Search for Higgs Boson Decays in the Di-muon Channel with the ATLAS Detector at $\sqrt{s} = 13$ TeV

Antony Nicholas Fray
Queen Mary University of London

Submitted in partial fulfilment of the requirements of the Degree of **Doctor of Philosophy**

Declaration

I, Antony Nicholas Fray, confirm that the research included within this thesis is my own work or that where it has been carried out in collaboration with, or supported by others, that this is duly acknowledged below and my contribution indicated. Previously published material is also acknowledged below.

I attest that I have exercised reasonable care to ensure that the work is original, and does not to the best of my knowledge break any UK law, infringe any third party's copyright or other Intellectual Property Right, or contain any confidential material.

I accept that the College has the right to use plagiarism detection software to check the electronic version of the thesis.

I confirm that this thesis has not been previously submitted for the award of a degree by this or any other university.

Signature: Date:

Details of collaboration and publications:

ATLAS Collaboration, *Search for the dimuon decay of the Higgs boson in pp collisions at* $\sqrt{s} = 13$ *TeV with the ATLAS detector* - Phys. Rev. Lett. 119 (2017) 051802, arXiv:1705.04582 [hep-ex].

Bona, M. et al., *Level 1 Calorimeter Trigger Efficiencies and Rates Optimisation* - 2018, ATL-COM-DAQ-2017-186.

ATLAS Collaboration, *A search for the rare decay of the Standard Model Higgs boson to dimuons in pp collisions at* $\sqrt{s} = 13$ *TeV with the ATLAS Detector* - 2018, ATLAS-CONF-2018-026.

The object and event selections outlined in Chapter 6 were implemented using a variant of the CxAODFramework, the base of which was maintained by a number of ATLAS collaborators, including the author.

All scale factors used in the analysis (and their associated systematics) were provided by the ATLAS Combined Performance Working Groups, with the exception of the $P_T^{\mu\mu}$ and $M_{\text{inv}}^{\mu\mu}$ re-weighting factors discussed in Chapter 7, which were derived by the author.

The Drell-Yan MC sample used for the study of the spurious signal systematics (as presented in Chapter 11) was produced privately by Yusheng Wu and Yanlin Liu. The

derivation of the correction factors and smearing of this sample was performed by the author, as was the determination of the associated systematics.

A framework written by Paul Thompson was utilised in the determination of the theoretical systematic uncertainties presented in Chapter 11 (although the implementation of the BDT selections and determination of the uncertainties was performed by the author).

The framework utilised for the extraction of the $H \to \mu\mu$ signal strength (and subsequently derived upper limit) was developed by Haifeng Li, having been modified by the author to incorporate the categories and systematics derived in this thesis. All other presented work (including the determination of the final results) was performed by the author unless otherwise stated.

This work was supported by the Science and Technology Facilities Council (STFC).

Abstract

A search was performed for the decay of a Standard Model (SM) Higgs boson in the di-muon channel, using pp collision data recorded at $\sqrt{s} = 13$ TeV with the ATLAS detector, corresponding to an integrated luminosity of 80.5 fb^{-1}. No significant excess of events was observed in the data. An observed (expected) upper limit at the 95% confidence level on the cross-section times branching ratio was set at 1.98 (2.13) times the SM expectation. The observed signal strength was measured to equal $\mu_s = -0.29^{+1.10}_{-1.12}$, corresponding to an observed (expected) significance of 0.00σ (0.82σ).

Acknowledgements

I would not have finished this thesis without the support of a vast number of people. I will do my best to thank you all in this section, but rest assured that even if not mentioned here, you have likely helped me in ways greater than you imagine.

Firstly, I would like to thank Eram Rizvi for his supervision over the past four years. Your constant guidance, patience and reassurance gave me the belief that I could finish this analysis. I've been lucky to have had the opportunity to work with you, and it has undoubtedly made me a better physicist.

I would like to thank all those within the PPRC for providing such a welcoming work environment. The discussions over lunch and coffee (or beers on the yearly occasion I went to the SCR) were enjoyable and enlightening. I never once felt out of place, and will miss you all. Particular thanks must go to Jon Hays for the coding advice in my first year, Adrian Bevan for his knowledge of statistical and machine learning techniques, and Tom Stevenson for his persistent willingness to help me, even with the most trivial of matters.

Thank you to all those I met while working on L1Calo (both in London and at CERN). The service work was an enjoyable distraction from my analysis, and gave me a better appreciation of the immeasurable amount of work done within ATLAS. I would particularly like to thank Ivana, Eduard, Bruce and Martin for sharing the joys of on-call shifts with myself, along with Andres, Adele, Eddie, Alison, Marcella and John, who were all a pleasure to work with.

To the $H \to \mu\mu$ team, thank you for the opportunity to contribute to such an interesting analysis. I've been lucky to work with such smart and talented people. I would particularly like to thank Paul, Andy, Yanlin, Yusheng, Haifeng, Miha, Giacomo, Hanna and Jan for their availability and willingness to troubleshoot issues I encountered. I wish you all the best of luck in working towards observation.

To all those I have played football with, thank you for supporting one of my main outlets of stress. To the members of the past four PPRC Bubble Chamber cup teams, I would like to think we have restored some level of pride to the reputation of Queen Mary on the UK physics football front. Thank you to the CERN Football Club for the opportunity to play in the annual Scottish Cup match, and to Alex for organising The Leftovers. Thank you to the members of Dynamo Weasels for the many training sessions, matches and meals. I'm very proud of what we achieved. I must also thank the various members of the postgraduate team at QM. Your tolerance of me attempting and failing to score a wonder goal every week did not go unappreciated.

I would like to thank the CERN UKLO team for organising my move to France, and supporting me while I lived there. Thanks must also go to the STFC for funding me the through the entire PhD.

Thank you to those I interacted with daily in the CERN Powerlifting Club (Florian,

Haydn, Stephanie, Ian, Hristo). We picked up heavy things, we put them down again, and we shared a lot of laughter.

To my friends from school, university and beyond, thank you for all of your understanding and support. Each time I've arisen from the dark depths of analysis, you've welcomed me back with open arms. Here's to many more years of adventures.

To my Mum and Dad, your love and support (and food) provides the foundation for everything I do. To Lucy and James, your words of advice (e.g. chowder) have been invaluable. I can't thank any of you (or the rest of our family) enough.

Finally, I must thank my partner Laura, who has been absolutely fantastic since this all began. You've supported me travelling all over the place, working all sorts of hours, and have patiently listened to me complain about what must seem incomprehensible nonsense. You keep me grounded, and focused on what's important in life. I'm not sure how I'll ever repay everything you've done for me, but how about we start with a nice meal? Yes, we can have a peshwari naan each.

Contents

List of Figures

List of Tables

Chapter 1

Introduction

What makes up the Universe within which we live? Why does it look and behave in the ways we observe it to? Questions such as these have plagued human minds for centuries, and are key to deriving a fundamental understanding of nature.

The Standard Model (SM) of particle physics plays a great role in answering parts of these questions. It describes both the elementary particles of which the Universe consists, and the fundamental forces with which they interact (with the exception of gravity). Since its formation in the 1970s, the SM theory has proven to be quite robust, consistently predicting results later derived from experimental data [1–7].

One long-standing issue was the lack of experimental evidence for a scalar Higgs boson, H. The existence of such a particle is key to the SM's explanation of how fundamental fermions (along with W and Z bosons) acquire mass [8–10]. The discovery of the Higgs was a key motivation in the construction of the most powerful particle collider to date, the Large Hadron Collider (LHC) [11].

In July 2012, the ATLAS (A Toroidal LHC ApparatuS) [12] and CMS (Compact Muon Solenoid) [13] experiments based at the LHC announced the detection of a signal consistent with a SM Higgs boson [14, 15]. The discovery paved the way for investigations into the particle's many properties, including the modes by which it can decay. Experimental observations of SM Higgs decays in the $b\bar{b}$, ZZ, W^+W^-, $\tau^+\tau^-$ and $\gamma\gamma$ channels have since been made [16, 20]. Evidence for a SM Higgs directly coupling to second generation fermions is however lacking. While studies have been made in the $H \to c\bar{c}$ channel, the di-charm final state's large multi-jet background remains a troublesome obstacle [21]. The di-strange final state is so multi-jet dominated, measurements of the coupling between the SM Higgs and the strange quark have been limited to indirect studies using mesons, such as $H \to \phi\gamma$ [22]. Similar studies have also been performed in the $H \to J/\psi\gamma$ channel, where a significant excess of events has yet to be observed [23].

The di-muon decay of a Higgs, denoted $H \to \mu^+\mu^-$, is a promising alternative. Since

Higgs-fermion couplings (known as Yukawa couplings) are mass dependent, $H \to \mu^+\mu^-$ is a relatively rare process, with it occurring over 1000 times less frequently than $H \to b\bar{b}$. The di-muon final state is however a very clean signature to detect. Certain regimes within the Minimal Supersymmetric Standard Model (MSSM) also provide regions of parameter space where Yukawa couplings to down-type fermions are enhanced, increasing the $H \to \mu\mu$ branching fraction [24]. $H \to \mu\mu$ could therefore also be used as a probe for physics Beyond the Standard Model (BSM).

Using proton-proton (pp) collision data collected between 2015 and 2016 at a centre-of-mass energy of $\sqrt{s} = 13$ TeV, CMS conducted a search for $H \to \mu^+\mu^-$, assuming a Higgs mass, m_H, of 125.09 GeV. While failing to find any evidence of the process, an upper limit at the 95% Confidence Level (CL) was set on the signal strength, μ_s, defined as the $H \to \mu^+\mu^-$ production rate normalised to the SM expectation. The observed (expected) upper limits on μ_s at the 95% CL were found to be 2.95 (2.45) times the SM prediction. When combined with data recorded at $\sqrt{s} = 7$ TeV and $\sqrt{s} = 8$ TeV between 2010 and 2012, the observed (expected) upper limit improved to 2.92 (2.16) times the SM value [25].

ATLAS conducted a similar search using pp collision data collected between 2010 and 2016, assuming $m_H = 125$ GeV, from which observed (expected) upper limits at the 95% CL on μ_s were set at 2.8 (2.9) times the SM expectation [26]. The result was later updated to incorporate data collected in 2017, from which the observed (expected) limits on μ_s at the 95% CL were reduced to 2.1 (2.0) times the SM expectation [27]. The author of this thesis contributed to both results; in the case of the former, the author contributed to the calculation and verification of the spurious signal systematics (the concept of which is described in Chapter 11 of this thesis), while also providing cut-flow tables to verify the implementation of the analysis' event selection. The author was a lead analyser of the more recent result, providing control and signal distributions, fits to signal and background MC samples (along with data), development of the analysis BDT and studies of its performance with respect to changing pile-up conditions, and provided inputs for the extraction of μ_s.

This thesis presents a search for $H \to \mu^+\mu^-$ using 80.5 fb^{-1} of pp collision data recorded by ATLAS at $\sqrt{s} = 13$ TeV, using updated methods to those shown in the previous ATLAS results. Chapter 2 presents an overview of the underlying theory of the SM, with particular focus given to its treatment of the Higgs boson. Chapter 3 describes the structure and components of the ATLAS detector, and how these are used in the recording of physics events. A discussion of the Monte Carlo samples used for simulation of the data is contained within Chapter 4. The MultiVariate Analysis (MVA) techniques used in the analysis are described in Chapter 5, with their implementation detailed in Chapter 9. The selections and definitions used for reconstructed objects and events are outlined in Chapter 6, while Chapter 7 details how different Monte Carlo generators

model their respective quantities. The modelling of variables key to the analysis is presented for both data and Monte Carlo samples in Chapter 8. Chapter 10 describes the analytical models used to fit the signal and background processes of interest, whilst Chapter 11 outlines the treatment of various sources of systematic uncertainty. Chapter 12 describes the statistical analysis techniques applied to the data, along with the derived results, while Chapter 13 summarises the analysis and discusses the future outlook of $H \to \mu^+\mu^-$ studies.

Chapter 2

Theory of the Standard Model

This chapter presents the underlying theoretical basis of the SM. Section 2.1 outlines the properties of the particles well described by the SM. Section 2.2 details the theories by which SM particles interact, with dedicated sections given to Quantum Electrodynamics (QED), Quantum Chromodynamics (QCD), Electroweak Theory and the Higgs mechanism. Section 2.3 describes the phenomenology of pp collisions, while Section 2.4 provides an overview of the production and decay modes of the SM Higgs boson, along with the key associated background processes.

2.1 Constituents of the Standard Model

A particle's intrinsic angular momentum can be quantised by its spin (S). Using spin, all particles can be sorted into one of two categories: fermions, which possess half-integer spin (in units of $\hbar$[1]) and comprise the matter and anti-matter of the Universe, and bosons, which possess integer spin and act as mediators of particle interactions. Fermions are further categorised into hadrons, which are comprised of quarks, and leptons, which contain no quarks and are thus considered fundamental.

All fermions have an equivalent anti-particle, which possess the same mass and spin as the original fermion, but with charge-parity-time (CPT) conjugated values of its quantum numbers. The majority of fermions within the SM are known to be Dirac fermions, meaning their particle and anti-particle states are distinctly different. The exception to this are neutrinos, who some hypothesise could be Majorana fermions, which possess identical particle anti-particle states.

The SM quarks are grouped into three generations of doublets, each consisting of an up-type quark and a down-type quark. A summary of their properties can be found in Table 2.1.1. The 1^{st} generation quarks possess a quantum number known as isospin (I),

[1] $\hbar$ is the Planck constant normalised to 2π.

with u and d assigned third component isospins (I_3) of $\frac{1}{2}$ and $-\frac{1}{2}$ respectively. Other quarks by contrast have $I_3 = 0$. Isospin is commonly used to distinguish bound quark states of similar mass.

All known quarks also possess a quantum number known as colour, which can take values of red, green or blue (or in the case of anti-quarks, anti-red, anti-green or anti-blue). Colour acts as the quantised charge of QCD, allowing quarks to interact via the strong nuclear force. Due to confinement, a phenomenon explored in Section 2.2.2, bound states are required to be colour-neutral. This prevents the existence of free quarks, leading to hadronisation, whereby bound multi-quark states are formed[2]. Bound states consisting of three quarks are known as baryons, while bound quark - anti-quark pairs are known as mesons. Evidence has also been found for the existence of candidate tetraquark and pentaquark states [28–31].

Property	$\begin{pmatrix} u \\ d \end{pmatrix}$	$\begin{pmatrix} c \\ s \end{pmatrix}$	$\begin{pmatrix} t \\ b \end{pmatrix}$
Electric Charge (e)	$\begin{pmatrix} +2/3 \\ -1/3 \end{pmatrix}$	$\begin{pmatrix} +2/3 \\ -1/3 \end{pmatrix}$	$\begin{pmatrix} +2/3 \\ -1/3 \end{pmatrix}$
Spin ($\hbar$)	$\begin{pmatrix} 1/2 \\ 1/2 \end{pmatrix}$	$\begin{pmatrix} 1/2 \\ 1/2 \end{pmatrix}$	$\begin{pmatrix} 1/2 \\ 1/2 \end{pmatrix}$
Mass (GeV)	$\begin{pmatrix} 0.0022 \\ 0.0047 \end{pmatrix}$	$\begin{pmatrix} 1.28 \\ 0.095 \end{pmatrix}$	$\begin{pmatrix} 173 \\ 4.18 \end{pmatrix}$

Table 2.1.1: Properties of the up (u), down (d), charm (c), strange (s), top (t) and bottom (b) type quarks described within the Standard Model. The generation doublets have been split into adjacent columns. Spin and electric charge are given in units of the Planck constant and electron charge respectively [32].

The SM leptons also exist in three generations of doublets, with each generation consisting of both a charged lepton and a neutral neutrino. There are three known types of lepton flavour: electron (e), muon (μ) and tau (τ). Each generation corresponds to a different lepton flavour. A summary of their properties can be found in Table 2.1.2. While the charged lepton masses are well defined, as of yet only upper limits have been set on the neutrino masses.

[2]An exception to this is the top quark, which decays into a bottom quark and a real W boson before hadronisation can occur, due to its large mass. Bound top quark states are therefore not observed.

Property	$\begin{pmatrix} e \\ \nu_e \end{pmatrix}$	$\begin{pmatrix} \mu \\ \nu_\mu \end{pmatrix}$	$\begin{pmatrix} \tau \\ \nu_\tau \end{pmatrix}$
Electric Charge (e)	$\begin{pmatrix} -1 \\ 0 \end{pmatrix}$	$\begin{pmatrix} -1 \\ 0 \end{pmatrix}$	$\begin{pmatrix} -1 \\ 0 \end{pmatrix}$
Spin ($\hbar$)	$\begin{pmatrix} 1/2 \\ 1/2 \end{pmatrix}$	$\begin{pmatrix} 1/2 \\ 1/2 \end{pmatrix}$	$\begin{pmatrix} 1/2 \\ 1/2 \end{pmatrix}$
Mass (MeV)	$\begin{pmatrix} 0.511 \\ < 2 \times 10^{-3} \end{pmatrix}$	$\begin{pmatrix} 106 \\ < 0.19 \end{pmatrix}$	$\begin{pmatrix} 1777 \\ < 18.2 \end{pmatrix}$

Table 2.1.2: Properties of the leptons described within the Standard Model. The generation doublets have been split into adjacent columns. Spin and electric charge are given in units of the Planck constant and electron charge respectively [32].

The gauge bosons of the SM act as mediators of the fundamental forces. Colour charged objects such as quarks interact via the strong nuclear force, the strongest of the fundamental forces. These interactions are mediated by the gluon (g). The photon (γ) mediates electromagnetic interactions, which are of infinite range and occur between electrically charged particles. The weak nuclear force is mediated by the W^+, W^- and Z bosons. Whilst a mediator of the gravitational force (known as the graviton) has been proposed, experimental evidence of its existence has yet to be uncovered, and construction of a Quantum Field Theory (QFT) consistent with its spin-2 nature has proved difficult. Gravity is thus not incorporated into the SM. A summary of the properties of the known gauge bosons is presented in Table 2.1.3. The properties of the scalar Higgs boson are also shown. Unlike the aforementioned bosons, the Higgs is not a force-carrying particle. It instead mediates interactions between massive particles and the Higgs field.

Property	$W^\pm$	Z	γ	g	H
Electric Charge (e)	$\pm$ 1	0	0	0	0
Spin ($\hbar$)	1	1	1	1	0
Mass (GeV)	80.38	91.19	0	0	125.18

Table 2.1.3: Properties of the gauge and Higgs bosons described within the Standard Model. Spin and electric charge are given in units of the Planck constant and electron charge respectively [32].

2.2 Standard Model Particle Interactions

The SM is built on a combination of field theory, special relativity and quantum mechanics, together forming a QFT. In such a theory, particles exist as fields permeating space-time; particles in the traditional sense can be thought of as excitations of these fields.

The equations of motion of such a system are governed by the Principle of Least Action, which denotes that the evolution of a system between two states will be such that the action (S) is minimised. It is defined as

$$S = \int d^4x \mathcal{L}[\phi(x^\mu), \partial_\mu \phi(x^\mu)], \tag{2.2.1}$$

where $\mathcal{L}[\phi(x^\mu), \partial_\mu \phi^\mu]$ represents the Lagrangian density of field $\phi(x^\mu)$. Four-vector notation has been used such that[3]:

$$x^\mu = (t, \mathbf{x}), \tag{2.2.2}$$

$$x_\mu = (t, -\mathbf{x}), \tag{2.2.3}$$

$$\partial_\mu \equiv \frac{\partial}{\partial x^\mu} = (\frac{\partial}{\partial t}, \nabla), \tag{2.2.4}$$

$$\partial^\mu \equiv \frac{\partial}{\partial x_\mu} = (\frac{\partial}{\partial t}, -\nabla). \tag{2.2.5}$$

From these principles, one can derive the Euler-Lagrange equation

$$\frac{\partial \mathcal{L}}{\partial \phi} = \partial_\mu \left(\frac{\partial \mathcal{L}}{\partial(\partial_\mu \phi)} \right), \tag{2.2.6}$$

from which the familiar equations of motion of particle physics (such as Newton's Second Law and Maxwell's equations) can be derived.

Through Lagrangian formalism, the SM can be encapsulated in the equation

$$\mathcal{L}_{\text{SM}} = \mathcal{L}_{\text{EWK}} + \mathcal{L}_{\text{QCD}} + \mathcal{L}_{\text{Higgs}} + \mathcal{L}_{\text{Yukawa}}. \tag{2.2.7}$$

Each of these contributions will be explored in the coming sections of this chapter.

2.2.1 Quantum Electrodynamics

The theory of QED encapsulates the electromagnetic interactions between the photon vector field A^μ and the charged fermion spinor fields ψ. Interactions between these spinor fields are described by the Dirac Lagrangian density,

$$\mathcal{L}_{\text{Dirac}} = \bar{\psi}(i\partial\!\!\!/ - m)\psi, \tag{2.2.8}$$

[3]In subsequent sections, the notation $x \equiv x^\mu$ shall be used.

with m representing the fermion mass, and $\bar{\psi} = \psi^\dagger \gamma^0$ the conjugate fermion spinor field. Feynman slash notation has been adopted such that $\not{\partial} = \gamma^\mu \partial_\mu$, with γ^μ the four-vector representation of the Dirac gamma matrices.

Equation 2.2.8 possesses a global U(1) symmetry, leaving it gauge invariant under phase transformations of the form

$$\psi(x) \to \psi'(x) = e^{iq\chi}\psi(x), \tag{2.2.9}$$

$$\bar{\psi}(x) \to \bar{\psi}'(x) = e^{-iq\chi}\bar{\psi}(x), \tag{2.2.10}$$

with χ a global phase and q the fermion charge. In the case of a local phase shift, such that $\chi = \chi(x)$, one finds the Dirac Lagrangian density loses its gauge invariance. Restoring this involves introducing a Lagrangian density term of the form

$$\mathcal{L}_{\text{Int}} = \bar{\psi}\gamma^\mu q A_\mu \psi, \tag{2.2.11}$$

which encapsulates fermion-photon interactions. A_μ transforms such that

$$A_\mu \to A'_\mu = A_\mu + \partial_\mu \chi(x). \tag{2.2.12}$$

Alongside this, we also introduce a gauge covariant derivative

$$D_\mu = \partial_\mu - iqA_\mu. \tag{2.2.13}$$

For a complete QED Lagrangian density, the kinematics of the A_μ field must also be considered. This is achieved through introduction of the field strength tensor $F^{\mu\nu}$, which can be written in terms of both the covariant derivative and the photon field:

$$F^{\mu\nu} = \partial^\mu A^\nu - \partial^\nu A^\mu, \tag{2.2.14}$$

$$= -\frac{i}{q}[D^\mu, D^\nu]. \tag{2.2.15}$$

This results in the QED Lagrangian density taking the form,

$$\mathcal{L}_{\text{QED}} = \bar{\psi}(i\not{D} - m)\psi - \frac{1}{4}F_{\mu\nu}F^{\mu\nu}. \tag{2.2.16}$$

It is of note that there are no terms present in Equation 2.2.16 to accommodate the self-interactions or mass of the A^μ field. Introduction of such terms ($\propto A^3$ and $\propto m^2 A^\mu A_\mu$ respectively) would remove the gauge-invariance of $\mathcal{L}_{\text{QED}}$, and thus their introduction is forbidden.

2.2.2 Quantum Chromodynamics

Interactions between colour charged objects are modelled by QCD, a non-abelian theory described by the special unitary gauge group SU(3). Quark fields carry one of three colours (red, green or blue), while anti-quark fields possess anti-colour values (anti-red, anti-green or anti-blue). Gluons carry colour - anti-colour combinations, leading to a total of 8 QCD gluons.

In a similar fashion to QED, it is desirable to preserve the local gauge invariance of the QCD Lagrangian density under transformations of the form

$$\psi(x) \rightarrow \psi'(x) = U(x)\psi = e^{i\chi_a(x)T^a}\psi(x), \tag{2.2.17}$$

where $\chi_a(x)$ is a local phase shift. $T^a = \frac{\lambda^a}{2}$ are the generators of SU(3), with λ^a representing the Gell-Mann matrices, and a the gluon colour charge index. Invariance is preserved by introducing a covariant derivative,

$$D_\mu = \partial_\mu + igT^aA^a_\mu, \tag{2.2.18}$$

with g the strong coupling constant and A^a_μ the gluon field of colour charge a, which transforms as

$$\boldsymbol{A_\mu} = T^aA^a_\mu \rightarrow \boldsymbol{A'_\mu} = UA_\mu U^\dagger + \frac{i}{g}(\partial_\mu U)U^\dagger. \tag{2.2.19}$$

The QCD field strength tensor is defined as

$$F^a_{\mu\nu} = \partial_\mu A^a_\nu - \partial_\nu A^a_\mu - gf^{abc}A^b_\mu A^c_\nu, \tag{2.2.20}$$

$$= -\frac{i}{g}[D_\mu, D_\nu], \tag{2.2.21}$$

where f^{abc} represent the structure constants of SU(3), which obey the commutation relation

$$[T^a, T^b] = if^{abc}T^c. \tag{2.2.22}$$

The $gf^{abc}A^b_\mu A^c_\nu$ term in Equation 2.2.20 arises from the non-abelian nature of QCD, and marks a key difference with respect to QED. Since gluons carry colour charge, they can self-interact, producing multi-gluon vertices. In contrast, the self-coupling of photons is forbidden under QED.

QCD interactions also exhibit asymptotic freedom. Unlike QED, where coupling strength deteriorates with distance, QCD interactions are strongest at large length scales (or, through $E = \frac{hc}{\lambda}$, low energy scales[4]). If one were to try to separate two quarks bound by a virtual gluon, by increasing their separation, the QCD coupling strength will increase, resulting in the generation of more virtual gluons. This would

[4] c represents the speed of light in a vacuum.

eventually produce quark - anti-quark pairs, which would bind to the original quarks. Free colour-charged states are thus forbidden.

The final gauge-invariant Lagrangian density of QCD is defined as

$$\mathcal{L}_{\mathrm{QCD}} = \sum_{f=1}^{n_f} \bar{\psi_f}(i\not{D} - m_f)\psi_f - \frac{1}{4}F^a_{\mu\nu}F^{\mu\nu}_a, \tag{2.2.23}$$

where m_f represents the mass of a quark of flavour f, and n_f the number of quark flavours [33].

2.2.3 Electroweak Theory

At the electroweak unification scale (≈ 250 GeV), the electromagnetic and weak nuclear forces unify. These so-called electroweak (EWK) interactions are described within the Glashow-Salam-Weinberg (GSW) model, constructed as a non-abelian $\mathrm{SU(2)_L} \otimes \mathrm{U(1)_Y}$ gauge theory. Weak isospin (T) contributions come from $\mathrm{SU(2)_L}$, where L denotes the handedness[5] of the fermions involved; only left-handed fermions undergo the gauge transformations of $\mathrm{SU(2)_L}$. Weak hypercharge (Y) contributions come from $\mathrm{U(1)_Y}$. The quantities relate to the fermion charge, Q, through the relation

$$Q = T^3 + \frac{Y}{2}, \tag{2.2.24}$$

with T^3 the third component of weak isospin.

The GSW model groups fermions into left-handed weak isospin doublets and right-handed weak isospin singlets of the form

$$Q_L = \left\{ \begin{pmatrix} u_L \\ d_L \end{pmatrix}, \begin{pmatrix} c_L \\ s_L \end{pmatrix}, \begin{pmatrix} t_L \\ b_L \end{pmatrix} \right\}, \tag{2.2.25}$$

$$L_L = \left\{ \begin{pmatrix} \nu_{e,L} \\ e_L \end{pmatrix}, \begin{pmatrix} \nu_{\mu,L} \\ \mu_L \end{pmatrix}, \begin{pmatrix} \nu_{\tau,L} \\ \tau_L \end{pmatrix} \right\}, \tag{2.2.26}$$

$$U_R = \{u_R, c_R, t_R\}, \tag{2.2.27}$$

$$D_R = \{d_R, s_R, b_R\}, \tag{2.2.28}$$

$$L_R = \{e_R, \mu_R, \tau_R\}, \tag{2.2.29}$$

where right-handed neutrinos are notably excluded. The Dirac Lagrangian of $\mathrm{SU(2)_L} \otimes \mathrm{U(1)_Y}$ is thus comprised of two components,

$$\mathcal{L}_{\mathrm{Dirac}} = \mathcal{L}_{\mathrm{Dirac},L} + \mathcal{L}_{\mathrm{Dirac},R}, \tag{2.2.30}$$

[5]Handedness relates to a quantum property of fermions known as chirality.

where

$$\mathcal{L}_{Dirac,L} = \sum_g \bar{Q}_L^g i\partial\!\!\!/ Q_L^g + \bar{L}_L^g i\partial\!\!\!/ L_L^g, \tag{2.2.31}$$

$$\mathcal{L}_{Dirac,R} = \sum_g \bar{U}_R^g i\partial\!\!\!/ U_R^g + \bar{D}_R^g i\partial\!\!\!/ D_R^g + \bar{L}_R^g i\partial\!\!\!/ L_R^g. \tag{2.2.32}$$

The summation over fermion generations (represented by index g) will be henceforth assumed.

For invariance of Equation 2.2.30 under local $\mathrm{U(1)_Y}$ and $\mathrm{SU(2)_L}$ transformations of the form

$$\psi(x) \to \psi'(x) = \mathrm{U_Y}(x)\psi = e^{i\beta(x)g'\frac{Y_i}{2}}\psi(x), \tag{2.2.33}$$

$$\psi(x) \to \psi'(x) = \mathrm{U_L}(x)\psi = e^{i\alpha^a(x)T^a}\psi(x), \tag{2.2.34}$$

where $\alpha^a(x)$ and $\beta(x)$ represent complex phases, and Y_i represents the hypercharge of fermion i, two covariant derivatives

$$D_\mu = \partial_\mu + i\frac{g'}{2}Y_i B_\mu, \tag{2.2.35}$$

$$\boldsymbol{D}_\mu = \partial_\mu + i\frac{g'}{2}Y_i B_\mu + ig_W T^a W_\mu^a, \tag{2.2.36}$$

are introduced. B^μ acts as the hypercharge gauge field of $\mathrm{U(1)_Y}$, with coupling constant g', and couples to all fermions. W_μ^a are the gauge fields of $\mathrm{SU(2)_L}$, which couple to particles with weak isospin (left-handed fermions) with strength g_W. $T^a = \frac{\sigma^a}{2}$ are the associated generators of $\mathrm{SU(2)_L}$, with σ^a the Pauli spin matrices, where a runs from 1 to 3.

The newly introduced gauge fields B^μ and W_μ^a transform such that

$$B_\mu \to B'_\mu = U_\mathrm{Y} B_\mu U_\mathrm{Y}^\dagger - (ig'\frac{Y_i}{2})^{-1} U_\mathrm{Y}^\dagger(\partial_\mu U_\mathrm{Y}), \tag{2.2.37}$$

$$\boldsymbol{W}_\mu \to \boldsymbol{W}'_\mu = U_\mathrm{L}\boldsymbol{W}_\mu U_\mathrm{L}^\dagger - (ig_W)^{-1}(\partial_\mu U_\mathrm{L})U_\mathrm{L}^\dagger, \tag{2.2.38}$$

where $\boldsymbol{W}_\mu = T^a W_\mu^a$.

The field strength tensors of $\mathrm{SU(2)_L} \otimes \mathrm{U(1)_Y}$ are defined as

$$B_{\mu\nu} = -(i\frac{g'}{2}Y_i)^{-1}[D_\mu, D_\nu], \tag{2.2.39}$$

$$= \partial_\mu B_\nu - \partial_\nu B_\mu, \tag{2.2.40}$$

$$\boldsymbol{W_{\mu\nu}} = -\frac{i}{g_W}[\boldsymbol{D_\mu}, \boldsymbol{D_\nu}], \tag{2.2.41}$$

$$= T^a W_{\mu\nu}^a, \tag{2.2.42}$$

where

$$W^a_{\mu\nu} = \partial_\mu W^a_\nu - \partial_\nu W^a_\mu - g\epsilon^{abc} W^b_\mu W^c_\nu. \tag{2.2.43}$$

ϵ^{abc} is known as the Levi-Civita symbol, and represents the structure constants of $\mathrm{SU(2)_L}$, obeying the commutation relation

$$[\sigma^a, \sigma^b] = i\epsilon^{abc}\sigma^c. \tag{2.2.44}$$

The $g\epsilon^{abc}W^b_\mu W^c_\nu$ term within Equation 2.2.43 permits the self-interactions of the W^a fields. All of this is encapsulated within the electroweak Lagrangian density

$$\begin{aligned}\mathcal{L}_{\mathrm{EWK}} = {} & \bar{Q}_L i\not{D} Q_L + \bar{L}_L i\not{D} L_L + \bar{U}_R i\not{D} U_R + \bar{D}_R i\not{D} D_R + \bar{L}_R i\not{D} L_R \\ & - \frac{1}{4} B_{\mu\nu} B^{\mu\nu} - \frac{1}{4} W^a_{\mu\nu} W^{\mu\nu,a},\end{aligned} \tag{2.2.45}$$

where the final two terms have been added to account for gauge field kinematics [33]. Similar to $\mathcal{L}_{\mathrm{QED}}$ and $\mathcal{L}_{\mathrm{QCD}}$, there are no terms present within $\mathcal{L}_{\mathrm{EWK}}$ to account for either fermion or gauge boson masses - their addition would violate the local $\mathrm{SU(2)_L} \otimes \mathrm{U(1)_Y}$ invariance.

2.2.4 Spontaneous Symmetry Breaking and the Higgs Mechanism

Spontaneous symmetry breaking provides the mechanism by which gauge boson masses can be introduced into the SM without violating the gauge invariance of $\mathrm{SU(2)_L} \otimes \mathrm{U(1)_Y}$.

Consider a scalar field theory of the form

$$\mathcal{L} = \frac{1}{2}(\partial_\mu \phi)^2 - V(\phi), \tag{2.2.46}$$

where

$$V(\phi) = \frac{1}{2}\mu^2\phi^2 + \frac{1}{4}\lambda\phi^4, \tag{2.2.47}$$

with $\lambda > 0$. $\mathcal{L}$ is invariant under gauge transformations of the form $\phi \to -\phi$.

To determine the minimum of $V(\phi)$, one must take its derivative,

$$\frac{dV}{d\phi} = (\mu^2 + \lambda\phi^2)\phi. \tag{2.2.48}$$

The value of ϕ which minimises the potential $V(\phi)$ is defined as the vacuum expectation value (v) of the field. For the case of $\mu^2 > 0$, $v = 0$, and the so-called vacuum state field configuration retains the $\phi \to -\phi$ gauge symmetry possessed by $\mathcal{L}$.

For the case of $\mu^2 < 0$ (i.e. $\mu^2 \to -|\mu^2|$), three solutions are present: a maximum at

$\phi = 0$, and two minima at $\phi = \pm\sqrt{(\frac{-\mu^2}{\lambda})}$. The shapes of $V(\phi)$ for $\mu^2 < 0$ and $\mu^2 > 0$ are shown below in Figure 2.2.1.

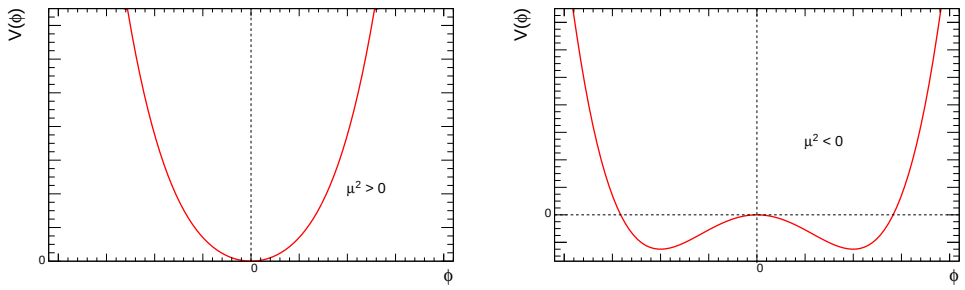

Figure 2.2.1: The scalar field potential of Equation 2.2.47 for the case of $\mu^2 > 0$ (left) and $\mu^2 < 0$ (right). When extended to three dimensions, the shape of $V(\phi)$ for $\mu^2 < 0$ forms the so-called Mexican hat potential.

For $v = \pm\sqrt{(\frac{-\mu^2}{\lambda})}$, the field can be re-defined as

$$\phi(x) = v + \eta(x), \tag{2.2.49}$$

with $\eta(x)$ representing a fluctuation of the field about v. $\mathcal{L}$ can thus be re-written in terms of v and $\eta(x)$ as

$$\mathcal{L}(v+\eta) = \frac{1}{2}(\partial_\mu \eta)^2 - \lambda v^2 \eta^2 - \lambda v \eta^3 - \frac{1}{4}\lambda \eta^4 + \frac{1}{4}\lambda v^4. \tag{2.2.50}$$

By comparing this result to the Klein-Gordon Lagrangian

$$\mathcal{L}_{KG} = \frac{1}{2}\partial_\mu \phi \partial^\mu \phi - \frac{1}{2}m^2\phi^2, \tag{2.2.51}$$

it is clear that in re-parametrising the field in terms of η, the mass term of $\mathcal{L}$ has changed from a wrong-sign (imaginary) configuration, $\frac{1}{2}|\mu^2|\phi^2$, to a right-sign (real) configuration, $-\lambda v^2 \eta^2$. While $\mathcal{L}$ retains the $\phi \to -\phi$ gauge symmetry from before (in the form $\eta \to -2v - \eta$), the vacuum field state configuration does not respect this symmetry. In choosing one of the degenerate $v = \pm\sqrt{(\frac{-\mu^2}{\lambda})}$ minima about which to expand, the system's original gauge invariance is spontaneously broken.

The Higgs mechanism describes the occurrence of spontaneous symmetry breaking within $\mathrm{SU(2)_L} \otimes \mathrm{U(1)_Y}$. Consider a complex scalar field doublet

$$\Phi = \begin{pmatrix} \phi^+ \\ \phi_0 \end{pmatrix} = \begin{pmatrix} \frac{1}{\sqrt{2}}(\phi_1 + i\phi_2) \\ \frac{1}{\sqrt{2}}(\phi_3 + i\phi_4) \end{pmatrix}, \tag{2.2.52}$$

where ϕ_i represent real scalar fields. The interactions of these fields are contained within the Lagrangian density term

$$\mathcal{L}_\Phi = (\boldsymbol{D}_\mu \Phi)^\dagger (\boldsymbol{D}^\mu \Phi) - V(\Phi^\dagger \Phi), \tag{2.2.53}$$

where

$$V(\Phi^\dagger \Phi) = \mu^2 \Phi^\dagger \Phi + \lambda |\Phi^\dagger \Phi|^2. \tag{2.2.54}$$

$\mathcal{L}_\Phi$ remains invariant under the $\mathrm{SU(2)_L}$ and $\mathrm{U(1)_Y}$ gauge transformations shown in Equations 2.2.33 and 2.2.34.

For the case of $\lambda > 0$ and $\mu^2 < 0$, one finds the potential is minimised when

$$|\Phi| = v' = \sqrt{-\frac{\mu^2}{2\lambda}}, \tag{2.2.55}$$

a condition satisfied by an infinite number of degenerate minima. Analogous to the scalar field theory case, one may re-parametrise Φ in terms of fields fluctuating about v'. This is most simply achieved in the unitary gauge, where the vacuum expectation values of ϕ_1, ϕ_2 and ϕ_4 are all zero, leaving

$$\Phi = v = \frac{1}{\sqrt{2}} \begin{pmatrix} 0 \\ \phi_3 \end{pmatrix}, \tag{2.2.56}$$

with $\phi_3 = h + v'$. h represents the neutral Higgs field, while ϕ_1, ϕ_2 and ϕ_4 are collectively known as massless Goldstone bosons. They are a result of Goldstone's theorem, which states that for a Lagrangian invariant under a continuous symmetry, a massless scalar boson will be generated for each spontaneously broken generator of the symmetry [34]. In this case, the symmetry of $\mathrm{SU(2)_L}$ is broken, leading to three Goldstone bosons (corresponding to the three generators of $\mathrm{SU(2)_L}$).

It is constructive to redefine the B_μ and $\boldsymbol{W}_\mu$ fields contained within $\boldsymbol{D}_\mu$ such that

$$W^\pm = \frac{W^1_\mu \mp i W^2_\mu}{\sqrt{2}}, \tag{2.2.57}$$

$$Z = \cos\theta_W W^3_\mu - \sin\theta_W B_\mu, \tag{2.2.58}$$

$$A = \sin\theta_W W^3_\mu + \cos\theta_W B_\mu, \tag{2.2.59}$$

$$\tag{2.2.60}$$

where

$$\cos\theta_W = \frac{g_W}{\sqrt{g_W^2 + g'^2}}, \tag{2.2.61}$$

with θ_W defined as the Weinberg angle. Substituting all of this into $\mathcal{L}_\Phi$ leaves

$$\begin{aligned}\mathcal{L}_{\text{Higgs}} = &\frac{1}{2}(\partial_\mu h)^2 \\ &+ \frac{1}{2}\left(\frac{1}{2}g_W v'\right)^2 (W^+W^- + \text{complex conjugate}) + \frac{1}{2}\left(\frac{\frac{1}{2}g_W v'}{\cos\theta_W}\right)^2 Z^2 \\ &+ g_W\left(\frac{1}{2}g_W v'\right) hW^+W^- + \frac{1}{4}v'\frac{g_W^2}{\cos^2\theta_W}hZ^2 \\ &+ \frac{1}{4}g_W^2 h^2 W^+W^- + \frac{1}{8}\frac{g_W^2}{\cos^2\theta_W}h^2Z^2 \\ &- V(\Phi^\dagger\Phi),\end{aligned} \tag{2.2.62}$$

where

$$V(\Phi^\dagger\Phi) = -\frac{1}{4}\lambda v'^4 + \lambda v'^2 h^2 + \lambda v' h^3 + \frac{1}{4}\lambda h^4. \tag{2.2.63}$$

Four massless scalar fields have evolved into a system of three massive gauge fields (the familiar W^+, W^- and Z bosons), one massless gauge field (γ) and a scalar Higgs field (h), all while preserving the $\mathrm{SU(2)_L} \otimes \mathrm{U(1)_Y}$ gauge invariance. In acquiring masses, the W and Z fields are said to have consumed the aforementioned Goldstone bosons. Their masses can be directly derived from $\mathcal{L}_{\text{Higgs}}$ as

$$m_W = \frac{1}{2}g_W v', \tag{2.2.64}$$

$$m_Z = \frac{1}{2}\frac{g_W v'}{\cos\theta_W}, \tag{2.2.65}$$

while the Higgs mass is parametrised as $m_H = \lambda v'^2$. The presence of terms of order h^3 and h^4 in $\mathcal{L}_{\text{Higgs}}$ demonstrates the Higgs field can also undergo self-interactions.

To include fermion masses within the SM, a further Lagrangian density is introduced,

$$\mathcal{L}_{\text{Yukawa}} = (-\mathcal{Y}_L \bar{L}_L^i \Phi_i L_R - \mathcal{Y}_D \bar{Q}_L^i \Phi_i D_R - \mathcal{Y}_U \epsilon_{ij} \bar{Q}_L^i \Phi^{*j} U_R) + \text{hermitian conjugate}, \tag{2.2.66}$$

where i and j represent the weak isospin components of the $\mathrm{SU(2)_L}$ doublets [33]. There is also an implicit sum over lepton and quark generations. The coupling strength between fermions and the Higgs field is represented by the Yukawa couplings ($\mathcal{Y}$), which parametrise fermion masses such that

$$m_f = \frac{1}{\sqrt{2}}\mathcal{Y}_f v'. \tag{2.2.67}$$

Higgs-fermion couplings are therefore fermion-mass dependent. It is also of note that within this formalism, neutrinos remain massless.

2.3 Particle Collider Phenomenology

A strong understanding of the proton is key to making full use of pp collision data. Protons are baryons which exist in a uud quark configuration. In the context of particle structure, these quarks are referred to as valence quarks. Since they possess colour charge, valence quarks interact with each other through virtual gluon exchange. In higher-order instances, virtual gluon fluctuations can produce virtual $q\bar{q}$ pairs, known as sea quarks. An example of this is shown below in Figure 2.3.1.

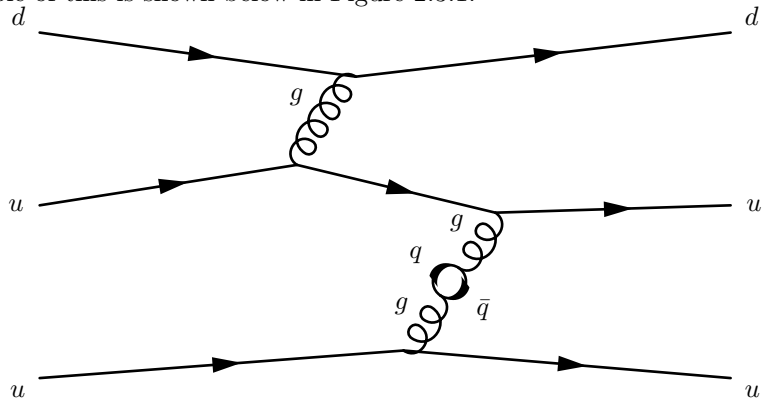

Figure 2.3.1: Exchange of virtual gluons and virtual $q\bar{q}$ pairs within the proton [35].

The Parton Model was proposed by Feynman to describe interactions involving the proton's constituents, collectively referred to as partons [36]. Partons carry a fraction of the proton's momentum, denoted x. Due to gluon exchange, the momentum fractions carried by partons are not fixed, but vary. These are expressed as Parton Distribution Functions (PDFs) $q(x, Q^2)$, where Q^2 defines the energy scale of the interactions in question. Gluon contributions to PDFs dominate at low x, while valence quark contributions dominate at high x.

At high energy scales (such as those at the LHC), pp collisions can be effectively treated as interactions between quarks and gluons. Many processes can be produced through these interactions. The probability of a specific process occurring is given by its cross-section, σ, which in particle physics is given in units of barns (1 b = 10^{-28} m^2). The cross-section of an interaction encodes both the initial high energy hard scatter, along with the associated low energy soft interactions that follow. Soft interaction contributions to σ prove difficult to determine through traditional methods, such as perturbation theory. A common treatment is to make use of Factorisation Theorem, wherein

$$\sigma = \int dx_1 \int dx_2 q_1(x_1, Q^2) q_2(x_2, Q^2) \hat{\sigma}(x_1, x_2, Q^2). \tag{2.3.1}$$

$\hat{\sigma}(x_1, x_2, Q^2)$ represents the cross-section of the hard scatter, which can be determined through perturbative means [37]. The PDFs of the interacting partons, q_1 and q_2,

encode the soft interactions of the partons, and can be determined through experimental methods.

It is constructive to determine the rate at which events of interest are produced, given by

$$\frac{dn}{dt} = \sigma L, \tag{2.3.2}$$

with L defined as the luminosity. More commonly referred to is

$$L_{\text{int}} = \int L dt, \tag{2.3.3}$$

the so-called integrated luminosity. For observation of rare processes (where σ is often low) with colliders such as the LHC, large integrated luminosities are required.

2.4 Properties of the Standard Model Higgs Boson

The four most prominent modes by which SM Higgs bosons can be produced are gluon-gluon fusion (ggF), vector boson fusion (VBF), associated production with a W or Z boson (VH) and associated production with a top quark pair ($t\bar{t}H$). All have been experimentally observed [19,20,38]. Figures 2.4.1 and 2.4.2 present the Feynman diagrams of these processes, while Table 2.4.1 shows theoretical predictions of their total production cross-sections for $m_H = 125$ GeV at $\sqrt{s} = 13$ TeV. Experimental measurements of the cross-sections have been found to be in agreement with SM predictions [39–41]. ggF is the dominant production mode, with its cross section an order of magnitude greater than the others. The taggable jets[6] associated with VBF are useful in distinguishing its topology from background processes.

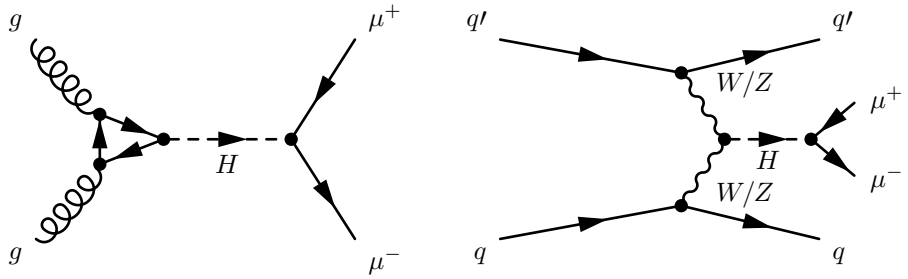

Figure 2.4.1: Feynman diagrams for the ggF (left) and VBF (right) Higgs production processes.

The dominant irreducible background of $H \to \mu^+\mu^-$ is the Drell-Yan process, shown below in Figure 2.4.3. Its cross section is around 40 times greater than the total SM Higgs production cross section. Other backgrounds of consideration include electroweak

[6]The definition of a particle jet is outlined in Chapter 6.

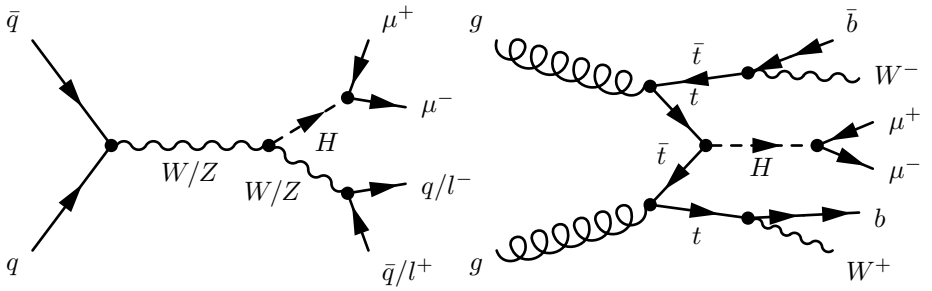

Figure 2.4.2: Feynman diagrams for the VH (left) and $t\bar{t}H$ (right) Higgs production processes.

	ggF	VBF	WH	ZH	$t\bar{t}H$	Total
σ (pb)	48.58	3.78	1.37	0.88	0.51	55.69

Table 2.4.1: Theoretical predictions of the total cross-sections for four production modes of a 125 GeV SM Higgs boson at $\sqrt{s} = 13$ TeV. The total value includes contributions from $b\bar{b}H$ and tH [42].

Z plus jets, di-boson (WW, ZZ and WZ), $t\bar{t}$ and single-top (tW), shown in Figures 2.4.5 and 2.4.6. Experimental measurements of their cross-sections at $\sqrt{s} = 13$ TeV are shown in Table 2.4.2.

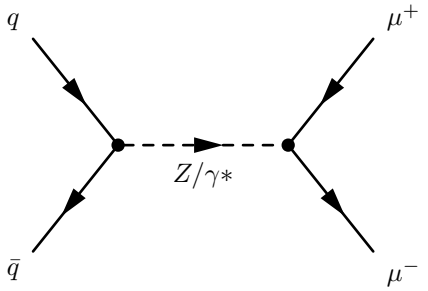

Figure 2.4.3: Feynman diagram for the Drell-Yan process, the primary background of this analysis.

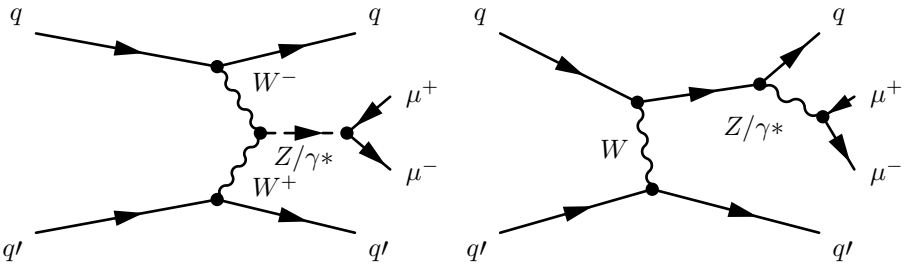

Figure 2.4.4: Feynman diagrams for the electroweak Z plus jets process.

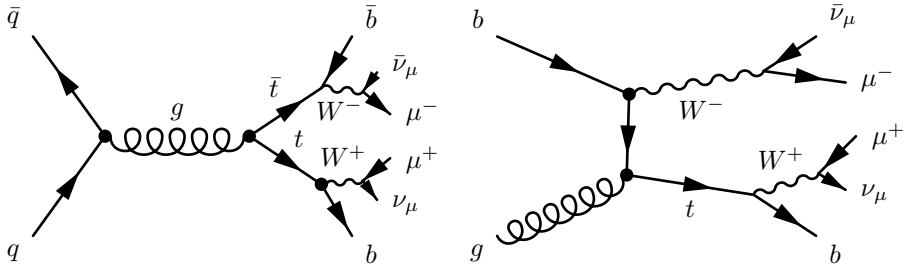

Figure 2.4.5: Feynman diagrams for the $t\bar{t}$ (left) and single top (right) background processes.

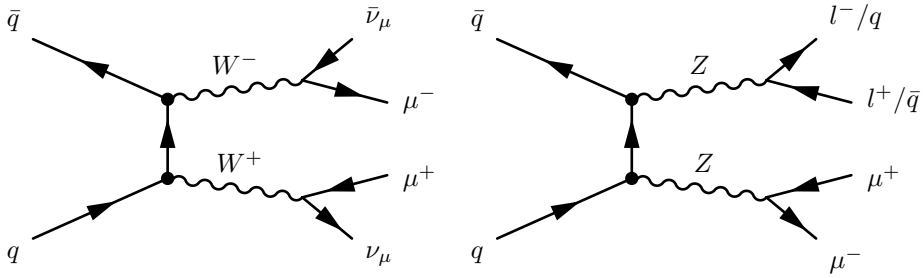

Figure 2.4.6: Feynman diagrams for the di-boson background processes.

	Drell-Yan	$t\bar{t}$	Ewk Z plus jets	tW	WW	WZ	ZZ
σ (pb)	1981	818	$534^\dagger$	94	$142^\dagger$	50.6	17.3

Table 2.4.2: Measurements of the cross-sections for the primary backgrounds considered when analysing the $H \to \mu\mu$ process at $\sqrt{s} = 13$ TeV [43–49]. All have been found to be in good agreement with the latest theoretical predictions. Values marked with † represent fiducial measurements, rather than total production cross-sections.

The branching ratios (BRs) of a particle are defined as the number of its decays to a particular final state, normalised by its total number of possible decays. The branching ratios of the SM Higgs boson are presented in Figure 2.4.7. The dominant decay mode is $H \to \bar{b}b$, which dominates roughly 57% of SM Higgs final states. For $m_H = 125$ GeV, the branching ratio of SM $H \to \mu^+\mu^-$ is 2.19×10^{-4}, three orders of magnitude lower than $H \to \bar{b}b$ [50]. $H \to \mu^+\mu^-$ is thus considered a rare decay mode of the SM Higgs boson.

Figure 2.4.8 presents the coupling strength of the SM Higgs boson as a function of particle mass. The rarity of $H \to \mu\mu$ is reflected in the size of the muon mass point's statistical error. All particles presented in the figure have been experimentally observed to couple to the SM Higgs boson, with the exception of the muon.

Using 5 fb^{-1} of $\sqrt{s} = 7$ TeV data and 20 fb^{-1} of $\sqrt{s} = 8$ TeV data, ATLAS and CMS produced a combined measurement of the mass of the SM Higgs boson of m_H

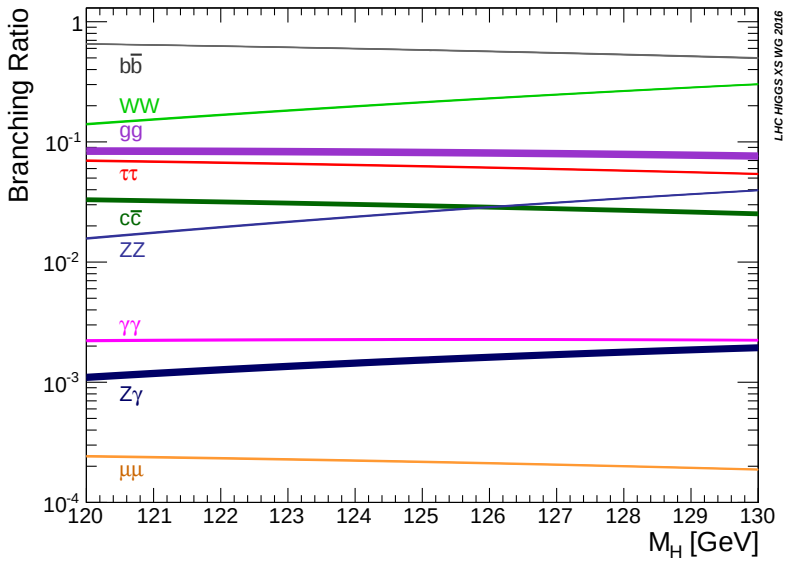

Figure 2.4.7: The branching ratios of the SM Higgs boson for $120 < m_H < 130$ GeV [42].

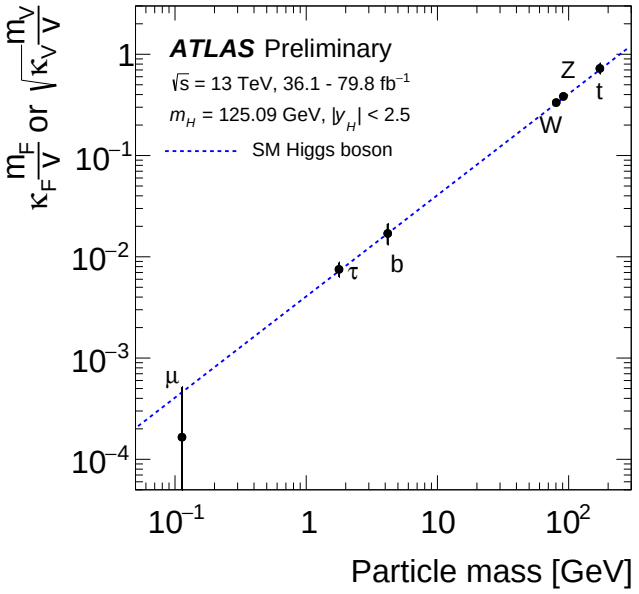

Figure 2.4.8: Coupling strength of the SM Higgs boson as a function of particle mass [51]. The parameters κ_F and κ_V represent reduced coupling strength modifiers of the SM Higgs boson to fermions and weak gauge bosons of masses m_F and m_V respectively, with V the vacuum expectation value of the Higgs field (246 GeV). The parameters form part of the κ framework, outlined in Reference [52].

$= 125.09 \pm 0.24$ GeV [53]. This was later updated by ATLAS (CMS) using 36.1 fb^{-1} (35.9 fb^{-1}) of 13 TeV data, finding $m_H = 124.97$ (125.26) $\pm$ 0.24 (0.21) GeV [54, 55]. Both experiments have also set upper limits on the total decay width of the SM Higgs boson, predicted to be 4.1 MeV by theoretical calculations [50]. Observed (expected) upper limits at the 95% CL were found to be 14.4 (15.2) MeV and 13.0 (26.0) MeV by ATLAS [56] and CMS [57] respectively. Separate analyses have also confirmed the SM Higgs to be a scalar boson (spin-0) with even symmetry under parity and charge conjugation transformations [58, 59].

Chapter 3

The Large Hadron Collider and the ATLAS Experiment

The LHC was built by the European Organization for Nuclear Research (CERN) in a 26.7 km circular tunnel on the France-Switzerland border [60]. It consists of two separate rings which accelerate and collide beams of protons (and lead ions). The collisions occur between 45 m and 170 m underground at four different interaction points (IPs), each surrounded by a different experiment. Their relative positions are shown below in Figure 3.0.1.

ATLAS and CMS are general purpose detectors, built for the study of the Higgs boson and to search for new physics. They are situated at Points 1 and 5 of the LHC respectively. The Large Hadron Collider Beauty experiment (LHCb) is situated at Point 8, and focuses on the interactions of b-hadrons, including their rare decay modes and CP-violation parameters. Lead-lead collisions are recorded at Point 2 by A Large Ion Collider Experiment (ALICE), dedicated to the study of quark-gluon plasma.

The LHC is sourced with protons from bottles of hydrogen gas, which are pumped into a duoplasmatron. Electrons emitted from an electric filament within the device ionise the gas, creating protons. Through application of an electric field, the protons form a beam, which is directed into a radio frequency quadrupole (RFQ), capable of accelerating the beam to 750 keV.

The beam then enters the first accelerator of the LHC injector chain, Linear Accelerator 2 (Linac 2), which makes use of RF cavities to charge cylindrical conductors, through which the beam passes. Adjacent cavities possess oppositely charged electric fields, causing the beam to repel and attract its way through the conductors. Quadrupole magnets ensure the beam retains a tight shape. By oscillating the electric fields of the cavities at a fixed frequency of 400 MHz, the beam can be continually accelerated up to energies of 50 MeV. The oscillations also cause protons within the beam to group

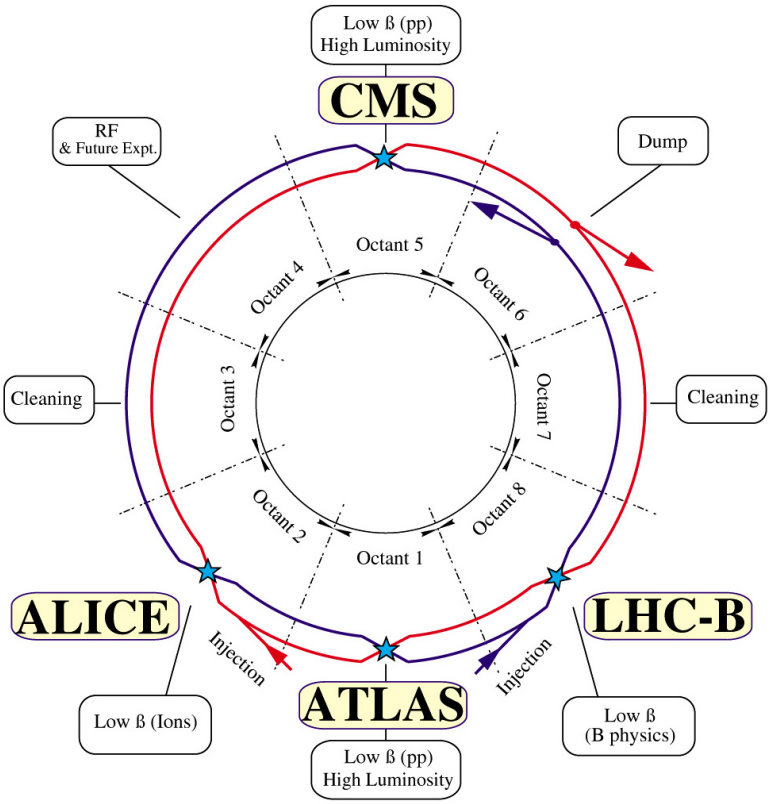

Figure 3.0.1: Schematic layout of the LHC. It is divided into eight Points, of which four house particle detectors [61].

together as bunches.

The Proton Synchrotron Booster (PSB) makes use of four superimposed synchrotron rings to further accelerate the beam to 1.4 GeV, after which it enters the Proton Synchrotron (PS), which provides an additional acceleration to 25 GeV. The second largest accelerator at CERN, the Super Proton Synchrotron (SPS), utilises a 6.9 km ring to accelerate the beam to 450 GeV, at which point it enters the LHC. The layout of the LHC with respect to its injector chain is shown below in Figure 3.0.2.

The LHC receives two proton beams from the SPS, and accelerates them in opposite directions around two separate rings. The beams are modelled as Gaussians with 16 μm widths, and reach energies of up to 7 TeV, giving a total centre-of-mass energy upon collision of 14 TeV. At its maximum intensity, the LHC can collide 2808 bunches of protons per beam, with each bunch containing 1.15×10^{11} protons. This produces luminosities of order 10^{34} cm^{-2}s^{-1}, given by

$$L = \frac{f n_b N_1 N_2}{4\pi\sigma_x\sigma_y}, \tag{3.0.1}$$

with n_b the number of bunches, N_1 and N_2 the number of protons per bunch from beams 1 and 2, f the LHC revolution frequency (11.245 kHz) and σ_x and σ_y the horizontal and vertical beam widths [62].

The trajectories of the beams are controlled by superconducting magnets which are cooled using superfluid helium to below 2 K. The temperature is maintained through application of a vacuum system, which insulates both the helium and the magnets from heat sources such as proton beam synchrotron radiation. A beam screen is also utilised for similar purposes. A separate vacuum system is employed for the beams themselves, used to minimise collisions with gas particles within the beam pipes.

During its Run-1 phase (2009-2013), the LHC operated at $\sqrt{s} = 7$ TeV (2010-2011) and $\sqrt{s} = 8$ TeV (2012), with bunch spacings of 50 ns, delivering a total integrated luminosity of 28.31 fb^{-1} of pp data. For Run-2 (2015-2018), the bunch spacings were reduced to 25 ns, with $\sqrt{s}$ increased to 13 TeV, resulting in a total delivered integrated luminosity of 158 fb^{-1}. This thesis presents results produced using the 2015-2017 portion of the latter dataset recorded by ATLAS (80.5 fb^{-1}).

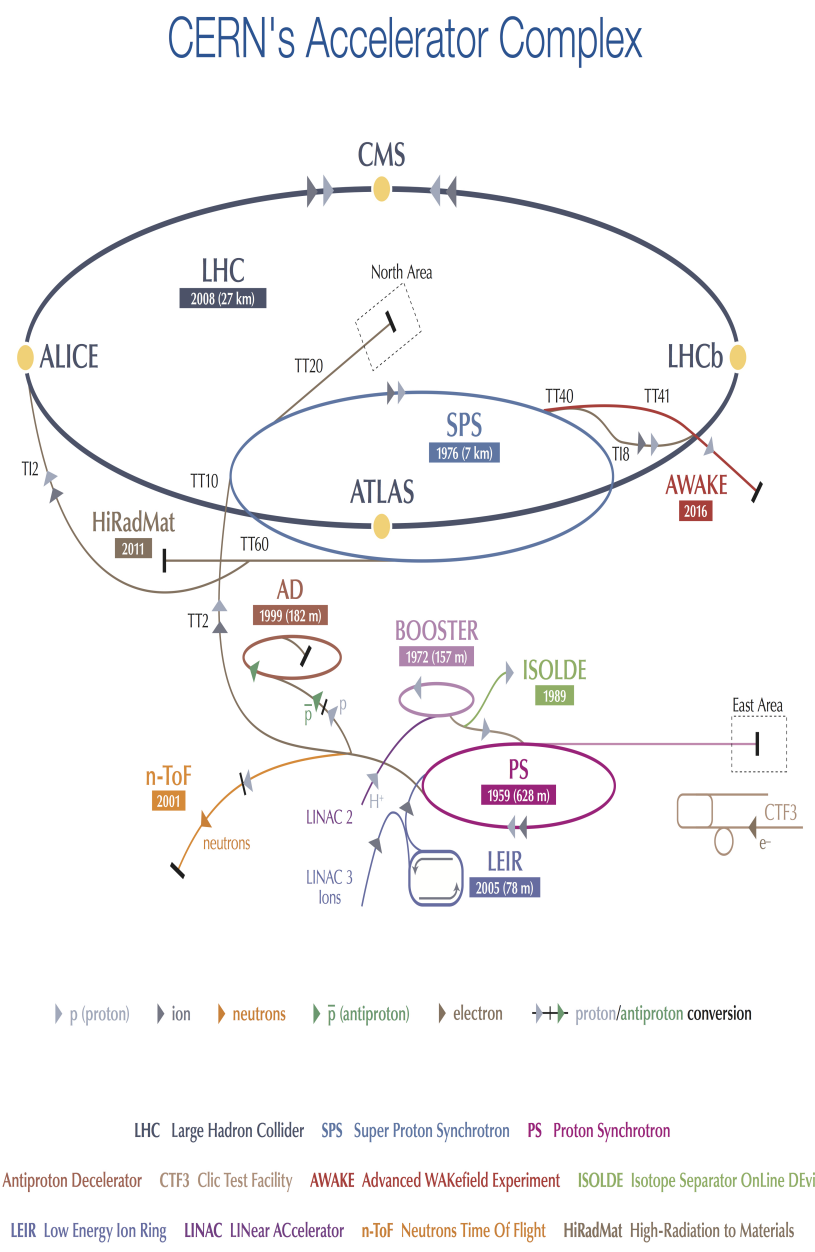

Figure 3.0.2: Schematic layout of the accelerator complex at CERN [63].

3.1 The ATLAS Detector

The layout of the ATLAS detector is shown below in Figure 3.1.1. It consists of four main subsystems which concentrically surround the IP; a magnet system, an inner detector, a calorimeter system and a muon spectrometer. These work alongside a dedicated trigger and data acquisition system, which identifies events of interest. The details of these components are discussed in the coming subsections of this chapter. Their interactions with various particles are depicted in Figure 3.1.2.

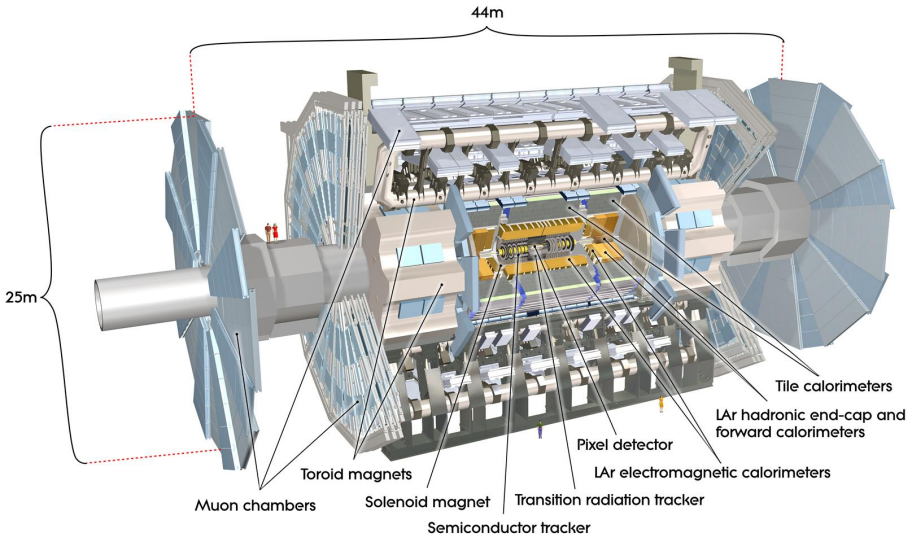

Figure 3.1.1: The layout of the ATLAS detector [12].

The coordinate system of ATLAS is centred on the nominal IP, with the anti-clockwise beam direction defining the positive z-axis [65]. The $x-y$ plane is transverse to the beam direction, with the positive x-axis pointing from the IP to the centre of the LHC ring, and the positive y-axis pointing upwards. The azimuthal angle, ϕ, is measured around the beam pipe, with $\phi = 0$ along the x-axis.

To study a high energy pp collision in its centre-of-mass frame, it is constructive to use Lorentz-invariant observables. One such quantity is the invariant mass,

$$M_{\text{inv}} = \sqrt{(\sum_i E_i)^2 + (\sum_i \boldsymbol{P}_i)^2}, \tag{3.1.1}$$

with E_i and $\boldsymbol{P}_i$ the energy and three-momentum of the ith particle involved in the collision. The component of a particle's momentum transverse to the beam line, P_T, is also of great use. Since initial state P_T is zero, the quantity is an effective identifier of post-collision high momentum states (which are typically the events of most interest).

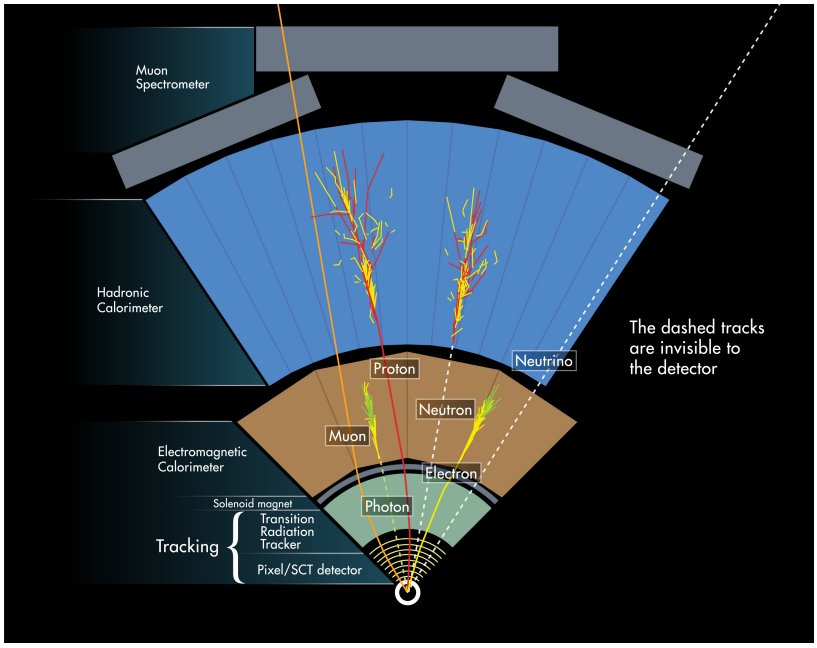

Figure 3.1.2: The interactions of various particles with the ATLAS detector [64]. Charged particles leave tracks in the inner detector, while neutral particles are identified by deposits in the calorimeters. Neutrinos escape the detector without directly measurable interactions, while muons penetrate through the calorimeters into the muon spectrometer.

Particle rapidity is defined as

$$y = \frac{1}{2} \ln \frac{(E + P_z)}{(E - P_z)}, \tag{3.1.2}$$

with P_z the longitudinal momentum of the particle. Differences in y are invariant under Lorentz boosts in the z direction. In the massless particle approximation, one may derive from y the pseudorapidity,

$$\eta = -\ln \tan(\frac{\theta}{2}), \tag{3.1.3}$$

with θ representing the polar angle measured from the z-axis, such that $\eta = 0$ points directly upward, and $\eta = \infty$ points along the beam line. Distances between particles are often defined in $\eta - \phi$ space as

$$\Delta R = \sqrt{(\Delta\eta)^2 + (\Delta\phi)^2}. \tag{3.1.4}$$

Two further quantities of use are the so-called transverse (d_0) and longitudinal (z_0) impact parameters. The former is defined as the distance of closest approach of a reconstructed particle to the beam line in the transverse plane, with negative values corresponding to tracks with positive angular momentum about the beam line [66]. The latter is then defined as the z value of the track at the point at which d_0 is measured.

In order to account for particles which ATLAS cannot directly detect (such as neutrinos), E_T^{miss} is often used. It is defined as the difference between the total transverse energy of all final state particles created in a collision, and the total transverse energy of all particles detected by ATLAS (E_T). The modelling of E_T^{miss} is therefore particularly susceptible to issues causing inaccuracies in event reconstruction, such as pile-up and jet miscalibrations. These effects are discussed more in Chapter 4.

3.1.1 Magnet System

Magnetic fields curve particle trajectories according to the Lorentz force, described in the non-relativistic case through

$$F = Bqv = \frac{mv^2}{r}, \tag{3.1.5}$$

where m, v and r represent the particle's mass, velocity and radius of trajectory respectively. B represents the magnetic flux density, with q the particle's electromagnetic charge. Equation 3.1.5 can be rearranged to

$$Bqr = mv = p. \tag{3.1.6}$$

Since q and B are known quantities (from SM theory and detector design respectively), one can use Equation 3.1.6 to determine particle momenta from track curvature. Momenta are most easily resolved for highly-curved tracks; an experiment's momentum resolution is therefore directly tied to the strength of its magnet system. These same conclusions hold true for relativistic collisions, such as those recorded at the LHC.

ATLAS makes use of four large superconducting magnets, forming a system 22 m in diameter and 26 m in length. Their layout is shown below in Figure 3.1.3.

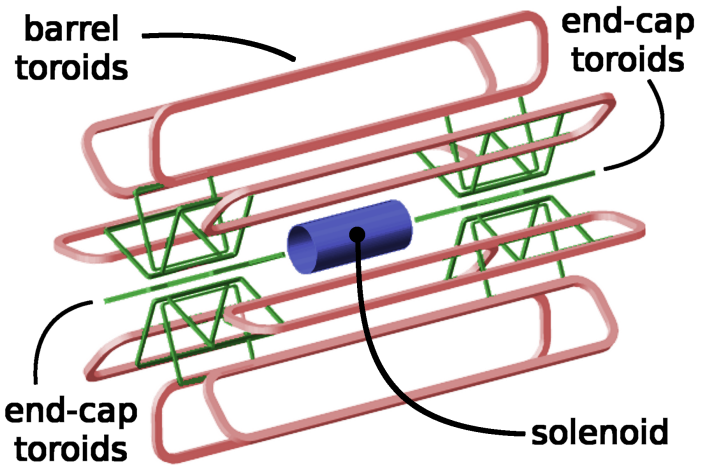

Figure 3.1.3: Geometry of the magnet system of ATLAS. The solenoid (blue) provides the magnetic field for the inner detector, while the toroid magnets (red and green) provide fields for the muon spectrometer [67].

A central solenoid of 5.8 m length, 2.4 m diameter and 4.5 cm thickness provides a 2 T axial field to the inner detector it encases. Due to its position, the solenoid risks blocking particles from entering the surrounding calorimeters. This drove the use of a high strength Al-stabilised NbTi conductor as the solenoid winding, providing a high strength field at an optimal thickness. The solenoid also shares the vacuum vessel of the Liquid Argon (LAr) calorimeter to reduce the number of walls which may inhibit particle trajectories. It operates at a nominal current of 7.73 kA, and is cooled by a system of internal, external and proximity cryogenics.

A barrel toroid consisting of eight coils provides the magnetic field for the cylindrical volume surrounding the calorimeters and end-cap toroids. The system is 25.3 m in length, with an outer diameter of 20.1 m, and operates at a nominal current of 20.5 kA. Each of the coils are housed in individual cryostats, and are supported by inner and outer rings of struts.

The two end-cap toroids consist of eight coils each, and are rotated 22.5° relative to the barrel toroid to optimise the bending power at the interface of the two systems. The end-cap toroids are housed in their own large cryostats, and possess stabilising keystone

wedges between their coils.

Both the barrel and end-cap toroids collectively provide the magnetic field of the muon spectrometer. The field is non-uniform, with magnetic flux densities of approximately 0.5 T and 1 T in the central and end-cap regions respectively. An Al-stabilised Nb/Ti/Cu conductor is used for the coil windings.

3.1.2 Inner Detector

The Inner Detector (ID) is the closest subsystem of ATLAS to the IP. It covers the range $|\eta| < 2.5$, and is immersed in a 2 T magnetic field provided by the superconducting solenoid. This curves the trajectories of charged particles, allowing the ID to perform vertex and momentum measurements with resolution

$$\frac{\sigma_{P_T}}{P_T} = 0.05\%\ P_T \oplus 1\%, \tag{3.1.7}$$

with P_T in GeV. The first term accounts for the resolution of track sagitta[1], while the latter accounts for multiple scattering effects.

The system consists of three independent subdetectors. The Pixel Detector (PD) and Semiconductor Tracker (SCT) are the innermost components, which make use of silicon pixel and microstrip technology, while the Transition Radiation Tracker (TRT) utilises straw tube elements. Their respective positions are shown below in Figure 3.1.4.

The PD is comprised of silicon pixels of minimum size $50 \times 400\ \mu\text{m}^2$ in $R^2 - \phi \times z$. Charged particles liberate electrons from silicon atoms within the pixels, generating electron-hole pairs. These can be directed via an electric field to anodes and cathodes respectively, producing a measurable current. Particle trajectories can then be reconstructed based on the position of the pixels registering signals. The pixels are arranged in layers on concentric cylinders surrounding the beam axis within the barrel, and on disks perpendicular to the beam axis in the end-cap regions. The intrinsic accuracies of the pixels are 10 μm ($R - \phi$) and 115 μm (z) in the barrel, and 10 μm ($R - \phi$) and 115 μm (R) in the end-caps. Particle tracks typically cover three layers of pixels, with the PD possessing approximately 80.4 million readout channels.

The SCT operates through similar means to the PD, but utilises silicon strips rather than pixels to cover a larger area. It encapsulates the PD with 4 coaxial cylindrical layers in the barrel region and 9 disk layers in each of the end-caps. The silicon strips consist of two 6.4 cm long daisy-chained sensors, with a mean strip separation of 80 μm. The rectangular strips of the barrel layer run parallel to the beam line, while the trapezoidal strips of the end-caps come in two varieties; some radial to the beam line and some at an angle of 40 mrad. The intrinsic accuracies of the strips are 17 μm ($R - \phi$) and 580

[1] Sagitta deformations bias the curvature of particle tracks. They are treated using corrections provided internally within ATLAS, as described in Chapter 4.

[2] R is the radial distance from the z-axis.

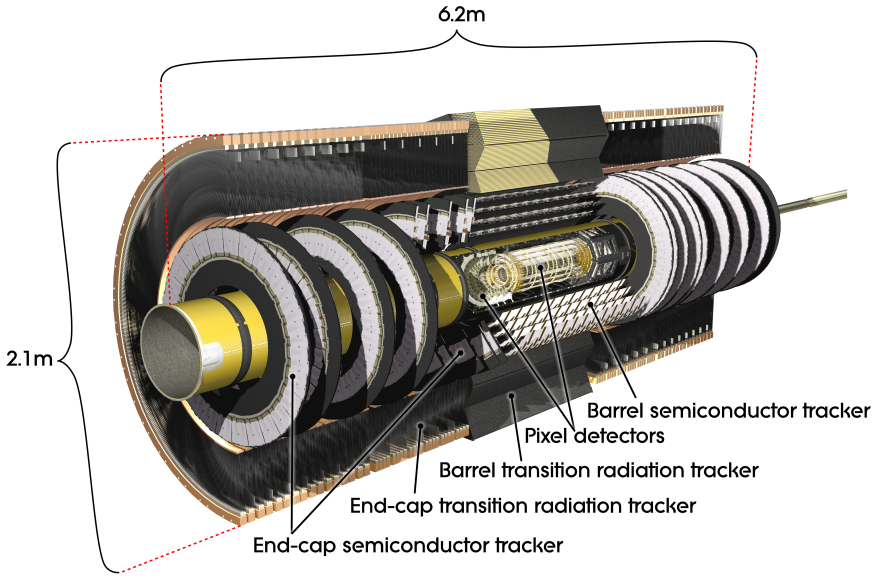

Figure 3.1.4: The inner detector of ATLAS. Its subdetector components are placed concentrically around the nominal IP. The Insertable B-Layer introduced in 2014 between the pixel detectors and the beam pipe is not shown [12].

μm (z) in the barrel, and 17 μm ($R-\phi$) and 580 μm (R) in the end-caps. The SCT contains roughly 6.3 million readout channels, with particle tracks typically covering eight layers of strips.

Due to their close proximity to the IP, both the PD and SCT are exposed to high levels of radiation. The silicon sensors are thus kept at low temperatures (-5 to -10°C) to minimise the effects of issues resulting from this, such as leakage currents. To help mitigate projected performance issues of the PD at increased luminosities, an extra detector component, the Insertable B-Layer (IBL), was installed between the beam pipe and the PD in 2014 [68]. The IBL utilises smaller pixels than the PD, with dimensions 50×250 μm^2, providing higher precision track measurements. Its introduction also improved the impact parameter reconstruction of tracks, resulting in improved b-tagging and vertexing performance.

The TRT utilises straw tubes of 4 mm diameter to track particles within the range $|\eta| < 2.0$. The tubes are filled with a gas mixture of Xe, CO_2 and O_2 (70/27/3), and are embedded in a matrix of polypropylene fibres. Charged particles emit transition radiation as they pass through the fibres, ionising the straw tube's gas mixture. Liberated electrons drift towards gold-plated tungsten wire anodes running through the centres of each straw, which connect directly to output electronics. Particles can be identified based on the strength of their signals measured by the TRT, since transition radiation

yields are proportional to the Lorentz factor[3], which is inversely proportional to particle mass. The straw tubes are arranged parallel to the beam line in the barrel, and radially in the end-caps, with lengths of 144 cm and 37 cm respectively. The TRT possesses approximately 351,000 total readout channels, with an accuracy of 130 μm per straw.

Figure 3.1.5 presents the performance of the ID in reconstructing tracks associated to particle jets[4], as a function of jet P_T. Track reconstruction efficiencies of 90-95% are achieved for central jets, whilst non-central jets are reconstructed with reduced efficiencies of 82-86%, largely due to the pile-up effects discussed in Chapter 4.

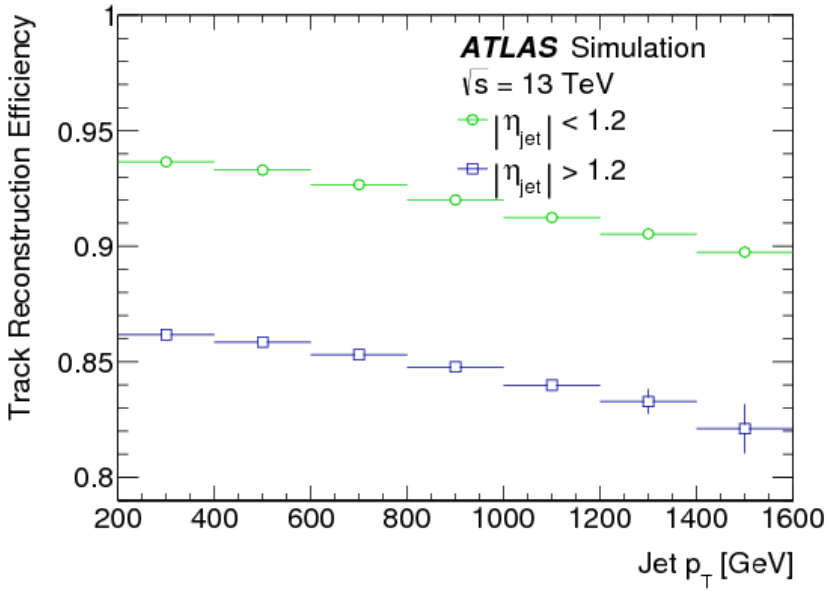

Figure 3.1.5: The track reconstruction efficiency of the ATLAS Inner Detector with respect to jet P_T, for different regions of η^{jet} [69]. The efficiencies were determined using simulated MC samples, found to effectively describe ATLAS data collected in 2015.

3.1.3 Calorimeters

The ATLAS calorimeter system measures the energy losses of particles within the range $|\eta| < 4.9$. The system is comprised of sampling calorimeters, which consist of alternating layers of passive and active materials. As incident particles strike the passive, high-density materials, particle showers are generated. These pass into the active material, within which ionisation radiation is produced and recorded. Since particle energy is

[3]The Lorentz factor, $\gamma = \frac{1}{\sqrt{1-\frac{v^2}{c^2}}}$, with v the particle's velocity and c the speed of light.

[4]The concept of particle jets is described in Chapter 6.

proportional to the amount of ionisation radiation emitted, calorimeter readings can be used to determine the energy of generated particles.

The calorimeters are designed with a thickness such that particle shower punch-through to the muon spectrometer is minimised. The innermost calorimeter possesses a thickness greater than 22 radiation lengths[5] in the barrel region, and greater than 24 in the end-caps.

ATLAS makes use of both electromagnetic (EM) and hadronic calorimeters. The former record the energies of electrons and photons through EM showers. The latter register the energy deposits of hadrons through hadronic showers. Since the radiation lengths of hadrons are much greater than those of electrons and photons, hadronic showers typically propagate deeper into the detector. The hadronic calorimeters are thus positioned further from the IP than the EM calorimeters, and use denser passive materials in the barrel region (steel rather than copper). Their respective layouts are shown in Figure 3.1.6.

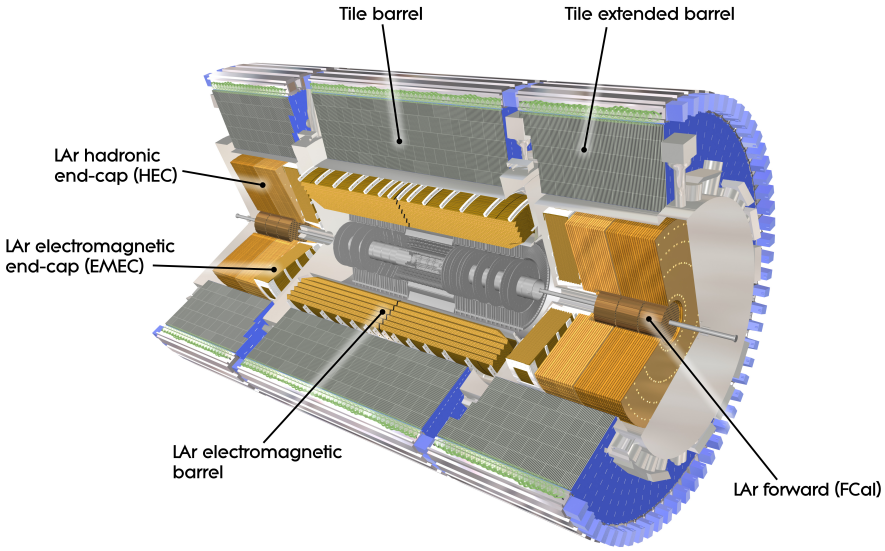

Figure 3.1.6: The calorimeter system of ATLAS [12].

The LAr EM calorimeter is the innermost component of the calorimeter system, capable of measuring particle energies with resolution

$$\frac{\sigma_E}{E} = \frac{10\%}{\sqrt{E}} \oplus 0.7\%, \tag{3.1.8}$$

[5]Radiation length is defined as the distance a particle can travel before losing $\frac{1}{e}$ its initial energy through radiative processes, with e representing Euler's number.

with E in GeV. The first term accounts for the stochastic sampling uncertainty of the calorimeter, while the latter accounts for effects due to non-uniformities of the detector, such as structure imperfections and radiation damage.

It consists of individual barrel and end-cap segments, contained within their own dedicated cryostats. The barrel calorimeter is comprised of two identical half-barrels, separated by 4 mm at $z = 0$, which collectively cover $|\eta| < 1.475$. The end-cap calorimeters each consist of an inner wheel and an outer wheel, covering ranges of $1.375 < |\eta| < 2.5$ and $2.5 < |\eta| < 3.2$ respectively. Lead plates arranged in an accordion geometry act as the passive material, while LAr is utilised as the active material. Signals are collected with copper readout electrodes located in the gaps between the lead plates. The barrel and end-caps are divided into modules, each consisting of three layers of calorimeter cells. Figure 3.1.7 presents the layout of an example barrel module. The system is complimented by a presampler placed between the first layer and the ID, which provides measurements and corrections for showers originating upstream of the calorimeter.

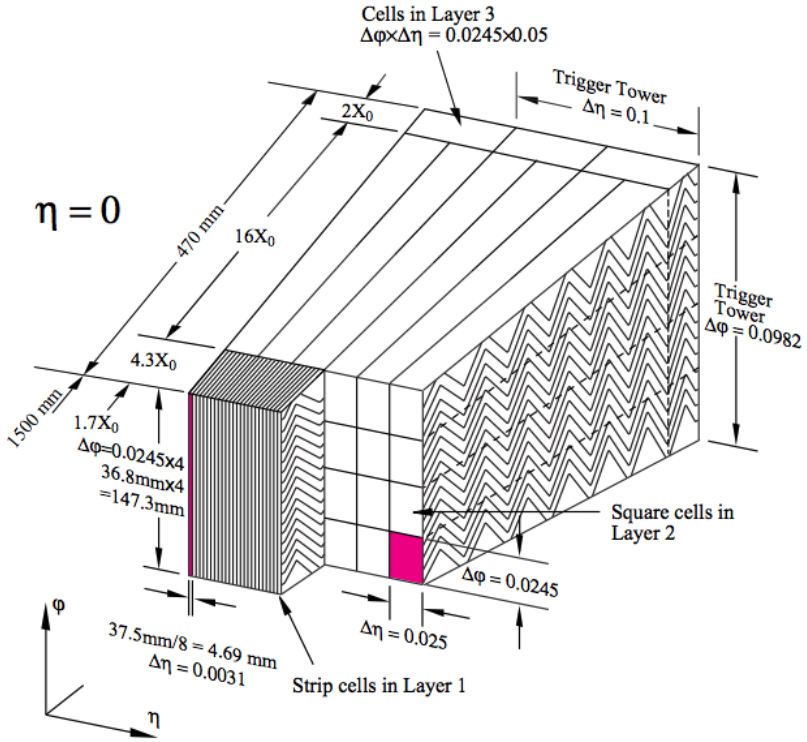

Figure 3.1.7: Sketch of a barrel module from the LAr EM calorimeter. The readout granularity of the calorimeter cells decreases when moving from Layer 1 to Layer 3. Trigger towers formed from clusters of calorimeter cells are utilised in the Level-1 Calorimeter Trigger System, described in Section 3.1.5 [12].

The hadronic tile calorimeter is located outside of the LAr EM calorimeter. It is

subdivided into a central barrel of 5.6 m length, covering $|\eta| < 1.0$, and two extended barrels, each 2.6 m in length and covering $0.8 < |\eta| < 1.7$. The barrels each consist of 64 modules, divided into three layers of steel plates and scintillating polystyrene tiles. As hadrons collide with the steel, hadronic showers are generated. These contain ionising particles, which produce ultraviolet scintillation light when passing through the tiles. Wavelength-shifting fibres convert the rays to visible light, after which Photo-Multiplier Tubes (PMTs) record their intensities. 10,000 PMTs are used for the tile calorimeter readout, compared to the 180,000 output channels of the LAr calorimeters.

The hadronic end-cap calorimeters extend the coverage of the hadronic calorimeter system to $1.5 < |\eta| < 3.2$. They are positioned directly behind the EM end-cap calorimeters, and share their LAr cryostats. Both end-caps consist of two independent wheels, each constructed with alternating layers of flat copper plates and an active LAr medium. They operate by the same methodology as the LAr EM calorimeter. Both the hadronic barrel and end-caps possess energy resolutions in GeV of

$$\frac{\sigma_E}{E} = \frac{40\%}{\sqrt{E}} \oplus 3\%. \tag{3.1.9}$$

The LAr forward calorimeters share the same cryostats as the end-cap calorimeters, and cover $3.1 < |\eta| < 4.9$. The system is split into one EM module (FCal1) and two hadronic modules (FCal2 and FCal3). While all utilise LAr as an active medium, their passive materials vary. FCal1 consists of copper plates punctured with copper rod electrodes, while FCal2 and FCal3 make use of tungsten rods, which are denser and therefore better suited for the containment of hadronic showers. The modules achieve energy resolutions in GeV of

$$\frac{\sigma_E}{E} = \frac{100\%}{\sqrt{E}} \oplus 10\%. \tag{3.1.10}$$

Figure 3.1.8 presents the performance of the LAr calorimeter in reconstructing the mass of the Z boson through its decays to electrons, using both simulated MC and data events recorded in 2018. Selected electrons were required to satisfy a selection largely similar to that presented in Chapter 6. The simulation appears to model the data well, indicating the performance of the system is in line with expectations. Also presented in Figure 3.1.8 is the ratio of the jet response measured in both simulated and 2015 data events as a function of jet P_T, for Z+jet, γ+jet and multi-jet calibrations. Jet response is often used in identifying miscalibrations of the tile calorimeter, which can affect jet energy measurements. The presented calibration techniques are in good agreement around

$$\frac{R_{\text{Data}}}{R_{\text{MC}}} = 1,$$

indicating the tile calorimeter is well calibrated (with analysis-level corrections accounting for what minor calibration discrepancies are present).

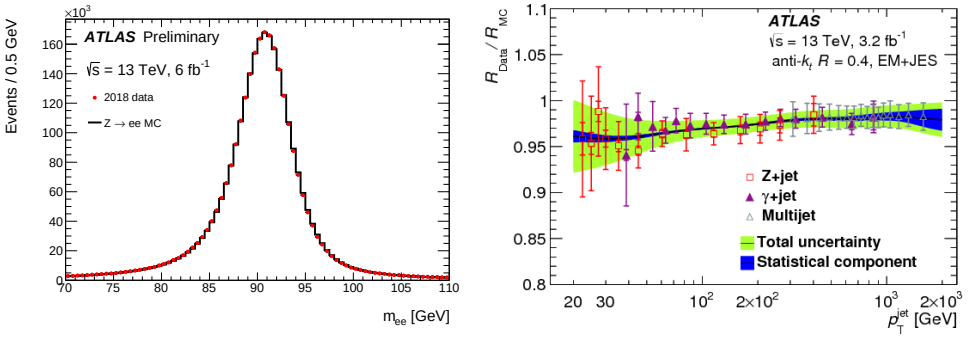

Figure 3.1.8: Performance of the LAr calorimeter in reconstructing the Z mass peak from di-electron events selected in both simulated and 2018 data events (left) [70]. Also presented is the ratio of the jet response measured in both simulated and 2015 data events as a function of jet P_T, as measured using the tile calorimeter (right) [71]. Both indicate good performance of the respective calorimeter sub-systems.

3.1.4 Muon Spectrometer

With their mass roughly 200 times greater than that of the electron, muons lose only a small fraction of their energy as they pass through the calorimeters, and can therefore penetrate further into the detector. The Muon Spectrometer (MS) is thus the outermost component of the ATLAS detector, designed to identify and measure the momenta of muons. Muon tracks are curved within the MS due to the magnetic fields of the toroids described in Section 3.1.1. Monitored Drift Tubes (MDTs) and Cathode Strip Chambers (CSCs) record these tracks across the range $|\eta| < 2.7$, achieving momentum resolutions of 10% for 1 TeV muons. A system of Resistive Plate Chambers (RPCs) and Thin Gap Chambers (TGCs) trigger on muon tracks within $|\eta| < 2.4$. Figure 3.1.9 illustrates the overall layout of the MS.

The 1150 MDT chambers of ATLAS cover the range $|\eta| < 2.7$, except for the innermost end-cap layer, which is limited to $|\eta| < 2.0$. The chambers form concentric layers which surround the beam pipe. They are shaped rectangularly in the barrel and trapezoidally in the end-cap, in order to maximise solid angle coverage while accommodating the support structures and magnetic coils of the detector. Each chamber consists of three to eight layers of drift tubes, with an average resolution of 35 μm per chamber. The tubes contain $ArCO_2$ at a pressure of 3 bar, and are 29.970 mm in diameter. Each contains a 50 μm tungsten-rhenium anode wire, kept at a potential of 3080 V. Incident particles ionise the $ArCO_2$ gas, creating electrons which drift towards the central wire, producing further electrons in the process. Upon contact with the anode, a change in voltage occurs. If the change is above a pre-defined threshold, the signal and time-stamp of the incident are recorded. Since the maximum drift time (700 ns) is known, the position of the original particle can be reconstructed based on the time taken for the signal to register.

MDTs are designed to safely operate up to counting rates of 150 Hz/cm^2, which are

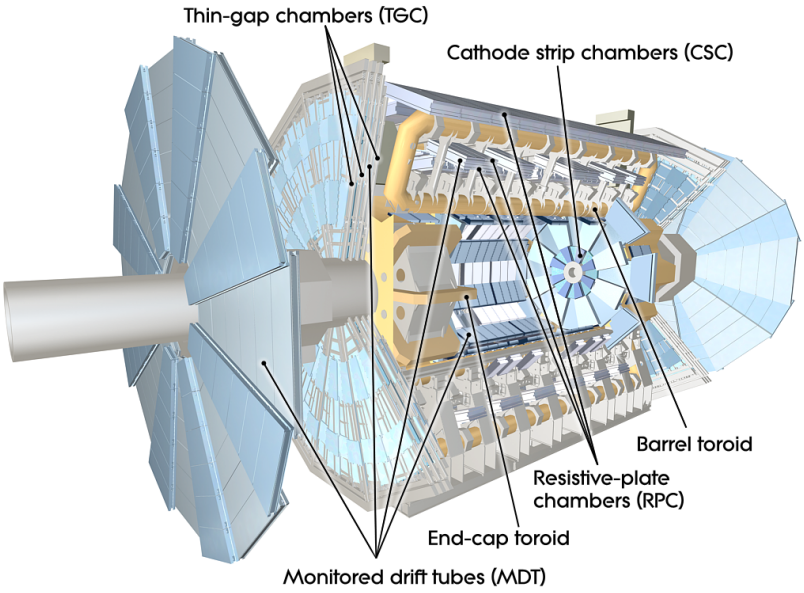

Figure 3.1.9: The Muon Spectrometer system of ATLAS [12].

exceeded within the first layer of the end-caps for $|\eta| > 2.0$. CSCs, capable of operating at up to 1000 Hz/cm^2, are instead utilised within these layers for $2.0 < |\eta| < 2.7$. The entire CSC system is comprised of two disks, each containing eight chambers, with four CSC planes per chamber. The planes consist of a sheet of polyurethane foam laminated with two sheets of 0.82 mm thick copper cladding. 17 μm copper strips run across the top of each sheet, forming cathodes. 30 μm diameter anode wires of gold-plated tungsten run perpendicular to these. CSCs thus provide two-dimensional tracking measurements, with average spatial resolutions per chamber of 40 μm and 5 mm in R and ϕ respectively. They operate with electron drift times of less than 40 ns, and utilise 30,720 readout channels.

606 RPCs form the trigger system of the barrel region of the MS. Three concentric layers of RPCs surround the beam axis, covering $|\eta| < 1.05$. The layers are denoted RPC1, RPC2 and RPC3, operating with detection efficiencies $\geq 98.5\%$. Their layout is shown below in Figure 3.1.10.

The RPCs consist of two parallel resistive plates made of plastic laminate, kept at a separation of 2 mm. A gas mixture of $C_2H_2F_4$/Iso-C_4H_{10}/SF_6 (94.7/5/0.3) is ionised by incident particles, producing electrons. An electric field directs the electrons towards metallic strips mounted on the outer faces of the plates, creating electron avalanches in the process. Contact with the metallic strips generates a signal, which can be passed on to the trigger system. RPC1 and RPC2 provide low P_T triggers in the range $6 - 9$ GeV, while RPC3 triggers on $9 - 35$ GeV tracks. They each possess resolutions of 10 mm $\times$ 10

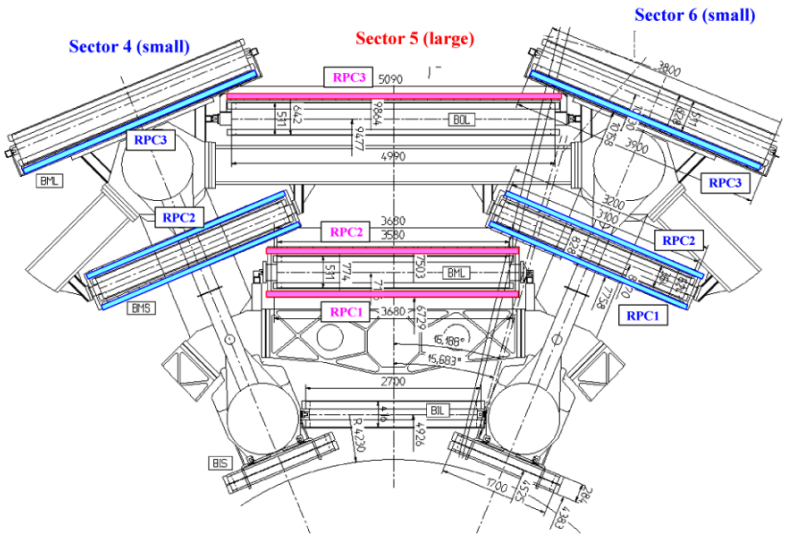

Figure 3.1.10: The cross-section of the upper portion of the barrel of the MS. The RPCs are marked in colour. In the middle chamber layer, RPC1 and RPC2 lie above and below their MDT partner. In the outer layer, RPC3 lies above the MDT in the large sector and below the MDT in the small sector [12].

mm in $z - \phi$, producing signals with time resolutions of 5 ns full width at half-maximum (FWHM).

Since muon momenta are greater in regions of large $|\eta|$, a higher granularity trigger system must be employed in the MS end-caps to achieve adequate resolution. TGCs are used for this purpose, providing trigger readouts for $1.05 < |\eta| < 2.4$. They are multi-wire proportional chambers, characterised by their wire-to-cathode distance (1.4 mm) being smaller than their wire-to-wire separation (1.8 mm). This layout provides time resolutions per chamber of 4 ns rms, with a trigger efficiency of 99.6% [72]. The chambers are filled with a CO_2 / n-pentane-C_5H_{12} gas mixture which, when ionised by incident particles, produces electrons. A potential difference directs the electrons (and their subsequent avalanches) to central arrays of anode wires, connected to readout electronics. Measurable signals are produced as electrons collect onto the anodes, with a strength proportional to the energy of the original particle. Trigger decisions are then made based on the properties of the signal, such as its strength and isolation. 3588 TGCs are utilised within the MS end-caps, spread across three layers (TGC1, TGC2 and TGC3), with resolutions per chamber of 2-6 mm $\times$ 3-7 mm in $R \times \phi$.

Figure 3.1.11 presents the efficiency with which ATLAS reconstructs muons in both simulated MC and 2018 data events, as functions of both muon P_T and η. Selected muons were required to satisfy the Medium identification requirement outlined in Chapter 6, and possess a $P_T > 10$ GeV, as is required in this analysis. Reconstruction efficiencies of

97-98% were achieved in both data and simulation with respect to P_T, and 99% with respect to η (for $|\eta| > 0.1$), demonstrating the high performance of the ATLAS muon system.

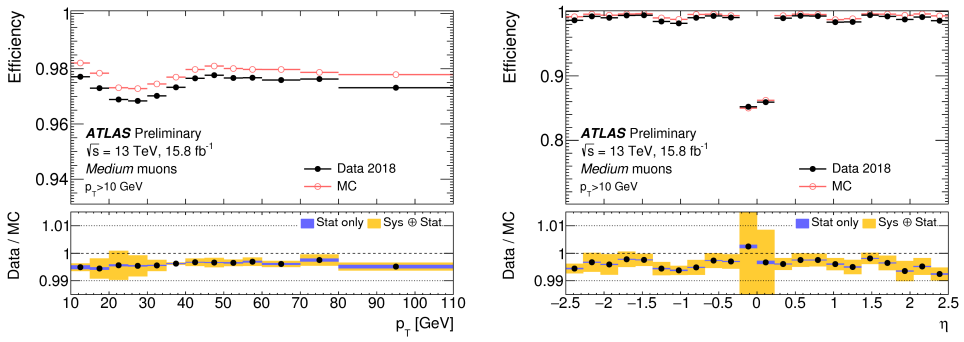

Figure 3.1.11: Reconstruction efficiencies of muons as functions of P_T and η in both MC and 2018 data [73].

3.1.5 Trigger and Data Acquisition System

With 25 ns bunch spacings, the LHC collides proton bunches with a frequency of 40 MHz. This produces far more data than ATLAS can record - the readout electronics are limited to a maximum rate of 1 kHz. ATLAS therefore utilises a trigger system to limit data taking to events of interest. For Run-1, a three-tiered trigger system was utilised. In moving to Run-2, an improved two-tier system was implemented, in order to account for the increased pile-up and luminosity associated with 13 TeV collisions. Its layout is shown below in Figure 3.1.12.

The Level-1 Trigger is comprised of four systems. The Level-1 Calorimeter Trigger (L1Calo) uses energy deposits in the calorimeters to identify high E_T objects of interest such as electrons, photons, taus and jets, along with high E_T^{miss} events. Signals are taken from trigger towers, formed from clusters of calorimeter cells. The clusters vary in size depending on the granularity of the calorimeters, with nominal sizes of 0.1×0.1 in $\Delta\eta \times \Delta\phi$ [75]. A sliding window algorithm searches for trigger towers with local energy maxima, known as Regions of Interest (RoI). Their information is passed to PreProcessor (PPr) modules which digitise the signals, identify the bunch-crossings from which they originate, and calibrate them for use in one of two algorithmic processors. The Cluster Processor (CS) applies electron, photon and tau identification algorithms, while the Jet Energy Processor (JEP) applies jet and E_T^{miss} reconstruction algorithms.

The Level-1 Muon Trigger (L1Muon) identifies high P_T muons by processing the information recorded by the RPCs and TGCs of the MS. Its algorithms depend on coincident hits of tracks in different trigger stations. Hits between stations are connected

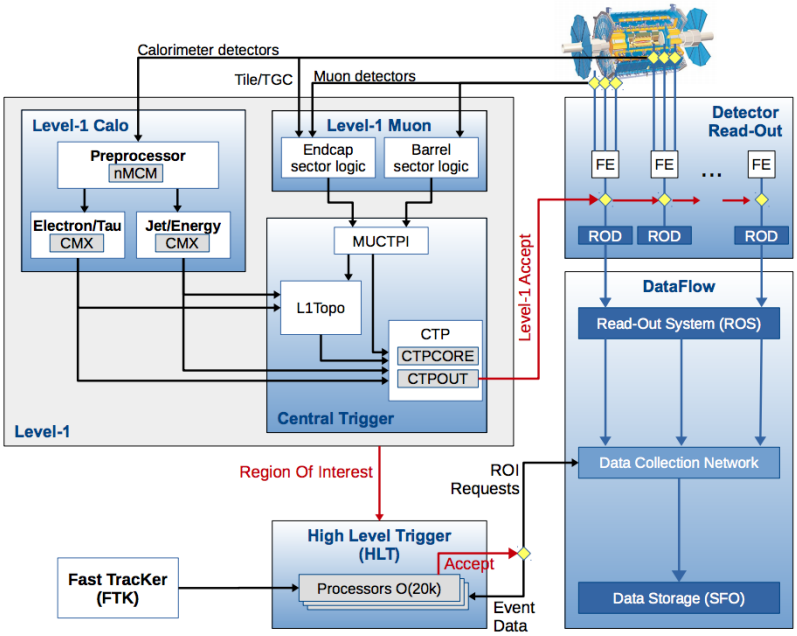

Figure 3.1.12: Layout of the Run-2 ATLAS trigger and data acquisition system. The FTK is planned to be fully integrated into the system for Run-3 [74].

by a road, the width of which varies with trigger P_T threshold. Six thresholds are evenly split between the low and high P_T triggers. The results are passed to the Muon to Central Trigger Processor Interface (MUCTPI), which combines the barrel and end-cap trigger information for each of the six P_T thresholds.

The outputs of L1Calo and L1Muon are known as Trigger Objects (TOBs), which are passed on to the Level-1 Topological Trigger (L1Topo). This applies cuts based on the angular separation, interaction hardness and invariant mass of reconstructed TOBs. The Central Trigger Processor (CTP) passes the resulting information (along with the TOB multiplicities provided by L1Calo and L1Muon) through look-up tables to determine the input signal trigger items. Providing the items satisfy the requirements listed in the Level-1 trigger menu, a Level-1 Accept (L1A) signal is sent to the High-Level Trigger (HLT), the second part of the ATLAS trigger system. Through this methodology, the L1 trigger system reduces input rates down to around 100 kHz, with a decision latency of 2 μm.

In contrast to the hardware-based approach of Level-1, the HLT is software-based. It applies reconstruction algorithms to the RoIs determined at Level-1, utilising fine-granularity information from all detector sub-systems (including those not available at Level-1, such as the ID) to determine events of interest. The algorithms typically operate in two stages; an initial fast reconstruction is used to tighten the selection on incident

objects, before a slower precision algorithm is utilised. In doing so, the HLT further lowers the event rate to roughly 1 kHz, after which the data are stored at the CERN Data Centre, where offline event reconstruction occurs (using algorithms identical to those used during online reconstruction).

For calorimeter objects, fast algorithms are used to build clusters of cells within either the RoIs identified at Level-1, or the full calorimeter system. The latter approach is applied for the reconstruction of jets and E_T^{miss}, while the former is used for the reconstruction of electrons, muons, taus and photons. Full online event reconstruction is then carried out by sliding window and topo-cluster algorithms, with the former favoured for electrons and photons.

The fast reconstruction of muon objects makes use of precision hits in MDT chambers to perform track fits to MS-only objects. The tracks are back-extrapolated to the IP, making use of CSC information where possible, and are combined with track information from the ID to form combined muon candidates. Muon trigger chain selection criteria are applied to reject fake muons, with those surviving passing to precision reconstruction algorithms. These make use of the refined RoI information from the previous step to perform a track reconstruction using the full MS system [76]. By combining with ID track information, combined muons are again formed. Alternate outside-in algorithms are also utilised to extrapolate ID tracks to the MS, for cases where the original algorithm fails.

Figure 3.1.13 presents the efficiency of the Level-1 muon trigger L1 MU15, along with the HLT triggers mu20_iloose and mu50, all of which were utilised in this analysis (as described in Chapter 6). The efficiencies were determined using $Z \to \mu\mu$ events selected from 2015 data with a tag-and-probe methodology, with the distributions presented as functions of the reconstructed probe's P_T. Separate distributions are presented depending on whether the probe was reconstructed in the barrel or end-caps of the detector. In both cases, trigger efficiencies $> 99\%$ are achieved for $P_T > 20$ GeV, as is required for the leading muons used in this analysis.

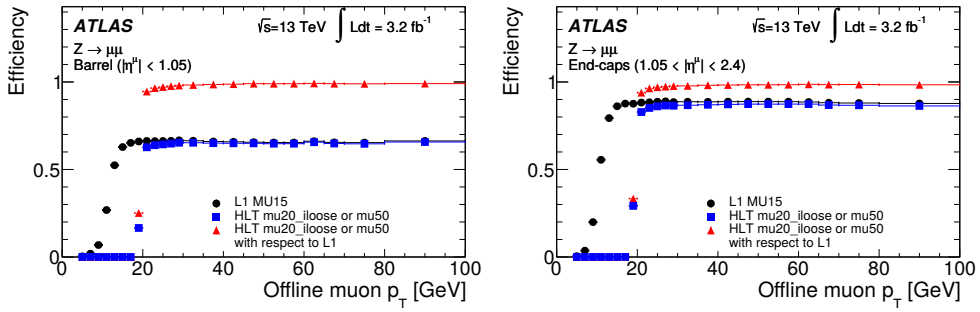

Figure 3.1.13: The efficiencies of the L1 MU15, HLT_mu20_iloose and HLT_mu50 triggers described in Chapter 6 as functions of probe muon P_T, in both the barrel and end-caps of the detector, determined using data recorded by ATLAS in 2015 [77].

The author of this thesis performed service work on L1Calo during 2017. Using pp collision data collected by ATLAS in 2016 at $\sqrt{s} = 13$ TeV, the variation of the rates and efficiencies of various electron triggers with respect to different noise and isolation configurations was studied, using di-electron events selected using a tag-and-probe approach, as detailed in Chapter 11. The methodology and results are documented in a separate note [78].

Chapter 4

Data and Monte Carlo Samples

Monte Carlo (MC) techniques are utilised in the simulation of theoretical models and particle detectors. They involve repeated random sampling over a given phase space to determine interaction cross-sections to a good approximation. Direct comparisons can then be made between existing theories and experimental data. MC techniques were utilised throughout this analysis for many purposes, including the simulation of signal and background processes, and the optimisation of the selection and categorisation of events.

MC events are typically generated in four stages. The first involves the simulation of the Matrix Element (ME) of the interaction, which describes the initial hard scatter, along with the decays of any resonant particles involved. MEs can be calculated to varying degrees of accuracy, depending on the number of particle emissions and virtual loop corrections involved. The calculations are performed using perturbation theory, where the ME is approximated to a power series of a certain order. Leading Order (LO) calculations ignore all loop contributions, and are the least computationally expensive. Next-to Leading Order (NLO) calculations include the next order of expansion terms, accounting for first order loop corrections and further particle emissions. In these instances, more accurate results are achieved at the expense of greater computing hours. The order to which calculations are performed, along with the choice of parton PDF and model parameters, varies between MC generators. This creates theoretical uncertainties which impact experimental results.

The showering of partons radiated in the initial and final states is then simulated. The order in which shower constituents are calculated depends on kinematic requirements unique to each MC generator. This choice leads to shower modelling uncertainties which analyses must also consider.

The Underlying Event (UE) of the interaction is then simulated, which contains all of the soft interactions not directly involved with the hard scatter. Parton hadronisations are finally simulated, along with the decays of the final state particles. The choice of hadronisation model again varies between MC generators, providing a further theoretical uncertainty.

The impact of the uncertainties discussed in this section is detailed in Chapter 11. The remaining sections of this chapter instead detail the data and MC samples used in this analysis, along with the various corrections applied to the them.

4.1 Data Samples

This analysis made use of 80.5 fb^{-1} of data recorded by ATLAS between 2015 and 2017. Only runs listed within the Good Run Lists (GRL) provided by the ATLAS Data Quality group were utilised [79]. The GRLs and their corresponding integrated luminosities are listed below in Table 4.1.1.

Year	Good Run List	Integrated Luminosity (fb^{-1})
2015	data15_13TeV.periodAllYear_ DetStatus-v89-pro21-02_ Unknown_PHYS_StandardGRL_ All_Good_25ns.xml	3.2
2016	data16_13TeV.periodAllYear_ DetStatus-v89-pro21-01_ DQDefects-00-02-04_PHYS_ StandardGRL_All_Good_25ns.xml	33.0
2017	data17_13TeV.periodAllYear_ DetStatus-v99-pro22-01_ Unknown_PHYS_StandardGRL_All_Good_ 25ns_Triggerno17e33prim.xml	44.3

Table 4.1.1: GRLs used in the analysis, and their corresponding integrated luminosities [79].

4.2 Monte Carlo Samples

All MC samples used in the analysis were passed through GEANT4 [80], which simulates the response of the ATLAS detector to incident processes. Each sample contained both truth-level (before GEANT4) and reco-level (after GEANT4) events. Signal MC samples covering the four primary SM $H \to \mu\mu$ production modes detailed in Section 2.4 were utilised, along with samples accounting for the dominant background processes. All of the former were produced with the simulated Higgs mass, branching ratio and decay width[1] set to 125 GeV, 2.19×10^{-4} and 4.07 MeV respectively [81], with the latter quantities determined using HDECAY [82, 83].

ggF signal processes were modelled using the POWHEG method within the POWHEG BOX MC generator [84, 85], capable of interfacing NLO QCD computations with parton-

[1]Decay width is defined as the Planck constant normalised by 2π, multiplied by the inverse of a particle's lifetime.

shower generators. NNLO accuracy was achieved through NNLOPS simulation [86, 87], within which the Higgs rapidity distribution is re-weighted to NNLO predictions using the HNNLO program [88]. The CTEQ6L1 PDF set [89] was utilised, with parton showering and hadronisation simulated with Pythia8 [90] using the AZNLO tune [91]. The samples were normalised to SM cross-sections predicted at N^3LO accuracy in QCD [92], with NLO EW corrections applied [93]. The values were determined using the PDF4LHC15 [94] and MRST2002 [95] PDF sets respectively.

VBF samples were generated with POWHEG BOX at NLO in QCD [96] using the same tuning and PDF sets as the ggF samples. Pythia8 was used for parton showering and hadronisation, with the samples normalised to cross-sections calculated at NNLO in QCD with the PDF4LHC15 prescription using VBF@NNLO [97, 98]. Further NLO EW corrections determined using the HAWK program [99–101] were also applied.

VH samples were produced with POWHEG BOX at NLO in QCD [102]. They were normalised to cross-sections calculated at NNLO with VH@NNLO [103] using PDF4LHC15, with NLO EW corrections applied through use of HAWK [104]. The cross-section of $gg \to ZH$ was independently determined at NNLO+Next-to-Leading-Logarithm (NLL) accuracy in QCD [105] with VH@NNLO.

$t\bar{t}H$ samples were produced with MadGraph5_aMC@NLO [106,107] with the NNPDF23LO PDF set [108], with Pythia8 used for parton showering. The samples were normalised to cross-sections calculated at NLO in QCD [109, 110] with NLO EW corrections applied [111], all determined using MadGraph5_aMC@NLO with the PDF4LHC15 PDF set.

Drell-Yan background samples sliced in H_T (the scalar P_T sum of all final state jets and leptons) were produced with Madgraph5_aMC@NLO and Pythia8 with the NNPDF23LO PDF set. Alternative Drell-Yan samples for MC generator studies were also produced, one set using Sherpa [112] with the NNPDF30NNLO PDF set [113], and the other using POWHEG with the CTEQ6L1 PDF set and the AZNLO Pythia8 tune.

The Sherpa MC generator was again utilised with the NNPDF30NNLO PDF set for the production of di-boson and electroweak Z plus jet samples, with the former accounting for ZZ, WZ and WW processes.

Top background processes ($t\bar{t}$, Wt) were accounted for using samples produced with Powheg+Pythia8 with NNPDF23LO.

A summary of the signal and background samples used in the analysis is presented below in Tables 4.2.1 - 4.2.4. Two sets of MC samples were produced: mc16a samples were used for comparisons with the 2015 and 2016 datasets, while mc16d samples were used for comparisons with data recorded in 2017. This was done to effectively model the differences in pile-up between the different datasets, an effect described in the following section. The events contained within the mc16d samples were different to those of mc16a to avoid statistical correlations.

DSID	Processes	Number of Events
344388	aMcAtNloPythia8EvtGen_A14_NNPDF23_NNPDF30nlo_ttH125_mumu	724000
345097	PowhegPythia8EvtGen_NNLOPS_nnlo_30_ggH125_mumu	1966000
345098	PowhegPythia8EvtGen_NNPDF3_AZNLO_ggZH125_Hmumu_Zinc	120000
345103	PowhegPythia8EvtGen_NNPDF30_AZNLO_ZH125J_Hmumu_Zincl_MINLO	119900
345104	PowhegPythia8EvtGen_NNPDF30_AZNLO_WpH125J_Hmumu_Wincl_MINLO	60000
345105	PowhegPythia8EvtGen_NNPDF30_AZNLO_WmH125J_Hmumu_Wincl_MINLO	60000
345106	PowhegPythia8EvtGen_NNPDF30_AZNLOCTEQ6L1_VBFH125_mumu	2000000

Table 4.2.1: The signal ggF, VBF, VH and $t\bar{t}H$ MC samples used in the analysis.

DSID	Processes	Number of Events
363123	MGPy8EG_N30NLO_Zmumu_Ht0_70_CVetoBVeto	3947000
363124	MGPy8EG_N30NLO_Zmumu_Ht0_70_CFilterBVeto	1152500
363125	MGPy8EG_N30NLO_Zmumu_Ht0_70_BFilter	1000000
363126	MGPy8EG_N30NLO_Zmumu_Ht70_140_CVetoBVeto	3619400
363127	MGPy8EG_N30NLO_Zmumu_Ht70_140_CFilterBVeto	2102400
363128	MGPy8EG_N30NLO_Zmumu_Ht70_140_BFilter	792440
363129	MGPy8EG_N30NLO_Zmumu_Ht140_280_CVetoBVeto	3960000
363130	MGPy8EG_N30NLO_Zmumu_Ht140_280_CFilterBVeto	1967400
363131	MGPy8EG_N30NLO_Zmumu_Ht140_280_BFilter	1557920
363132	MGPy8EG_N30NLO_Zmumu_Ht280_500_CVetoBVeto	1579000
363133	MGPy8EG_N30NLO_Zmumu_Ht280_500_CFilterBVeto	797000
363134	MGPy8EG_N30NLO_Zmumu_Ht280_500_BFilter	473000
363135	MGPy8EG_N30NLO_Zmumu_Ht500_700_CVetoBVeto	396000
363136	MGPy8EG_N30NLO_Zmumu_Ht500_700_CFilterBVeto	411000
363137	MGPy8EG_N30NLO_Zmumu_Ht500_700_BFilter	48000
363138	MGPy8EG_N30NLO_Zmumu_Ht700_1000_CVetoBVeto	10000
363139	MGPy8EG_N30NLO_Zmumu_Ht700_1000_CFilterBVeto	10000
363140	MGPy8EG_N30NLO_Zmumu_Ht700_1000_BFilter	9000
363141	MGPy8EG_N30NLO_Zmumu_Ht1000_2000_CVetoBVeto	9000
363142	MGPy8EG_N30NLO_Zmumu_Ht1000_2000_CFilterBVeto	2000
363143	MGPy8EG_N30NLO_Zmumu_Ht1000_2000_BFilter	2000
363144	MGPy8EG_N30NLO_Zmumu_Ht2000_E_CMS_CVetoBVeto	2000
363145	MGPy8EG_N30NLO_Zmumu_Ht2000_E_CMS_CFilterBVeto	2000
363146	MGPy8EG_N30NLO_Zmumu_Ht2000_E_CMS_BFilter	2000

Table 4.2.2: The Drell-Yan MC samples used in the analysis that were generated with Madgraph. To increase the number of generated events, three samples were produced for each H_T range: one where events containing either c- or b-jets were vetoed, a second where a filter was applied to increase the number of c-jets, with b-jets still vetoed, and a third with a filter used to increase the number of b-jets.

DSID	Processes	Number of Events
308093	Sherpa_221_NNPDF30NNLO_Zmm2jets_Min_N_TChannel	1130000
361107	PowhegPythia8EvtGen_AZNLOCTEQ6L1_Zmumu	158223000
364100	Sherpa_221_NNPDF30NNLO_Zmumu_MAXHTPTV0_70_CVetoBVeto	17639000
364101	Sherpa_221_NNPDF30NNLO_Zmumu_MAXHTPTV0_70_CFilterBVeto	9936500
364102	Sherpa_221_NNPDF30NNLO_Zmumu_MAXHTPTV0_70_BFilter	17604000
364103	Sherpa_221_NNPDF30NNLO_Zmumu_MAXHTPTV70_140_CVetoBVeto	13461000
364104	Sherpa_221_NNPDF30NNLO_Zmumu_MAXHTPTV70_140_CFilterBVeto	4491600
364105	Sherpa_221_NNPDF30NNLO_Zmumu_MAXHTPTV70_140_BFilter	11960800
364106	Sherpa_221_NNPDF30NNLO_Zmumu_MAXHTPTV140_280_CVetoBVeto	11244000
364107	Sherpa_221_NNPDF30NNLO_Zmumu_MAXHTPTV140_280_CFilterBVeto	6750000
364108	Sherpa_221_NNPDF30NNLO_Zmumu_MAXHTPTV140_280_BFilter	17457800
364109	Sherpa_221_NNPDF30NNLO_Zmumu_MAXHTPTV280_500_CVetoBVeto	3960500
364110	Sherpa_221_NNPDF30NNLO_Zmumu_MAXHTPTV280_500_CFilterBVeto	2249000
364111	Sherpa_221_NNPDF30NNLO_Zmumu_MAXHTPTV280_500_BFilter	4497700
364112	Sherpa_221_NNPDF30NNLO_Zmumu_MAXHTPTV500_1000	5993500
364113	Sherpa_221_NNPDF30NNLO_Zmumu_MAXHTPTV1000_E_CMS	2247000

Table 4.2.3: The extra Drell-Yan and Electroweak Z plus jets MC samples used in the analysis.

DSID	Processes	Number of Events
363356	Sherpa_221_NNPDF30NNLO_ZqqZll	10800000
363358	Sherpa_221_NNPDF30NNLO_WqqZll	10779000
364250	Sherpa_222_NNPDF30NNLO_llll	53838800
364253	Sherpa_222_NNPDF30NNLO_lllv	47651700
364254	Sherpa_222_NNPDF30NNLO_llvv	44971000
410015	PowhegPythiaEvtGen_P2012_Wt_dilepton_top	1130000
410016	PowhegPythiaEvtGen_P2012_Wt_dilepton_antitop	1130000
410470	PhPy8EG_A14_ttbar_hdamp258p75_nonallhad	129824000

Table 4.2.4: The top and di-boson MC samples used in the analysis. The nonallhad label refers to all allowed decay modes which aren't fully hadronic.

4.3 Monte Carlo Corrections

Scale factors were applied to the MC samples to correct for differences between the MC and the data. In doing so, the MC's description of the data was improved. Each scale factor was typically of the form

$$\text{Scale Factor} = \frac{\text{Data}}{\text{MC}}, \tag{4.3.1}$$

and were provided by the Combined Performance groups within ATLAS.

Trigger scale factors were used to correct for the inefficiencies of triggers used in the selection of events. b-tagging scale factors were applied to correct the differences in performance seen when applying b-tagging algorithms to data rather than MC. Muon reconstruction scale factors accounted for inefficiencies in ATLAS' reconstruction of muons, while muon isolation scale factors accounted for inefficiencies in the reconstruction of material surrounding muons (which determines the muon's degree of isolation). Track-to-Vertex-Association (TTVA) scale factors accounted for the efficiency with which muon tracks were associated to the primary vertex. These corrections were applied to all MC samples used in the analysis. The methods by which they were derived, along with their associated systematic uncertainties, are discussed in Chapter 11. Their average values when applied to the ggF and Drell-Yan samples used in the analysis as functions of $P_T^{\mu,\text{Leading}}$, $P_T^{\mu,\text{Subleading}}$, $P_T^{\mu\mu}$, $\eta^{\mu,\text{Leading}}$, $\eta^{\mu,\text{Subleading}}$, $y^{\mu\mu}$ and $M_{\text{inv}}^{\mu\mu}$ are shown below in Figures 4.3.1 to 4.3.4. Trigger scale factors correct the MC sample normalisations by up to 4%, while the other aforementioned scale factors induce corrections of 1-2%. The scale factor shapes are largely uniform as functions of the chosen variables, with the exception of the trigger scale factor, due to the limited coverage of the RPCs. Impacts of the scale factors on the other MC samples used in the analysis are shown in Appendix A.

Despite its largely accurate description of ATLAS, GEANT4 fails to achieve the energy and momentum resolutions outlined in Chapter 3. Muon resolution and scale corrections were therefore applied to all MC samples, along with further calibration corrections for jet energy scale and resolution measurements. Due to misalignments within the ID of ATLAS, deformations are also present within the tracks of reconstructed muons. This generates a charge-dependent bias in the associated P_T spectra which must be corrected. In this analysis, sagitta corrections provided by the ATLAS Muon Combined Performance Working Group were utilised, which were applied to data events, rather than MC.

As the average number of interactions per bunch crossing ($<\mu>$) grows, so too does a detrimental effect known as pile-up. In-time pile-up occurs when multiple proton-proton collisions occur within the same bunch. Out-of-time pile-up results from signals from previous bunch crossings lingering within the detector, an effect enhanced when detector response times are greater than the incident bunch crossing frequency. In order for MC

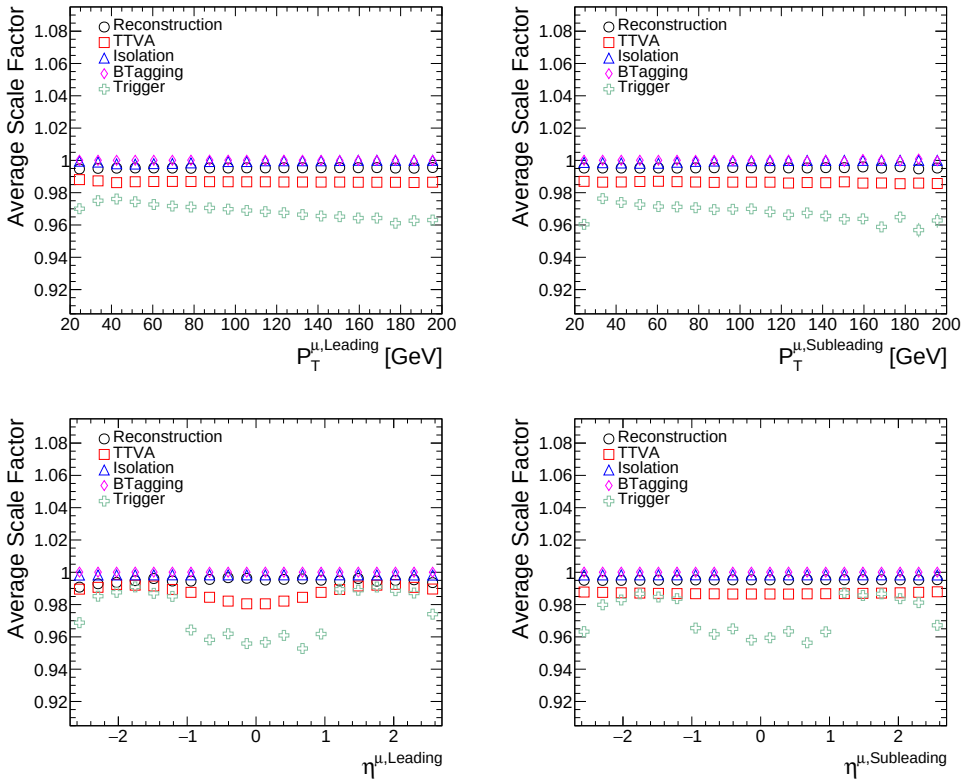

Figure 4.3.1: Average values of the muon reconstruction, muon TTVA, muon isolation, b-tagging and trigger scale factors used in the analysis, as a function of $P_T^{\mu,\text{Leading}}$ (top left), $P_T^{\mu,\text{Subleading}}$ (top right), $\eta^{\mu,\text{Leading}}$ (bottom left) and $\eta^{\mu,\text{Subleading}}$ (bottom right) for the ggF MC sample. The full object and event selections detailed in Chapter 6 have been applied, with the exception of the cut on $M_{\text{inv}}^{\mu\mu}$. Only MC statistical errors are shown.

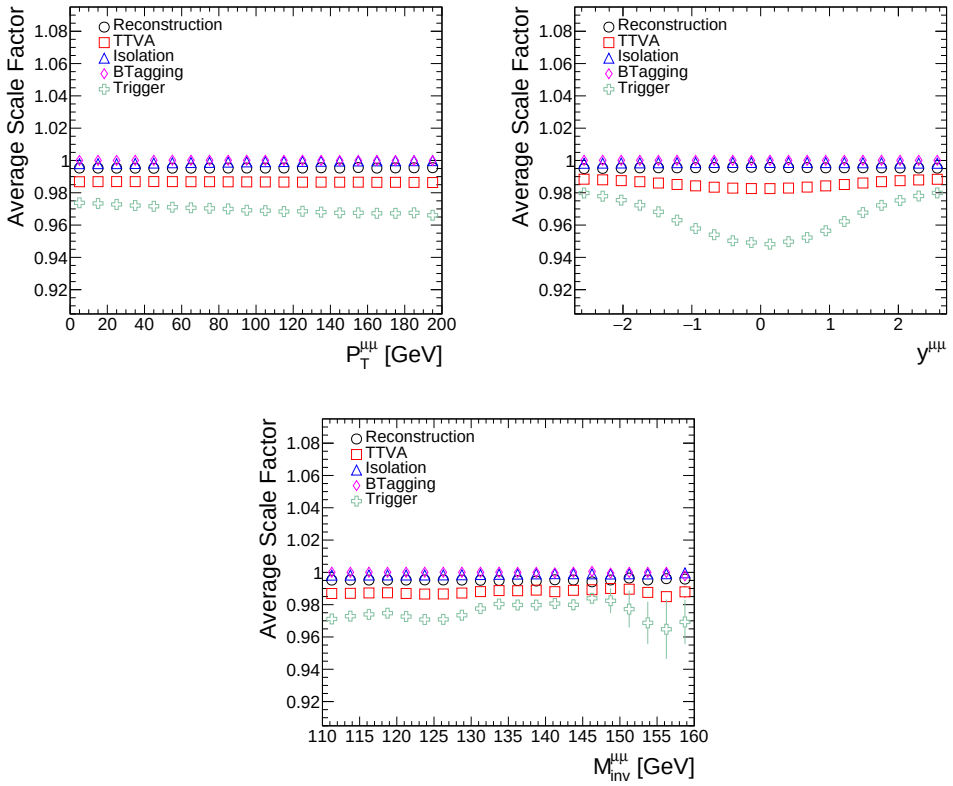

Figure 4.3.2: Average values of the muon reconstruction, muon TTVA, muon isolation, b-tagging and trigger scale factors used in the analysis, as a function of $P_{\mathrm{T}}^{\mu\mu}$ (top left), $y^{\mu\mu}$ (top right) and $M_{\mathrm{inv}}^{\mu\mu}$ (bottom) for the ggF MC sample. The full object and event selections detailed in Chapter 6 have been applied, with the exception of the cut on $M_{\mathrm{inv}}^{\mu\mu}$. Only MC statistical errors are shown.

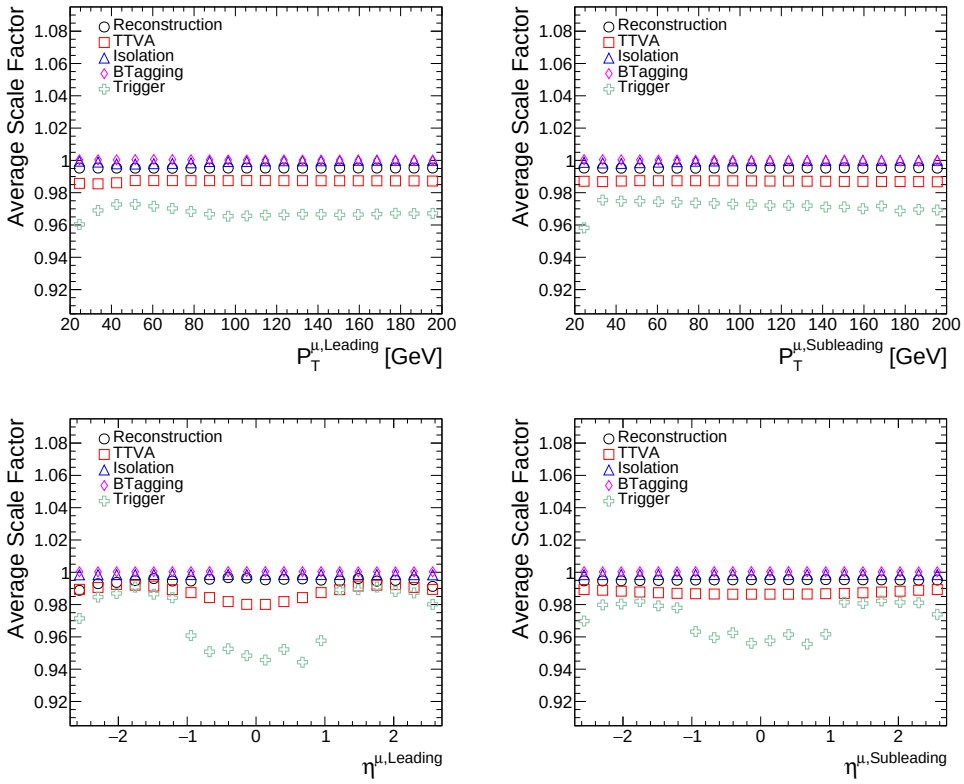

Figure 4.3.3: Average values of the muon reconstruction, muon TTVA, muon isolation, b-tagging and trigger scale factors used in the analysis, as a function of $P_T^{\mu,\text{Leading}}$ (top left), $P_T^{\mu,\text{Subleading}}$ (top right), $\eta^{\mu,\text{Leading}}$ (bottom left) and $\eta^{\mu,\text{Subleading}}$ (bottom right) for the Drell-Yan MC samples generated with Madgraph. The full object and event selections detailed in Chapter 6 have been applied, with the exception of the cut on $M_{\text{inv}}^{\mu\mu}$. Only MC statistical errors are shown.

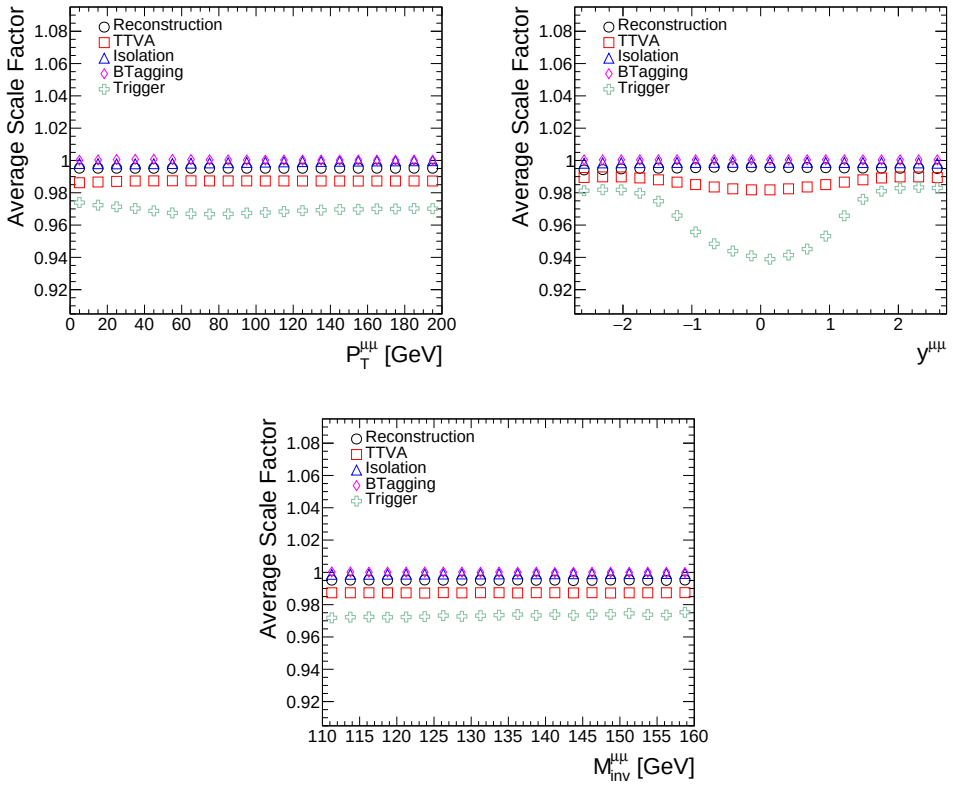

Figure 4.3.4: Average values of the muon reconstruction, muon TTVA, muon isolation, b-tagging and trigger scale factors used in the analysis, as a function of $P_{\mathrm{T}}^{\mu\mu}$ (top left), $y^{\mu\mu}$ (top right) and $M_{\mathrm{inv}}^{\mu\mu}$ (bottom) for the Drell-Yan MC samples generated with Madgraph. The full object and event selections detailed in Chapter 6 have been applied, with the exception of the cut on $M_{\mathrm{inv}}^{\mu\mu}$. Only MC statistical errors are shown.

to accurately describe data, these effects must be accounted for. This is achieved through pile-up re-weighting, wherein the $<\mu>$ distribution of the MC is re-weighted to that of the data.

Due to the changing beam conditions, the $<\mu>$ distributions recorded by ATLAS vary by year. The variation of recorded luminosity with $<\mu>$ over the course of Run-2 is shown below in Figure 4.3.5. To account for these differences, separate pile-up reweighting files were used for the mc16a and mc16d samples respectively.

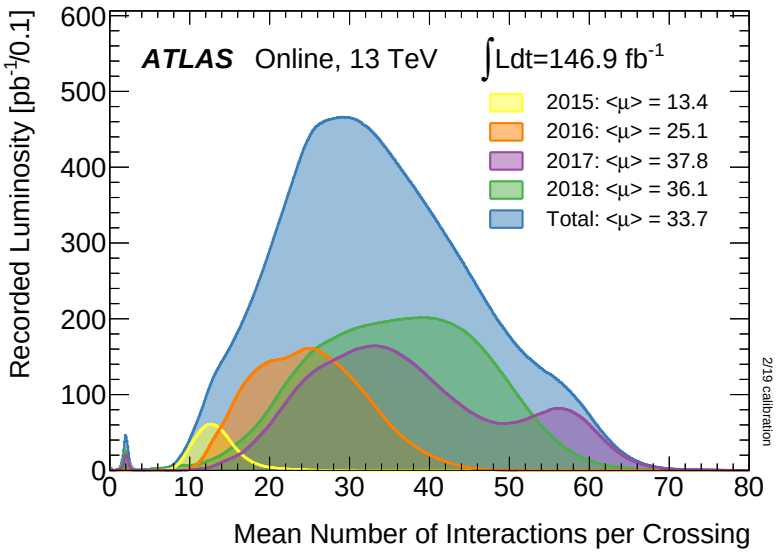

Figure 4.3.5: Recorded luminosity as a function of $<\mu>$ recorded by ATLAS during Run-2. Both pile-up and $<\mu>$ increased on a yearly basis in an attempt to maximise the total integrated luminosity [114].

Chapter 5

Theory of Boosted Decision Trees

To optimise a search analysis, one must maximise sensitivity to the desired signal by as much as possible. This is commonly achieved by constructing regions of phase-space where the ratio of signal to the square root of background event yields, $\frac{S}{\sqrt{B}}$, is greatest[1]. While simple cut-based methods have proved popular for this means for some time, support of Multi-Variate Analysis (MVA) techniques is rapidly growing.

The most commonly used framework for application of MVA techniques in High Energy Physics (HEP) is TMVA [116], an integrated part of the ROOT analysis framework [117]. Both are made use of in this thesis. While an abundance of MVA techniques exist, this analysis makes sole use of Boosted Decision Trees (BDTs), due to their simplicity of implementation, and high performance with limited optimisation. Future iterations of $H \to \mu\mu$ analyses could undoubtedly explore and compare other methods, such as Support Vector Machines and Neural Networks, in order to potentially further optimise signal-background separation.

It is of note that the BDT usage outlined above is motivated as a means to solve a classification problem, where events are to be sorted into discrete categories (signal and background). However, MVA techniques can also be used for regression analyses, where the final goal is to measure a continuous variable. While HEP analyses often employ MVAs to solve both sets of problems, regression techniques will not be explored in this thesis.

[1]This is an approximation of the form, $\sqrt{2\left((S+B)\ln(1+\frac{S}{B})) - S\right)}$, for the case where S is small relative to the background, as is the case in this analysis [115].

5.1 Boosted Decision Trees

Decision trees are classifiers which apply a series of binary cuts (pass/fail) until a stop criterion is satisfied. They are an example of a supervised learning algorithm, which receives training events (with a known desired output) from the user and sorts them into discrete categories. Once trained, a BDT can be applied to previously unseen datasets, identifying the class of events (signal or background) that may not be known a priori. For analyses such as this, the goal is to train a BDT using MC samples (where the constituent events are known to be signal or background), and apply it to ATLAS data, with the hopes of identifying $H \to \mu\mu$ signal events.

An example of a decision tree is presented in Figure 5.1.1. Given a series of discriminating variables x_i, the tree splits the input dataset at each node (or leaf) using the variable best satisfying the separation criteria at each point. Each connected set of branches represents its own region in hyperspace, driving decision trees to outperform typical cut-based analyses (which are often limited to single hyperspace regions).

In this analysis, the default TMVA BDT separation criterion was utilised, the Gini Index (GI), defined as

$$GI = p(1-p), \tag{5.1.1}$$

where p, the signal purity, is defined as

$$p = \frac{n_S}{n_S + n_B}, \tag{5.1.2}$$

with n_S and n_B the number of signal and background events respectively. Optimal signal/background separation is achieved for either large or small purities, both resulting in GI values close to 0. Selected variables therefore best minimise GI at each node. This is in contrast to $\frac{S}{\sqrt{B}}$, where when acting as a separation criterion, only large signal purities are desirable. Whilst the latter criterion is more relevant to this analysis, GI was favoured due to its ease of implementation in TMVA.

Decision tree algorithms are however limited in a number of regards. They are particularly susceptible to statistical fluctuations in the input data, which can influence node decisions, creating a knock-on effect for the proceeding branches. This can lead to overtraining, where the decision tree over-fits the input dataset, deteriorating its performance when applied to previously unseen test datasets. In a HEP analysis, for example, a decision tree overtrained on MC events may misclassify data events it later encounters. Various techniques can be utilised to improve the robustness of decision trees to such effects, along with improving their performance in general. These are explored in the following sections.

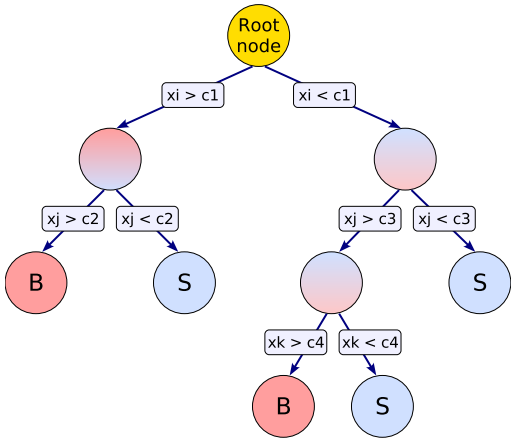

Figure 5.1.1: Schematic layout of a decision tree. At each node, a cut, c, is applied to one of the variables, x, taken from the input dataset. Cuts are decided based on which variable best satisfies the separation criteria at that point. Leaf nodes are labelled as signal (S) or background (B) depending on the majority type of events in the respective nodes [116].

5.1.1 Boosting and Bagging

Boosting is a method by which an MVA algorithm's classification performance and insensitivity to statistical fluctuations can be improved. Its use is typically focused towards so-called weak learners, which in the context of decision trees refer to trees of limited depth, which by themselves have little discriminating power. In boosting, weak learners are retrained within a re-parametrised learning model, and combined into an ensemble (or forest), from which a majority vote on the classification of events is determined. This is weighted by the prediction accuracy of each individual tree. The process is iterated until classification performance reaches an optimal level. By building an ensemble of low depth trees, rather than one tree of large depth, the sensitivity of the BDT to statistical fluctuations is reduced, while also still typically outperforming a simple tree.

Consider a function $F(\mathbf{x})$ mapping the classification response of a BDT to input data containing the group of variables $\mathbf{x}$. The function is constructed as a weighted sum of weak learners, $f(x; a_m)$, with x a variable of set $\mathbf{x}$ and a_m a discrete label (signal/background) assigned by learner m. $F(\mathbf{x})$ can be represented as an expansion of the form

$$F(\mathbf{x}; P) = \sum_{m=0}^{M} \beta_m f(x; a_m), \tag{5.1.3}$$

$$P \in \{\beta_m; a_m\}_0^M, \tag{5.1.4}$$

with M the total number of trees considered, β_m a boosting factor controlling the learning rate of the algorithm, and P the parameters of the model (such as variable cuts). A loss function, $L(F(\mathbf{x}), y)$, is used to quantify the difference between the true value of the data, y, and the response of the model, $F(\mathbf{x})$. The boosting procedure involves modifying P and re-training the model until $L(F(\mathbf{x}), y)$ is minimised. In subsequent iterations, input events that were previously misclassified are given higher weights.

The functional form of $L(F(\mathbf{x}), y)$ varies between boosting methods. In this analysis, the Gradient Boosting method [118] of TMVA is adopted, where

$$L(F(\mathbf{x}), y) = \ln\left(1 + e^{-2F(\mathbf{x})y}\right). \tag{5.1.5}$$

This loss function is considered more robust in noisy settings than those of other methods (such as Adaptive Boost).

The robustness of Gradient Boosted BDTs to overtraining can be enhanced by reducing the learning rate of the algorithm, controlled in TMVA by the shrinkage parameter. Low shrinkage values force the growth of more trees of limited depth.

Classifiers can be further stabilised through Bootstrap Aggregating (Bagging), where learners are repeatedly trained using randomly re-sampled subsets of the input dataset. A combined classifier is then formed from an average of the individual learners. The procedure helps to reduce the sensitivity of the classifier to statistical fluctuations in the input data. Unlike the case of boosting, combined classifiers produced through bagging are formed using simple averages, rather than weighted averages (where higher weights are given to better performing classifiers). Boosting also trains its models sequentially (using modified weights from previous steps), whereas bagging trains each learner in parallel. Bagging thus produces multiple independent models, whereas boosting focuses on improving the performance of previously identified weak learners.

5.1.2 Cross-Validation

An effective classifier must be generalised such that high performance is maintained when exposed to previously unseen datasets. Cross-validation methods are often employed for such purposes, wherein datasets are divided into subsets specific for training and testing the classifier.

The simplest form of cross-validation is known as hold-out, where the dataset is split once. The classifier is then repeatedly trained on the training subset until performance is optimised, after which its performance is tested on the remaining events. While this reduces the likelihood of overtraining with respect to training on the full dataset, the method is sensitive to how the data is split.

A more robust approach involves splitting the data more than once. While still sensitive to the splitting method, the classifier's performance may be tested multiple

times, and quantified with an averaged error rate. With k-fold cross-validation, the dataset is randomly split into k folds of equal size. The classifier is then trained using $k-1$ folds, and tested on the single fold remaining. The process is repeated using all combinations of folds, after which an averaged error rate of the classifier (or some other quantifier of its performance) may be calculated. This method benefits from utilising the entirety of the dataset, which is useful when the number of events is limited. k can in principle take very large values, but in reality this choice is limited by computation time and the amount of available data. In cases where folds contain too few events, the classifier is subject to large statistical fluctuations, making the results of algorithms such as BDTs unreliable.

In this analysis, two-fold cross-validation was utilised. It is explored in more detail in Chapter 9.

Chapter 6

Object and Event Selection

Despite the large amount of data recorded by ATLAS during Run-2, a large proportion of it was irrelevant for this analysis, containing no di-muon final states. Selection criteria were therefore applied to reconstructed events and objects in order to identify events of interest. These criteria are outlined in the following sections.

6.1 Muons

The selection of muons was performed using the official Muon Selector Tool provided by the ATLAS Muon Combined Performance (MCP) group [119]. Their recommendations were followed throughout the analysis.

Muons are reconstructed using information from the ID, MS and calorimeters of ATLAS. Different types of muon can be specified, depending on the number of subdetectors involved in their reconstruction:

- Combined (CB) muons are the most prominent, having hits in both the ID and MS which are independently reconstructed into tracks. In the majority of cases the MS tracks are reconstructed first, and then extrapolated inward to match an ID track, in a process known as outside-in pattern recognition. Inside-out pattern recognition (where ID tracks are extrapolated and matched to MS tracks) is also used as a complementary approach.

- Segment-tagged (ST) muons are identified by associating a track in the ID with at least one local track segment in the MDT/CSC chambers. They are typically low P_T muons falling into regions of low MS acceptance.

- Calorimeter-tagged (CT) muons are identified by matching an ID track to energy deposits in the calorimeters compatible with that of a minimum-ionising particle.

They have momenta in the range $15 < P_T < 100$ GeV, and are within $|\eta| < 0.1$, corresponding to cabling and service regions of the MS, where acceptance is low.

- Extrapolated (ME) or Stand-Alone (SA) muons are reconstructed purely from MS tracks that are loosely compatible with the original interaction point, and are most often used to extend muon reconstruction coverage to $2.5 < |\eta| < 2.7$, where ID coverage is missing. Since the Level-1 Muon triggers are limited to $|\eta| \leq 2.4$, ME muons cannot satisfy the trigger requirements of the analysis event selection, outlined later in this chapter.

No direct requirement was made on muon type in this analysis.

Standardised muon identification selections are provided by MCP to allow analyses to specify their desired quality of reconstructed muons. The selections aim to suppress background muons originating from kaon and pion decays while still maintaining a high prompt muon selection efficiency. Track-related variables are utilised as discriminators, since muons originating from in-flight hadron decays typically show an identifiable kink in their tracks. Requirements are also made on the number of hits in the ID and MS in order to ensure a robust momentum measurement. Loose muons were used for this analysis, designed to maximise muon reconstruction efficiency while still maintaining good quality tracks. The selection requires CB muons within $|\eta| < 0.1$ to register at least one hit in an MDT layer, increasing to three or more hits for $|\eta| > 0.1$. ME muons are required to have three or more hits across the MDT/CSC layers, and are used solely within $2.5 < |\eta| < 2.7$. CT and ST muons are allowed within $|\eta| < 0.1$. The absolute value of the difference between the ratio of the charge and momentum of muons measured in the ID and MS, divided by the sum in quadrature of their uncertainties, is required to be less than 7. For $4 < P_T < 20$ GeV and $20 < P_T < 100$ GeV, Loose muons are reconstructed with efficiencies of 96.7% and 98.1% respectively, alongside background muon reconstruction efficiencies of 0.53% and 0.76% [119].

All analysis muons were restricted to $|\eta| < 2.7$, the total region within which ATLAS can reconstruct muons. A $P_T > 15$ GeV requirement was also imposed to suppress background muons from QCD multi-jet processes.

To suppress muons originating from pile-up and cosmic interactions, impact parameters cuts were also applied. The absolute significance of the distance of closest approach of a muon to the beam line (BL) in the transverse plane, $|d_0^{BL}\text{significance}|$, was required to be less than 3. The corresponding longitudinal impact parameter, z_0, was also utilised in the requirement $|\Delta z_0^{PV} \times \sin(\theta)| < 0.5$ mm, with PV the Primary Vertex of the event (defined in Section 6.6). Both cuts were recommended by the ATLAS Tracking Combined Performance Group. Muons from boson decays are typically well separated from other event particles, as opposed to muons produced in semi-leptonic meson decays, which are typically embedded in jets. Selections were therefore also imposed on the isolation of muon candidates to further reduce the prominence of background muons. In this analysis,

muons were required to satisfy the LooseTrackOnly isolation criteria. The working point utilises a track-based isolation variable, $P_T^{\text{varcone30}}$, defined as the scalar sum of the P_T of tracks with $P_T > 1$ GeV within a cone of size $\Delta R = \min(\frac{10\text{GeV}}{P_T^\mu}, 0.3)$ around a muon with transverse momentum P_T^μ, excluding the momentum of the muon track itself [119]. LooseTrackOnly applies cuts to the ratio of $P_T^{\text{varcone30}}$ to P_T^μ in (η^μ, P_T^μ) bins such that a flat 99% muon reconstruction efficiency is observed.

A summary of all muon object cuts used in the analysis is presented in Table 6.1.1.

Variable	Requirement
P_T	> 15 GeV
$\lvert\eta\rvert$	< 2.7
Isolation	LooseTrackOnly
Identification	Loose
d_0	$\lvert d_0^{BL}\text{significance}\rvert < 3$
z_0	$\lvert\Delta z_0^{PV} \times \sin(\theta)\rvert < 0.5$ mm

Table 6.1.1: The muon object selection used in the analysis.

6.2 Jets

Jets are highly-collimated collections of particles originating from partons produced in high energy collisions. They are most simply defined using cone algorithms, which structure jets as collections of partons within a cone of radius R. The cone's axis is chosen such that jet energy is maximised, with jet momentum defined as the sum of the constituent parton's momenta. Such algorithms take topological calorimeter cell deposits as inputs; starting from a seed cell of high significance (defined as the ratio of the cell energy to its average expected noise), a growing-volume algorithm [120] combines the seed with neighbouring cells satisfying specific growth requirements to form proto-clusters. Those containing two or more local maxima undergo cluster splitting, so as to enable the study of jet substructure. Resulting topological cell clusters contain both shape and location information, benefiting the calibration of calorimeter signals and the later reconstruction of physics objects.

Complications with cone algorithms arise in instances where cones overlap. Clustering algorithms offer an alternative approach to jet formulation, where partons separated by less than a set amount are iteratively combined. This analysis makes use of the anti-k_t

clustering algorithm, which uses distance measures

$$d_{ij} = \min(k_{ti}^{-2}, k_{tj}^{-2}) \frac{\Delta_{ij}^2}{R^2}, \tag{6.2.1}$$

$$d_{iB} = k_{ti}^{-2}, \tag{6.2.2}$$

with B the beamline, $\Delta_{ij}^2 = (y_i - y_j)^2 + (\phi_i - \phi_j)^2$ and k_{ti}, y_i and ϕ_i the transverse momentum, rapidity and azimuthal angle of the ith particle respectively [121]. The algorithm considers all object combinations, combining particles i and j when $d_{ij} < d_{iB}$. R was set to the recommended value of 0.4 in this analysis. Jets reconstructed with this criteria were henceforth referred to as AntiKt4EMTopo jets, with EM referring to the energy scale of the reconstructed jets (ElectroMagnetic).

Once reconstructed, analysis jets were required to possess a $P_T > 25$ (30) GeV for $|\eta| < 2.4$ ($2.4 < |\eta| < 4.5$). The increased P_T requirement in forward regions was imposed to reduce the contributions of jets originating from pile-up interactions.

To identify and remove fake jets originating from cosmic muon showers, beam-induced backgrounds and calorimeter cell bursts, analysis jets were required to pass the BadLoose selection detailed in [122]. The selection makes use of the fractional energy deposits of jets in different regions of ATLAS, along with the average pulse quality of the calorimeter cells, and possesses a 99.5% selection efficiency for jets with $P_T > 20$ GeV.

Pile-up jets were further suppressed through requiring a cut on the output of the Jet Vertex Tagger (JVT) [123] provided by the ATLAS JetEtMiss group. The discriminant is constructed as a 2D likelihood based on the k-Nearest Neighbour algorithm [116], utilising two variables: R_{P_T}, the scalar P_T sum of all tracks associated with a jet that originate from the primary vertex, normalised to the fully calibrated jet P_T, and corrJVF, which shares the same numerator as R_{P_T} but is instead normalised by the scalar P_T sum of all associated tracks (with pile-up corrections applied). The analysis required each jet with $P_T < 60$ GeV and $|\eta| < 2.4$ to have a JVT output value greater than 0.59, in accordance with the recommendations of the ATLAS JetEtMiss group, corresponding to jet selection efficiencies of up to 92%.

Jets identified to have originated from b-quarks were labelled b-jets and were subject to a cut using the officially provided MV2c10 tagger [124], in order to reduce $t\bar{t}$ background contributions. The MV2 algorithms are BDTs trained to separate b-jets (signal) from light (u, d, s-quark or gluon)-jets and c-jets (background). The ratio of light to charm jets used in the background training samples varies between taggers, and for MV2c10 is 90:10. Events containing b-jets passing the 60% selection efficiency working point of MV2c10, corresponding to a cut of 0.9349, were then vetoed. Higher selection efficiencies were avoided due to the risk of vetoing $H \to \mu\mu$ signal events.

A summary of all jet object cuts used in the analysis is presented in Table 6.2.1.

Variable	Requirement
Algorithm	AntiKt4EMTopo
P_T	> 25 GeV for $\|\eta\| \leq 2.4$
	> 30 GeV for $2.4 < \|\eta\| < 4.5$
$\|\eta\|$	< 4.5
Cleaning	No "BadLoose" Jets
JVT	JVT > 0.59 for $P_T < 60$ GeV and $\|\eta\| < 2.4$

Table 6.2.1: The jet object selection used in the analysis.

6.3 Electrons

While electrons were not directly studied in the analysis, since their contributions to the $H \to \mu\mu$ final state are minimal, they were involved in the overlap removal procedure (see Section 6.5), and were thus subject to the following selection criteria.

Small regions of the EM calorimeter contain faulty electronics, such as dead front end boards, heavy voltage power supplies and cell cores. To avoid electrons reconstructed near these parts (which may lead to measurement inefficiencies), the BADCLUSELECTRON cut provided by the ATLAS e/γ group was applied. The cut considers the position of analysis electrons, and vetoes those reconstructed within the aforementioned faulty regions.

Each electron was required to possess a P_T greater than 7 GeV, and be reconstructed within $|\eta| < 2.47$. Those reconstructed between the barrel and end-caps of the EM calorimeter ($1.37 < |\eta| < 1.52$) were vetoed, due to the region's reduced resolution. The pile-up robust FCLoose isolation working point was utilised, requiring $\frac{E_T^{\text{topocone20}}}{P_T^e} < 0.2$, with $E_T^{\text{topocone20}}$ defined as the pile-up corrected sum of the energies of the topological clusters within a cone of size $\Delta R = 0.2$ around an electron. The energies of clusters within $\Delta R < 0.1$ are removed to exclude the energy deposits of the electron itself. For electrons with

- $|d_0^{BL}\text{significance}| < 3$,
- $|\Delta z_0^{PV} \times \sin(\theta)| < 0.5$ mm,
- $P_T^e > 1$ GeV,

$\frac{P_T^{\text{varcone20}}}{P_T^e} < 0.15$ was also required.

Electrons were required to pass impact parameter requirements of $|d_0^{BL}\text{significance}| < 3$ and $|\Delta z_0^{PV} \times \sin(\theta)| < 0.5$ mm in order to reduce pile-up and cosmic contributions. Candidates were also required to satisfy the Medium Likelihood identification criteria

provided by the ATLAS e/γ group, found to select electrons and background events with efficiencies (as functions of E_T) of roughly 90% and 0.003% respectively [125]. The selection utilises discriminants formed using the likelihood-based method, where the probability density functions of input variables are combined to determine the likelihood an electron candidate is signal or background. Such input variables include electron shower shapes, impact parameters and tracking information from the TRT.

A summary of all electron object cuts used in the analysis is presented in Table 6.3.1.

Variable	Requirement
P_T	> 7 GeV
$\|\eta\|$	< 2.47
	exclude $1.37 < \|\eta\| < 1.52$
Isolation	FCLoose
Identification	Medium Likelihood
Quality	Exclude BADCLUSELECTRON
d_0	$\|d_0^{BL}\text{significance}\| < 3$
z_0	$\|\Delta z_0^{PV} \times \sin(\theta)\| < 0.5$ mm

Table 6.3.1: The electron object selection used in the analysis.

6.4 E_T^{miss}

E_T^{miss} was calculated using the kinematic contributions of muons, electrons and jets passing the aforementioned selections. The calculation also included a Track-based Soft Term (TST) accounting for the energies of ID tracks not associated to physics objects [126]. It was performed using the official METMaker package provided by the ATLAS JetEtMiss group.

6.5 Overlap Removal

Pile-up, final state radiation and bremsstrahlung (among other effects) often result in the reconstruction of multiple overlapping objects. Overlap removal outlines the precedence with which such objects are retained, reducing the likelihood of double counting objects from the same event, and helping to preserve the objects of greatest interest to the analysis. The ΔR separation of the objects in question was used as the figure of merit. The following criteria were applied:

- Jets resolved within $\Delta R < 0.2$ of an electron were removed.

- Electrons resolved within $0.2 < \Delta R < 0.4$ of a jet were removed.
- Jets resolved within $\Delta R < 0.4$ of a muon were removed (unless more than 2 tracks were associated to the jet, in which case the muon was removed).
- Electrons sharing a track with an identified muon were removed.

Both taus and photons were not used for overlap removal within the analysis, and thus no explicit selections were defined. This was thought to have little impact on the final result, since the majority of tau decays are hadronic, and those involving muons typically have an identifiable kink in their track, allowing them to be vetoed.

6.6 Event Selection

Data events were required to belong to one of the GRLs listed in Table 4.1.1, during which data was taken in good detector conditions. The events also underwent event cleaning, in which those deemed incomplete, or found to contain LAr noise bursts, or corruptions in the Tile Calorimeter and/or SCT were removed. Events found to contain jets failing the BadLoose selection described in Section 6.2 were removed.

All data and MC events were required to contain a primary vertex. Candidate vertices were selected by performing a vertex fit to clusters of tracks, with PV(s) identified based on their compatibility with the beam line (using the z-coordinate of their distance of closest approach).

Events from (or modelling) the 2015 dataset were required to pass either the HLT_mu20_iloose_L1MU15 or HLT_mu50 triggers, while 2016 and 2017 events were required to fire either the HLT_mu26_ivarmedium or HLT_mu50 triggers. A muon was required to be within $\Delta R < 0.1$ of each trigger fired in each event. While HLT_mu20_iloose_L1MU15 and HLT_mu26_ivarmedium were the lowest unprescaled triggers of their respective datasets, allowing for the study of lower P_T muons, their inclusive isolation requirements (iloose and ivarmedium) risked lowering the muon selection efficiency. This motivated the combined use of the HLT_mu50 trigger, which has no such requirement.

Exactly two muons of opposite charge were required to be present in each event. To ensure the aforementioned triggers fired, the leading muon was required to possess a $P_T > 27$ GeV, with the subleading muon P_T limited to > 15 GeV by the previously detailed muon object selection.

To reduce contributions from top and di-boson processes, events with $E_T^{\text{miss}} > 80$ GeV were vetoed. $t\bar{t}$ events were suppressed through application of the b-jet veto cut outlined in Section 6.2.

Successfully selected events were then sorted into different categories based on their respective $M_{\text{inv}}^{\mu\mu}$ values. Signal region events were defined to lie within $110 \leq M_{\text{inv}}^{\mu\mu} \leq 160$

GeV, with the Signal Plus Jets region containing events with two or more jets from the same mass window. The $120 \leq M_{\text{inv}}^{\mu\mu} \leq 130$ GeV portion of both regions was blinded while the analysis underwent validation. This entailed studying the kinematic distributions of muons in regions thought to be well modelled, such as around the Z mass peak. Major discrepancies here would highlight issues with the analysis selection and approach, which might bias the final result. This motivated the definition of the Z and Z Plus Jets control regions, defined as $76 \leq M_{\text{inv}}^{\mu\mu} \leq 106$ GeV and $76 \leq M_{\text{inv}}^{\mu\mu} \leq 106$ GeV + 2 $\leq$ jets respectively. Control distributions of kinematic variables in each of these regions are presented in Chapter 8, while Table 6.6.1 summarises the event selection criteria used in the analysis.

Variable	Requirement
Good Run List	Pass
Event Clean	Pass
Number of Muons	2
Trigger	HLT_mu20_iloose_L1MU15 OR HLT_mu50 (2015 data)
	HLT_mu26_ivarmedium OR HLT_mu50 (2016/2017 data)
Trigger Matching	Yes
P_T^{μ}	$P_T^{\mu,\text{Leading}} > 27$ GeV
	$P_T^{\mu,\text{Subleading}} > 15$ GeV
Muon Charge	Opposite charge sign for selected muons
E_T^{miss}	$E_T^{\text{miss}} < 80$ GeV
b-jet Veto	Reject if pass MV2c10 60% WP for $P_T^{\text{jet}} > 20$ GeV and $\lvert\eta^{\text{jet}}\rvert < 2.5$
$M_{\text{inv}}^{\mu\mu}$	$76 \leq M_{\text{inv}}^{\mu\mu} \leq 106$ GeV (Z control region)
	$76 \leq M_{\text{inv}}^{\mu\mu} \leq 106$ GeV + ≥ 2 jets (Z Plus Jets control region)
	$110 \leq M_{\text{inv}}^{\mu\mu} \leq 160$ GeV (Signal region)
	$110 \leq M_{\text{inv}}^{\mu\mu} \leq 160$ GeV + ≥ 2 jets (Signal Plus Jets region)

Table 6.6.1: The event selection used in the analysis.

Table 6.6.2 presents the efficiencies of the cuts listed in Table 6.6.1. Efficiencies are presented for both signal and background MC samples, along with data. Each efficiency was calculated with respect to the previous cut, with event weights not yet applied to the MC. Along with the full object selections detailed in Tables 6.1.1 to 6.3.1, a loose pre-selection had already been applied to each sample, prior to entering the cut-flow. This included GRL and event cleaning cuts for data, along with loose P_T^{μ}, η^{μ} and NLepton requirements, applied so as to reduce the number of events being processed during later stages of the analysis. These cuts are summarised in Table 6.6.3.

Selection efficiencies of 89%, 88%, 63% and 13% were achieved in the Signal region for ggF, VBF, VH and $t\bar{t}H$ respectively. The selection efficiencies of VH and $t\bar{t}H$ were lowered significantly by the two muon, E_T^{miss} and b-jet veto cuts, which were optimised during previous $H \to \mu\mu$ analyses [27] where the focus was only on ggF and VBF events. Since the expected event yields for these processes with 80.5 fb^{-1} are 95% and 98% (40% and 86%) lower than those of ggF (VBF), their contributions to the analysis would be minimal. Their selection efficiencies were thus deemed acceptable. Future analyses using greater luminosities could of course benefit from optimising the event selection to accept more VH and $t\bar{t}H$ events.

The current selection did however reject 97% of Drell-Yan events within the Signal region, along with 95%, 94% and 75% rejection efficiencies for electroweak Z plus jet, di-boson and top events. For Drell-Yan, the largest losses came from the trigger, b-jet veto and mass cuts, with di-boson and top also showing 13 - 49% losses due to the E_T^{miss} cut. While it may seem desirable to lower the 25% selection efficiency of top events in the Signal region, after weighting the events, Drell-Yan was seen to contribute two orders of magnitude more events in the majority of analysis categories than the considered top processes. The issue was therefore deemed unimportant.

2.29% of the total data events were selected within the Signal region. The largest losses arose from the trigger and mass cuts. The data selection efficiencies closely match those of Drell-Yan, highlighting the domination of Drell-Yan events within the analysis.

Cut	ggF		VBF		VH		$t\bar{t}H$		Drell-Yan		Ewk Z+Jets		Di-boson		Top		Data	
Input	1299302	-	1373390	-	246211	-	549666	-	11886238	-	630305	-	32550189	-	22415315	-	73306692	-
Two Muons	1297516	99.86	1370734	99.81	226902	92.16	425598	77.43	11857950	99.76	629169	99.82	18907690	58.09	7859115	35.06	70778107	96.55
Trigger	1219394	93.98	1284318	93.70	212074	93.47	395997	93.04	10664321	89.93	563073	89.49	16407223	86.78	6812746	86.69	62396998	88.16
Trigger Matching	1219372	100.00	1284264	100.00	211971	99.95	394221	99.55	10662800	99.99	563034	99.99	16382582	99.85	6804407	99.88	62395188	100.00
$P_T^{\mu,\text{Leading}} > 27$ GeV	1216480	99.76	1283310	99.93	211834	99.94	393931	99.93	10591949	99.34	559448	99.36	16186741	98.80	6728359	98.88	60934223	97.66
$P_T^{\mu,\text{Subleading}} > 15$ GeV	1216480	100.00	1283310	100.00	211834	100.00	393931	100.00	10591949	100.00	559448	100.00	16186741	100.00	6728359	100.00	60934223	100.00
Opposite Sign	1216448	100.00	1283241	99.99	210137	99.20	378850	96.17	10590673	99.99	559406	99.99	15482453	95.65	6640810	98.70	60892854	99.93
$E_T^{\text{miss}} < 80$ GeV	1209293	99.41	1268364	98.84	181546	86.39	274305	72.40	10478233	98.94	552185	98.71	13525184	87.36	4096510	61.69	60515297	99.38
b-jet Veto	1194354	98.76	1245363	98.19	162101	89.29	75017	27.35	9717701	92.74	541205	98.01	13067621	96.62	1181797	28.85	59737220	98.71
$66 < M_{\text{inv}}^{\mu\mu} < 106$ GeV	31926	2.67	32861	2.64	4638	2.86	2326	3.10	8787547	90.43	454668	84.01	8993308	68.82	247735	20.96	53577974	89.69
$110 < M_{\text{inv}}^{\mu\mu} < 160$ GeV	1157606	96.92	1206584	96.89	156059	96.27	71146	94.84	263631	2.71	23462	4.34	782449	5.99	295937	25.04	1366004	2.29

Table 6.6.2: Cut-flow table for the event selection used in the analysis. For each sample, the number of remaining events after each cut is shown, along with the percentage difference with respect to the previous cut. A loose pre-selection was applied to all samples before undergoing the selection, and no event weights were yet applied. The $M_{\text{inv}}^{\mu\mu}$ cuts are orthogonal, and were used to define the Z control region and Signal region respectively. The total number of data events processed (before pre-selection) corresponded to an integrated luminosity of 80.5 fb^{-1}.

Cut	Requirement
Good Run List	Yes
Event Clean	Yes
N_{Leptons}	$N_{\text{Muons}} + N_{\text{Electrons}} > 1$
$P_T^{\mu,\text{Leading}}$	> 17 GeV
$P_T^{\mu,\text{Subleading}}$	> 7 GeV
$\lvert\eta^{\mu}\rvert$	< 2.7

Table 6.6.3: Pre-selection applied to all samples from which the cut-flow presented in Table 6.6.2 was calculated.

Chapter 7

Drell-Yan Monte Carlo Generator Comparisons

Since the previous ATLAS $H \to \mu\mu$ analyses utilised Madgraph for the generation of their Drell-Yan MC samples, one may be tempted to follow suit. However, both Sherpa and Powheg provide alternative Drell-Yan samples, as listed in Table 4.2.2. This chapter presents a study comparing how each of the aforementioned MC generators model variables of interest in both the control and Signal regions.

7.1 $P_T^{\mu\mu}$ and $M_{\mathbf{inv}}^{jj}$ Re-weightings

The $P_T^{\mu\mu}$ distribution of the data was modelled poorly by each of the MC generators considered, due to initial state radiation (ISR) and soft gluon interactions complicating the determination of the sample cross-sections. Re-weighting factors were thus derived for each generator to correct the discrepancies. For each of the four regions considered (Z control region, Z Plus Jets control region, Signal region and Signal Plus Jets region) a 6th order polynomial was fit to the ratio of $P_T^{\mu\mu}$ between data and Drell-Yan MC (where all other MC contributions had been subtracted from the data). Correction factors derived from the fit were then applied to all Drell-Yan MC samples used in the analysis (with the exception of the spurious signal systematic sample described in Chapter 11). The factors were both derived and applied at the reconstructed event level.

A similarly-motivated M_{inv}^{jj} re-weighting factor was also derived for the Madgraph, Sherpa and Powheg Drell-Yan samples in each region. 3rd order polynomial fits were made to the ratio of M_{inv}^{jj} between data and Drell-Yan MC (where all other MC contributions had been subtracted from the data, and $P_T^{\mu\mu}$ corrections already applied). The resulting correction factors were applied to all Drell-Yan MC samples used in the analysis (with the spurious signal systematic sample again the exception). It should be noted that

events containing fewer than two jets had no associated M_{inv}^{jj} value, and thus did not undergo M_{inv}^{jj} re-weighting.

Figures 7.1.1 and 7.1.2 present fits to the ratios between the Madgraph, Sherpa and Powheg Drell-Yan MC samples and data, as functions of $P_T^{\mu\mu}$ and M_{inv}^{jj}, in the Z and Z Plus Jets control regions. The fits perform adequately in most instances, although there is room for improvement. All of the fits appear to be pulled by the overflow bins at 200 GeV, which have low statistical errors. These could in principle be ignored in future fits. The distorted shape of the Madgraph $P_T^{\mu\mu}$ distributions below 65 GeV appear to disrupt the fit significantly. The Sherpa $P_T^{\mu\mu}$ distributions lack smoothness in general, due to the sliced nature of the input samples. This undoubtedly affected the fit detrimentally. A discrepancy at low $P_T^{\mu\mu}$ is also seen in the Powheg distributions. One may expect better agreement than what is shown for each generator before any re-weighting is applied. These discrepancies in normalisation are likely due to the E_T^{miss} and b-veto cuts outlined in Chapter 6, which affect the normalisation cross-sections of the samples. While these cuts could in principle be removed from the control regions, they have been kept to maintain consistency with the Signal region selections.

The M_{inv}^{jj} fits perform reasonably well for the Madgraph and Sherpa distributions. The Powheg fits perform poorly, with discrepancies as large as 30%. This is likely due to the known limitations of the generator in modelling multi-jet events. Spline fits were attempted as an alternative solution, but their over-sensitivity to statistical fluctuations in the $P_T^{\mu\mu}$ and M_{inv}^{jj} distributions made them an overall less stable choice.

Figures 7.1.3 and 7.1.4 present data-MC comparisons of the $P_T^{\mu\mu}$ and M_{inv}^{jj} distributions of the Madgraph, Sherpa and Powheg samples in the Z control region before and after application of the aforementioned re-weighting factors. Only statistical errors are presented. The $P_T^{\mu\mu}$ re-weighting factor improves the $P_T^{\mu\mu}$ modelling of Sherpa and Powheg by $\geq 10\%$ in general, with Madgraph's improvements smaller and more prominent in the low/high $P_T^{\mu\mu}$ regions. The M_{inv}^{jj} re-weighting factor improves M_{inv}^{jj} modelling in Madgraph and Sherpa by 5-10%, but shows little benefit for Powheg, which presents data-MC discrepancies larger than 20% throughout. The re-weighting also deteriorates the data-MC agreement shown in the Sherpa $P_T^{\mu\mu}$ distribution. This is likely due to inaccurate re-weighting factors derived from bins poorly modelled by the polynomial fits, identifying a general flaw of this methodology. Thus, despite Sherpa best modelling M_{inv}^{jj} after application of both re-weighting factors, Madgraph provides the best modelling of $P_T^{\mu\mu}$.

Figures 7.1.5 and 7.1.6 present polynomial fits to the $P_T^{\mu\mu}$ and M_{inv}^{jj} data-MC ratios in the Signal and Signal Plus Jets regions, using Madgraph, Sherpa and Powheg Drell-Yan MC samples. The ratios were derived after subtracting all non Drell-Yan MC samples from the data. The reduced number of events in the Signal regions lead to large statistical errors in the distributions. The fits are of similar quality to those of

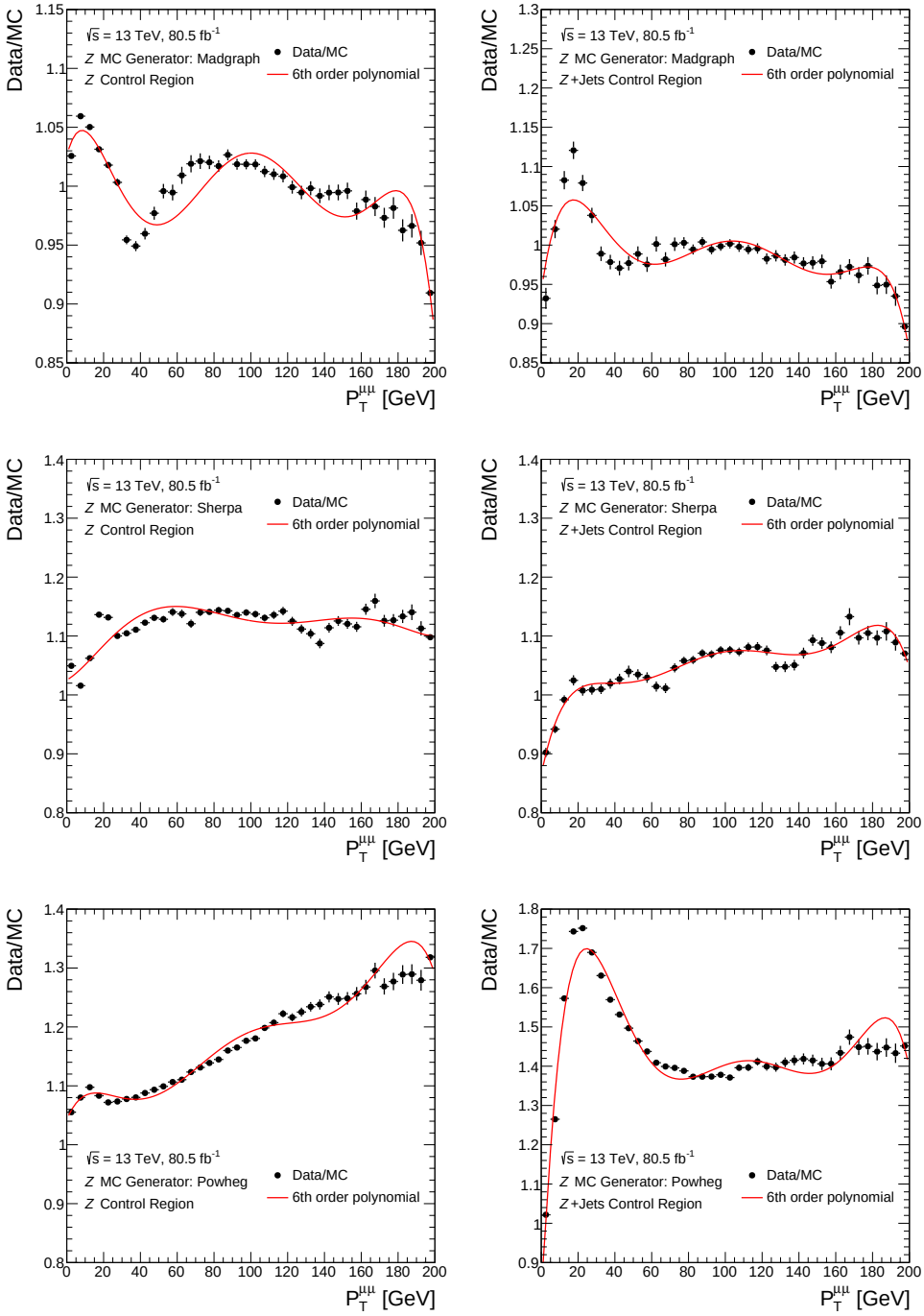

Figure 7.1.1: Fitting of a 6^{th} order polynomial to the data/MC $P_T^{\mu\mu}$ ratios in the Z (left) and Z plus jets (right) control regions. Separate fits are performed using Madgraph (top), Sherpa (middle) and Powheg (bottom) for the generation of the Drell-Yan MC.

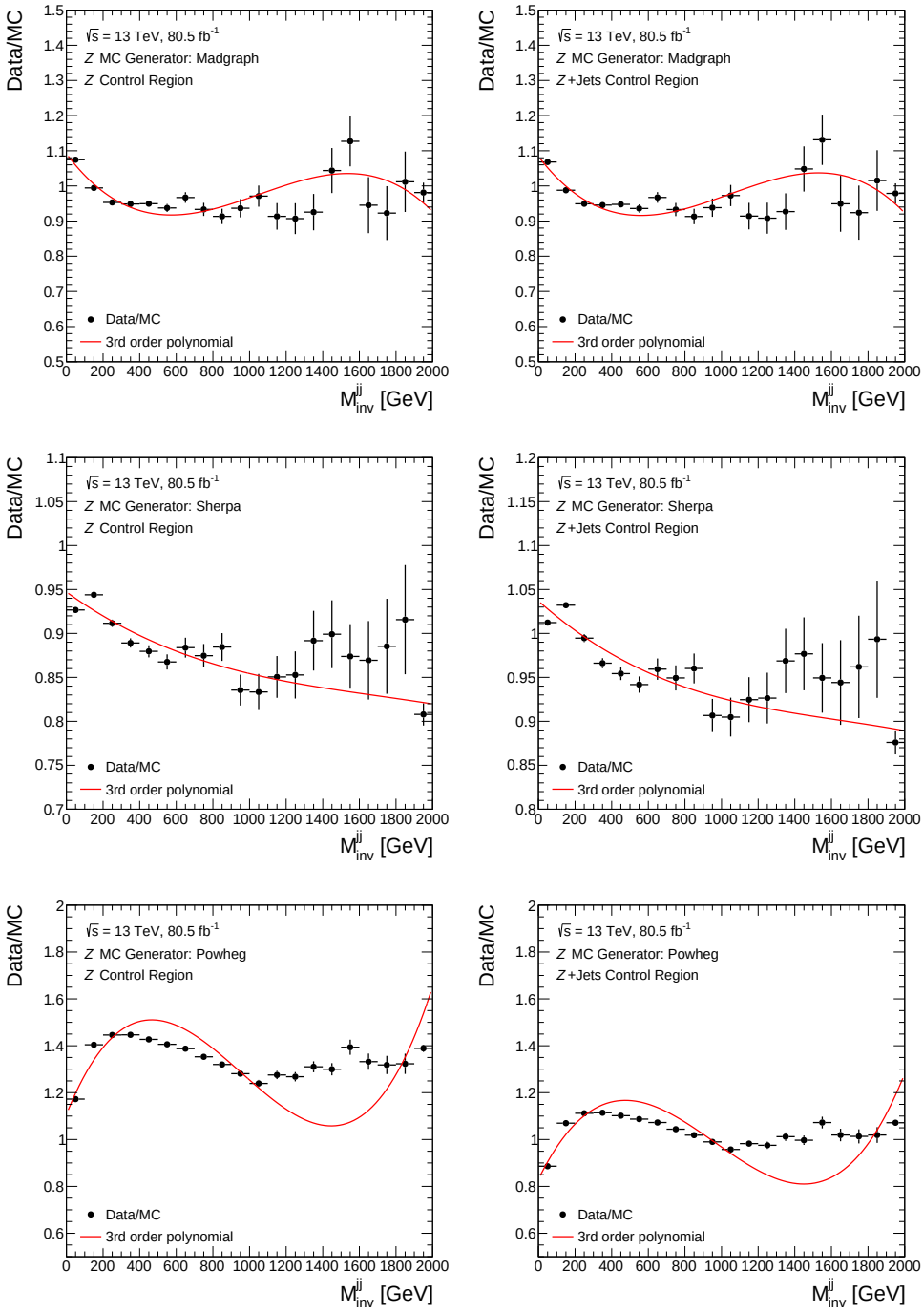

Figure 7.1.2: Fitting of a 3$^{\text{rd}}$ order polynomial to the data/MC M^{jj}_{inv} ratios in the Z (left) and Z plus jets (right) control regions. Separate fits are performed using Madgraph (top), Sherpa (middle) and Powheg (bottom) for the generation of the Drell-Yan MC.

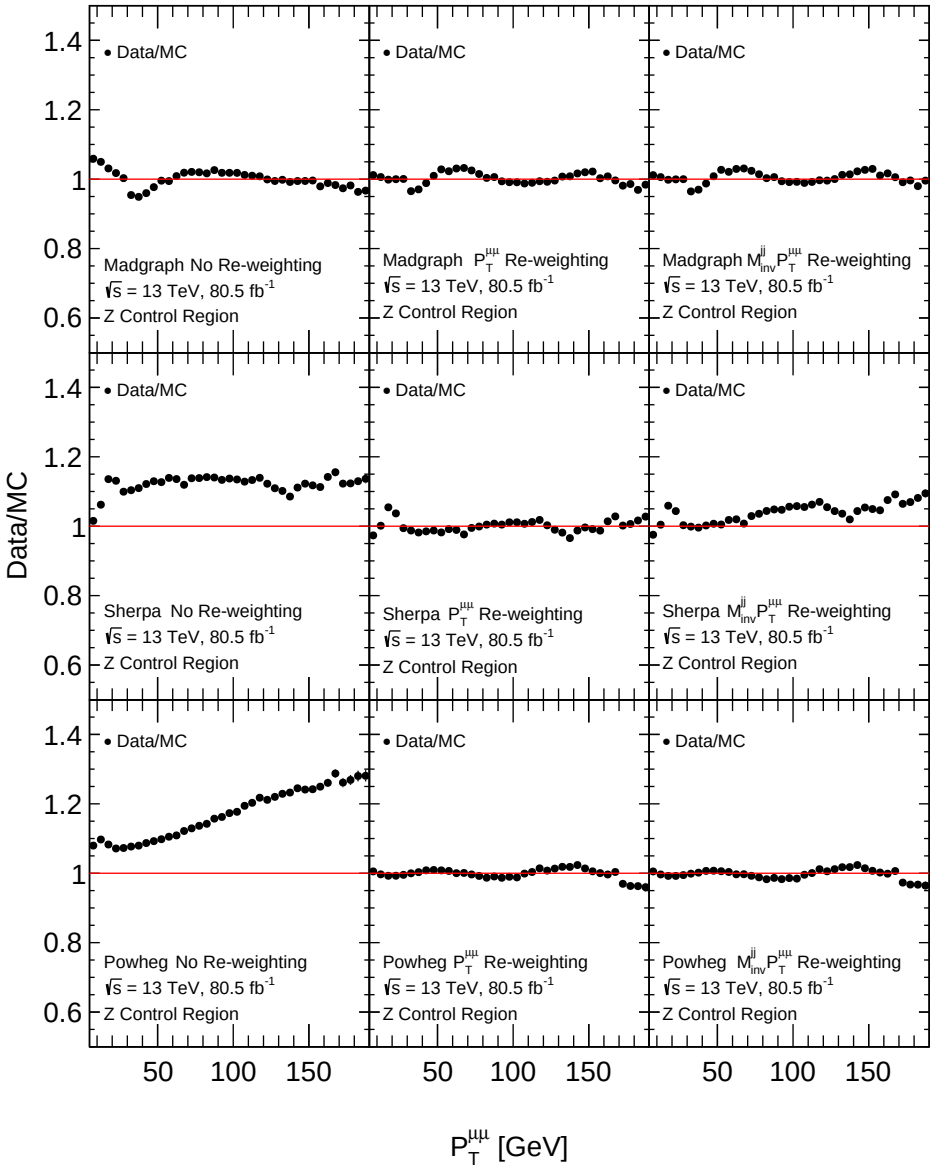

Figure 7.1.3: Comparisons between data and MC for $P_T^{\mu\mu}$ in the Z control region before (left) and after the application of the $P_T^{\mu\mu}$ (middle) and $M_{\rm inv}^{jj}$ (right) re-weightings described in Section 7.1. Madgraph, Sherpa and Powheg have been used for the generation of the Drell-Yan MC used in the top, middle and bottom rows respectively.

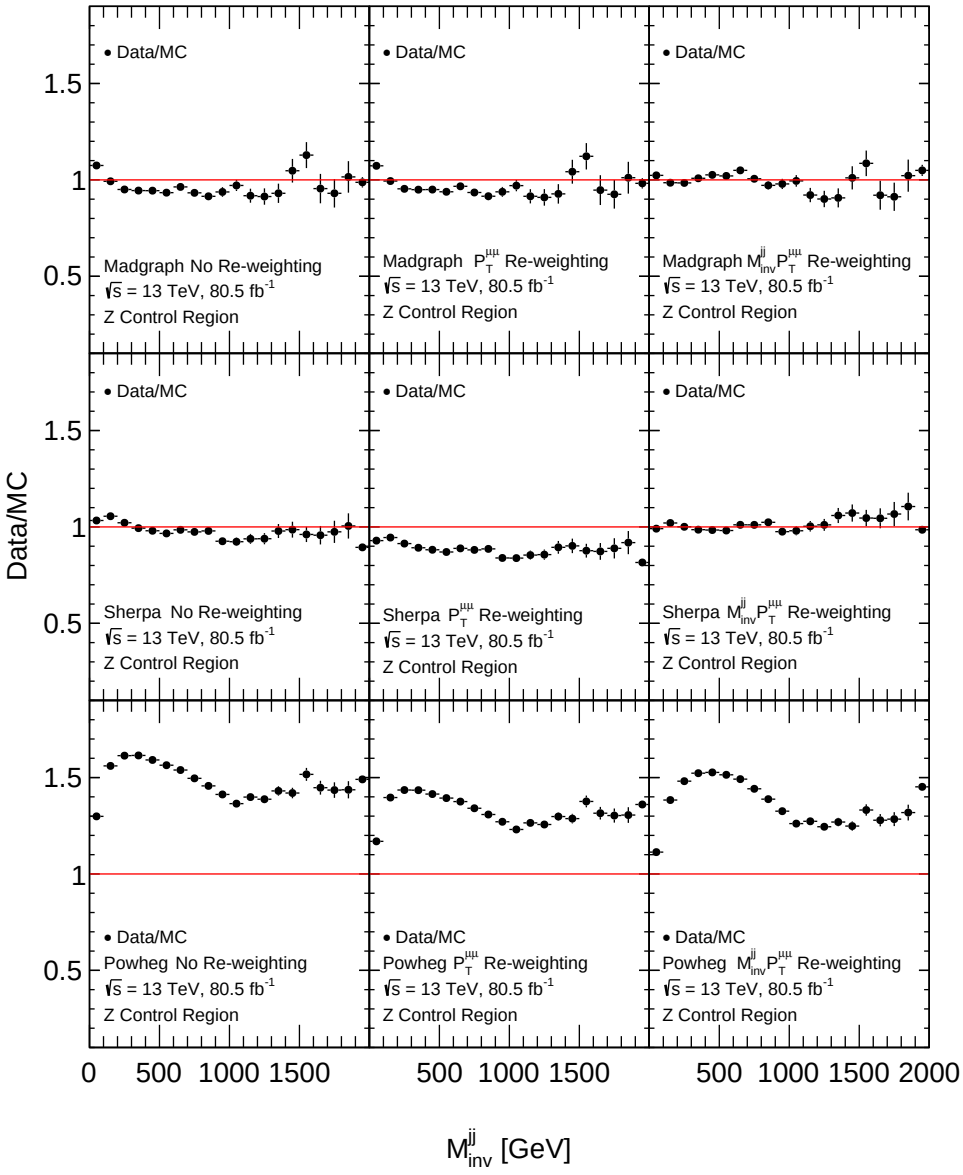

Figure 7.1.4: Comparisons between data and MC for $M_{\rm inv}^{jj}$ in the Z control region before (left) and after the application of the $P_T^{\mu\mu}$ (middle) and $M_{\rm inv}^{jj}$ (right) re-weightings described in Section 7.1. Madgraph, Sherpa and Powheg have been used for the generation of the Drell-Yan MC used in the top, middle and bottom rows respectively.

the control regions. The post-corrected $P_T^{\mu\mu}$ and M_{inv}^{jj} distributions are presented in Figures 7.1.7 and 7.1.8. The $P_T^{\mu\mu}$ re-weighting appears to have the largest effect on the Powheg distribution, reducing discrepancies by around 20%. Madgraph and Sherpa appear to model the distributions similarly well after re-weighting, with agreement within 20%, with Powheg again struggling to model M_{inv}^{jj}. The Powheg modelling of M_{inv}^{jj} deteriorates after application of the M_{inv}^{jj} re-weighting, due to the inaccuracy of its 3rd order polynomial fits.

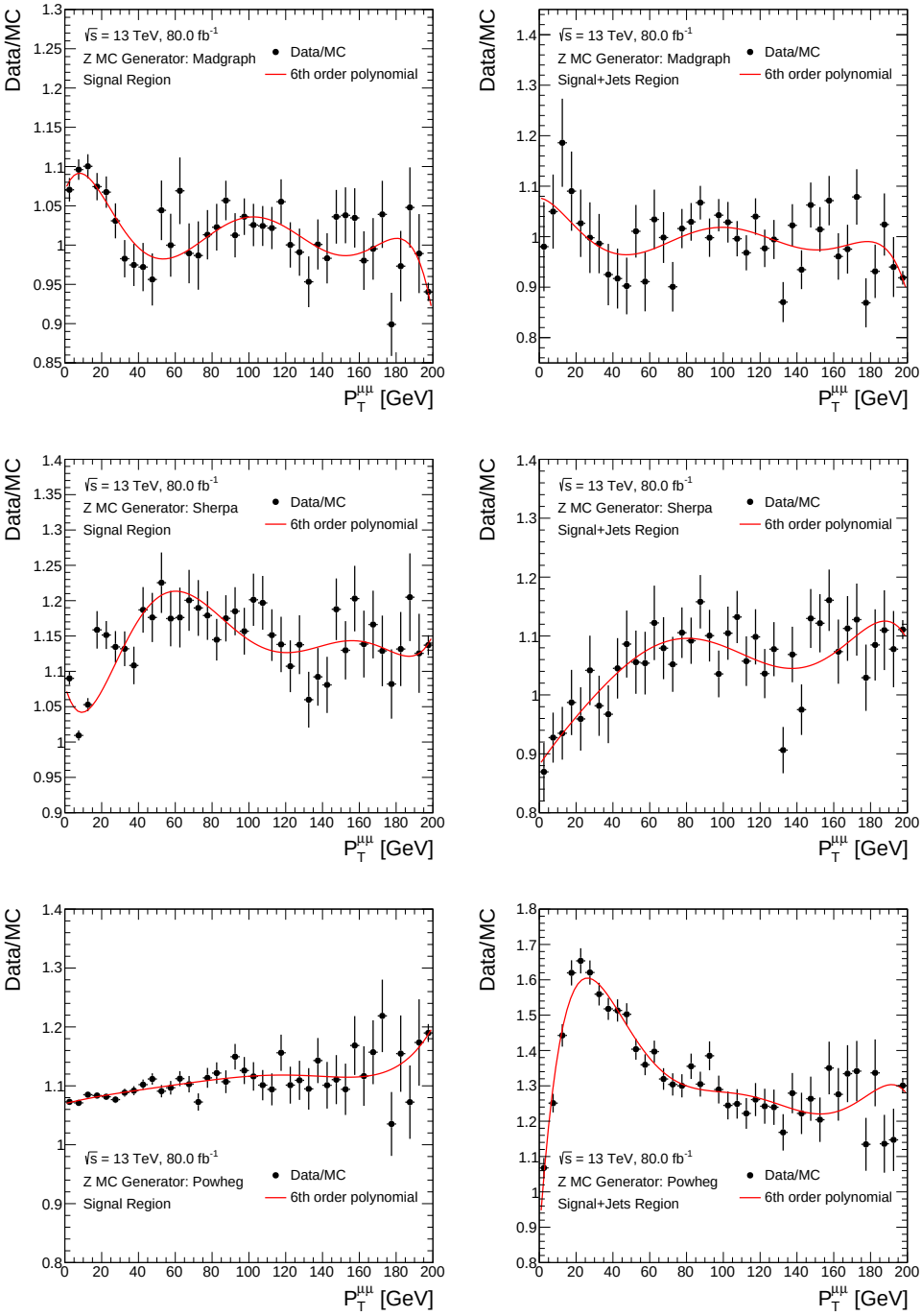

Figure 7.1.5: Fitting of a 6^{th} order polynomial to the data/MC $P_T^{\mu\mu}$ ratios in the Signal (left) and Signal plus jets (right) regions. Separate fits are performed using Madgraph (top), Sherpa (middle) and Powheg (bottom) for the generation of the Drell-Yan MC.

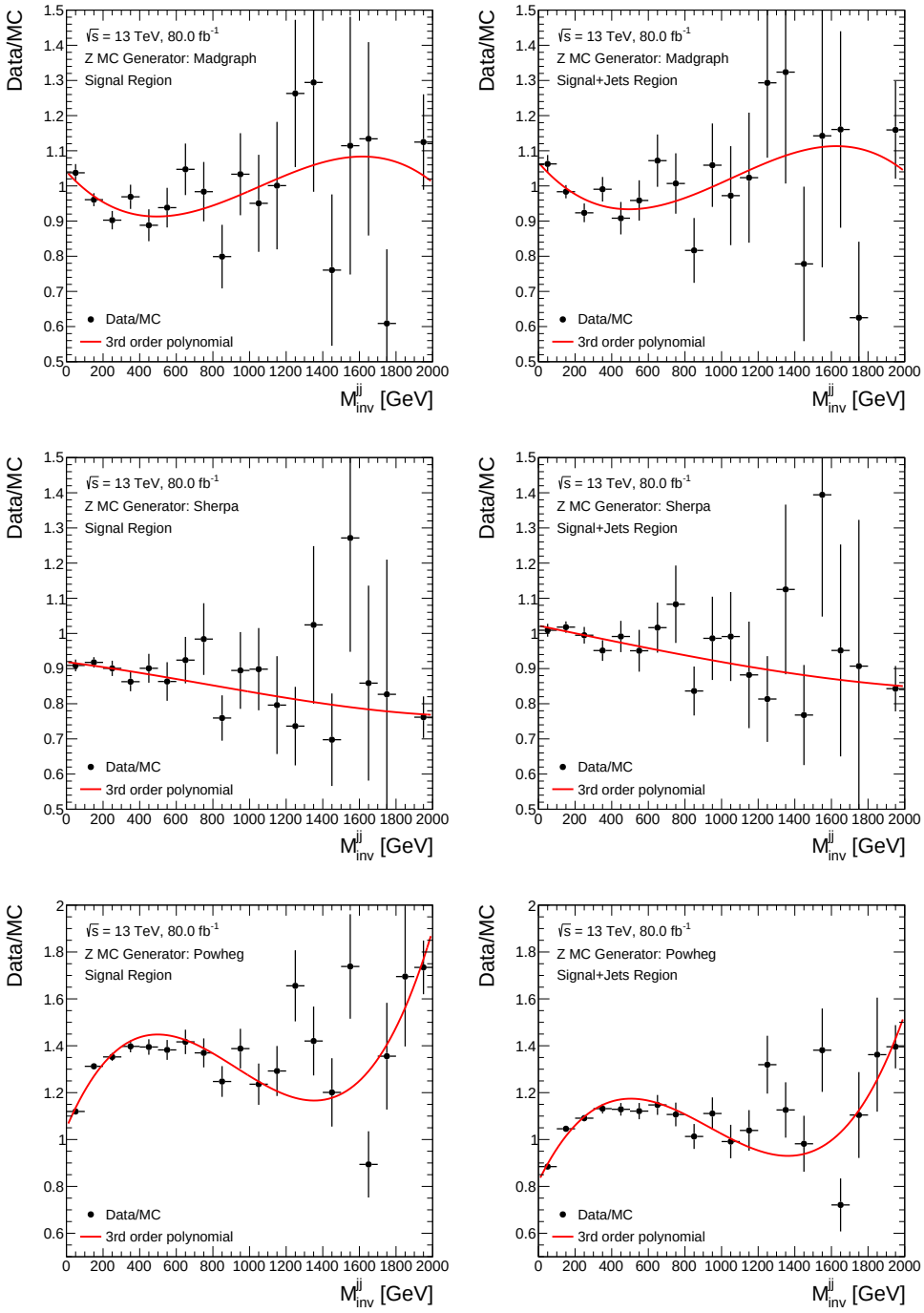

Figure 7.1.6: Fitting of a 3$^{\text{rd}}$ order polynomial to the data/MC M_{inv}^{jj} ratios in the Signal (left) and Signal plus jets (right) regions. Separate fits are performed using Madgraph (top), Sherpa (middle) and Powheg (bottom) for the generation of the Drell-Yan MC.

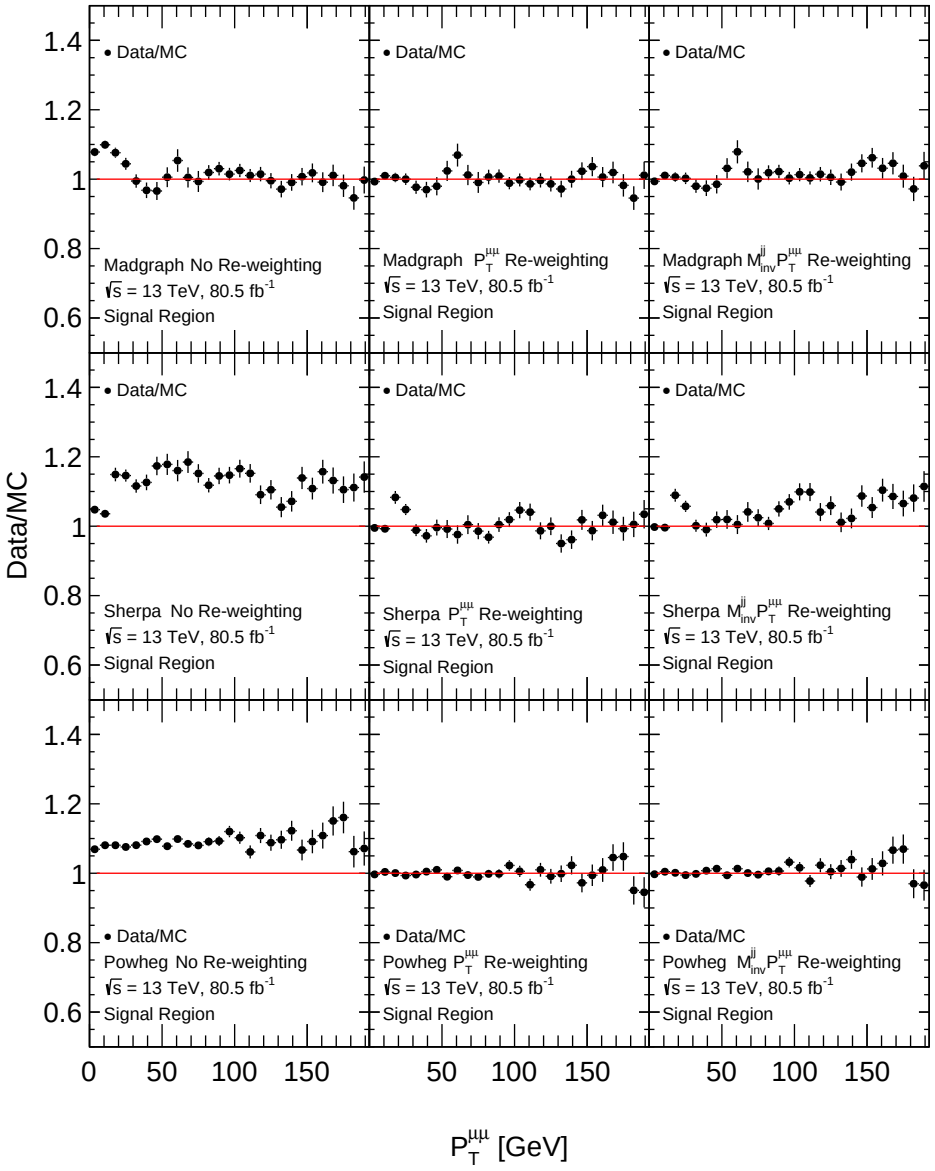

Figure 7.1.7: Comparisons between data and MC for $P_T^{\mu\mu}$ in the Signal region before (left) and after the application of the $P_T^{\mu\mu}$ (middle) and M_{inv}^{jj} (right) re-weightings described in Section 7.1. Madgraph, Sherpa and Powheg have been used for the generation of the Drell-Yan MC used in the top, middle and bottom rows respectively.

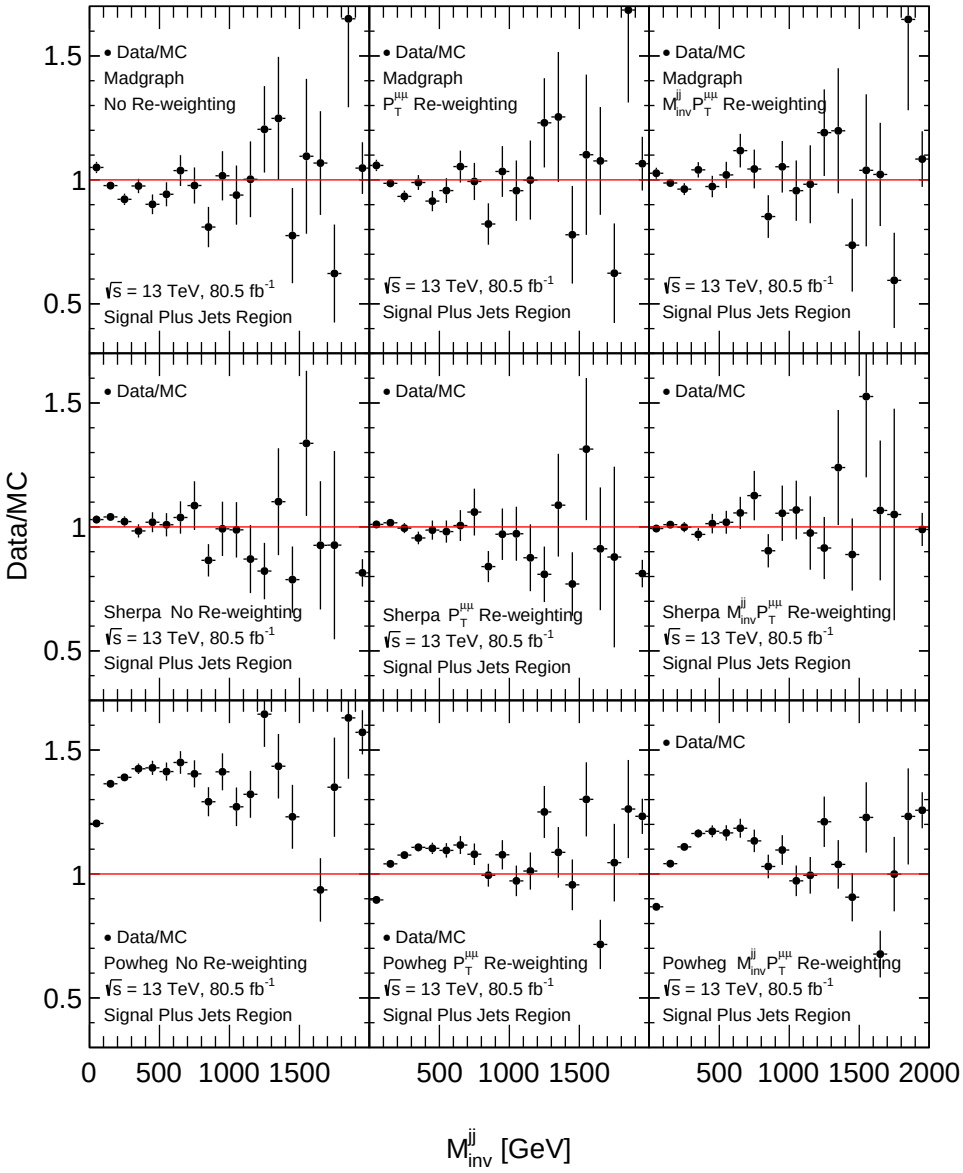

Figure 7.1.8: Comparisons between data and MC for $M^{jj}_{\rm inv}$ in the Signal plus jets region before (left) and after the application of the $P_T^{\mu\mu}$ (middle) and $M^{jj}_{\rm inv}$ (right) re-weightings described in Section 7.1. Madgraph, Sherpa and Powheg have been used for the generation of the Drell-Yan MC used in the top, middle and bottom rows respectively.

7.2 Distribution Comparisons

A major part of the analysis involved categorisation of events using Boosted Decision Trees (described fully in Chapter 9). For a classifier to correctly treat data, it must be trained using MC which accurately describes said data. It was therefore imperative that, as the dominant contributor to the data, the Drell-Yan MC sample used in the analysis accurately described the data as functions of each variable used to train the BDTs. Data-MC comparisons were therefore produced using Madgraph, Sherpa and Powheg Drell-Yan MC samples for each re-weighting step mentioned in the previous section. While the BDTs used in the analysis would only be trained and applied in the Signal regions, for the sake of completeness, the comparison studies were performed in all analysis regions. Since it was not known initially which variables would be used to train the BDTs, the comparisons were performed for a large number of variables thought to be potentially relevant to the analysis. The decision as to which variables were relevant was performed intuitively.

An example of one such comparison is presented below in Figure 7.2.1, where the $M_{\text{inv}}^{\mu\mu}$ distributions of data and Powheg, Sherpa and Madgraph Drell-Yan MC is compared in the Z control region. Without $P_T^{\mu\mu}$ or M_{inv}^{jj} re-weightings, normalisation discrepancies of 2-9% (depending on the MC generator) are seen, thought to be due to the cross-section predictions failing to describe the phase space regions with the E_T^{miss} and b-veto cuts applied. After corrections, agreement within 5% is seen for each generator, with Powheg presenting the smoothest distribution. Comparisons for other variables are presented in Appendix B.

To better quantify the levels of data-MC agreement, reduced-χ^2 values were computed between the data and MC distributions in each region, for each variable considered. The derived values are presented in Tables 7.2.1 to 7.2.4. While the reduced-χ^2 values are larger than what is typically acceptable (≈ 1), to determine the best re-weighting/MC sample combination, identifying the lowest reduced-χ^2 value per variable was all that was required. Such values are highlighted in bold in the tables, with the total number of bold values per column summarised in the bottom rows. Madgraph in combination with the $P_T^{\mu\mu}$ and M_{inv}^{jj} re-weightings was found to best model the largest number of variables across the majority of regions, with the nominal Sherpa configuration performing best in the Signal Plus Jets region. Since the latter result was a narrow victory, for the sake of completeness and convenience, $P_T^{\mu\mu}$+M_{inv}^{jj} re-weighted Madgraph was chosen for use in the remainder of the analysis. In general, Madgraph was found to best model jet variables, with Sherpa better modelling muon quantities. Since both sets of variables were used throughout the analysis, this was not considered an important distinction.

To factor out MC normalisation discrepancies, the study was also performed with the data and MC distributions normalised by the sum of their respective weights. This allowed the shapes of the distributions to be directly compared. Madgraph in combination

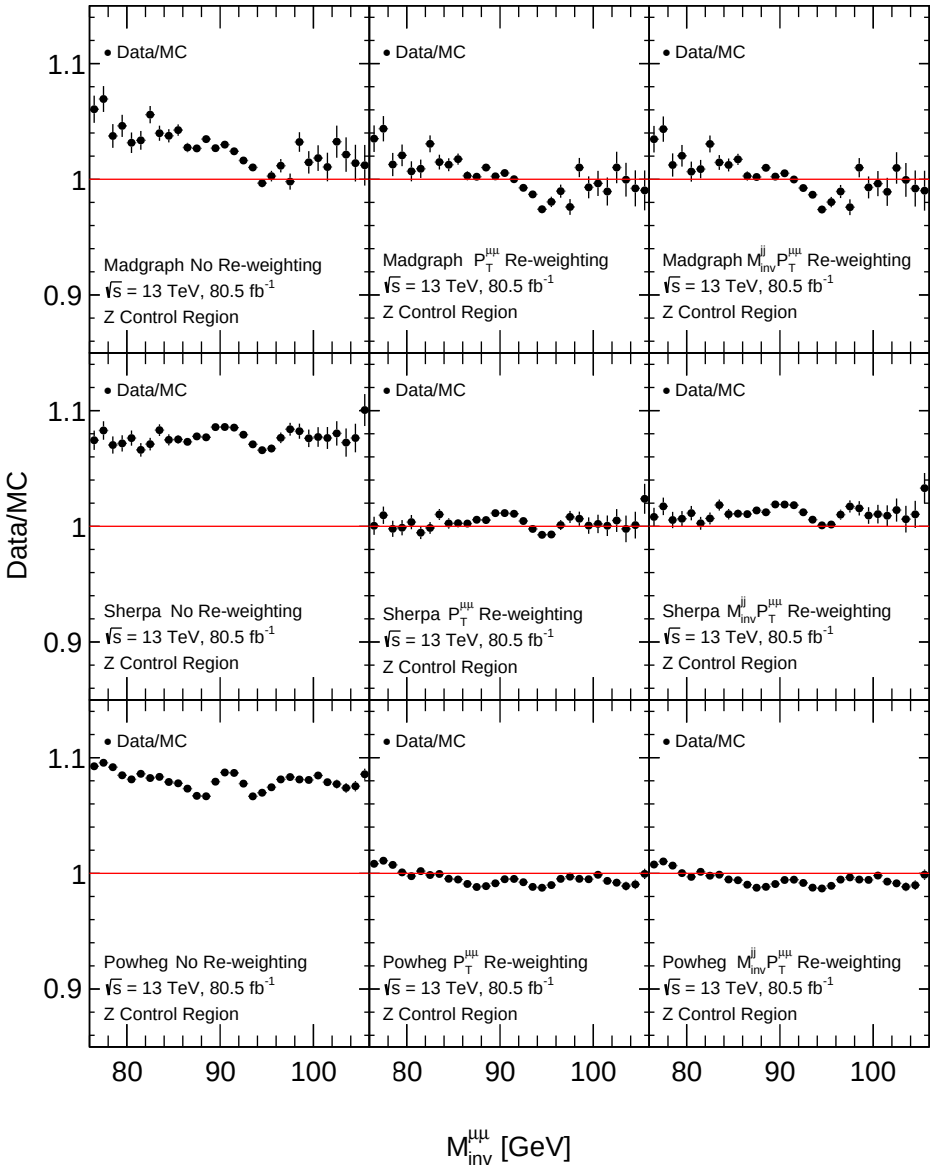

Figure 7.2.1: Comparisons between data and MC for $M_{\rm inv}^{\mu\mu}$ in the Z control region before (left) and after the application of the $P_T^{\mu\mu}$ (middle) and $M_{\rm inv}^{jj}$ (right) re-weightings described in Section 7.1. Madgraph, Sherpa and Powheg have been used for the generation of the Drell-Yan MC used in the top, middle and bottom rows respectively.

with the $P_T^{\mu\mu}$ and M_{inv}^{jj} re-weightings was again found to best model the data.

Variable	χ^2/NDF								
	Madgraph			Sherpa			Powheg		
	Nominal	$P_T^{\mu\mu}$	$M_{\text{inv}}^{jj} P_T^{\mu\mu}$	Nominal	$P_T^{\mu\mu}$	$M_{\text{inv}}^{jj} P_T^{\mu\mu}$	Nominal	$P_T^{\mu\mu}$	$M_{\text{inv}}^{jj} P_T^{\mu\mu}$
$P_T^{\mu,\text{Leading}}$	91.19	**4.40**	7.19	62.73	9.20	23.93	353.55	105.81	107.49
$P_T^{\mu,\text{Subleading}}$	31.31	6.91	9.06	20.25	**6.32**	12.60	136.85	66.82	71.44
$P_T^{\mu\mu}$	122.09	**17.95**	27.37	169.06	47.05	92.19	487.98	31.24	33.41
d_0^{BL}significance	548.60	542.55	**541.63**	968.01	958.84	966.69	6578.61	7252.38	7251.67
$\Delta z_0^{PV} \sin\theta$	707.46	700.38	**698.94**	1227.97	1224.65	1219.80	9986.99	10343.50	10339.30
$\eta^{\mu,\text{Leading}}$	28.64	28.31	28.15	**11.60**	11.99	11.75	111.00	109.09	109.15
$\eta^{\mu,\text{Subleading}}$	22.09	21.96	22.10	13.24	**12.30**	12.46	71.08	70.48	70.30
E_T^{miss}	**13.43**	31.76	31.53	179.83	151.41	112.94	2637.89	1936.72	1914.29
$M_{\text{inv}}^{\mu\mu}$	7.90	7.29	7.29	3.58	3.37	**3.04**	41.09	12.21	12.20
$\Delta\phi^{\mu\mu}$	**140.06**	177.66	179.01	884.81	525.13	600.26	4778.55	3358.79	3323.96
$y^{\mu\mu}$	2.64	2.65	**2.63**	4.86	4.95	4.50	34.70	25.76	25.71
$\phi^{\mu,\text{Leading}}$	**3.82**	**3.82**	**3.82**	7.84	7.70	7.68	43.44	43.01	43.00
$\phi^{\mu,\text{Subleading}}$	3.18	**3.16**	**3.16**	3.98	3.91	3.90	31.72	31.80	31.84
$\phi^{\mu\mu}$	2.70	2.71	2.70	2.41	**2.35**	2.69	17.20	17.20	17.25
$< \mu >$	28756.70	28706.30	**28678.90**	44550.80	44162.00	44421.40	179329.00	179294.00	179241.00
$\Delta R^{\mu\mu}$	63.88	10.06	14.56	87.41	**8.54**	41.91	521.36	107.19	107.60
M_{inv}^{jj}	35.62	32.30	5.89	19.82	16.78	**4.50**	780.62	708.72	1396.62
Jet Multiplicity	**25010.40**	27559.30	27456.80	38819.80	31762.10	35556.10	330352.00	257940.00	255960.00
$P_T^{j,\text{Leading}}$	273.38	162.85	**69.01**	108.47	87.68	91.07	2816.59	1709.85	2083.29
$P_T^{j,\text{Subleading}}$	155.23	123.33	56.59	55.61	52.28	**51.62**	9259.87	7964.06	8881.10
$\Delta\eta^{jj}$	23.79	23.10	**5.88**	78.98	76.59	56.88	809.21	711.39	276.12
$\eta_{j1} \times \eta_{j2}$	21.03	15.54	**7.99**	33.26	41.67	32.48	344.41	260.55	200.54
H_T	**8580.94**	9677.14	9974.93	12462.40	10542.50	12428.40	80679.70	59870.10	59706.00
Centrality	262.51	234.08	**97.95**	175.56	204.46	147.23	1117.82	1159.62	569.68
$\eta^{j,\text{Leading}}$	31.08	26.54	28.70	**15.00**	18.57	21.70	215.82	159.87	153.74
$\eta^{j,\text{Subleading}}$	22.28	23.35	**20.27**	26.93	26.21	26.75	863.68	783.19	634.91
$\phi^{j,\text{Leading}}$	3.89	3.81	**3.78**	5.02	5.03	5.02	17.08	16.99	17.08
$\phi^{j,\text{Subleading}}$	4.41	4.41	**4.38**	6.47	6.49	6.53	24.06	23.90	24.05
ΔR^{jj}	20.77	24.27	**7.58**	68.58	66.13	54.14	1750.34	1979.50	2296.32
$\Delta\phi^{jj}$	**2.36**	2.84	2.54	5.33	7.83	9.98	2879.56	3294.80	3519.82
P_T^{jj}	81.49	20.35	**9.30**	23.06	16.37	19.73	699.29	973.39	988.90
$y^{\mu\mu jj}$	90.02	78.51	76.39	34.73	31.12	**28.63**	500.22	653.53	687.72
$y^{\mu\mu j,\text{Leading}}$	155.51	135.34	142.67	5.62	**2.32**	4.03	963.60	1283.98	1347.77
$y^{\mu\mu j,\text{Subleading}}$	4.79	**4.58**	6.80	20.75	16.88	9.12	949.36	836.66	519.01
$P_T^{\mu\mu jj}$	46.94	45.07	48.79	21.33	22.15	**15.75**	1272.77	1159.86	1274.30
$P_T^{\mu\mu j,\text{Leading}}$	80.18	63.30	**37.98**	63.32	69.93	62.19	6974.12	6220.12	6793.83
$P_T^{\mu\mu j,\text{Subleading}}$	167.98	84.16	**32.88**	68.75	47.20	55.38	1325.39	736.66	867.13
Number of Best χ2/NDF	6	5	17	2	5	5	0	0	0

Table 7.2.1: Comparison of χ^2/NDF values between data and MC in the Z control region before and after the application of the $P_T^{\mu\mu}$ and M_{inv}^{jj} re-weightings described in Section 7.1. Separate values are shown depending on whether Madgraph, Sherpa or Powheg have been used for the generation of the Drell-Yan MC used. Values highlighted in bold are the lowest of their respective rows.

Variable	χ^2/NDF								
	Madgraph			Sherpa			Powheg		
	Nominal	$P_T^{\mu\mu}$	$M_{\rm inv}^{jj}P_T^{\mu\mu}$	Nominal	$P_T^{\mu\mu}$	$M_{\rm inv}^{jj}P_T^{\mu\mu}$	Nominal	$P_T^{\mu\mu}$	$M_{\rm inv}^{jj}P_T^{\mu\mu}$
$P_T^{\mu,\rm Leading}$	56.81	1.83	4.98	25.02	**1.73**	2.78	162.29	17.55	19.01
$P_T^{\mu,\rm Subleading}$	14.22	3.97	6.97	12.95	**1.72**	2.83	16.68	15.95	19.76
$P_{\rm T}^{\mu\mu}$	61.43	7.32	16.48	42.37	**3.58**	7.48	534.80	27.66	35.04
d_0^{BL}significance	90.43	88.07	**86.77**	112.80	116.57	115.29	550.01	539.45	538.49
$\Delta z_0^{PV}\sin\theta$	129.35	124.26	**121.44**	175.54	182.61	179.34	771.96	749.28	744.74
$\eta^{\mu,\rm Leading}$	12.98	12.93	13.12	**4.92**	5.17	5.11	30.56	29.49	30.35
$\eta^{\mu,\rm Subleading}$	3.03	**2.91**	3.01	7.39	7.39	7.32	25.42	26.03	26.72
$E_T^{\rm miss}$	21.39	20.38	22.99	3.15	1.97	**1.47**	517.43	570.45	492.02
$M_{\rm inv}^{\mu\mu}$	2.15	1.87	1.84	**1.07**	1.19	1.20	5.04	3.23	3.15
$\Delta\phi^{\mu\mu}$	14.49	2.52	3.58	23.11	**1.37**	1.80	271.59	16.97	21.32
$y^{\mu\mu}$	2.75	2.85	3.05	**2.34**	2.45	**2.34**	28.40	30.73	32.77
$\phi^{\mu,\rm Leading}$	**0.79**	**0.79**	0.80	2.26	2.25	2.24	4.59	4.59	4.59
$\phi^{\mu,\rm Subleading}$	**0.80**	0.81	**0.80**	0.94	0.94	0.93	1.78	1.74	1.72
$\phi^{\mu\mu}$	**0.98**	**0.98**	0.99	1.56	1.59	1.59	2.60	2.81	2.84
$<\mu>$	6195.79	6079.23	**6031.40**	8726.91	8904.45	8909.56	20990.50	20670.30	20708.20
$\Delta R^{\mu\mu}$	30.91	5.90	12.02	38.54	**2.32**	4.50	182.51	16.85	21.70
$M_{\rm inv}^{jj}$	35.62	30.57	6.06	19.82	20.47	**4.76**	780.62	812.01	1530.42
Jet Multiplicity	**86.43**	102.95	136.19	134.32	177.84	139.16	9157.50	9848.19	10429.60
$P_T^{j,\rm Leading}$	273.38	128.85	**55.35**	108.47	79.28	62.82	2816.59	3846.96	4403.85
$P_T^{j,\rm Subleading}$	155.23	110.94	51.96	55.61	52.24	**43.40**	9259.87	10754.00	11833.00
$\Delta\eta^{jj}$	23.79	24.77	**6.22**	78.98	75.83	53.79	809.21	931.03	414.77
$\eta_{j1}\times\eta_{j2}$	21.03	16.58	**8.44**	33.26	44.07	34.13	344.41	328.64	252.83
H_T	95.66	36.17	**16.61**	53.97	49.95	31.52	1728.93	2307.91	2589.13
Centrality	262.51	242.48	**107.14**	175.56	216.16	146.60	1117.82	1296.99	674.18
$\eta^{j,\rm Leading}$	31.08	25.73	27.63	**15.00**	20.24	23.98	215.82	238.99	222.00
$\eta^{j,\rm Subleading}$	22.28	22.80	**19.99**	26.93	26.59	27.50	863.68	804.10	661.96
$\phi^{j,\rm Leading}$	3.89	3.81	**3.78**	5.02	5.10	5.09	17.08	16.88	16.96
$\phi^{j,\rm Subleading}$	4.41	4.37	**4.35**	6.47	6.58	6.62	24.06	23.62	23.74
ΔR^{jj}	20.77	28.22	**8.74**	68.58	68.26	56.72	1750.34	1625.59	1817.70
$\Delta\phi^{jj}$	2.36	3.10	**2.16**	5.33	9.81	12.90	2879.56	2757.51	2948.78
P_T^{jj}	81.49	10.09	**5.77**	23.06	10.78	6.24	699.29	551.07	599.22
$y^{\mu\mu jj}$	90.02	76.12	73.98	34.73	32.69	**26.96**	500.22	420.09	452.25
$y^{\mu\mu j,\rm Leading}$	155.51	130.46	137.20	5.62	**3.92**	5.25	963.60	857.55	894.41
$y^{\mu\mu j,\rm Subleading}$	4.79	**4.50**	6.76	20.75	15.66	8.15	949.36	867.13	562.16
$P_T^{\mu\mu jj}$	46.94	43.42	47.47	21.33	27.83	**18.53**	1272.77	1455.74	1568.47
$P_T^{\mu\mu j,\rm Leading}$	80.18	59.09	**37.57**	63.32	67.98	57.40	6974.12	8101.36	8761.03
$P_T^{\mu\mu j,\rm Subleading}$	167.98	62.49	**27.94**	68.75	35.43	28.44	1325.39	2039.99	2289.84
Number of Best χ2/NDF	3	4	17	4	6	6	0	0	0

Table 7.2.2: Comparison of χ^2/NDF values between data and MC in the Z Plus Jets control region before and after the application of the $P_T^{\mu\mu}$ and $M_{\rm inv}^{jj}$ re-weightings described in Section 7.1. Separate values are shown depending on whether Madgraph, Sherpa or Powheg have been used for the generation of the Drell-Yan MC used. Values highlighted in bold are the lowest of their respective rows.

Variable	χ^2/NDF								
	Madgraph			Sherpa			Powheg		
	Nominal	$P_T^{\mu\mu}$	$M_{\text{inv}}^{jj} P_T^{\mu\mu}$	Nominal	$P_T^{\mu\mu}$	$M_{\text{inv}}^{jj} P_T^{\mu\mu}$	Nominal	$P_T^{\mu\mu}$	$M_{\text{inv}}^{jj} P_T^{\mu\mu}$
$P_T^{\mu,\text{Leading}}$	6.84	2.06	2.71	2.04	**1.81**	2.36	3.01	1.94	1.91
$P_T^{\mu,\text{Subleading}}$	2.71	**1.64**	1.77	2.72	1.75	2.13	7.65	6.59	7.00
$P_{\text{T}}^{\mu\mu}$	10.66	**0.99**	2.31	7.49	2.51	4.76	3.80	1.00	1.27
d_0^{BL}significance	21.31	21.17	**21.09**	33.31	32.63	32.54	259.29	259.13	259.14
$\Delta z_0^{PV} \sin\theta$	24.20	23.79	**23.73**	35.95	35.50	35.17	297.92	298.34	298.26
$\eta^{\mu,\text{Leading}}$	**2.25**	2.45	2.47	2.51	2.38	2.48	6.73	6.80	6.83
$\eta^{\mu,\text{Subleading}}$	2.80	2.85	2.86	**1.35**	**1.35**	1.37	4.42	4.44	4.46
E_T^{miss}	**1.26**	2.75	3.19	2.62	1.73	1.67	72.65	72.08	79.42
$M_{\text{inv}}^{\mu\mu}$	1.45	1.67	1.69	**1.32**	1.34	**1.32**	1.62	1.82	1.88
$\Delta\phi^{\mu\mu}$	3.75	**1.94**	2.46	5.31	2.17	2.65	3.54	2.66	3.17
$y^{\mu\mu}$	**1.26**	1.38	1.45	1.85	1.82	1.78	4.47	4.83	4.78
$\phi^{\mu,\text{Leading}}$	**0.58**	0.59	**0.58**	0.99	0.98	1.01	3.44	3.43	3.43
$\phi^{\mu,\text{Subleading}}$	**0.78**	0.79	0.79	2.10	2.10	2.07	2.32	2.32	2.33
$\phi^{\mu\mu}$	1.56	1.57	1.56	1.19	1.18	**1.16**	2.16	2.16	2.16
$< \mu >$	734.00	**726.95**	727.27	1123.79	1109.46	1112.59	4676.29	4669.10	4678.83
$\Delta R^{\mu\mu}$	5.23	**1.53**	1.82	3.63	3.16	3.27	3.46	3.22	3.19
M_{inv}^{jj}	2.01	1.85	1.29	1.64	1.47	**1.17**	16.93	17.56	32.09
Jet Multiplicity	13.58	**8.00**	10.08	17.72	32.93	12.33	561.00	582.86	655.26
$P_T^{j,\text{Leading}}$	5.62	2.32	**1.45**	3.19	3.51	3.69	35.91	30.15	35.58
$P_T^{j,\text{Subleading}}$	3.27	2.08	**1.10**	2.57	3.17	3.54	202.37	208.12	217.48
$\Delta\eta^{jj}$	29.15	29.31	**27.89**	29.47	32.84	30.30	34.52	36.16	28.13
$\eta_{j1} \times \eta_{j2}$	2.47	2.18	1.99	**1.33**	1.54	1.44	3.97	3.88	2.29
H_T	8.71	1.80	**1.36**	2.62	6.79	2.28	74.78	64.94	76.58
Centrality	14.33	12.73	7.93	4.78	5.14	**4.04**	51.00	48.36	31.25
$\eta^{j,\text{Leading}}$	2.47	2.17	2.24	**0.83**	0.89	1.03	4.11	4.11	4.41
$\eta^{j,\text{Subleading}}$	1.46	1.54	**1.43**	1.77	1.74	1.84	12.79	12.82	10.57
$\phi^{j,\text{Leading}}$	0.52	0.51	**0.50**	1.12	1.14	1.14	1.75	1.74	1.74
$\phi^{j,\text{Subleading}}$	1.05	1.06	**1.03**	1.31	1.31	1.33	1.32	1.33	1.34
ΔR^{jj}	1.22	1.30	**0.84**	2.88	2.93	2.55	44.24	48.04	57.20
$\Delta\phi^{jj}$	1.17	1.17	1.19	**0.99**	**0.99**	1.02	71.81	77.41	82.17
P_T^{jj}	3.09	**1.47**	1.51	1.62	1.70	1.97	23.66	26.18	26.52
$y^{\mu\mu jj}$	46141.60	46697.30	45467.50	2.91	3.29	**2.89**	54.88	53.04	54.02
$y^{\mu\mu j,\text{Leading}}$	10.46	8.91	9.42	1.30	**1.29**	1.42	62.12	64.13	67.49
$y^{\mu\mu j,\text{Subleading}}$	8.10	8.25	8.52	**0.63**	0.69	0.40	5.94	7.09	3.42
$P_T^{\mu\mu jj}$	3.47	3.75	3.93	1.15	1.30	**1.04**	21.23	25.52	25.64
$P_T^{\mu\mu j,\text{Leading}}$	1.97	**1.54**	1.62	2.20	2.89	2.73	129.09	135.67	139.75
$P_T^{\mu\mu j,\text{Subleading}}$	4.08	1.76	**1.39**	2.49	2.30	2.63	22.00	17.98	19.91
Number of Best χ2/NDF	5	8	12	6	4	6	0	0	0

Table 7.2.3: Comparison of χ^2/NDF values between data and MC in the Signal region before and after the application of the $P_T^{\mu\mu}$ and M_{inv}^{jj} re-weightings described in Section 7.1. Separate values are shown depending on whether Madgraph, Sherpa or Powheg have been used for the generation of the Drell-Yan MC used. Values highlighted in bold are the lowest of their respective rows.

Variable	χ^2/NDF								
	Madgraph			Sherpa			Powheg		
	Nominal	$P_T^{\mu\mu}$	$M_{\rm inv}^{jj}P_T^{\mu\mu}$	Nominal	$P_T^{\mu\mu}$	$M_{\rm inv}^{jj}P_T^{\mu\mu}$	Nominal	$P_T^{\mu\mu}$	$M_{\rm inv}^{jj}P_T^{\mu\mu}$
$P_T^{\mu,\rm Leading}$	3.15	1.60	1.79	1.90	**1.15**	1.16	7.12	0.86	0.88
$P_T^{\mu,\rm Subleading}$	1.50	1.04	1.05	1.19	**0.89**	0.91	2.62	2.17	2.28
$P_{\rm T}^{\mu\mu}$	3.28	1.09	1.52	3.33	**0.78**	0.93	20.94	1.45	1.69
d_0^{BL}significance	8.22	8.08	7.98	**6.60**	6.79	6.92	28.94	28.21	28.18
$\Delta z_0^{PV}\sin\theta$	11.00	10.82	10.77	**8.80**	9.15	9.03	32.34	30.70	30.65
$\eta^{\mu,\rm Leading}$	1.64	1.65	1.68	**0.86**	0.87	0.89	5.35	3.85	3.80
$\eta^{\mu,\rm Subleading}$	3.00	3.02	3.03	**1.56**	1.59	1.59	1.76	1.76	1.76
$E_T^{\rm miss}$	1.91	1.80	1.90	**1.15**	1.37	1.43	16.21	4.10	3.44
$M_{\rm inv}^{\mu\mu}$	0.85	0.84	0.83	**0.80**	**0.80**	**0.80**	5.40	1.78	1.75
$\Delta\phi^{\mu\mu}$	1.69	1.56	1.67	2.17	**1.16**	1.17	10.46	1.69	1.85
$y^{\mu\mu}$	1.42	1.45	1.48	0.54	0.55	**0.52**	31.24	37.89	37.92
$\phi^{\mu,\rm Leading}$	0.75	0.75	0.75	1.41	1.43	1.43	**0.51**	0.59	0.59
$\phi^{\mu,\rm Subleading}$	0.67	0.67	**0.65**	1.67	1.67	1.65	0.72	0.76	0.77
$\phi^{\mu\mu}$	0.80	0.80	**0.79**	1.54	1.53	1.55	1.11	1.08	1.07
$<\mu>$	196.20	193.04	**192.08**	304.76	313.28	313.99	745.40	702.65	703.83
$\Delta R^{\mu\mu}$	3.00	2.32	2.36	1.80	**1.17**	1.21	5.92	1.27	1.38
$M_{\rm inv}^{jj}$	2.01	1.91	1.30	1.64	1.59	**1.18**	16.93	24.05	42.10
Jet Multiplicity	**6.87**	7.70	9.37	7.14	8.91	7.11	138.03	227.92	239.38
$P_T^{j,\rm Leading}$	5.62	2.48	**1.45**	3.19	1.92	1.73	35.91	83.05	94.62
$P_T^{j,\rm Subleading}$	3.27	2.27	**1.15**	2.57	1.99	2.62	202.37	303.21	322.88
$\Delta\eta^{jj}$	29.15	28.74	**27.92**	29.47	30.17	30.24	34.52	46.96	36.96
$\eta_{j1}\times\eta_{j2}$	2.47	2.25	2.04	**1.33**	1.80	1.59	3.97	6.16	4.43
H_T	2.79	1.29	1.06	1.51	1.56	**0.95**	28.11	61.42	67.89
Centrality	14.33	13.12	8.02	4.78	6.05	**4.17**	51.00	43.34	26.50
$\eta^{j,\rm Leading}$	2.47	2.24	2.29	**0.83**	1.04	1.18	4.11	4.50	4.50
$\eta^{j,\rm Subleading}$	1.46	1.53	**1.43**	1.77	1.80	1.91	12.79	15.09	12.60
$\phi^{j,\rm Leading}$	0.52	0.51	**0.50**	1.12	1.14	1.15	1.75	1.75	1.75
$\phi^{j,\rm Subleading}$	1.05	1.06	**1.03**	1.31	1.32	1.34	1.32	1.27	1.28
ΔR^{jj}	1.22	1.27	**0.84**	2.88	2.88	2.67	44.24	40.13	46.65
$\Delta\phi^{jj}$	1.17	1.17	1.20	**0.99**	1.08	1.17	71.81	63.79	68.46
P_T^{jj}	3.09	1.54	1.54	1.62	1.05	**1.01**	23.66	12.17	13.24
$y^{\mu\mu jj}$	46141.60	45665.20	45468.80	**2.91**	3.19	2.92	54.88	29.89	29.73
$y^{\mu\mu j,\rm Leading}$	10.46	9.40	9.78	**1.30**	1.60	1.71	62.12	35.91	37.49
$y^{\mu\mu j,\rm Subleading}$	8.10	8.19	8.45	0.63	0.43	**0.34**	5.94	13.03	8.04
$P_T^{\mu\mu jj}$	3.47	3.58	3.94	1.15	1.28	**1.07**	21.23	44.00	46.38
$P_T^{\mu\mu j,\rm Leading}$	1.97	**1.55**	1.62	2.20	2.32	2.36	129.09	200.10	211.03
$P_T^{\mu\mu j,\rm Subleading}$	4.08	1.74	1.28	2.49	1.15	**1.07**	22.00	47.70	53.16
Number of Best χ2/NDF	1	1	10	11	6	9	1	0	0

Table 7.2.4: Comparison of χ^2/NDF values between data and MC in the Signal Plus Jets region before and after the application of the $P_T^{\mu\mu}$ and $M_{\rm inv}^{jj}$ re-weightings described in Section 7.1. Separate values are shown depending on whether Madgraph, Sherpa or Powheg have been used for the generation of the Drell-Yan MC used. Values highlighted in bold are the lowest of their respective rows.

7.3 Boosted Decision Tree Training Comparisons

When analysing the results of the previous section, all variables were treated with equal importance - the better modelling of key analysis quantities (such as $M_{\text{inv}}^{\mu\mu}$) was not factored into the final decision of which Drell-Yan MC generator to use. In principle, however, the better modelling of certain variables (such as those used to train the analysis BDTs) will have a larger effect on the derived $H \to \mu\mu$ signal strength than others. The effects of this were studied in the following section, where separate BDTs were trained using Madgraph, Sherpa and Powheg Drell-Yan MC, with the goal of separating VBF events from the surrounding backgrounds (as was done in the previous ATLAS Run-2 $H \to \mu\mu$ analyses). In each case, VBF signal MC was trained against di-boson, top, electroweak Z plus jets and Drell-Yan background MC samples. The BDTs were trained using the same parameters and methodology as those described in Chapter 9 (including 2-fold cross-validation). Events used in the BDT training and testing were required to possess two or more jets, and lie within $110 \leq M_{\text{inv}}^{\mu\mu} \leq 160$ GeV, with the training variables the same as those used for the 2018 ATLAS $H \to \mu\mu$ analysis BDT [27]. The variables were chosen to exploit the forward positioning and large η separation signature of jets from the VBF process.

The variable rankings associated with the folds of each BDT are presented in Tables 7.3.1 to 7.3.3. Variations in variable importance between folds of the same BDT are seen due to statistical fluctuations in the MC samples. Importances also vary between BDTs due to the variable modelling differences of the MC generators.

Figure 7.3.1 presents the Receiver Operating Characteristic (ROC) curves of both folds of the BDTs. The curves compare the background rejection and signal acceptance efficiencies of each BDT, with curves lying closer to the top-right of the plots indicating better performing BDTs. Training with Powheg Drell-Yan MC gave the best performance, although the improvement was minimal. To quantify these improvements, the integrals of each ROC curve were taken, with the values summarised in Table 7.3.4. The choice of Drell-Yan MC generator was found to vary signal-background separation by less than 1%. Slight performance differences were seen between BDT folds due to statistical fluctuations in the MC samples.

Since Powheg was demonstrated to give the worst description of the data in the previous section, these improvements could be due to conveniently mismodelled variables, rather than the exploitation of genuine trends in the data. Were this to be true, the Powheg BDT would classify Drell-Yan MC and data events considerably differently. To test this idea, data-MC comparisons of the BDT responses to the full analysis samples were produced, shown below in Figure 7.3.2. Only MC statistical errors are presented in each case. As suspected, data-MC discrepancies of 10-20% are seen in the Powheg distribution, with the Madgraph and Sherpa BDTs presenting data-MC agreements largely within 5%. The Powheg Drell-Yan MC sample was therefore an inappropriate

Rank	Variable	Variable Importance
1	$\Delta\eta^{jj}$	0.104
2	$P_T^{\mu\mu}$	0.084
3	E_T^{miss}	0.083
4	M_{inv}^{jj}	0.082
5	$\Delta y^{\mu\mu j,\text{Subleading}}$	0.080
6	$\Delta y^{jj\mu\mu}$	0.078
7	$\Delta y^{\mu\mu j,\text{Leading}}$	0.075
8	$P_T^{jj\mu\mu}$	0.074
9	ΔR^{jj}	0.074
10	$P_T^{\mu\mu j,\text{Leading}}$	0.066
11	H_T	0.059
12	$P_T^{\mu\mu j,\text{Subleading}}$	0.055
13	P_T^{jj}	0.052
14	Centrality	0.033

Rank	Variable	Variable Importance
1	$\Delta\eta^{jj}$	0.103
2	$P_T^{\mu\mu}$	0.093
3	$\Delta y^{\mu\mu j,\text{Leading}}$	0.084
4	M_{inv}^{jj}	0.082
5	$\Delta y^{\mu\mu j,\text{Subleading}}$	0.074
6	ΔR^{jj}	0.073
7	$P_T^{jj\mu\mu}$	0.071
8	H_T	0.070
9	$\Delta y^{jj\mu\mu}$	0.069
10	E_T^{miss}	0.068
11	$P_T^{\mu\mu j,\text{Leading}}$	0.067
12	P_T^{jj}	0.052
13	$P_T^{\mu\mu j,\text{Subleading}}$	0.049
14	Centrality	0.045

Table 7.3.1: Ranking of the input variables used to train folds 1 (left) and 2 (right) of the BDTs utilising Madgraph Drell-Yan MC.

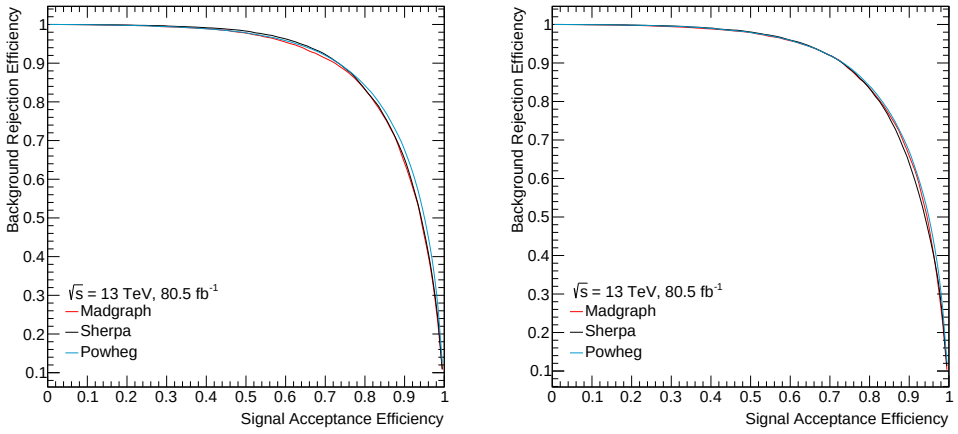

(a) Fold 1.

(b) Fold 2.

Figure 7.3.1: ROC curves for the nominal analysis BDT, trained and tested using Drell-Yan MC produced with Madgraph (red), Sherpa (black) and Powheg (blue). Both Folds 1 (left) and 2 (right) of each BDT are presented.

choice for the training of further analysis BDTs.

By placing cuts on the BDT output distributions, categories of large $\frac{S}{\sqrt{B}}$ could be

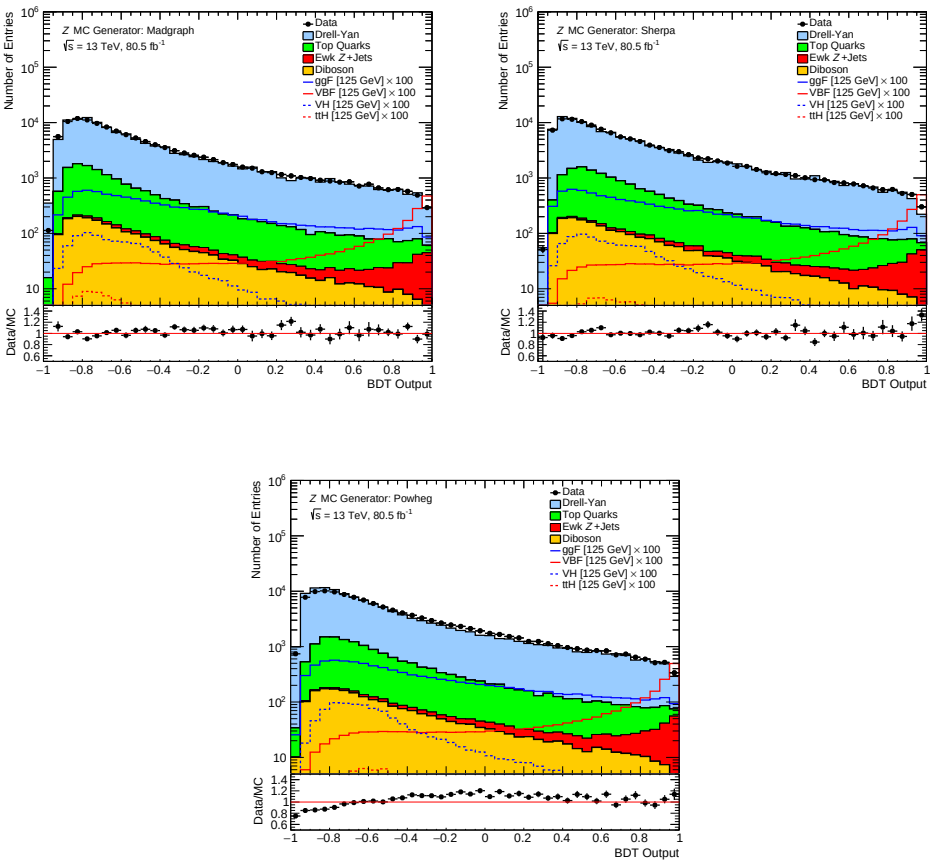

Figure 7.3.2: Data-MC comparisons of the responses of BDTs trained using Madgraph, Sherpa and Powheg Drell-Yan MC. Only MC statistical uncertainties are shown. The BDTs were trained using a two-fold approach, where the BDT trained using Fold 1 events was applied exclusively to events in Fold 2 (and vice versa). The presented distributions contain events from both folds, post-classification from the respective BDTs.

Rank	Variable	Variable Importance
1	M_{inv}^{jj}	0.098
2	$P_T^{jj\mu\mu}$	0.095
3	$\Delta\eta^{jj}$	0.093
4	$P_T^{\mu\mu}$	0.085
5	$P_T^{\mu\mu j,\text{Leading}}$	0.077
6	$\Delta y^{jj\mu\mu}$	0.076
7	ΔR^{jj}	0.076
8	$\Delta y^{\mu\mu j,\text{Subleading}}$	0.071
9	$\Delta y^{\mu\mu j,\text{Leading}}$	0.070
10	E_T^{miss}	0.067
11	H_T	0.059
12	$P_T^{\mu\mu j,\text{Subleading}}$	0.057
13	Centrality	0.047
14	P_T^{jj}	0.028

Rank	Variable	Variable Importance
1	$\Delta\eta^{jj}$	0.099
2	$P_T^{jj\mu\mu}$	0.091
3	M_{inv}^{jj}	0.089
4	$P_T^{\mu\mu}$	0.087
5	$\Delta y^{jj\mu\mu}$	0.080
6	E_T^{miss}	0.079
7	$P_T^{\mu\mu j,\text{Leading}}$	0.072
8	ΔR^{jj}	0.070
9	$\Delta y^{\mu\mu j,\text{Leading}}$	0.068
10	$\Delta y^{\mu\mu j,\text{Subleading}}$	0.064
11	H_T	0.061
12	$P_T^{\mu\mu j,\text{Subleading}}$	0.058
13	Centrality	0.046
14	P_T^{jj}	0.037

Table 7.3.2: Ranking of the input variables used to train folds 1 (left) and 2 (right) of the BDTs utilising Sherpa Drell-Yan MC.

devised, allowing for an effective measure of the analysis' signal sensitivity. In the aforementioned $H \to \mu\mu$ analyses, so-called VBF Tight and VBF Loose categories were defined by cutting the BDT output distribution at points corresponding to 98% and 95% signal purity respectively. Equivalent purity cuts for the Madgraph, Sherpa and Powheg BDTs of this analysis are listed in Appendix B, along with the BDT output distributions.

Events failing these cuts were sorted into one of six ggF categories, based on $P_T^{\mu\mu}$ (low ($P_T^{\mu\mu} < 15$ GeV), medium ($15 \leq P_T^{\mu\mu} < 50$ GeV) and high ($50 \leq P_T^{\mu\mu}$ GeV)) and η^{μ} (central ($|\eta^{\mu_1}| < 1$ and $|\eta^{\mu_2}| < 1$) and non-central ($|\eta^{\mu_1}| \geq 1$ or $|\eta^{\mu_2}| \geq 1$)).

Table 7.3.5 summarises the event yields obtained when applying this categorisation to signal and background MC samples, along with data, in the region $120 < M_{\text{inv}}^{\mu\mu} < 130$ GeV, after application of the full event selection. Results are presented in three separate instances, depending on whether the Madgraph, Sherpa or Powheg BDTs have been applied. The highest significance categories were found to be VBF Tight and Non-Central High $P_T^{\mu\mu}$ for all BDTs tested. The combined significance achieved when using the Sherpa BDT was 2.4% greater than the Madgraph and Powheg alternatives. Since Tables 7.2.3 and 7.2.4 demonstrated Madgraph best modelled the data overall, this improvement is likely due to statistical fluctuations. This is demonstrated in the VBF Tight event yields of the Sherpa BDT, where the total background and data yields disagree by 25% (rather

Rank	Variable	Variable Importance
1	M_{inv}^{jj}	0.100
2	$P_T^{\mu\mu}$	0.087
3	$P_T^{jj\mu\mu}$	0.086
4	$P_T^{\mu\mu j,\text{Leading}}$	0.086
5	$\Delta\eta^{jj}$	0.082
6	E_T^{miss}	0.077
7	ΔR^{jj}	0.077
8	$\Delta y^{\mu\mu j,\text{Leading}}$	0.071
9	$\Delta y^{\mu\mu j,\text{Subleading}}$	0.067
10	$\Delta y^{jj\mu\mu}$	0.066
11	$P_T^{\mu\mu j,\text{Subleading}}$	0.064
12	H_T	0.053
13	Centrality	0.042
14	P_T^{jj}	0.042

Rank	Variable	Variable Importance
1	$P_T^{jj\mu\mu}$	0.096
2	M_{inv}^{jj}	0.095
3	$P_T^{\mu\mu j,\text{Leading}}$	0.088
4	$P_T^{\mu\mu}$	0.084
5	$\Delta\eta^{jj}$	0.079
6	$\Delta y^{\mu\mu j,\text{Leading}}$	0.073
7	ΔR^{jj}	0.072
8	E_T^{miss}	0.070
9	$\Delta y^{jj\mu\mu}$	0.067
10	$\Delta y^{\mu\mu j,\text{Subleading}}$	0.066
11	H_T	0.062
12	$P_T^{\mu\mu j,\text{Subleading}}$	0.061
13	Centrality	0.047
14	P_T^{jj}	0.043

Table 7.3.3: Ranking of the input variables used to train folds 1 (left) and 2 (right) of the BDTs utilising Powheg Drell-Yan MC.

	Madgraph		Sherpa		Powheg	
	Fold 1	Fold 2	Fold 1	Fold 2	Fold 1	Fold 2
ROC Integral	0.893	0.896	0.896	0.895	0.900	0.899
Fold Averaged ROC Integral	0.895		0.896		0.900	
% Improvement	-		0.112		0.559	

Table 7.3.4: ROC integral comparisons between the folds of BDTs trained using Madgraph, Sherpa and Powheg Drell-Yan MC. The bottom row is calculated with respect to the ROC integral of the Madgraph BDT, averaged across both folds.

than the 3% discrepancy seen with Madgraph). The Madgraph samples were therefore deemed the most appropriate to use for the rest of the analysis.

Category	ggF	VBF	VH	$t\bar{t}H$	Drell-Yan	EWK Z+ Jets	Di-boson	Top	Total Signal	Total Background	$\frac{S}{\sqrt{B}}$	Data
Madgraph - Central, Low $P_T^{\mu\mu}$	26.41 ± 0.11	0.22 ± 0.00	0.12 ± 0.00	0.00 ± 0.00	23032.80 ± 882.15	1.59 ± 0.26	49.88 ± 4.03	51.75 ± 2.36	26.75 ± 0.11	23136.03 ± 882.16	0.18	24178
Madgraph - Non-central, Low $P_T^{\mu\mu}$	69.94 ± 0.19	0.62 ± 0.00	0.40 ± 0.01	0.01 ± 0.00	88582.79 ± 1809.80	6.38 ± 0.58	135.19 ± 6.63	212.24 ± 4.76	70.97 ± 0.19	88936.59 ± 1809.82	0.24	90169
Madgraph - Central, Medium $P_T^{\mu\mu}$	49.51 ± 0.15	1.65 ± 0.01	0.94 ± 0.01	0.03 ± 0.00	18054.26 ± 764.38	9.93 ± 0.67	333.73 ± 10.21	195.18 ± 4.64	52.13 ± 0.15	18593.11 ± 764.46	0.38	19830
Madgraph - Non-Central, Medium $P_T^{\mu\mu}$	128.92 ± 0.26	4.53 ± 0.01	2.87 ± 0.02	0.08 ± 0.00	66983.75 ± 1535.48	43.02 ± 1.51	1171.02 ± 19.61	973.56 ± 10.50	136.40 ± 0.26	69171.34 ± 1535.64	0.52	71726
Madgraph - Central, High $P_T^{\mu\mu}$	37.30 ± 0.13	4.08 ± 0.01	2.75 ± 0.02	0.21 ± 0.00	7495.43 ± 306.48	22.84 ± 1.10	735.79 ± 15.17	158.40 ± 3.73	44.34 ± 0.13	8412.46 ± 306.88	0.48	8630
Madgraph - Non-Central, High $P_T^{\mu\mu}$	85.34 ± 0.21	9.95 ± 0.02	7.12 ± 0.04	0.37 ± 0.00	24333.50 ± 618.59	65.78 ± 1.90	2217.33 ± 27.02	712.51 ± 9.63	102.78 ± 0.21	27329.12 ± 619.26	0.62	27782
Madgraph - VBF Loose	4.13 ± 0.05	4.17 ± 0.01	0.08 ± 0.00	0.01 ± 0.00	518.81 ± 48.78	17.56 ± 0.97	43.32 ± 3.50	9.26 ± 0.82	8.39 ± 0.05	588.95 ± 48.93	0.35	557
Madgraph - VBF Tight	1.73 ± 0.03	6.19 ± 0.02	0.01 ± 0.00	0.00 ± 0.00	149.34 ± 15.85	16.61 ± 0.92	7.87 ± 1.49	2.08 ± 0.30	7.93 ± 0.04	175.90 ± 15.95	0.60	169
Madgraph - Inclusive	403.27 ± 0.45	31.41 ± 0.03	14.29 ± 0.05	0.70 ± 0.01	229150.68 ± 2734.00	183.72 ± 3.12	4694.14 ± 39.04	2314.97 ± 16.36	449.57 ± 0.45	236343.50 ± 2734.33	1.26	243041
Sherpa - Central, Low $P_T^{\mu\mu}$	26.40 ± 0.11	0.21 ± 0.00	0.12 ± 0.00	0.00 ± 0.00	23885.65 ± 538.96	1.59 ± 0.26	49.88 ± 4.03	51.73 ± 2.36	26.73 ± 0.11	23988.85 ± 538.98	0.17	24178
Sherpa - Non-central, Low $P_T^{\mu\mu}$	69.91 ± 0.19	0.60 ± 0.00	0.40 ± 0.01	0.01 ± 0.00	90304.51 ± 1074.33	6.34 ± 0.58	134.86 ± 6.62	212.22 ± 4.76	70.92 ± 0.19	90657.93 ± 1074.36	0.24	90149
Sherpa - Central, Medium $P_T^{\mu\mu}$	49.51 ± 0.15	1.64 ± 0.01	0.94 ± 0.01	0.03 ± 0.00	19191.48 ± 688.77	9.81 ± 0.66	333.81 ± 10.21	195.83 ± 4.67	52.12 ± 0.15	19730.93 ± 688.86	0.37	19823
Sherpa - Non-Central, Medium $P_T^{\mu\mu}$	128.90 ± 0.26	4.50 ± 0.01	2.87 ± 0.02	0.08 ± 0.00	65655.88 ± 1345.17	42.60 ± 1.50	1171.00 ± 19.61	973.41 ± 10.50	136.35 ± 0.26	67842.89 ± 1345.36	0.52	71712
Sherpa - Central, High $P_T^{\mu\mu}$	37.06 ± 0.13	3.92 ± 0.01	2.74 ± 0.02	0.20 ± 0.00	7337.07 ± 306.77	21.45 ± 1.05	732.48 ± 15.14	157.56 ± 3.73	43.92 ± 0.13	8248.56 ± 307.17	0.48	8574
Sherpa - Non-Central, High $P_T^{\mu\mu}$	84.96 ± 0.21	9.60 ± 0.02	7.09 ± 0.04	0.36 ± 0.00	24601.20 ± 570.14	63.43 ± 1.86	2209.11 ± 26.95	710.83 ± 9.63	102.01 ± 0.21	27584.58 ± 570.86	0.61	27698
Sherpa - VBF Loose	4.07 ± 0.05	3.45 ± 0.01	0.10 ± 0.00	0.01 ± 0.00	535.16 ± 51.02	16.80 ± 0.98	46.95 ± 3.82	9.73 ± 0.67	7.63 ± 0.05	608.64 ± 51.18	0.31	638
Sherpa - VBF Tight	2.46 ± 0.03	7.49 ± 0.02	0.02 ± 0.00	0.00 ± 0.00	173.89 ± 30.63	21.69 ± 1.05	16.06 ± 2.13	3.65 ± 0.39	9.97 ± 0.04	215.29 ± 30.72	0.68	269
Sherpa - Inclusive	403.27 ± 0.45	31.41 ± 0.03	14.29 ± 0.05	0.70 ± 0.01	231684.83 ± 2037.47	183.72 ± 3.12	4694.14 ± 39.04	2314.97 ± 16.36	449.57 ± 0.45	238877.65 ± 2037.91	1.29	243041
Powheg - Central, Low $P_T^{\mu\mu}$	26.41 ± 0.11	0.22 ± 0.00	0.12 ± 0.00	0.00 ± 0.00	23431.53 ± 169.31	1.67 ± 0.26	49.88 ± 4.03	51.75 ± 2.36	26.75 ± 0.11	23534.84 ± 169.37	0.17	24179
Powheg - Non-central, Low $P_T^{\mu\mu}$	69.94 ± 0.19	0.62 ± 0.00	0.40 ± 0.01	0.01 ± 0.00	89991.75 ± 340.06	6.30 ± 0.57	134.53 ± 6.61	212.26 ± 4.76	70.97 ± 0.19	90344.83 ± 340.16	0.24	90164
Powheg - Central, Medium $P_T^{\mu\mu}$	49.49 ± 0.15	1.63 ± 0.01	0.94 ± 0.01	0.03 ± 0.00	19787.81 ± 160.01	9.73 ± 0.66	333.58 ± 10.21	195.84 ± 4.67	52.09 ± 0.15	20326.96 ± 160.40	0.37	19824
Powheg - Non-Central, Medium $P_T^{\mu\mu}$	128.87 ± 0.26	4.47 ± 0.01	2.87 ± 0.02	0.08 ± 0.00	71274.29 ± 311.24	42.09 ± 1.49	1168.73 ± 19.59	973.10 ± 10.51	136.29 ± 0.26	73458.20 ± 312.04	0.50	71700
Powheg - Central, High $P_T^{\mu\mu}$	37.23 ± 0.13	4.05 ± 0.01	2.74 ± 0.02	0.20 ± 0.00	8568.07 ± 107.18	21.13 ± 1.04	732.73 ± 15.14	158.14 ± 3.73	44.22 ± 0.13	9480.07 ± 108.31	0.45	8612
Powheg - Non-Central, High $P_T^{\mu\mu}$	85.20 ± 0.21	9.89 ± 0.02	7.10 ± 0.04	0.36 ± 0.00	26188.29 ± 193.20	64.37 ± 1.88	2209.67 ± 26.96	710.56 ± 9.63	102.55 ± 2.36	29172.89 ± 195.32	0.60	27708
Powheg - VBF Loose	4.14 ± 0.05	3.84 ± 0.01	0.09 ± 0.00	0.01 ± 0.00	586.16 ± 33.79	18.15 ± 1.03	50.59 ± 3.96	10.01 ± 0.65	8.35 ± 0.05	664.90 ± 34.04	0.31	632
Powheg - VBF Tight	1.99 ± 0.03	6.70 ± 0.02	0.02 ± 0.00	0.00 ± 0.00	128.00 ± 14.60	20.27 ± 1.01	14.44 ± 2.01	3.31 ± 0.35	8.71 ± 0.04	166.02 ± 14.78	0.68	222
Powheg - Inclusive	403.27 ± 0.45	31.41 ± 0.03	14.29 ± 0.05	0.70 ± 0.01	239955.89 ± 562.98	183.72 ± 3.12	4694.14 ± 39.04	2314.97 ± 16.36	449.57 ± 0.45	247148.72 ± 564.58	1.26	243041

Table 7.3.5: Expected event yields (normalised to 80.5 fb^{-1}) for different signal and background processes in eight signal categories, in the window 120 GeV $< M_{\text{inv}}^{\mu\mu} <$ 130 GeV. Results are presented for categories derived from BDTs trained with Drell-Yan MC produced with Madgraph, Sherpa and Powheg respectively. The significances of the inclusive rows are equal to the quadrature sums of the significances of the preceding categories.

Chapter 8

Variable Modelling in the Control and Signal Regions

To ensure the BDTs developed during the latter stages of the analysis were effective when applied to data, cross-checks were made to ensure the MC samples used for their training accurately described the data. This chapter presents data-MC comparisons for the different kinematic variables used to train these BDTs, with all events and physics objects having undergone the selections outline in Chapter 6.

8.1 Z Control Region

Comparisons were initially made in the Z and Z Plus Jets control regions to validate the analysis selection, since the region surrounding the Z mass has been studied extensively in the past, and is thought to be well described by the latest theoretical predictions.

Figure 8.1.1 presents the $P_T^{\mu,\text{Leading}}$, $P_T^{\mu,\text{Subleading}}$, $\eta^{\mu,\text{Leading}}$, $\eta^{\mu,\text{Subleading}}$, $\phi^{\mu,\text{Leading}}$ and $\phi^{\mu,\text{Subleading}}$ distributions of muons selected within the Z control region. MC statistical errors are contained within the error bands, along with the experimental systematic uncertainties detailed in Chapter 11, and $P_T^{\mu\mu}$ and M_{inv}^{jj} re-weighting uncertainties. The latter were computed as the difference between the re-weighted and nominal distributions. The P_T distributions show agreement within 5-10%, with discrepancies more prominent at high P_T, where track curvature is reduced. The distributions show distorted shapes, due in part to the imperfect modelling used for the $P_T^{\mu\mu}$ re-weighting. The η distributions show agreement within 5%, apart from the $|\eta| > 2.5$ regions which lack ID coverage. The distorted shapes are due to issues with Madgraph, rather than the analysis selection, as can be seen in the smoother Sherpa and Powheg distributions presented in Appendix B. The ϕ distributions are well modelled, with data-MC agreement within 2-3%.

Figure 8.1.2 presents the $P_T^{\mu\mu}$, E_T^{miss}, $\Delta R^{\mu\mu}$, $\Delta\phi^{\mu\mu}$, $y^{\mu\mu}$ and Jet Multiplicity distri-

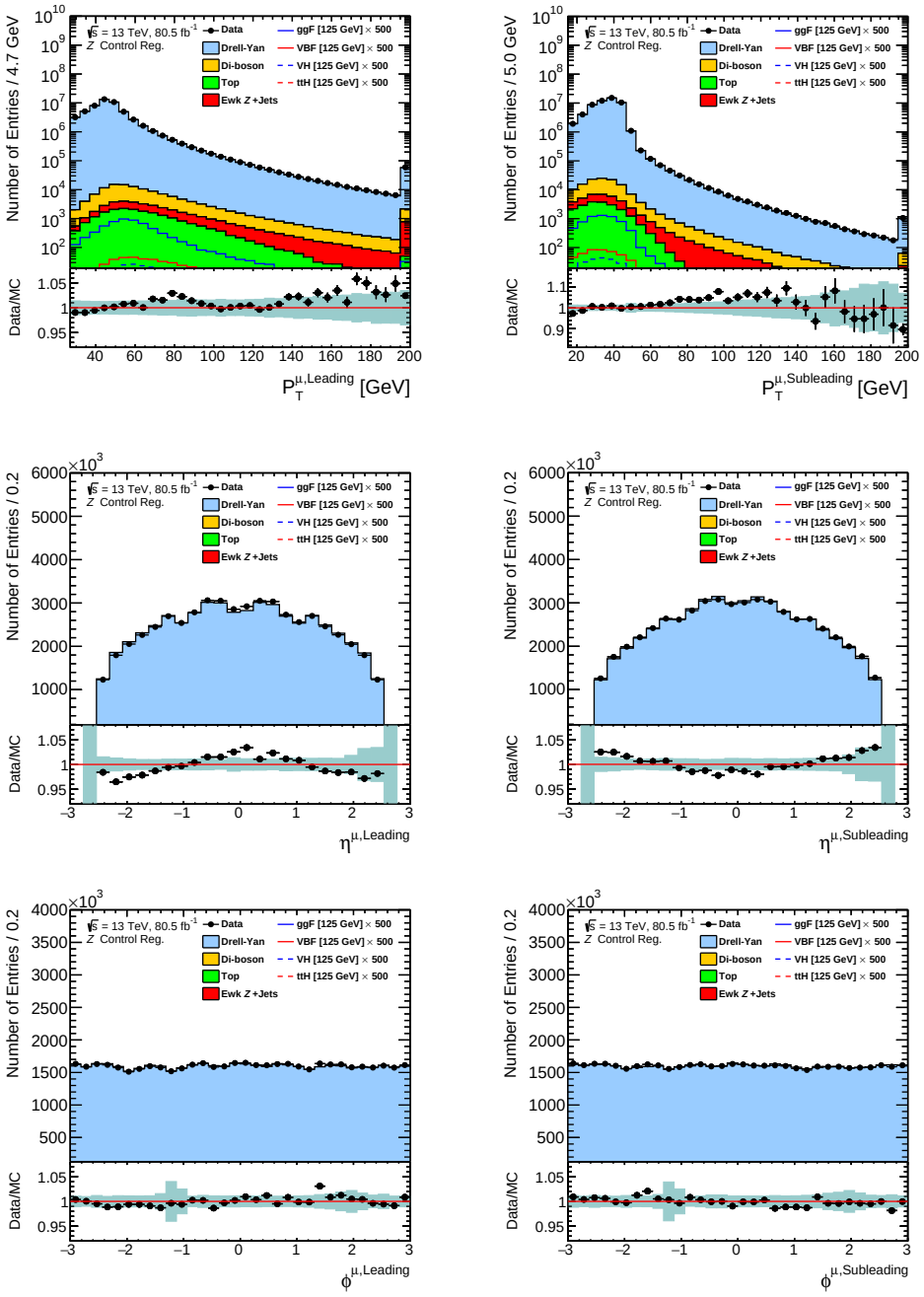

Figure 8.1.1: Comparisons between data and MC samples for $P_T^{\mu,\text{Leading}}$ (top left), $P_T^{\mu,\text{Subleading}}$ (top right), $\eta^{\mu,\text{Leading}}$ (middle left), $\eta^{\mu,\text{Subleading}}$ (middle right), $\phi^{\mu,\text{Leading}}$ (bottom left) and $\phi^{\mu,\text{Subleading}}$ (bottom right) in the Z control region. MC statistical and experimental systematic uncertainties are included within the error bands, along with $P_T^{\mu\mu}$ and M_{inv}^{jj} re-weighting uncertainties. The MC samples have been normalised to 80.5 fb^{-1}, corresponding to the luminosity of the data, apart from the signal samples, which have been scaled by a further factor of 500. For the $P_T^{\mu,\text{Leading}}$ and $P_T^{\mu,\text{Subleading}}$ distributions, entries with $P_T^{\mu} > 200$ GeV are collectively presented in overflow bins.

butions of events selected within the Z control region. The $P_T^{\mu\mu}$ distribution shows a distorted shape, despite the applied $P_T^{\mu\mu}$ re-weighting, due to the imperfect performance of the 6th order polynomial fit. However, data-MC agreement within 5% is still achieved. E_T^{miss} remains well modelled throughout the analysed phase space, with discrepancies typically less than 5%. While discrepancies of 10% are seen in the high E_T^{miss} region, they are contained within the systematic error bands. The $\Delta R^{\mu\mu}$ ratio remains largely flat, with agreement within 1-2%, growing to 10% in the low $\Delta R^{\mu\mu}$ region where muon identification becomes more difficult. Both $\Delta\phi^{\mu\mu}$ and $y^{\mu\mu}$ are well modelled, with data-MC discrepancies within 2-3%. While discrepancies greater than 5% are seen in the $|y^{\mu\mu}| > 2.5$ region, the number of events present is very limited, such that impact on the analysis is negligible. The Jet Multiplicity appears well modelled up to NJets < 8, with agreement within 10-20% and within the systematic uncertainty bands. There is however a 50% mismodelling of zero-jet events. This could be due to miscalibration of the MC jets, rather than the MC generator, since the effect is seen using Madgraph, Sherpa and Powheg Drell-Yan MC (as can be seen in Figure B.0.5 of Appendix B). The effect is also absent within the Signal region, as presented later in Figure 8.3.2, so was thought to have little effect on the analysis.

Figure 8.1.3 presents the $M_{\text{inv}}^{\mu\mu}$, $\cos(\theta^*)$, Jet Multiplicity ($|\eta \leq 2.5|$) and Jet Multiplicity ($|\eta > 2.5|$) distributions within the Z control region. The $M_{\text{inv}}^{\mu\mu}$ distribution presents data-MC agreement within 5%, with fluctuations largely contained within the error bands. $\cos(\theta^*)$, defined as

$$\cos(\theta^*) = \frac{P_T^{\mu\mu}(P_{T,1}^{\mu^+}P_{T,2}^{\mu^-} - P_{T,1}^{\mu^-}P_{T,2}^{\mu^+})}{M_{\text{inv}}^{\mu\mu}|P_T^{\mu\mu}|\sqrt{(M_{\text{inv}}^{\mu\mu})^2 + (P_T^{\mu\mu})^2}}, \tag{8.1.1}$$

where

$$P_{T,i}^{\mu^\pm} = E_i \pm P_{Z,i}, \tag{8.1.2}$$

with $i = 1(2)$ representing the negatively charged muon (positively charged anti-muon), and P_Z the longitudinal component of the muon's momenta [127], is often used to study the symmetry of boson decays. Since the Z and Higgs bosons are of differing spin (1 and 0 respectively), one can discriminate between their decay products through analysing angular variables such as $\cos(\theta^*)$. In this case, the data-MC modelling of $\cos(\theta^*)$ is seen to agree within 1-2%. Both of the Jet Multiplicity distributions display the same 50% discrepancy of zero-jet events as seen in the previous figure. Above this multiplicity, the $|\eta \leq 2.5|$ distribution exhibits agreement of 5-10%. The $|\eta > 2.5|$ distribution appears well modelled for events with four or fewer jets, with discrepancies greater than 50% arising above this. Such events are four orders of magnitude less prominent than their lower multiplicity counterparts, and thus have a limited impact on the analysis. Forward region events with high jet multiplicities are largely impacted by pile-up, so the

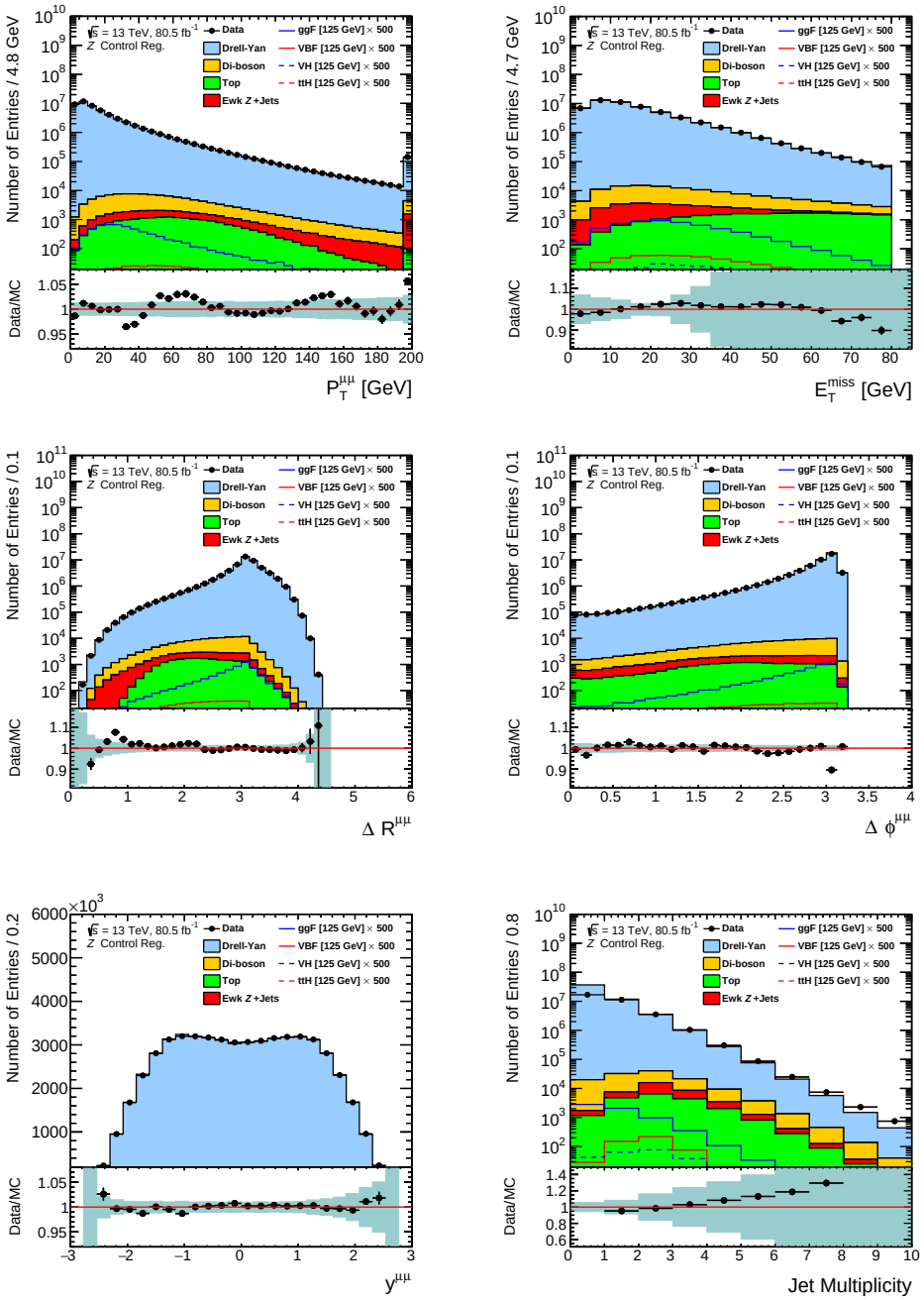

Figure 8.1.2: Comparisons between data and MC samples for $P_T^{\mu\mu}$ (top left), E_T^{miss} (top right), $\Delta R^{\mu\mu}$ (middle left), $\Delta\phi^{\mu\mu}$ (middle right), $y^{\mu\mu}$ (bottom left) and Jet Multiplicity (bottom right) in the Z control region. MC statistical and experimental systematic uncertainties are included within the error bands, along with $P_T^{\mu\mu}$ and M_{inv}^{jj} re-weighting uncertainties. The MC samples have been normalised to 80.5 fb^{-1}, corresponding to the luminosity of the data, with the signal samples scaled by a further factor of 500. For the $P_T^{\mu\mu}$ distribution, entries with $P_T^{\mu\mu} > 200$ GeV are collectively presented in an overflow bin.

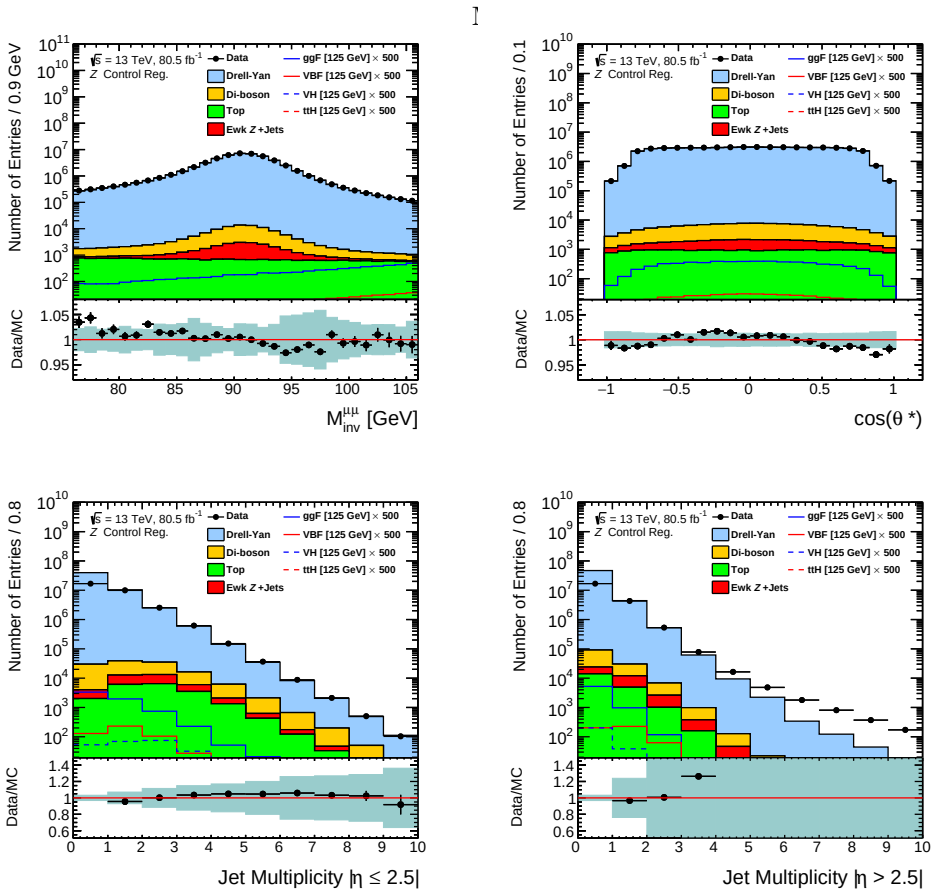

Figure 8.1.3: Comparisons between data and MC samples for $M_{\text{inv}}^{\mu\mu}$ (top left), $\cos(\theta*)$ (top right), Jet Multiplicity for $|\eta \leq 2.5|$ (bottom left) and Jet Multiplicity for $|\eta > 2.5|$ (bottom right) in the Z control region. MC statistical and experimental systematic uncertainties are included within the error bands, along with $P_T^{\mu\mu}$ and M_{inv}^{jj} re-weighting uncertainties. The MC samples have been normalised to 80.5 fb^{-1}, corresponding to the luminosity of the data, with the signal samples scaled by a further factor of 500.

8.2 Z Plus Jets Control Region

The Z Plus Jets control region was devised to study phase spaces of the Z control region where VBF contributions were enhanced. VBF events typically possess two forward jets with a large separation in rapidity. BDTs used for identifying VBF events are thus often trained using jet and rapidity related quantities. The modelling of such variables in both data and MC is considered in this section.

Figure 8.2.1 presents data-MC comparisons as functions of $P_T^{j,\text{Leading}}$, $P_T^{j,\text{Subleading}}$, $\eta^{j,\text{Leading}}$, $\eta^{j,\text{Subleading}}$, $\phi^{j,\text{Leading}}$ and $\phi^{j,\text{Subleading}}$. The P_T^j distributions show data-

MC agreement largely within 20%. A gradual deterioration in agreement is seen with increasing P_T^j, although the dominant VBF contributions come from events with $P_T^j < 200$ GeV, where agreement is within 10%. Both the η^j and ϕ^j distributions appear well modelled, with agreement within 20% and 10% for the former and latter respectively. All fluctuations are contained within the error bands.

Figure 8.2.2 presents distributions of P_T^{jj}, H_T, ΔR^{jj}, $\Delta\phi^{jj}$, M_{inv}^{jj} and Centrality, with the latter defined as

$$\text{Centrality} = \frac{y^{\mu\mu} - \frac{y^{j,\text{Leading}}+y^{j,\text{Subleading}}}{2}}{|y^{j,\text{Leading}} - y^{j,\text{Subleading}}|}. \tag{8.2.1}$$

H_T was defined as the scalar sum of the P_T of all final state muons and jets, and shows a similar level of modelling to the P_T^j distributions - an initial agreement within 5% deteriorates to 20-30% in the high H_T tail. This could be due to poor jet calibration in the high P_T regions, but ultimately this region of phase space contains limited signal, and will thus contribute little to the final result. The large fluctuations in the systematic errors of the distribution are due to jet and pile-up related effects. P_T^{jj} appears better modelled with agreement within 5%, increasing to 10% above 400 GeV. The remaining distributions present data-MC agreement within 10%, demonstrating the data is well described in this region.

Figure 8.2.3 presents data-MC comparisons for $\Delta y^{\mu\mu jj}$, $\Delta y^{\mu\mu j,\text{Leading}}$, $\Delta y^{\mu\mu j,\text{Subleading}}$, $P_T^{\mu\mu jj}$, $P_T^{\mu\mu j,\text{Leading}}$ and $P_T^{\mu\mu j,\text{Subleading}}$, all (with the exception of $\Delta y^{\mu\mu jj}$) used for training Chapter 9's VBF BDT. The labels refer to four-vector combinations of the di-muon and di-jet systems present in the selected final states. The Δy distributions are well modelled, with agreement largely within 10%. The P_T distributions again demonstrate a deterioration of agreement with increasing P_T, although fluctuations are generally contained within the presented uncertainties, and the regions most sensitive to VBF ($P_T^j < 200$) GeV present data-MC agreement to within 5%.

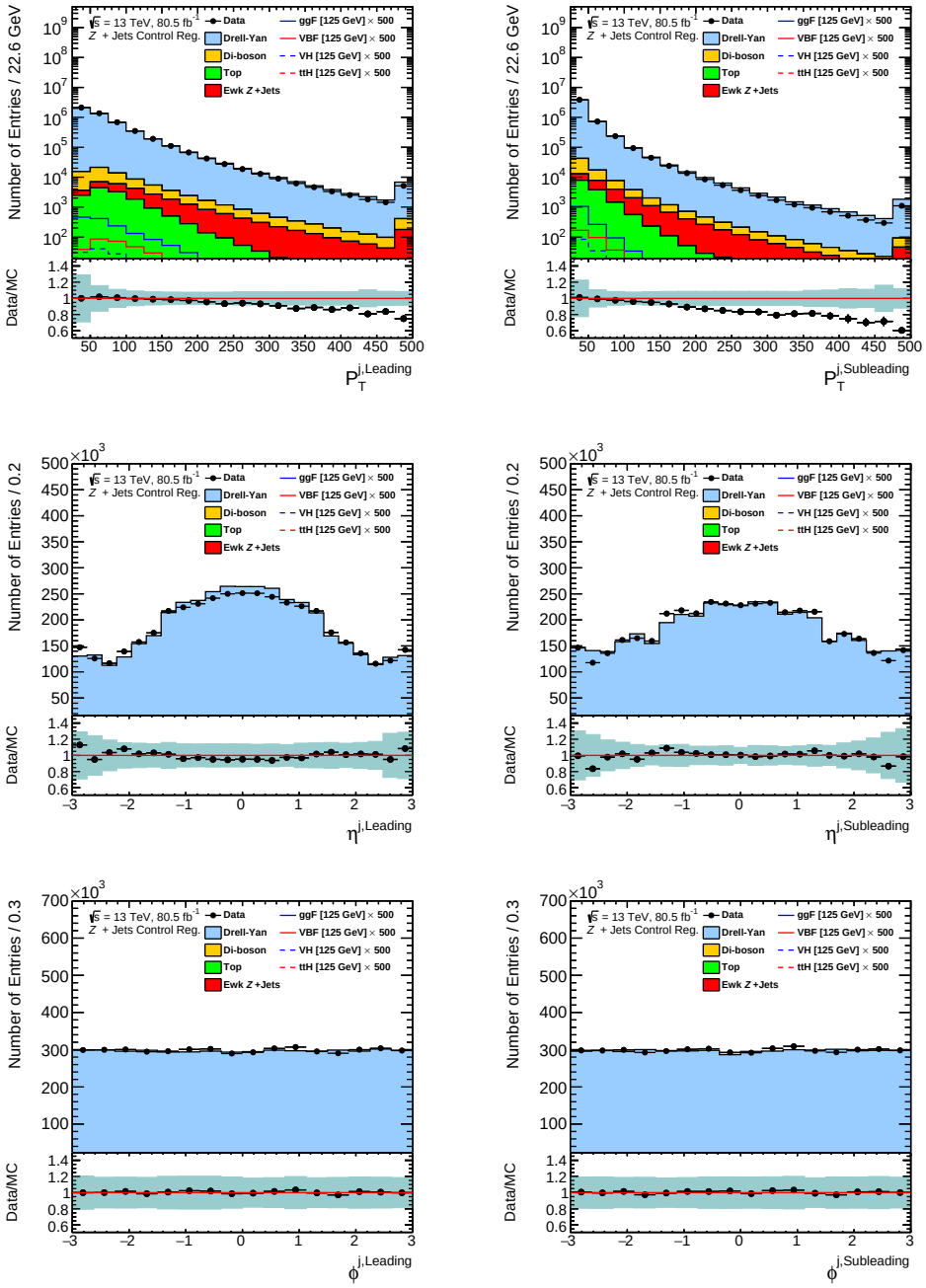

Figure 8.2.1: Comparisons between data and MC samples for $P_T^{j,\text{Leading}}$ (top left), $P_T^{j,\text{Subleading}}$ (top right), $\eta^{j,\text{Leading}}$ (middle left), $\eta^{j,\text{Subleading}}$ (middle right), $\phi^{j,\text{Leading}}$ (bottom left) and $\phi^{j,\text{Subleading}}$ (bottom right) in the Z Plus Jets control region. MC statistical and experimental systematic uncertainties are included within the error bands, along with $P_T^{\mu\mu}$ and M_{inv}^{jj} re-weighting uncertainties. The MC samples have been normalised to 80.5 fb^{-1}, corresponding to the luminosity of the data, with the signal samples scaled by a further factor of 500. For the $P_T^{j,\text{Leading}}$ and $P_T^{j,\text{Subleading}}$ distributions, entries with $P_T^j > 500$ GeV are collectively presented in overflow bins.

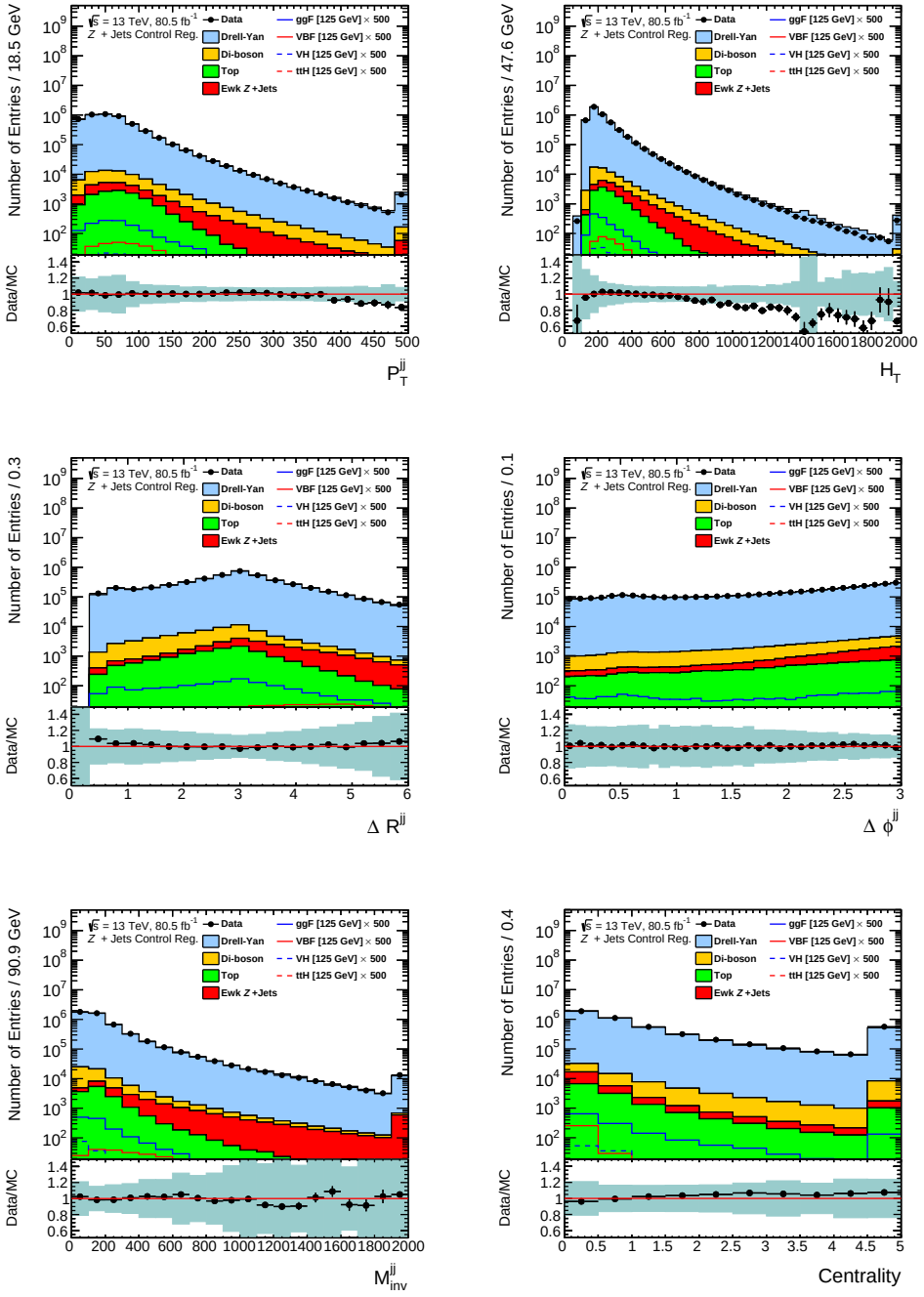

Figure 8.2.2: Comparisons between data and MC samples for P_T^{jj} (top left), H_T (top right), ΔR^{jj} (middle left), $\Delta\phi^{jj}$ (middle right), M_{inv}^{jj} (bottom left) and Centrality (bottom right) in the Z Plus Jets control region. MC statistical and experimental systematic uncertainties are included within the error bands, along with $P_T^{\mu\mu}$ and M_{inv}^{jj} re-weighting uncertainties. The MC samples have been normalised to 80.5 fb^{-1}, corresponding to the luminosity of the data, with the signal samples scaled by a further factor of 500. For the P_T^{jj}, H_T, M_{inv}^{jj} and Centrality distributions, the rightmost bin contains an overflow of entries above the presented ranges.

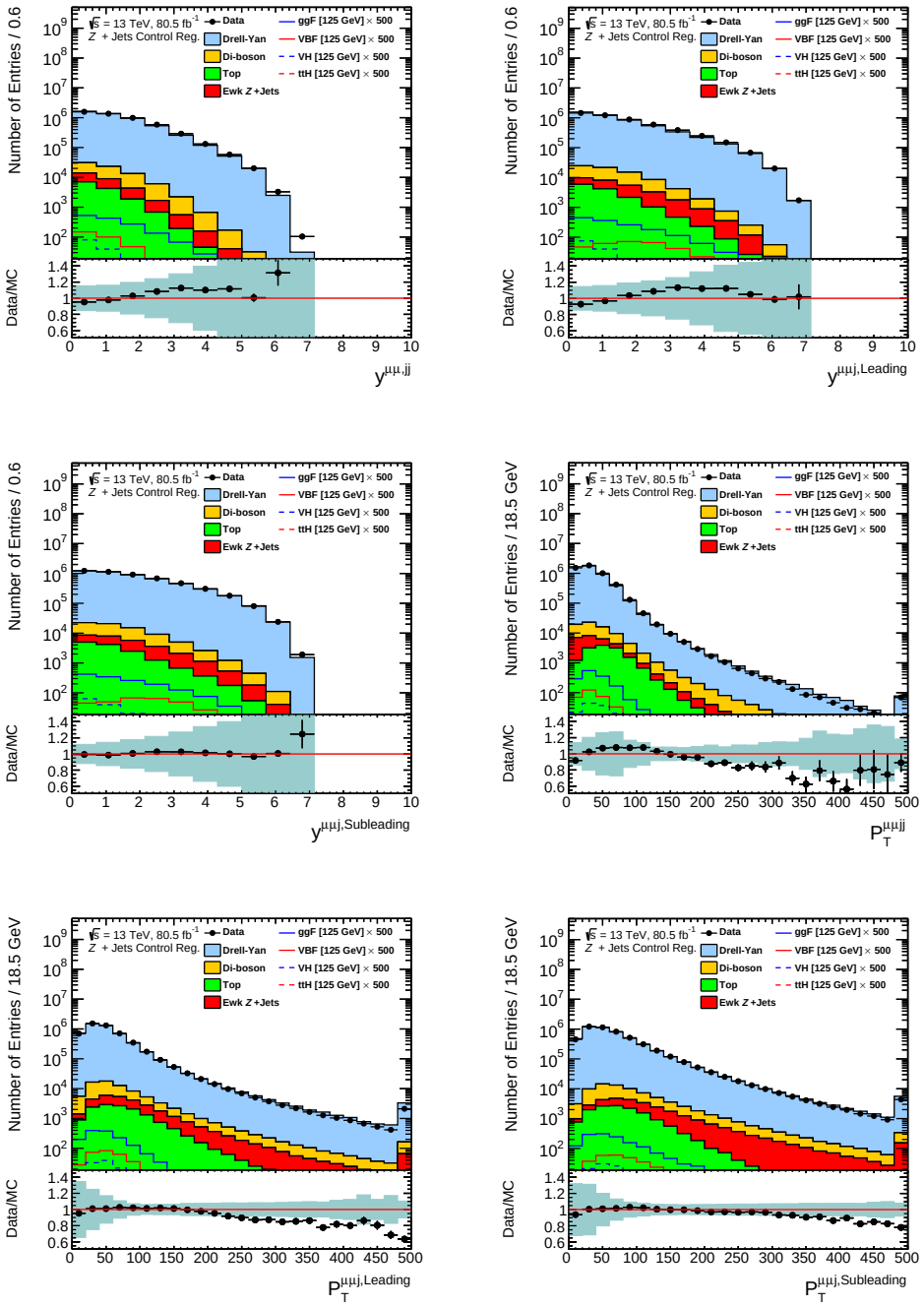

Figure 8.2.3: Comparisons between data and MC samples for $\Delta y^{\mu\mu jj}$ (top left), $\Delta y^{\mu\mu j,\mathrm{Leading}}$ (top right), $\Delta y^{\mu\mu j,\mathrm{Subleading}}$ (middle left), $P_T^{\mu\mu jj}$ (middle right), $P_T^{\mu\mu j,\mathrm{Leading}}$ (bottom left) and $P_T^{\mu\mu j,\mathrm{Subleading}}$ (bottom right) in the Z Plus Jets control region. MC statistical and experimental systematic uncertainties are included within the error bands, along with $P_T^{\mu\mu}$ and M_{inv}^{jj} re-weighting uncertainties. The MC samples have been normalised to 80.5 fb^{-1}, corresponding to the luminosity of the data, with the signal samples scaled by a further factor of 500. For the $P_T^{\mu\mu jj}$, $P_T^{\mu\mu j,\mathrm{Leading}}$ and $P_T^{\mu\mu j,\mathrm{Subleading}}$ distributions, the rightmost bin contains an overflow of entries above the presented ranges.

8.3 Signal Region

Having implemented a selection capable of accurately describing the Z mass peak, a Signal region selection was devised, allowing the analysis of events surrounding the Higgs mass peak. This section presents data-MC comparisons of various distributions within this region. The ratio panels contain error bands representing MC statistical, experimental systematic and $P_T^{\mu\mu}$ and M_{inv}^{jj} re-weighting uncertainties.

Figure 8.3.1 presents the $P_T^{\mu,\text{Leading}}$, $P_T^{\mu,\text{Subleading}}$, $\eta^{\mu,\text{Leading}}$, $\eta^{\mu,\text{Subleading}}$, $\phi^{\mu,\text{Leading}}$ and $\phi^{\mu,\text{Subleading}}$ distributions of muons selected within $110 < M_{\text{inv}}^{\mu\mu} < 160$ GeV. The P_T distributions present data-MC agreement within 10%, with fluctuations largely contained within the associated error bands. The η and ϕ distributions are well modelled, with agreement within 5%.

Figure 8.3.2 presents the $P_T^{\mu\mu}$, E_T^{miss}, $\Delta R^{\mu\mu}$, $\Delta\phi^{\mu\mu}$, $y^{\mu\mu}$ and Jet Multiplicity distributions of events selected within the Signal region. All variables are well modelled, with data-MC agreements typically within 5-10%. The discrepancies seen in Figures 8.1.2 and 8.1.3 for zero-jet events were not reproduced within this region, with data and MC instead agreeing to within 5%. This was an important result, since many of the BDTs of Chapter 9 were trained using events divided into categories of differing Jet Multiplicity. This was undertaken to further exploit the kinematic differences between signal and background events in these regions. For example, VBF contributions are larger in events with two or more jets, with the opposite true for ggF. To effectively divide events into such categories, accurate modelling of Jet Multiplicity was thus required, and was achieved in this case.

Figure 8.3.3 presents the $M_{\text{inv}}^{\mu\mu}$, $\cos(\theta^*)$, Jet Multiplicity ($|\eta \leq 2.5|$) and Jet Multiplicity ($|\eta > 2.5|$) distributions within the Signal region. The $M_{\text{inv}}^{\mu\mu}$ distribution is reasonably smooth, with the data and MC agreeing to within 10%. The presented fluctuations are all contained within the considered uncertainties. Both $\cos(\theta^*)$ and the central Jet Multiplicity are also well modelled, with discrepancies typically smaller than 10%. Data-MC discrepancies greater than 50% are seen in the forward Jet Multiplicity distribution for events with four or more jets. As discussed previously, this is likely due to mismodelling of pile-up jets, and will have had little effect on the analysis. Firstly, each BDT trained using the forward Jet Multiplicity in Chapter 9 found the variable to be of minimal importance, so misclassification of data due to this mismodelling is unlikely to have occurred. More importantly, the extraction of $H \to \mu\mu$ (presented in Chapter 12) was performed using the $M_{\text{inv}}^{\mu\mu}$ distributions of data, not MC. Providing the BDTs used to categorise the data were trained with variables uncorrelated to $M_{\text{inv}}^{\mu\mu}$, the final $M_{\text{inv}}^{\mu\mu}$ distributions should be unbiased with respect to the data-MC mismodelling seen in this chapter. This is true for all presented distributions, and is one of the reasons MC shape systematic uncertainties were neglected in the extraction of μ_s, as discussed in Chapter 11.

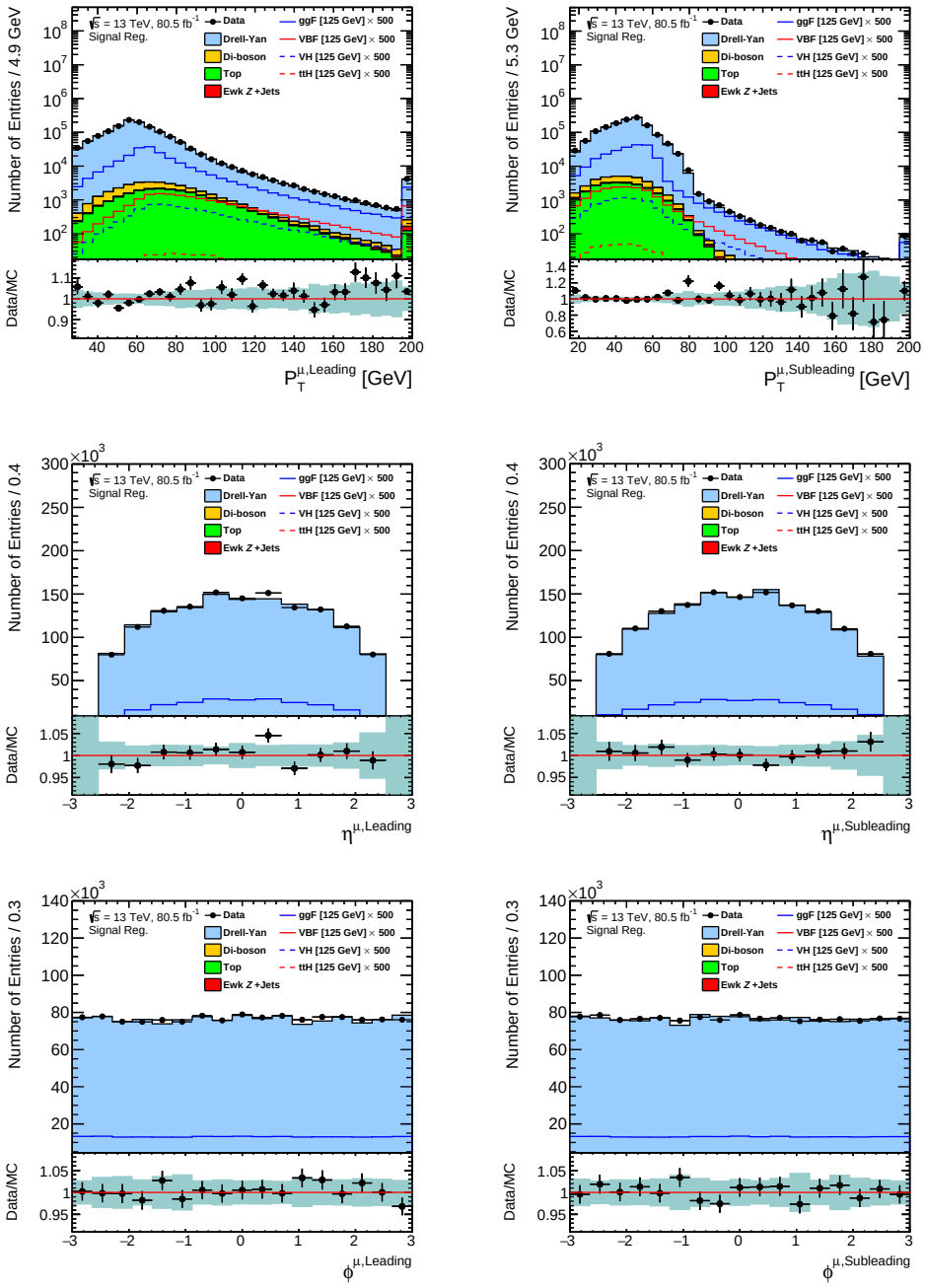

Figure 8.3.1: Comparisons between data and MC samples for $P_T^{\mu,\text{Leading}}$ (top left), $P_T^{\mu,\text{Subleading}}$ (top right), $\eta^{\mu,\text{Leading}}$ (middle left), $\eta^{\mu,\text{Subleading}}$ (middle right), $\phi^{\mu,\text{Leading}}$ (bottom left) and $\phi^{\mu,\text{Subleading}}$ (bottom right) in the Signal region. MC statistical and experimental systematic uncertainties are included within the error bands, along with $P_T^{\mu\mu}$ and M_{inv}^{jj} re-weighting uncertainties. The MC samples have been normalised to 80.5 fb^{-1}, corresponding to the luminosity of the data, with the signal samples scaled by a further factor of 500. For the $P_T^{\mu,\text{Leading}}$ and $P_T^{\mu,\text{Subleading}}$ distributions, entries with $P_T^{\mu} > 200$ GeV are collectively presented in overflow bins.

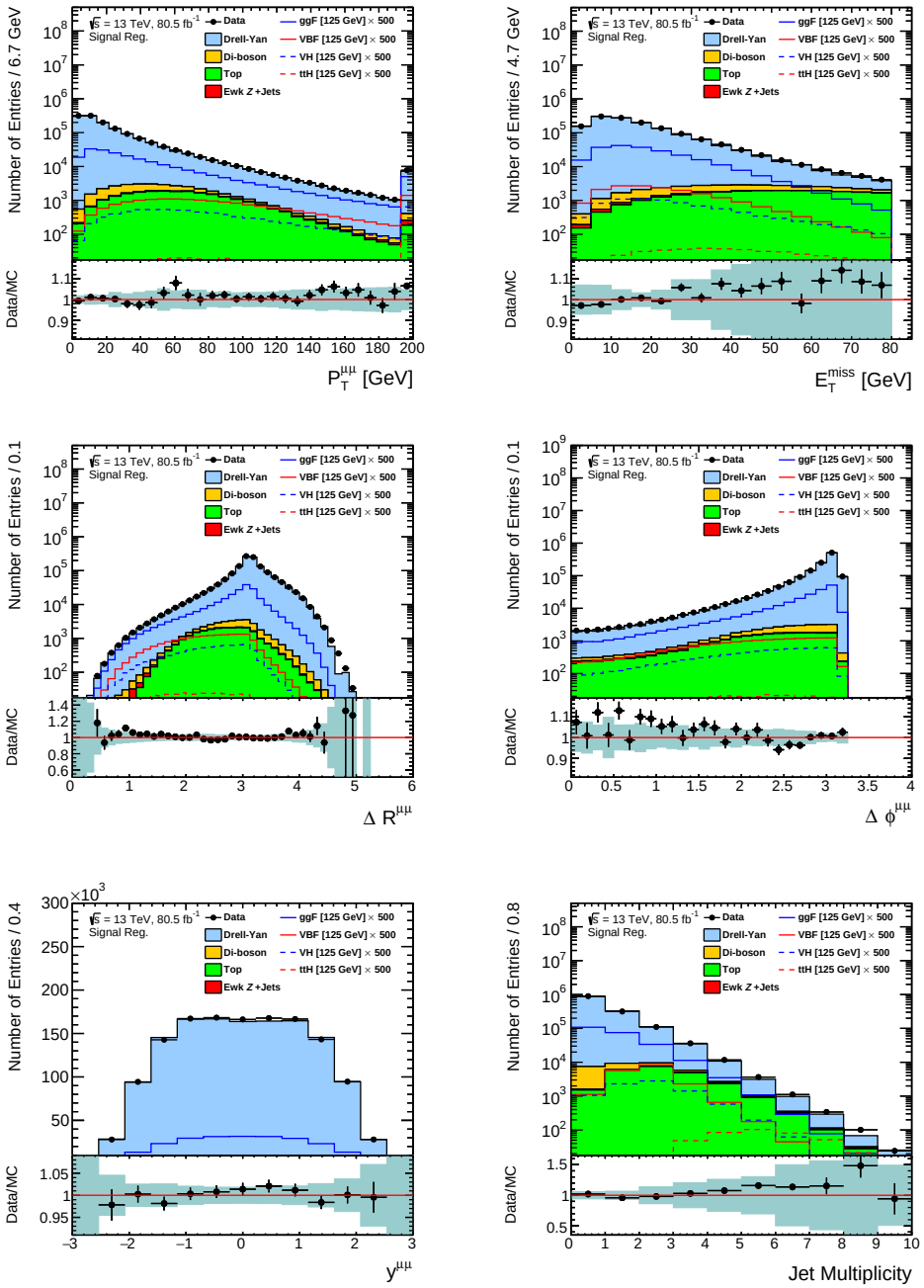

Figure 8.3.2: Comparisons between data and MC samples for $P_T^{\mu\mu}$ (top left), E_T^{miss} (top right), $\Delta R^{\mu\mu}$ (middle left), $\Delta\phi^{\mu\mu}$ (middle right), $y^{\mu\mu}$ (bottom left) and Jet Multiplicity (bottom right) in the Signal region. MC statistical and experimental systematic uncertainties are included within the error bands, along with $P_T^{\mu\mu}$ and M_{inv}^{jj} re-weighting uncertainties. The MC samples have been normalised to 80.5 fb^{-1}, corresponding to the luminosity of the data, with the signal samples scaled by a further factor of 500. For the $P_T^{\mu\mu}$ distribution, entries with $P_T^{\mu\mu} > 200$ GeV are collectively presented in an overflow bin.

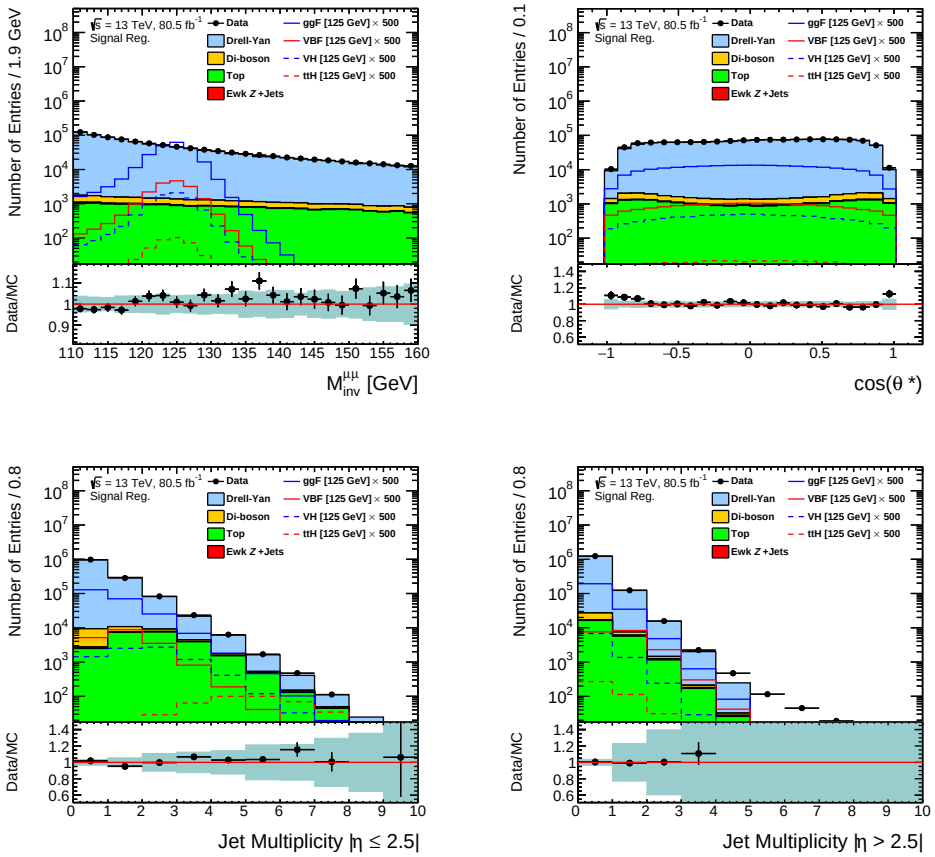

Figure 8.3.3: Comparisons between data and MC samples for $M_{\text{inv}}^{\mu\mu}$ (top left), $\cos(\theta*)$ (top right), Jet Multiplicity for $|\eta \leq 2.5|$ (bottom left) and Jet Multiplicity for $|\eta > 2.5|$ (bottom right) in the Signal region. MC statistical and experimental systematic uncertainties are included within the error bands, along with $P_T^{\mu\mu}$ and M_{inv}^{jj} re-weighting uncertainties. The MC samples have been normalised to 80.5 fb^{-1}, corresponding to the luminosity of the data, with the signal samples scaled by a further factor of 500.

8.4 Signal Plus Jets Region

Signal region events with two or more jets were studied in a dedicated region to validate the MC modelling of events used to train the VBF and Multi-Jet BDTs of Chapter 9.

Figure 8.4.1 presents data-MC comparisons as functions of $P_T^{j,\text{Leading}}$, $P_T^{j,\text{Subleading}}$, $\eta^{j,\text{Leading}}$, $\eta^{j,\text{Subleading}}$, $\phi^{j,\text{Leading}}$ and $\phi^{j,\text{Subleading}}$. The η^j and ϕ^j distributions present data-MC agreement within 10-20%, with fluctuations contained within the considered uncertainties. Both $P_T^{j,\text{Leading}}$ and $P_T^{j,\text{Subleading}}$ appear well modelled over the considered phase space, with the data and MC samples agreeing within 10-20% on average. Some deterioration in agreement is seen for high $P_T^{j,\text{Subleading}}$, although considering the large MC statistical uncertainties present, this is likely due to the limited number of events.

Figures 8.4.2 and 8.4.3 presents distributions of P_T^{jj}, H_T, ΔR^{jj}, $\Delta\phi^{jj}$, M_{inv}^{jj}, Centrality, $\Delta y^{\mu\mu jj}$, $\Delta y^{\mu\mu j,\text{Leading}}$, $\Delta y^{\mu\mu j,\text{Subleading}}$, $P_T^{\mu\mu jj}$, $P_T^{\mu\mu j,\text{Leading}}$ and $P_T^{\mu\mu j,\text{Subleading}}$. All variables appear to be well modelled in both sets of samples, with data-MC agreement typically within 10-20%, and fluctuations contained within the considered uncertainties. There are 40-50% discrepancies in the H_T distribution for $H_T < 100$ GeV and $H_T > 1400$ GeV, although these regions possess large statistical uncertainties. Regardless, H_T was not used in the training of any BDTs, due to its high correlation with $M_{\text{inv}}^{\mu\mu}$, and thus its modelling is purely demonstrative, and had no effect on the analysis.

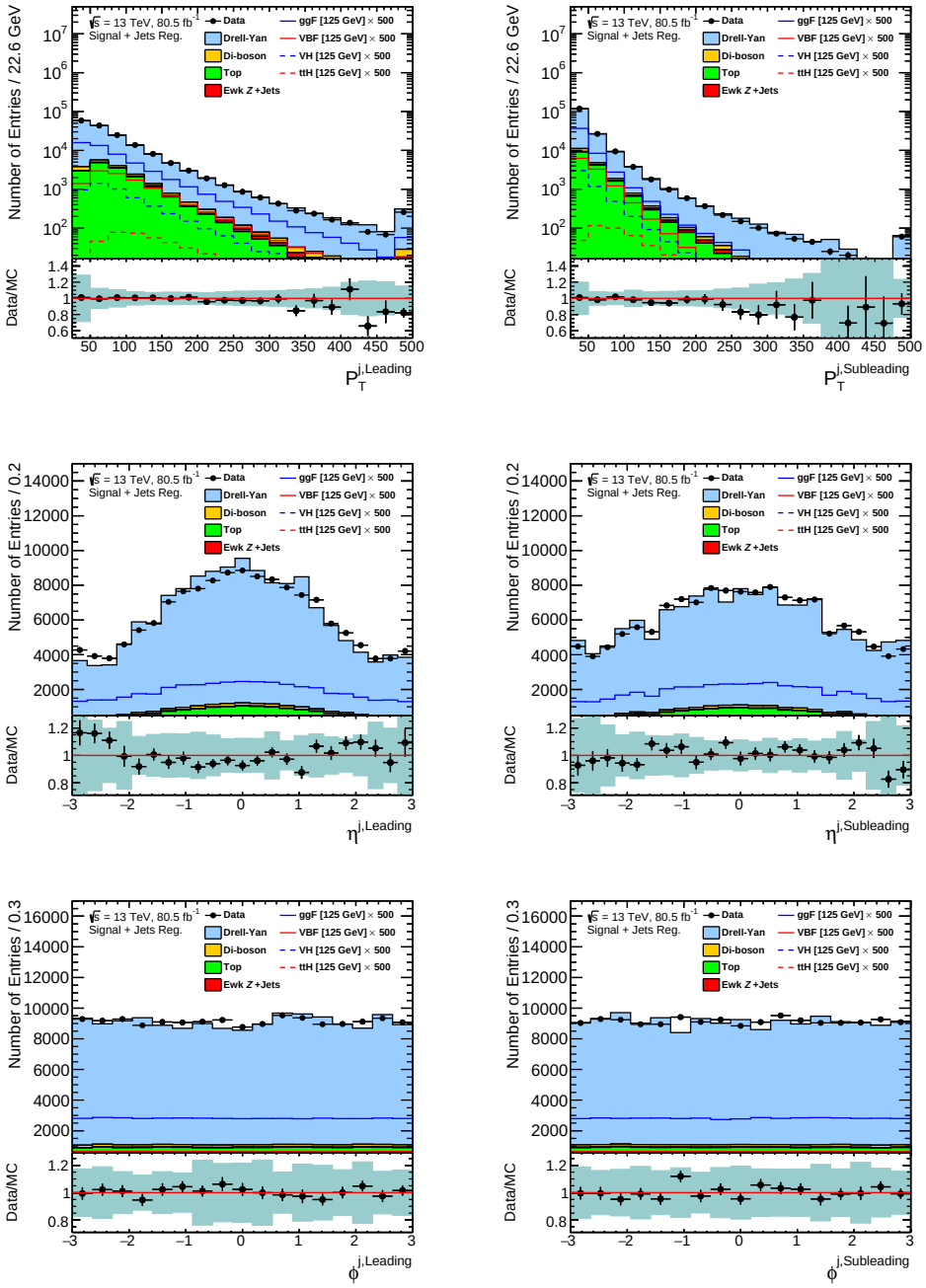

Figure 8.4.1: Comparisons between data and MC samples for $P_T^{j,\text{Leading}}$ (top left), $P_T^{j,\text{Subleading}}$ (top right), $\eta^{j,\text{Leading}}$ (middle left), $\eta^{j,\text{Subleading}}$ (middle right), $\phi^{j,\text{Leading}}$ (bottom left) and $\phi^{j,\text{Subleading}}$ (bottom right) in the Signal Plus Jets control region. MC statistical and experimental systematic uncertainties are included within the error bands, along with $P_T^{\mu\mu}$ and M_{inv}^{jj} re-weighting uncertainties. The MC samples have been normalised to 80.5 fb^{-1}, corresponding to the luminosity of the data, with the signal samples scaled by a further factor of 500. For the $P_T^{j,\text{Leading}}$ and $P_T^{j,\text{Subleading}}$ distributions, entries with $P_T^j > 500$ GeV are collectively presented in overflow bins.

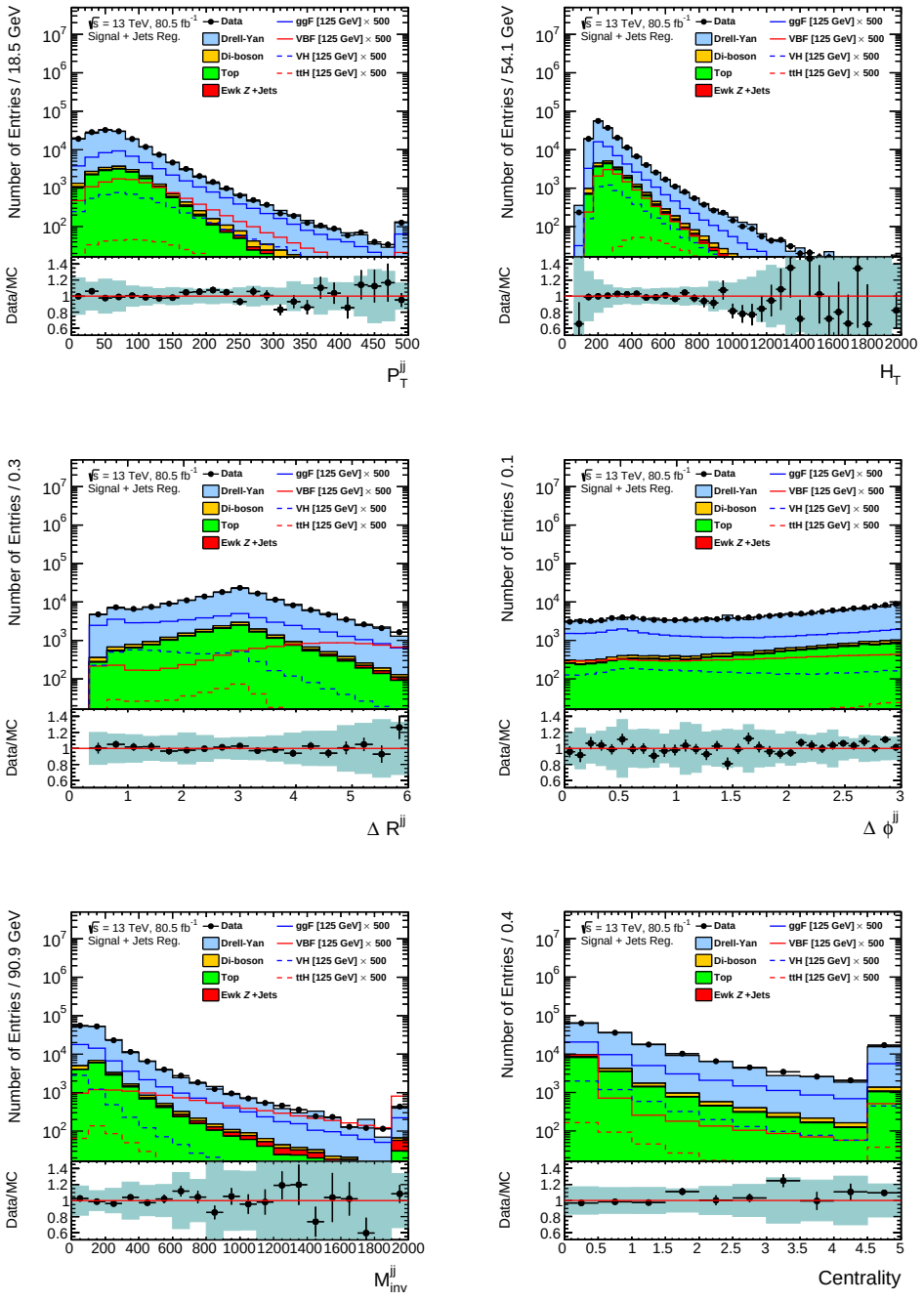

Figure 8.4.2: Comparisons between data and MC samples for P_T^{jj} (top left), H_T (top right), ΔR^{jj} (middle left), $\Delta\phi^{jj}$ (middle right), M_{inv}^{jj} (bottom left) and Centrality (bottom right) in the Signal Plus Jets control region. MC statistical and experimental systematic uncertainties are included within the error bands, along with $P_T^{\mu\mu}$ and M_{inv}^{jj} re-weighting uncertainties. The MC samples have been normalised to 80.5 fb^{-1}, corresponding to the luminosity of the data, with the signal samples scaled by a further factor of 500. For the P_T^{jj}, H_T, M_{inv}^{jj} and Centrality distributions, the rightmost bin contains an overflow of entries above the presented ranges.

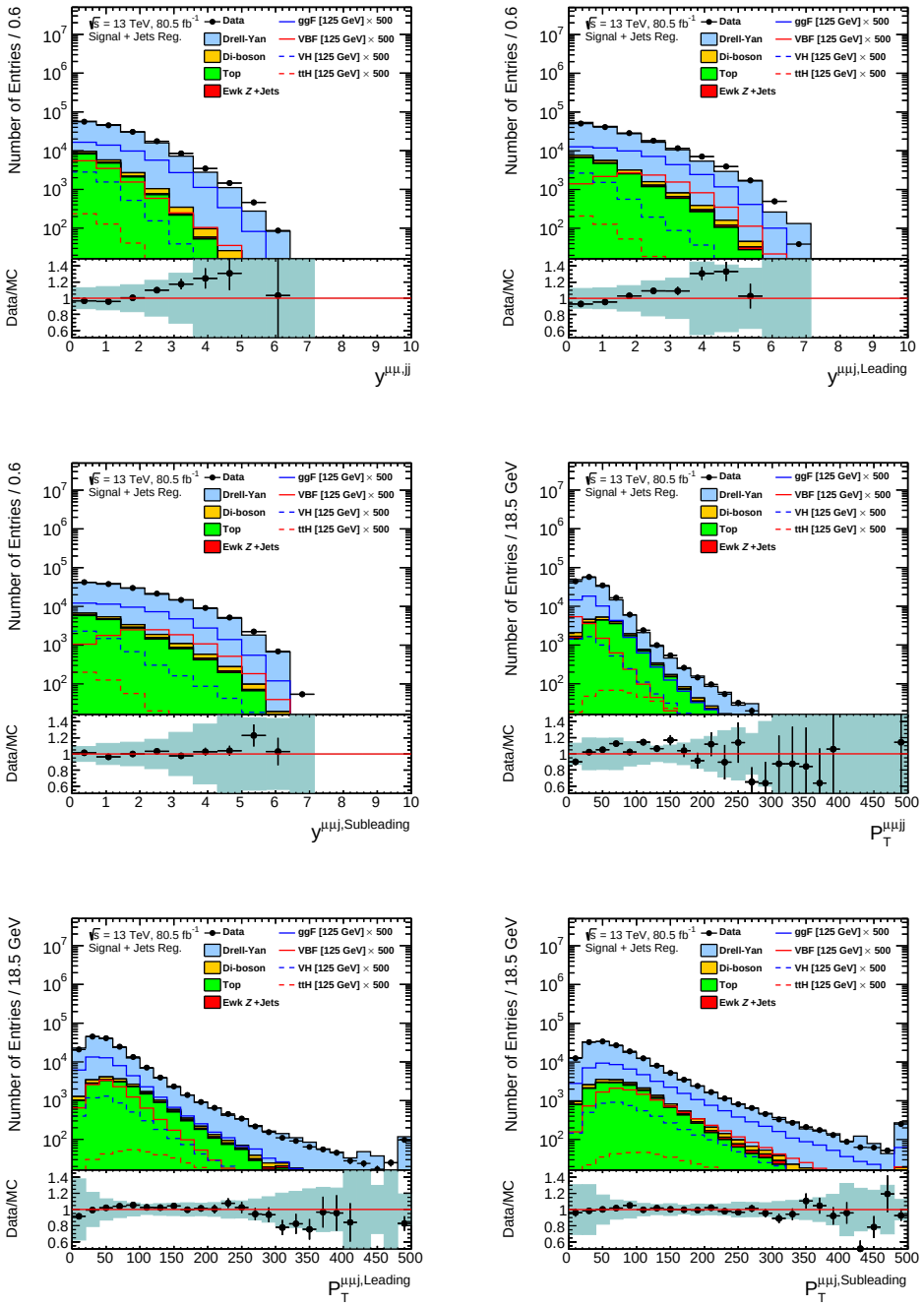

Figure 8.4.3: Comparisons between data and MC samples for $\Delta y^{\mu\mu jj}$ (top left), $\Delta y^{\mu\mu j,\text{Leading}}$ (top right), $\Delta y^{\mu\mu j,\text{Subleading}}$ (middle left), $P_T^{\mu\mu jj}$ (middle right), $P_T^{\mu\mu j,\text{Leading}}$ (bottom left) and $P_T^{\mu\mu j,\text{Subleading}}$ (bottom right) in the Signal Plus Jets control region. MC statistical and experimental systematic uncertainties are included within the error bands, along with $P_T^{\mu\mu}$ and M_{inv}^{jj} re-weighting uncertainties. The MC samples have been normalised to 80.5 fb^{-1}, corresponding to the luminosity of the data, with the signal samples scaled by a further factor of 500. For the $P_T^{\mu\mu jj}$, $P_T^{\mu\mu j,\text{Leading}}$ and $P_T^{\mu\mu j,\text{Subleading}}$ distributions, the rightmost bin contains an overflow of entries above the presented ranges.

Chapter 9

Category Optimisation with Boosted Decision Trees

In many analyses (such as this), the $H \to \mu\mu$ signal strength is extracted by performing a combined signal plus background fit to the $M_{\text{inv}}^{\mu\mu}$ distributions of data within the Signal region. Signal sensitivity can be maximised by sorting events into categories of large $\frac{S}{\sqrt{B}}$, and simultaneously fitting the $M_{\text{inv}}^{\mu\mu}$ distributions of each.

In Chapter 7, a BDT was used to define two categories sensitive to the VBF process, with events failing the BDT selection sorted into orthogonal ggF categories, split by detector geometry and $P_T^{\mu\mu}$. This chapter presents three alternative methods by which events can be categorised through the use of BDTs, with their respective category sensitivities compared. The first involved training a single BDT using all available signal and background MC samples. The second involved training a BDT to separate the dominant background processes of $H \to \mu\mu$, after which subsequent BDTs sorted signal events from each isolated background component. The third involved training a BDT capable of identifying VBF events, with those failing the selection subject to a ggF-optimised BDT. In each case, categories were derived directly from the BDT output distributions, with all events having passed the Signal region selection outlined in Chapter 6.

Table 9.0.1 presents the full list of variables considered for the training and testing of the analysis BDTs. The variables were chosen based on the quality of their modelling in both data and MC, as presented in Chapter 8. A number were also chosen based on their use in the training of the BDTs of other analyses, such as the most recent ATLAS $H \to \mu\mu$ study. For each method outlined above, BDTs were trained using events with zero, one, and two or more jets separately, so as to maximise signal-background separation. The number of variables available for training the BDTs thus varied, based on the jet multiplicity of the event. For each method, a BDT was also trained on

inclusively selected events for comparison. All BDTs in this chapter underwent two-fold cross-validation, with the TRandom3 class of ROOT (based on the Mersenne Twister pseudo-random number generator [128]) utilised for sample splitting[1]. In each case, one BDT was trained on Fold 1 and tested on (and eventually applied to) Fold 2, with a second BDT trained and tested on the opposite folds.

The end goal of the analysis was to measure the $H \to \mu\mu$ signal strength through applying signal plus background fits to the $M_{\text{inv}}^{\mu\mu}$ distributions of data in each of the analysis categories (described in detail in the coming chapters). In order to validate the performance of the fits without biasing oneself to trends in the data, fits were initially performed on the $M_{\text{inv}}^{\mu\mu}$ distributions of background MC. As seen in Figure 8.3.3, the total background $M_{\text{inv}}^{\mu\mu}$ distributions should fall smoothly within the $110 \leq M_{\text{inv}}^{\mu\mu} < 160$ GeV region. However, when training a BDT with variables highly correlated with $M_{\text{inv}}^{\mu\mu}$, the $M_{\text{inv}}^{\mu\mu}$ distributions of subsequently derived categories can become distorted, leading to fitting biases. To avoid this effect, a BDT was trained (using two-fold cross-validation) with all of the variables listed in Table 9.0.1, along with $M_{\text{inv}}^{\mu\mu}$, and variables found to be highly correlated with $M_{\text{inv}}^{\mu\mu}$ were removed from future BDT trainings. The output linear correlation coefficient matrices for the background events of each fold of the BDT trained on inclusive events are shown below in Figures 9.0.1 and 9.0.2. Similar plots for BDTs trained with zero-jet, single-jet and multi-jet events are shown in Appendix C. ggF, VBF, VH and $t\bar{t}H$ processes were utilised as signal inputs, while Drell-Yan, di-boson, top and electroweak Z plus jet events were used as backgrounds. H_T, $P_T^{\mu,\text{Leading}}$ and $P_T^{\mu,\text{Subleading}}$ all presented linear correlation coefficients greater than 10% with respect to $M_{\text{inv}}^{\mu\mu}$ across all BDTs considered, and were thus ignored from further BDT trainings. In the Multi-Jet case, $\Delta R^{\mu\mu}$ was also removed, since it's correlation with $M_{\text{inv}}^{\mu\mu}$ exceeded 10% in Fold 2.

[1] Although not used in the BDT training, the data samples used in the analysis were also split in this way for consistency.

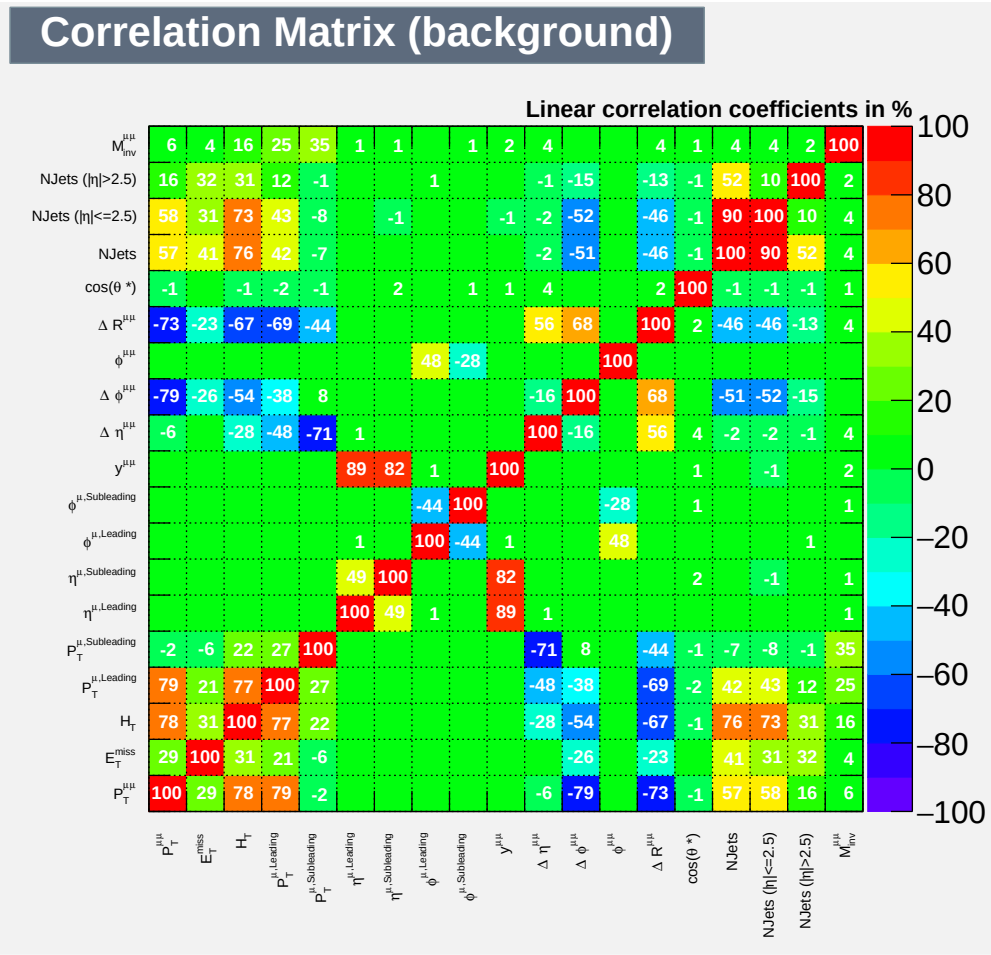

Figure 9.0.1: Correlations between variables considered for training the Inclusive selection BDTs. Correlations are presented for Fold 1 of the combined Drell-Yan, di-boson, top and electroweak Z plus jet backgrounds.

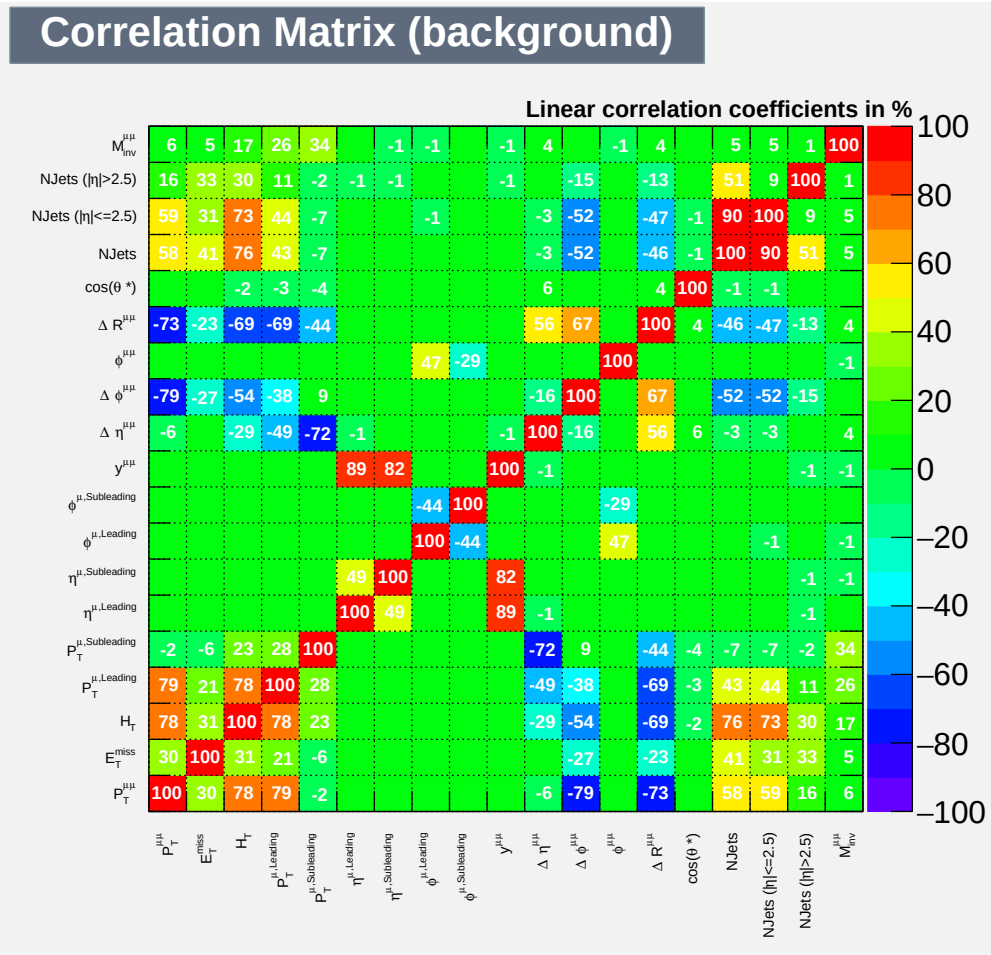

Figure 9.0.2: Correlations between variables considered for training the Inclusive selection BDTs. Correlations are presented for Fold 2 of the combined Drell-Yan, di-boson, top and electroweak Z plus jet backgrounds.

Variable	Inclusive	≥ 2 jets	1-jet	0-jet
$P_T^{\mu,\text{Leading}}$	✓	✓	✓	✓
$P_T^{\mu,\text{Subleading}}$	✓	✓	✓	✓
$\eta^{\mu,\text{Leading}}$	✓	✓	✓	✓
$\eta^{\mu,\text{Subleading}}$	✓	✓	✓	✓
$\phi^{\mu,\text{Leading}}$	✓	✓	✓	✓
$\phi^{\mu,\text{Subleading}}$	✓	✓	✓	✓
$y^{\mu\mu}$	✓	✓	✓	✓
$\Delta\eta^{\mu\mu}$	✓	✓	✓	✓
$\Delta\phi^{\mu\mu}$	✓	✓	✓	✓
$\phi^{\mu\mu}$	✓	✓	✓	✓
$\Delta R^{\mu\mu}$	✓	✓	✓	✓
$\cos(\theta^*)$	✓	✓	✓	✓
$P_T^{\mu\mu}$	✓	✓	✓	✓
E_T^{miss}	✓	✓	✓	✓
H_T	✓	✓	✓	✓
Jet Multiplicity	✓	✓	×	×
Jet Multiplicity ($\lvert\eta^j\rvert \leq 2.5$)	✓	✓	×	×
Jet Multiplicity ($\lvert\eta^j\rvert > 2.5$)	✓	✓	×	×
$\Delta\eta^{jj}$	×	✓	×	×
ΔR^{jj}	×	✓	×	×
Centrality	×	✓	×	×
M_{inv}^{jj}	×	✓	×	×
P_T^{jj}	×	✓	×	×
$\Delta y^{\mu\mu j,\text{Leading}}$	×	✓	×	×
$P_T^{\mu\mu j,\text{Leading}}$	×	✓	×	×
$\Delta y^{\mu\mu j,\text{Subleading}}$	×	✓	×	×
$P_T^{\mu\mu j,\text{Subleading}}$	×	✓	×	×
$\Delta y^{\mu\mu jj}$	×	✓	×	×
$P_T^{\mu\mu jj}$	×	✓	×	×
$P_T^{j,\text{Leading}}$	×	✓	✓	×
$\eta^{j,\text{Leading}}$	×	✓	✓	×
$\phi^{j,\text{Leading}}$	×	✓	✓	×
$P_T^{j,\text{Subleading}}$	×	✓	×	×
$\eta^{j,\text{Subleading}}$	×	✓	×	×
$\phi^{j,\text{Subleading}}$	×	✓	×	×

Table 9.0.1: Variables considered for the training and testing of the analysis BDTs.

The baseline parameters used for training the analysis BDTs are presented in Table 9.0.2. The number of trees and cuts (NTrees and NCuts respectively), along with the BDT depth (MaxDepth) were all limited to avoid overtraining, quantified as the difference in number of events between the test and training samples in each bin of the BDT output distributions. The GradientBoost algorithm was used alongside a bagged resampling procedure, with a BaggedSampleFraction of 0.5 recommended by the TMVA user manual [116]. The Shrinkage parameter, controlling the weights of individual trees, was set to 0.1 in order to limit the learning rate of the classifiers. This encouraged the growth of more trees, helping to reduce the classifier's sensitivity to overtraining. Negative weights were ignored during training to avoid complications with boosting (although the associated events were still utilised when evaluating BDT performance).

BDT Parameter	Value
NTrees	200
MaxDepth	4
NCuts	20
Shrinkage	0.1
BoostType	Grad
UseBaggedBoost	True
BaggedSampleFraction	0.5
IgnoreNegWeightsInTraining	True

Table 9.0.2: Benchmark parameters used for training the analysis BDTs.

For each of the methods explored in this chapter, category optimisation was performed in two distinct steps. A variable-optimisation algorithm was applied to each BDT to determine the best performing sets of variables. BDT performance was quantified by integrating under the associated ROC curves (as explained in Chapter 7). All pair-wise combinations of allowed variables were considered, after which variables were sequentially added to the best-performing pair until performance could not be improved by more than 0.01%. To ensure maximal optimisation, all combinations of all allowed variables were considered at each stage. In the case of k-folded samples, the optimisation was performed for each fold individually, with only variables common to both folds taken forward. This was done to avoid overtraining with respect to a particular fold. Figure 9.0.3 presents the evolution of the ROC curve of a BDT undergoing the variable-optimisation procedure. The optimisation was performed using inclusively selected events, with all signal and background MC samples utilised. For the BDTs trained with two variables (black), performance between variable combinations varies by up 11%. Performance was further improved through training with additional variables, represented by the red (three), green

(four), blue (five), magenta (six) and cyan (seven) lines. The addition of a third variable to the best performing pair further improved performance by 0.45%, with improvements as little as 0.06% seen when moving from six to seven variables.

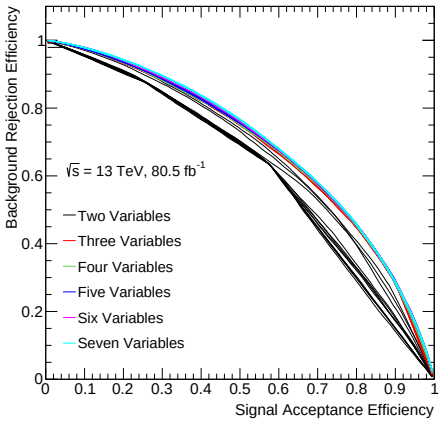

Figure 9.0.3: The evolution of the ROC curve of a BDT undergoing the variable-optimisation procedure described in Chapter 9. The black lines represent BDTs trained using all pair-wise combinations of available variables. The best performing pair was taken as the basis of the three variable BDTs, represented in red. Subsequent BDTs trained using four (green), five (blue), six (magenta) and seven (cyan) variables are also presented. The number of variables considered for training the BDTs was increased until the ROC curve integrals improved by less than 0.01%.

Trained BDTs were then subject to a boundary-optimisation algorithm, tasked with cutting the BDT output distributions into categories such that the combined signal sensitivity ($\frac{S}{\sqrt{B}}$) was maximised. For a given step-size, the algorithm cut on the BDT output distribution at all available points, and identified the cut producing the categories of highest combined sensitivity. The procedure was performed iteratively, with more cuts introduced until the addition of further categories no longer improved sensitivity. For a reasonably performing BDT, signal sensitivity is largest in high BDT score regions, corresponding to the right-hand side of the output distribution. Categories defined in such regions are therefore often of greatest sensitivity. To prevent the devaluing of existing cuts and to save on computation time, successive iterations of the algorithm therefore only considered cuts to the left of existing categories.

A step-size of 0.01 was found to be most optimal; in moving from 0.1 to 0.01, the combined category sensitivity was improved by roughly 2%, with only a moderate increase in computation time. A step-size of 0.001 showed large increases in computation time ($\mathcal{O}$(hours) rather than $\mathcal{O}$(minutes)) with sensitivity improvements under 1%. Smaller step-sizes also proved more sensitive to statistical fluctuations in the BDT output distributions, leading to the definition of categories where data-MC modelling was poor.

To ensure subsequent background fits performed well, a minimum of 50 background events were required for a category to be accepted. This is roughly equal to the lowest number of background events found in the VBF Tight category of the 36 fb^{-1} $H \to \mu\mu$ analysis performed by ATLAS [26], where the event count was large enough for the fits to converge successfully.

9.1 Inclusive Signal Plus Background BDTs

Following the approaches taken by other analyses [25], a single BDT was trained using all signal and background MC samples, referred to as the Inclusive BDT strategy. Separate BDTs were trained using zero-jet, single-jet and multi-jet events, alongside an inclusive selection BDT for comparison. Events were divided in this way so as to enhance the kinematic differences between the different signal and background processes. For example, VBF events typically dominate the phase space with two or more jets, while ggF events are more prominent at lower jet multiplicities.

The variables used to train the inclusive selection BDT are presented in Table 9.1.1, and are ranked in order of importance. Importance was quantified by the number of times a variable was used to split decision tree nodes, weighted by the number of events in the node and the square of the separation gain[2] achieved by the cut [116]. $y^{\mu\mu}$ was found to be the most important variable across both folds. Small variations of importance values are seen between folds due to statistical fluctuations within the training samples.

Rank	Variable	Variable Importance
1	$y^{\mu\mu}$	0.150
2	$\Delta\phi^{\mu\mu}$	0.143
3	E_T^{miss}	0.135
4	$\cos(\theta^*)$	0.126
5	$\Delta\eta^{\mu\mu}$	0.125
6	$P_T^{\mu\mu}$	0.115
7	Jet Multiplicity	0.080
8	Jet Multiplicity ($\lvert\eta^j\rvert > 2.5$)	0.063
9	Jet Multiplicity ($\lvert\eta^j\rvert \leq 2.5$)	0.063

Rank	Variable	Variable Importance
1	$y^{\mu\mu}$	0.151
2	$\Delta\phi^{\mu\mu}$	0.145
3	E_T^{miss}	0.142
4	$\Delta\eta^{\mu\mu}$	0.133
5	$\cos(\theta^*)$	0.125
6	$P_T^{\mu\mu}$	0.112
7	Jet Multiplicity	0.080
8	Jet Multiplicity ($\lvert\eta^j\rvert \leq 2.5$)	0.060
9	Jet Multiplicity ($\lvert\eta^j\rvert > 2.5$)	0.052

Table 9.1.1: Ranking of the input variables used to train Folds 1 (left) and 2 (right) of the inclusive selection BDTs.

The BDT response of the inclusive selection BDT is shown below in Figure 9.1.1. The signal and background shapes are largely consistent across both folds. The signal MC test and training sample responses are consistent within 5% across the entirety of both distributions. Discrepancies increase by a further 10% in the background, likely due to the large statistical errors of the Madgraph Drell-Yan samples.

[2]The quantifier of separation gain was the Gini Index, defined in Chapter 5.

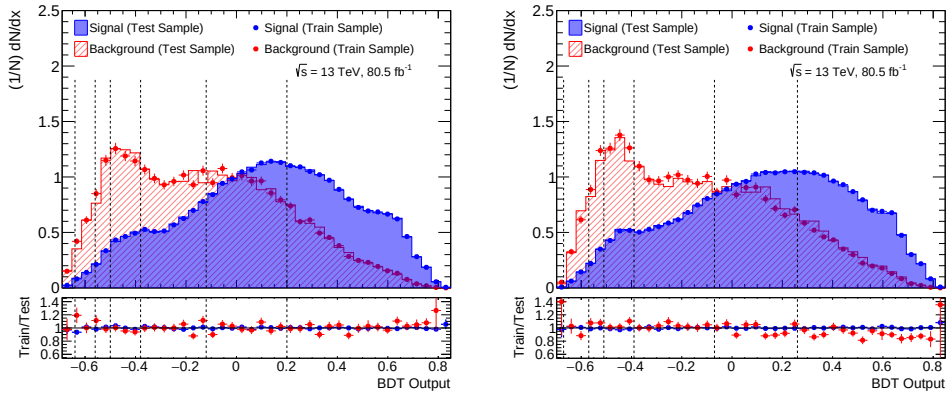

Figure 9.1.1: Output distributions of Folds 1 (left) and 2 (right) of the Inclusive Strategy BDTs, trained and tested with inclusive events. The dotted lines correspond to the boundaries of categories derived from the distributions. The bottom panels display the ratio between the training and test samples of the signal (blue) and background (red) MC.

The category boundaries derived from the BDT are shown in Table 9.1.2. Differences are seen between folds, likely due to statistical fluctuations in the background MC. Category boundaries derived from the BDT trained with Fold 1 were applied to Fold 2 (and vice versa).

After application of the BDT, Folds 1 and 2 were recombined, and the event yields of the signal and background MC samples in each category were derived. These are presented in Table 9.1.3, along with the data yields and $\frac{S}{\sqrt{B}}$ significances. The right-hand most category (Category 1) was found to be the most sensitive, validating the performance of the boundary-optimisation algorithm. The total combined significance was 1.13, 11.5% less sensitive than the $P_T^{\mu\mu}$/detector geometry categorisation approach presented in Table 7.3.5 of Chapter 7.

Category	BDT Output Range	
	Fold 1	Fold 2
Inclusive 1	$0.20 \leq x$	$0.26 \leq x$
Inclusive 2	$-0.12 < x \leq 0.20$	$-0.07 < x \leq 0.26$
Inclusive 3	$-0.38 < x \leq -0.12$	$-0.39 < x \leq -0.07$
Inclusive 4	$-0.50 < x \leq -0.38$	$-0.51 < x \leq -0.39$
Inclusive 5	$-0.56 < x \leq -0.50$	$-0.57 < x \leq -0.51$
Inclusive 6	$-0.64 < x \leq -0.56$	$-0.67 < x \leq -0.57$
Inclusive 7	$x \leq -0.64$	$x \leq -0.67$

Table 9.1.2: Category boundaries for both folds of the Inclusive Strategy BDTs trained with inclusive events. Cuts derived from the Fold 1 BDT were applied to the Fold 2 samples (and vice versa).

Category	ggF	VBF	VH	$t\bar{t}H$	Drell-Yan	EWK Z + Jets	Di-boson	Top	Total Signal	Total Background	$\frac{S}{\sqrt{B}}$	Data
Inclusive 1	146.84 ± 0.27	25.03 ± 0.03	9.55 ± 0.04	0.54 ± 0.01	36056.61 ± 830.15	125.66 ± 2.58	2550.56 ± 28.74	940.73 ± 10.86	181.96 ± 0.27	39673.56 ± 830.72	0.91	40497
Inclusive 2	138.40 ± 0.26	5.28 ± 0.01	3.84 ± 0.03	0.14 ± 0.00	64774.44 ± 1483.45	46.07 ± 1.58	1715.01 ± 23.64	952.00 ± 10.18	147.66 ± 0.26	67487.52 ± 1483.67	0.57	69826
Inclusive 3	79.04 ± 0.20	0.96 ± 0.01	0.71 ± 0.01	0.02 ± 0.00	66446.61 ± 1525.67	10.23 ± 0.70	386.97 ± 11.15	330.66 ± 6.08	80.73 ± 0.20	67174.47 ± 1525.72	0.31	68624
Inclusive 4	25.97 ± 0.11	0.11 ± 0.00	0.07 ± 0.00	0.00 ± 0.00	34930.45 ± 1115.82	1.19 ± 0.24	27.66 ± 3.05	61.04 ± 2.48	26.15 ± 0.11	35020.34 ± 1115.83	0.14	36678
Inclusive 5	7.87 ± 0.06	0.03 ± 0.00	0.01 ± 0.00	0.00 ± 0.00	14352.00 ± 741.95	0.34 ± 0.12	10.69 ± 2.17	17.98 ± 1.32	7.91 ± 0.06	14381.01 ± 741.95	0.07	14892
Inclusive 6	4.73 ± 0.05	0.01 ± 0.00	0.01 ± 0.00	0.00 ± 0.00	11326.01 ± 639.38	0.24 ± 0.11	2.96 ± 0.91	11.72 ± 1.10	4.75 ± 0.05	11340.92 ± 639.38	0.04	11293
Inclusive 7	0.42 ± 0.01	0.00 ± 0.00	0.00 ± 0.00	0.00 ± 0.00	1036.82 ± 212.49	0.00 ± 0.00	0.29 ± 0.29	0.82 ± 0.31	0.42 ± 0.01	1037.94 ± 212.49	0.01	1231
Inclusive Combined	403.27 ± 0.45	31.41 ± 0.03	14.19 ± 0.05	0.70 ± 0.01	228922.94 ± 2732.57	183.72 ± 6.30	4694.14 ± 39.04	2314.97 ± 16.36	449.57 ± 0.45	236115.76 ± 2732.90	1.13	243041

Table 9.1.3: Expected event yields (normalised to 80.5 fb^{-1}) for different signal and background processes in the seven categories defined by the inclusive selection BDTs of the Inclusive BDT strategy, in the window 120 GeV $< M_{\text{inv}}^{\mu\mu} <$ 130 GeV. The significance of the combined row is equal to the quadrature sum of the significances of the preceding categories.

Tables 9.1.4, 9.1.5 and 9.1.6 present the importance of the variables used to train the Multi-Jet, Single-Jet and Zero-Jet BDTs of the Inclusive Strategy. Both $y^{\mu\mu}$ and $P_T^{\mu\mu}$ present large importances throughout. The corresponding BDT output distributions are shown in Figures 9.1.2, 9.1.3 and 9.1.4. The Multi-Jet BDT was particularly sensitive to overtraining, and was thus limited to 100 trees and a maximum depth of 3. While minimal overtraining is seen throughout the distributions for the signal MC, discrepancies of 20-30% are seen between the training and test samples of the background. Considering the low number of variables used to train the BDTs, along with the lack of overtraining in the signal, this is likely a detrimental effect caused by the limited number of events within the background MC samples. While Drell-Yan samples with a greater number of events were available, such as those generated by Powheg and Sherpa, as demonstrated in Chapter 7, their modelling of the data was poorer. BDTs trained with these samples would thus be less reliable.

Rank	Variable	Variable Importance
1	$\Delta y^{\mu\mu j,\text{Leading}}$	0.228
2	$\Delta\eta^{jj}$	0.217
3	$P_T^{\mu\mu}$	0.209
4	E_T^{miss}	0.202
5	$P_T^{j,\text{Leading}}$	0.144

Rank	Variable	Variable Importance
1	$\Delta y^{\mu\mu j,\text{Leading}}$	0.235
2	$\Delta\eta^{jj}$	0.233
3	$P_T^{\mu\mu}$	0.210
4	E_T^{miss}	0.194
5	$P_T^{j,\text{Leading}}$	0.128

Table 9.1.4: Ranking of the input variables used to train Folds 1 (left) and 2 (right) of the Multi-Jet category BDTs.

Rank	Variable	Variable Importance
1	$\eta^{j,\text{Leading}}$	0.217
2	$y^{\mu\mu}$	0.201
3	E_T^{miss}	0.174
4	$\Delta\eta^{\mu\mu}$	0.168
5	$P_T^{\mu\mu}$	0.160
6	$P_T^{j,\text{Leading}}$	0.080

Rank	Variable	Variable Importance
1	$\eta^{j,\text{Leading}}$	0.207
2	$y^{\mu\mu}$	0.188
3	$\Delta\eta^{\mu\mu}$	0.178
4	$P_T^{\mu\mu}$	0.169
5	E_T^{miss}	0.162
6	$P_T^{j,\text{Leading}}$	0.096

Table 9.1.5: Ranking of the input variables used to train Folds 1 (left) and 2 (right) of the Single-Jet category BDTs.

The category boundaries derived from the jet-split BDTs are shown below in Table 9.1.7. Boundary differences were again seen between folds due to statistical fluctuations in the background MC. The resulting category event yields are presented in Table 9.1.8. A combined significance of 1.23 was achieved, an 8.8% improvement over the inclusive selection BDT. The strategy did however yield a lower overall significance than the

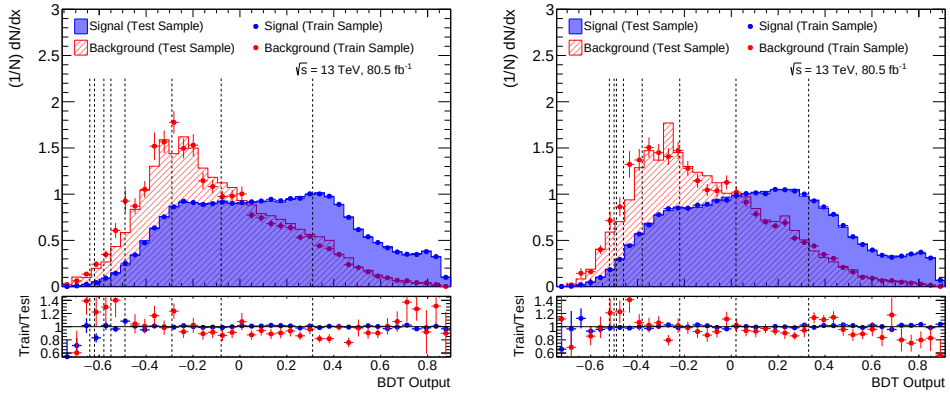

Figure 9.1.2: Output distributions of Folds 1 (left) and 2 (right) of the Inclusive Strategy BDTs, trained and tested with multi-jet events. The dotted lines correspond to the boundaries of categories derived from the distributions. The bottom panels display the ratio between the training and test samples of the signal (blue) and background (red) MC.

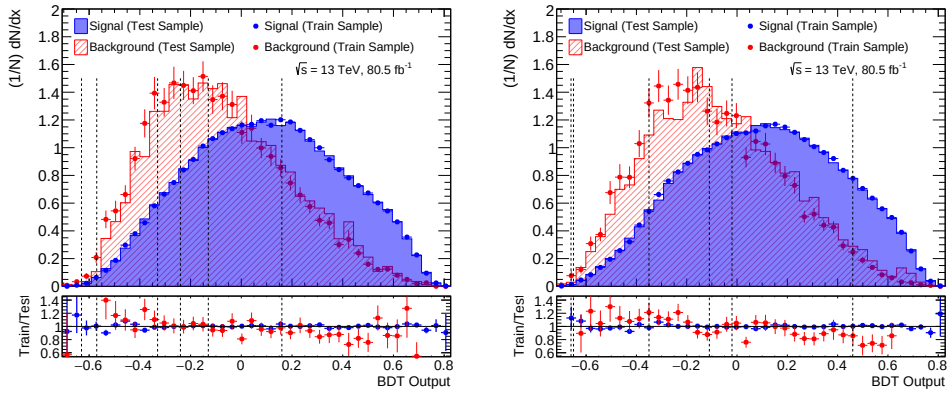

Figure 9.1.3: Output distributions of Folds 1 (left) and 2 (right) of the Inclusive Strategy BDTs, trained and tested with single-jet events. The dotted lines correspond to the boundaries of categories derived from the distributions. The bottom panels display the ratio between the training and test samples of the signal (blue) and background (red) MC.

Rank	Variable	Variable Importance
1	$\cos(\theta^*)$	0.371
2	$y^{\mu\mu}$	0.369
3	$P_T^{\mu\mu}$	0.260

Rank	Variable	Variable Importance
1	$\cos(\theta^*)$	0.368
2	$y^{\mu\mu}$	0.366
3	$P_T^{\mu\mu}$	0.265

Table 9.1.6: Ranking of the input variables used to train Folds 1 (left) and 2 (right) of the Zero-Jet category BDTs.

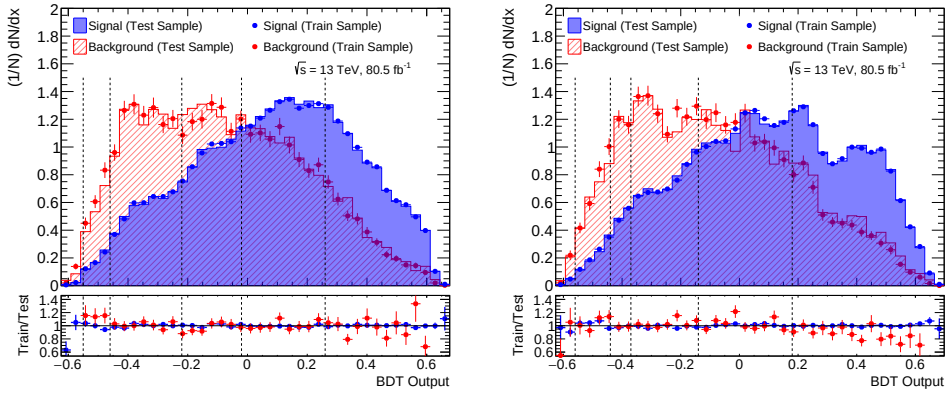

Figure 9.1.4: Output distributions of Folds 1 (left) and 2 (right) of the Inclusive Strategy BDTs, trained and tested with zero-jet events. The dotted lines correspond to the boundaries of categories derived from the distributions. The bottom panels display the ratio between the training and test samples of the signal (blue) and background (red) MC.

approach of Chapter 7 by 2.4%. Given the Single-Jet and Multi-Jet BDTs were slightly under-optimised to account for the MC statistical uncertainties, this difference could likely be compensated for by training with larger background MC samples.

Category	BDT Output Range	
	Fold 1	Fold 2
Zero-Jet 1	$0.26 \leq x$	$0.18 \leq x$
Zero-Jet 2	$-0.02 < x \leq 0.26$	$-0.14 < x \leq 0.18$
Zero-Jet 3	$-0.22 < x \leq -0.02$	$-0.37 < x \leq -0.14$
Zero-Jet 4	$-0.46 < x \leq -0.22$	$-0.44 < x \leq -0.37$
Zero-Jet 5	$-0.55 < x \leq -0.46$	$-0.56 < x \leq -0.44$
Zero-Jet 6	$x \leq -0.55$	$x \leq -0.56$
Single-Jet 1	$0.16 \leq x$	$0.46 \leq x$
Single-Jet 2	$-0.13 < x \leq 0.16$	$-0.02 < x \leq 0.46$
Single-Jet 3	$-0.24 < x \leq -0.13$	$-0.11 < x \leq -0.02$
Single-Jet 4	$-0.33 < x \leq -0.24$	$-0.35 < x \leq -0.11$
Single-Jet 5	$-0.57 < x \leq -0.33$	$-0.65 < x \leq -0.35$
Single-Jet 6	$-0.63 < x \leq -0.57$	$-0.66 < x \leq -0.65$
Single-Jet 7	$x \leq -0.63$	$x \leq -0.66$
Multi-Jet 1	$0.31 \leq x$	$0.33 \leq x$
Multi-Jet 2	$-0.08 < x \leq 0.31$	$0.02 < x \leq 0.33$
Multi-Jet 3	$-0.29 < x \leq -0.08$	$-0.22 < x \leq 0.02$
Multi-Jet 4	$-0.49 < x \leq -0.29$	$-0.38 < x \leq -0.22$
Multi-Jet 5	$-0.55 < x \leq -0.49$	$-0.46 < x \leq -0.38$
Multi-Jet 6	$-0.58 < x \leq -0.55$	$-0.49 < x \leq -0.46$
Multi-Jet 7	$-0.62 < x \leq -0.58$	$-0.50 < x \leq -0.49$
Multi-Jet 8	$-0.64 < x \leq -0.62$	$-0.52 < x \leq -0.50$
Multi-Jet 9	$x \leq -0.64$	$x \leq -0.52$

Table 9.1.7: Category boundaries for both folds of the Inclusive Strategy BDTs trained with zero-jet, single-jet and multi-jet events. Cuts derived from the Fold 1 BDTs were applied to the Fold 2 samples (and vice versa).

Category	ggF	VBF	VH	$t\bar{t}H$	Drell-Yan	EWK Z + Jets	Di-boson	Top	Total Signal	Total Background	$\frac{S}{\sqrt{B}}$	Data
Zero-Jet 1	64.66 ± 0.18	1.23 ± 0.01	1.38 ± 0.02	0.00 ± 0.00	23673.11 ± 870.97	10.47 ± 0.73	247.22 ± 8.73	728.44 ± 9.45	67.37 ± 0.18	24659.25 ± 871.07	0.43	26964
Zero-Jet 2	68.05 ± 0.18	0.51 ± 0.00	0.31 ± 0.01	0.00 ± 0.00	47318.12 ± 1289.61	5.71 ± 0.54	47.41 ± 3.83	308.79 ± 5.89	68.87 ± 0.18	47680.04 ± 1289.63	0.32	49608
Zero-Jet 3	34.91 ± 0.13	0.14 ± 0.00	0.07 ± 0.00	0.00 ± 0.00	40765.98 ± 1191.00	1.42 ± 0.26	8.89 ± 1.57	100.33 ± 3.20	35.12 ± 0.13	40876.62 ± 1191.01	0.17	41212
Zero-Jet 4	16.68 ± 0.09	0.05 ± 0.00	0.02 ± 0.00	0.00 ± 0.00	25687.59 ± 958.87	0.62 ± 0.17	3.00 ± 1.24	35.42 ± 1.87	16.75 ± 0.09	25726.64 ± 958.87	0.10	28561
Zero-Jet 5	4.01 ± 0.05	0.01 ± 0.00	0.00 ± 0.00	0.00 ± 0.00	10286.10 ± 635.14	0.05 ± 0.05	0.72 ± 0.43	9.98 ± 0.95	4.02 ± 0.05	10296.86 ± 635.15	0.04	10117
Zero-Jet 6	0.35 ± 0.01	0.00 ± 0.00	0.00 ± 0.00	0.00 ± 0.00	841.16 ± 168.72	0.11 ± 0.08	0.29 ± 0.29	0.49 ± 0.25	0.35 ± 0.01	842.05 ± 168.72	0.01	1069
Zero-Jet Combined	188.66 ± 0.31	1.94 ± 0.01	1.79 ± 0.02	0.00 ± 0.00	148572.07 ± 2278.48	18.39 ± 1.96	307.53 ± 9.76	1183.46 ± 11.78	192.39 ± 0.31	150081.45 ± 2278.53	0.57	157531
Single-Jet 1	34.46 ± 0.13	5.22 ± 0.01	0.82 ± 0.01	0.00 ± 0.00	6385.53 ± 381.18	19.27 ± 1.00	238.33 ± 8.91	123.36 ± 3.83	40.50 ± 0.13	6766.48 ± 381.31	0.49	7624
Single-Jet 2	54.56 ± 0.16	3.68 ± 0.01	1.87 ± 0.02	0.00 ± 0.00	20238.17 ± 793.76	20.49 ± 1.01	569.18 ± 13.52	281.60 ± 7.60	60.11 ± 0.16	21109.45 ± 793.92	0.41	20810
Single-Jet 3	13.16 ± 0.08	0.48 ± 0.00	0.43 ± 0.01	0.00 ± 0.00	7846.29 ± 549.21	3.71 ± 0.43	127.51 ± 6.14	65.83 ± 3.00	14.07 ± 0.08	8043.34 ± 549.25	0.16	7290
Single-Jet 4	17.49 ± 0.09	0.50 ± 0.00	0.54 ± 0.01	0.00 ± 0.00	12121.16 ± 657.61	4.73 ± 0.50	158.48 ± 7.31	96.24 ± 3.50	18.53 ± 0.09	12380.61 ± 657.66	0.17	11667
Single-Jet 5	9.80 ± 0.07	0.18 ± 0.00	0.25 ± 0.01	0.00 ± 0.00	9098.32 ± 638.29	2.04 ± 0.30	80.08 ± 5.18	61.52 ± 2.86	10.23 ± 0.07	9241.95 ± 638.31	0.11	8567
Single-Jet 6	0.14 ± 0.01	0.00 ± 0.00	0.00 ± 0.00	0.00 ± 0.00	80.64 ± 47.17	0.00 ± 0.00	2.50 ± 0.85	1.87 ± 0.43	0.14 ± 0.01	85.02 ± 47.18	0.02	141
Single-Jet 7	0.04 ± 0.01	0.00 ± 0.00	0.00 ± 0.00	0.00 ± 0.00	56.36 ± 39.85	0.06 ± 0.06	1.69 ± 0.71	0.52 ± 0.18	0.04 ± 0.01	58.63 ± 39.86	0.01	46
Single-Jet Combined	129.65 ± 0.25	10.06 ± 0.02	3.92 ± 0.03	0.01 ± 0.00	55826.46 ± 1385.88	50.29 ± 3.23	1177.79 ± 19.53	630.94 ± 10.11	143.64 ± 0.25	57685.48 ± 1386.06	0.69	56145
Multi-Jet 1	19.27 ± 0.10	11.31 ± 0.02	1.13 ± 0.01	0.07 ± 0.00	2166.43 ± 73.31	39.54 ± 1.46	174.75 ± 7.41	42.89 ± 1.49	31.78 ± 0.10	2423.61 ± 73.71	0.65	2638
Multi-Jet 2	31.58 ± 0.13	4.88 ± 0.01	3.36 ± 0.03	0.23 ± 0.00	7325.70 ± 307.85	35.18 ± 1.37	646.88 ± 14.39	130.23 ± 2.48	40.05 ± 0.13	8137.99 ± 308.20	0.44	8529
Multi-Jet 3	19.62 ± 0.10	2.10 ± 0.01	2.21 ± 0.02	0.16 ± 0.00	7244.20 ± 312.33	23.07 ± 1.12	814.17 ± 16.22	135.59 ± 2.81	24.09 ± 0.10	8217.03 ± 312.76	0.27	8482
Multi-Jet 4	11.04 ± 0.08	0.85 ± 0.01	1.32 ± 0.02	0.13 ± 0.00	5967.38 ± 361.38	12.14 ± 0.84	826.11 ± 16.37	119.99 ± 2.61	13.34 ± 0.08	6925.61 ± 361.76	0.16	6883
Multi-Jet 5	2.09 ± 0.03	0.16 ± 0.00	0.29 ± 0.01	0.05 ± 0.00	1017.16 ± 114.60	2.33 ± 0.38	307.48 ± 10.05	33.90 ± 1.33	2.59 ± 0.03	1360.87 ± 115.05	0.07	1499
Multi-Jet 6	0.53 ± 0.02	0.04 ± 0.00	0.06 ± 0.00	0.01 ± 0.00	280.99 ± 69.34	0.86 ± 0.24	121.90 ± 6.61	11.64 ± 0.78	0.64 ± 0.02	415.39 ± 69.66	0.03	459
Multi-Jet 7	0.19 ± 0.01	0.01 ± 0.00	0.03 ± 0.00	0.01 ± 0.00	127.74 ± 52.84	0.39 ± 0.13	71.67 ± 5.01	6.64 ± 0.52	0.24 ± 0.01	206.44 ± 53.08	0.02	218
Multi-Jet 8	0.20 ± 0.01	0.02 ± 0.00	0.03 ± 0.00	0.01 ± 0.00	72.81 ± 18.34	0.18 ± 0.09	52.59 ± 4.37	5.69 ± 0.52	0.26 ± 0.01	131.27 ± 18.86	0.02	179
Multi-Jet 9	0.44 ± 0.02	0.03 ± 0.00	0.06 ± 0.00	0.02 ± 0.00	322.00 ± 73.76	1.34 ± 0.29	193.26 ± 8.09	14.00 ± 0.86	0.55 ± 0.02	530.60 ± 74.21	0.02	478
Multi-Jet Combined	84.96 ± 0.21	19.41 ± 0.03	8.48 ± 0.04	0.69 ± 0.01	24524.40 ± 595.65	115.03 ± 5.04	3208.82 ± 32.36	500.57 ± 5.17	113.54 ± 0.22	28348.83 ± 596.57	0.85	29365
All Combined	403.27 ± 0.45	31.41 ± 0.07	14.19 ± 0.05	0.70 ± 0.01	228922.94 ± 2732.57	183.71 ± 6.30	4694.14 ± 39.04	2314.97 ± 16.36	449.57 ± 0.45	236115.76 ± 2732.90	1.23	243041

Table 9.1.8: Expected event yields (normalised to 80.5 fb^{-1}) for different signal and background processes in the twenty-two categories defined by the Zero-Jet, Single-Jet and Multi-Jet selection BDTs of the Inclusive BDT strategy, in the window 120 GeV $< M_{\text{inv}}^{\mu\mu} <$ 130 GeV. The significances of the combined rows are equal to the quadrature sums of the significances of the preceding categories.

9.2 Background Separation BDTs

An alternative Background Separation approach was inspired by the idea of utilising BDTs to separate the various backgrounds of the analysis, after which subsequent BDTs could separate signals from the individual background components.

Table 9.2.1 presents the ROC curve integrals of BDTs of different background configurations trained against each other, averaged over the respective BDT folds, while Figure 9.2.1 presents the ROC curves of each individual fold. All variables within the Inclusive column of Table 9.0.1 were utilised for BDT training. Configurations isolating the electroweak Z plus jets MC were not utilised, due to the sample's large statistical uncertainties. The largest separation was seen when training top MC against all others, outperforming the weakest BDT considered by nearly 13%.

Configuration	Averaged ROC Integral
Top vs (Di-boson + Drell-Yan + EWK Z+Jets)	0.955
(Top + EWK Z+Jets) vs (Di-boson + Drell-Yan)	0.953
(Drell-Yan + EWK Z+Jets) vs (Top + Di-boson)	0.919
Drell-Yan vs (Top + Di-boson + EWK Z+Jets)	0.918
Di-boson vs (Top + Drell-Yan + EWK Z+Jets)	0.847
(Di-boson + EWK Z+Jets) vs (Top + Drell-Yan)	0.846

Table 9.2.1: ROC curve integral comparisons of BDTs trained with different background sample configurations, averaged across both training folds.

9.2.1 Background Separation

To optimise the separation of top processes from the surrounding background, the variable-optimisation algorithm outlined in Section 9.1 was utilised. Due to the limited number of top MC events available in the Signal region, the choice was made to train only one BDT at this stage, using an inclusive selection (rather than training multiple BDTs based on the jet multiplicity of events). This would ensure a satisfactory number of top events would remain for optimising the subsequent Signal vs Top-Like BDTs without overtraining.

Table 9.2.2 presents the importance of variables used to train the optimised background separation BDT, with E_T^{miss} having the largest impact. The associated BDT output distributions of each fold are shown in Figure 9.2.2, along with their respective purities. Throughout the distributions, the test and training sample responses are in agreement within 20%, limited by the statistical uncertainties of the MC samples. A top-purity cut of 95% was chosen to separate the background samples for the next BDT training stage, corresponding to output distribution cuts of 0.657 and 0.653 for Folds 1 and 2

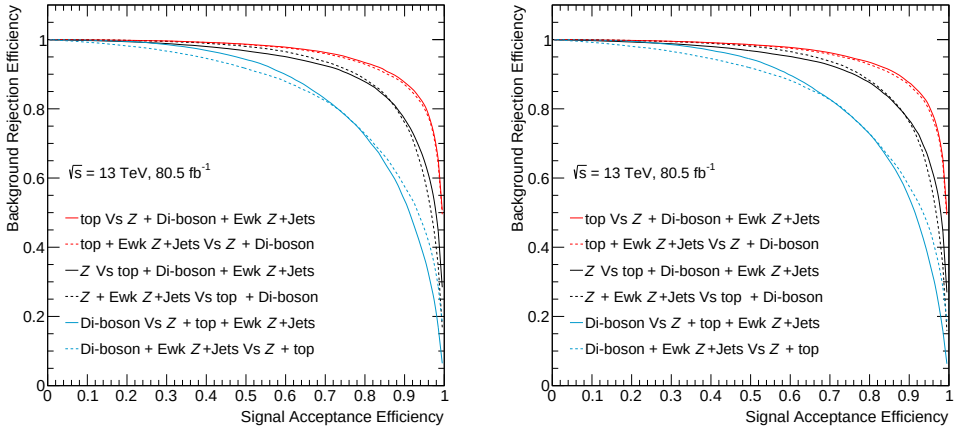

Figure 9.2.1: ROC curve comparisons for Folds 1 (left) and 2 (right) of different background training sample configurations. The best separation is achieved when training top samples against combined Drell-Yan, di-boson and electroweak Z plus jet backgrounds.

respectively. While cutting at 98% purity was tested, this led to too few top events being available for successfully training the Signal vs Top-Like BDTs.

Rank	Variable	Variable Importance
1	E_T^{miss}	0.213
2	$P_T^{\mu\mu}$	0.141
3	$y^{\mu\mu}$	0.141
4	$\cos(\theta^*)$	0.132
5	$\Delta R^{\mu\mu}$	0.105
6	Jet Multiplicity	0.098
7	Jet Multiplicity ($\lvert\eta^j\rvert \leq 2.5$)	0.094
8	Jet Multiplicity ($\lvert\eta^j\rvert > 2.5$)	0.076

Rank	Variable	Variable Importance
1	E_T^{miss}	0.208
2	$y^{\mu\mu}$	0.138
3	$P_T^{\mu\mu}$	0.138
4	$\cos(\theta^*)$	0.132
5	$\Delta R^{\mu\mu}$	0.110
6	Jet Multiplicity	0.106
7	Jet Multiplicity ($\lvert\eta^j\rvert \leq 2.5$)	0.100
8	Jet Multiplicity ($\lvert\eta^j\rvert > 2.5$)	0.068

Table 9.2.2: Ranking of the input variables used to train Folds 1 (left) and 2 (right) of the initial Background Separation BDTs.

9.2.2 Signal-Background Separation

Upon application of the Background Separation BDT to all MC samples (and data), events were sorted into one of two categories:

- Events falling within the 95% purity cut-off were deemed Top-Like.
- Events falling outside the 95% purity cut-off were deemed Boson-Like.

Two subsequent classes of BDTs (Signal vs Top-Like and Signal vs Boson-Like) were then trained. Variables used for training the previous Background Separation BDT

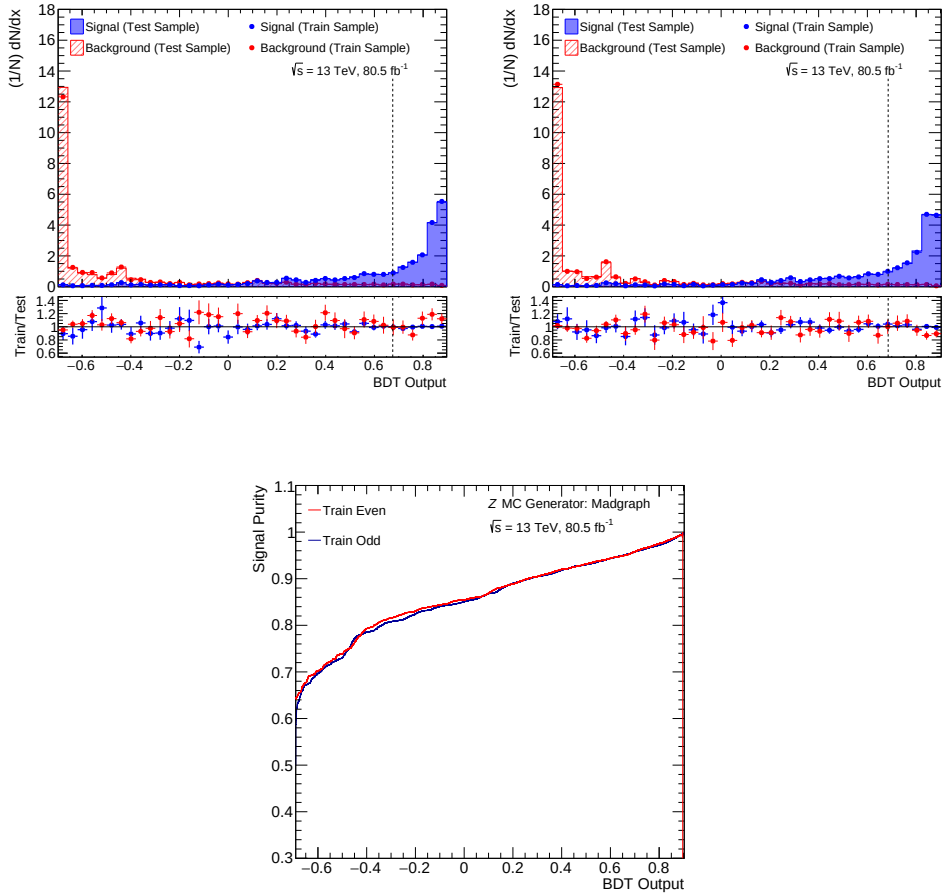

Figure 9.2.2: Output distributions of Folds 1 (left) and 2 (right) of the Background Separation BDTs, along with the purity of the respective folds (bottom), trained and tested with inclusive events. The dotted line represents the category decision boundary, corresponding to a top background purity of 95%. The bottom panels of the output distribution plots display the ratio between the training and test samples of the Top-Like (blue) and Boson-Like (red) MC samples.

were left out to avoid overtraining. Due to the limited number of available top events, zero-jet and single-jet events were grouped together for training and testing the Signal vs Top-Like BDTs. The same approach was taken with the Signal vs Boson-Like BDTs for simplicity. BDTs were also trained on multi-jet events, and inclusively-selected events for comparison.

Tables 9.2.3 and 9.2.4 present the importance of the variables used to train the Top-Like and Boson-Like BDTs with the inclusive selection. $\Delta\phi^{\mu\mu}$ and $\Delta\eta^{\mu\mu}$ proved most important in the Top-Like cases, with the pseudorapidity of the leading and subleading muons possessing greater importance in the Boson-Like cases.

Rank	Variable	Variable Importance
1	$\Delta\phi^{\mu\mu}$	0.258
2	$\Delta\eta^{\mu\mu}$	0.214
3	$\eta^{\mu\mu}$	0.200
4	$\eta^{\mu,\text{Subleading}}$	0.164
5	$\eta^{\mu,\text{Leading}}$	0.164

Rank	Variable	Variable Importance
1	$\Delta\phi^{\mu\mu}$	0.253
2	$\Delta\eta^{\mu\mu}$	0.210
3	$\eta^{\mu\mu}$	0.203
4	$\eta^{\mu,\text{Leading}}$	0.181
5	$\eta^{\mu,\text{Subleading}}$	0.153

Table 9.2.3: Ranking of the input variables used to train Folds 1 (left) and 2 (right) of the Signal vs Top-Like background BDTs using the inclusive selection.

Rank	Variable	Variable Importance
1	$\eta^{\mu,\text{Leading}}$	0.282
2	$\eta^{\mu,\text{Subleading}}$	0.249
3	$\Delta\phi^{\mu\mu}$	0.236
4	$\eta^{\mu\mu}$	0.234

Rank	Variable	Variable Importance
1	$\eta^{\mu,\text{Leading}}$	0.268
2	$\eta^{\mu,\text{Subleading}}$	0.262
3	$\Delta\phi^{\mu\mu}$	0.243
4	$\eta^{\mu\mu}$	0.228

Table 9.2.4: Ranking of the input variables used to train Folds 1 (left) and 2 (right) of the Signal vs Boson-Like background BDTs using the inclusive selection.

Figures 9.2.3 and 9.2.4 present the output distributions of the Top-Like and Boson-Like BDTs trained with the inclusive selection, while Table 9.2.5 lists the category boundaries derived from the distributions. Signal overtraining of up to 10% is seen in some regions of the Top-Like BDT, alongside background overtraining of 20-30%. This is likely due to the relatively high purity cut of the previous stage limiting the number of available events, leading to large statistical uncertainties in the MC. Minimal overtraining ($\leq 10\%$) is exhibited by the Boson-Like BDT, in part due to it having been trained with a reduced maximum depth of 3. Although similar settings were tested for the Top-Like case, they produced insufficient signal-background separation.

The MC and data event yields derived from this categorisation are presented in Table 9.2.6. The largest sensitivity categories arise from the Boson-Like BDT, although this could in part be due to the majority of signal events possessing a Boson-Like topology,

rather than Top-Like. A total combined significance of 1.10 was achieved, the lowest presented thus far.

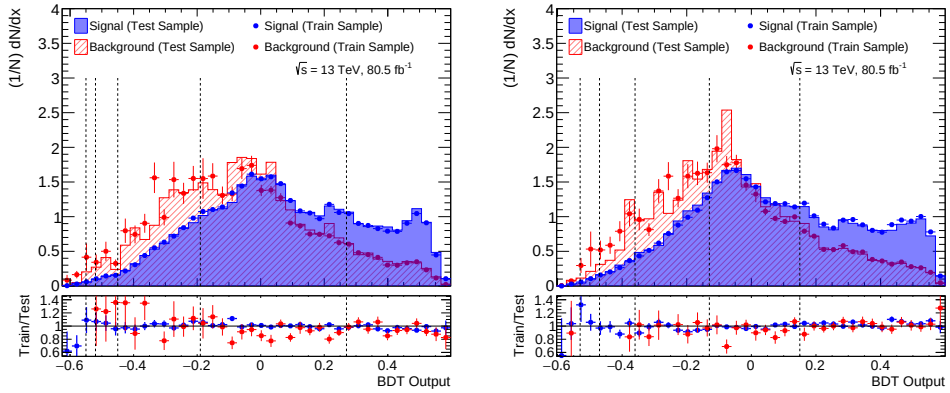

Figure 9.2.3: Output distributions of Folds 1 (left) and 2 (right) of the Signal vs Top-Like background BDTs, trained and tested with inclusive events. The dotted lines correspond to the boundaries of categories derived from the distributions. The bottom panels display the ratio between the training and test samples of the signal (blue) and background (red) MC.

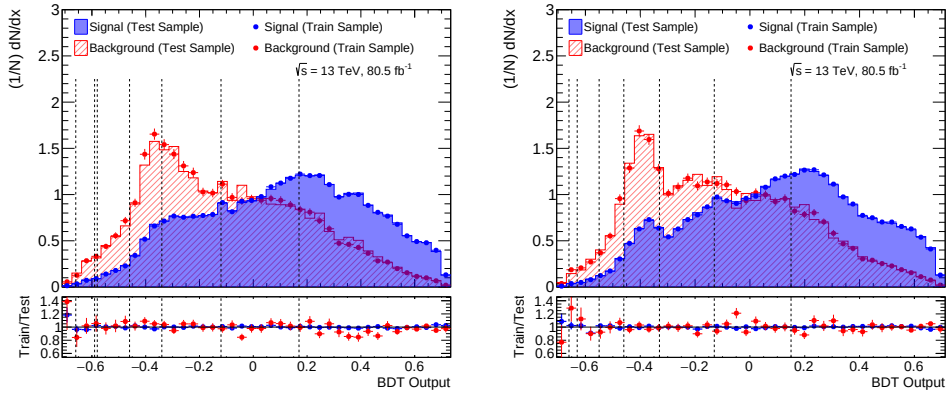

Figure 9.2.4: Output distributions of Folds 1 (left) and 2 (right) of the Signal vs Boson-Like background BDTs, trained and tested with inclusive events. The dotted lines correspond to the boundaries of categories derived from the distributions. The bottom panels display the ratio between the training and test samples of the signal (blue) and background (red) MC.

Tables 9.2.7 and 9.2.8 present the importance of variables used to train the Zero/Single-Jet and Multi-Jet Top-Like BDTs, whilst Tables 9.2.9 and 9.2.10 present the same

Category	BDT Output Range	
	Fold 1	Fold 2
Top-like Inclusive 1	$0.27 \leq x$	$0.15 \leq x$
Top-like Inclusive 2	$-0.19 < x \leq 0.27$	$-0.13 < x \leq 0.15$
Top-like Inclusive 3	$-0.45 < x \leq -0.19$	$-0.36 < x \leq -0.13$
Top-like Inclusive 4	$-0.52 < x \leq -0.45$	$-0.47 < x \leq -0.36$
Top-like Inclusive 5	$-0.55 < x \leq -0.52$	$-0.53 < x \leq -0.47$
Top-like Inclusive 6	$x \leq -0.55$	$x \leq -0.53$
Boson-like Inclusive 1	$0.17 \leq x$	$0.15 \leq x$
Boson-like Inclusive 2	$-0.12 < x \leq 0.17$	$-0.13 < x \leq 0.15$
Boson-like Inclusive 3	$-0.34 < x \leq -0.12$	$-0.33 < x \leq -0.13$
Boson-like Inclusive 4	$-0.46 < x \leq -0.34$	$-0.46 < x \leq -0.33$
Boson-like Inclusive 5	$-0.58 < x \leq -0.46$	$-0.55 < x \leq -0.46$
Boson-like Inclusive 6	$-0.59 < x \leq -0.58$	$-0.63 < x \leq -0.55$
Boson-like Inclusive 7	$-0.66 < x \leq -0.59$	$-0.66 < x \leq -0.63$
Boson-like Inclusive 8	$x \leq -0.66$	$x \leq -0.66$

Table 9.2.5: Category boundaries for both folds of the Background Separation Strategy BDTs trained with inclusive events. Cuts derived from the Fold 1 BDTs were applied to the Fold 2 samples (and vice versa).

information for the Boson-Like BDTs. Both $\Delta\phi^{\mu\mu}$ and $\eta^{\mu,\text{Leading}}$ show large importances throughout, along with $\Delta y^{\mu\mu j,\text{Leading}}$ for the Multi-Jet instances. Large importance differences are seen between the folds of the Zero/Single-jet Top-Like BDT, likely due to statistical fluctuations in the background MC. To counteract overtraining, the Top-Like BDTs were trained with a reduced number of trees (100), and maximum depths of 2. Despite this, both the Zero/Single-Jet and Multi-Jet Top-Like BDTs exhibited large amounts of overtraining, as seen in Figures 9.2.5 and 9.2.6. For the Zero/Single-Jet case, overtraining in excess of 40% is seen, putting the reliability of the BDT into question. The output distributions of the jet-split Boson-Like BDTs are presented in Figures 9.2.6 to 9.2.8. While minimal overtraining is seen for the Zero/Single-Jet case, discrepancies between the background training and test samples of 30-40% are seen for the Multi-Jet case.

The category boundaries derived from the BDTs are presented in Table 9.2.11. Large boundary differences are seen between the folds due to the prominence of statistical fluctuations in the background MC samples. Sensitivity to these effects is a notable flaw of the boundary-optimisation algorithm.

The event yields of this categorisation are presented in Table 9.2.12. The largest sensitivities are again seen in the Boson-Like categories. Despite the overtraining seen in some of the BDTs, reasonable agreement (within 20%) was achieved between the total background MC and data yields in each category. A total significance of 1.22 was attained, a gain of 11% with respect to the inclusive selection case, and within

Category	ggF	VBF	VH	$t\bar{t}H$	Drell-Yan	EWK Z + Jets	Di-boson	Top	Total Signal	Total Background	$\frac{S}{\sqrt{B}}$	Data
Top-like Inclusive 1	7.31 ± 0.06	1.40 ± 0.01	0.92 ± 0.01	0.18 ± 0.00	1096.97 ± 28.50	8.82 ± 0.73	328.32 ± 10.06	55.98 ± 1.52	9.81 ± 0.06	1490.09 ± 30.27	0.25	1642
Top-like Inclusive 2	12.26 ± 0.08	1.82 ± 0.01	1.40 ± 0.02	0.21 ± 0.00	3101.44 ± 243.25	14.68 ± 0.90	1465.60 ± 21.85	215.16 ± 4.14	15.69 ± 0.08	4796.88 ± 244.27	0.23	5174
Top-like Inclusive 3	4.60 ± 0.05	0.52 ± 0.00	0.47 ± 0.01	0.07 ± 0.00	1615.42 ± 162.29	5.12 ± 0.56	849.03 ± 16.69	140.75 ± 3.56	5.66 ± 0.05	2610.31 ± 163.18	0.11	2919
Top-like Inclusive 4	0.57 ± 0.02	0.05 ± 0.00	0.04 ± 0.00	0.01 ± 0.00	355.03 ± 99.62	0.68 ± 0.22	127.66 ± 6.50	22.42 ± 1.42	0.67 ± 0.02	505.80 ± 99.84	0.03	499
Top-like Inclusive 5	0.12 ± 0.01	0.01 ± 0.00	0.01 ± 0.00	0.00 ± 0.00	91.66 ± 51.39	0.15 ± 0.09	26.43 ± 2.98	4.68 ± 0.61	0.14 ± 0.01	122.93 ± 51.48	0.01	129
Top-like Inclusive 6	0.04 ± 0.01	0.00 ± 0.00	0.00 ± 0.00	0.00 ± 0.00	4.88 ± 1.98	0.00 ± 0.00	11.77 ± 2.04	1.84 ± 0.43	0.04 ± 0.01	18.50 ± 2.87	0.01	48
Top-like Inclusive Combined	24.90 ± 0.12	3.81 ± 0.01	2.84 ± 0.02	0.46 ± 0.01	6265.41 ± 314.47	29.45 ± 2.53	2808.81 ± 30.21	440.83 ± 5.90	32.01 ± 0.12	9544.51 ± 315.98	0.36	10411
Boson-like Inclusive 1	159.04 ± 0.28	21.63 ± 0.03	8.35 ± 0.04	0.20 ± 0.00	45594.39 ± 1048.84	106.40 ± 2.37	1248.72 ± 20.21	887.20 ± 11.03	189.22 ± 0.28	47836.71 ± 1049.10	0.87	48452
Boson-like Inclusive 2	115.42 ± 0.24	4.49 ± 0.01	2.19 ± 0.02	0.03 ± 0.00	62320.72 ± 1458.19	33.56 ± 1.31	462.91 ± 12.13	631.42 ± 8.51	122.13 ± 0.24	63448.60 ± 1458.26	0.48	64446
Boson-like Inclusive 3	63.32 ± 0.18	1.10 ± 0.01	0.60 ± 0.01	0.01 ± 0.00	56055.51 ± 1416.65	10.29 ± 0.71	126.16 ± 6.34	239.03 ± 5.17	65.03 ± 0.18	56430.99 ± 1416.67	0.27	58341
Boson-like Inclusive 4	29.21 ± 0.12	0.30 ± 0.00	0.17 ± 0.01	0.00 ± 0.00	38330.29 ± 1160.42	2.65 ± 0.37	32.59 ± 3.24	83.11 ± 2.92	29.68 ± 0.12	38448.65 ± 1160.43	0.15	40793
Boson-like Inclusive 5	8.34 ± 0.06	0.07 ± 0.00	0.03 ± 0.00	0.00 ± 0.00	14033.26 ± 747.14	0.95 ± 0.21	12.24 ± 2.05	24.30 ± 1.54	8.44 ± 0.06	14070.76 ± 747.15	0.07	13897
Boson-like Inclusive 6	1.52 ± 0.03	0.01 ± 0.00	0.01 ± 0.00	0.00 ± 0.00	3182.77 ± 338.77	0.10 ± 0.06	1.20 ± 0.60	3.13 ± 0.65	1.54 ± 0.03	3187.20 ± 338.78	0.03	3078
Boson-like Inclusive 7	1.21 ± 0.02	0.01 ± 0.00	0.00 ± 0.00	0.00 ± 0.00	2505.64 ± 308.02	0.20 ± 0.09	0.87 ± 0.51	4.11 ± 0.72	1.22 ± 0.02	2510.81 ± 308.02	0.02	2791
Boson-like Inclusive 8	0.32 ± 0.01	0.00 ± 0.00	0.00 ± 0.00	0.00 ± 0.00	634.94 ± 142.54	0.10 ± 0.07	0.64 ± 0.45	1.83 ± 0.40	0.32 ± 0.01	637.51 ± 142.54	0.01	832
Boson-like Inclusive Combined	378.37 ± 0.43	27.60 ± 0.03	11.35 ± 0.05	0.24 ± 0.00	222657.52 ± 2714.41	154.26 ± 5.77	1885.33 ± 24.73	1874.13 ± 15.26	417.56 ± 0.43	226571.25 ± 2714.57	1.04	232630
All Combined	403.27 ± 0.45	31.41 ± 0.03	14.19 ± 0.05	0.70 ± 0.01	228922.93 ± 2732.57	183.71 ± 6.30	4694.14 ± 39.04	2314.96 ± 16.36	449.57 ± 0.45	236115.76 ± 2732.90	1.10	243041

Table 9.2.6: Expected event yields (normalised to 80.5 fb^{-1}) for different signal and background processes in the fourteen categories defined by the inclusive selection BDTs of the Background Separation strategy, in the window 120 GeV $< M_{\text{inv}}^{\mu\mu} <$ 130 GeV. The significances of the combined rows are equal to the quadrature sums of the significances of the preceding categories.

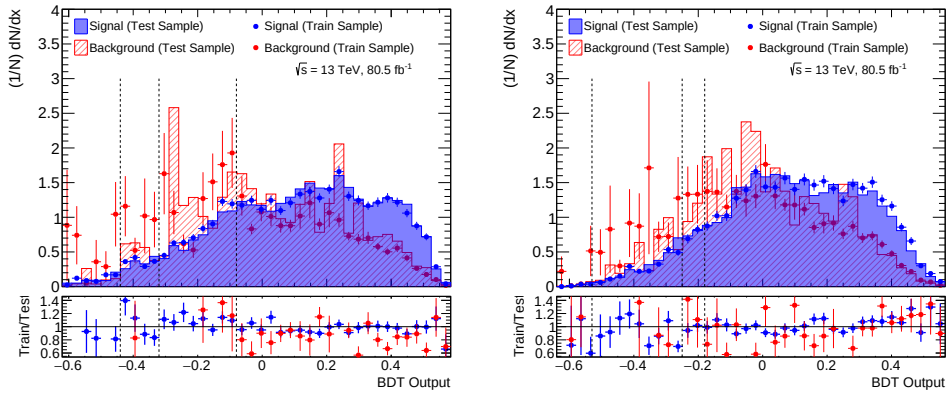

Figure 9.2.5: Output distributions of Folds 1 (left) and 2 (right) of the Signal vs Top-Like background BDTs, trained and tested with zero/single-jet events. The dotted lines correspond to the boundaries of categories derived from the distributions. The bottom panels display the ratio between the training and test samples of the signal (blue) and background (red) MC.

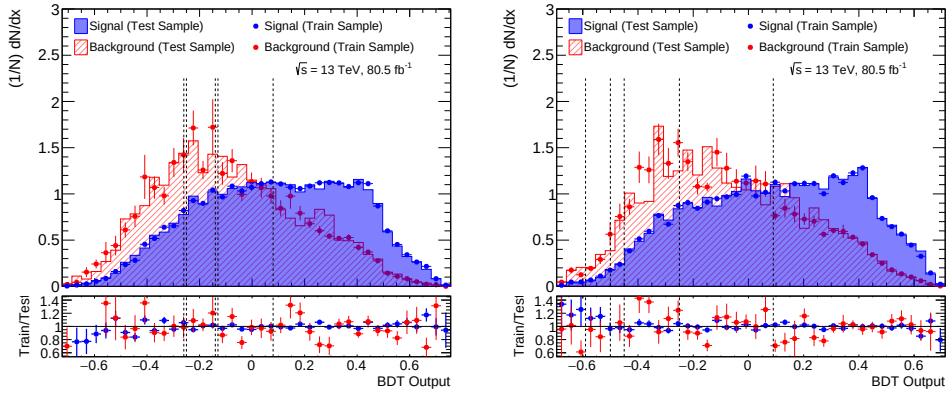

Figure 9.2.6: Output distributions of Folds 1 (left) and 2 (right) of the Signal vs Top-Like background BDTs, trained and tested with multi-jet events. The dotted lines correspond to the boundaries of categories derived from the distributions. The bottom panels display the ratio between the training and test samples of the signal (blue) and background (red) MC.

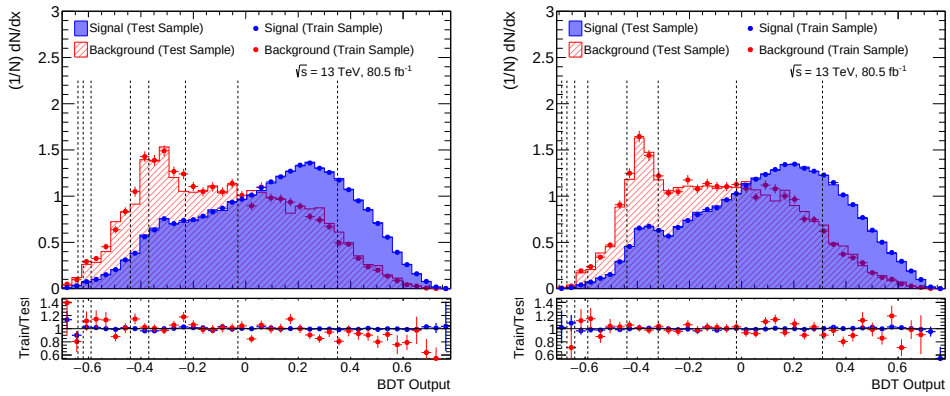

Figure 9.2.7: Output distributions of Folds 1 (left) and 2 (right) of the Signal vs Boson-Like background BDTs, trained and tested with zero/single-jet events. The dotted lines correspond to the boundaries of categories derived from the distributions. The bottom panels display the ratio between the training and test samples of the signal (blue) and background (red) MC.

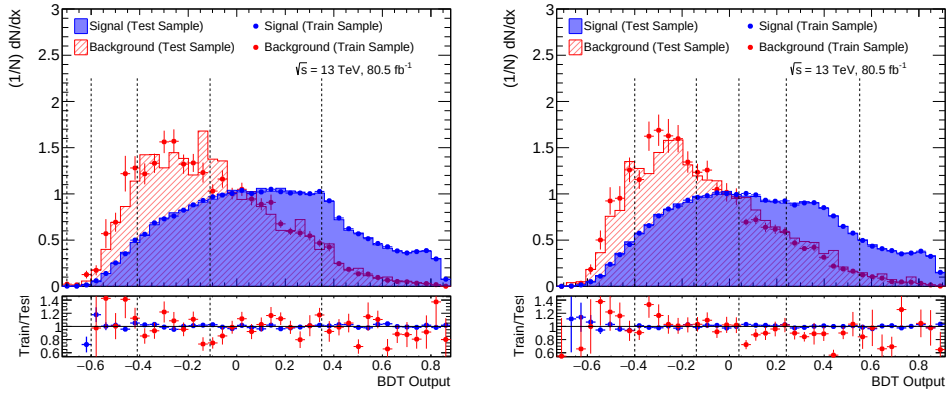

Figure 9.2.8: Output distributions of Folds 1 (left) and 2 (right) of the Signal vs Boson-Like background BDTs, trained and tested with multi-jet events. The dotted lines correspond to the boundaries of categories derived from the distributions. The bottom panels display the ratio between the training and test samples of the signal (blue) and background (red) MC.

Rank	Variable	Variable Importance
1	$\Delta\phi^{\mu\mu}$	0.357
2	$\eta^{\mu,\text{Leading}}$	0.352
3	$\Delta\eta^{\mu\mu}$	0.292

Rank	Variable	Variable Importance
1	$\Delta\phi^{\mu\mu}$	0.418
2	$\eta^{\mu,\text{Leading}}$	0.296
3	$\Delta\eta^{\mu\mu}$	0.286

Table 9.2.7: Ranking of the input variables used to train Folds 1 (left) and 2 (right) of the Signal vs Top-Like background BDTs using the Zero/Single-Jet selection.

Rank	Variable	Variable Importance
1	$\Delta y^{\mu\mu j,\text{Leading}}$	0.292
2	$\Delta\phi^{\mu\mu}$	0.280
3	$\Delta\eta^{\mu\mu}$	0.228
4	$\eta^{\mu,\text{Leading}}$	0.200

Rank	Variable	Variable Importance
1	$\Delta\phi^{\mu\mu}$	0.277
2	$\Delta y^{\mu\mu j,\text{Leading}}$	0.267
3	$\Delta\eta^{\mu\mu}$	0.248
4	$\eta^{\mu,\text{Leading}}$	0.208

Table 9.2.8: Ranking of the input variables used to train Folds 1 (left) and 2 (right) of the Signal vs Top-Like background BDTs using the Multi-Jet selection.

Rank	Variable	Variable Importance
1	$\eta^{\mu,\text{Leading}}$	0.222
2	$\eta^{\mu,\text{Subleading}}$	0.206
3	$\eta^{\mu\mu}$	0.189
4	$\Delta\phi^{\mu\mu}$	0.186
5	$\eta^{j,\text{Leading}}$	0.112
6	$P_T^{j,\text{Leading}}$	0.085

Rank	Variable	Variable Importance
1	$\eta^{\mu,\text{Subleading}}$	0.214
2	$\eta^{\mu,\text{Leading}}$	0.201
3	$\Delta\phi^{\mu\mu}$	0.189
4	$\eta^{\mu\mu}$	0.182
5	$\eta^{j,\text{Leading}}$	0.130
6	$P_T^{j,\text{Leading}}$	0.084

Table 9.2.9: Ranking of the input variables used to train Folds 1 (left) and 2 (right) of the Signal vs Boson-Like background BDTs using the Zero/Single-Jet selection.

Rank	Variable	Variable Importance
1	$\Delta y^{\mu\mu j,\text{Leading}}$	0.128
2	$\Delta\phi^{\mu\mu}$	0.119
3	$\Delta\eta^{jj}$	0.109
4	$\eta^{\mu\mu}$	0.104
5	ΔR^{jj}	0.104
6	$\eta^{\mu,\text{Subleading}}$	0.101
7	$\Delta y^{\mu\mu j,\text{Subleading}}$	0.096
8	$\eta^{\mu,\text{Leading}}$	0.093
9	$P_T^{\mu\mu j,\text{Subleading}}$	0.082
10	$P_T^{\mu\mu j,\text{Leading}}$	0.050
11	$P_T^{j,\text{Subleading}}$	0.012

Rank	Variable	Variable Importance
1	$\Delta\phi^{\mu\mu}$	0.115
2	$\eta^{\mu,\text{Leading}}$	0.114
3	$\Delta y^{\mu\mu j,\text{Leading}}$	0.114
4	$\Delta\eta^{jj}$	0.112
5	$\Delta y^{\mu\mu j,\text{Subleading}}$	0.102
6	$\eta^{\mu,\text{Subleading}}$	0.092
7	$\eta^{\mu\mu}$	0.090
8	ΔR^{jj}	0.089
9	$P_T^{\mu\mu j,\text{Subleading}}$	0.081
10	$P_T^{\mu\mu j,\text{Leading}}$	0.053
11	$P_T^{j,\text{Subleading}}$	0.038

Table 9.2.10: Ranking of the input variables used to train Folds 1 (left) and 2 (right) of the Signal vs Boson-Like background BDTs using the Multi-Jet selection.

Category	BDT Output Range	
	Fold 1	Fold 2
Top-like Zero/Single-Jet 1	$-0.08 \leq x$	$-0.18 \leq x$
Top-like Zero/Single-Jet 2	$-0.32 < x \leq -0.08$	$-0.25 < x \leq -0.18$
Top-like Zero/Single-Jet 3	$-0.44 < x \leq -0.32$	$-0.53 < x \leq -0.25$
Top-like Zero/Single-Jet 4	$x \leq -0.44$	$x \leq -0.53$
Top-like Multi-Jet 1	$0.08 \leq x$	$0.09 \leq x$
Top-like Multi-Jet 2	$-0.13 < x \leq 0.08$	$-0.25 < x \leq 0.09$
Top-like Multi-Jet 3	$-0.14 < x \leq -0.13$	$-0.45 < x \leq -0.25$
Top-like Multi-Jet 4	$-0.25 < x \leq -0.14$	$-0.50 < x \leq -0.45$
Top-like Multi-Jet 5	$-0.26 < x \leq -0.25$	$-0.59 < x \leq -0.50$
Top-like Multi-Jet 6	$x \leq -0.26$	$x \leq -0.59$
Boson-like Zero/Single-Jet 1	$0.35 \leq x$	$0.31 \leq x$
Boson-like Zero/Single-Jet 2	$-0.03 < x \leq 0.35$	$-0.02 < x \leq 0.26$
Boson-like Zero/Single-Jet 3	$-0.23 < x \leq -0.03$	$-0.32 < x \leq -0.02$
Boson-like Zero/Single-Jet 4	$-0.37 < x \leq -0.23$	$-0.44 < x \leq -0.32$
Boson-like Zero/Single-Jet 5	$-0.44 < x \leq -0.37$	$-0.59 < x \leq -0.44$
Boson-like Zero/Single-Jet 6	$-0.59 < x \leq -0.44$	$-0.64 < x \leq -0.59$
Boson-like Zero/Single-Jet 7	$-0.62 < x \leq -0.59$	$-0.67 < x \leq -0.64$
Boson-like Zero/Single-Jet 8	$-0.64 < x \leq -0.62$	$-0.69x \leq -0.67$
Boson-like Zero/Single-Jet 9	$x \leq -0.64$	$x \leq -0.69$
Boson-like Multi-Jet 1	$0.35 \leq x$	$0.55 \leq x$
Boson-like Multi-Jet 2	$-0.11 < x \leq 0.35$	$0.24 < x \leq 0.55$
Boson-like Multi-Jet 3	$-0.41 < x \leq -0.11$	$0.04 < x \leq 0.24$
Boson-like Multi-Jet 4	$-0.60 < x \leq -0.41$	$-0.14 < x \leq 0.04$
Boson-like Multi-Jet 5	$-0.70 < x \leq -0.60$	$-0.40 < x \leq -0.14$
Boson-like Multi-Jet 6	$x \leq -0.70$	$x \leq -0.40$

Table 9.2.11: Category boundaries for both folds of the Background Separation Strategy BDTs trained with zero-jet, single-jet and multi-jet events. Cuts derived from the Fold 1 BDTs were applied to the Fold 2 samples (and vice versa).

1% agreement of the jet-split Inclusive Strategy BDT result. The method was again limited by large MC statistical uncertainties, most prominent in the Zero/Single-Jet BDT categories. It would be interesting to investigate in future analyses how different event splittings (such as Zero/Single/Di-Jet and 3 $\leq$ jet categories) could impact this issue, and how the method might perform given an increased number of MC events with which to train and test the BDTs.

Category	ggF	VBF	VH	$t\bar{t}H$	Drell-Yan	EWK Z + Jets	Di-boson	Top	Total Signal	Total Background	$\frac{S}{\sqrt{B}}$	Data
Top-like Zero/Single-Jet 1	3.72 ± 0.04	0.62 ± 0.00	0.40 ± 0.01	0.00 ± 0.00	729.94 ± 95.14	2.63 ± 0.36	358.00 ± 10.66	118.29 ± 3.83	4.74 ± 0.04	1208.86 ± 95.81	0.14	1535
Top-like Zero/Single-Jet 2	0.52 ± 0.02	0.07 ± 0.00	0.05 ± 0.00	0.00 ± 0.00	245.86 ± 85.00	0.54 ± 0.16	88.03 ± 5.19	32.63 ± 2.10	0.64 ± 0.02	367.05 ± 85.18	0.03	329
Top-like Zero/Single-Jet 3	0.32 ± 0.01	0.03 ± 0.00	0.03 ± 0.00	0.00 ± 0.00	163.07 ± 63.76	0.33 ± 0.12	42.57 ± 3.76	20.05 ± 1.77	0.38 ± 0.01	226.02 ± 63.90	0.03	236
Top-like Zero/Single-Jet 4	0.04 ± 0.00	0.00 ± 0.00	0.00 ± 0.00	0.00 ± 0.00	3.98 ± 2.29	0.06 ± 0.05	4.87 ± 1.26	2.41 ± 0.61	0.04 ± 0.00	11.33 ± 2.68	0.01	35
Top-like Zero/Single-Jet Combined	4.61 ± 0.05	0.72 ± 0.01	0.48 ± 0.01	0.00 ± 0.00	1142.85 ± 142.64	3.56 ± 0.81	493.48 ± 12.50	173.38 ± 4.75	5.81 ± 0.05	1813.27 ± 143.27	0.14	2135
Top-like Multi-Jet 1	10.21 ± 0.07	1.93 ± 0.01	0.98 ± 0.01	0.20 ± 0.00	1689.84 ± 193.78	13.11 ± 0.91	480.01 ± 12.19	79.48 ± 1.73	13.32 ± 0.07	2262.44 ± 194.17	0.28	2489
Top-like Multi-Jet 2	5.90 ± 0.06	0.75 ± 0.01	0.72 ± 0.01	0.13 ± 0.00	1610.86 ± 129.62	7.22 ± 0.62	792.43 ± 16.11	88.67 ± 2.08	7.50 ± 0.06	2499.17 ± 130.64	0.15	2799
Top-like Multi-Jet 3	1.39 ± 0.03	0.13 ± 0.00	0.24 ± 0.01	0.04 ± 0.00	532.81 ± 80.53	1.81 ± 0.36	333.87 ± 10.66	33.24 ± 1.28	1.80 ± 0.03	901.73 ± 81.24	0.06	974
Top-like Multi-Jet 4	1.21 ± 0.03	0.13 ± 0.00	0.17 ± 0.01	0.03 ± 0.00	409.13 ± 58.15	1.84 ± 0.32	230.97 ± 8.74	23.00 ± 1.02	1.54 ± 0.03	664.95 ± 58.82	0.06	753
Top-like Multi-Jet 5	0.19 ± 0.01	0.02 ± 0.00	0.03 ± 0.00	0.01 ± 0.00	196.46 ± 64.60	0.21 ± 0.09	56.93 ± 4.27	5.15 ± 0.53	0.25 ± 0.01	258.75 ± 64.75	0.01	149
Top-like Multi-Jet 6	1.40 ± 0.03	0.13 ± 0.00	0.23 ± 0.01	0.05 ± 0.00	683.46 ± 100.76	1.71 ± 0.31	421.13 ± 11.83	37.90 ± 1.40	1.81 ± 0.03	1144.20 ± 101.46	0.05	1112
Top-like Multi-Jet Combined	20.30 ± 0.10	3.09 ± 0.01	2.36 ± 0.02	0.46 ± 0.01	5122.56 ± 280.26	25.89 ± 2.40	2315.34 ± 27.50	267.45 ± 3.49	26.21 ± 0.10	7731.24 ± 281.64	0.33	8276
Boson-like Zero/Single-Jet 1	67.24 ± 0.18	6.65 ± 0.02	2.21 ± 0.02	0.00 ± 0.00	16369.49 ± 642.63	28.09 ± 1.21	418.08 ± 11.65	485.40 ± 8.96	76.10 ± 0.18	17301.06 ± 642.80	0.58	18216
Boson-like Zero/Single-Jet 2	137.36 ± 0.26	3.80 ± 0.01	2.44 ± 0.02	0.00 ± 0.00	66678.01 ± 1515.29	28.93 ± 1.22	462.43 ± 12.15	790.13 ± 9.80	143.6 ± 0.26	67959.51 ± 1515.37	0.55	68921
Boson-like Zero/Single-Jet 3	65.24 ± 0.18	0.64 ± 0.00	0.44 ± 0.01	0.00 ± 0.00	57721.90 ± 1455.40	5.83 ± 0.51	89.13 ± 5.45	251.02 ± 5.45	66.32 ± 0.18	58067.89 ± 1455.42	0.28	57492
Boson-like Zero/Single-Jet 4	27.90 ± 0.12	0.14 ± 0.00	0.09 ± 0.00	0.00 ± 0.00	35036.40 ± 1123.66	1.33 ± 0.24	14.78 ± 2.04	72.91 ± 2.77	28.13 ± 0.12	35125.41 ± 1123.67	0.15	38016
Boson-like Zero/Single-Jet 5	9.98 ± 0.07	0.03 ± 0.00	0.03 ± 0.00	0.00 ± 0.00	16284.48 ± 771.08	0.50 ± 0.16	4.09 ± 1.41	24.32 ± 1.61	10.04 ± 0.07	16313.39 ± 771.08	0.08	17071
Boson-like Zero/Single-Jet 6	5.20 ± 0.05	0.02 ± 0.00	0.01 ± 0.00	0.00 ± 0.00	9757.42 ± 591.36	0.35 ± 0.12	3.34 ± 1.02	15.11 ± 1.29	5.23 ± 0.05	9776.21 ± 591.37	0.05	9728
Boson-like Zero/Single-Jet 7	0.44 ± 0.01	0.00 ± 0.00	0.00 ± 0.00	0.00 ± 0.00	800.18 ± 194.20	0.10 ± 0.07	0.00 ± 0.00	1.19 ± 0.39	0.44 ± 0.01	801.47 ± 194.20	0.02	1141
Boson-like Zero/Single-Jet 8	0.18 ± 0.01	0.00 ± 0.00	0.00 ± 0.00	0.00 ± 0.00	349.49 ± 106.61	0.00 ± 0.00	0.00 ± 0.00	0.28 ± 0.20	0.18 ± 0.01	349.77 ± 106.61	0.01	460
Boson-like Zero/Single-Jet 9	0.18 ± 0.01	0.00 ± 0.00	0.00 ± 0.00	0.00 ± 0.00	349.49 ± 106.61	0.00 ± 0.00	0.00 ± 0.00	0.28 ± 0.20	0.18 ± 0.01	349.77 ± 106.61	0.01	460
Boson-like Zero/Single-Jet Combined	313.71 ± 0.39	11.28 ± 0.02	5.22 ± 0.03	0.00 ± 0.00	203346.86 ± 2663.56	65.12 ± 3.69	991.84 ± 17.89	1640.64 ± 14.78	330.21 ± 0.39	206044.47 ± 2663.67	0.86	211505
Boson-like Multi-Jet 1	8.60 ± 0.07	7.90 ± 0.02	0.35 ± 0.01	0.01 ± 0.00	796.22 ± 39.28	26.11 ± 1.18	43.68 ± 3.89	16.02 ± 1.07	16.86 ± 0.07	882.03 ± 39.51	0.57	1022
Boson-like Multi-Jet 2	24.02 ± 0.11	4.85 ± 0.01	2.30 ± 0.02	0.08 ± 0.00	5161.73 ± 255.60	28.78 ± 1.23	243.39 ± 9.11	61.29 ± 1.93	31.25 ± 0.11	5495.19 ± 255.77	0.42	5544
Boson-like Multi-Jet 3	14.72 ± 0.09	1.90 ± 0.01	1.47 ± 0.02	0.06 ± 0.00	5277.24 ± 278.76	15.91 ± 0.89	244.91 ± 8.81	59.88 ± 1.92	18.15 ± 0.09	5597.95 ± 278.91	0.24	5850
Boson-like Multi-Jet 4	7.99 ± 0.06	0.90 ± 0.01	0.86 ± 0.01	0.04 ± 0.00	2820.73 ± 182.65	9.22 ± 0.68	138.75 ± 6.80	37.43 ± 1.46	9.79 ± 0.06	3006.13 ± 182.78	0.18	3401
Boson-like Multi-Jet 5	7.44 ± 0.06	0.66 ± 0.01	0.86 ± 0.01	0.04 ± 0.00	3732.10 ± 245.90	6.84 ± 0.61	178.10 ± 7.42	41.06 ± 1.62	9.00 ± 0.06	3958.11 ± 246.02	0.14	3849
Boson-like Multi-Jet 6	1.90 ± 0.03	0.10 ± 0.00	0.28 ± 0.01	0.01 ± 0.00	1613.81 ± 194.54	2.27 ± 0.40	44.66 ± 3.75	17.43 ± 1.09	2.29 ± 0.03	1678.17 ± 194.58	0.06	1423
Boson-like Multi-Jet Combined	64.67 ± 0.18	16.32 ± 0.02	6.12 ± 0.03	0.23 ± 0.00	19401.84 ± 525.60	89.14 ± 4.43	893.48 ± 17.06	233.12 ± 3.81	87.34 ± 0.18	20617.58 ± 525.91	0.78	21089
All Combined	403.27 ± 0.45	31.41 ± 0.03	14.19 ± 0.05	0.70 ± 0.01	228922.93 ± 2732.57	183.71 ± 6.30	4694.14 ± 39.04	2314.96 ± 16.36	449.57 ± 0.45	236115.76 ± 2732.90	1.22	243041

Table 9.2.12: Expected event yields (normalised to 80.5 fb^{-1}) for different signal and background processes in the twenty-five categories defined by the jet-split selection BDTs of the Background Separation strategy, in the window 120 GeV $< M^{\mu\mu}_{\text{inv}} <$ 130 GeV. The significances of the combined rows are equal to the quadrature sums of the significances of the preceding categories.

9.3 Dedicated Signal BDTs

For the Dedicated Signal strategy, an initial BDT was trained with the focus on identifying VBF signatures, with events failing the selection passed into a ggF-optimised BDT. Dedicated BDTs for the VH and $t\bar{t}H$ processes were not trained, due to the low expected event yield contributions from these processes with 80.5 fb^{-1}. Two-fold cross-validation was again utilised for all BDTs involved.

The VBF BDT, trained using VBF signal and di-boson, top, Drell-Yan and electroweak Z plus jet background MC, was subject to the variable-optimisation algorithm detailed in Section 9.1. Since the VBF topology typically involves at least two jets, the Multi-Jet variable selection of Table 9.0.1 was utilised. The importance of the variables selected by the algorithm are detailed in Table 9.3.1, with $\Delta\eta^{jj}$ of greatest importance for both folds. Comparisons of the normalised distributions of the signal and background events used to train the BDT can be found in Appendix D.

The BDT output distributions are presented in Figure 9.3.1, along with the signal purities of each fold, and the resultant output of applying the BDT to data and MC samples (with the error bands containing statistical, experimental systematic and $P_T^{\mu\mu}$ and M_{inv}^{jj} re-weighting uncertainties). The signal purities of the folds were largely consistent as functions of BDT response, allowing for the definition of two VBF categories of 95% and 98% signal purity. Events falling outside these regions were categorised using the ggF BDTs, described later in this section. The VBF category boundaries are listed in Table 9.3.3.

While minimal overtraining is seen in the signal MC, background discrepancies between training and test samples as large as 20% are seen in some regions. Despite this, the response of the BDT to the data and MC samples is within 10% agreement, and comfortably within the statistical and experimental systematic error bands. The exhibited overtraining was thus not deemed detrimental to the data-MC modelling of the analysis.

While a data-MC discrepancy $\geq 50\%$ is present in the lowest BDT output bin, the signal sensitivity in this region is minimal, such that its effect on the analysis was deemed negligible.

Figure 9.3.2 compares the ROC curves of the newly developed VBF BDT and the Madgraph BDT presented in Chapter 7. Averaged across both folds, the new BDT outperformed its competitor by 0.35%, a minimal improvement.

9.3.1 ggF BDT

All signal (ggF, VBF, VH and $t\bar{t}H$) and background events failing the VBF BDT selection were used for training and testing a set of ggF BDTs, using a two-fold cross-validation approach. Three BDTs were trained with zero-jet, single-jet and multi-jet

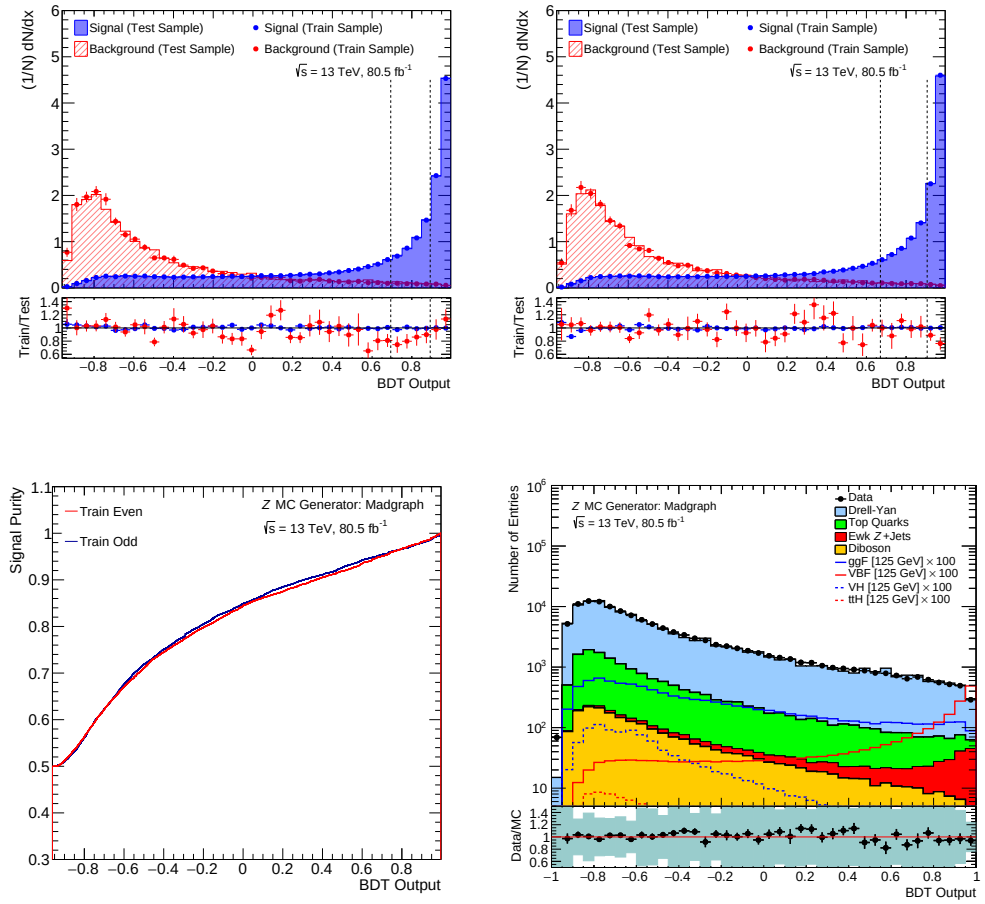

Figure 9.3.1: Output distributions of Folds 1 (top left) and 2 (top right) of the dedicated VBF BDTs, along with the purity of the respective folds (bottom left), trained and tested with inclusive events. The bottom panels of the output distributions display the ratio between the training and test samples of the signal (blue) and background (red) MC. A comparison between data and MC predictions for the BDT output distribution is also presented (bottom right), with the ratio panel containing statistical, experimental systematic, $P_T^{\mu\mu}$ and M_{inv}^{jj} re-weighting uncertainties. The dotted lines represent the category decision boundaries, corresponding to VBF signal purities of 95% and 98% respectively.

Rank	Variable	Variable Importance
1	$\Delta\eta^{jj}$	0.112
2	$P_T^{\mu\mu}$	0.099
3	$\Delta y^{\mu\mu j,\text{Subleading}}$	0.093
4	M_{inv}^{jj}	0.090
5	$\Delta y^{\mu\mu j,\text{Leading}}$	0.085
6	E_T^{miss}	0.082
7	$P_T^{j,\text{Leading}}$	0.075
8	$P_T^{\mu\mu j,\text{Leading}}$	0.071
9	Centrality	0.069
10	$P_T^{\mu\mu jj}$	0.066
11	$P_T^{\mu\mu j,\text{Subleading}}$	0.061
12	Jet Multiplicity ($\lvert\eta^j\rvert \leq 2.5$)	0.052
13	Jet Multiplicity ($\lvert\eta^j\rvert > 2.5$)	0.046

Rank	Variable	Variable Importance
1	$\Delta\eta^{jj}$	0.114
2	M_{inv}^{jj}	0.099
3	$P_T^{\mu\mu}$	0.097
4	$\Delta y^{\mu\mu j,\text{Subleading}}$	0.088
5	$\Delta y^{\mu\mu j,\text{Leading}}$	0.086
6	$P_T^{j,\text{Leading}}$	0.082
7	E_T^{miss}	0.080
8	$P_T^{\mu\mu j,\text{Leading}}$	0.077
9	$P_T^{\mu\mu jj}$	0.073
10	Centrality	0.063
11	$P_T^{\mu\mu j,\text{Subleading}}$	0.056
12	Jet Multiplicity ($\lvert\eta^j\rvert > 2.5$)	0.046
13	Jet Multiplicity ($\lvert\eta^j\rvert \leq 2.5$)	0.040

Table 9.3.1: Ranking of the input variables used to train Folds 1 (left) and 2 (right) of the VBF category BDTs.

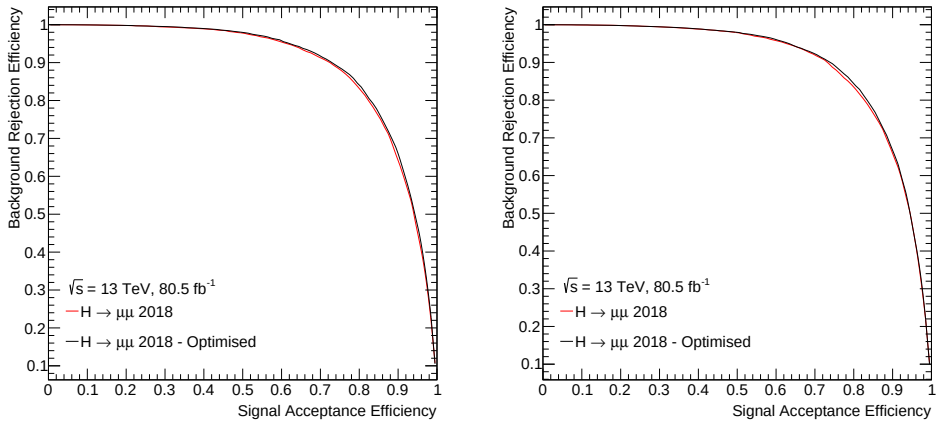

Figure 9.3.2: ROC curve comparisons between an optimised form of the BDT presented in Chapter 7, and its nominal configuration. Performance improvements of 0.41% and 0.28% are seen for Folds 1 and 2 with respect to the nominal.

events respectively, with an inclusive selection BDT trained for comparison. All were subject to the variable and boundary-optimisation algorithms detailed in Section 9.1. Variables used to train the VBF BDT in the previous step were not used to avoid overtraining.

Table 9.3.2 presents the optimally-chosen variables used for the inclusive selection BDT. Similar to the Signal vs Boson-Like BDTs, $\Delta\phi^{\mu\mu}$ and $\eta^{\mu,\text{Leading}}$ held the most importance. Comparisons of the normalised distributions of the signal and background events used to train the BDT can be found in Appendix D.

The output distributions of the BDT are shown in Figure 9.3.3. The signal appears overtrained by less than 5%, with background overtraining largely within 10%. The

background overtraining appears more prominently in Fold 1, highlighting a potential limitation of the method by which the variable-optimisation algorithm treats k-folding - in this case, it appears the chosen variables were overly optimised with respect to a particular fold. This could be reduced in future by reducing the number of trees and depth with which the BDT is trained.

Comparisons of the BDT score between data and MC are presented in Figure 9.3.3, with agreement comfortably within the statistical and systematic error bands, and within 5-10% overall.

Rank	Variable	Variable Importance
1	$\eta^{\mu,\text{Leading}}$	0.210
2	$\Delta\phi^{\mu\mu}$	0.181
3	$\cos(\theta^*)$	0.175
4	$\Delta R^{\mu\mu}$	0.172
5	$\Delta\eta^{\mu\mu}$	0.157
6	Jet Multiplicity	0.104

Rank	Variable	Variable Importance
1	$\eta^{\mu,\text{Leading}}$	0.209
2	$\Delta\phi^{\mu\mu}$	0.188
3	$\Delta R^{\mu\mu}$	0.173
4	$\cos(\theta^*)$	0.169
5	$\Delta\eta^{\mu\mu}$	0.162
6	Jet Multiplicity	0.099

Table 9.3.2: Ranking of the input variables used to train Folds 1 (left) and 2 (right) of the inclusive ggF category BDTs.

The category boundaries derived from the BDT are listed in Table 9.3.3, with the associated event yields presented in Table 9.3.4. In combination with the VBF categories, a combined significance of 1.24 was achieved, outperforming the previously tested methods by 1-2%. Across all categories, the data yields agree with the MC predictions within statistical errors.

Category	BDT Output Range	
	Fold 1	Fold 2
ggF Inclusive 1	$0.18 \leq x$	$0.12 \leq x$
ggF Inclusive 2	$-0.05 < x \leq 0.18$	$-0.17 < x \leq 0.12$
ggF Inclusive 3	$-0.32 < x \leq -0.05$	$-0.30 < x \leq -0.17$
ggF Inclusive 4	$-0.39 < x \leq -0.32$	$-0.42 < x \leq -0.30$
ggF Inclusive 5	$-0.42 < x \leq -0.39$	$-0.52 < x \leq -0.42$
ggF Inclusive 6	$-0.55 < x \leq -0.42$	$-0.56 < x \leq -0.52$
ggF Inclusive 7	$x \leq -0.55$	$x \leq -0.56$
VBF Inclusive 1	$0.89 \leq x$	$0.91 \leq x$
VBF Inclusive 2	$0.69 < x \leq 0.89$	$0.67 < x \leq 0.91$

Table 9.3.3: Category boundaries for both folds of the Dedicated Signal Strategy BDTs trained with inclusive events. Cuts derived from the Fold 1 BDTs were applied to the Fold 2 samples (and vice versa).

The variables used to train the dedicated ggF BDTs with zero-jet, single-jet and multi-jet events are listed in Tables 9.3.5 to 9.3.7. The correlation between $\Delta R^{\mu\mu}$

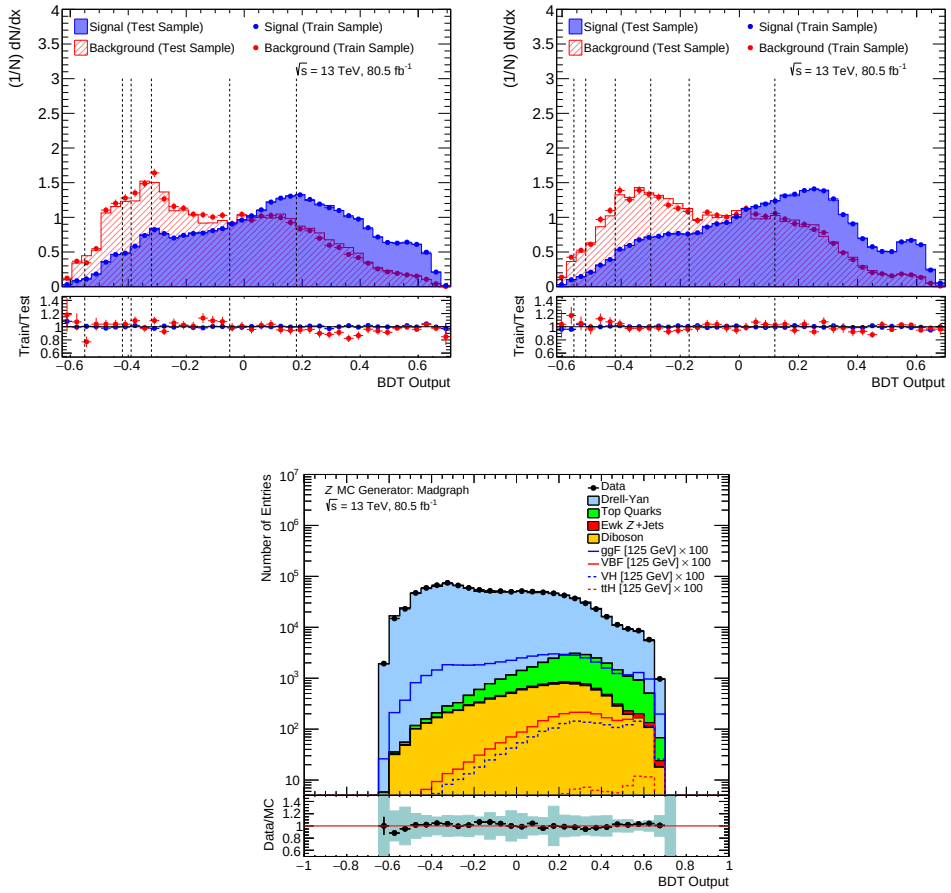

Figure 9.3.3: Output distributions of Folds 1 (top left) and 2 (top right) of the dedicated ggF BDTs, trained and tested with multi-jet events. The dotted lines correspond to the boundaries of categories derived from the distributions. The bottom panels display the ratio between the training and test samples of the signal (blue) and background (red) MC. A comparison between data and MC predictions for the BDT output distribution is also presented (bottom), with the ratio panel containing statistical, experimental systematic, $P_T^{\mu\mu}$ and M_{inv}^{jj} re-weighting uncertainties.

Category	ggF	VBF	VH	$t\bar{t}H$	Drell-Yan	EWK Z + Jets	Di-boson	Top	Total Signal	Total Background	$\frac{S}{\sqrt{B}}$	Data
ggF Inclusive 1	171.20 ± 0.29	15.33 ± 0.02	10.83 ± 0.05	0.63 ± 0.01	49700.89 ± 1069.02	99.25 ± 2.31	3516.47 ± 33.90	1193.80 ± 11.87	197.99 ± 0.30	54510.40 ± 1069.63	0.85	55129
ggF Inclusive 2	112.35 ± 0.24	4.11 ± 0.01	2.51 ± 0.02	0.06 ± 0.00	59455.08 ± 1438.29	35.70 ± 1.39	915.08 ± 17.03	691.54 ± 8.86	119.03 ± 0.24	61097.39 ± 1438.42	0.48	63811
ggF Inclusive 3	65.89 ± 0.18	0.98 ± 0.01	0.58 ± 0.01	0.01 ± 0.00	55766.21 ± 1409.88	10.71 ± 0.70	182.08 ± 7.81	268.04 ± 5.65	67.46 ± 0.18	56227.04 ± 1409.92	0.28	57155
ggF Inclusive 4	26.51 ± 0.12	0.18 ± 0.00	0.10 ± 0.00	0.00 ± 0.00	29730.97 ± 1021.01	1.60 ± 0.27	15.85 ± 2.12	80.17 ± 2.88	26.79 ± 0.12	29828.59 ± 1021.01	0.16	32115
ggF Inclusive 5	9.55 ± 0.07	0.05 ± 0.00	0.03 ± 0.00	0.00 ± 0.00	15041.71 ± 758.89	0.49 ± 0.15	7.07 ± 1.63	31.66 ± 1.81	9.63 ± 0.07	15080.94 ± 758.90	0.08	14914
ggF Inclusive 6	9.79 ± 0.07	0.05 ± 0.00	0.04 ± 0.00	0.00 ± 0.00	14801.83 ± 711.34	0.68 ± 0.18	2.07 ± 0.78	31.41 ± 1.85	9.88 ± 0.07	14836.00 ± 711.34	0.08	15645
ggF Inclusive 7	1.80 ± 0.03	0.01 ± 0.00	0.00 ± 0.00	0.00 ± 0.00	3700.47 ± 374.65	0.10 ± 0.07	1.29 ± 0.59	7.63 ± 0.87	1.81 ± 0.03	3709.49 ± 374.65	0.03	3480
ggF Inclusive Combined	397.09 ± 0.45	20.72 ± 0.03	14.09 ± 0.05	0.69 ± 0.01	228197.16 ± 2732.03	148.53 ± 5.66	4639.90 ± 38.84	2304.26 ± 16.34	432.59 ± 0.45	235289.85 ± 2732.36	1.03	242249
VBF 1	1.85 ± 0.03	6.55 ± 0.02	0.01 ± 0.00	0.00 ± 0.00	165.32 ± 16.00	18.14 ± 0.98	7.57 ± 1.43	2.19 ± 0.33	8.41 ± 0.04	193.23 ± 16.09	0.61	181
VBF 2	4.33 ± 0.05	4.14 ± 0.01	0.08 ± 0.00	0.01 ± 0.00	560.45 ± 51.56	17.05 ± 0.93	46.66 ± 3.67	8.51 ± 0.60	8.56 ± 0.05	632.68 ± 51.70	0.34	611
VBF Combined	6.18 ± 0.06	10.69 ± 0.02	0.09 ± 0.00	0.01 ± 0.00	725.78 ± 53.98	35.19 ± 2.77	54.24 ± 3.94	10.71 ± 0.69	16.97 ± 0.06	825.91 ± 54.20	0.69	792
Combined	403.27 ± 0.45	31.41 ± 0.07	14.19 ± 0.05	0.70 ± 0.01	228922.94 ± 2732.57	183.71 ± 6.30	4694.14 ± 39.04	2314.97 ± 16.36	449.57 ± 0.45	236115.76 ± 2732.90	1.24	243041

Table 9.3.4: Expected event yields (normalised to 80.5 fb^{-1}) for different signal and background processes in the nine categories defined by the VBF BDT and the inclusive ggF BDTs, in the window 120 GeV $< M_{\text{inv}}^{\mu\mu} <$ 130 GeV. The significances of the combined rows are equal to the quadrature sums of the significances of the preceding categories.

and $M_{\text{inv}}^{\mu\mu}$ in the Single-Jet and Multi-Jet BDTs was found to be minimal, and so was allowed in these cases. Both BDTs were highly sensitive to overtraining, and were thus trained with a reduced number of trees (100) and reduced maximum depths (2 and 3 respectively). The allowed number of training variables for each was also limited relative to the recommendations of the variable-optimisation algorithm. Comparisons of the normalised distributions of the signal and background events used to train the BDTs can be found in Appendix D.

The resulting BDT output distributions are shown in Figures 9.3.4 to 9.3.6. Signal overtraining was found to be minimal in all cases. Background overtraining $\geq 20\%$ was seen in some regions, with the Multi-Jet BDT exhibiting more evidence of overtraining in general. Large background MC statistical uncertainties were a large contributor to these effects. Despite this, the BDT scores of the data and MC (also shown in Figures 9.3.4 to 9.3.6) agree within 10%, suggesting the effects of overtraining are negligible to the treatment of data and MC in these regions.

Rank	Variable	Variable Importance
1	$\cos(\theta^*)$	0.225
2	$\Delta\phi^{\mu\mu}$	0.204
3	$\eta^{\mu,\text{Subleading}}$	0.200
4	$\eta^{\mu,\text{Leading}}$	0.193
5	$y^{\mu\mu}$	0.177

Rank	Variable	Variable Importance
1	$\cos(\theta^*)$	0.234
2	$\Delta\phi^{\mu\mu}$	0.199
3	$\eta^{\mu,\text{Leading}}$	0.196
4	$\eta^{\mu,\text{Subleading}}$	0.190
5	$y^{\mu\mu}$	0.182

Table 9.3.5: Ranking of the input variables used to train Folds 1 (left) and 2 (right) of the Zero-Jet ggF category BDTs.

Rank	Variable	Variable Importance
1	$\eta^{j,\text{Leading}}$	0.371
2	$\Delta R^{\mu\mu}$	0.315
3	$\eta^{\mu,\text{Leading}}$	0.315

Rank	Variable	Variable Importance
1	$\eta^{j,\text{Leading}}$	0.349
2	$\Delta R^{\mu\mu}$	0.331
3	$\eta^{\mu,\text{Leading}}$	0.320

Table 9.3.6: Ranking of the input variables used to train Folds 1 (left) and 2 (right) of the Single-Jet ggF category BDTs.

The categories derived from the BDT output distributions are listed in Table 9.3.8. Boundary definitions vary between folds due to statistical fluctuations in the MC. The associated event yields are listed in Table 9.3.9, with data yields agreeing with MC predictions within statistical errors for most categories. A total combined significance of 1.28 is attained, the largest of all BDT categorisations considered. This categorisation was thus utilised for the final $H \to \mu\mu$ signal strength extraction. Given a larger amount of MC events with which to train the BDTs, or perhaps dedicated VH and $t\bar{t}H$ BDTs, it is likely this significance could be further improved.

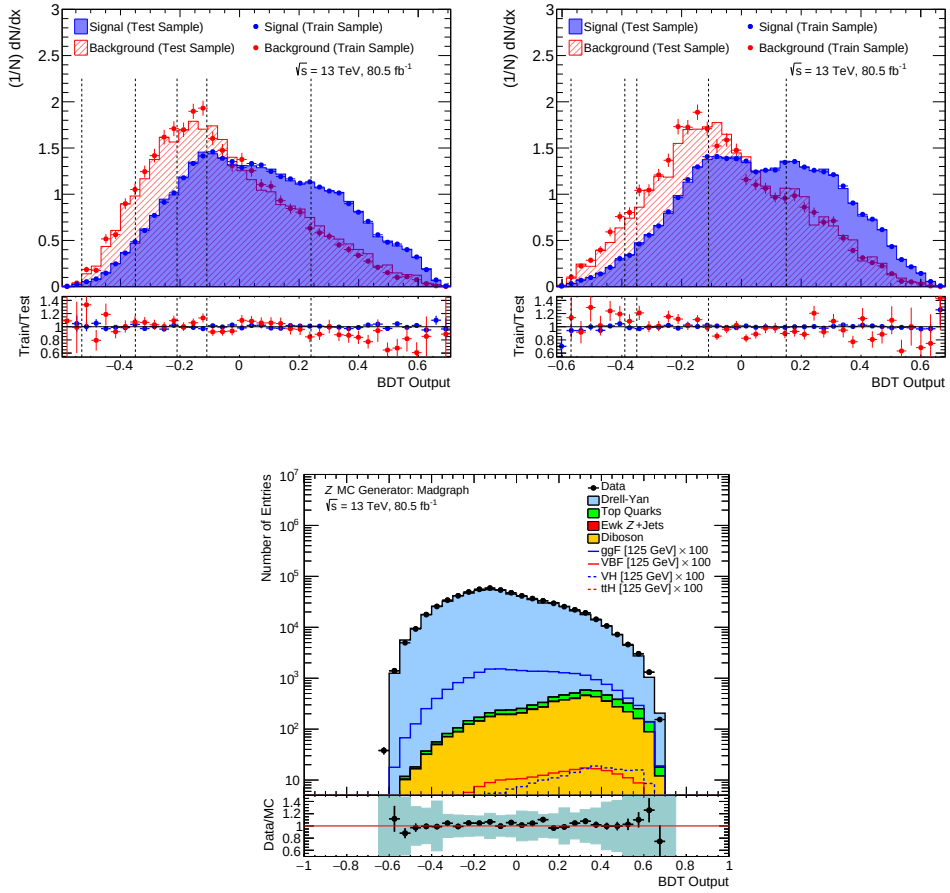

Figure 9.3.4: Output distributions of Folds 1 (top left) and 2 (top right) of the dedicated ggF BDTs, trained and tested with zero-jet events. The dotted lines correspond to the boundaries of categories derived from the distributions. The bottom panels display the ratio between the training and test samples of the signal (blue) and background (red) MC. A comparison between data and MC predictions for the BDT output distribution is also presented (bottom), with the ratio panel containing statistical, experimental systematic, $P_T^{\mu\mu}$ and M_{inv}^{jj} re-weighting uncertainties.

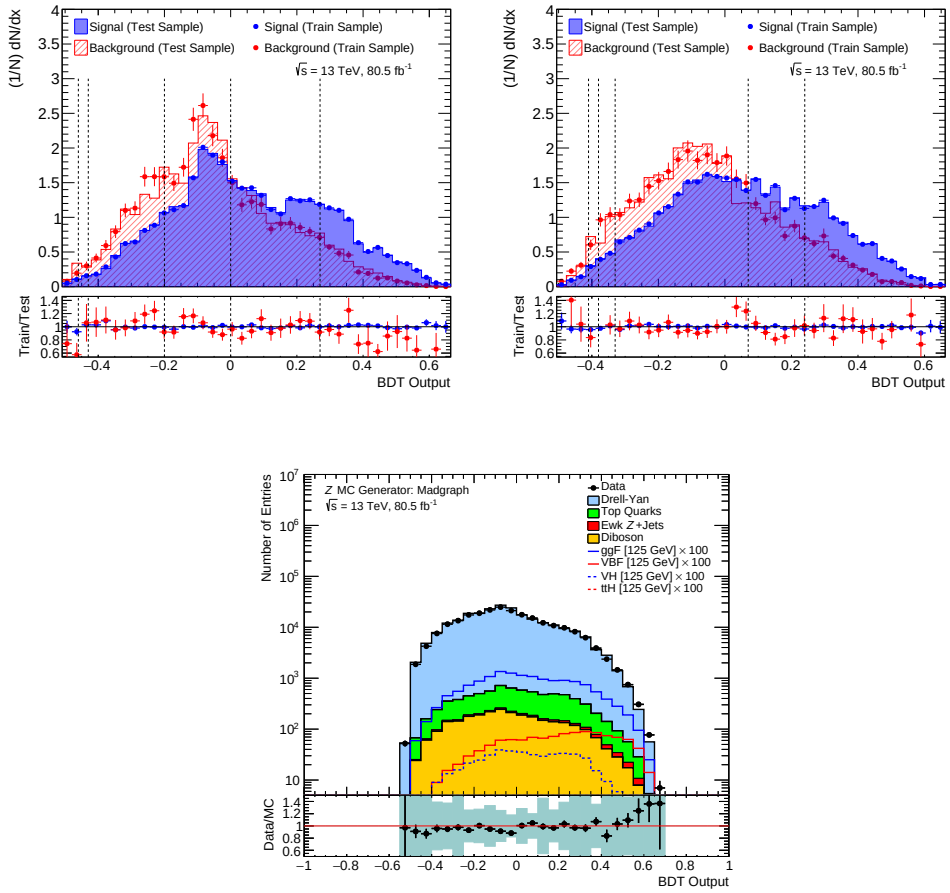

Figure 9.3.5: Output distributions of Folds 1 (top left) and 2 (top right) of the dedicated ggF BDTs, trained and tested with single-jet events. The dotted lines correspond to the boundaries of categories derived from the distributions. The bottom panels display the ratio between the training and test samples of the signal (blue) and background (red) MC. A comparison between data and MC predictions for the BDT output distribution is also presented (bottom), with the ratio panel containing statistical, experimental systematic, $P_T^{\mu\mu}$ and M_{inv}^{jj} re-weighting uncertainties.

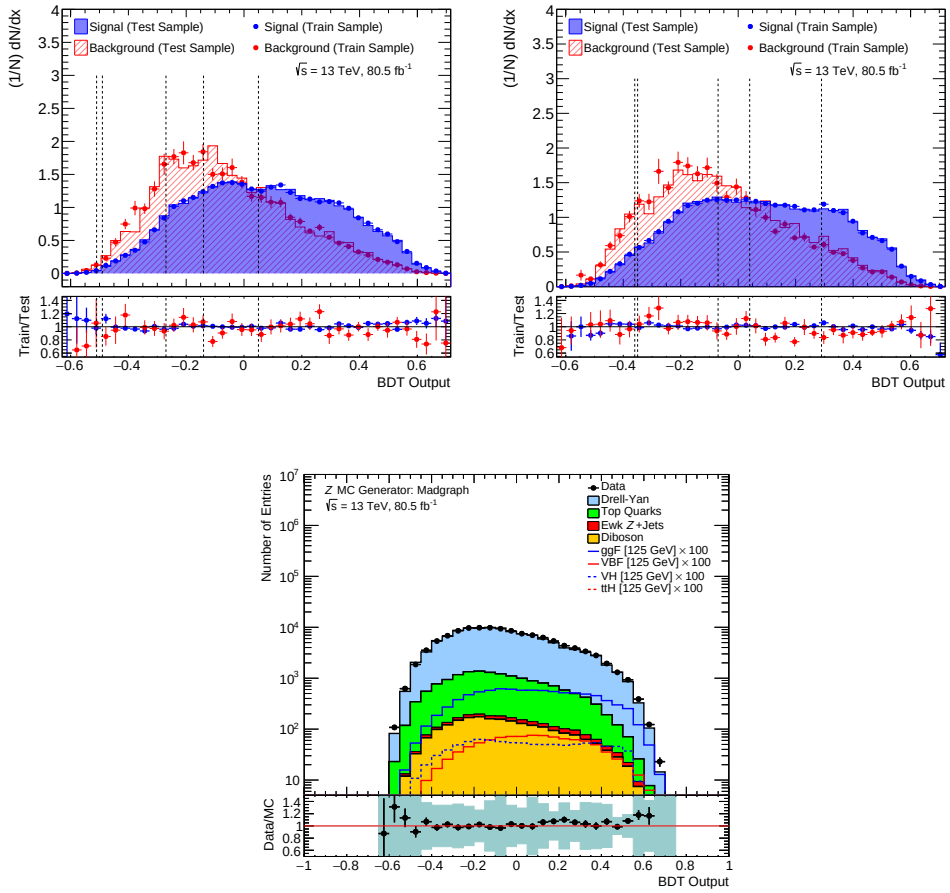

Figure 9.3.6: Output distributions of Folds 1 (top left) and 2 (top right) of the dedicated ggF BDTs, trained and tested with multi-jet events. The dotted lines correspond to the boundaries of categories derived from the distributions. The bottom panels display the ratio between the training and test samples of the signal (blue) and background (red) MC. A comparison between data and MC predictions for the BDT output distribution is also presented (bottom), with the ratio panel containing statistical, experimental systematic, $P_T^{\mu\mu}$ and M_{inv}^{jj} re-weighting uncertainties.

Rank	Variable	Variable Importance
1	$\Delta R^{\mu\mu}$	0.219
2	$\eta^{j,\text{Leading}}$	0.214
3	ΔR^{jj}	0.189
4	$y^{\mu\mu}$	0.159
5	$\eta^{\mu,\text{Leading}}$	0.129
6	$P_T^{j,\text{Subleading}}$	0.089

Rank	Variable	Variable Importance
1	$\Delta R^{\mu\mu}$	0.230
2	$\eta^{j,\text{Leading}}$	0.217
3	ΔR^{jj}	0.168
4	$y^{\mu\mu}$	0.157
5	$\eta^{\mu,\text{Leading}}$	0.156
6	$P_T^{j,\text{Subleading}}$	0.071

Table 9.3.7: Ranking of the input variables used to train Folds 1 (left) and 2 (right) of the Multi-Jet ggF category BDTs.

Category	BDT Output Range	
	Fold 1	Fold 2
ggF Zero-Jet 1	$0.24 \leq x$	$0.15 < x$
ggF Zero-Jet 2	$-0.11 < x \leq 0.24$	$-0.11 < x \leq 0.15$
ggF Zero-Jet 3	$-0.21 < x \leq -0.11$	$-0.35 < x \leq -0.11$
ggF Zero-Jet 4	$-0.35 < x \leq -0.21$	$-0.39 < x \leq -0.35$
ggF Zero-Jet 5	$-0.53 < x \leq -0.35$	$-0.57 < x \leq -0.39$
ggF Zero-Jet 6	$x \leq -0.53$	$x \leq -0.57$
ggF Single-Jet 1	$0.27 \leq x$	$0.24 \leq x$
ggF Single-Jet 2	$0.0 < x \leq 0.27$	$0.07 < x \leq 0.24$
ggF Single-Jet 3	$-0.20 < x \leq 0.0$	$-0.33 < x \leq 0.07$
ggF Single-Jet 4	$-0.43 < x \leq -0.20$	$-0.38 < x \leq -0.33$
ggF Single-Jet 5	$-0.46 < x \leq -0.43$	$-0.41 < x \leq -0.38$
ggF Single-Jet 6	$x \leq -0.46$	$x \leq -0.41$
ggF Multi-Jet 1	$0.05 \leq x$	$0.29 \leq x$
ggF Multi-Jet 2	$-0.14 < x \leq 0.05$	$0.04 < x \leq 0.29$
ggF Multi-Jet 3	$-0.27 < x \leq -0.14$	$-0.07 < x \leq 0.04$
ggF Multi-Jet 4	$-0.49 < x \leq -0.27$	$-0.35 < x \leq -0.07$
ggF Multi-Jet 5	$-0.51 < x \leq -0.49$	$-0.36 < x \leq -0.35$
ggF Multi-Jet 6	$x \leq -0.51$	$x \leq -0.36$

Table 9.3.8: Category boundaries for both folds of the Dedicated Signal Strategy BDTs trained with zero-jet, single-jet and multi-jet events. Cuts derived from the Fold 1 BDTs were applied to the Fold 2 samples (and vice versa).

Category	ggF	VBF	VH	$t\bar{t}H$	Drell-Yan	EWK Z + Jets	Di-boson	Top	Total Signal	Total Background	$\frac{S}{\sqrt{B}}$	Data
ggF Zero-Jet 1	62.13 ± 0.17	1.06 ± 0.01	1.18 ± 0.02	0.00 ± 0.00	25236.94 ± 922.51	9.06 ± 0.68	222.20 ± 8.28	685.59 ± 8.98	64.37 ± 0.03	26153.78 ± 922.59	0.40	27547
ggF Zero-Jet 2	75.50 ± 0.19	0.60 ± 0.00	0.43 ± 0.01	0.00 ± 0.00	56749.72 ± 1390.37	6.41 ± 0.58	63.12 ± 4.44	341.92 ± 6.46	76.53 ± 0.19	57161.17 ± 1390.39	0.32	60057
ggF Zero-Jet 3	33.06 ± 0.13	0.19 ± 0.00	0.11 ± 0.00	0.00 ± 0.00	38020.36 ± 1180.59	1.80 ± 0.28	14.18 ± 2.18	96.11 ± 3.20	33.36 ± 0.13	38132.45 ± 1180.59	0.17	40545
ggF Zero-Jet 4	11.78 ± 0.08	0.06 ± 0.00	0.04 ± 0.00	0.00 ± 0.00	16929.23 ± 770.56	0.68 ± 0.17	5.72 ± 1.26	38.84 ± 1.99	11.88 ± 0.08	16974.47 ± 770.56	0.09	17315
ggF Zero-Jet 5	6.06 ± 0.06	0.03 ± 0.00	0.02 ± 0.00	0.00 ± 0.00	11444.67 ± 643.84	0.40 ± 0.14	2.32 ± 0.79	20.28 ± 1.44	6.11 ± 0.06	11467.67 ± 643.84	0.06	11806
ggF Zero-Jet 6	0.13 ± 0.01	0.00 ± 0.00	0.00 ± 0.00	0.00 ± 0.00	191.15 ± 72.31	0.04 ± 0.04	0.00 ± 0.00	0.72 ± 0.28	0.13 ± 0.01	191.92 ± 72.31	0.01	261
ggF Zero-Jet Combined	188.66 ± 0.31	1.94 ± 0.01	1.79 ± 0.02	0.00 ± 0.00	148572.07 ± 2278.48	18.39 ± 1.96	307.53 ± 9.76	1183.46 ± 11.78	192.39 ± 0.31	150081.46 ± 2278.53	0.55	157531
ggF Single-Jet 1	26.32 ± 0.11	4.45 ± 0.01	0.78 ± 0.01	0.00 ± 0.00	4889.82 ± 293.07	13.74 ± 0.87	206.51 ± 8.13	94.06 ± 3.15	31.55 ± 0.11	5204.12 ± 293.20	0.44	5426
ggF Single-Jet 2	37.23 ± 0.14	2.73 ± 0.01	1.18 ± 0.02	0.00 ± 0.00	12201.05 ± 628.80	13.51 ± 0.82	366.98 ± 11.02	169.23 ± 6.65	41.14 ± 0.14	12750.78 ± 628.93	0.36	13092
ggF Single-Jet 3	53.74 ± 0.16	2.44 ± 0.01	1.58 ± 0.02	0.00 ± 0.00	30258.87 ± 1075.59	17.00 ± 0.92	472.12 ± 12.38	275.23 ± 5.92	57.65 ± 0.16	31023.22 ± 1075.67	0.33	28588
ggF Single-Jet 4	10.45 ± 0.07	0.39 ± 0.00	0.31 ± 0.01	0.00 ± 0.00	6995.14 ± 470.41	5.10 ± 0.49	104.48 ± 5.60	74.23 ± 3.22	11.15 ± 0.07	7178.96 ± 470.46	0.13	7497
ggF Single-Jet 5	0.96 ± 0.02	0.03 ± 0.00	0.04 ± 0.00	0.00 ± 0.00	887.34 ± 207.92	0.46 ± 0.14	11.12 ± 1.86	8.23 ± 1.04	1.03 ± 0.02	907.14 ± 207.93	0.03	804
ggF Single-Jet 6	0.95 ± 0.02	0.02 ± 0.00	0.03 ± 0.00	0.00 ± 0.00	594.25 ± 134.09	0.48 ± 0.15	16.57 ± 2.38	9.96 ± 1.27	1.00 ± 0.02	621.27 ± 134.12	0.04	738
ggF Single-Jet Combined	129.65 ± 0.25	10.06 ± 0.02	3.92 ± 0.03	0.01 ± 0.00	55826.46 ± 1385.88	50.29 ± 3.23	1177.79 ± 19.53	630.94 ± 10.11	143.64 ± 0.25	57685.48 ± 1386.06	0.67	56145
ggF Multi-Jet 1	29.59 ± 0.12	3.27 ± 0.01	3.14 ± 0.02	0.24 ± 0.00	5072.60 ± 228.87	22.48 ± 1.12	603.91 ± 13.85	112.15 ± 2.44	36.24 ± 0.12	5811.14 ± 229.30	0.48	6039
ggF Multi-Jet 2	21.54 ± 0.11	2.66 ± 0.01	1.95 ± 0.02	0.16 ± 0.00	6251.51 ± 322.40	23.26 ± 1.14	832.85 ± 16.56	126.09 ± 2.64	26.31 ± 0.11	7233.71 ± 322.83	0.31	7455
ggF Multi-Jet 3	11.09 ± 0.08	1.22 ± 0.01	1.15 ± 0.02	0.10 ± 0.00	4143.27 ± 262.73	12.60 ± 0.82	582.47 ± 13.97	83.56 ± 2.09	13.56 ± 0.08	4821.89 ± 263.12	0.20	5060
ggF Multi-Jet 4	14.69 ± 0.09	1.41 ± 0.01	1.81 ± 0.02	0.16 ± 0.00	6968.53 ± 320.93	18.04 ± 0.98	939.59 ± 17.49	141.22 ± 2.73	18.07 ± 0.09	8067.38 ± 321.42	0.20	8449
ggF Multi-Jet 5	0.27 ± 0.01	0.02 ± 0.00	0.04 ± 0.00	0.00 ± 0.00	149.49 ± 49.71	0.26 ± 0.11	23.50 ± 2.89	3.70 ± 0.47	0.33 ± 0.01	176.94 ± 49.79	0.03	208
ggF Multi-Jet 6	1.61 ± 0.03	0.13 ± 0.00	0.30 ± 0.01	0.03 ± 0.00	1213.23 ± 145.16	3.21 ± 0.47	172.27 ± 7.49	23.14 ± 1.11	2.07 ± 0.03	1411.85 ± 145.36	0.06	1362
ggF Multi-Jet Combined	78.78 ± 0.20	8.72 ± 0.02	8.39 ± 0.04	0.69 ± 0.01	23798.62 ± 593.20	79.84 ± 4.21	3154.58 ± 32.12	489.87 ± 5.12	96.58 ± 0.21	27522.92 ± 594.11	0.64	28573
VBF 1	1.85 ± 0.03	6.55 ± 0.02	0.01 ± 0.00	0.00 ± 0.00	165.32 ± 16.00	18.14 ± 0.98	7.57 ± 1.43	2.19 ± 0.33	8.41 ± 0.04	193.23 ± 16.09	0.61	181
VBF 2	4.33 ± 0.05	4.14 ± 0.01	0.08 ± 0.00	0.01 ± 0.00	560.45 ± 51.56	17.05 ± 0.93	46.66 ± 3.67	8.51 ± 0.60	8.56 ± 0.05	632.68 ± 51.70	0.34	611
VBF Combined	6.18 ± 0.06	10.69 ± 0.02	0.09 ± 0.00	0.01 ± 0.00	725.78 ± 53.98	35.19 ± 2.77	54.24 ± 3.94	10.71 ± 0.69	16.97 ± 0.06	825.91 ± 54.20	0.69	792
Combined	403.27 ± 0.45	31.41 ± 0.07	14.19 ± 0.05	0.70 ± 0.01	228922.94 ± 2732.57	183.71 ± 6.30	4694.14 ± 39.04	2314.97 ± 16.36	449.57 ± 0.45	236115.76 ± 2732.90	1.28	243041

Table 9.3.9: Expected event yields (normalised to 80.5 fb^{-1}) for different signal and background processes in the twenty categories defined by the VBF BDT and the Zero-Jet, Single-Jet and Multi-Jet ggF BDTs, in the window 120 GeV $< M_{\text{inv}}^{\mu\mu} <$ 130 GeV. The significances of the combined rows are equal to the quadrature sums of the significances of the preceding categories.

To summarise, this chapter has presented three different methods by which selected events can be categorised through the use of BDTs. The first involved training a single BDT using all available signal and background MC samples. The second involved training an initial BDT capable of separating the different background components of the analysis, after which a subsequent BDT could attempt to separate signal processes from the individual background components. The third involved training an initial BDT focused on identifying VBF events, with those failing its selection subject to a separate BDT trained to identify non-VBF events. For each method, BDTs were trained using zero-jet, single-jet and multi-jet events separately, in order to maximise signal-background separation. Categories were then defined based on the output distributions of the BDTs. The third method was found to produce the highest overall signal sensitivity, and thus its categorisation was used for the remainder of the analysis. The categories derived from the other methods are thus ignored for the remainder of this thesis.

9.3.2 $M^{\mu\mu}_{\mathbf{inv}}$ Distributions for the Dedicated Signal BDT Categories

Figures 9.3.7 to 9.3.11 present the $M^{\mu\mu}_{\text{inv}}$ distributions of data and MC in each of the Zero-Jet, Single-Jet, Multi-Jet, Inclusive and VBF categories defined by the Dedicated Signal BDTs. All samples have been normalised to 80.5 fb^{-1}. While Drell-Yan samples produced with Madgraph were used for training the BDTs, when split into categories, the sample statistical errors were too large to allow for smoothly falling background $M^{\mu\mu}_{\text{inv}}$ distributions. The Powheg Drell-Yan samples by comparison possess an order of magnitude greater number of events. Thus, in each category Powheg Drell-Yan samples normalised to the event yields of Madgraph were utilised. The $M^{\mu\mu}_{\text{inv}}$ distributions using Madgraph are presented in Appendix E.

Across all categories, data-MC discrepancies are generally smaller than 10%, and within the bounds of the presented statistical, experimental systematic and $P_T^{\mu\mu}$ and M^{jj}_{inv} re-weighting uncertainties. Despite the re-normalisation procedure outlined above, the Zero-Jet 6 and Multi-Jet 5 categories show notable fluctuations in their overall background MC distributions, with systematic uncertainties greater than 500% seen in some bins. These categories were thus excluded from the $H \to \mu\mu$ signal extraction fits. Since the expected significances of these categories is small (0.01 and 0.03 respectively), the total expected combined significance (1.28) remains unchanged with their removal from the analysis.

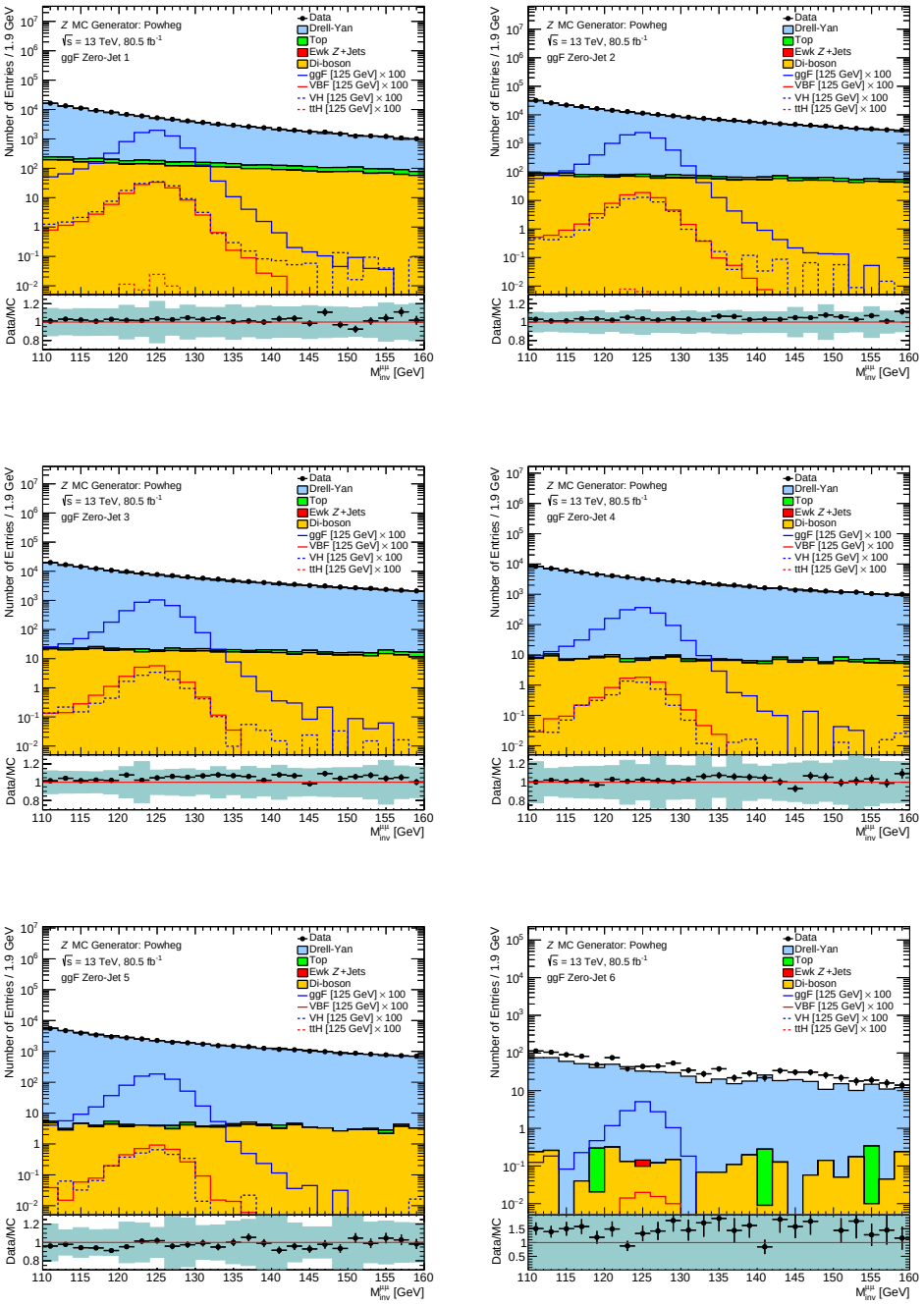

Figure 9.3.7: Comparison of the $M^{\mu\mu}_{\text{inv}}$ distributions of data and MC in the ggF Zero-Jet 1 (top left), ggF Zero-Jet 2 (top right), ggF Zero-Jet 3 (middle left), ggF Zero-Jet 4 (middle right), ggF Zero-Jet 5 (bottom left) and ggF Zero-Jet 6 (bottom right) categories. The MC samples have been normalised to 80.5 fb^{-1}. For a smooth background shape, Drell-Yan events produced with Powheg were utilised, normalised to the event yields of Madgraph Drell-Yan samples. The systematic bands include statistical, experimental systematic, $P_T^{\mu\mu}$ and M^{jj}_{inv} re-weighting uncertainties.

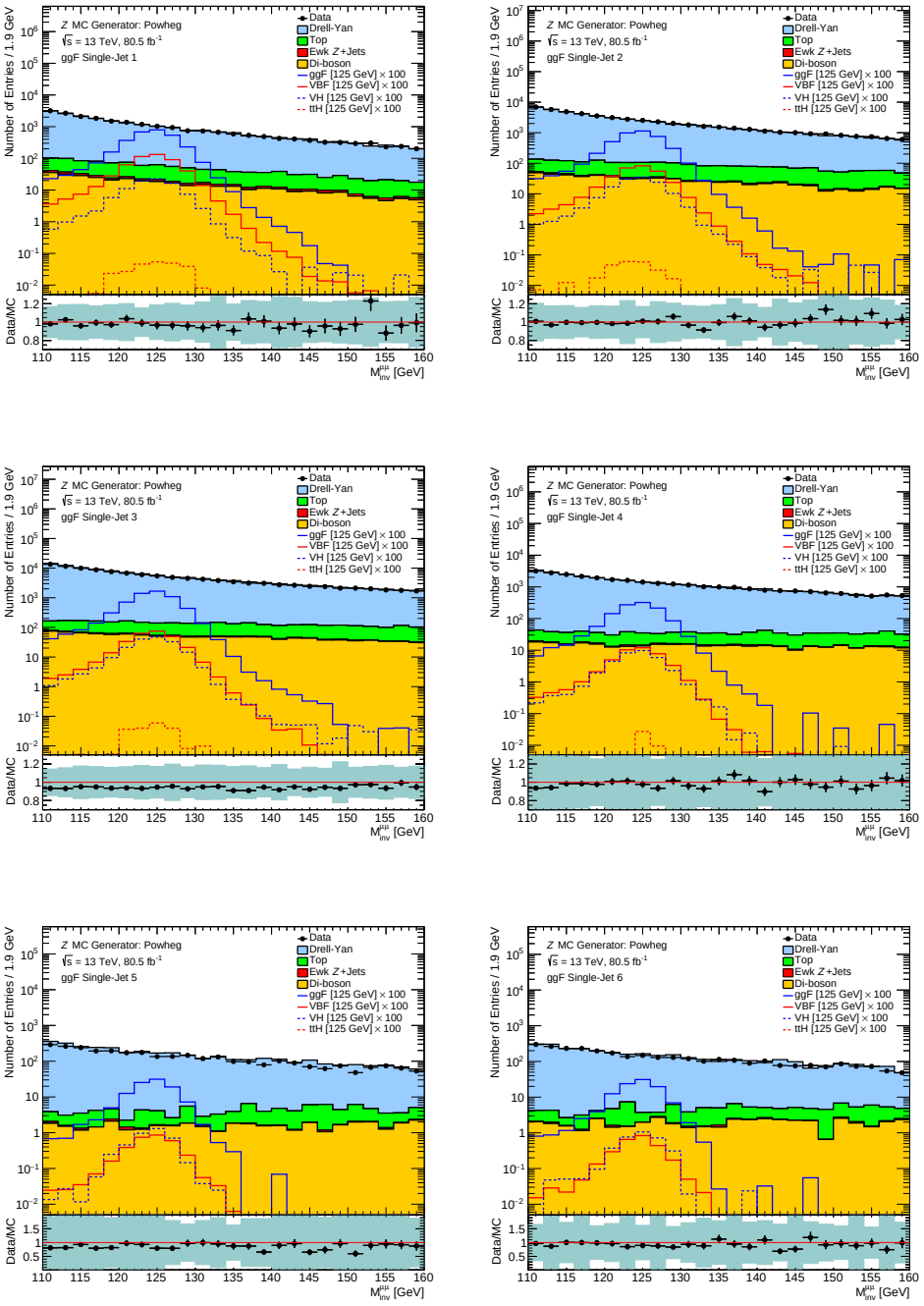

Figure 9.3.8: Comparison of the $M_{\text{inv}}^{\mu\mu}$ distributions of data and MC in the ggF Single-Jet 1 (top left), ggF Single-Jet 2 (top right), ggF Single-Jet 3 (middle left), ggF Single-Jet 4 (middle right), ggF Single-Jet 5 (bottom left) and ggF Single-Jet 6 (bottom right) categories. The MC samples have been normalised to 80.5 fb^{-1}. For a smooth background shape, Drell-Yan events produced with Powheg were utilised, normalised to the event yields of Madgraph Drell-Yan samples. The systematic bands include statistical, experimental systematic, $P_T^{\mu\mu}$ and M_{inv}^{jj} re-weighting uncertainties.

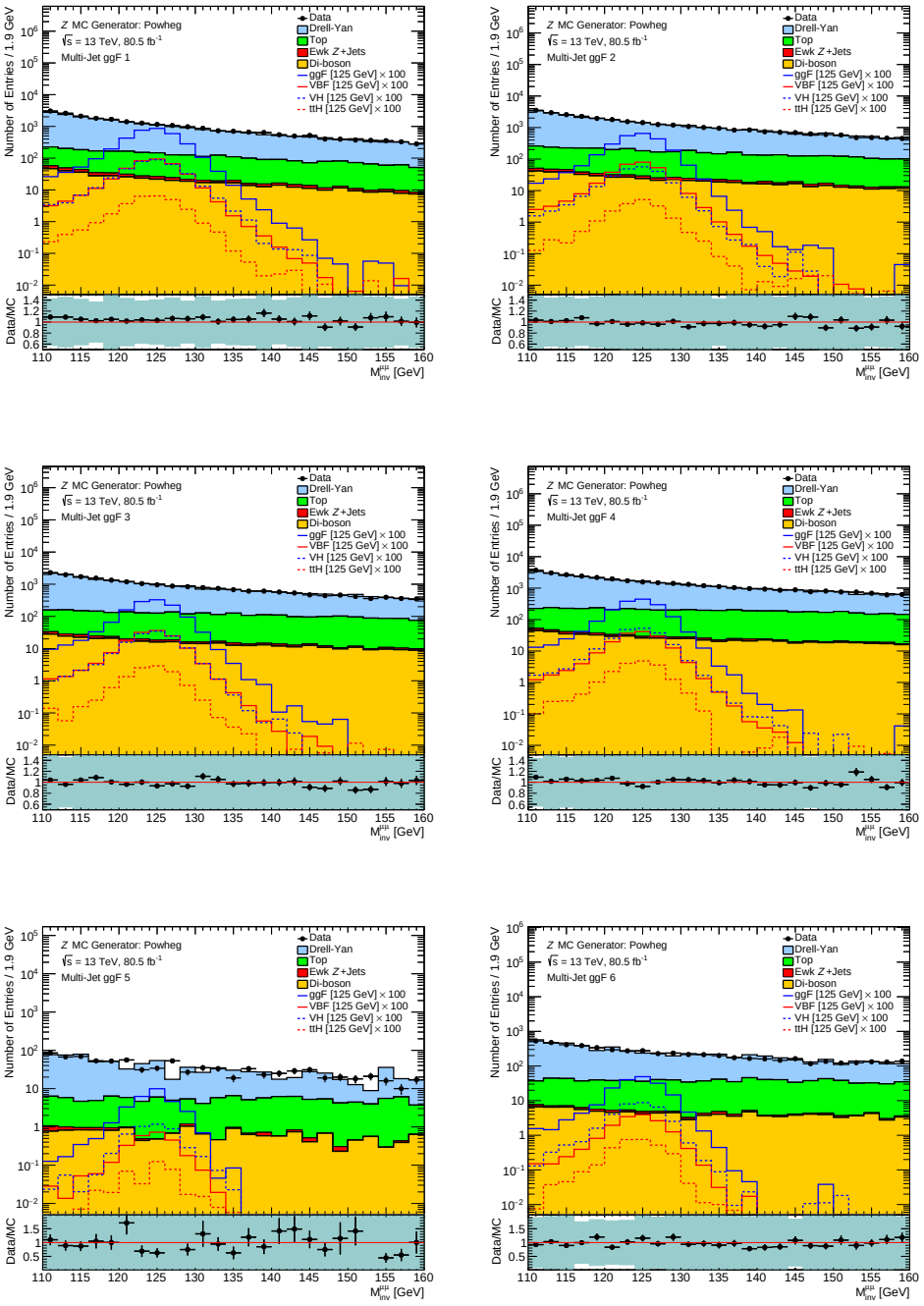

Figure 9.3.9: Comparison of the $M_{\text{inv}}^{\mu\mu}$ distributions of data and MC in the ggF Multi-Jet 1 (top left), ggF Multi-Jet 2 (top right), ggF Multi-Jet 3 (middle left), ggF Multi-Jet 4 (middle right), ggF Multi-Jet 5 (bottom left) and ggF Multi-Jet 6 (bottom right) categories. The MC samples have been normalised to 80.5 fb^{-1}. For a smooth background shape, Drell-Yan events produced with Powheg were utilised, normalised to the event yields of Madgraph Drell-Yan samples. The systematic bands include statistical, experimental systematic, $P_T^{\mu\mu}$ and M_{inv}^{jj} re-weighting uncertainties.

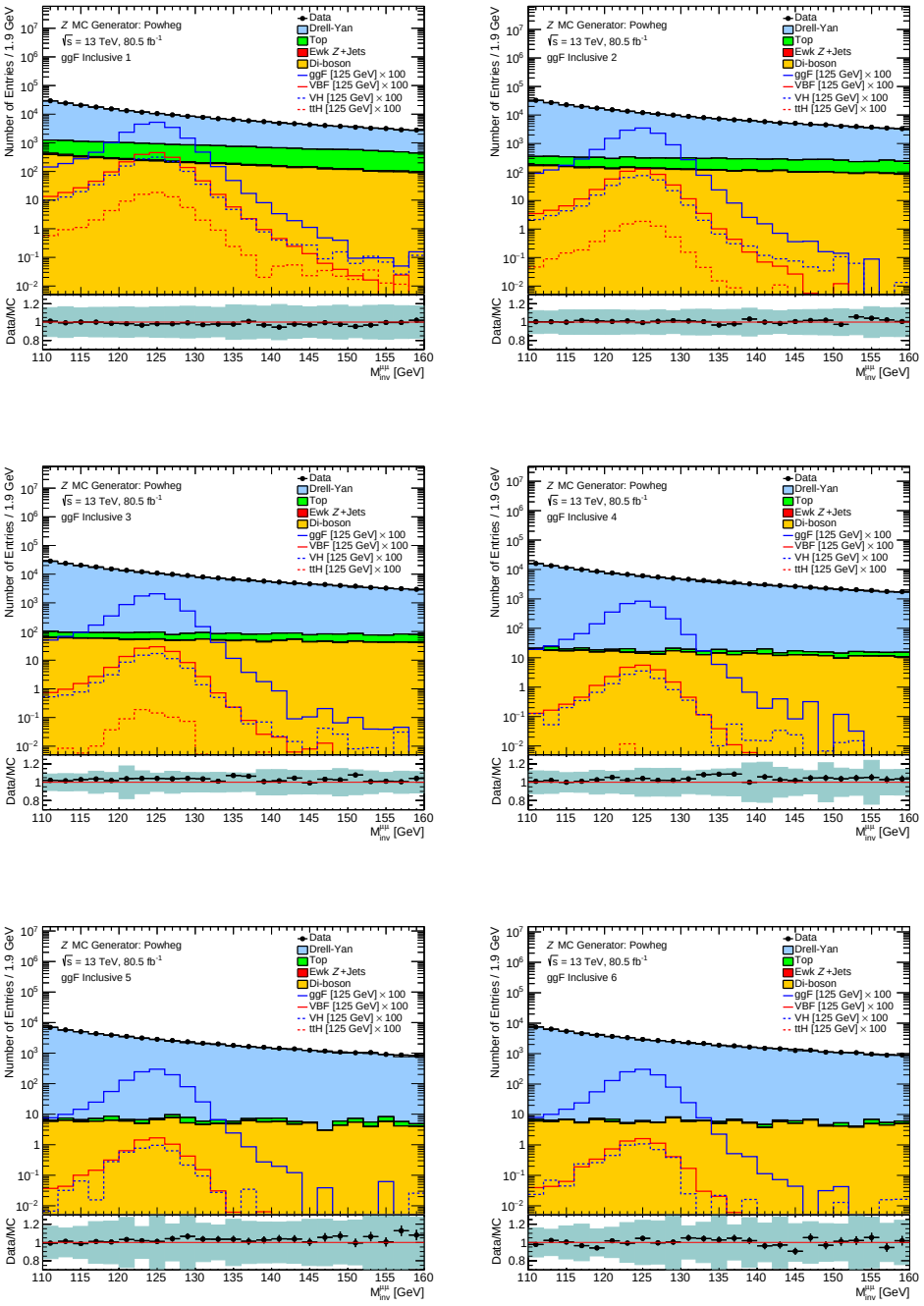

Figure 9.3.10: Comparison of the $M^{\mu\mu}_{\text{inv}}$ distributions of data and MC in the ggF Inclusive 1 (top left), ggF Inclusive 2 (top right), ggF Inclusive 3 (middle left), ggF Inclusive 4 (middle right), ggF Inclusive 5 (bottom left) and ggF Inclusive 6 (bottom right) categories. The MC samples have been normalised to 80.5 fb^{-1}. For a smooth background shape, Drell-Yan events produced with Powheg were utilised, normalised to the event yields of Madgraph Drell-Yan samples. The systematic bands include statistical, experimental systematic, $P_T^{\mu\mu}$ and M^{jj}_{inv} re-weighting uncertainties.

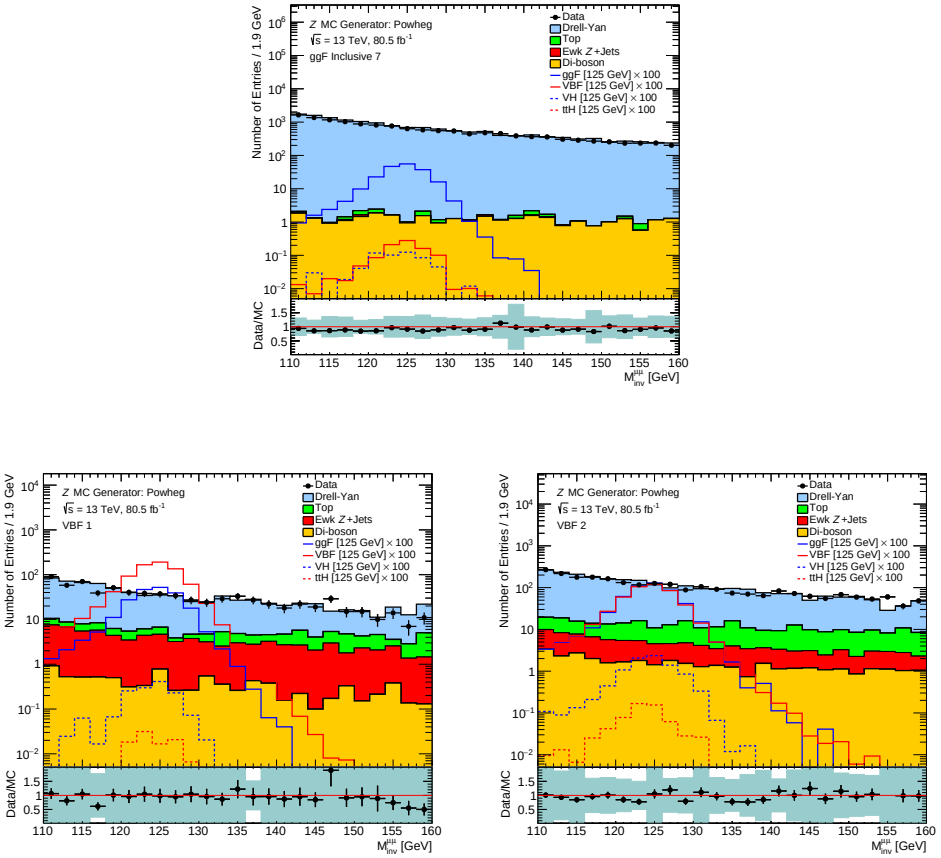

Figure 9.3.11: Comparison of the $M^{\mu\mu}_{\text{inv}}$ distributions of data and MC in the ggF Inclusive 7 (top), VBF 1 (bottom left) and VBF 2 (bottom right) categories. The MC samples have been normalised to 80.5 fb^{-1}. For a smooth background shape, Drell-Yan events produced with Powheg were utilised, normalised to the event yields of Madgraph Drell-Yan samples. The systematic bands include statistical, experimental systematic, $P_T^{\mu\mu}$ and M^{jj}_{inv} re-weighting uncertainties.

Chapter 10

Signal and Background Modelling

To extract the $H \to \mu\mu$ signal strength from the $M_{\text{inv}}^{\mu\mu}$ distributions presented in Chapter 9, functions capable of modelling both signal and background contributions within the data required development. This chapter presents the parametrisation of the signal and background models used in the analysis, along with their performance when applied to MC and data samples.

10.1 Signal Fits

The $H \to \mu\mu$ signal is theorised to exist as a resonance of 4.1 MeV width centred on the 125 GeV mass point. When studied experimentally, its shape is expected to be driven by the muon momentum resolution of the detector, commonly modelled with a Gaussian function, along with Final State Radiation (FSR) photon contributions in the lower mass regions, often modelled using exponentials.

During the early parts of Run-1, where evidence for the SM Higgs boson had yet to be observed, $H \to \mu\mu$ searches considered multiple Higgs mass points, ranging from 100 to 150 GeV [129]. The theorised signal widths associated with these mass points varied from 2.85 to 17.5 MeV. Candidate signal models were therefore required to be flexible enough to account for both variations in signal width, along with width and resolution differences between categories. The most effective model for $H \to \mu\mu$, a Gaussian combined with a Crystal Ball distribution, was used continually up to the most recent result [27]. With the SM Higgs resonance now firmly established at 125 GeV, such mass scans are no longer necessary for SM Higgs searches such as this. The structure of the signal model was thus revisited, with the aim of improving its modelling of 125 GeV Higgs events.

Various functional forms were considered, with the most effective found to be a triple

Gaussian of the form

$$
\begin{aligned}
&f_{\text{sig}}(M_{\text{inv}}^{\mu\mu}, f_1, f_2, \mu_{G_1}, \sigma_{G_1}, \mu_{G_2}, \sigma_{G_2}, \mu_{G_3}, \sigma_{G_3}) = \\
&f_1 \cdot G_1(M_{\text{inv}}^{\mu\mu}, \mu_{G_1}, \sigma_{G_1}) + \\
&(1 - f_1)\Big(f_2 \cdot G_2(M_{\text{inv}}^{\mu\mu}, \mu_{G_2}, \sigma_{G_2}) + (1 - f_2) \cdot G_3(M_{\text{inv}}^{\mu\mu}, \mu_{G_3}, \sigma_{G_3})\Big),
\end{aligned}
\tag{10.1.1}
$$

with f_{sig} the combined functional form, G_1, G_2 and G_3 the individual Gaussian components, f_1 and f_2 factors controlling the fractional contributions of each Gaussian to f_{sig}, and μ_i and σ_i the mean and width of Gaussian i.

The chosen functional form was motivated such that one Gaussian could model muon momentum resolution effects, one could account for FSR photon contributions in the tail[1], and one could provide additional resolution corrections due to finer effects. A similar functional form was utilised for the most recent CMS $H \to \mu\mu$ analysis [25].

Table 10.1.1 presents the initial values and allowed ranges for the parameters when performing fits to signal MC samples. μ_{G_1} and μ_{G_2} were initially set to the predicted Higgs mass, whilst μ_{G_3} was fixed to 120 GeV, where FSR photon contributions were more prominent. This was done to reduce the number of degrees of freedom, allowing more meaningful conclusions to be derived from the fit's performance. The allowed ranges and initial values for the other parameters were determined through trial and error, based on improving the average reduced-χ^2 of the fits across all categories and signal samples.

Parameter	Unit	Initial Value	Allowed Range
f_1	-	0.3	$0 \leq f_1 \leq 1$
f_2	-	0.6	$0 \leq f_2 \leq 1$
μ_{G_1}	GeV	125	$123 \leq \mu_{G_1} \leq 127$
σ_{G_1}	GeV	5	$0.01 \leq \sigma_{G_1} \leq 10$
μ_{G_2}	GeV	125	$120 \leq \mu_{G_2} \leq 130$
σ_{G_2}	GeV	5	$0.01 \leq \sigma_{G_2} \leq 10$
μ_{G_3}	GeV	120	-
σ_{G_3}	GeV	4	$0.01 \leq \sigma_{G_3} \leq 10$

Table 10.1.1: Summary of the initial values and allowed ranges of the parameters of the signal model used in the analysis. μ_{G_3} was fixed to reduce the number of fit constraints.
.

Figures 10.1.1 to 10.1.4 present the results of fitting the signal model to the $M_{\text{inv}}^{\mu\mu}$ distributions of ggF MC samples in the ggF Zero-Jet, ggF Single-Jet, ggF Multi-Jet and VBF categories, while Figures 10.1.5 to 10.1.8 present the same fits applied to VBF MC

[1]This choice is more phenomenological than physics based.

samples. Also presented are the associated pull distributions, defined as

$$\text{pull} = \frac{N^{\text{fit}} - N^{\text{data}}}{\sigma^{\text{fit}}}, \tag{10.1.2}$$

with N^{data} the number of data events in a given bin, N^{fit} the number of events of said bin used in the fitting, and σ^{fit} the bin's fitting error. Given enough events, pulls are expected to be Gaussian distributed about zero for an unbiased fit. Pull distributions were therefore presented to highlight issues with the fitting model.

No significant fitting biases were present within any of the categories considered for both the ggF and VBF MC samples, with pulls typically no larger than ± 2 . The reduced-χ^2 values lie on average between 0.7 and 1.5, providing further confidence in the signal model. The ggF Zero-Jet 2 category fit to ggF presents a reduced-χ^2 of 2.06, but shows no significant bias in its pull distribution. The ggF Zero-Jet 6 fit to VBF performs reasonably well, despite the large statistical uncertainties.

The signal model was also fit to WH, ZH and $t\bar{t}H$ samples, where MC statistical uncertainties were considerably larger. Since these processes contribute little to the analysis, their fits are presented in Appendix F. The signal model performed reasonably well in the majority of cases, with no obvious consistent biases present.

For the final signal plus background fits to data, the signal components were fixed to the values obtained from the above MC fits. This was done to ensure the final fits minimised with respect to genuine $H \to \mu\mu$ signal, rather than other effects (such as statistical fluctuations).

Table 10.1.2 presents the Full Width at Half Maximum (FWHM) values of the ggF and VBF MC samples used to test the signal model. The values were calculated from binned MC histograms, rather than the signal model fits. To improve the precision of the calculation, variants of the MC histograms with quadruple the standard binning (0.125 GeV rather than 0.5 GeV precision) were utilised. The signal widths are seen to vary by 1-2 GeV between categories, likely due to a number of reasons. Events within the forward regions of the detector will typically have larger resolutions, due to the muons possessing higher P_T values on average, and thus reduced track curvatures. Due to the complicated nature of the BDT output distributions from which the categories were defined, it is difficult to identify which categories for a given BDT correspond to such events. Poorer resolutions also occur in events with large amounts of initial and final state radiation. This is demonstrated by the larger signal widths seen in the VBF and ggF Multi-Jet categories. The finest resolutions were seen in the ggF Multi-Jet 5 category, although as demonstrated in the previous chapter, the MC modelling of such events was poor, and the category was thus ignored for the final μ_s calculation. A 10 GeV width was seen in the ggF Zero-Jet 6 category for VBF, due to the large MC statistical uncertainties of the sample.

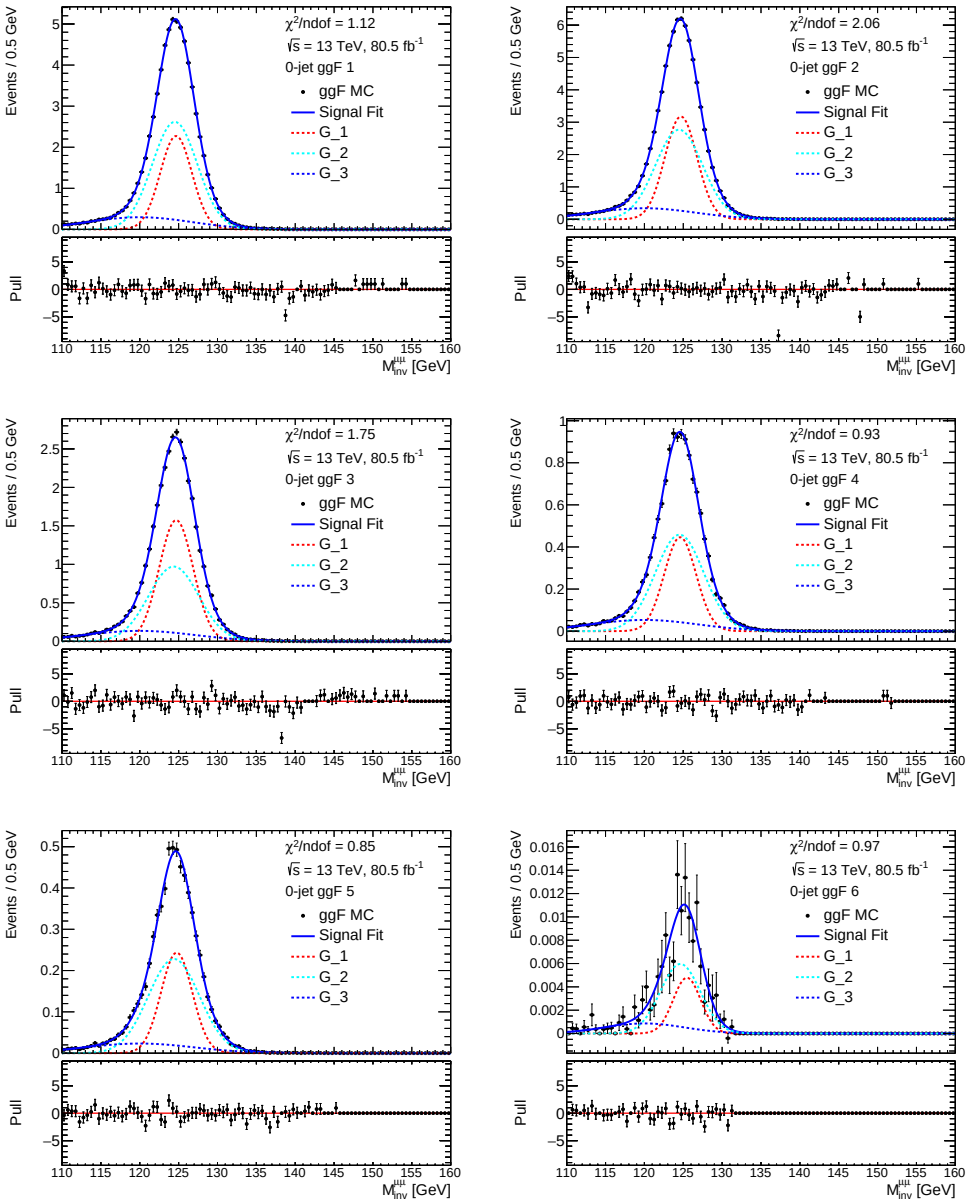

Figure 10.1.1: The $M_{\text{inv}}^{\mu\mu}$ distributions of ggF MC events in the ggF Zero-Jet 1 (top left), ggF Zero-Jet 2 (top right), ggF Zero-Jet 3 (middle left), ggF Zero-Jet 4 (middle right), ggF Zero-Jet 5 (bottom left) and ggF Zero-Jet 6 (bottom right) categories, fitted using the triple Gaussian signal model described in Chapter 10. The combined signal model is represented by the solid blue line, with the individual Gaussian components represented by the dashed red, cyan and blue lines. The distributions are normalised to 80.5 fb^{-1}, corresponding to the luminosity of the data.

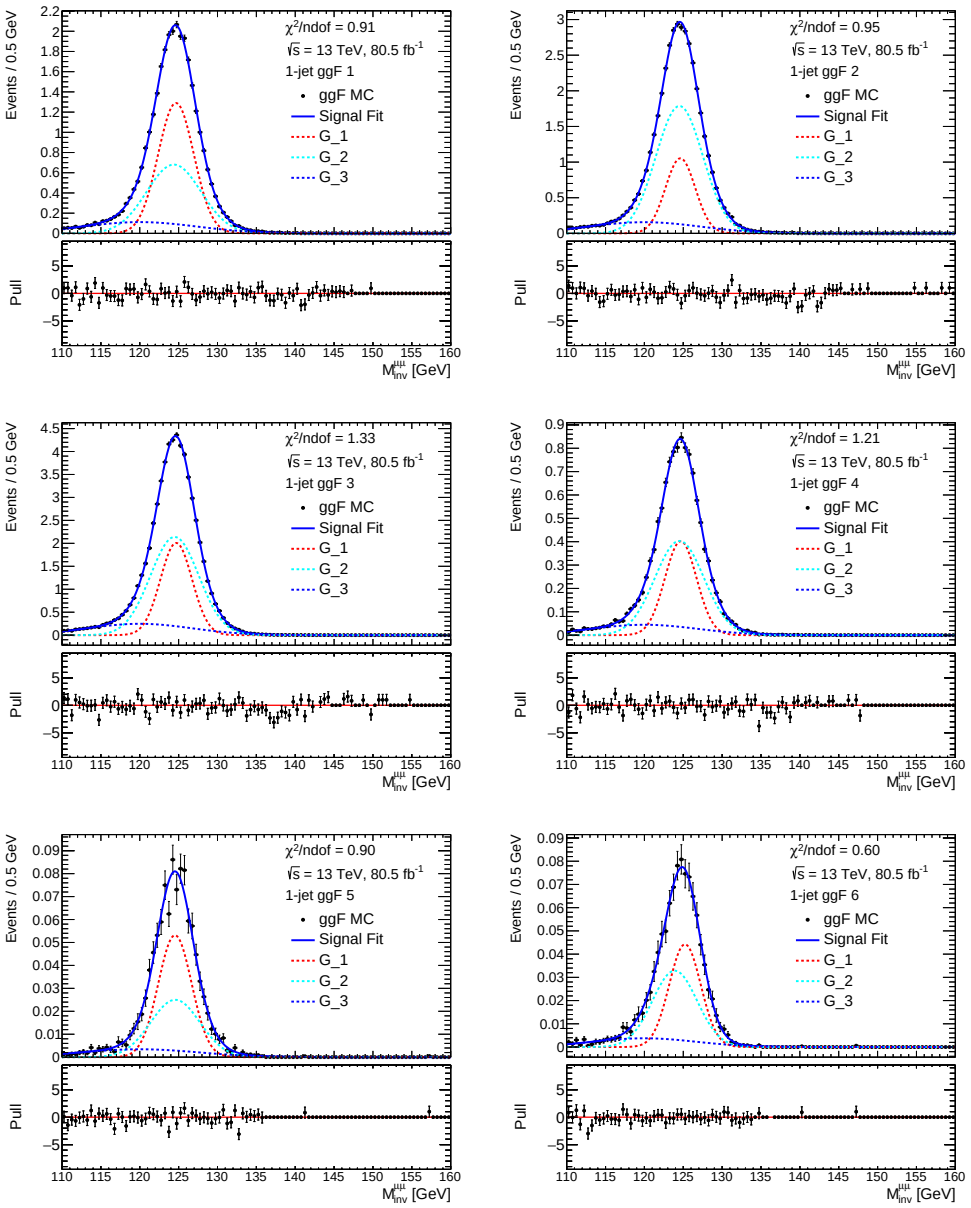

Figure 10.1.2: The $M_{\text{inv}}^{\mu\mu}$ distributions of ggF MC events in the ggF Single-Jet 1 (top left), ggF Single-Jet 2 (top right), ggF Single-Jet 3 (middle left), ggF Single-Jet 4 (middle right), ggF Single-Jet 5 (bottom left) and ggF Single-Jet 6 (bottom right) categories, fitted using the triple Gaussian signal model described in Chapter 10. The combined signal model is represented by the solid blue line, with the individual Gaussian components represented by the dashed red, cyan and blue lines. The distributions are normalised to 80.5 fb^{-1}, corresponding to the luminosity of the data.

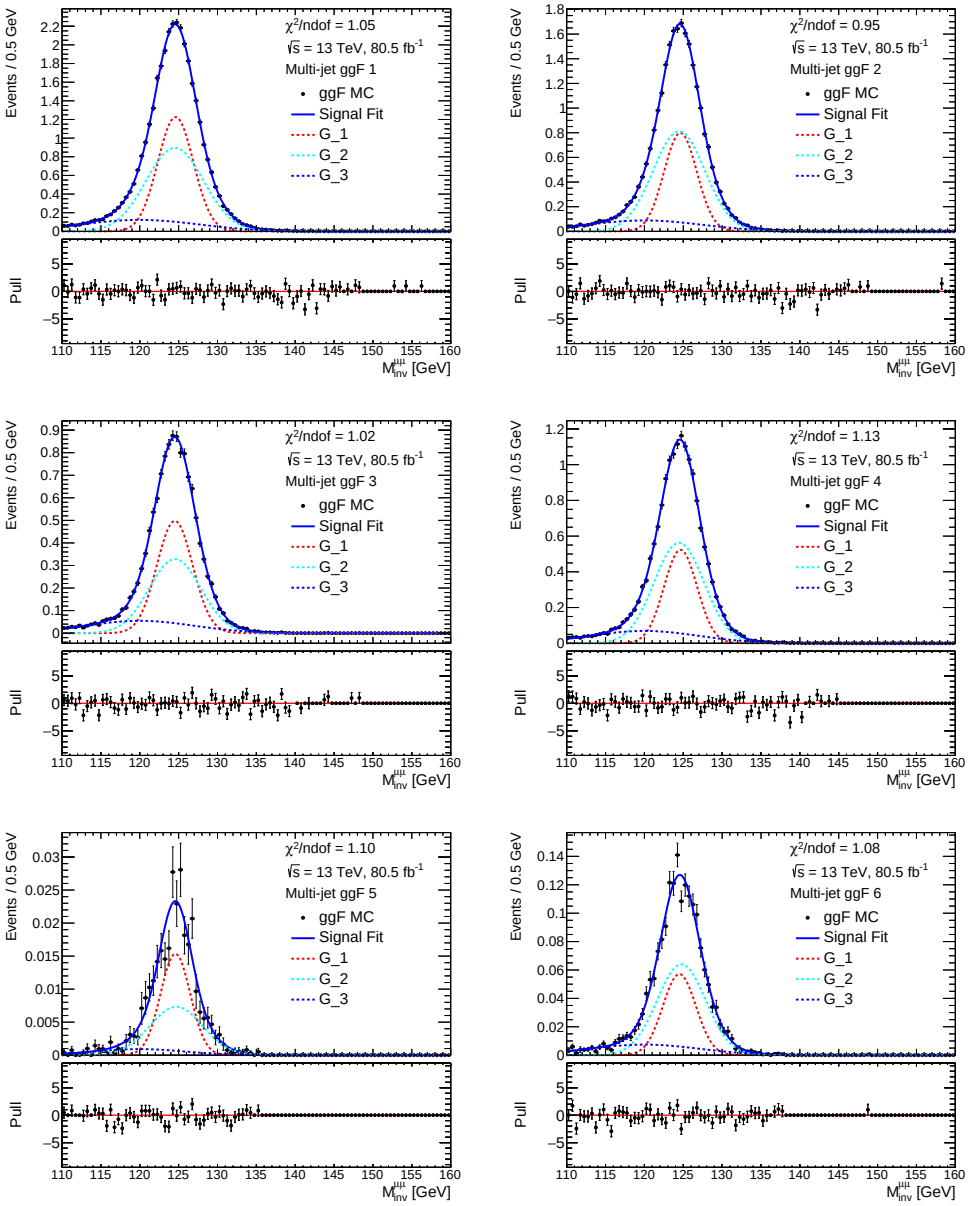

Figure 10.1.3: The $M_{\text{inv}}^{\mu\mu}$ distributions of ggF MC events in the ggF Multi-Jet 1 (top left), ggF Multi-Jet 2 (top right), ggF Multi-Jet 3 (middle left), ggF Multi-Jet 4 (middle right), ggF Multi-Jet 5 (bottom left) and ggF Multi-Jet 6 (bottom right) categories, fitted using the triple Gaussian signal model described in Chapter 10. The combined signal model is represented by the solid blue line, with the individual Gaussian components represented by the dashed red, cyan and blue lines. The distributions are normalised to 80.5 fb^{-1}, corresponding to the luminosity of the data.

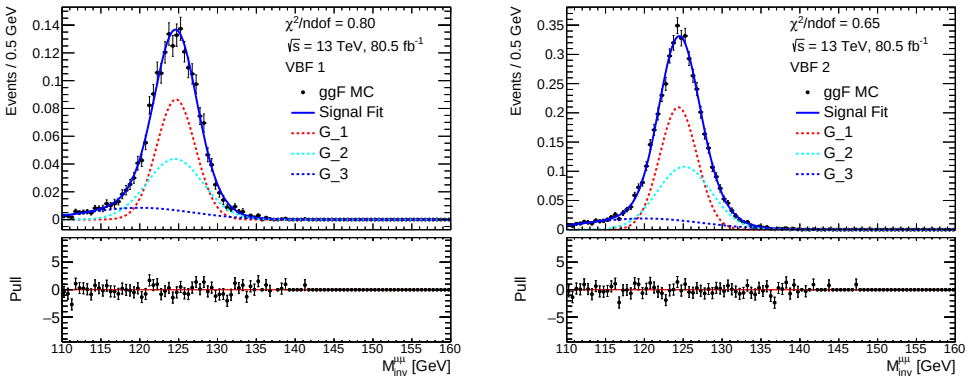

Figure 10.1.4: The $M_{\text{inv}}^{\mu\mu}$ distributions of ggF MC events in the VBF 1 (left) and VBF 2 (right) categories, fitted using the triple Gaussian signal model described in Chapter 10. The combined signal model is represented by the solid blue line, with the individual Gaussian components represented by the dashed red, cyan and blue lines. The distributions are normalised to 80.5 fb^{-1}, corresponding to the luminosity of the data.

Category	Width [GeV]	
	ggF	VBF
ggF Zero-Jet 1	5.5	5.3
ggF Zero-Jet 2	5.9	5.5
ggF Zero-Jet 3	5.4	6.0
ggF Zero-Jet 4	6.0	6.3
ggF Zero-Jet 5	5.4	5.5
ggF Zero-Jet 6	5.3	10.0
ggF Single-Jet 1	5.6	5.3
ggF Single-Jet 2	5.9	5.8
ggF Single-Jet 3	5.8	5.9
ggF Single-Jet 4	5.4	5.0
ggF Single-Jet 5	5.3	4.4
ggF Single-Jet 6	5.3	4.4
ggF Multi-Jet 1	6.5	6.5
ggF Multi-Jet 2	6.1	6.3
ggF Multi-Jet 3	6.3	6.3
ggF Multi-Jet 4	6.0	6.4
ggF Multi-Jet 5	4.4	4.6
ggF Multi-Jet 6	5.4	6.4
VBF 1	7.0	6.5
VBF 2	6.3	6.6

Table 10.1.2: The Full With at Half Maximum (FWHM) values of the ggF and VBF MC samples used to test the signal fitting model, for each of the analysis categories. The values were derived from 0.125 GeV binned histograms, rather than the signal model fits.

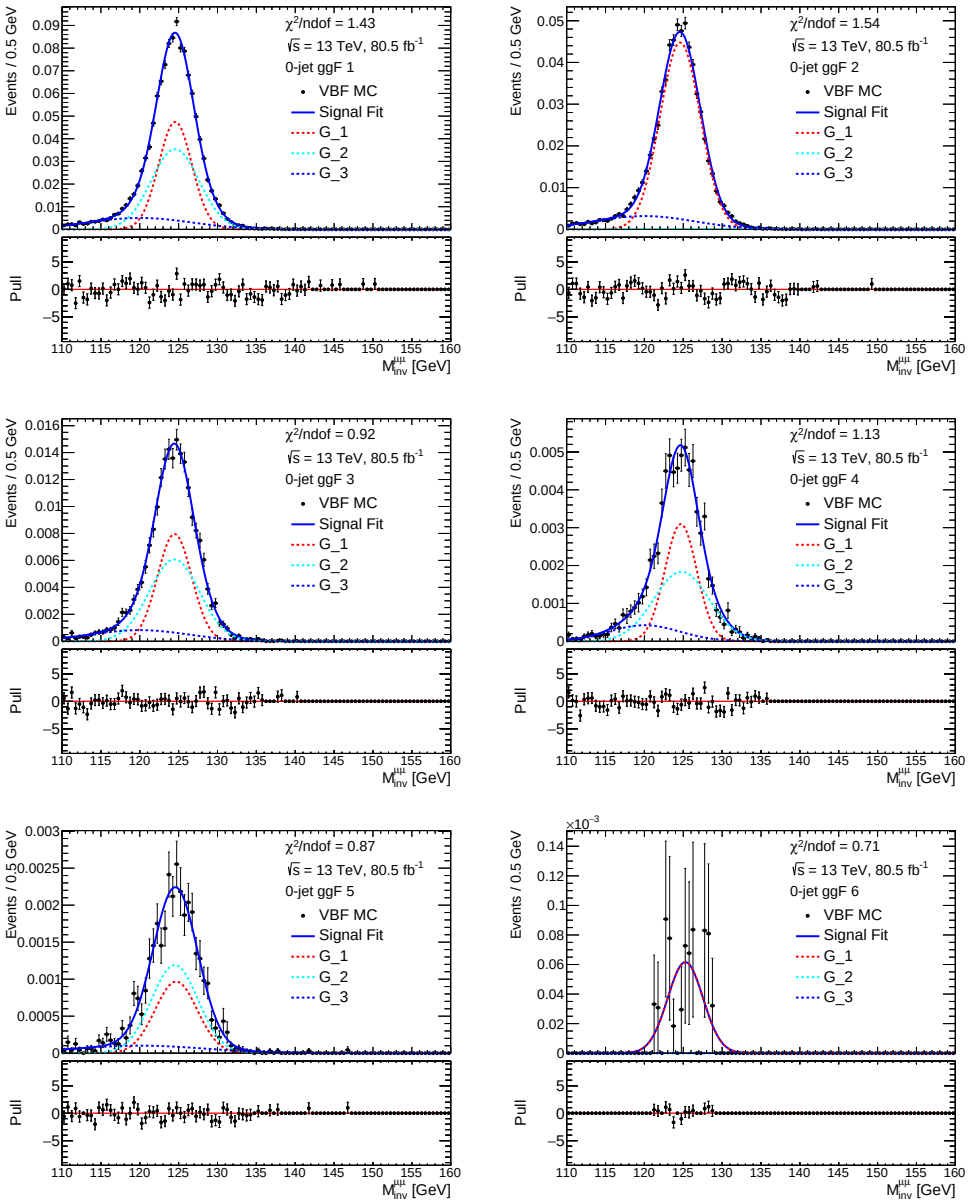

Figure 10.1.5: The $M_{\text{inv}}^{\mu\mu}$ distributions of VBF MC events in the ggF Zero-Jet 1 (top left), ggF Zero-Jet 2 (top right), ggF Zero-Jet 3 (middle left), ggF Zero-Jet 4 (middle right), ggF Zero-Jet 5 (bottom left) and ggF Zero-Jet 6 (bottom right) categories, fitted using the triple Gaussian signal model described in Chapter 10. The combined signal model is represented by the solid blue line, with the individual Gaussian components represented by the dashed red, cyan and blue lines. The distributions are normalised to 80.5 fb^{-1}, corresponding to the luminosity of the data.

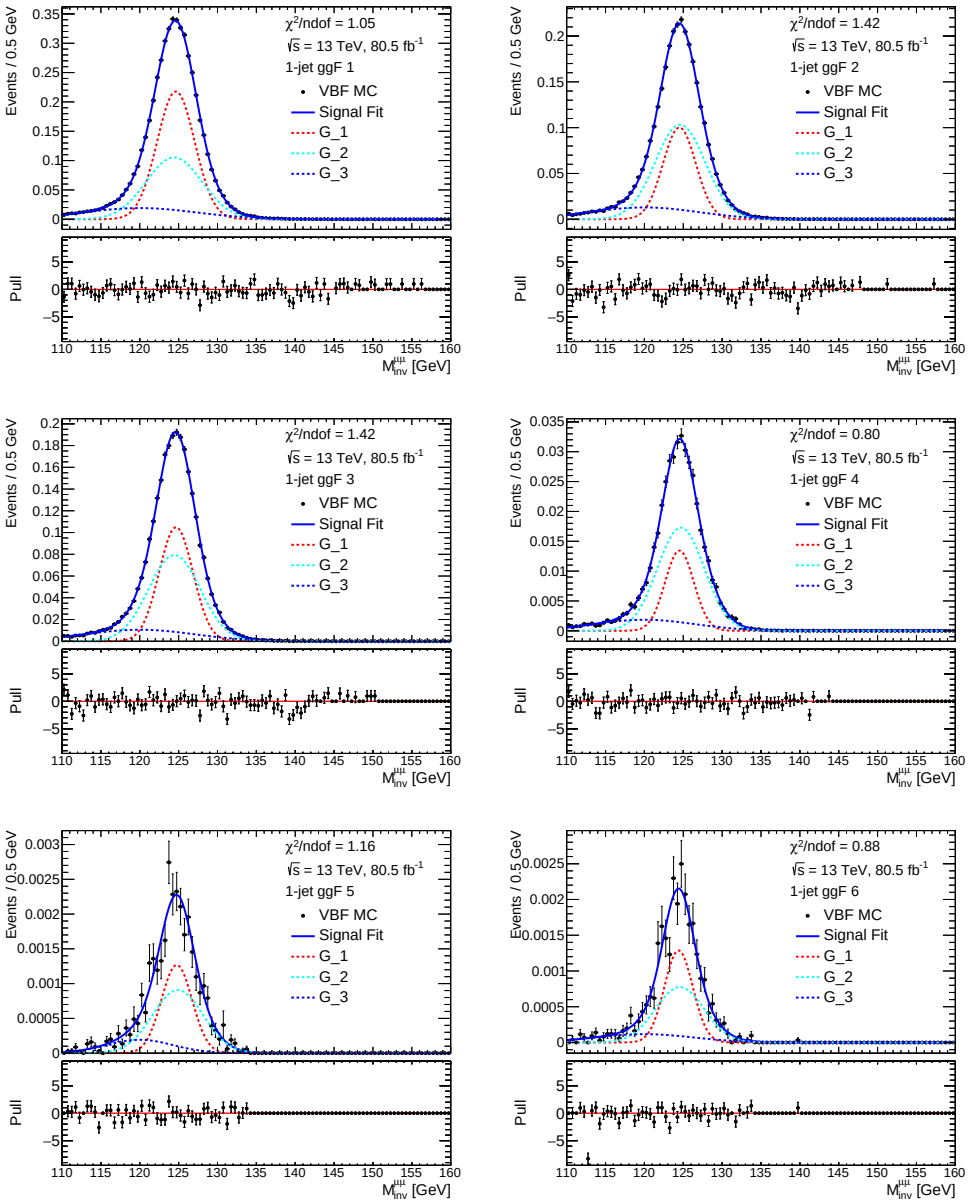

Figure 10.1.6: The $M_{\text{inv}}^{\mu\mu}$ distributions of VBF MC events in the ggF Single-Jet 1 (top left), ggF Single-Jet 2 (top right), ggF Single-Jet 3 (middle left), ggF Single-Jet 4 (middle right), ggF Single-Jet 5 (bottom left) and ggF Single-Jet 6 (bottom right) categories, fitted using the triple Gaussian signal model described in Chapter 10. The combined signal model is represented by the solid blue line, with the individual Gaussian components represented by the dashed red, cyan and blue lines. The distributions are normalised to 80.5 fb^{-1}, corresponding to the luminosity of the data.

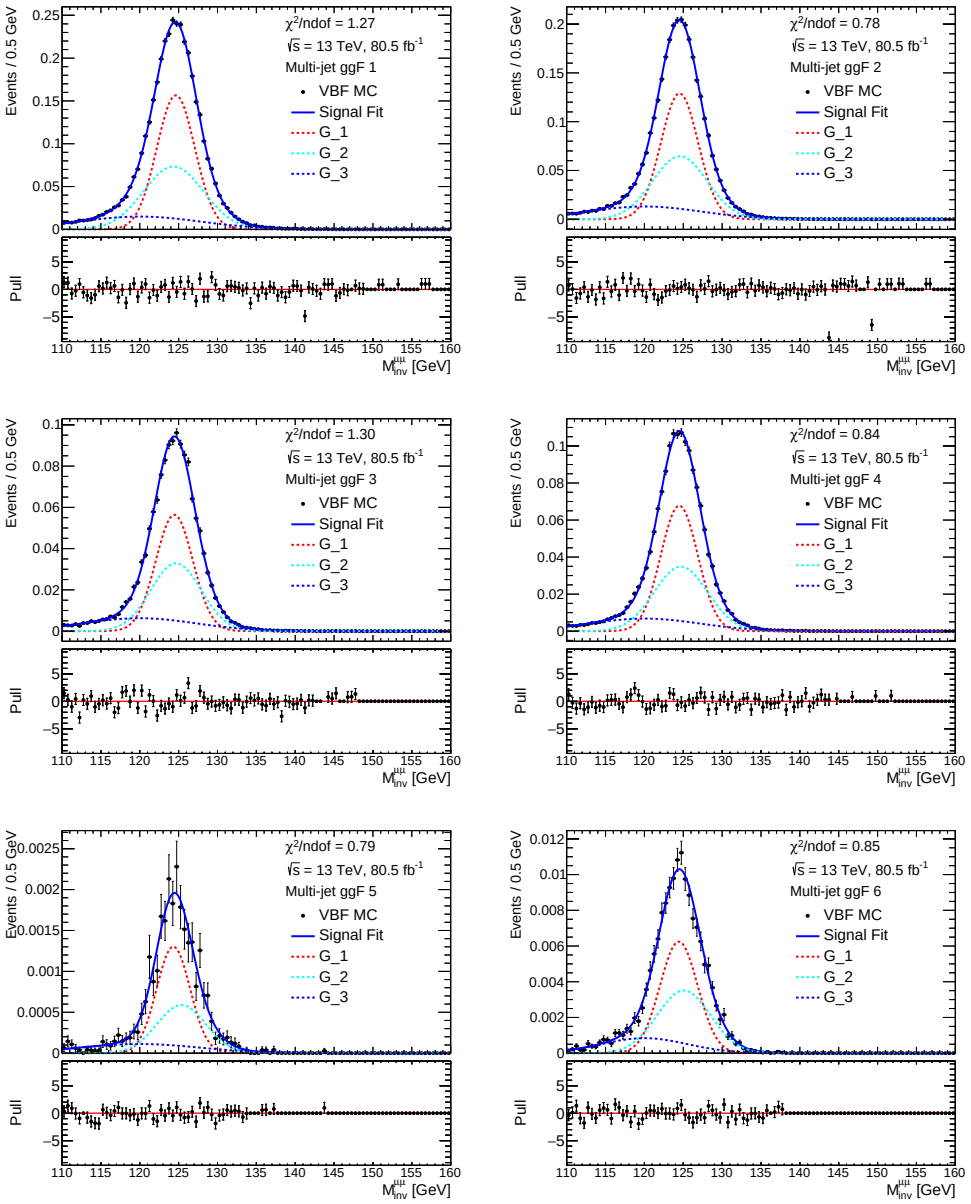

Figure 10.1.7: The $M_{\text{inv}}^{\mu\mu}$ distributions of VBF MC events in the ggF Multi-Jet 1 (top left), ggF Multi-Jet 2 (top right), ggF Multi-Jet 3 (middle left), ggF Multi-Jet 4 (middle right), ggF Multi-Jet 5 (bottom left) and ggF Multi-Jet 6 (bottom right) categories, fitted using the triple Gaussian signal model described in Chapter 10. The combined signal model is represented by the solid blue line, with the individual Gaussian components represented by the dashed red, cyan and blue lines. The distributions are normalised to 80.5 fb^{-1}, corresponding to the luminosity of the data.

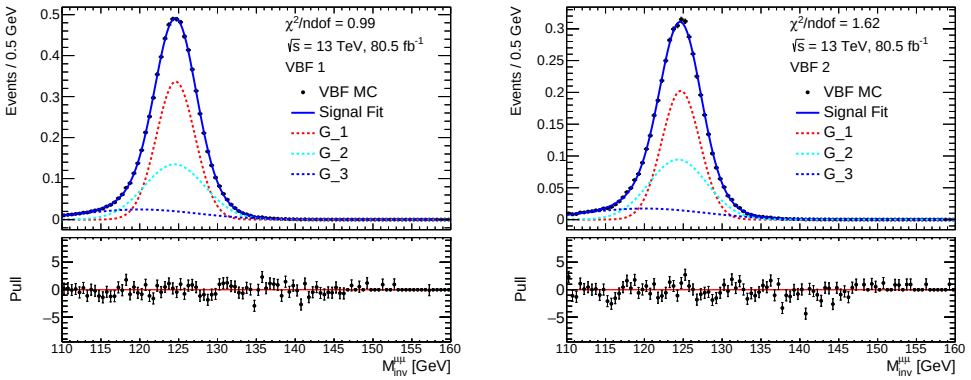

Figure 10.1.8: The $M_{\text{inv}}^{\mu\mu}$ distributions of VBF MC events in the VBF 1 (left) and VBF 2 (right) categories, fitted using the triple Gaussian signal model described in Chapter 10. The combined signal model is represented by the solid blue line, with the individual Gaussian components represented by the dashed red, cyan and blue lines. The distributions are normalised to 80.5 fb^{-1}, corresponding to the luminosity of the data.

10.2 Background Fits

A background model was devised capable of modelling the smoothly falling Z mass peak, which dominates the data distributions in the Signal region. The model is more complicated than that used for the signal processes, and was taken from the Run-1 and Run-2 ATLAS $H \to \mu\mu$ analyses, during which it underwent rigorous testing [129].

A Breit-Wigner (BW) distribution was initially taken to model the falling Z mass resonance. The distribution was convolved with a Gaussian to account for detector resolution effects. A further $\frac{e^x}{x^3}$ term was added to account for di-boson and top quark contributions.

The total function is represented as

$$\begin{aligned} &f_{\text{bkg}}(M_{\text{inv}}^{\mu\mu}, f, \mu_{BW}, \Gamma_{BW}, \sigma_G, B) = \\ &f \cdot \Big(BW(M_{\text{inv}}^{\mu\mu}, \mu_{BW}, \Gamma_{BW}) \circledast G(M_{\text{inv}}^{\mu\mu}, \sigma_G)\Big) + (1-f) \cdot \Big(\frac{\exp^{Bx}}{x^3}\Big), \end{aligned} \tag{10.2.1}$$

where

$$BW(M_{\text{inv}}^{\mu\mu}, \mu_{BW}, \Gamma_{BW}) = \frac{1}{(x-\mu_{BW})^2 + (\frac{\Gamma_{BW}}{2})^2} \tag{10.2.2}$$

The BW and Gaussian terms were implemented using the RooVoigtian class of RooFit [130], consisting of Voigt profiles (pre-convolved BW and Gaussian objects). The profiles take the BW mean (μ_{BW}), BW decay width (Γ_{BW}) and Gaussian width (σ_G) as arguments. The fractional contributions of the Drell-Yan and top/di-boson terms were represented by f, with B an additional factor used to vary the exponent of the final

term.

Table 10.2.1 summarises the initial values and allowed ranges given to the background model parameters during the fitting procedure. Both μ_{BW} and Γ_{BW} were fixed to values given by the Particle Data Group [32]. f and B were allowed to vary, with their ranges and initial values determined through trial and error. σ_G was initially allowed to float, but when applying the background fit to the spurious signal samples of Chapter 11, it was found to largely influence the fit bias in certain categories. Such parameter sensitivity was absent when applying the fit to the official Drell-Yan MC samples (shown in Appendix F), or to data (shown in this chapter). The effect was likely due to the spurious signal samples poorly modelling certain variables, leading to inaccurate classification with the analysis BDTs, and potential shaping of the associated $M_{\text{inv}}^{\mu\mu}$ distributions. A more detailed discussion is given in the next chapter.

To combat this effect, iterative background fits were applied to the spurious signal samples, with σ_G increased in 0.1 GeV steps from 1 to 10 GeV. All other parameters were treated as described in Table 10.2.1. The σ_G value producing the lowest reduced-χ^2 value for a given category was taken forward as the fixed value for that category for the final signal plus background fits. The results are summarised in Table 10.2.2. The ggF Zero-Jet 1 category was separately iterated in steps of 0.01 GeV, due to more prominent biases in this region.

Parameter	Unit	Initial Value	Allowed Range
f	-	0.2	$0 \leq f \leq 1$
μ_{BW}	GeV	91.2	-
Γ_{BW}	GeV	2.49	-
σ_G	GeV	See Table 10.2.2	-
B	-	-0.1	$-1 \leq B \leq 1$

Table 10.2.1: Summary of the initial values and allowed ranges of the parameters of the background model used in the analysis. μ_{BW} and Γ_{BW} were fixed to values given by the Particle Data Group [32]. σ_G was fixed to category-dependent values, described in Table 10.2.2.

For consistency, the presented σ_G values were also used when fitting the official Drell-Yan MC and data $M_{\text{inv}}^{\mu\mu}$ distributions. The former fits are described in Appendix F, and were used to validate the analysis. Once a satisfactory level of performance was achieved, the analysis was unblinded and background fits were applied to the data. These fits are presented in Figures 10.2.1 to 10.2.4 for all categories. Also presented are the associated pull distributions. No fitting biases of note appeared in any of the categories, with the majority of reduced-χ^2 values between 0.8 and 1.5. The exception to this was ggF Multi-Jet 5, which presented a reduced-χ^2 of 1.79. The category was however ignored in the final μ_s extraction, so the effect is unimportant.

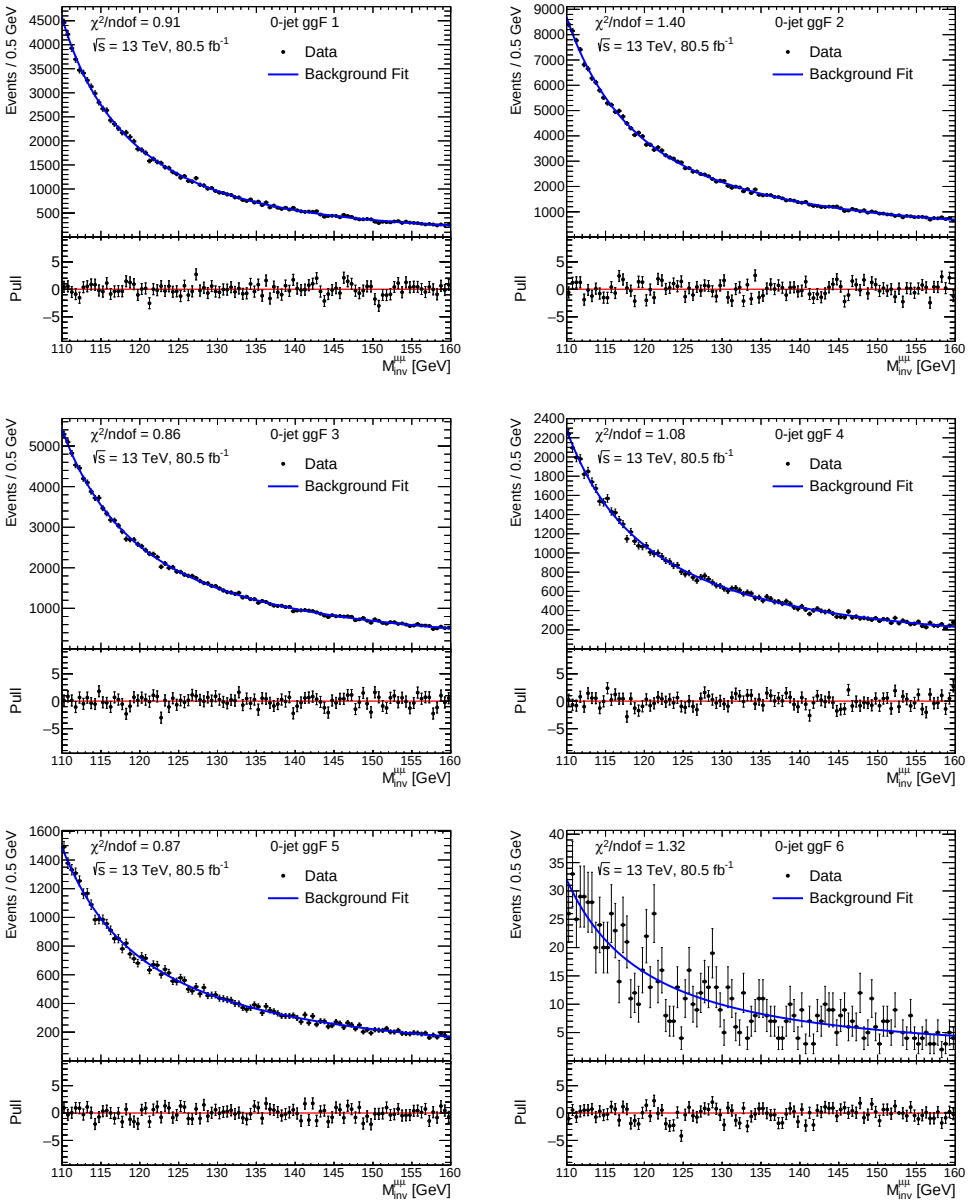

Figure 10.2.1: The $M_{\text{inv}}^{\mu\mu}$ distributions of data events in the ggF Zero-Jet 1 (top left), ggF Zero-Jet 2 (top right), ggF Zero-Jet 3 (middle left), ggF Zero-Jet 4 (middle right), ggF Zero-Jet 5 (bottom left) and ggF Zero-Jet 6 (bottom right) categories, fitted using the background model described in Chapter 10.

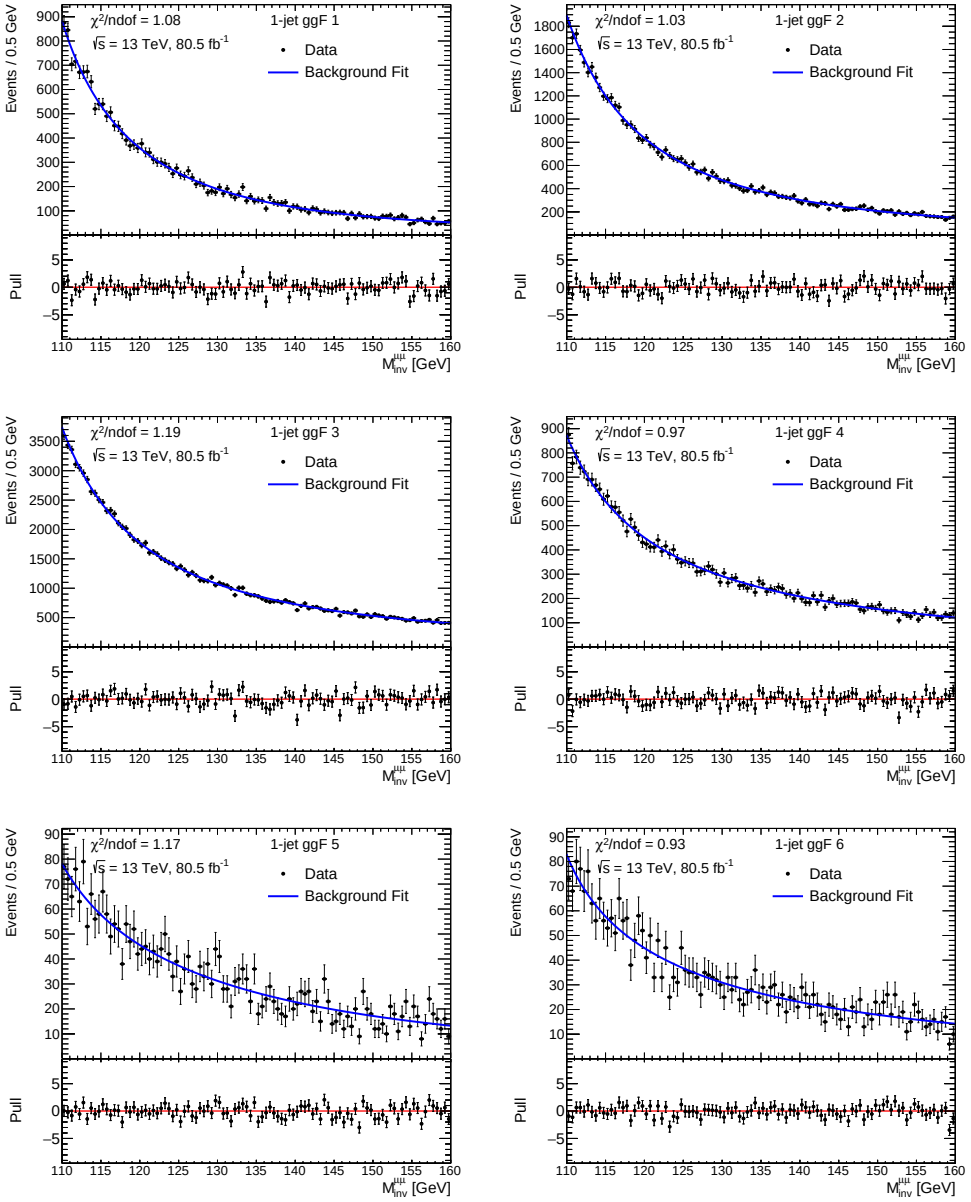

Figure 10.2.2: The $M_{\text{inv}}^{\mu\mu}$ distributions of data events in the ggF Single-Jet 1 (top left), ggF Single-Jet 2 (top right), ggF Single-Jet 3 (middle left), ggF Single-Jet 4 (middle right), ggF Single-Jet 5 (bottom left) and ggF Single-Jet 6 (bottom right) categories, fitted using the background model described in Chapter 10.

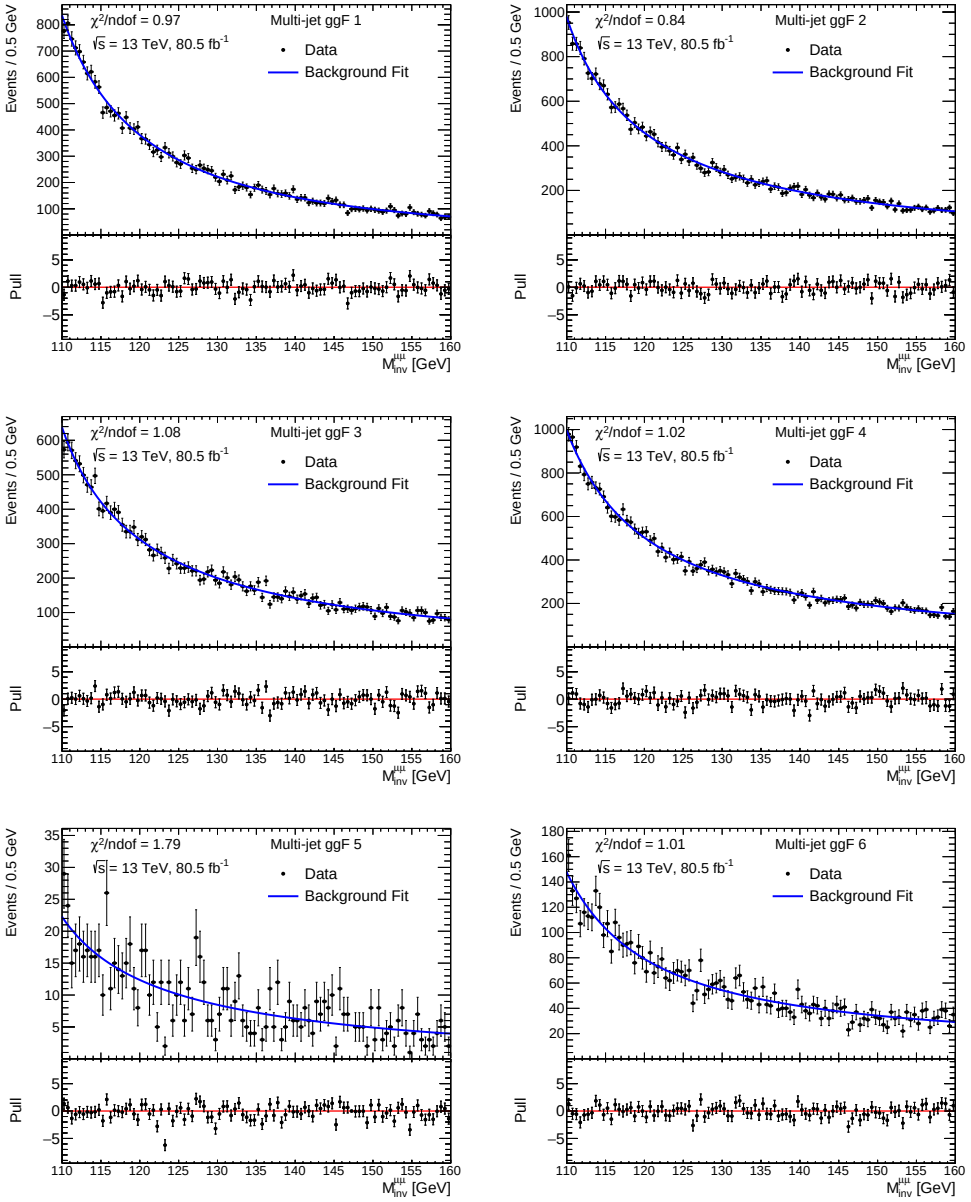

Figure 10.2.3: The $M_{\text{inv}}^{\mu\mu}$ distributions of data events in the ggF Multi-Jet 1 (top left), ggF Multi-Jet 2 (top right), ggF Multi-Jet 3 (middle left), ggF Multi-Jet 4 (middle right), ggF Multi-Jet 5 (bottom left) and ggF Multi-Jet 6 (bottom right) categories, fitted using the background model described in Chapter 10.

Category	σ_G [GeV]
ggF Zero-Jet 1	4.39
ggF Zero-Jet 2	2.60
ggF Zero-Jet 3	2.20
ggF Zero-Jet 4	2.20
ggF Zero-Jet 5	2.00
ggF Zero-Jet 6	2.30
ggF Single-Jet 1	3.90
ggF Single-Jet 2	2.60
ggF Single-Jet 3	1.30
ggF Single-Jet 4	3.00
ggF Single-Jet 5	3.50
ggF Single-Jet 6	4.60
ggF Multi-Jet 1	3.60
ggF Multi-Jet 2	4.30
ggF Multi-Jet 3	4.20
ggF Multi-Jet 4	3.40
ggF Multi-Jet 5	3.40
ggF Multi-Jet 6	2.20
VBF 1	1.10
VBF 2	4.60

Table 10.2.2: Values of σ_G which gave the lowest reduced-χ^2 values when applying the background model to the $M^{\mu\mu}_{\text{inv}}$ distributions of the spurious signal sample of Chapter 11 in each category. For the final signal plus background fits, the σ_G values of the background model were fixed to the above values.

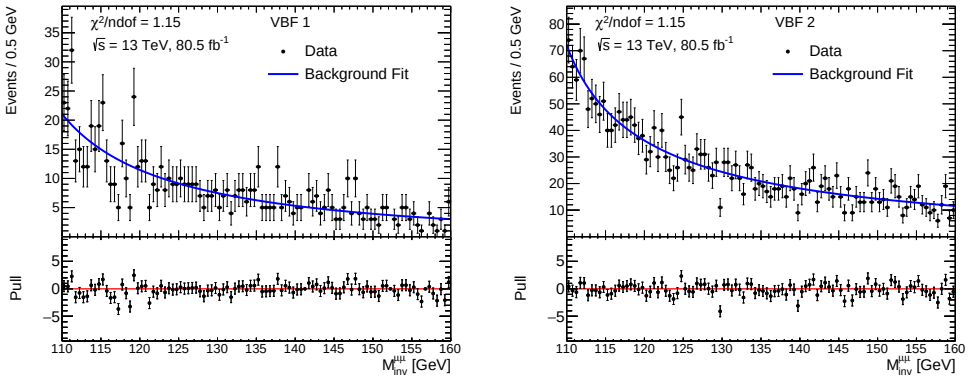

Figure 10.2.4: The $M^{\mu\mu}_{\text{inv}}$ distributions of data events in the VBF 1 (left) and VBF 2 (right) categories, fitted using the background model described in Chapter 10.

Chapter 11

Systematics

The measurement of μ_s is sensitive to a large number of systematic effects, such as the shape and normalisation of the fitted $M_{\text{inv}}^{\mu\mu}$ distributions and biases in the fitting models themselves. This chapter outlines the origin and effects of various systematics affecting the analysis. Section 11.1 details experimental systematic uncertainty contributions arising from inefficiencies in detector performance and MC simulation. Section 11.2 describes the systematic uncertainties associated with the theoretical modelling of the $H \to \mu\mu$ process. Section 11.3 presents the impact of biases in the background fitting function, known as spurious signal systematics. All systematics are included as Nuisance Parameter (NP) terms in the likelihood fitting functions outlined in Chapter 12.

11.1 Experimental Systematic Uncertainties

All experimental systematic variations described in this section were provided by the ATLAS Combined Performance Working Groups. With the exception of the luminosity error, their impact on the analysis was computed through comparing the event yields of the $M_{\text{inv}}^{\mu\mu}$ distributions of ggF and VBF MC samples between 110 and 160 GeV with and without application of each systematic variation. The impact of every variation was determined for each category individually, with the results used as signal normalisation uncertainties in the calculation of μ_s. Background normalisation uncertainties were not treated, since the final μ_s extraction was performed using fits to data, rather than background MC.

The combined luminosity error for the 2015, 2016 and 2017 datasets was determined through scale calibrations using x-y beam-separation scans [131], and was found to be 2.0%.

Systematic contributions from pile-up were also assessed. When comparing the NVertex vs μ distributions of data and MC, the latter were found to consistently over-

predict the number of reconstructed vertices in the data. Before the pile-up re-weighting corrections of Chapter 4 could be derived, this discrepancy was first accounted for through application of a fixed scale factor (provided internally within ATLAS), known as the pile-up data scale factor. Due to the MC μ distributions being integer based, this correction was uniquely applied as an inverse scale factor to the data, rather than a standard MC scale factor. Systematic variations were then defined based on applying either no correction, or double the standard correction [132]. These variations were found to impact the signal event yields in each category by 1-3% on average.

Statistical and systematic uncertainties were assigned to the muon scale factors described in Chapter 4. The scale factors were determined using $Z \to \mu\mu$ and $J/\psi \to \mu\mu$ events selected from the 2015 ATLAS dataset [119]. By assuming the scale factors to be normally distributed, statistical uncertainties were derived by varying the scale factors by $\pm 1\sigma$ of their distributions, while systematic uncertainties were determined through varying the event selections. The uncertainties impacted the signal event yields by around 1% in the most sensitive categories, rising to 30% in lower sensitivity categories such as Zero-Jet Category 6. Uncertainties were also associated with the muon scale, track and sagitta corrections outlined in Chapter 4. They were determined through varying the parametrisation of the formulae from which the corrections were derived. In the most sensitive categories, the uncertainties were found to have an impact on the Signal region event yields of 1-2%.

Uncertainties related to the resolution and calibration of jets were also considered. Jet Energy Resolution (JER) corrections were originally derived using Run-1 ATLAS data [133], with the methodology later applied to the 2015 dataset [134]. Jet resolutions were determined through Gaussian fits to the P_T asymmetry of di-jet events, with systematics derived through varying the event selection. Jet calibration corrections were by comparison derived over a number of steps [71]. Pile-up based corrections were obtained using jet density variables, with supporting residual corrections determined using fits to jet P_T as functions of η, μ and $N_{\mathrm{PrimaryVertices}}$. Jet Energy Scale (JES) corrections derived from Gaussian fits to $E^{\mathrm{reco}}/E^{\mathrm{truth}}$ were then applied to correct the jet four-momenta. Global sequential calibration was performed to further improve JES resolution, after which in-situ methods corrected for imperfect detector responses. At each stage of the calibration, the MC response was corrected to that of the data, with systematic variations obtained through varying the fit parameters at each step. The initial 80 JES systematic uncertainties were then reduced to a set of five through various reduction schemes. When propagated to the categories of this analysis, the largest variations in event yield came from JET_SR1_JET_GroupedNP_1, where variations ranged from 5% to 19%.

Also treated were the systematic uncertainties associated with the tagging algorithms used in the analysis. JVT uncertainties arise from performance differences when applied

to different MC generators, along with the mismodelling of variables used to train the discriminant. They were found to impact the Signal region event yields by less than 1% in most categories. Flavour tagging systematics have a number of origins, including the simulation models used to generate the tagger training samples, and the parametrisation of the models used to fit the jet's tracks. Average variations were found to be 1-2% and 1-5% for ggF and VBF events respectively.

Systematic uncertainties relating to the E_T^{miss} scale and resolution were also treated. The uncertainties were dependent on the relative uncertainties of the objects from which E_T^{miss} was calculated, along with the associated soft term. Comparisons were made between data and MC for variables quantifying the difference between the soft and hard E_T^{miss} terms of $Z \to \mu\mu$ events. To correct the differences, Gaussian smearing corrections were applied to the MC, with systematic uncertainties arising from changes to the smearing needed to account for different MC generators and shower models [126]. The uncertainties were found to impact the Signal region event yields in each category by 1-2% on average.

The combined impact of the experimental systematic uncertainties on the ggF and VBF event yields in each category is summarised below in Table 11.1.1. The individual contributions of each systematic in each category are listed in Appendix G. The ggF and VBF MC samples were normalised to 80.5 fb^{-1} before calculation of the event yields and their variations. Uncertainties are typically larger for categories defined in the leftmost regions of the BDT output distributions, due to the increased signal MC statistical uncertainty in these regions. In the Zero-Jet categories, VBF uncertainties are 7-50% larger than those of ggF. This is likely due to the large VBF MC statistical uncertainties in these regions, since most VBF events contain two or more jets (and are thus categorised in the Multi-Jet and VBF categories). The opposite effect is true for ggF, where the largest uncertainties are seen in the VBF and Multi-Jet categories. In total, the experimental systematic uncertainties were found to have a 2% impact on the final μ_s result.

The uncertainties associated with the $P_T^{\mu\mu}$ and $M_{\text{inv}}^{\mu\mu}$ re-weighting factors of Chapter 7 were not included in the determination of μ_s, since these corrections were only applied to the background Drell-Yan MC samples, while the final μ_s extraction was performed using the distributions of the data.

Category	Up (ggF) [%]	Down (ggF) [%]	Up (VBF) [%]	Down (VBF) [%]
ggF Zero-Jet 1	10.51	10.39	17.34	19.81
ggF Zero-Jet 2	6.48	6.09	14.32	15.41
ggF Zero-Jet 3	5.45	5.20	13.29	16.14
ggF Zero-Jet 4	6.33	6.02	23.63	18.01
ggF Zero-Jet 5	6.27	5.43	21.33	21.98
ggF Zero-Jet 6	23.14	23.26	76.02	86.92
ggF Single-Jet 1	5.75	5.32	9.86	9.79
ggF Single-Jet 2	1.64	1.35	7.73	7.08
ggF Single-Jet 3	4.83	5.17	6.39	5.69
ggF Single-Jet 4	7.00	8.46	6.18	5.87
ggF Single-Jet 5	13.00	12.12	21.11	23.34
ggF Single-Jet 6	9.32	13.43	12.67	12.95
ggF Multi-Jet 1	8.28	8.46	6.52	5.92
ggF Multi-Jet 2	16.21	13.50	7.33	7.84
ggF Multi-Jet 3	15.97	16.16	8.41	8.23
ggF Multi-Jet 4	17.98	15.49	8.22	7.07
ggF Multi-Jet 5	23.01	27.67	22.64	20.94
ggF Multi-Jet 6	18.36	14.22	11.77	9.95
VBF 1	13.82	10.38	5.59	6.24
VBF 2	11.65	10.30	4.87	5.05

Table 11.1.1: Variations of ggF and VBF MC event yields between $110 \leq M_{\text{inv}}^{\mu\mu} \leq 160$ GeV due to experimental systematic variations, for all analysis categories.

11.2 Theoretical Systematic Uncertainties

Table 11.2.1 summarises the uncertainties on the cross-sections of the signal production modes considered in the analysis. The values were taken from the LHC Cross-Section Working Group [135]. QCD uncertainties were measured by varying the renormalisation and factorisation scales, while variation of the chosen PDF sets provided PDF and α_s[1] uncertainties. Separate entries were provided for the $pp \to ZH$ and $gg \to ZH$ mechanisms due to large differences in their QCD scale uncertainties (which dominate on average). Although the scale uncertainties reach 25% for $gg \to ZH$, event yield contributions from this channel are small, and contribute little to the final result.

Also provided by the LHC Cross-Section Working Group was the theoretical uncertainty on the $H \to \mu\mu$ branching ratio, found to be $\pm 1.23\%$ [135].

Production Mode	QCD [%]	PDF [%]	α_s [%]
ggF	± 3.9	± 1.9	± 2.6
VBF	$^{+0.4}_{-0.3}$	± 2.1	± 0.5
WH	$^{+0.5}_{-0.7}$	± 1.7	± 0.9
$pp \to ZH$	$^{+3.8}_{-3.1}$	± 1.3	± 0.9
$gg \to ZH$	$^{+25.1}_{-18.9}$	± 1.8	± 1.6
$t\bar{t}H$	$^{+5.8}_{-9.2}$	± 3.0	± 2.0

Table 11.2.1: The impact of various theoretical systematic variations on the ggF, VBF, WH, ZH and $t\bar{t}H$ production cross-sections [135].

Theoretical uncertainties on the acceptance of ggF and VBF events in each category were calculated using truth-level samples produced with Powheg+Pythia8 with the AZNLO tune. A dedicated sample was produced for each variation considered. The full analysis Signal region selection was applied to each sample, after which they were passed through the Dedicated Signal BDT network described in Chapter 9. Acceptance was defined as the number of events in a given category normalised to the total number of available events before BDT selection. QCD scale variations were determined by varying the factorisation and renormalisation scales up and down by factors of two. PDF and α_s uncertainties were assessed using samples produced with the CT10, MSTW and NNPDF PDF sets. Underlying event and parton shower uncertainties were determined by modifying Gaussian distributed variables within AZNLO by $\pm 1\sigma$. Such variables included the number of multi-parton interactions simulated (MPI), the renormalisation scale (Ren), and the P_T of the shower remnants (Var1 and Var2). Uncertainties were determined by comparing the $P_T^{\mu\mu,\text{truth}}$ distributions of each variation in each category. The histograms

[1] α_s was previously labelled g in Chapter 2.

were integrated to compare the number of events associated to each variation relative to the nominal configuration. Examples of these distributions for ggF and VBF events in the ggF Zero-Jet 1 category are presented in Figure 11.2.1. While QCD, PDF and α_s variations are largely constant as functions of $P_T^{\mu\mu,\text{truth}}$, shower variations increase noticeably at high $P_T^{\mu\mu}$. For both ggF and VBF samples, the dominating uncertainty arises from QCD scale, ranging from 6% to 25% depending on the category.

A summary of the combined theoretical acceptance uncertainties in each category is presented in Table 11.2.2. The largest uncertainties for ggF events are seen in the Multi-Jet and VBF categories, where the statistical uncertainties of the samples are greatest. The opposite is largely true for VBF events, where theoretical uncertainties are greatest in the Zero-Jet and Single-Jet categories. When introduced to the signal strength calculation outlined in Chapter 12, the theoretical acceptance uncertainties were found to affect μ_s by less than 1%. A more detailed summary of the theoretical acceptance uncertainties is presented in Appendix H.

Category	ggF Acceptance Uncertainty [%]	VBF Acceptance Uncertainty [%]
ggF Zero-Jet 1	6.87	17.85
ggF Zero-Jet 2	6.80	16.88
ggF Zero-Jet 3	7.27	20.72
ggF Zero-Jet 4	7.80	16.99
ggF Zero-Jet 5	7.57	29.06
ggF Zero-Jet 6	6.29	18.46
ggF Single-Jet 1	13.02	14.14
ggF Single-Jet 2	12.76	14.73
ggF Single-Jet 3	12.96	14.43
ggF Single-Jet 4	13.33	15.20
ggF Single-Jet 5	15.86	18.27
ggF Single-Jet 6	12.92	14.19
ggF Multi-Jet 1	20.48	11.65
ggF Multi-Jet 2	20.73	10.46
ggF Multi-Jet 3	20.78	14.82
ggF Multi-Jet 4	21.70	10.91
ggF Multi-Jet 5	29.45	62.48
ggF Multi-Jet 6	20.08	11.65
VBF 1	25.32	10.63
VBF 2	17.45	10.53

Table 11.2.2: Summary of the total acceptance uncertainties of ggF and VBF events in each analysis category due to the variation of PDF, QCD scale and α_s, along with shower and underlying event modelling parameters.

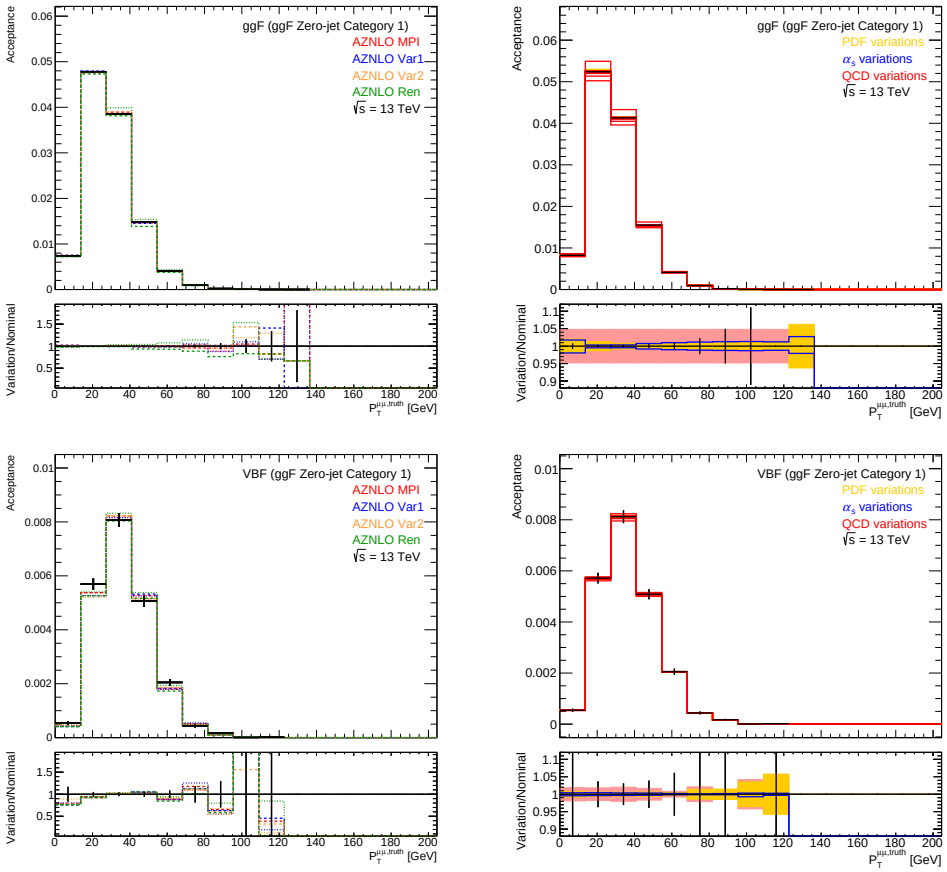

Figure 11.2.1: Variation of underlying event and parton shower (left) parameters as a function of $P_T^{\mu\mu,\text{truth}}$ for ggF (top) and VBF (bottom) samples in the ggF Zero-Jet 1 category. Also presented is the variation in QCD scale, PDF set and α_s (right). The full analysis selection has been applied to each sample at truth level.

11.3 Spurious Signal Systematic Uncertainties

To extract the $H \to \mu\mu$ signal strength, the signal plus background fit outlined in Chapter 10 must be applied to the $M_{\text{inv}}^{\mu\mu}$ distributions of the data in each category. One must be careful to ensure the signal identified by the fit is genuine $H \to \mu\mu$ signal, and not the result of biases in the fitting model. Spurious signal systematics are thus derived in an attempt to quantify these biases. There are many methods by which such systematics can be determined. In this section, the methodology common to previous ATLAS $H \to \mu\mu$ [27] analyses was applied.

To identify a signal as background-dominated as $H \to \mu\mu$, an accurate understanding of the surrounding background is crucial. MC predictions can only provide an approximation of the true background distribution found in the data, with the predictions often limited by the statistical uncertainty of the MC. One may try to overcome this obstacle by producing as large a MC sample as possible. Since detector simulation of MC samples is time consuming, it is common practice to generate the sample at truth-level, before applying smearing functions to approximate the detector's response. The signal plus background fit may then be applied to the corrected sample. For a background-only MC sample, the resultant fits should identify zero signal events if no bias is present. Any signal events identified are thus labelled spurious signal events.

This analysis utilised a 5000 fb^{-1} Drell-Yan MC sample privately generated using Powheg and Pythia8[2]. Despite Chapter 7 having demonstrated Madgraph to best model Drell-Yan events, Powheg was chosen due to its high efficiency in generating large numbers of events, allowing for a smoothly falling background $M_{\text{inv}}^{\mu\mu}$ distribution. To minimise file size and computation time, generated events were restricted to $95 \leq M_{\text{inv}}^{\mu\mu} \leq 200$ GeV, thus avoiding the Z mass peak. Given the signal plus background fits were to be performed in the Signal region ($110 \leq M_{\text{inv}}^{\mu\mu} \leq 160$ GeV), the cut was expected to have a minimal effect on the spurious signal yields. The cut was applied at born level, corresponding to the hard scatter final state before the emission of any muon FSR. Surviving muons were then dressed, a procedure through which FSR photons within $\Delta R < 0.1$ of each muon were added to the respective muon four-momentum vectors.

The detector response to the aforementioned sample was approximated in two steps. The first involved the application of a smearing correction to the muon momenta, to account for the detector's limited momentum resolution. Muon reconstruction efficiency corrections were then applied to each event. The corrections were derived from the official truth-and reco-level Powheg Drell-Yan MC samples produced during the mc15c campaign. While mc16 versions of these samples were available, the mc15c versions were preferred to better match the Powheg configuration options used to produce the private sample. Variable modelling differences between the production campaigns were later

[2]The generation of this sample was performed by Yusheng Wu and Yanlin Liu, rather than the author of this thesis.

accounted for through a polynomial re-weighting procedure, discussed further into this section. The choice of official sample was therefore thought to have little impact on the overall analysis.

Both the official and private samples were subject to the full analysis selection outlined in Chapter 6, with the exception of the $M^{\mu\mu}_{\text{inv}}$ cut. Muon momentum corrections were determined from distributions of $P_T^{\mu,\text{reco}}/P_T^{\mu,\text{truth}} - 1$ taken from the official samples. To approximate the momentum resolution to a sufficient degree of accuracy, corrections were determined in 338 bins of $P_T^{\mu,\text{truth}}$ and $\eta^{\mu,\text{truth}}$. The $\eta^{\mu,\text{truth}}$ bins were of 0.2 width, and were evenly distributed between $-2.6 \leq \eta^{\mu,\text{truth}} \leq 2.6$. The $P_T^{\mu,\text{truth}}$ bins are listed in Table 11.3.1, and correspond to those used in the most recent $H \to \mu\mu$ analysis [27].

Bin	Range [GeV]
1	$0 \leq P_T^{\mu,\text{truth}} < 20$
2	$20 \leq P_T^{\mu,\text{truth}} < 25$
3	$25 \leq P_T^{\mu,\text{truth}} < 30$
4	$30 \leq P_T^{\mu,\text{truth}} < 35$
5	$35 \leq P_T^{\mu,\text{truth}} < 40$
6	$40 \leq P_T^{\mu,\text{truth}} < 50$
7	$50 \leq P_T^{\mu,\text{truth}} < 60$
8	$60 \leq P_T^{\mu,\text{truth}} < 70$
9	$70 \leq P_T^{\mu,\text{truth}} < 80$
10	$80 \leq P_T^{\mu,\text{truth}} < 90$
11	$90 \leq P_T^{\mu,\text{truth}} < 100$
12	$100 \leq P_T^{\mu,\text{truth}} < 150$
13	$150 \leq P_T^{\mu,\text{truth}}$

Table 11.3.1: Bins of $P_T^{\mu,\text{truth}}$ from which the muon momentum resolution corrections for the spurious signal systematic sample were derived.

The $P_T^{\mu,\text{reco}}/P_T^{\mu,\text{truth}} - 1$ distributions of the $2.2 \leq \eta^{\mu,\text{truth}} \leq 2.4$ and $2.4 \leq \eta^{\mu,\text{truth}} \leq 2.6$ bins are shown below in Figure 11.3.1. The distributions associated with the remaining bins are presented in Appendix I. For each $\eta^{\mu,\text{truth}}$ range considered, the muon momentum resolution appears to degrade with increasing P_T. This is indicative of track curvature decreasing as a function of muon P_T. Smearing corrections were computed from random numbers derived from the probability density functions associated with the shown distributions. Efforts were initially made to instead derive random numbers from parametrised fits to the distributions, but this approach was found to produce a less effective smearing. As detailed in Chapter 3, the muon momentum resolution of

ATLAS runs inversely with P_T. Smearing corrections derived from $\frac{1}{P_T^{\mu,\text{reco}}}/\frac{1}{P_T^{\mu,\text{truth}}} - 1$ distributions were therefore also considered, but were found to produce similarly effective results as those obtained with the chosen approach.

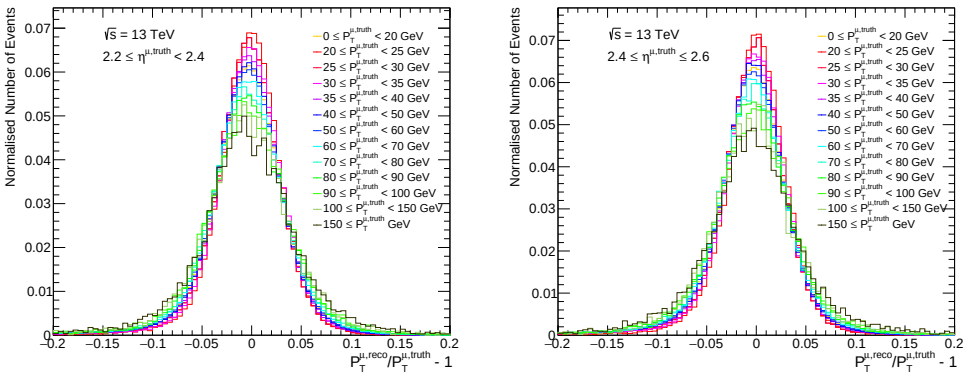

Figure 11.3.1: The difference in P_T between truth- and reco-level muons in bins of $P_T^{\mu,\text{truth}}$ and $\eta^{\mu,\text{truth}}$. The distributions are normalised to $P_T^{\mu,\text{truth}}$. $P_T^{\mu,\text{truth}}$ bins are represented by differently coloured histograms, with each plot corresponding to a different $\eta^{\mu,\text{truth}}$ bin. Shown here are the $2.2 \leq \eta^{\mu,\text{truth}} < 2.4$ (left) and $2.4 \leq \eta^{\mu,\text{truth}} \leq 2.6$ (right) $\eta^{\mu,\text{truth}}$ ranges. The PDFs associated with the distributions are used to perform a binned smearing of truth-level muons in the spurious signal systematic sample to reco-level.

Muon reconstruction efficiency corrections were derived from the official samples using a tag-and-probe approach. The muon object selection of Chapter 6 was applied to a given muon, after which the reconstruction efficiency of the second muon was measured. The full analysis event selection was applied, with the exception of the mass and subleading P_T cuts. The corrections were determined in bins of $P_T^{\mu,\text{truth}}$ and $\eta^{\mu,\text{truth}}$, using a finer binning than that of the previous step: $\eta^{\mu,\text{truth}}$ bins were of 0.1 width, while $P_T^{\mu,\text{truth}}$ bins were of 5, 1, 10 and 50 GeV widths between $0 \leq P_T^{\mu,\text{truth}} < 30$ GeV, $30 \leq P_T^{\mu,\text{truth}} < 50$ GeV, $50 \leq P_T^{\mu,\text{truth}} < 100$ GeV and $100 \leq$ GeV respectively. Figure 11.3.2 presents the derived reconstruction efficiencies, which are greater than 95% for the majority of the phase space considered. Efficiencies of 50% are seen for $|\eta^{\mu,\text{truth}}| < 0.1$, where trajectories are close to the beam line and therefore more difficult to reconstruct. Efficiencies of 5% or lower are seen for $|\eta^{\mu,\text{truth}}| > 2.6$, where ID coverage is lost, and $P_T^{\mu,\text{truth}} < 15$ GeV, where muon identification is limited.

To test the effectiveness of the smearing and reconstruction efficiency corrections with respect to the full detector simulation, comparisons were made between the official truth-level sample, smeared using the previously shown corrections, and the official reco-level sample. These comparisons are shown in Figure 11.3.3. Also shown is a comparison between the smeared private and official reco-level samples. The η distributions were found to agree within 1-2%. The P_T distributions show agreement largely within 10%,

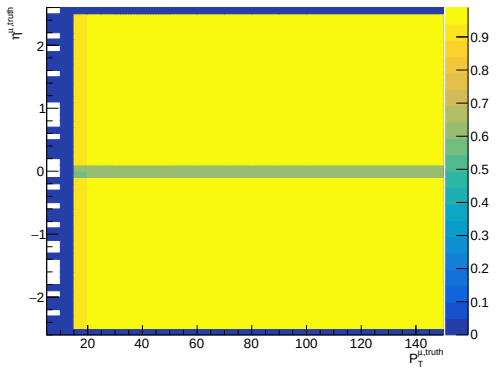

Figure 11.3.2: The selection efficiency of truth-level muons in bins of $P_T^{\mu,\text{truth}}$ and $\eta^{\mu,\text{truth}}$. The efficiencies were determined through a tag-and-probe methodology.

apart from the high $P_T^{\mu,\text{Subleading}}$ region, where statistical errors are large. A structure in the $P_T^{\mu,\text{Leading}}$ ratio can be seen between 140 and 160 GeV. This is likely due to inefficiencies with the smearing mechanism in this region, and could be improved through calculation of smearing factors using a finer binning between $100 \leq P_T^{\mu,\text{truth}} \leq 200$ GeV, or through smoothly interpolating the smearing corrections between bins. The $M_{\text{inv}}^{\mu\mu}$ distributions of the official samples agree within 5% for the majority of the phase space considered. Some larger discrepancies are seen for $M_{\text{inv}}^{\mu\mu} \leq 100$ GeV and $M_{\text{inv}}^{\mu\mu} \geq 180$ GeV between the private and official reco-level samples. These are likely due to the born-level mass cuts placed when generating the private sample, and are largely irrelevant, since good agreement is seen in the Signal region ($110 \leq M_{\text{inv}}^{\mu\mu} \leq 160$).

Once smeared, the private sample was processed using the BDTs described in Chapter 9 such that $M_{\text{inv}}^{\mu\mu}$ distributions for each category could be produced. As a closure test, the resultant distributions were compared to those shown in Chapter 9, which were used as input for the final μ_s calculation. For consistency, the private $M_{\text{inv}}^{\mu\mu}$ distributions were also normalised to the events yields derived from the Madgraph samples. A comparison between the smeared private sample and the official fitting input in the ggF Zero-Jet 1 category is shown on the left hand side of Figure 11.3.4. A consistent shape discrepancy is present between the distributions. This was thought to be caused by the samples presenting shape differences for variables used by the analysis BDTs. Since the smearing corrections were only applied to muons, these differences were likely present within the jet distributions. The VBF BDT was trained using a number of jet related quantities. Shape discrepancies at this point could therefore affect the VBF BDT decision, which would in turn have consequences for the subsequently applied ggF BDTs.

To correct these effects, the private $M_{\text{inv}}^{\mu\mu}$ distributions were re-weighted to their reco-level counterparts through application of a first-order polynomial fit to their ratio.

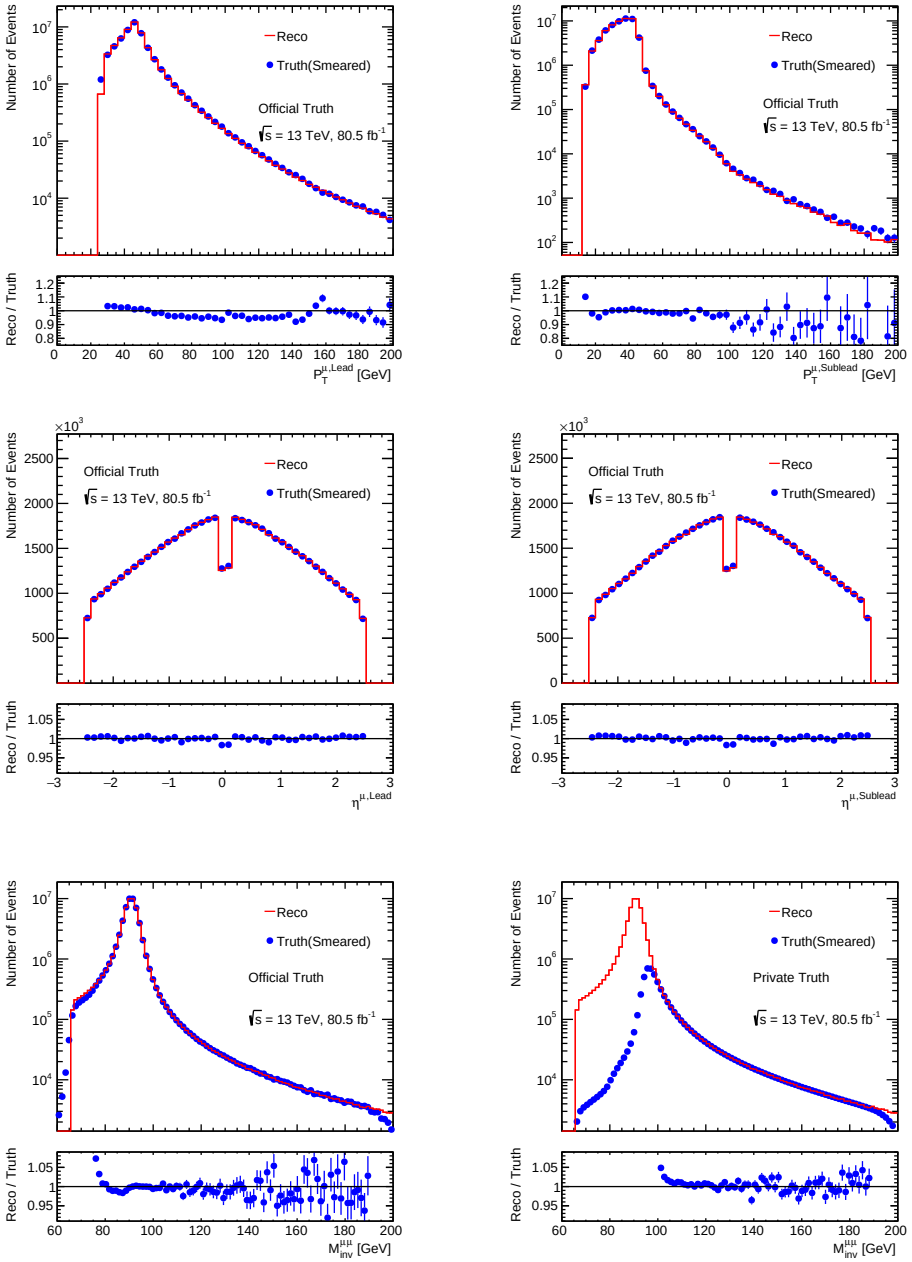

Figure 11.3.3: Comparisons between the official reco-level Powheg Drell-Yan MC (red) and the official truth-level Powheg Drell-Yan MC (blue), with the latter having undergone the smearing mechanism detailed in Section 11.3. Comparisons are shown for $P_T^{\mu,\text{Leading}}$ (top left), $P_T^{\mu,\text{Subleading}}$ (top right), $\eta^{\mu,\text{Leading}}$ (middle left), $\eta^{\mu,\text{Subleading}}$ (middle right) and $M_{\text{inv}}^{\mu\mu}$ (bottom left). Also shown are the $M_{\text{inv}}^{\mu\mu}$ distributions of the official reco-level Powheg Drell-Yan MC and the privately generated truth-level Powheg Drell-Yan MC (bottom right), where the latter has been smeared, and undergone born-level cuts of $M_{\text{inv}}^{\mu\mu} > 95$ GeV and $M_{\text{inv}}^{\mu\mu} < 200$ GeV. Only MC statistical errors are shown throughout.

An example of the fit can be seen in the lower left quadrant of Figure 11.3.4, where it converges to the MC reasonably well. The re-weighting performance of the fit is demonstrated on the right hand side of Figure 11.3.4, where the distributions agree within 10%. This re-weighting procedure was carried out for all categories, with the exception of ggF Multi-Jet 5, VBF 1 and VBF 2, where the reco-level distribution statistical errors were too large for a reliable fit.

Comparisons between the reco-level and re-weighted distributions are shown in Figures 11.3.5 to 11.3.8. In the majority of ggF categories, the distributions show agreement within 5-10%, suggesting the smearing and re-weighting procedures were effective. Discrepancies of up to 20% are seen in some categories, such as Zero-Jet 6, Single-Jet 5 and 6 and Multi-Jet 5 and 6, an effect likely correlated with the large statistical errors of the corresponding reco-level distributions. The same explanation is likely true for the VBF categories, where discrepancies greater than 20% are seen. Despite this, the smeared truth distributions are smoothly falling in all categories, which was the ultimate goal of the procedure. The aforementioned discrepancies were therefore considered tolerable.

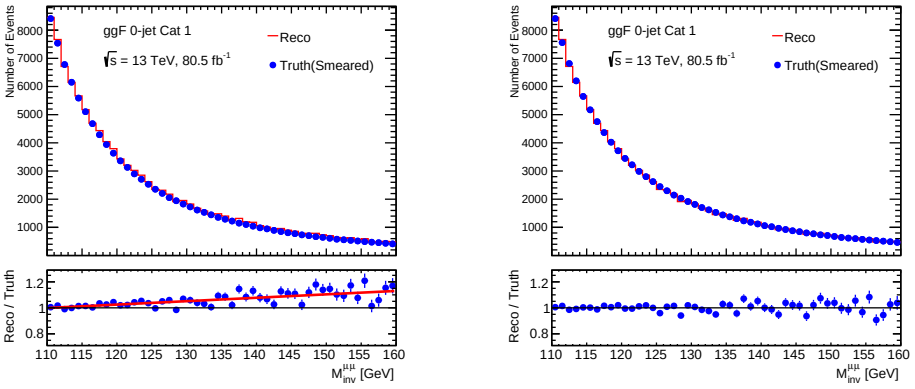

Figure 11.3.4: Comparisons between the $M_{\text{inv}}^{\mu\mu}$ distributions of the official reco-level Powheg Drell-Yan MC (red) and the privately generated truth-level Powheg Drell-Yan MC (blue), with the latter having undergone the smearing mechanism detailed in Section 11.3. The distributions are presented before (left) and after (right) application of a first-order polynomial re-weighting to the privately generated sample. The corresponding fit is shown in the bottom left ratio panel. Comparisons are made in the ggF Zero-Jet 1 category. Only MC statistical errors are shown throughout.

Figures 11.3.9 to 11.3.12 present the results of applying the signal plus background fits to the smeared truth distributions in each category. The distributions are normalised to 5000 fb^{-1}, corresponding to the luminosity of the privately generated sample. Di-boson, top and electroweak Z plus jets MC samples were not included in the fits, due to their large statistical errors relative to the smeared Drell-Yan sample. In any case, their

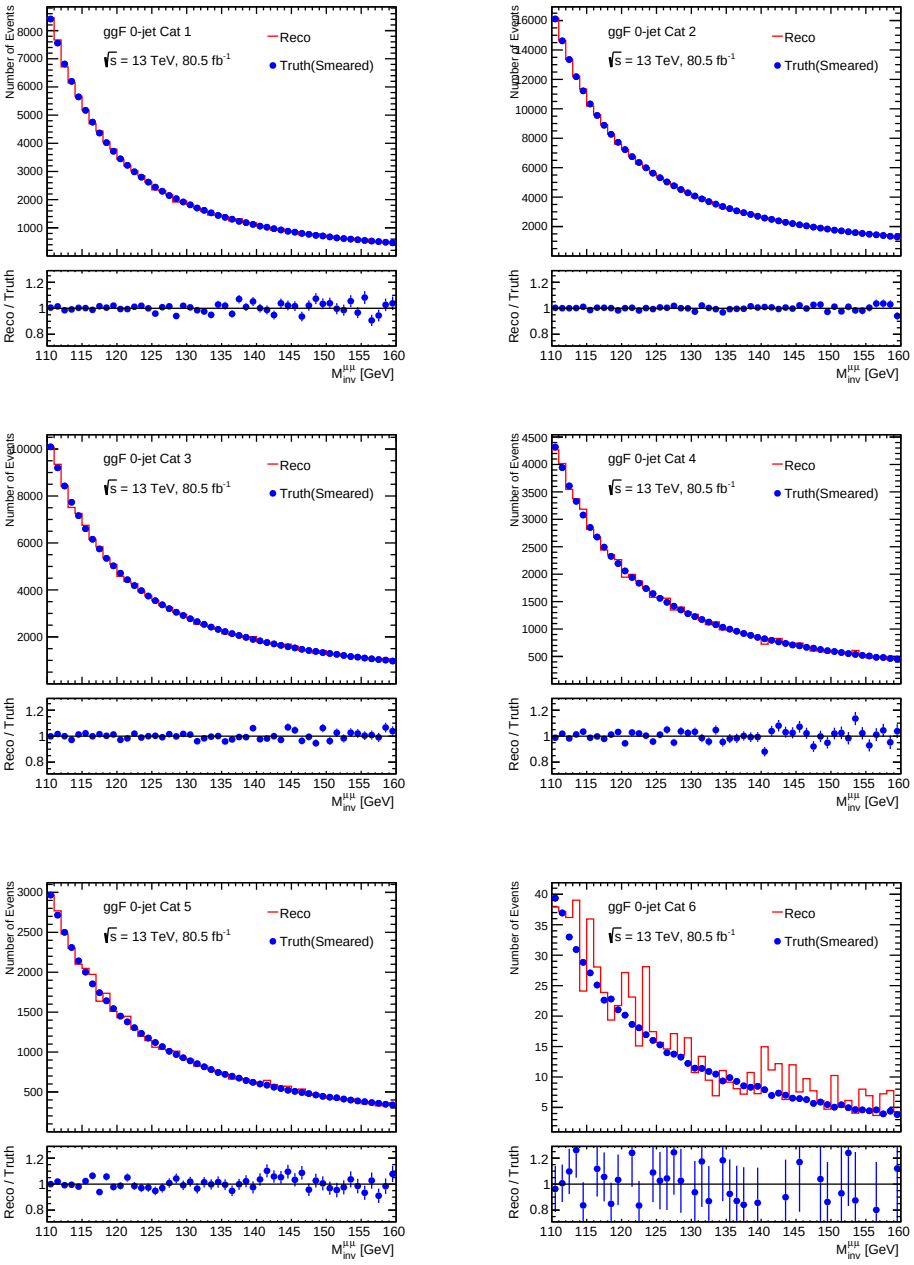

Figure 11.3.5: Comparisons between the $M_{\text{inv}}^{\mu\mu}$ distributions of the official reco-level Powheg Drell-Yan MC (red) and the privately generated truth-level Powheg Drell-Yan MC (blue), with the latter having undergone the smearing mechanism detailed in Section 11.3. Comparisons are made in the ggF Zero-Jet 1 (top left), ggF Zero-Jet 2 (top right), ggF Zero-Jet 3 (middle left), ggF Zero-Jet 4 (middle right), ggF Zero-Jet 5 (bottom left) and ggF Zero-Jet 6 (bottom right) categories. Only MC statistical errors are shown throughout.

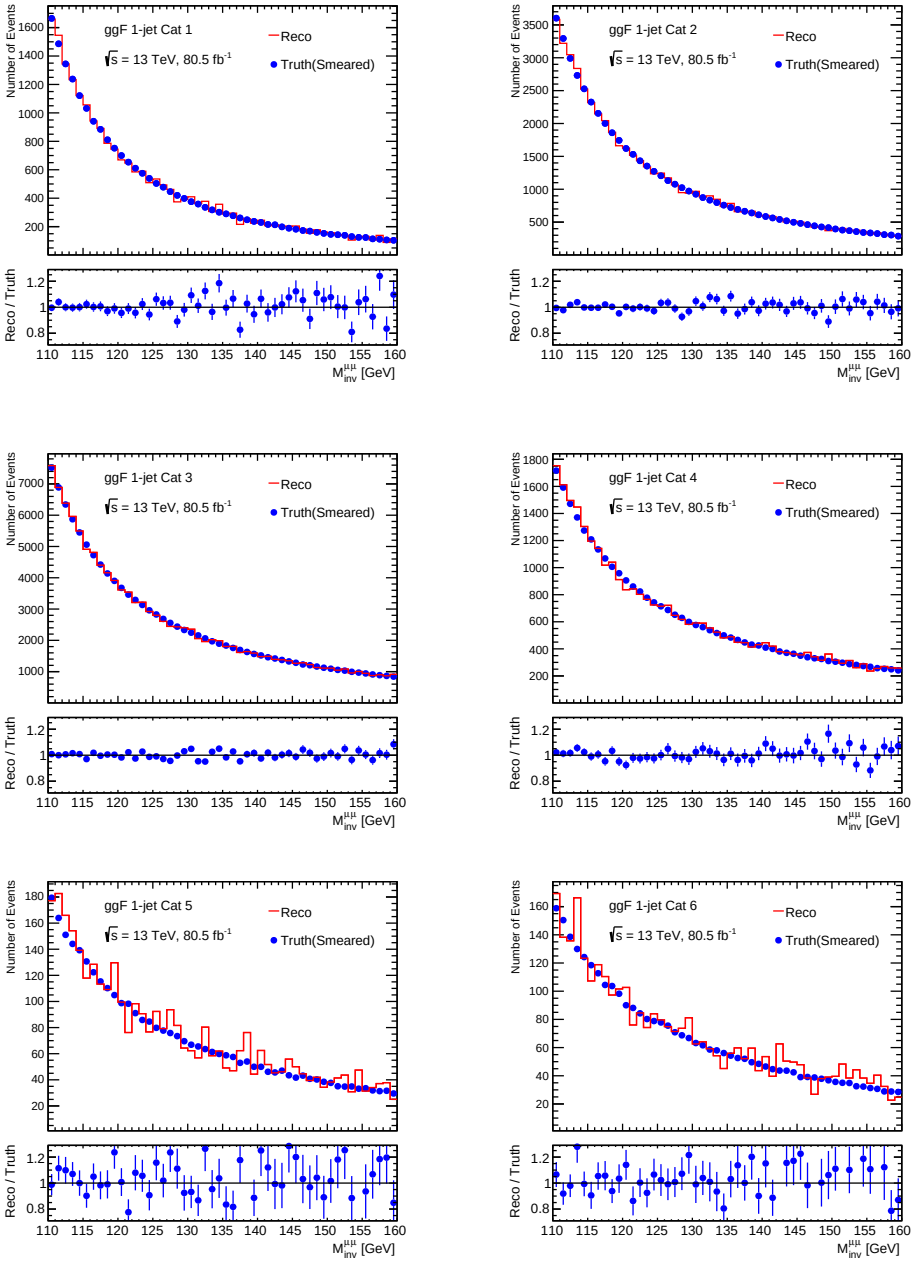

Figure 11.3.6: Comparisons between the $M^{\mu\mu}_{\text{inv}}$ distributions of the official reco-level Powheg Drell-Yan MC (red) and the privately generated truth-level Powheg Drell-Yan MC (blue), with the latter having undergone the smearing mechanism detailed in Section 11.3. Comparisons are made in the ggF Single-Jet 1 (top left), ggF Single-Jet 2 (top right), ggF Single-Jet 3 (middle left), ggF Single-Jet 4 (middle right), ggF Single-Jet 5 (bottom left) and ggF Single-Jet 6 (bottom right) categories. Only MC statistical errors are shown throughout.

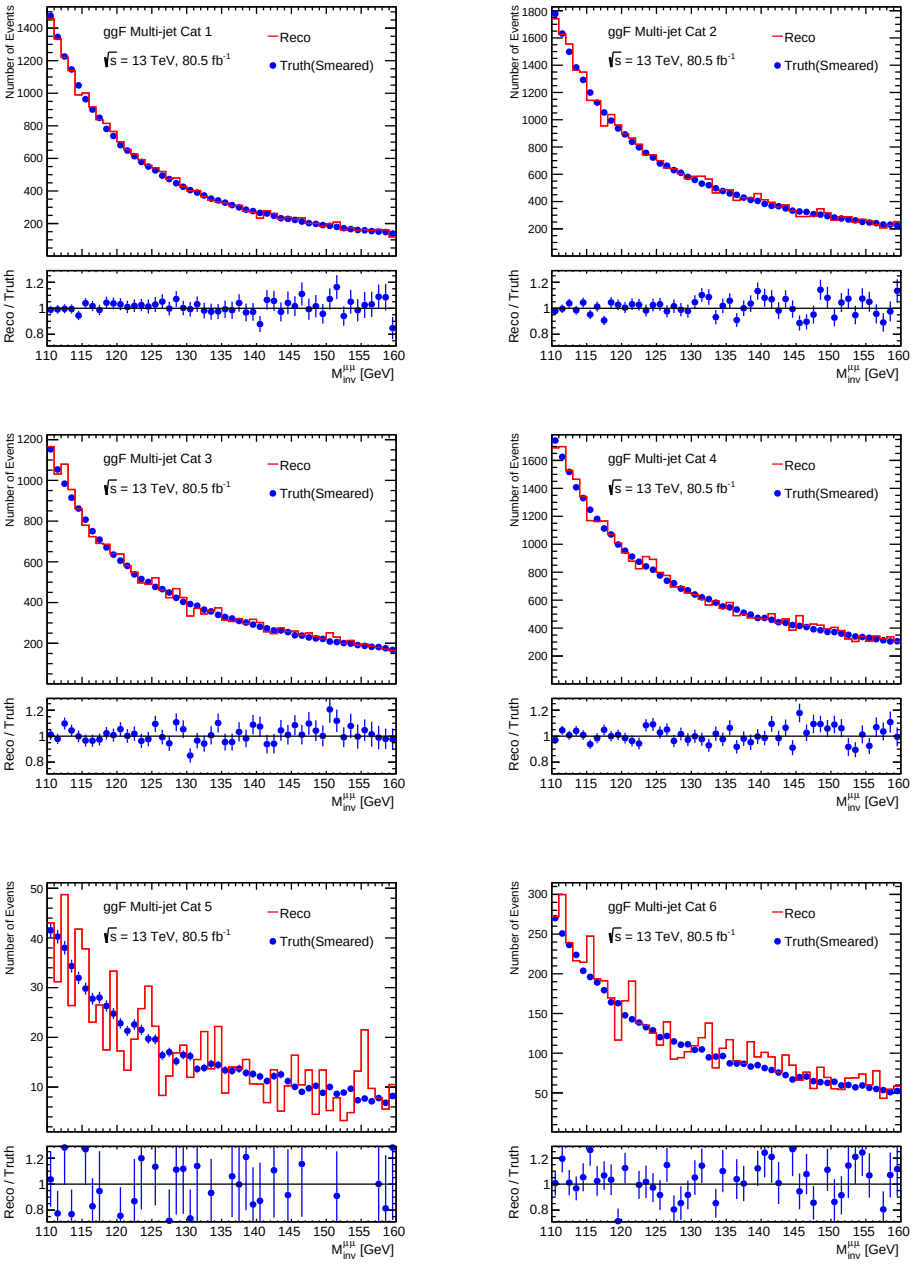

Figure 11.3.7: Comparisons between the $M_{\text{inv}}^{\mu\mu}$ distributions of the official reco-level Powheg Drell-Yan MC (red) and the privately generated truth-level Powheg Drell-Yan MC (blue), with the latter having undergone the smearing mechanism detailed in Section 11.3. Comparisons are made in the ggF Multi-Jet 1 (top left), ggF Multi-Jet 2 (top right), ggF Multi-Jet 3 (middle left), ggF Multi-Jet 4 (middle right), ggF Multi-Jet 5 (bottom left) and ggF Multi-Jet 6 (bottom right) categories. Only MC statistical errors are shown throughout.

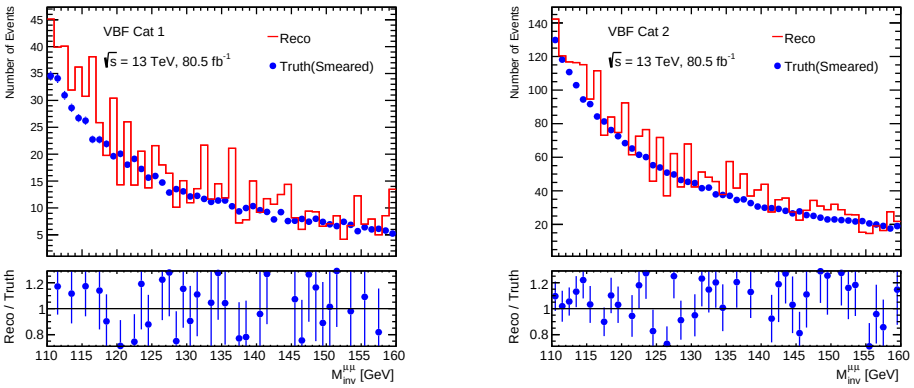

Figure 11.3.8: Comparisons between the $M_{\text{inv}}^{\mu\mu}$ distributions of the official reco-level Powheg Drell-Yan MC (red) and the privately generated truth-level Powheg Drell-Yan MC (blue), with the latter having undergone the smearing mechanism detailed in Section 11.3. Comparisons are made in the VBF 1 (left) and VBF 2 (right) categories. Only MC statistical errors are shown throughout.

contributions to the overall background shape were not thought to be significant in most categories. The background components of the fits are represented by the dashed blue (Voigtian) and red ($\frac{e^x}{x^3}$) lines, with the solid red line representing the signal component, fixed to the parameters obtained from the signal MC fits presented in Chapter 10. Overlaid in magenta are the combined ggF, VBF, VH and $t\bar{t}H$ $M_{\text{inv}}^{\mu\mu}$ distributions in each category, scaled by a factor of 100 (or in the case of the VBF categories, a factor of 10). The signal distributions are presented for demonstrative purposes, and were not directly involved in the fitting procedure. Spurious signal strength (μ_{spurious}) values were computed as the ratio of the number of signal events identified by the fit to the number of signal events predicted by the signal MC presented in Chapter 10 (normalised to 5000 fb^{-1}). The fitted signal yields were allowed to take on negative values to account for cases where spurious signal events arise from statistical fluctuations in the fitted distributions. Also presented are the pull distributions of the fits, using the same pull definition as the previous chapter. The fits appear to perform without significant bias in the majority of categories, with the corresponding reduced-χ^2 values all below 2. The exception to this is the ggF Zero-Jet 1 category, presenting a reduced-χ^2 of 2.31, with pull fluctuations of 3 to 4 seen between 110 and 120 GeV. This could be due to slight shaping of the $M_{\text{inv}}^{\mu\mu}$ distribution, a result of the BDT's response to ineffectively smeared variables. Since the fluctuations are minimal around the 125 GeV mass point, the effect was tolerated. Furthermore, the spurious signal yield in the category was found to be negative, suggesting the dominating uncertainty in the region is instead the statistical uncertainty of the MC. Future iterations of the analysis could develop an improved background fitting function for this region, or implement more robust cross-checks when

training the BDTs to prevent any form of mass shaping.

Table 11.3.2 summarises the absolute spurious signal yields (N_{Spur}) obtained in each category, alongside the statistical uncertainty on the background MC between $110 < M_{\text{inv}}^{\mu\mu} < 160$ GeV ($\sqrt{B}$). All categories remain dominated by the statistical uncertainty of the MC background (which roughly translates to the statistical uncertainty of the data, given the background-dominated nature of the analysis). The spurious signal yields were found to impact the final μ_s result by 1%. The means by which they were implemented are discussed in the following chapter.

It is of note that in a number of categories, the error associated with the spurious signal yields was larger than the yields themselves. When such instances occurred in previous ATLAS $H \to \mu\mu$ studies, the absolute error on the yield was instead taken as the NP for the μ_s calculation. When applying this methodology to this analysis, the spurious signal yields were inflated to $\pm 200\%$ the statistical uncertainty of the data, leading to technical issues with the μ_s computation. The approach is perhaps overly conservative in any case, and thus was not implemented for this analysis.

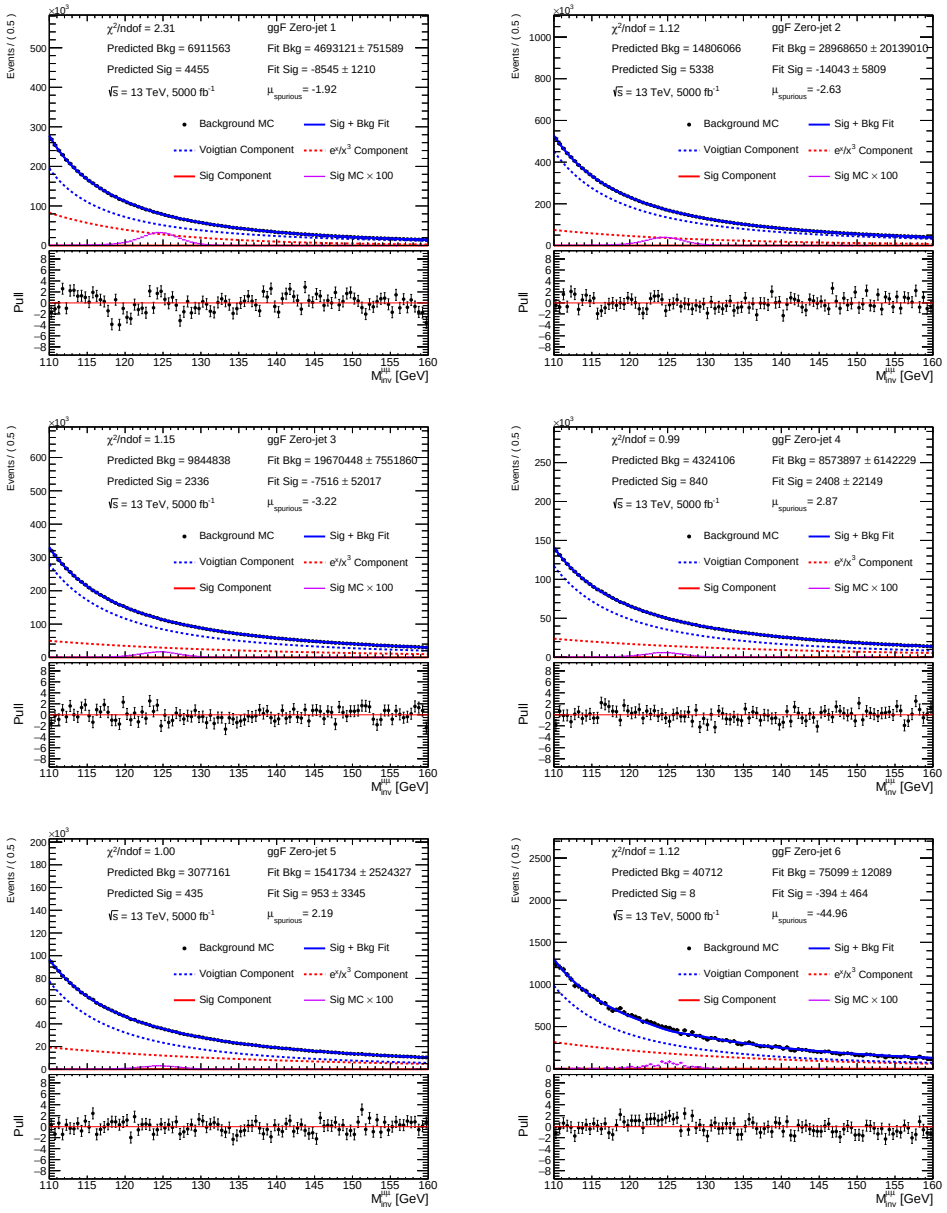

Figure 11.3.9: Signal plus background fits to the smeared $M_{\text{inv}}^{\mu\mu}$ distributions of the ggF Zero-Jet categories, as presented in Figure 11.3.5. The distributions are normalised to 5000 fb^{-1}, corresponding to the integrated luminosity of the privately generated truth-level Powheg Drell-Yan MC sample. The predicted number of signal and background events in each region was determined from integrating the signal and background MC distributions presented in Chapter 10 and Appendix F. The combined $M_{\text{inv}}^{\mu\mu}$ distributions of the signal samples are presented in magenta, having been scaled by a factor of 100. These distributions were not directly involved in the fitting procedure. μ_{spurious} values were defined as the ratio of the signal yields derived from the fit to the signal yields predicted by the signal MC. Fits are performed in the ggF Zero-Jet 1 (top left), ggF Zero-Jet 2 (top right), ggF Zero-Jet 3 (middle left), ggF Zero-Jet 4 (middle right), ggF Zero-Jet 5 (bottom left) and ggF Zero-Jet 6 (bottom right) categories.

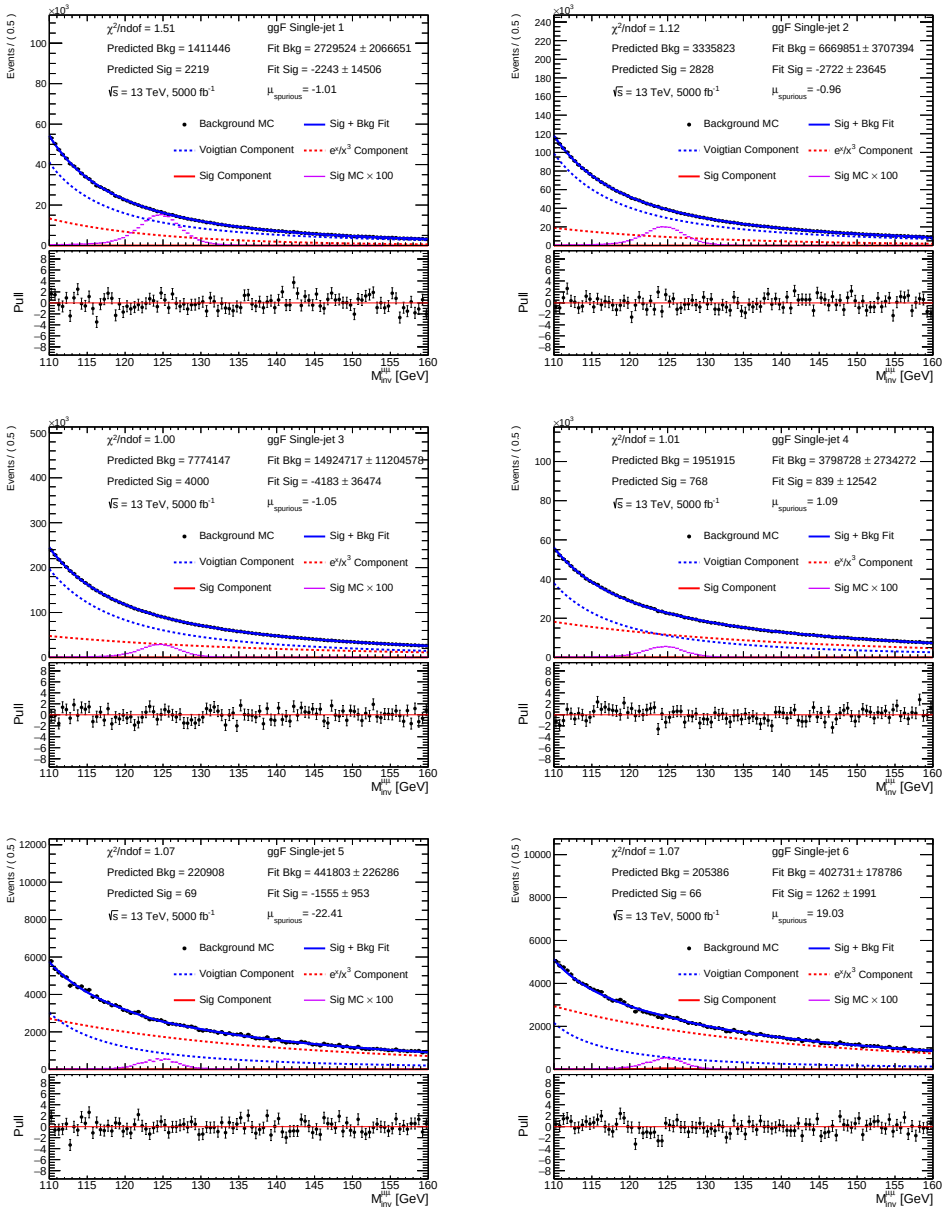

Figure 11.3.10: Signal plus background fits to the smeared $M_{\text{inv}}^{\mu\mu}$ distributions of the ggF Single-Jet categories, as presented in Figure 11.3.6. The distributions are normalised to 5000 fb^{-1}, corresponding to the integrated luminosity of the privately generated truth-level Powheg Drell-Yan MC sample. The predicted number of signal and background events in each region was determined from integrating the signal and background MC samples presented in Chapter 10 and Appendix F. The combined $M_{\text{inv}}^{\mu\mu}$ distributions of the signal samples are presented in magenta, having been scaled by a factor of 100. These distributions were not directly involved in the fitting procedure. μ_{spurious} values were defined as the ratio of the signal yields derived from the fit to the signal yields predicted by the signal MC. Fits are performed in the ggF Single-Jet 1 (top left), ggF Single-Jet 2 (top right), ggF Single-Jet 3 (middle left), ggF Single-Jet 4 (middle right), ggF Single-Jet 5 (bottom left) and ggF Single-Jet 6 (bottom right) categories.

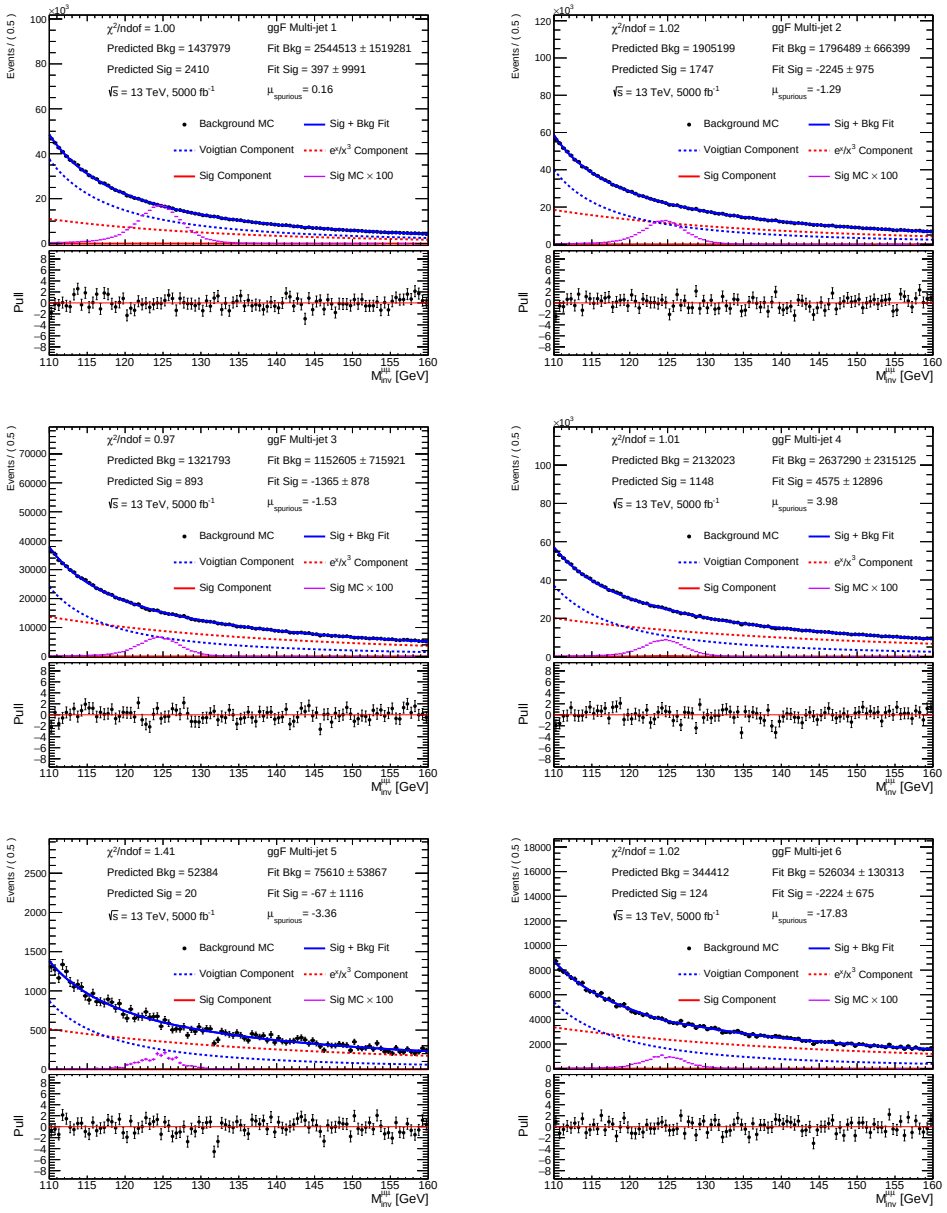

Figure 11.3.11: Signal plus background fits to the smeared $M_{\text{inv}}^{\mu\mu}$ distributions of the ggF Multi-Jet categories, as presented in Figure 11.3.7. The distributions are normalised to 5000 fb^{-1}, corresponding to the integrated luminosity of the privately generated truth-level Powheg Drell-Yan MC sample. The predicted number of signal and background events in each region was determined from integrating the signal and background MC samples presented in Chapter 10 and Appendix F. The combined $M_{\text{inv}}^{\mu\mu}$ distributions of the signal samples are presented in magenta, having been scaled by a factor of 100. These distributions were not directly involved in the fitting procedure. μ_{spurious} values were defined as the ratio of the signal yields derived from the fit to the signal yields predicted by the signal MC. Fits are performed in the ggF Multi-Jet 1 (top left), ggF Multi-Jet 2 (top right), ggF Multi-Jet 3 (middle left), ggF Multi-Jet 4 (middle right), ggF Multi-Jet 5 (bottom left) and ggF Multi-Jet 6 (bottom right) categories.

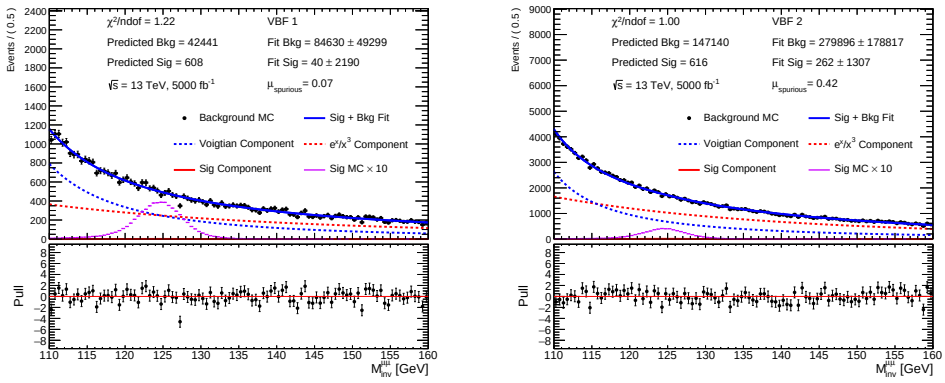

Figure 11.3.12: Signal plus background fits to the smeared $M_{\text{inv}}^{\mu\mu}$ distributions of the VBF categories, as presented in Figure 11.3.8. The distributions are normalised to 5000 fb^{-1}, corresponding to the integrated luminosity of the privately generated truth-level Powheg Drell-Yan MC sample. The predicted number of signal and background events in each region was determined from integrating the signal and background MC samples presented in Chapter 10 and Appendix F. The combined $M_{\text{inv}}^{\mu\mu}$ distributions of the signal samples are presented in magenta, having been scaled by a factor of 10. These distributions were not directly involved in the fitting procedure. μ_{spurious} values were defined as the ratio of the signal yields derived from the fit to the signal yields predicted by the signal MC. Fits are performed in the VBF 1 (left) and VBF 2 (right) categories.

Category	N_{Spur}	$\sqrt{B}$	$\frac{N_{\text{Spur}}}{\sqrt{B}}$
ggF Zero-Jet 1	137.59	333.85	0.41
ggF Zero-Jet 2	226.09	488.37	0.46
ggF Zero-Jet 3	121.01	398.33	0.30
ggF Zero-Jet 4	38.77	264.20	0.15
ggF Zero-Jet 5	15.34	222.95	0.07
ggF Zero-Jet 6	6.34	27.23	0.23
ggF Single-Jet 1	36.11	151.28	0.24
ggF Single-Jet 2	43.82	232.03	0.19
ggF Single-Jet 3	67.35	354.04	0.19
ggF Single-Jet 4	13.51	177.82	0.08
ggF Single-Jet 5	25.04	60.88	0.41
ggF Single-Jet 6	20.32	58.66	0.35
ggF Multi-Jet 1	6.39	152.84	0.04
ggF Multi-Jet 2	36.16	175.87	0.21
ggF Multi-Jet 3	21.98	146.73	0.15
ggF Multi-Jet 4	73.66	185.98	0.40
ggF Multi-Jet 5	1.08	29.43	0.04
ggF Multi-Jet 6	35.82	76.97	0.47
VBF 1	0.64	28.65	0.02
VBF 2	4.23	51.71	0.08

Table 11.3.2: The absolute spurious signal yields taken from fitting the smeared truth $M_{\text{inv}}^{\mu\mu}$ distributions presented in Figures 11.3.5 to 11.3.8. The yields have been normalised to 80.5 fb^{-1}. Also presented is the combined statistical error of the Drell-Yan, electroweak Z plus jets, di-boson and top background MC samples used in the analysis, having been normalised to 80.5 fb^{-1}. The values are equivalent to those of Table 9.3.9 in the case where the mass range has been extended from $120 < M_{\text{inv}}^{\mu\mu} < 130$ GeV to $110 < M_{\text{inv}}^{\mu\mu} < 160$ GeV.

Chapter 12

Results

In search analyses, it is traditional to define the null hypothesis, H_0, as the case where the data contains only background processes. The alternate hypothesis, H_1, instead proposes the data consists of both signal and background contributions. When setting limits on a production process, the signal plus background model forms H_0, with H_1 the background-only hypothesis. One may quantify the level of agreement between a given hypothesis and the data by computing a p-value, corresponding to the probability of obtaining a result of equal or greater incompatibility with the data than that observed, assuming H_0 to be true. For p-values lower than 0.05 (the 95% Confidence Level (CL)), one may exclude H_0.

In this analysis, the compatibility of the data observed in the signal region with the SM background-only hypothesis (H_0) was computed using a maximum likelihood approach, parametrised in terms of the signal strength μ_s. H_0 corresponded to the $\mu_s = 0$ case, with $\mu_s = 1$ the $H \to \mu\mu$ signal hypothesis (H_1). Due to the large statistical uncertainties associated with the determined μ_s value, upper limits were also set on the signal strength, in which case H_0 and H_1 were reversed.

The full likelihood function was constructed as a product of Poisson probabilities,

$$\mathcal{L}(\mu_s, \theta) = \prod_{c=1}^{N_c} \mathcal{L}_c(\mu_s, \theta), \tag{12.0.1}$$

with $\mathcal{L}_c$ the likelihood function of category c, defined as

$$\mathcal{L}_c(\mu_s, \theta) = \prod_{j=1}^{N_{\text{bin}}^c} \frac{(\mu_s s_j + b_j + \tilde{s}_j)^{n_j}}{n_j!} e^{-(\mu_s s_j + b_j + \tilde{s}_j)}, \tag{12.0.2}$$

where

$$s_j = \sum_{p=1}^{N_{\text{prod}}} N^c_{\text{Ev},p} \int_{\text{bin}_j} f_p(x;\theta_p)dx, \tag{12.0.3}$$

$$b_j = N^c_{\text{Ev},b} \int_{\text{bin}_j} f_b(x;\theta_b)dx, \tag{12.0.4}$$

$$\tilde{s}_j = N^c_{\text{Ev},\tilde{s}} \sum_{p=1}^{N_{\text{prod}}} \int_{\text{bin}_j} f_p(x;\theta_p)dx. \tag{12.0.5}$$

N_c represents the total number of categories, with N^c_{bin} the total number of bins in category c, and n_j the number of events in bin j. $N^c_{\text{Ev},p}$ represents the total number of events in category c originating from process p, with $N^c_{\text{Ev},\tilde{s}}$ the corresponding number of spurious signal events. p sums over the number of signal production processes considered, N_{prod}, equal to 4 (ggF, VBF, VH and $t\bar{t}H$). The Probability Density Functions (PDFs) of these processes are contained within $f_p(x;\theta_p)$, with x in this instance representing $M^{\mu\mu}_{\text{inv}}$, and θ_p the signal normalisation nuisance parameters (corresponding to the experimental and theoretical systematic uncertainties outlined in the previous chapter). $f_b(x;\theta_b)$ represents the background PDF, dependent on both x and θ_b, the background normalisation nuisance parameters (which were not considered for this thesis).

To determine the nominal μ_s result, $-\ln\mathcal{L}$ was minimised with respect to μ_s and the aforementioned nuisance parameters. The obtained value was $\mu_s = -0.29^{+1.10}_{-1.12}$, with the largest uncertainties arising from the statistical uncertainty of the data. This corresponded to an observed (expected) significance of 0.00σ (0.82σ), with the expected value computed using the Asimov dataset, defined later in this chapter. The difference between the observed and expected significances is due to statistical fluctuations in the data.

With no significant excess of events observed in the data, upper limits were set on μ_s at the 95% CL. To compute said limits, the profile likelihood ratio

$$\lambda(\mu_s) = \frac{\mathcal{L}(\mu_s, \hat{\hat{\theta}})}{\mathcal{L}(\hat{\mu_s}, \hat{\theta})} \tag{12.0.6}$$

was defined, with $\hat{\mu_s}$ and $\hat{\theta}$ (the so-called Maximum-Likelihood Estimators (MLEs)) the values of μ_s and θ which maximise $\mathcal{L}$, and $\hat{\hat{\theta}}$ the value of θ maximising $\mathcal{L}$ for a given μ_s. $\hat{\mu_s}$ is an effective estimator of the true signal strength μ_s, and is allowed to take on negative values (providing $\mu_s s_j + b_j$ remains positive overall). The ratio is limited to the range $0 \leq \lambda(\mu_s) \leq 1$, with values close to 1 implying good agreement between the data and the hypothesised signal strength.

It is convenient to then define a test statistic

$$\tilde{q}_{\mu_s} = -2 \ln \lambda(\mu_s), \tag{12.0.7}$$

with large values of $\tilde{q}_{\mu_s}$ corresponding to low values of $\lambda(\mu_s)$, and thus poor agreement between μ_s and the data [115].

When calculating upper limits on μ_s, instances with $\hat{\mu_s} > \mu_s$ provide no indication of incompatibility between data and μ_s. $\tilde{q}_{\mu_s} = 0$ is thus used in such cases. Furthermore, in models (such as the SM) where $\mu_s \geq 0$, for $\hat{\mu_s} < 0$, the best compatibility between model and data is achieved for $\mu_s = 0$. The test statistic can therefore be expressed as

$$\tilde{q}_{\mu_s} = \begin{cases} -2 \ln \frac{\mathcal{L}(\mu_s, \hat{\hat{\theta}}(\mu_s))}{\mathcal{L}(0, \hat{\hat{\theta}}(0))}) & \hat{\mu_s} < 0 \\ -2 \ln \frac{\mathcal{L}(\mu_s, \hat{\hat{\theta}}(\mu_s))}{\mathcal{L}(\hat{\mu_s}, \hat{\theta})}) & 0 \leq \hat{\mu_s} \leq \mu_s \\ 0 & \hat{\mu_s} > \mu_s. \end{cases} \tag{12.0.8}$$

In order to quantify discrepancies between the data and the chosen hypothesis, one may construct p-values of the form

$$p_s = \int_{\tilde{q}^{\text{obs}}_{\mu_s}}^{\infty} f(\tilde{q}_{\mu_s} | \mu_s, \hat{\theta}^{\text{obs}}_{\mu_s}) d\tilde{q}_{\mu_s}, \tag{12.0.9}$$

$$p_b = 1 - \int_{\tilde{q}^{\text{obs}}_{0}}^{\infty} f(\tilde{q}_{\mu_s} | 0, \hat{\theta}^{\text{obs}}_{0}) d\tilde{q}_{\mu_s}, \tag{12.0.10}$$

where $\tilde{q}^{\text{obs}}_{\mu_s}$ and $\hat{\theta}^{\text{obs}}_{\mu_s}$ define the values of $\tilde{q}$ and $\hat{\theta}$ observed in the data, and $f(\tilde{q}_{\mu_s} | \mu_s, \hat{\theta}^{\text{obs}}_{\mu_s})$ defines the PDF of $\tilde{q}_{\mu_s}$ for the hypothesised signal strength μ_s, which can be approximately computed using the prescription outlined in [115].

The final exclusion limits were computed using the CL_s method [136], where

$$CL_s(\mu_s) = \frac{p_{\mu_s}}{1 - p_b}. \tag{12.0.11}$$

Upper limits were determined through scanning values of μ_s, and identifying the values for which $CL_s = 0.05$. All values of μ_s for which $CL_s < 0.05$ were thus excluded by the limit. The results are listed in Table 12.0.1. The observed limit was obtained using the recorded data. The expected limit was obtained using the so-called Asimov dataset, constructed such that when computing the likelihoods, $\hat{\mu_s}$ and $\hat{\theta}$ were found equal to their true values μ and θ. The Asimov dataset was thus insensitive to statistical fluctuations, and a better estimator of the analysis' signal sensitivity. The deviation between the observed and expected limits (as well as the significances presented earlier) is due to statistical fluctuations, with the observed result (1.98) lying within the $\pm 1\sigma$ band of the Asimov result (2.13).

The expected limit is 5% worse than that found by the most recent ATLAS $H \to \mu\mu$ analysis, despite the 2% improvement projected by the newly introduced BDT categorisation. This is likely due to a combination of factors, including the different signal models used between analyses, differences in object calibrations and varied statistical uncertainties between the different categorisations.

Observed	$+2\sigma$	$+1\sigma$	Expected	-1σ	-2σ
1.98	3.98	2.94	2.13	1.53	1.14

Table 12.0.1: Observed and expected upper limits on μ_s at the 95% Confidence Level.

The impact of the leading 25 NPs on the derived signal strength is presented in Figure 12.0.1. Uncertainties on $\hat{\mu_s}$ are presented for each NP, with both pre-fit (yellow) and post-fit (striped blue) uncertainties considered. The variations were computed through comparing the nominal $\hat{\mu_s}$ value to that obtained when each NP was fixed to its MLE value, $\pm$ the pre-/post-fit uncertainty. Also presented are the respective pulls of the NPs. The largest deviations come from the spurious signal systematics, where variations of up to $\pm 5\%$ are seen.

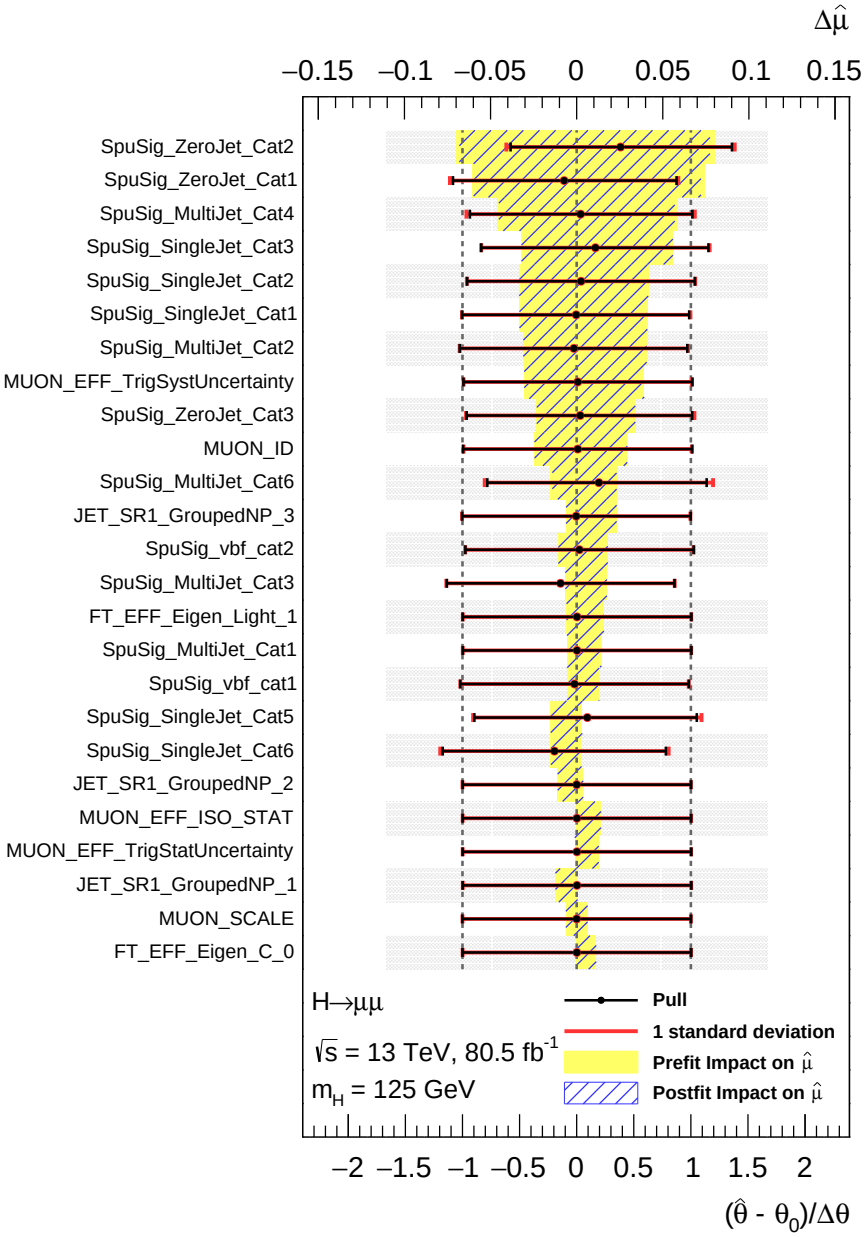

Figure 12.0.1: The pre-fit and post-fit uncertainties on $\hat{\mu_s}$ from the 25 largest NPs considered in the analysis. The uncertainties were determined when applying fits to data events, and were computed through comparing the nominal value of $\hat{\mu_s}$ obtained from the fit to the value obtained when fixing each NP to its Maximum-Likelihood Estimator (MLE) value, $\pm$ the pre-fit/post-fit uncertainties. The uncertainties are represented by the shaded yellow (pre-fit) and striped blue (post-fit) error bars. The data points are plotted relative to the bottom axis, representing the pulls of the NPs on the likelihood fits. $\hat{\theta}$ represents the MLE of the NP in question, with θ_0 its nominal value and $\Delta\theta$ the pre-fit standard deviation of the NP. The largest deviations arise due to the spurious signal systematics.

Chapter 13

Conclusion and Future Developments

A search was performed for the decay of a Standard Model Higgs boson in the di-muon channel, using pp collision data recorded at $\sqrt{s} = 13$ TeV with the ATLAS detector, corresponding to an integrated luminosity of 80.5 fb^{-1}. No significant excess of events was observed in the data, with the $H \to \mu\mu$ signal strength measured as $\mu_s = -0.29^{+1.10}_{-1.12}$, corresponding to an observed (expected) significance of 0.00σ (0.82σ). An observed (expected) upper limit at the 95% confidence level on the cross-section times branching ratio was set at 1.98 (2.13) times the SM expectation. The findings are competitive with those recently published by ATLAS [27], and will likely remain world-leading until the publication of full Run-2 results by either ATLAS or CMS. Both will benefit greatly from the increased signal sensitivity associated the inclusion of data recorded in 2018.

There are a number of potential causes for the 5% loss in expected sensitivity compared to the most recent ATLAS result [27]. The signal model utilised for the previous result was found to possess biases in a number of categories, which could have contributed to upward fluctuations in sensitivity. This thesis made use of newer jet and muon calibrations provided by the ATLAS Combined Performance Working Groups, which would have impacted the modelling of variables used to train the BDTs. Changes to the BDT output distributions would have affected the categorisation of events, and thus the derived signal sensitivity. This analysis also changed the categorisation of events through implementation of a network of BDTs, producing 20 new categories (as opposed to the previous 8). This increase in category number likely caused the overall statistical uncertainty of the likelihood fits to increase, reducing the overall analysis sensitivity. The truth of this will become more apparent as the recorded luminosity of the LHC grows.

Despite this, there are already a number of improvements which could be implemented to future $H \to \mu\mu$ analyses to increase signal sensitivity. One such example would be the

implementation of an FSR recovery algorithm. $H \to \mu\mu$ decays often include photons radiated from the di-muon final state. By associating candidate photons with nearby muons, the photon and muon four-vectors can be combined, improving the di-muon mass resolution and signal event yields about the Higgs mass peak. The technique has been proven to increase the selection efficiency of $H \to ZZ \to 4l$ decays by 3% [137], and could provide similar benefits for $H \to \mu\mu$.

Three separate event categorisations were explored in Chapter 9, all utilising the same multivariate algorithm (Boosted Decision Trees). It would be of interest to study the performance of other algorithms, such as Support Vector Machines and Neural Networks. The performance of the Background Separation BDTs was significantly limited by a lack of MC events available for training. This could be easily remedied given enough computing time for further event generation, and could allow the potential sensitivity improvements of the method to be better explored in the future. The algorithmic approach to which all of the BDTs were trained proved effective as a first attempt, but contains room for improvement. The minimum number of events allowed per category could be better optimised, as could the hyper-parameters used for training. Dedicated categories and BDTs for the VH and $t\bar{t}H$ processes could also provide improvements in sensitivity as the amount of available data increases.

The treatment of the spurious signal systematics in Chapter 11 followed the standard prescription used by many ATLAS analyses. While this approach is valid, it could be more rigorous. For example, previous $H \to \gamma\gamma$ searches have tested multiple background models for each independent analysis category, choosing that with the lowest bias [14, 16]. Rather than producing a large MC sample to approximate the true background, some analyses instead devise a range of plausible background models (such as exponentials, power-law functions and Bernstein polynomials), and assess the spread of spurious signal yields attained using the different functions [140]. It would be interesting to compare these differing approaches in future analyses, and see how they impact the derived spurious signal yields. Both methods would avoid the variable mismodelling and mass shaping issues encountered in this analysis when processing the spurious signal samples through the BDT network. As the leading source of systematic uncertainty, the treatment of the spurious signal systematics will grow in importance as more data is recorded, and statistical uncertainties reduce.

For the time being, however, the analysis remains dominated by the statistical uncertainty of the data, and in this respect the future of $H \to \mu\mu$ is bright. The addition of the 60 fb^{-1} of data recorded in 2018, as well as the 300 fb^{-1} projected to be recorded during Run-3 [138] will help drive the analysis sensitivity ever higher. By scaling the number of events in each category of the analysis, naive projections on the required luminosity for achieving evidence (3σ) and discovery (5σ) of $H \to \mu\mu$ were produced. The respective requirements were found to be 440 fb^{-1} and 1221 fb^{-1} respectively. While the

projections fail to account for increases in systematic uncertainty, as well as the increased pile-up associated with Run-3's $\sqrt{s} = 14$ TeV conditions, they give fair indication that evidence for $H \to \mu\mu$ could be obtained within the next 5 years (perhaps even sooner were CMS and ATLAS to produce a combined result). Experimental observation of $H \to \mu\mu$ will be likely postponed until the advent of the HL-LHC, projected to record upwards of 3000 fb^{-1} [139]. A separate analysis recently studied the projected performance of a $H \to \mu\mu$ search under such conditions, using 3000 fb^{-1} MC samples with $\sqrt{s} = 14$ TeV and $<\mu>= 200$ [141]. The applied event selection was largely similar to that of this analysis, with the categorisation the same as that of Chapter 7, except only one VBF category was defined (without the use of a BDT). Only theoretical and experimental luminosity uncertainties were considered. Utilising the same signal and background models as the previous ATLAS $H \to \mu\mu$ analysis, the projected significance was found to be over 9σ, well above the standardised 5σ limit for claiming discovery.

With all of this considered, $H \to \mu\mu$ remains an analysis of growing interest and importance to the field of high energy physics. It holds an important role in our understanding of the Higgs boson, and the influence it imparts upon the Standard Model. With its experimental observation on the horizon, there has never been a better time to join the search effort. It is the author's hope that the work presented within this thesis provides the basis of such future analyses, from which our understanding of the Universe can continue to grow.

Bibliography

[1] UA1 Collaboration, *Experimental observation of isolated large transverse energy electrons with associated missing energy at* $\sqrt{s} = 540\ GeV$ - 1983, Phys. Lett. B 122 (1983) 1, pp.103-116, doi:10.1016/0370-2693(83)91177-2.

[2] UA2 Collaboration, *Observation of single isolated electrons of high transverse momentum in events with missing transverse energy at the CERN* $\bar{p}p$ *collider* - 1983, Phys. Lett. B 122 (1983) 5-6, pp.476-485, doi:10.1016/0370-2693(83)91605-2.

[3] UA1 Collaboration, *Experimental observation of lepton pairs of invariant mass around 95* GeV/c^2 *at the CERN SPS collider* - 1983, Phys. Lett. B 126 (1983) 5, pp.338-410, doi:10.1016/0370-2693(83)90188-0.

[4] UA2 Collaboration, *Evidence for* $Z^0 \rightarrow e^+e^-$ *at the CERN pp collider* - 1983, Phys. Lett. B 129 (1983) 1-2, pp.130-140, doi:10.1016/0370-2693(83)90744-X.

[5] D0 Collaboration, *Observation of the Top Quark* - 1995, Phys. Rev. Lett. 74, 2632, doi:10.1103/PhysRevLett.74.2632.

[6] CDF Collaboration, *Observation of Top Quark Production in* $\bar{p}p$ *Collisions with the Collider Detector at Fermilab* - 1995, Phys. Rev. Lett. 74, 2626, doi:10.1103/PhysRevLett.74.2626.

[7] Hasert, F.J. et al., *Observation of Neutrino-Like Interactions Without Muon or Electron in the Gargamelle Neutrino Experiment* - 1973, Phys. Lett. B. 46 (1973) 138.

[8] Higgs, P.W., *Broken Symmetries and the Masses of Gauge Bosons* - 1964, Phys. Rev. Lett. 13, 508, doi:10.1103/PhysRevLett.13.508.

[9] Brout, R. and Englert, F., *Broken Symmetry and the Mass of Gauge Vector Mesons* - 1964, Phys. Rev. Lett. 13, 321, doi:10.1103/PhysRevLett.13.321.

[10] Guralnik, G.S., Hagen, C.R. and Kibble, T.W.B., *Global Conservation Laws and Massless Particles* - 1964, Phys. Rev. Lett. 13, 585, doi:10.1103/PhysRevLett.13.585.

[11] Bruning, O.S. et al., *LHC Design Report* - 2004, CERN-2004-003-V-1.

[12] The ATLAS Collaboration, *The ATLAS Experiment at the CERN Large Hadron Collider* - 2008, JINST 3 S08003, doi:10.1088/1748-0221/3/08/S08003.

[13] The CMS Collaboration, *The CMS Experiment at the CERN LHC* - 2008, JINST 3 S08004, doi:10.1088/1748-0221/3/08/S08003.

[14] The ATLAS Collaboration, *Observation of a new particle in the search for the Standard Model Higgs boson with the ATLAS detector at the LHC* - 2012, Phys.Lett. B 716 (2012) 1-29, arXiv:1207.7214 [hep-ex].

[15] The CMS Collaboration, *Observation of a new boson at a mass of 125 GeV with the CMS experiment at the LHC* - 2012, Phys. Lett. B 716 (2012) 30, arXiv:1207.7235 [hep-ex].

[16] The CMS Collaboration, *Observation of the diphoton decay of the Higgs boson and measurement of its properties* - 2014, Eur. Phys. J. C(2014) 74:3076, arXiv:1407.0558v2 [hep-ex].

[17] The ATLAS Collaboration, *Measurements of Higgs boson production and couplings in diboson final states with the ATLAS detector at the LHC* - 2013, Phys. Lett. B 726 (2013) 88-119, doi:10.1016/j.physletb.2013.08.010.

[18] The ATLAS Collaboration, *Observation and measurement of Higgs boson decays to WW^* with the ATLAS detector* - 2015, Phys. Rev. D 92, 012006, doi:10.1103/PhysRevD.92.012006.

[19] The ATLAS Collaboration, *Measurements of the Higgs boson production and decay rates and constraints on its couplings from a combined ATLAS and CMS analysis of the LHC pp collision data at $\sqrt{s} = 7$ and 8 TeV* - 2016, JHEP08(2016)045.

[20] The ATLAS Collaboration, *Observation of $H \to b\bar{b}$ decays and VH production with the ATLAS detector* - 2018, arXiv:1808.08238 [hep-ex].

[21] The ATLAS Collaboration, *Search for the Decay of the Higgs Boson to Charm Quarks with the ATLAS Experiment* - 2018, Phys. Rev. Lett. 120, 211802, arXiv:1802.04329 [hep-ex].

[22] The ATLAS Collaboration, *Search for the exclusive Higgs and Z boson decays to $\phi\gamma$ and $\rho\gamma$ with the ATLAS detector* - 2017, arXiv:1712.02758v1 [hep-ex].

[23] The ATLAS Collaboration, *Searches for exclusive Higgs and Z boson decays into $J/\psi\gamma, \psi(2S)\gamma$, and $\upsilon(nS)\gamma$ at $\sqrt{s} = 13$ TeV with the ATLAS detector* - 2018, doi:10.1016/j.physletb.2018.09.024.

[24] Djouadi, A., *The Anatomy of Electro-Weak Symmetry Breaking. II: The Higgs bosons in the Minimal Supersymmetric Model* - 2005, Phys.Rept.459:1-241,2008, arXiv:hep-ph/0503173 [hep-ph].

[25] The CMS Collaboration, *Search for the Higgs boson decaying to two muons in proton-proton collisions at* $\sqrt{s}$ *= 13 TeV* - 2018, Submitted to Phys. Rev. Lett., arXiv:1807.06325 [hep-ex].

[26] The ATLAS Collaboration, *Search for the dimuon decay of the Higgs boson in pp collisions at* $\sqrt{s} = 13$ *TeV with the ATLAS detector* - 2017, Phys. Rev. Lett. 119, 051802, arXiv:1705.04582v1 [hep-ex].

[27] The ATLAS Collaboration, *A search for the rare decay of the Standard Model Higgs boson to dimuons in pp collisions at* $\sqrt{s} = 13$ *TeV with the ATLAS Detector* - 2018, ATLAS-CONF-2018-026.

[28] BESIII Collaboration, *Observation of a charged charmoniumlike structure in* $e^+e^- \to \pi^+\pi^- J/\psi$ *at* $\sqrt{s} = 4.26$ *GeV* - 2013, Phys. Rev. Lett. 110, 252001, arXiv:1303.5949 [hep-ex].

[29] Belle Collaboration, *Study of* $e^+e^- \to \pi^+\pi^- J/\psi$ *and Observation of a Charged Charmonium-like State at Belle* - 2013, Phys. Rev. Lett. 110, 252002, arXiv:1304.0121 [hep-ex].

[30] BESIII Collaboration, *Observation of* $Z_C(3900)^0$ *in* $e^+e^- \to \pi^0\pi^0 J/\psi$ - 2015, Phys. Rev. Lett. 115, 112003, arXiv:1506.06018 [hep-ex].

[31] LHCb Collaboration, *Observation of* $J/\psi p$ *resonances consistent with pentaquark states in* $\Lambda_b^0 \to J/\psi K^- p$ *decays* - 2015, Phys. Rev. Lett. 115, 072001, arXiv:1507.03414 [hep-ex].

[32] M. Tanabashi et al. (Particle Data Group), *The Review of Particle Physics* - 2018, Phys. Rev. D 98, 030001.

[33] Hamilton, K., *The Standard Model Part II* - 2015, Lecture Notes, Unpublished

[34] Goldstone, J., Salam, A. and Weinberg, S., *Broken Symmetries* - 1962, Phys.Rev. 127 (1962) pp. 965-970, doi:10.1103/PhysRev.127.965.

[35] Thomson, M., *Modern Particle Physics* - 2013, Cambridge University Press.

[36] Feynman, R. P., *Very High-Energy Collisions of Hadrons* - 1969, Phys. Rev. Lett. 23 (1969), pp.1415 - 1417, doi:10.1103/PhysRevLett.23.1415.

[37] Collins, J.C., Soper, D.E. and Sterman, G., *Factorization of Hard Processes in QCD* - 1988, Adv.Ser.Direct.High Energy Phys.5:1-91 - arXiv:hep-ph/0409313v1.

[38] The ATLAS Collaboration, *Observation of Higgs boson production in association with a top quark pair at the LHC with the ATLAS detector* - 2018, Phys. Lett. B. 784, pp.173-191, arXiv:1806.00425 [hep-ex].

[39] The ATLAS Collaboration, *Combined measurement of differential and total cross sections in the $H \to \gamma\gamma$ and the $H \to ZZ^* \to 4l$ decay channels at $\sqrt{s} = 13$ TeV with the ATLAS detector* - 2018, Submitted to Phys. Lett. B., arXiv:1805.10197 [hep-ex].

[40] The ATLAS Collaboration, *Measurements of gluon-gluon fusion and vector-boson fusion Higgs boson production cross-sections in the $H \to WW^* \to e\nu\mu\nu$ decay channel in pp collisions at $\sqrt{s} = 13$ TeV with the ATLAS detector* - 2018, Submitted to Phys. Lett. B., arXiv:1808.09054v1 [hep-ex] .

[41] The ATLAS Collaboration, *Measurements of Higgs boson properties in the diphoton decay channel with 36 fb^{-1} of pp collision data at $\sqrt{s} = 13$ TeV with the ATLAS detector* - 2018, Phys. Rev. D 98, 052005, arXiv:1802.04146 [hep-ex].

[42] D. de Florian et al., *Handbook of LHC Higgs Cross Sections: 4. Deciphering the Nature of the Higgs Sector* - 2016, arXiv:1610.07922 [hep-ph].

[43] The ATLAS Collaboration, *Measurement of $W^{\pm}$ and Z-boson production cross sections in pp collisions at $\sqrt{s} = 13$ TeV with the ATLAS detector* - 2016, Phys. Lett. B 759 (2016) 601, arXiv:1603.09222 [hep-ex].

[44] The ATLAS Collaboration, *Measurement of the $t\bar{t}$ production cross-section using e events with b-tagged jets in pp collisions at $\sqrt{s} = 13TeV$ with the ATLAS detector* - 2016, Phys. Lett. B. 761, pp.136-157, doi:10.1016/j.physletb.2016.08.019.

[45] The ATLAS Collaboration, *Measurement of the cross-section for producing a W boson in association with a single top quark in pp collisions at $\sqrt{s} = 13$ TeV with ATLAS* - 2018, JHEP01 (2018) 063, arXiv:1612.07231 [hep-ex].

[46] The ATLAS Collaboration, *Measurement of the W^+W production cross section in pp collisions at a centre-of-mass energy of $\sqrt{s} = 13$ TeV with the ATLAS experiment* - 2017, Phys. Lett. B. 773, pp.354-374, arXiv:1702.04519 [hep-ex].

[47] The ATLAS Collaboration, *Measurement of the $W^{\pm}Z$ boson pair-production cross section in pp collisions at $\sqrt{s} = 13$ TeV with the ATLAS detector* - 2016, Phys. Lett. B. 762, pp.1-22, arXiv:1606.04017 [hep-ex].

[48] The ATLAS Collaboration, *$ZZ \to l^+l^-l^+l^-$ cross-section measurements and search for anomalous triple gauge couplings in 13 TeV pp collisions with the ATLAS detector* - 2018, Phys. Rev. D 97, 032005, arXiv:1709.07703 [hep-ex].

[49] The CMS Collaboration, *Electroweak production of two jets in association with a Z boson in proton-proton collisions at* $\sqrt{s} = 13$ *TeV* - 2018, Eur. Phys. J. C (2018) 78: 589, arXiv:1712.09814 [hep-ex].

[50] LHC Higgs Cross Section Working Group, *Handbook of LHC Higgs cross sections: 3. Higgs Properties* - 2013, pp.264, arXiv:1307.1347v2 [hep-ph].

[51] The ATLAS Collaboration, *Combined measurements of Higgs boson production and decay using up to 80* fb^{-1} *of proton-proton collision data at* $\sqrt{s} = 13$ *TeV collected with the ATLAS experiment* - 2018, ATLAS-CONF-2018-031.

[52] LHC Higgs Cross Section Working Group, *LHC HXSWG interim recommendations to explore the coupling structure of a Higgs-like particle* - 2012, arXiv:1209.0040 [hep-ph].

[53] The ATLAS and CMS Collaborations, *Combined measurement of the Higgs boson mass in pp collisions at* $\sqrt{s}$ *= 7 and 8 TeV with the ATLAS and CMS experiments* - 2015, Phys. Rev. Lett. 114 (2015) 191803, arXiv:1503.07589 [hep-ex].

[54] The ATLAS Collaboration, *Measurement of the Higgs boson mass in the* $H \to ZZ^* \to 4l$ *and* $H \to \gamma\gamma$ *channe;s with* $\sqrt{s} = 13$ *TeV pp collisions using the ATLAS detector* - 2018, Phys. Lett. B. 784, pp.345-366, arXiv:1806.00242 [hep-ex].

[55] The CMS Collaboration, *Measurements of properties of the Higgs boson decaying into the four-lepton final state in pp collisions at* $\sqrt{s} = 13$ *TeV* - 2017, J. High Energ. Phys. (2017) 2017: 47, arXiv:1706.09936v2 [hep-ex].

[56] The ATLAS Collaboration, *Constraints on off-shell Higgs boson production and the Higgs boson total width in* $ZZ \to 4l$ *and* $ZZ \to 2l2\nu$ *final states with the ATLAS detector* - 2018, arXiv:1808.01191v2 [hep-ex].

[57] The CMS Collaboration, *Search for Higgs boson off-shell production in proton-proton collisions at 7 and 8 TeV and derivation of constraints on its total decay width* - 2016, J. hHgh Energy Phys. 09 (2016) 051, arXiv:1605.02329 [hep-ex].

[58] The ATLAS Collaboration, *Study of the spin and parity of the Higgs boson in diboson decays with the ATLAS detector* - 2015, Eur. Phys. J. C (2015) 75: 476, arXiv:1506.05669 [hep-ex].

[59] The CMS Collaboration, *Constraints on the spin-parity and anomalous HVV couplings of the Higgs boson in proton collisions at 7 and 8 TeV* - 2015, Phys. Rev. D 92, 012004, arXiv:1411.3441 [hep-ex].

[60] Evans, L. and Bryant, P., *The CERN Large Hadron Collider: Accelerator and Experiments - LHC Machine* - 2008, JINST 3 S08001, doi:10.1088/1748-0221/3/08/S08001.

[61] Caron, J.L., *LHC Layout. Schema general du LHC.* - 1997, LHC-PHO-1997-060.

[62] Benedikt, M. et. al (CERN), *LHC Design Report Volume III The LHC Injector Chain* - 2004, doi:10.5170/CERN-2004-003-V-3.

[63] Haffner, J., *The CERN accelerator complex* - 2013, OPEN-PHO-ACCEL-2013-056

[64] Pequenao, J. and Schaffner, P., *An computer generated image representing how ATLAS detects particles* - 2013, CERN-EX-1301009.

[65] Strauss, E., *Online measurement of LHC beam parameters with the ATLAS High Level Trigger* - 2012, Journal of Physics: Conference Series, Vol. 368, 1., pp.1, doi:10.1088/1742-6596/368/1/012003.

[66] Dankers, R.J., *The Physics Performance Of And Level 2 Trigger For The Inner Detector of ATLAS* - 1998, Universiteit Twente, Chapter 3 pp.35-36.

[67] Goodson, J., http://www.jetgoodson.com/images/thesisImages/magnetSystems.png Accessed 18/07/2018.

[68] The ATLAS Collaboration, *ATLAS Insertable B-Layer Technical Design Report* - 2010, CERN-LHCC-2010-013, ATLAS-TDR-19.

[69] The ATLAS Collaboration, *Performance of the ATLAS track reconstruction algorithms in dense environments in LHC Run 2* - 2017, doi:10.1140/epjc/s10052-017-5225-7.

[70] The ATLAS Collaboration, *Z to ee mass distribution for early 2018 data* - 2018, EGAM-2018-003.

[71] The ATLAS Collaboration, *Jet energy scale measurements and their systematic uncertainties in proton-proton collisions at* $\sqrt{s} = 13$ *TeV with the ATLAS detector* - 2017, arXiv:1703.09665 [hep-ex].

[72] Palestini, S., *The Muon Spectrometer of the ATLAS Experiment* - 2003, Nuclear Physics B., Vol. 125, pp. 337-345, doi:10.1016/S0920-5632(03)91013-9.

[73] Junggeburth, J.J. et al., *MCP preliminary public plots based on 2018 data* - 2018, ATL-COM-PHYS-2018-1236.

[74] A Ruiz Martinez and The ATLAS Collaboration, *The Run-2 ATLAS Trigger System* - 2016, J.Phys.: Conf. Ser. 762 012003, doi:10.1088/1742-6596/762/1/012003.

[75] Achenbach, R. et al., *The ATLAS Level-1 Calorimeter Trigger* - 2008, JINST 3 P03001.

[76] Morgenstern, M.M., *Performance of the ATLAS Muon Trigger in Run 2* - 2017, ATL-DAQ-PROC-2017-046.

[77] The ATLAS Collaboration, *Performance of the ATLAS trigger system in 2015* - 2017, doi:10.1140/epjc/s10052-017-4852-3 .

[78] Bona, M. et al., *Level 1 Calorimeter Trigger Efficiencies and Rates Optimisation* - 2018, ATL-COM-DAQ-2017-186.

[79] ATLAS Data Quality Group, *Good Run Lists for Analysis Run-2* - https://twiki.cern.ch/twiki/bin/viewauth/AtlasProtected/GoodRunListsForAnalysisRun2, Accessed 01/08/2018.

[80] Agostinelli, S. et al., *GEANT4 - A Simulation Toolkit* - 2003, Nuclear Instruments and Methods in Physics Vol. 506, Issue 3, pp. 250-303, doi:10.1016/S0168-9002(03)01368-8.

[81] LHC Higgs Cross Section Working Group, *Handbook of LHC Higgs Cross Sections: 1. Inclusive Observables* - 2011, pp.78, arXiv:1101.0593 [hep-ph].

[82] Djouadi, A., Kalinowski, J. and Spira, M., *HDECAY: a Program for Higgs Boson Decays in the Standard Model and its Supersymmetric Extension* - 1998, Comput.Phys.Commun.108:56-74, arXiv:hep-ph/9704448.

[83] Djouadi, A., Kalinowski, J., Mühlleitner and Spira, M., *THE TOOLS AND MONTE CARLO WORKING GROUP Summary Report from the Les Houches 2009 Workshop on TeV Colliders - An update on the program HDECAY* - 2009, arXiv:1003.1643 [hep-ph].

[84] Frixione, S., Nason, P. and Oleari, C., *Matching NLO QCD computations with Parton Shower simulations: the POWHEG method* - 2007, arXiv:0709.2092 [hep-ph].

[85] Alioli, S., Nason, P., Oleari, C. and Re., E., *A general framework for implementing NLO calculations in shower Monte Carlo programs: the POWHEG BOX* - 2010, arXiv:1002.2581 [hep-ph].

[86] Hamilton, K., Nason, P., Re, E. and Zanderighi, G., *NNLOPS simulation of Higgs boson production* - 2013, arXiv:1309.0017 [hep-ph].

[87] Hamilton, K., Nason, P., Oleari, C. and Zanderighi, G., *Merging H/W/Z + 0 and 1 jet at NLO with no merging scale: a path to parton shower + NNLO matching* - 2013, arXiv:1212.4504 [hep-ph].

[88] Catani, S. and Grazzini, M., *An NNLO subtraction formalism in hadron collisions and its application to Higgs boson production at the LHC* - 2007, arXiv:hep-ph/0703012.

[89] Pumplin, J., Stump, D.R., Huston, J., Lai, H.L., Nadolsky, P. and Tung, W.K., *New Generation of Parton Distributions with Uncertainties from Global QCD Analysis* - 2002, arXiv:hep-ph/0201195.

[90] Sjöstrand, T., Mrenna, S. and Skands, P., *A Brief Introduction to PYTHIA 8.1* - 2007, arXiv:0710.3820 [hep-ph].

[91] The ATLAS Collaboration, *Measurement of the $Z/\gamma*$ boson transverse momentum distribution in pp collisions at $\sqrt{s} = 7$ TeV with the ATLAS detector* - 2014, arXiv:1406.3660 [hep-ex].

[92] Anastasiou, C. et al. *High precision determination of the gluon fusion Higgs boson cross-section at the LHC* - 2016, arXiv:1602.00695 [hep-ph].

[93] Actis, S., Passarino, G., Sturm, C. and Uccirati, S., *NLO Electroweak Corrections to Higgs Boson Production at Hadron Colliders* - 2008, arXiv:0809.1301 [hep-ph].

[94] Butterworth, J. et al., *PDF4LHC recommendations for LHC Run II* - 2015, arXiv:1510.03865 [hep-ph].

[95] Martin, A.D., Roberts, R.G., Stirling, W.J. and Thorne, R.S., *Uncertainties of predictions from parton distributions. 1: experimental errors* - 2002, arXiv:hep-ph/0211080.

[96] Nason, P. and Oleari, C., *NLO Higgs boson production via vector-boson fusion matched with shower in POWHEG* - 2010, arXiv:0911.5299 [hep-ph].

[97] Bolzoni, P., Maltoni, P., Moch, S.O. and Zaro, M., *Higgs production via vector-boson fusion at NNLO in QCD* - 2010, arXiv:1003.4451 [hep-ph].

[98] Bolzoni, P., Maltoni, P., Moch, S.O. and Zaro, M., *Vector boson fusion at NNLO in QCD: SM Higgs and beyond* - 2012, arXiv:1109.3717 [hep-ph].

[99] Denner, A., Dittmaier, S., Kallweit, S. and Mück, A., *HAWK 2.0: A Monte Carlo program for Higgs production in vector-boson fusion and Higgs strahlung at hadron colliders* - 2014, arXiv:1412.5390 [hep-ph].

[100] Ciccolini, M., Denner, A. and Dittmaier, S., *Strong and electroweak corrections to the production of Higgs+2jets via weak interactions at the LHC* - 2007, arXiv:0707.0381 [hep-ph].

[101] Ciccolini, M., Denner, A. and Dittmaier, S., *Electroweak and QCD corrections to Higgs production via vector-boson fusion at the LHC* - 2007, arXiv:0710.4749 [hep-ph].

[102] Mimasu, K., Sanz, V. and Williams, C., *Higher Order QCD predictions for Associated Higgs production with anomalous couplings to gauge bosons* - 2015, arXiv:1512.02572 [hep-ph].

[103] Brein, O., Harlander, R.V. and Zirke, T. J. E., *vh@nnlo - Higgs Strahlung at hadron colliders* - 2012, arXiv:1210.5347 [hep-ph].

[104] Denner, A., Dittmaier, S., Kallweit, S. and Mück, A., *Electroweak corrections to Higgs-strahlung off W/Z bosons at the Tevatron and the LHC with HAWK* - 2011, arXiv:1112.5142 [hep-ph].

[105] Altenkamp, L. et al., *Gluon-induced Higgs-strahlung at next-to-leading order QCD* - 2012, arXiv:1211.5015 [hep-ph].

[106] Alwall, J. et al., *The automated computation of tree-level and next-to-leading order differential cross sections, and their matching to parton shower simulations* - 2014, arXiv:1405.0301 [hep-ph].

[107] Alwall, J. et al., *MadGraph 5 : Going Beyond* - 2011, arXiv:1106.0522 [hep-ph].

[108] The NNPDF Collaboration, *Parton distributions with LHC data* - 2012, arXiv:1207.1303 [hep-ph].

[109] Beenakker, W. et al., *NLO QCD corrections to t anti-t H production in hadron collisions* - 2002, arXiv:hep-ph/0211352.

[110] Dawson, S. et al., *Associated Higgs production with top quarks at the Large Hadron Collider: NLO QCD corrections* - 2003, arXiv:hep-ph/0305087.

[111] Yu, Z. et al., *QCD NLO and EW NLO corrections to $t\bar{t}H$ production with top quark decays at hadron collider* - 2014, arXiv:1407.1110 [hep-ph].

[112] Gleisberg, T. et al., *Event generation with SHERPA 1.1* - 2008, arXiv:0811.4622 [hep-ph].

[113] The NNPDF Collaboration, *Parton distributions for the LHC Run II* - 2014, arXiv:1410.8849 [hep-ph].

[114] ATLAS Experiment © 2018 CERN.

[115] Cowan, G., Cranmer, K., Gross, E. and Vitells, O. *Asymptotic formulae for likelihood-based tests for new physics* - 2013, arXiv:1007.1727 [physics.data-an].

[116] A. Hoecker et al., *TMVA - Toolkit for Multivariate Data Analysis* - 2007, arXiv:physics/0703039 [physics.data-an].

[117] . Brun, R. and Rademakers, F., *ROOT - An Object Oriented Data Analysis Framework* - 1997, Nuclear Instruments and Methods in Physics Research A 389, pp. 81-86. doi:10.1016/S0168-9002(97)00048-X.

[118] Friedman, J., *Greedy Function Approximation: A Gradient Boosting Machine* - 2001, The Annals of Statistics, Vol. 29, No. 5, pp. 1189-1232, JSTOR.

[119] The ATLAS Collaboration, *Muon reconstruction performance of the ATLAS detector in proton-proton collision data at* $\sqrt{s} = 13\ TeV$ - 2016, arXiv:1603.05598 [hep-ex].

[120] The ATLAS Collaboration, *Topological cell clustering in the ATLAS calorimeters and its performance in LHC Run 1* - 2017, arXiv:1603.02934 [hep-ex].

[121] Cacciari, M., Salam, G. and Soyez, G., *The anti-k_t jet clustering algorithm* - 2008, arXiv:0802.1189v2 [hep-ph].

[122] The ATLAS Collaboration, *Selection of jets produced in 13 TeV proton-proton collisions with the ATLAS detector* - 2015, ATLAS-CONF-2015-029.

[123] The ATLAS Collaboration, *Tagging and suppression of pileup jets with the ATLAS detector* - 2014, ATLAS-CONF-2014-018.

[124] The ATLAS Collaboration, *Expected performance of the ATLAS b-tagging algorithms in Run02* - 2015, ATL-PHYS-PUB-2015-022.

[125] The ATLAS Collaboration, *Electron efficiency measurements with the ATLAS detector using the 2015 LHC proton-proton collision data* - 2016, ATLAS-CONF-2016-024.

[126] The ATLAS Collaboration, *Performance of missing transverse momentum reconstruction with the ATLAS detector using proton-proton collisions at* $\sqrt{s} = 13\ TeV$ - 2018, arXiv:1802.08168v2 [hep-ex] .

[127] The ATLAS Collaboration, *Measurement of the Drell-Yan triple-differential cross section in pp collisions at* $\sqrt{s} = 8\ TeV$ - 2017, J. High Energ. Phys. (2017) 2017: 59, doi.org/10.1007/JHEP12(2017)059.

[128] Matsumoto, M. and Nishimura, T., *Mersenne Twister: a 623-dimensionally equidistributed uniform pseudo-random number generator* - 1998, ACM Transactions on Modeling and Computer Simulation, Vol. 8 Issue 1, pp. 3-30, doi:10.1145/272991.272995.

[129] The ATLAS Collaboration, *Search for the Standard Model Higgs boson decay to* $\mu^+\mu^-$ *with the ATLAS detector* - 2014, arXiv:1406.7663 [hep-ex].

[130] Verkerke, W. and Kirkby, D., *The RooFit toolkit for data modeling* - 2003, arXiv:physics/0306116 [physics.data-an].

[131] The ATLAS Collaboration, *Luminosity determination in pp collisions at* $\sqrt{s} = 8$ *TeV using the ATLAS detecotr at the LHC* - 2016, arXiv:1608.03953 [hep-ex].

[132] The ATLAS Collaboration, *Measurement of the Inelastic Proton-Proton Cross Section at* $\sqrt{s} = 13$ *TeV with the ATLAS Detector at the LHC* - 2016, arXiv:1606.02625 [hep-ex].

[133] The ATLAS Collaboration, *Jet energy resolution in proton-proton collisions at* $\sqrt{s} = 7$ *TeV recorded in 2010 with the ATLAS detector* - 2012, arXiv:1210.6210v1 [hep-ex] .

[134] The ATLAS Collaboration, *Jet Calibration and Systematic Uncertainties for Jets Reconstructed in the ATLAS Detector at* $\sqrt{s} = 13$ *TeV* - 2016, ATLAS-PHYS-PUB-2015-015.

[135] LHC higgs Cross Section Working Group, *Handbook of LHC Higgs cross sections: 4. Deciphering the nature of the Higgs sector* - 2017, arXiv:1610.07922v2 [hep-ph] .

[136] Read, A.L., *Presentation of search results: the* CL_s *technique* - 2002, J. Phys. G: Nucl. Part. Phys. 28 2693.

[137] The CMS Collaboration, *Measurement of the properties of a Higgs boson in the four-lepton final state* - 2014, arXiv:1312.5353v3 [hep-ex] .

[138] Chen, X., *Prospects of LHC Higgs Physics at the end of Run III* - 2017, ATL-PHYS-PROC-2017-019.

[139] Apollinari, G. et al., *High Luminosity Large Hadron Collider HL-LHC* - 2017, arXiv:1705.08830 [physics.acc-ph].

[140] Dauncey, P.D. et. al., *Handling uncertainties in background shapes: the discrete profiling method* - 2015, arXiv:1408.6865v5 [physics.data-an].

[141] The ATLAS Collaboration, *Prospects for the measurement of the rare Higgs boson decay* $H \to \mu\mu$ *with 3000* fb^1 *of pp collisions collected at* $\sqrt{s} = 14$ *TeV by the ATLAS experiment* - 2018, ATL-PHYS-PUB-2018-006.

Appendix A

Impact of Scale Factors on MC Sample Normalisation

Figures A.0.1 to A.0.18 present the average values of the muon reconstruction, muon isolation, muon TTVA, b-tagging and trigger scale factors used on MC samples in the analysis as functions of $P_T^{\mu,\text{Leading}}$, $P_T^{\mu,\text{Subleading}}$, $P_{\text{T}}^{\mu\mu}$, $\eta^{\mu,\text{Leading}}$, $\eta^{\mu,\text{Subleading}}$, $y^{\mu\mu}$ and $M_{\text{inv}}^{\mu\mu}$. The same distributions for the ggF and Madgraph Drell-Yan samples are shown in Chapter 4. The scale factors have a similar impact on each sample, with the exception of the b-tagging scale factor, which corrects the $t\bar{t}H$ and top sample normalisations by a further 2-3% on average, due to the prominence of b-jets in such processes.

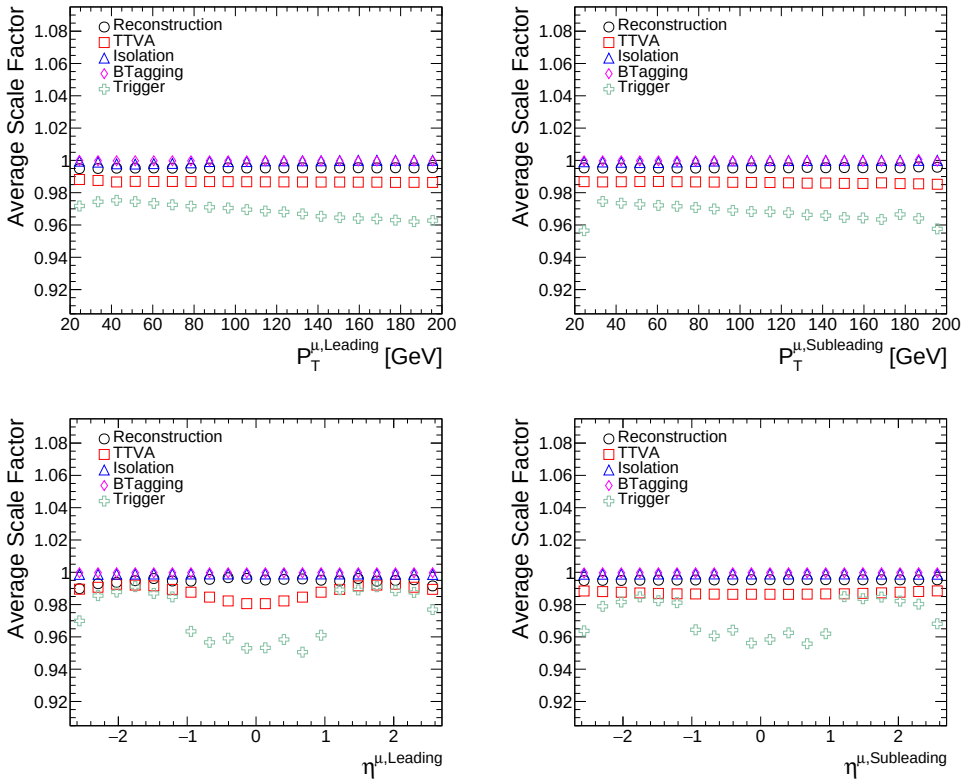

Figure A.0.1: Average values of the muon reconstruction, muon TTVA, muon isolation, b-tagging and trigger scale factors used in the analysis, as a function of $P_T^{\mu,\text{Leading}}$ (top left), $P_T^{\mu,\text{Subleading}}$ (top right), $\eta^{\mu,\text{Leading}}$ (bottom left), and $\eta^{\mu,\text{Subleading}}$ (bottom right) for the VBF MC samples. The full object and event selections detailed in Chapter 6 have been applied, with the exception of the cut on $M_{\text{inv}}^{\mu\mu}$. Only MC statistical errors are shown.

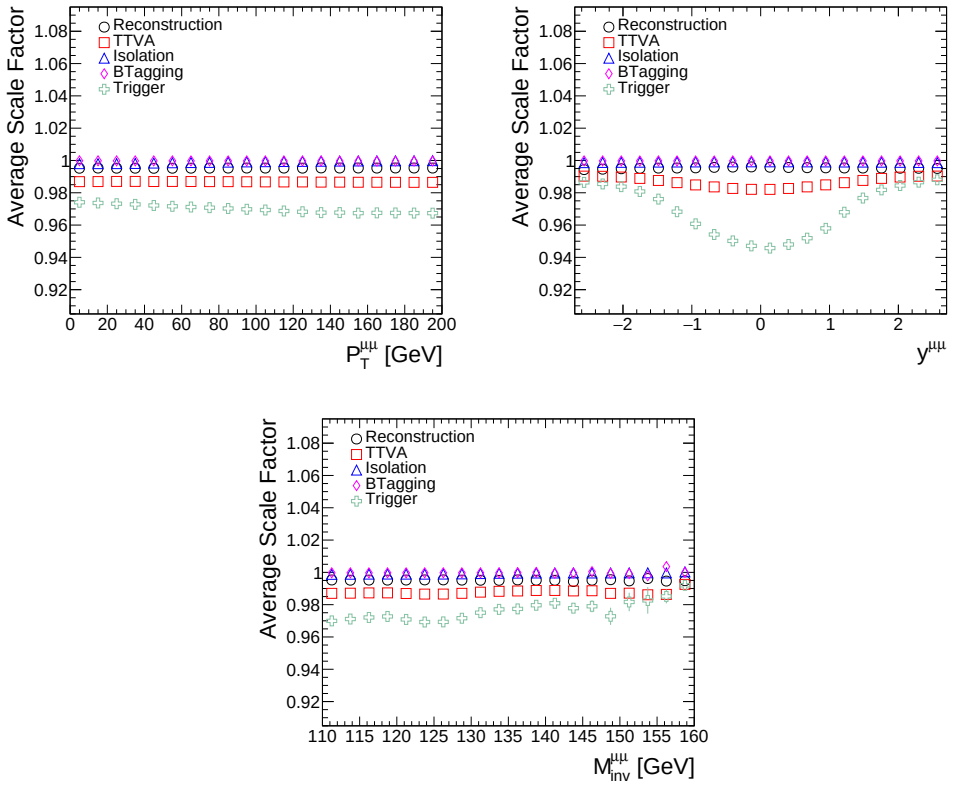

Figure A.0.2: Average values of the muon reconstruction, muon TTVA, muon isolation, b-tagging and trigger scale factors used in the analysis, as a function of $P_{\mathrm{T}}^{\mu\mu}$ (top left), $y^{\mu\mu}$ (top right) and $M_{\mathrm{inv}}^{\mu\mu}$ (bottom) for the VBF MC samples. The full object and event selections detailed in Chapter 6 have been applied, with the exception of the cut on $M_{\mathrm{inv}}^{\mu\mu}$. Only MC statistical errors are shown.

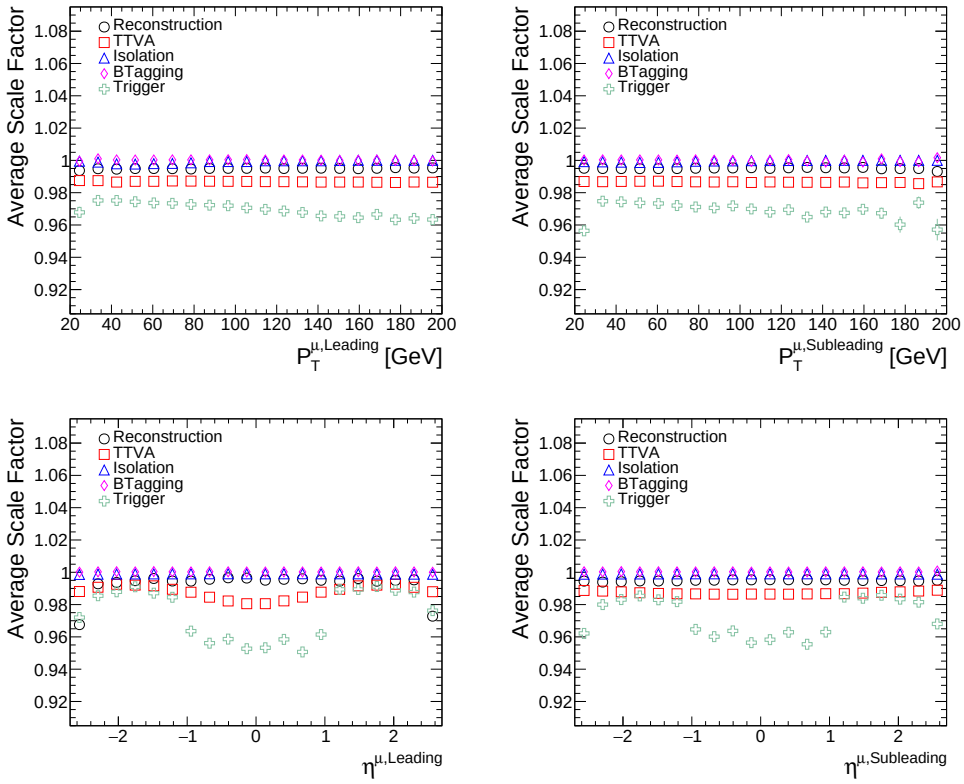

Figure A.0.3: Average values of the muon reconstruction, muon TTVA, muon isolation, b-tagging and trigger scale factors used in the analysis, as a function of $P_T^{\mu,\text{Leading}}$ (top left), $P_T^{\mu,\text{Subleading}}$ (top right), $\eta^{\mu,\text{Leading}}$ (bottom left) and $\eta^{\mu,\text{Subleading}}$ (bottom right) for the VH MC samples. The full object and event selections detailed in Chapter 6 have been applied, with the exception of the cut on $M_{\text{inv}}^{\mu\mu}$. Only MC statistical errors are shown.

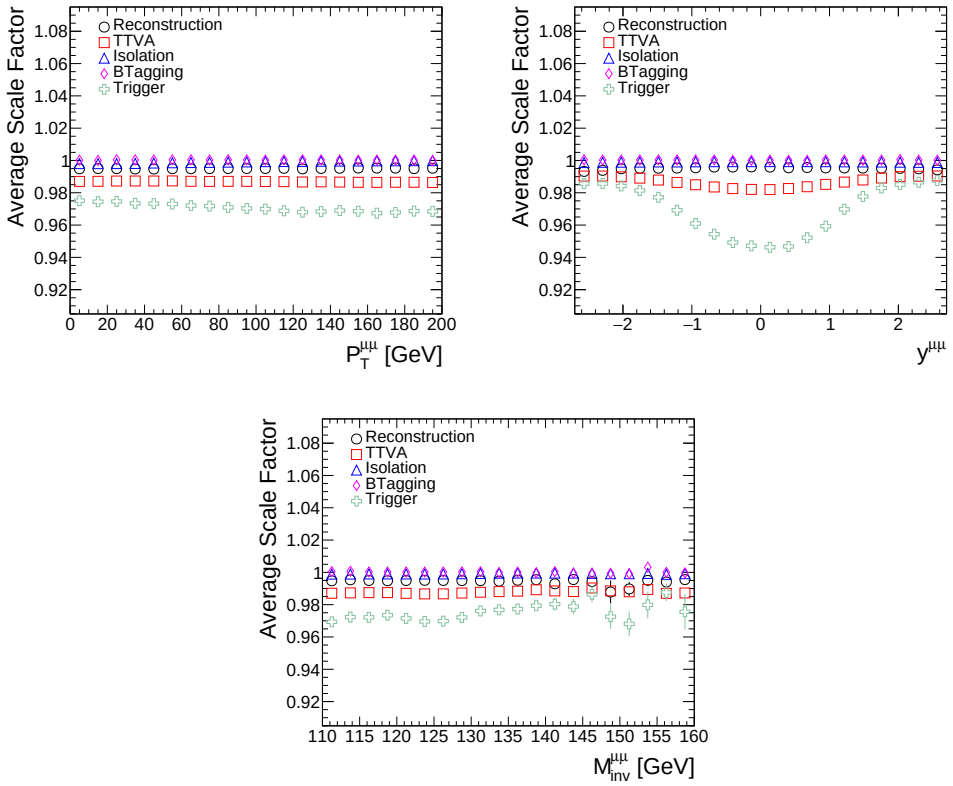

Figure A.0.4: Average values of the muon reconstruction, muon TTVA, muon isolation, b-tagging and trigger scale factors used in the analysis, as a function of $P_{\mathrm{T}}^{\mu\mu}$ (top left), $y^{\mu\mu}$ (top right) and $M_{\mathrm{inv}}^{\mu\mu}$ (bottom) for the VH MC samples. The full object and event selections detailed in Chapter 6 have been applied, with the exception of the cut on $M_{\mathrm{inv}}^{\mu\mu}$. Only MC statistical errors are shown.

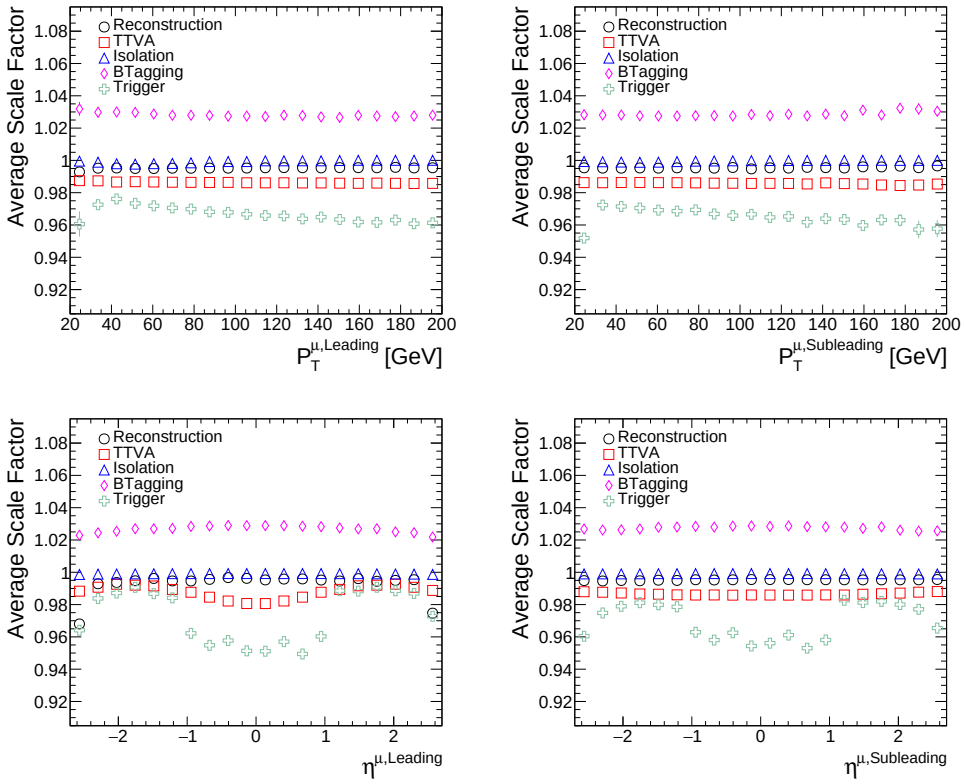

Figure A.0.5: Average values of the muon reconstruction, muon TTVA, muon isolation, b-tagging and trigger scale factors used in the analysis, as a function of $P_T^{\mu,\text{Leading}}$ (top left), $P_T^{\mu,\text{Subleading}}$ (top right), $\eta^{\mu,\text{Leading}}$ (bottom left), and $\eta^{\mu,\text{Subleading}}$ (bottom right) for the $t\bar{t}H$ MC samples. The full object and event selections detailed in Chapter 6 have been applied, with the exception of the cut on $M_{\text{inv}}^{\mu\mu}$. Only MC statistical errors are shown.

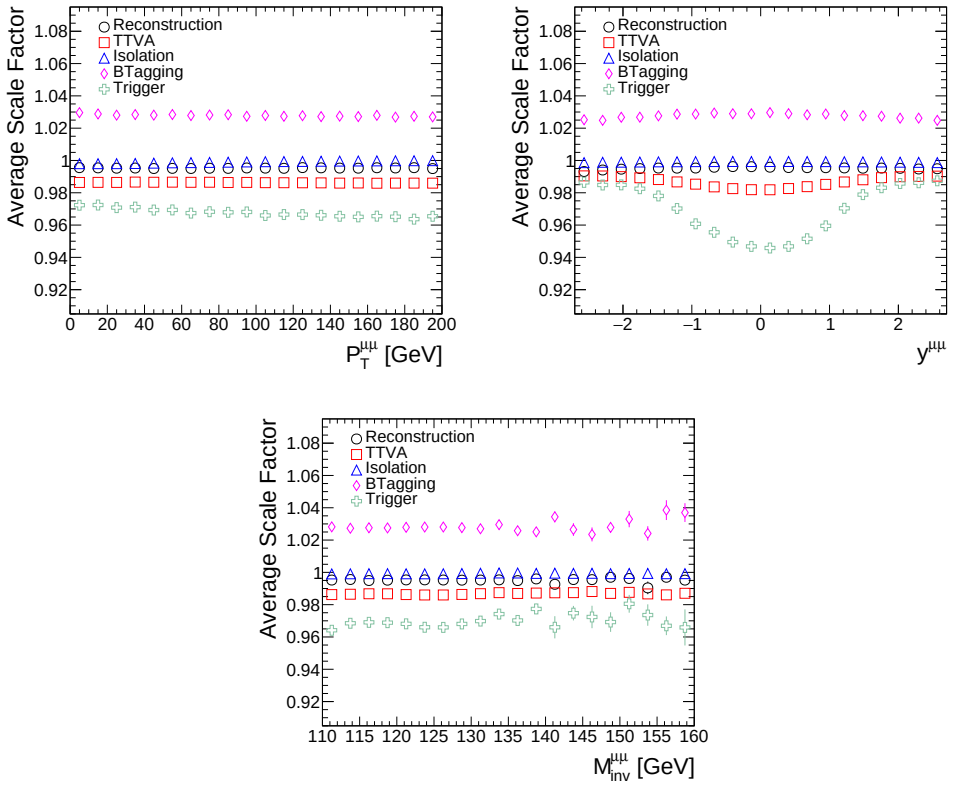

Figure A.0.6: Average values of the muon reconstruction, muon TTVA, muon isolation, b-tagging and trigger scale factors used in the analysis, as a function of $P_{\mathrm{T}}^{\mu\mu}$ (top left), $y^{\mu\mu}$ (top right) and $M_{\mathrm{inv}}^{\mu\mu}$ (bottom) for the $t\bar{t}H$ MC samples. The full object and event selections detailed in Chapter 6 have been applied, with the exception of the cut on $M_{\mathrm{inv}}^{\mu\mu}$. Only MC statistical errors are shown.

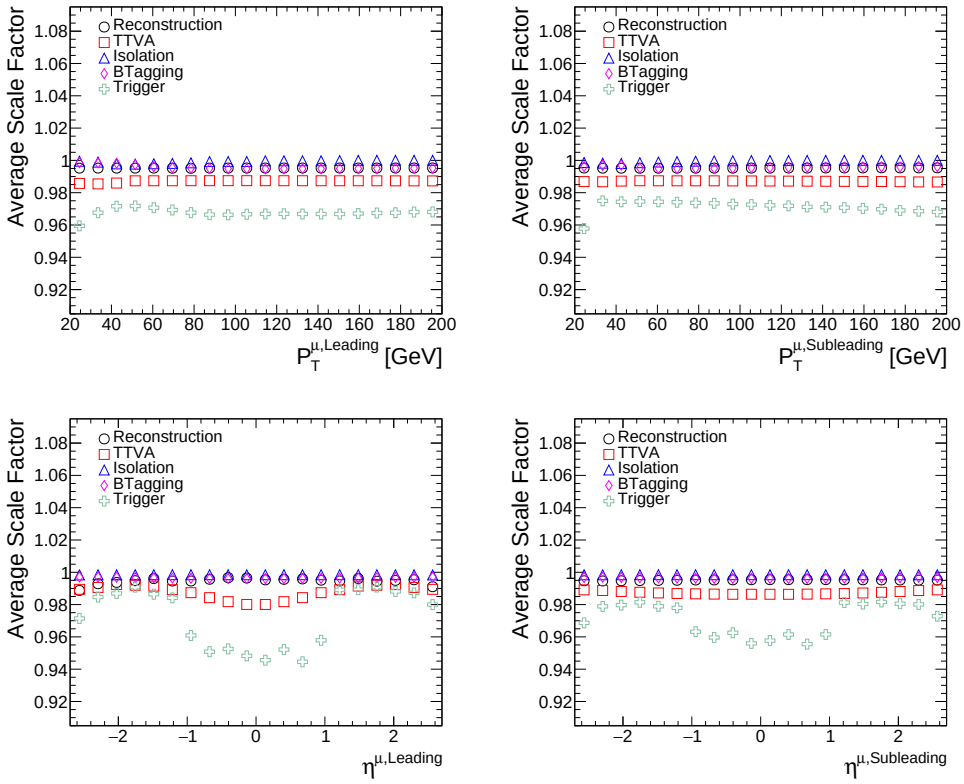

Figure A.0.7: Average values of the muon reconstruction, muon TTVA, muon isolation, b-tagging and trigger scale factors used in the analysis, as a function of $P_T^{\mu,\text{Leading}}$ (top left), $P_T^{\mu,\text{Subleading}}$ (top right), $\eta^{\mu,\text{Leading}}$ (bottom left) and $\eta^{\mu,\text{Subleading}}$ (bottom right) for the Drell-Yan MC samples generated with Sherpa. The full object and event selections detailed in Chapter 6 have been applied, with the exception of the cut on $M_{\text{inv}}^{\mu\mu}$. Only MC statistical errors are shown.

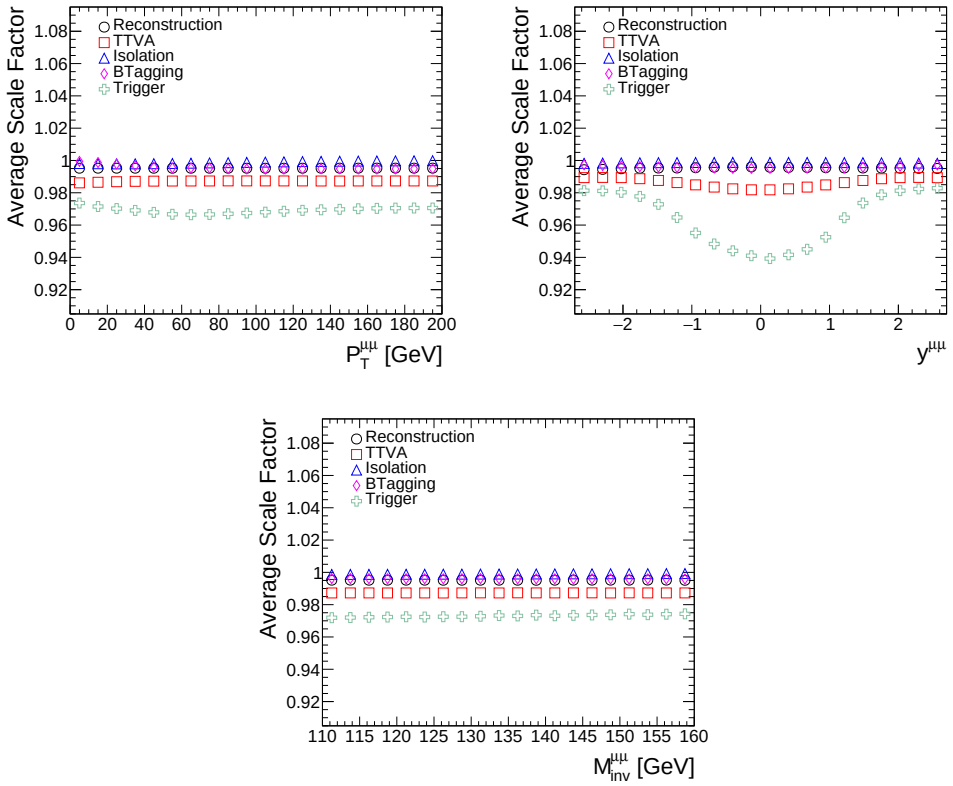

Figure A.0.8: Average values of the muon reconstruction, muon TTVA, muon isolation, b-tagging and trigger scale factors used in the analysis, as a function of $P_{\mathrm{T}}^{\mu\mu}$ (top left), $y^{\mu\mu}$ (top right) and $M_{\mathrm{inv}}^{\mu\mu}$ (bottom) for the Drell-Yan MC samples generated with Sherpa. The full object and event selections detailed in Chapter 6 have been applied, with the exception of the cut on $M_{\mathrm{inv}}^{\mu\mu}$. Only MC statistical errors are shown.

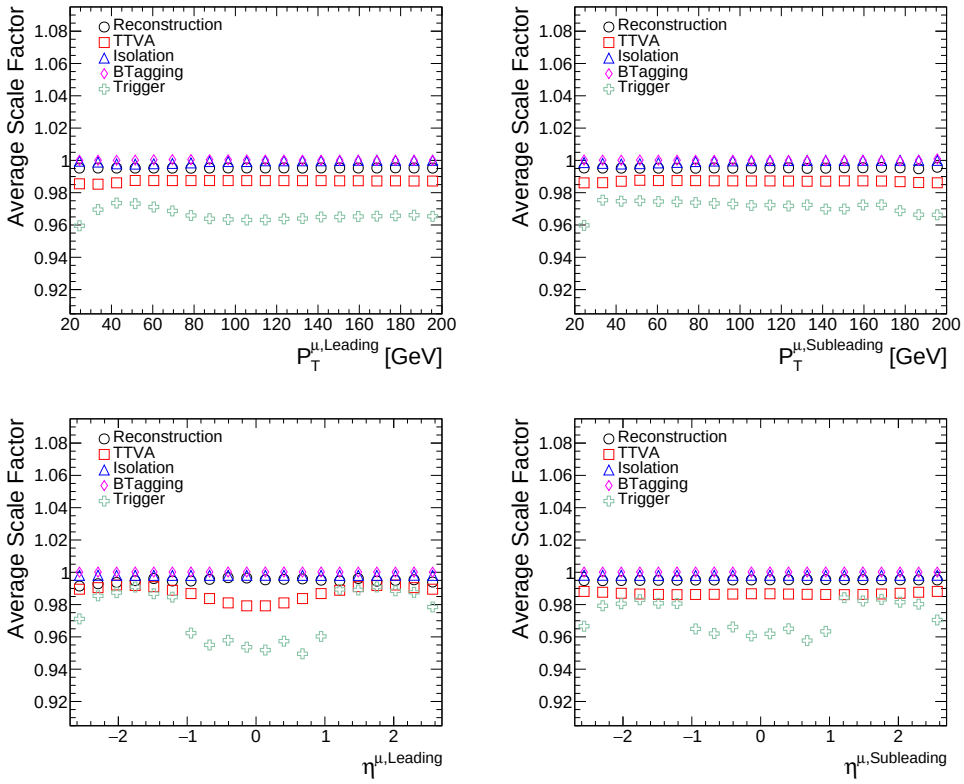

Figure A.0.9: Average values of the muon reconstruction, muon TTVA, muon isolation, b-tagging and trigger scale factors used in the analysis, as a function of $P_T^{\mu,\text{Leading}}$ (top left), $P_T^{\mu,\text{Subleading}}$ (top right), $\eta^{\mu,\text{Leading}}$ (bottom left) and $\eta^{\mu,\text{Subleading}}$ (bottom right) for the Drell-Yan MC samples generated with Powheg. The full object and event selections detailed in Chapter 6 have been applied, with the exception of the cut on $M_{\text{inv}}^{\mu\mu}$. Only MC statistical errors are shown.

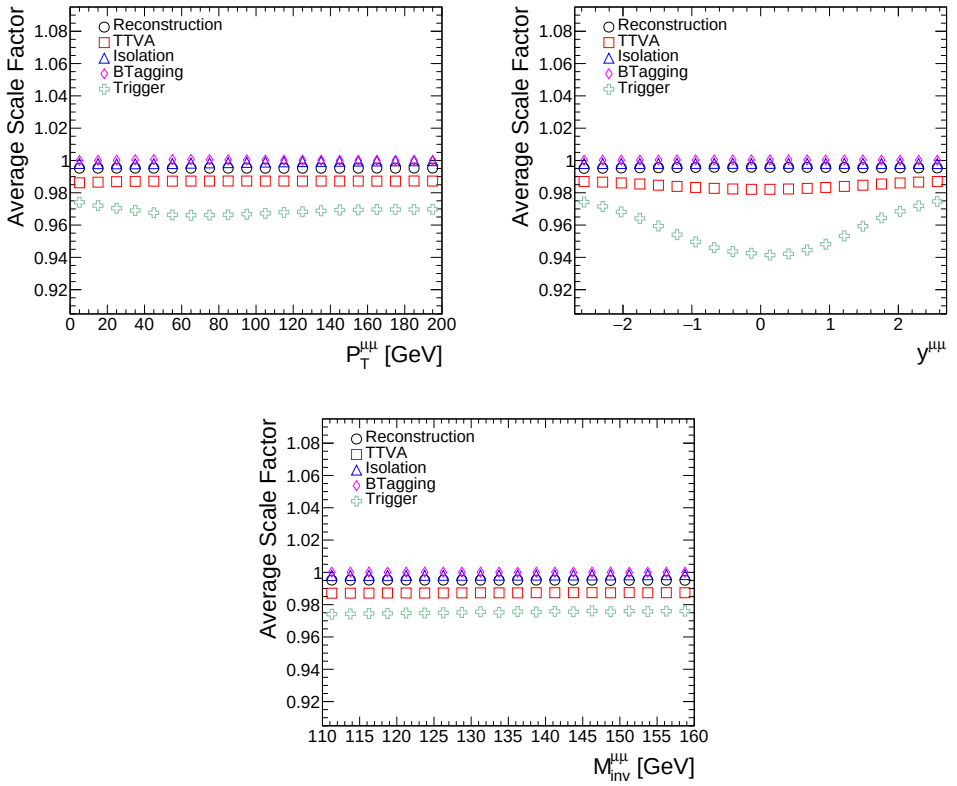

Figure A.0.10: Average values of the muon reconstruction, muon TTVA, muon isolation, b-tagging and trigger scale factors used in the analysis, as a function of $P_{\mathrm{T}}^{\mu\mu}$ (top left), $y^{\mu\mu}$ (top right) and $M_{\mathrm{inv}}^{\mu\mu}$ (bottom) for the Drell-Yan MC samples generated with Powheg. The full object and event selections detailed in Chapter 6 have been applied, with the exception of the cut on $M_{\mathrm{inv}}^{\mu\mu}$. Only MC statistical errors are shown.

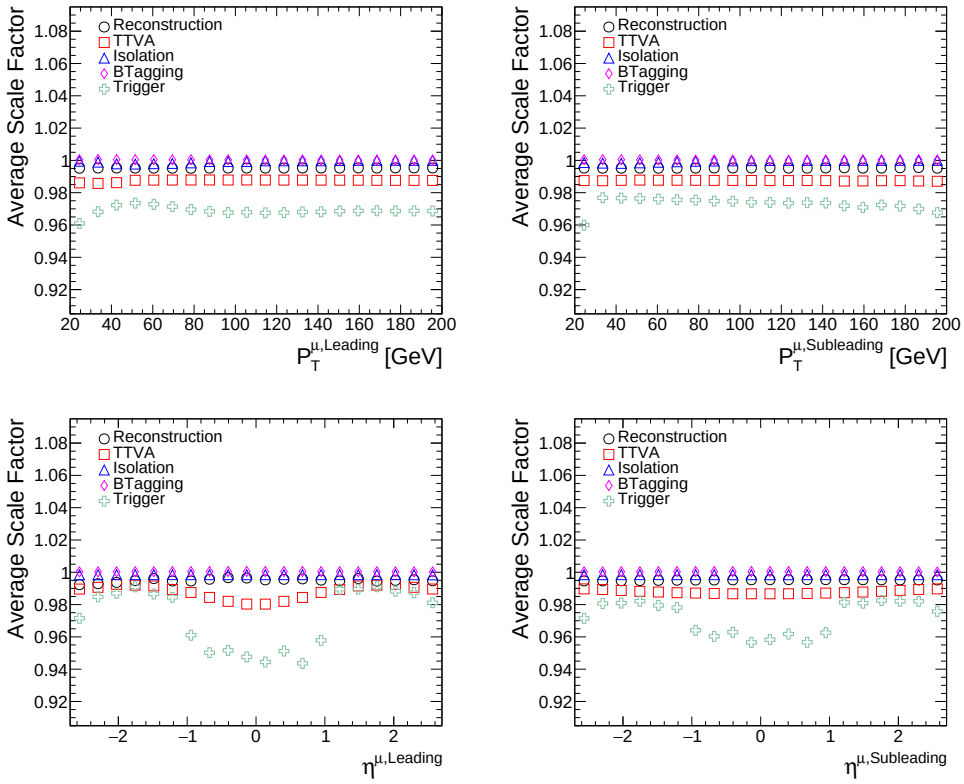

Figure A.0.11: Average values of the muon reconstruction, muon TTVA, muon isolation, b-tagging and trigger scale factors used in the analysis, as a function of $P_T^{\mu,\text{Leading}}$ (top left), $P_T^{\mu,\text{Subleading}}$ (top right), $\eta^{\mu,\text{Leading}}$ (bottom left) and $\eta^{\mu,\text{Subleading}}$ (bottom right) for the Drell-Yan MC samples generated with Madgraph with a VBF filter applied. The full object and event selections detailed in Chapter 6 have been applied, with the exception of the cut on $M_{\text{inv}}^{\mu\mu}$. Only MC statistical errors are shown.

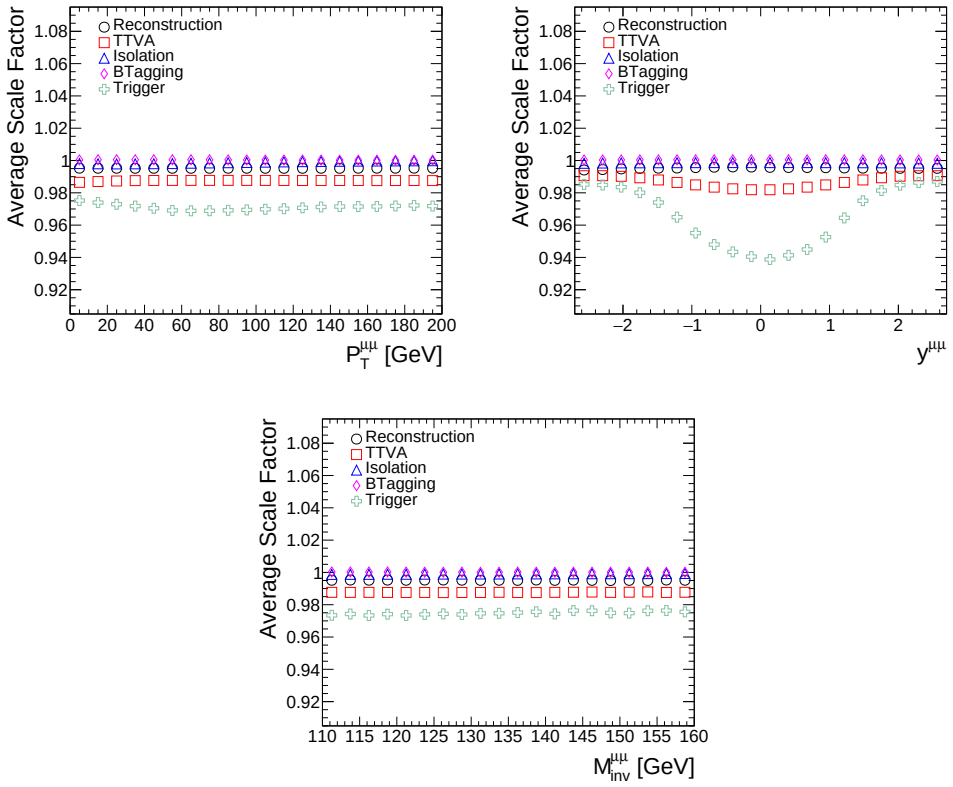

Figure A.0.12: Average values of the muon reconstruction, muon TTVA, muon isolation, b-tagging and trigger scale factors used in the analysis, as a function of $P_{\mathrm{T}}^{\mu\mu}$ (top left), $y^{\mu\mu}$ (top right) and $M_{\mathrm{inv}}^{\mu\mu}$ (bottom) for the Drell-Yan MC samples generated with Madgraph with a VBF filter applied. The full object and event selections detailed in Chapter 6 have been applied, with the exception of the cut on $M_{\mathrm{inv}}^{\mu\mu}$. Only MC statistical errors are shown.

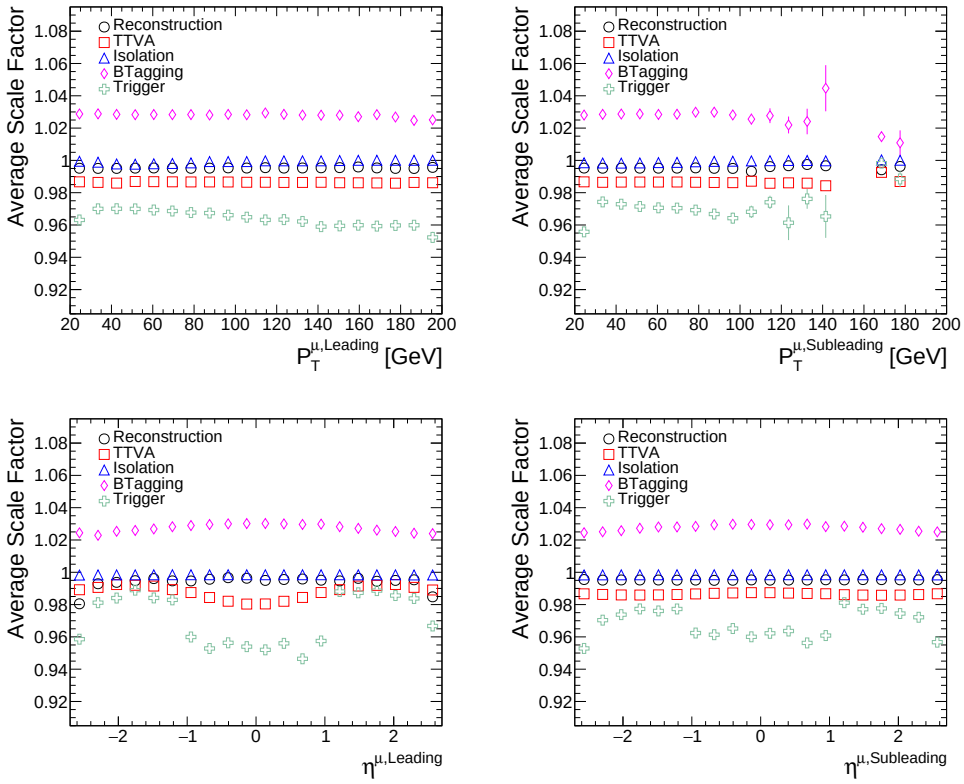

Figure A.0.13: Average values of the muon reconstruction, muon TTVA, muon isolation, b-tagging and trigger scale factors used in the analysis, as a function of $P_T^{\mu,\text{Leading}}$ (top left), $P_T^{\mu,\text{Subleading}}$ (top right), $\eta^{\mu,\text{Leading}}$ (bottom left) and $\eta^{\mu,\text{Subleading}}$ (bottom right) for the top MC samples. The full object and event selections detailed in Chapter 6 have been applied, with the exception of the cut on $M_{\text{inv}}^{\mu\mu}$. Only MC statistical errors are shown.

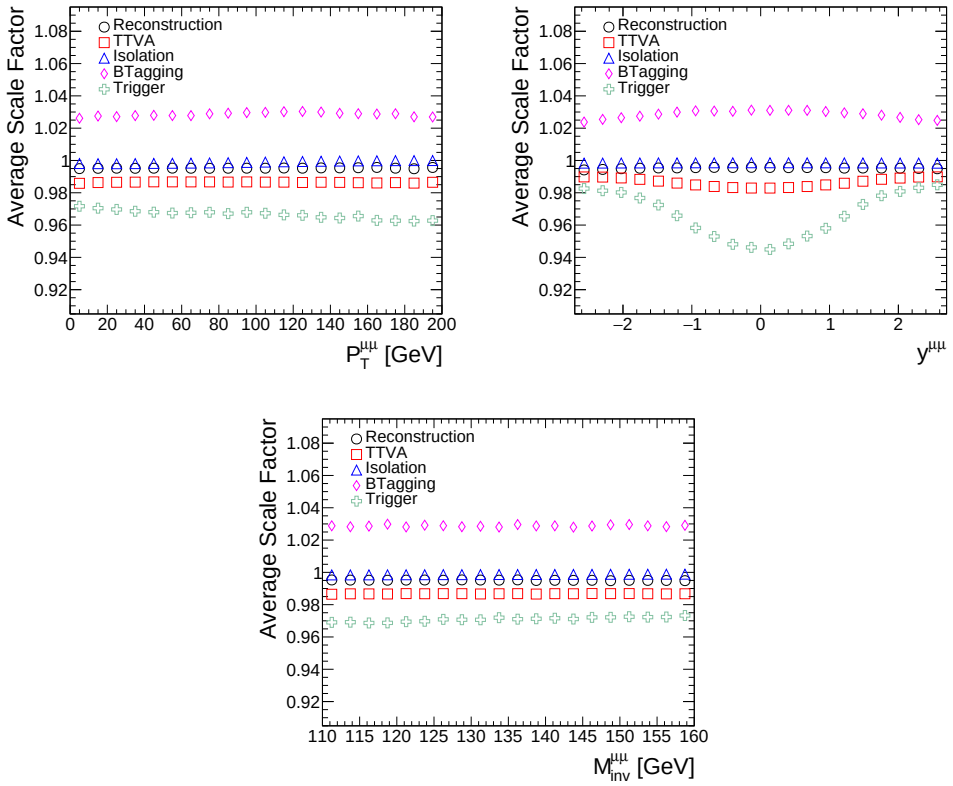

Figure A.0.14: Average values of the muon reconstruction, muon TTVA, muon isolation, b-tagging and trigger scale factors used in the analysis, as a function of $P_{\mathrm{T}}^{\mu\mu}$ (top left), $y^{\mu\mu}$ (top right) and $M_{\mathrm{inv}}^{\mu\mu}$ (bottom) for the top MC samples. The full object and event selections detailed in Chapter 6 have been applied, with the exception of the cut on $M_{\mathrm{inv}}^{\mu\mu}$. Only MC statistical errors are shown.

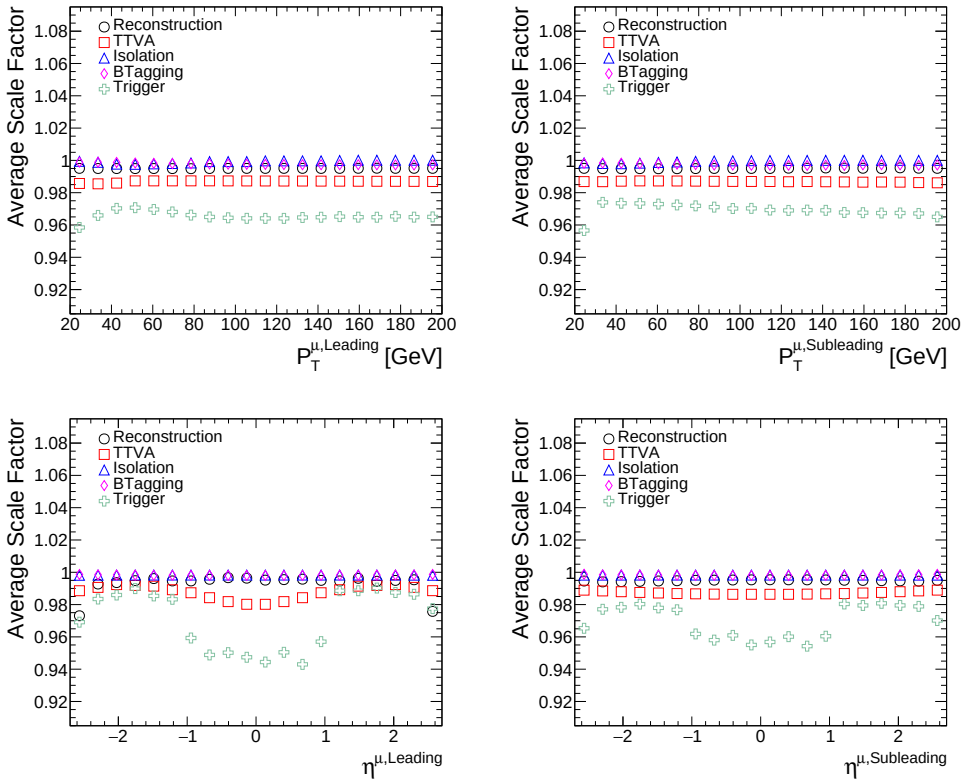

Figure A.0.15: Average values of the muon reconstruction, muon TTVA, muon isolation, b-tagging and trigger scale factors used in the analysis, as a function of $P_T^{\mu,\text{Leading}}$ (top left), $P_T^{\mu,\text{Subleading}}$ (top right), $\eta^{\mu,\text{Leading}}$ (bottom left) and $\eta^{\mu,\text{Subleading}}$ (bottom right) for the di-boson MC samples. The full object and event selections detailed in Chapter 6 have been applied, with the exception of the cut on $M_{\text{inv}}^{\mu\mu}$. Only MC statistical errors are shown.

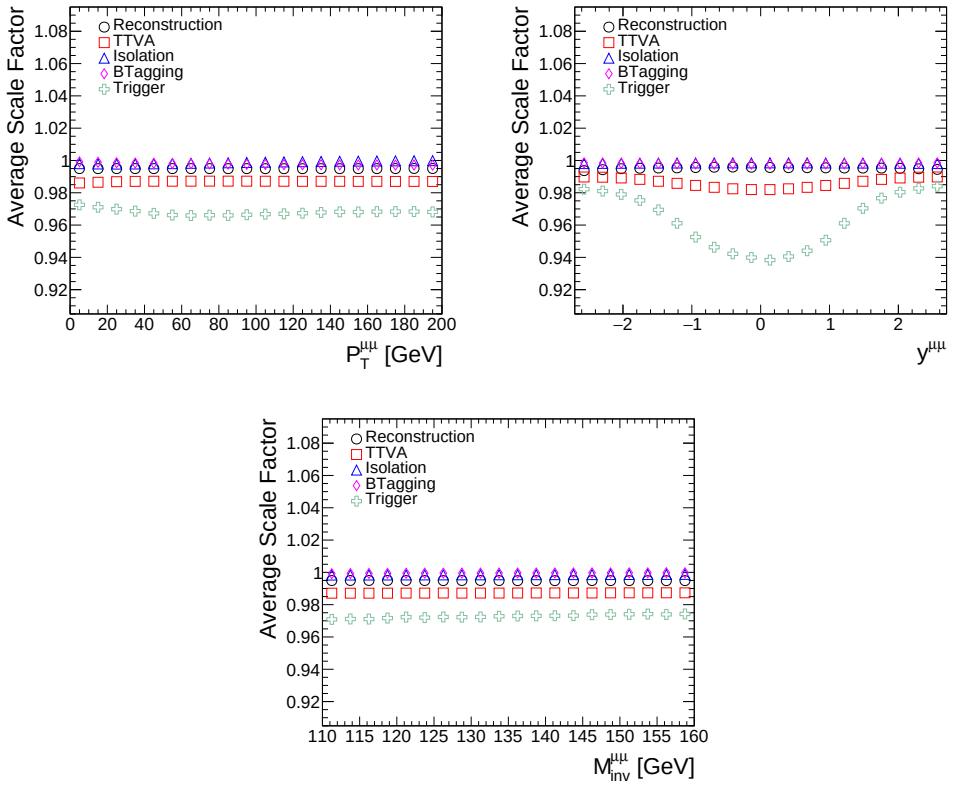

Figure A.0.16: Average values of the muon reconstruction, muon TTVA, muon isolation, b-tagging and trigger scale factors used in the analysis, as a function of $P_{\mathrm{T}}^{\mu\mu}$ (top left), $y^{\mu\mu}$ (top right) and $M_{\mathrm{inv}}^{\mu\mu}$ (bottom) for the di-boson MC samples. The full object and event selections detailed in Chapter 6 have been applied, with the exception of the cut on $M_{\mathrm{inv}}^{\mu\mu}$. Only MC statistical errors are shown.

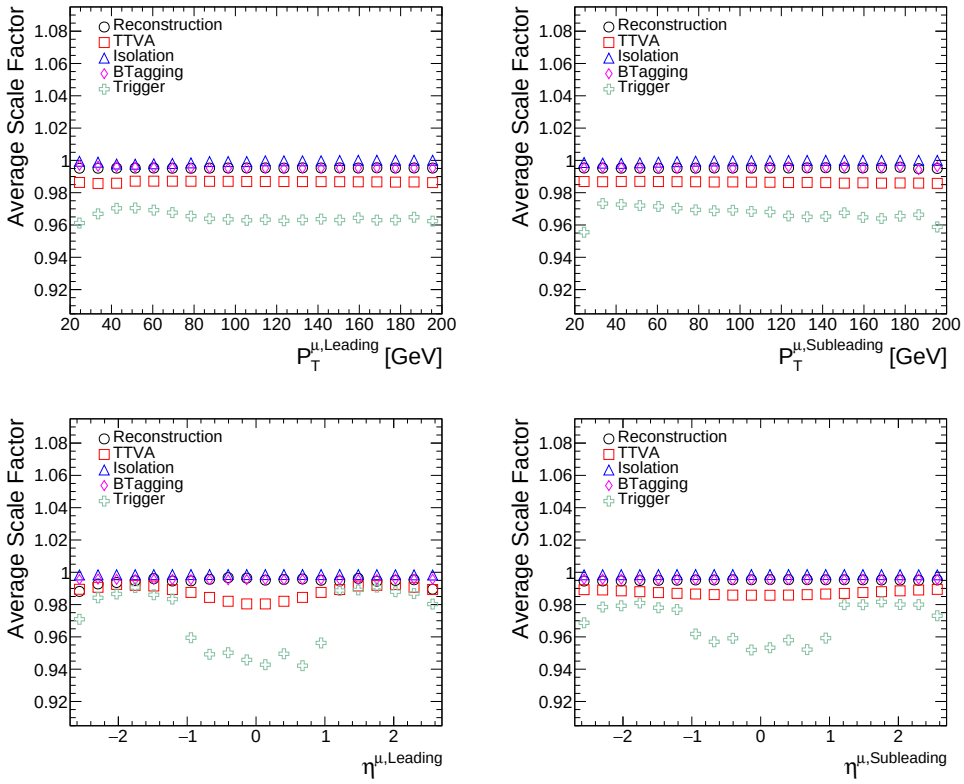

Figure A.0.17: Average values of the muon reconstruction, muon TTVA, muon isolation, b-tagging and trigger scale factors used in the analysis, as a function of $P_T^{\mu,\text{Leading}}$ (top left), $P_T^{\mu,\text{Subleading}}$ (top right), $\eta^{\mu,\text{Leading}}$ (bottom left) and $\eta^{\mu,\text{Subleading}}$ (bottom right) for the electroweak Z+jets MC samples. The full object and event selections detailed in Chapter 6 have been applied, with the exception of the cut on $M_{\text{inv}}^{\mu\mu}$. Only MC statistical errors are shown.

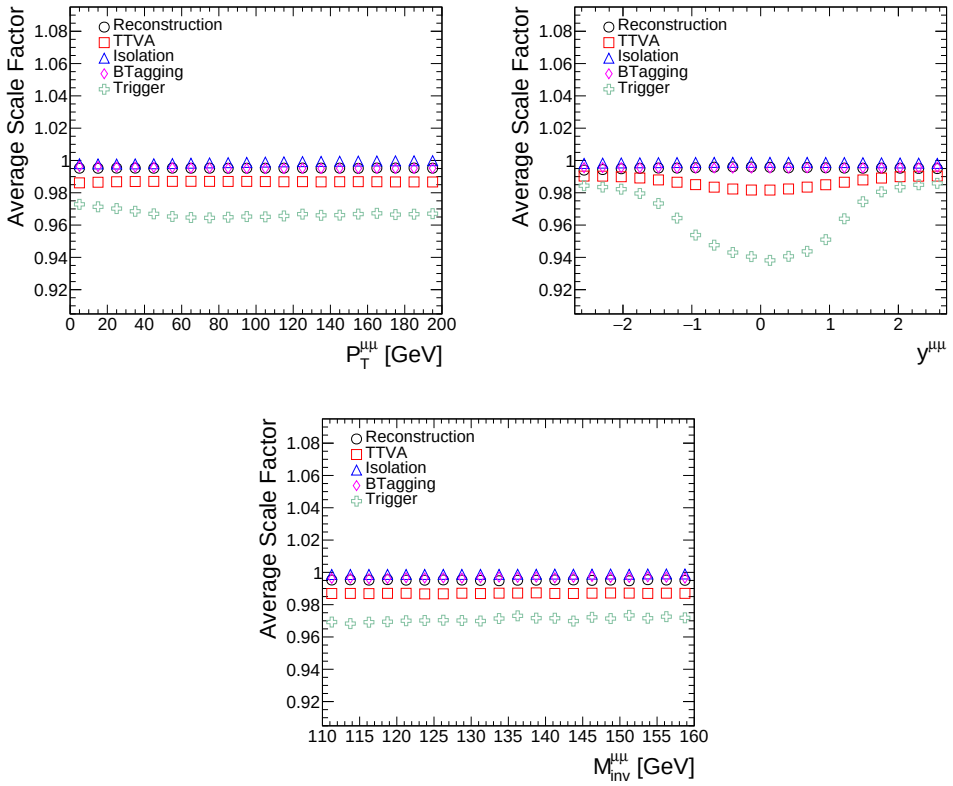

Figure A.0.18: Average values of the muon reconstruction, muon TTVA, muon isolation, b-tagging and trigger scale factors used in the analysis, as a function of $P_{\mathrm{T}}^{\mu\mu}$ (top left), $y^{\mu\mu}$ (top right) and $M_{\mathrm{inv}}^{\mu\mu}$ (bottom) for the electroweak Z+jets MC samples. The full object and event selections detailed in Chapter 6 have been applied, with the exception of the cut on $M_{\mathrm{inv}}^{\mu\mu}$. Only MC statistical errors are shown.

Appendix B

Drell-Yan Monte-Carlo Generator Comparisons

This chapter presents the data-MC comparisons from which Tables 7.2.1 to 7.2.4 of Chapter 7 were derived. Comparisons were made using Madgraph, Sherpa and Powheg Drell-Yan MC with and without $P_T^{\mu\mu}$ and M_{inv}^{jj} re-weightings. Figures B.0.1 to B.0.9 present comparisons as functions of $P_T^{\mu,\text{Leading}}$, $P_T^{\mu,\text{Subleading}}$, $\eta^{\mu,\text{Leading}}$, $\eta^{\mu,\text{Subleading}}$, Jet Multiplicity, $P_T^{j,\text{Leading}}$, $P_T^{j,\text{Subleading}}$, $\eta^{j,\text{Leading}}$ and $\eta^{j,\text{Subleading}}$ in the Z control region, while Figures B.0.10 to B.0.18 present the same distributions in the Signal region. Discrepancies between data and MC vary from 5% to 40% or greater, depending on the configuration considered. Powheg shows consistent issues modelling jet-related quantities, while Madgraph and Sherpa show similar levels of performance.

Figure B.0.19 presents the BDT output distributions of the BDTs trained using the $P_T^{\mu\mu}$ and M_{inv}^{jj} re-weighted Madgraph, Sherpa and Powheg Drell-Yan MC samples. Overtraining of around 5% is seen in the Madgraph and Sherpa background distributions due to MC statistical fluctuations in the training folds. The cuts applied to each distribution to define the respective VBF Tight and VBF Loose categories are summarised in Table B.0.1. The cuts vary by 1-2% between MC generators, with differences between folds due to statistical fluctuations. As demonstrated in Chapter 7, these variations between generators lead to overall significance differences after categorisation of 1-2%.

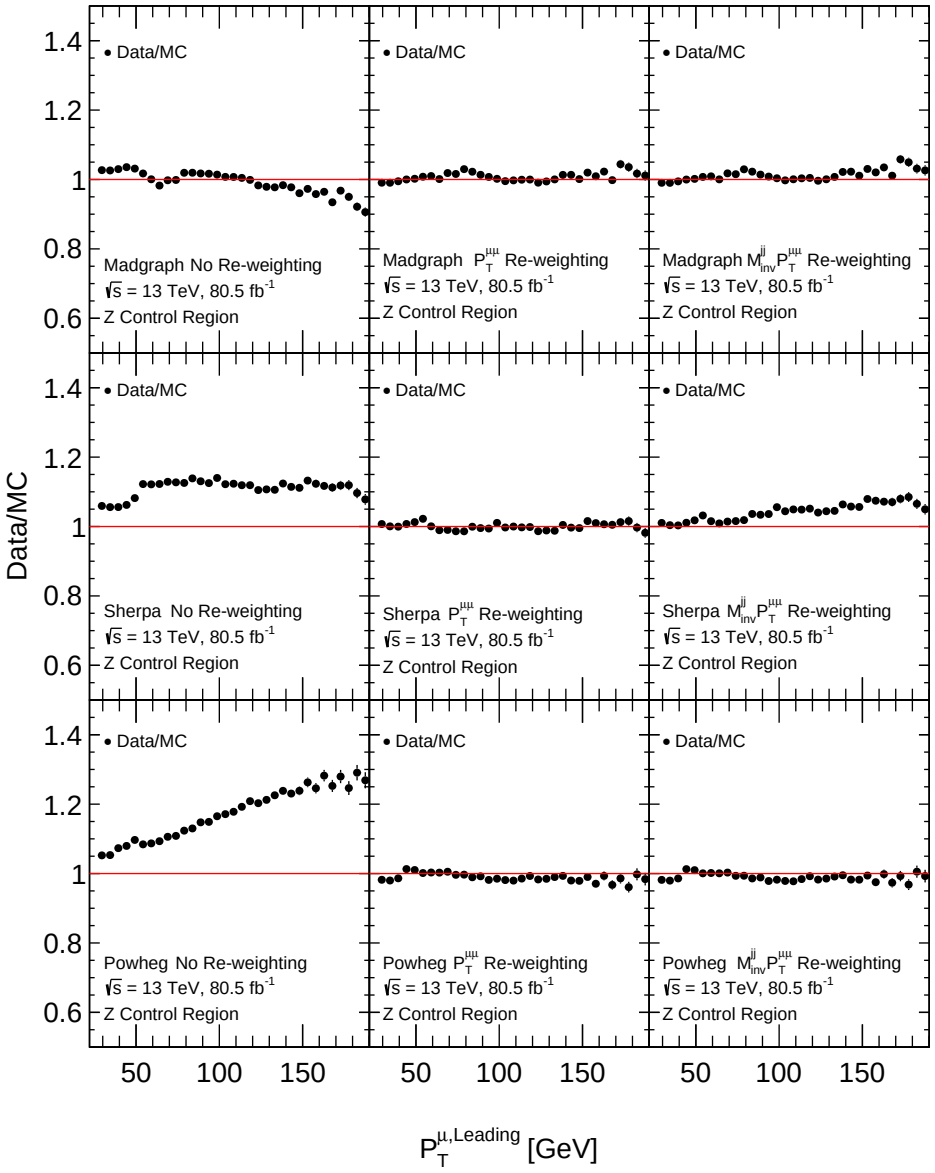

Figure B.0.1: Comparisons between data and MC for $P_T^{\mu,\text{Leading}}$ in the Z control region before (left) and after the application of the $P_T^{\mu\mu}$ (middle) and M_{inv}^{jj} (right) re-weightings described in Section 7.1. Madgraph, Sherpa and Powheg have been used for the generation of the Drell-Yan MC used in the top, middle and bottom rows respectively.

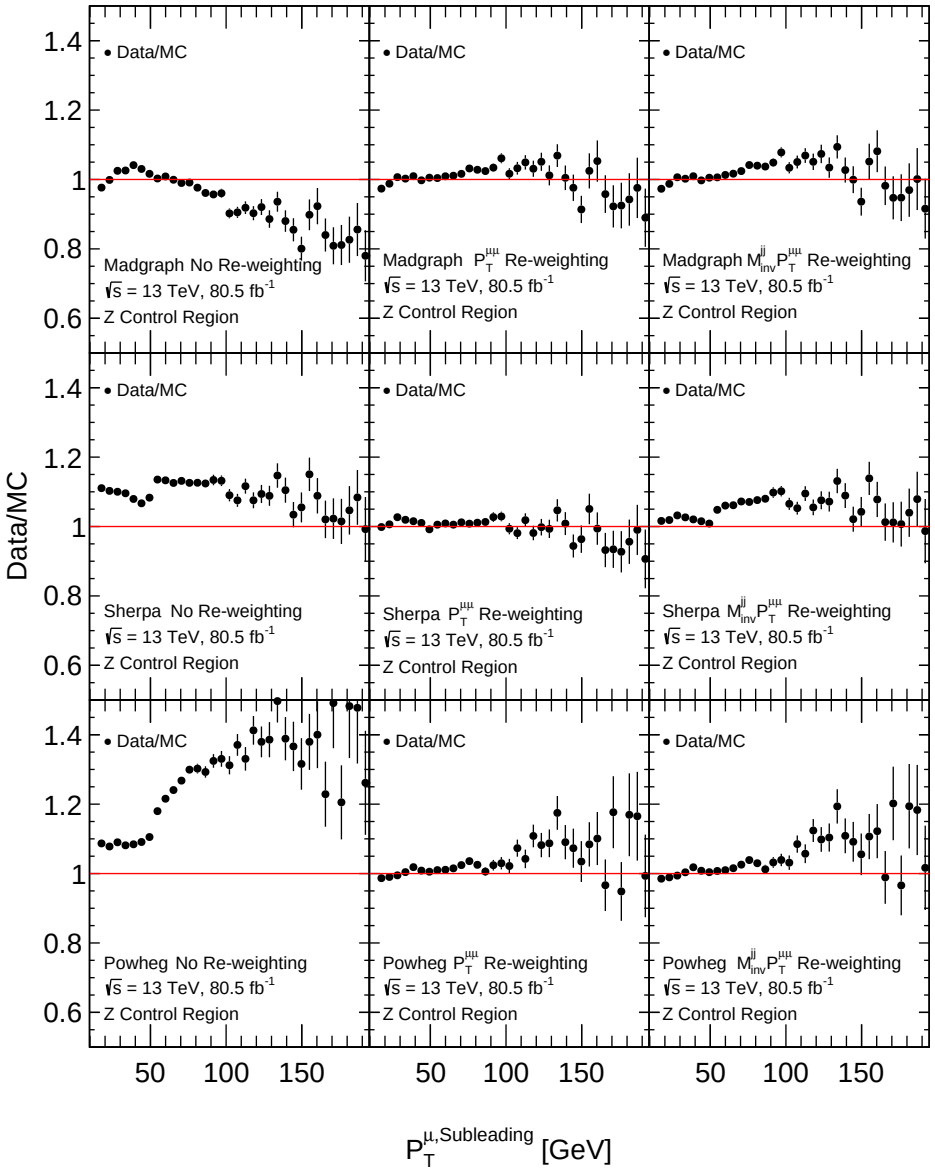

Figure B.0.2: Comparisons between data and MC for $P_T^{\mu,\text{Subleading}}$ in the Z control region before (left) and after the application of the $P_T^{\mu\mu}$ (middle) and M_{inv}^{jj} (right) re-weightings described in Section 7.1. Madgraph, Sherpa and Powheg have been used for the generation of the Drell-Yan MC used in the top, middle and bottom rows respectively.

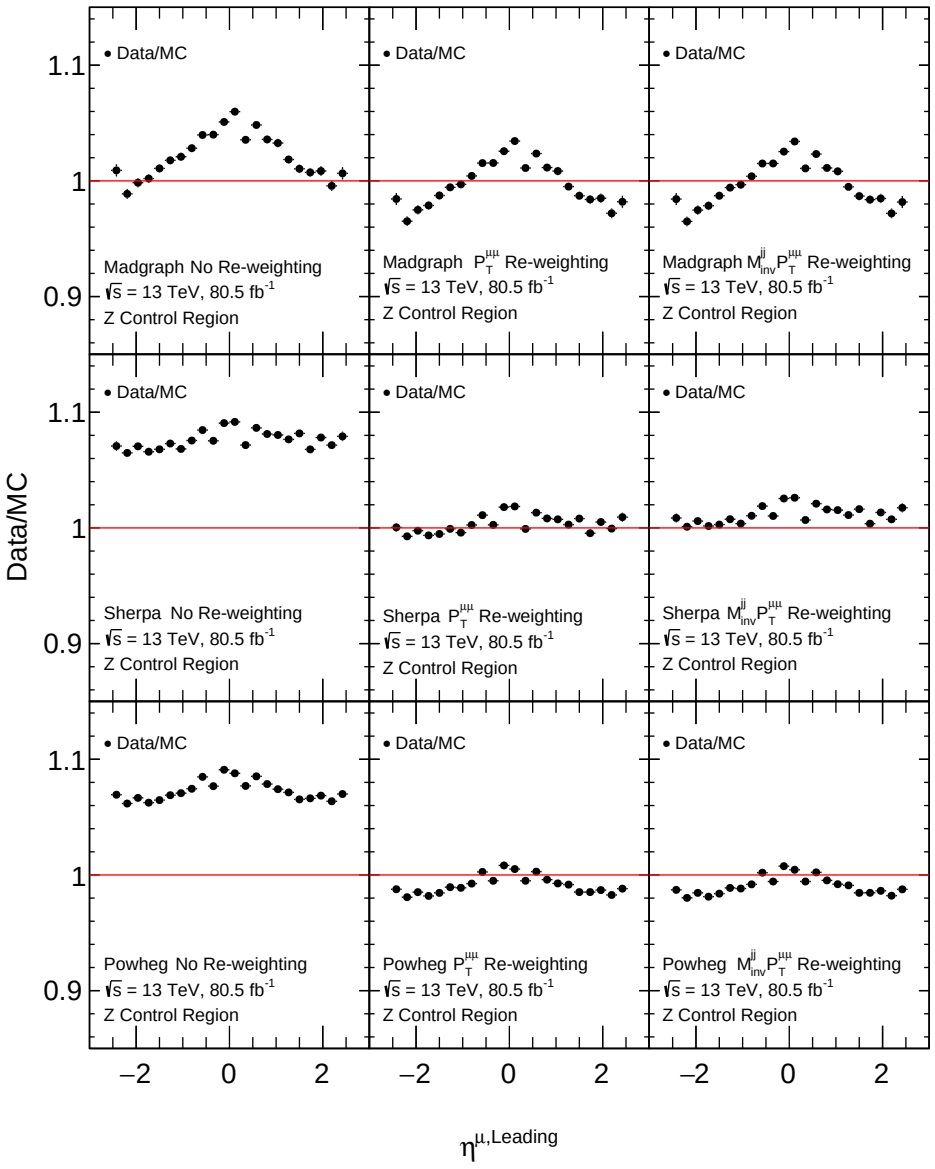

Figure B.0.3: Comparisons between data and MC for $\eta^{\mu,\text{Leading}}$ in the Z control region before (left) and after the application of the $P_T^{\mu\mu}$ (middle) and M_{inv}^{jj} (right) re-weightings described in Section 7.1. Madgraph, Sherpa and Powheg have been used for the generation of the Drell-Yan MC used in the top, middle and bottom rows respectively.

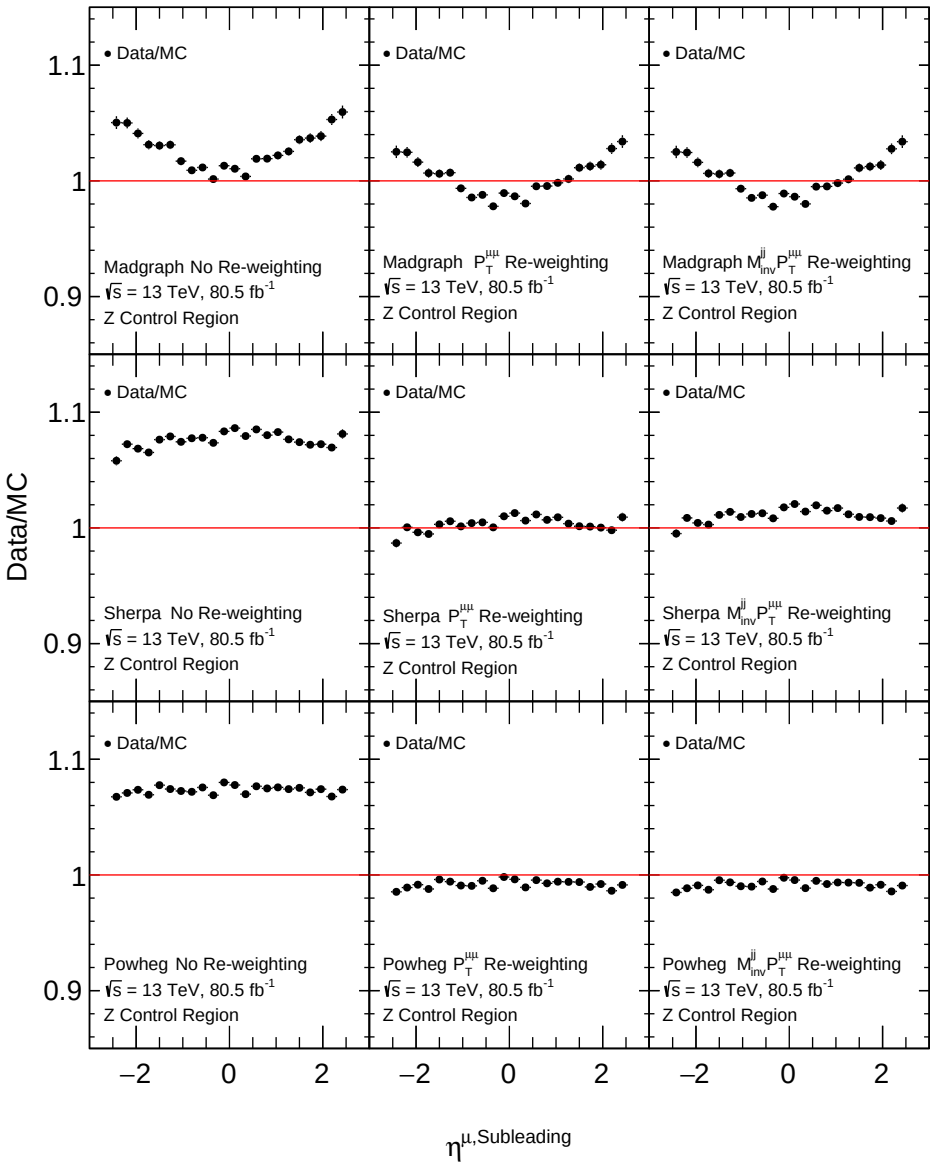

Figure B.0.4: Comparisons between data and MC for $\eta^{\mu,\text{Subleading}}$ in the Z control region before (left) and after the application of the $P_T^{\mu\mu}$ (middle) and M_{inv}^{jj} (right) re-weightings described in Section 7.1. Madgraph, Sherpa and Powheg have been used for the generation of the Drell-Yan MC used in the top, middle and bottom rows respectively.

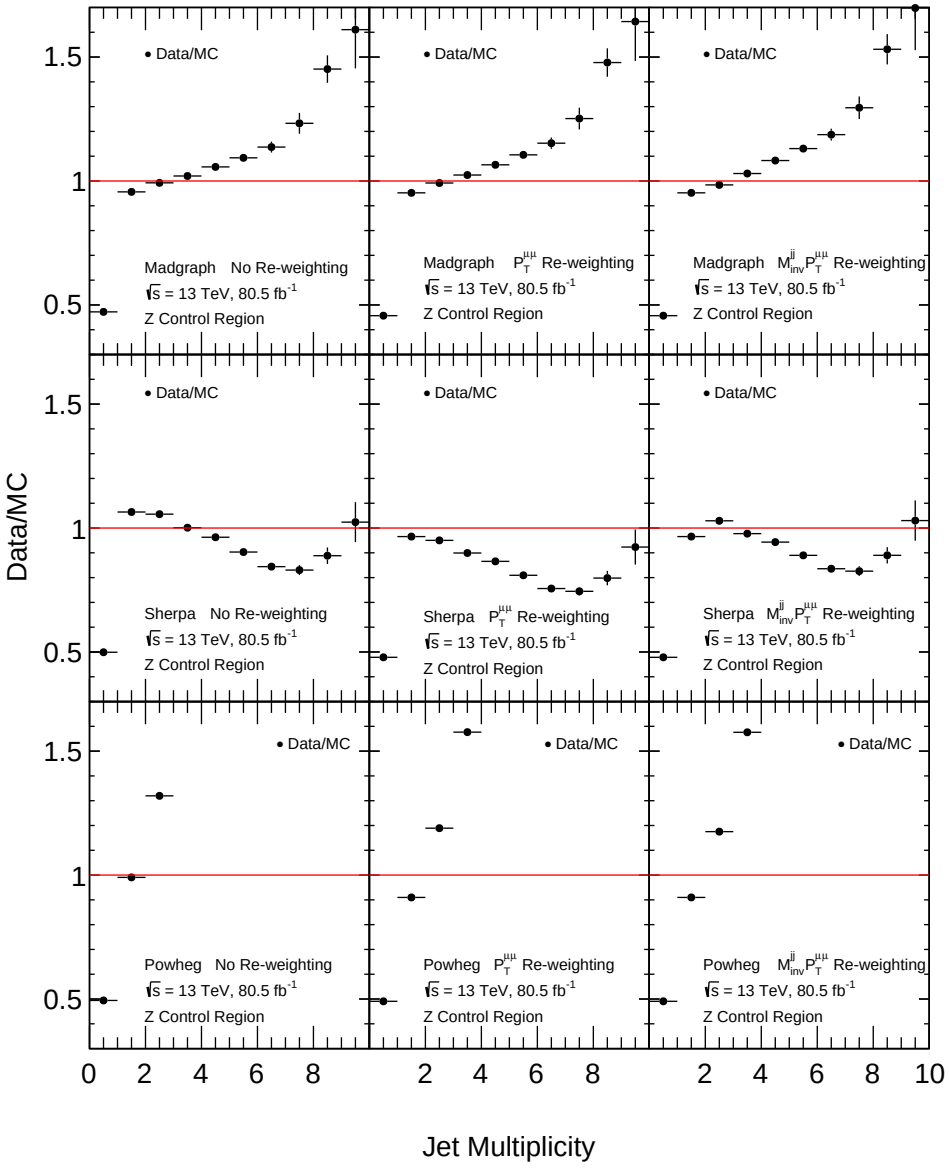

Figure B.0.5: Comparisons between data and MC for jet multiplicity in the Z control region before (left) and after the application of the $P_T^{\mu\mu}$ (middle) and M_{inv}^{jj} (right) re-weightings described in Section 7.1. Madgraph, Sherpa and Powheg have been used for the generation of the Drell-Yan MC used in the top, middle and bottom rows respectively.

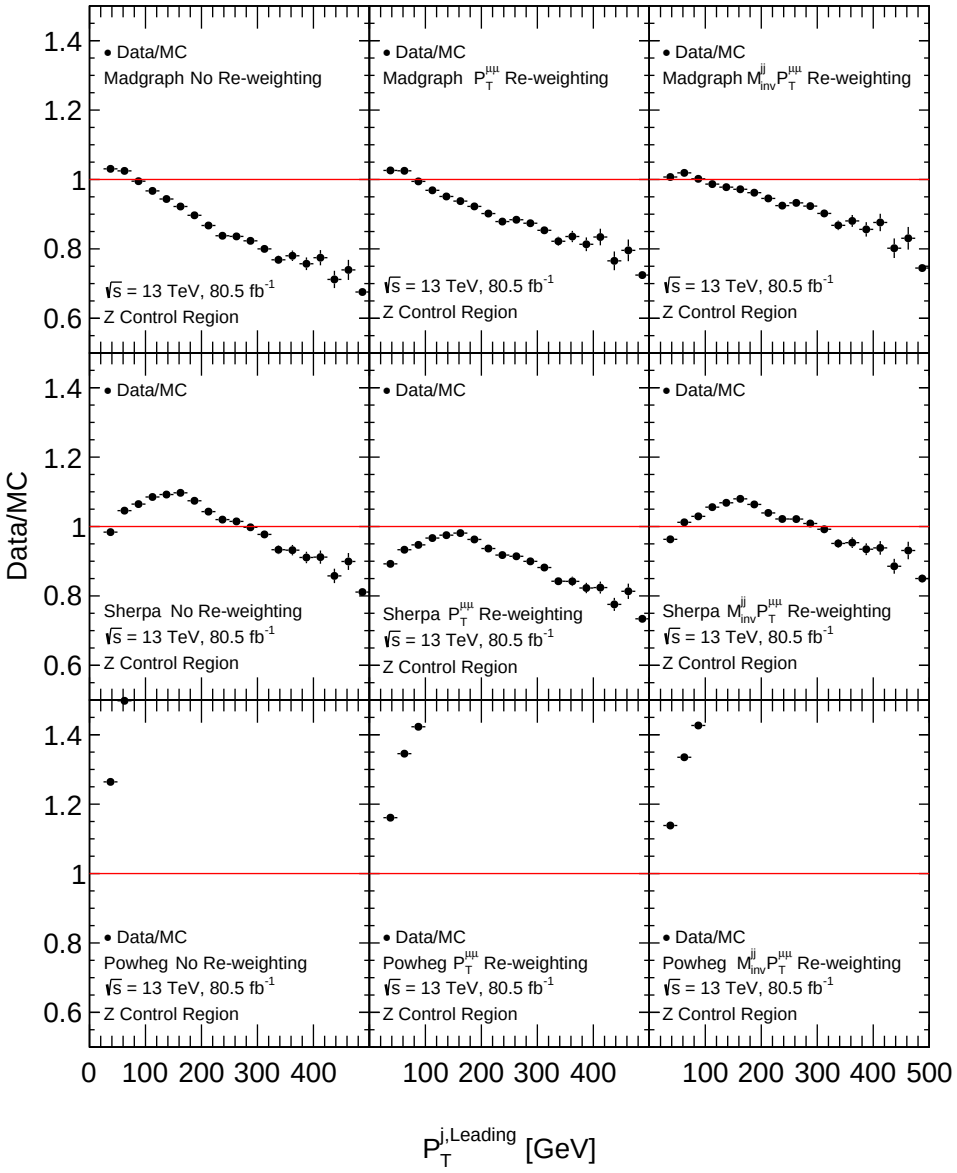

Figure B.0.6: Comparisons between data and MC for $P_T^{j,\text{Leading}}$ in the Z control region before (left) and after the application of the $P_T^{\mu\mu}$ (middle) and M_{inv}^{jj} (right) re-weightings described in Section 7.1. Madgraph, Sherpa and Powheg have been used for the generation of the Drell-Yan MC used in the top, middle and bottom rows respectively.

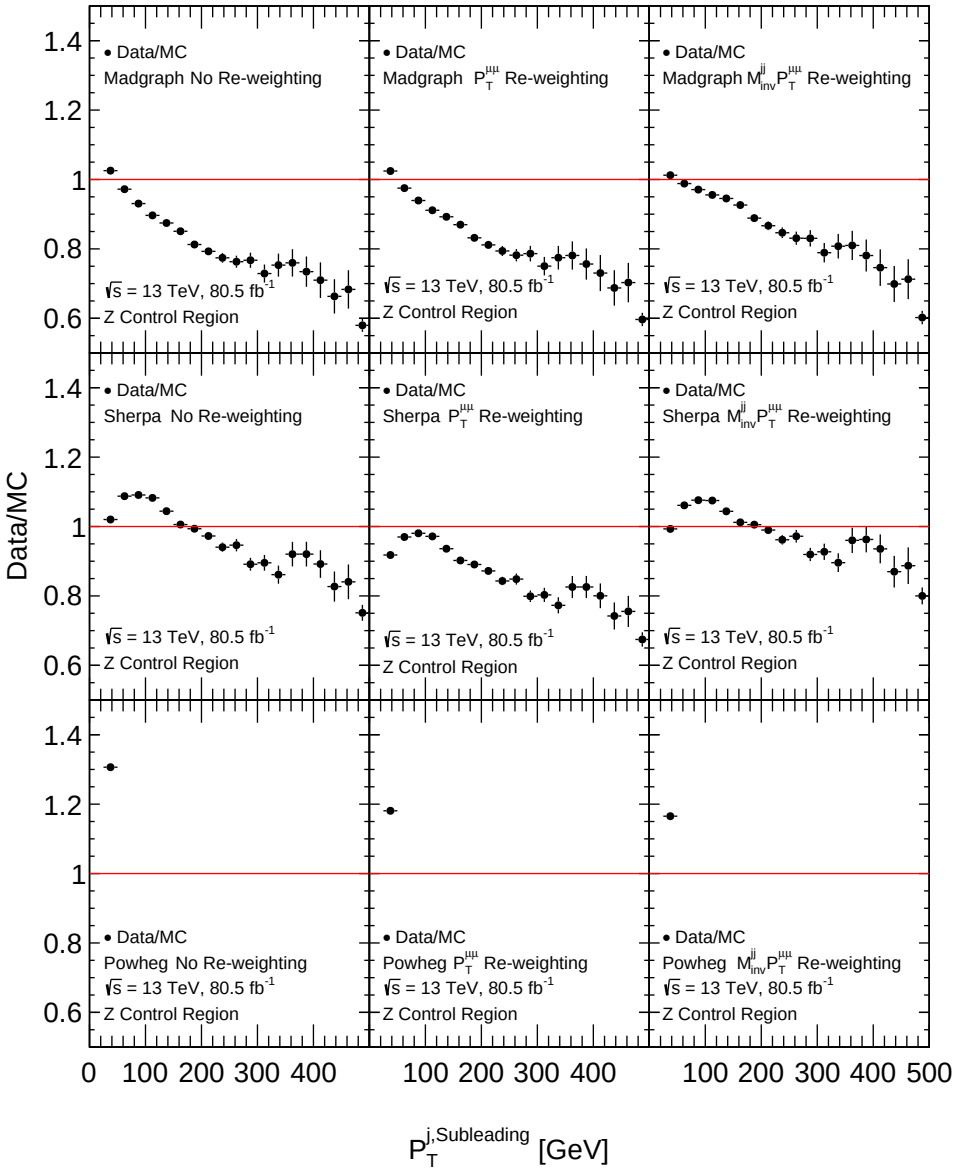

Figure B.0.7: Comparisons between data and MC for $P_T^{j,\text{Subleading}}$ in the Z control region before (left) and after the application of the $P_T^{\mu\mu}$ (middle) and M_{inv}^{jj} (right) re-weightings described in Section 7.1. Madgraph, Sherpa and Powheg have been used for the generation of the Drell-Yan MC used in the top, middle and bottom rows respectively.

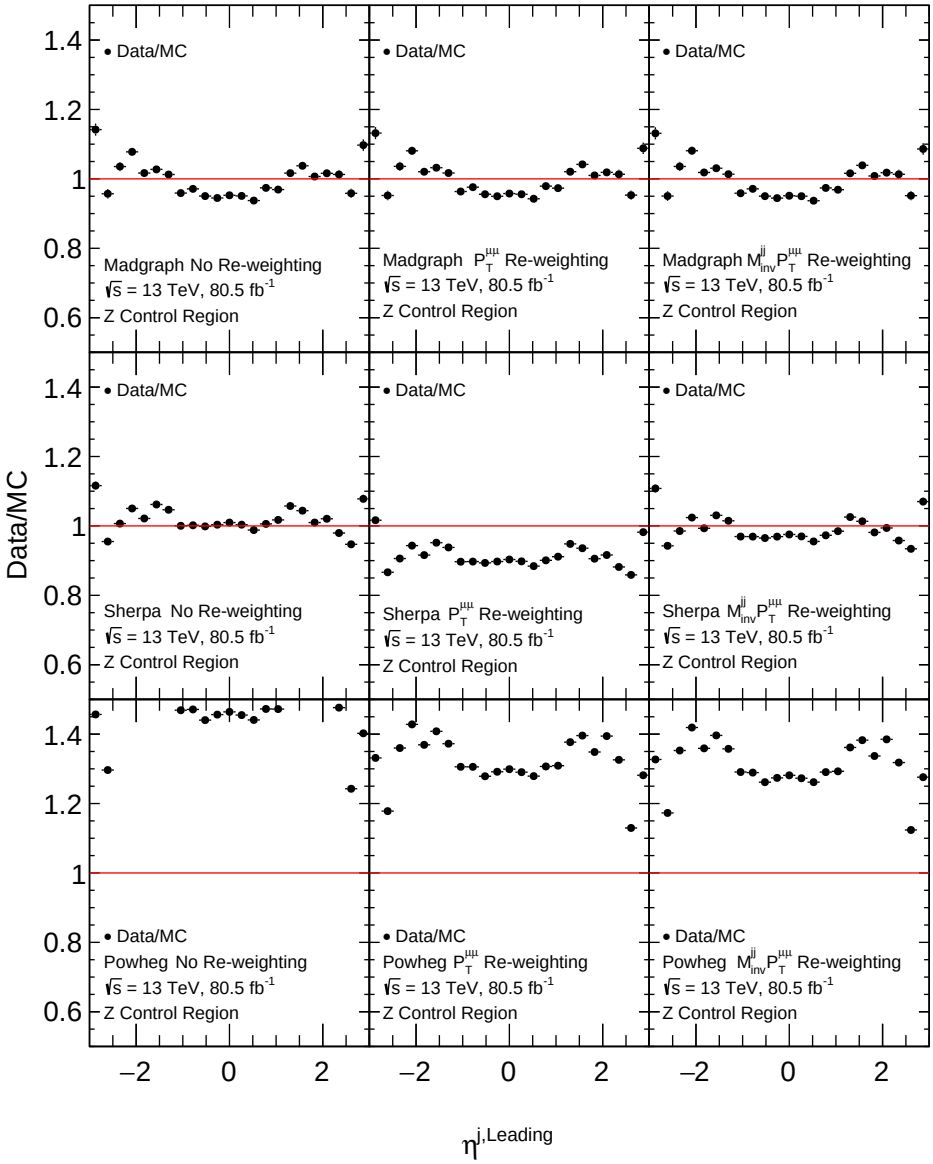

Figure B.0.8: Comparisons between data and MC for $\eta^{j,\text{Leading}}$ in the Z control region before (left) and after the application of the $P_T^{\mu\mu}$ (middle) and M_{inv}^{jj} (right) re-weightings described in Section 7.1. Madgraph, Sherpa and Powheg have been used for the generation of the Drell-Yan MC used in the top, middle and bottom rows respectively.

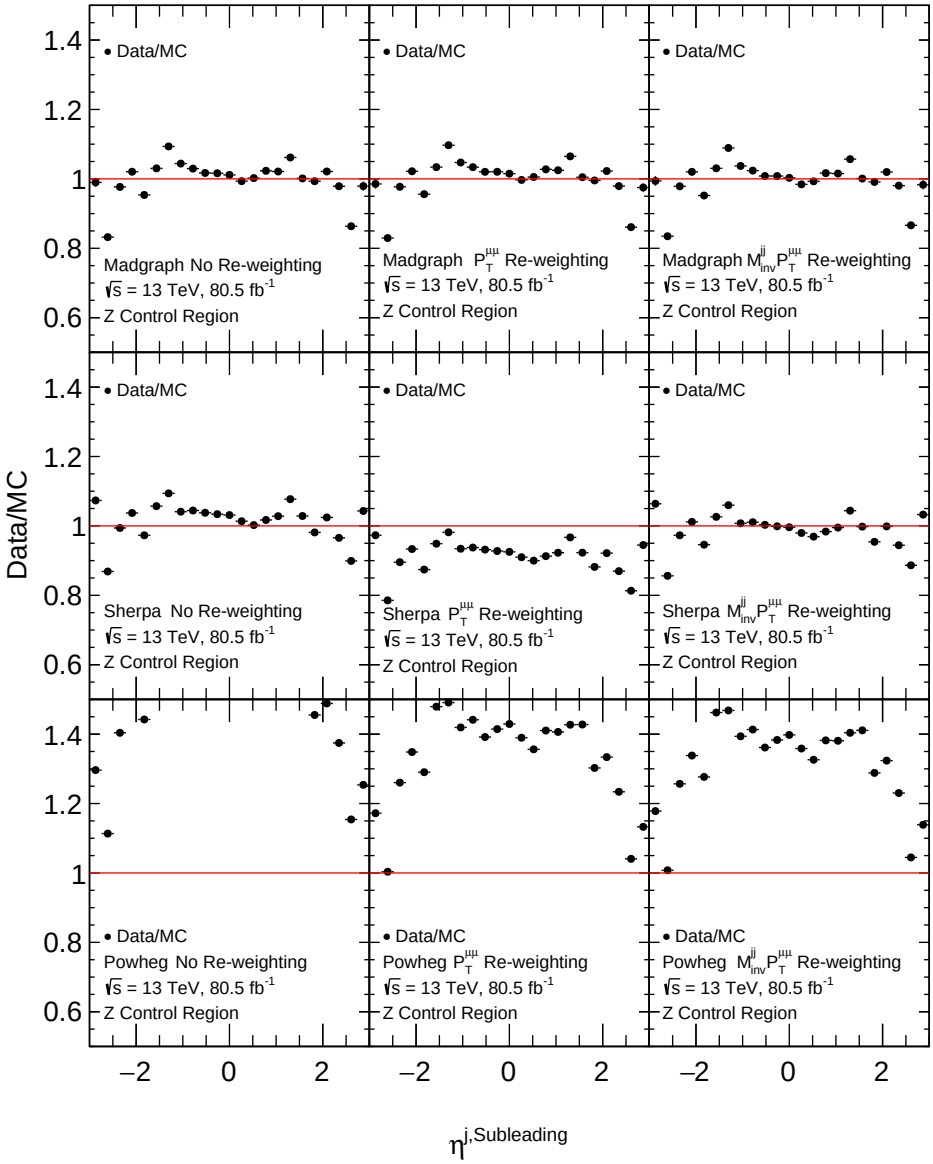

Figure B.0.9: Comparisons between data and MC for $\eta^{j,\text{Subleading}}$ in the Z control region before (left) and after the application of the $P_T^{\mu\mu}$ (middle) and M_{inv}^{jj} (right) re-weightings described in Section 7.1. Madgraph, Sherpa and Powheg have been used for the generation of the Drell-Yan MC used in the top, middle and bottom rows respectively.

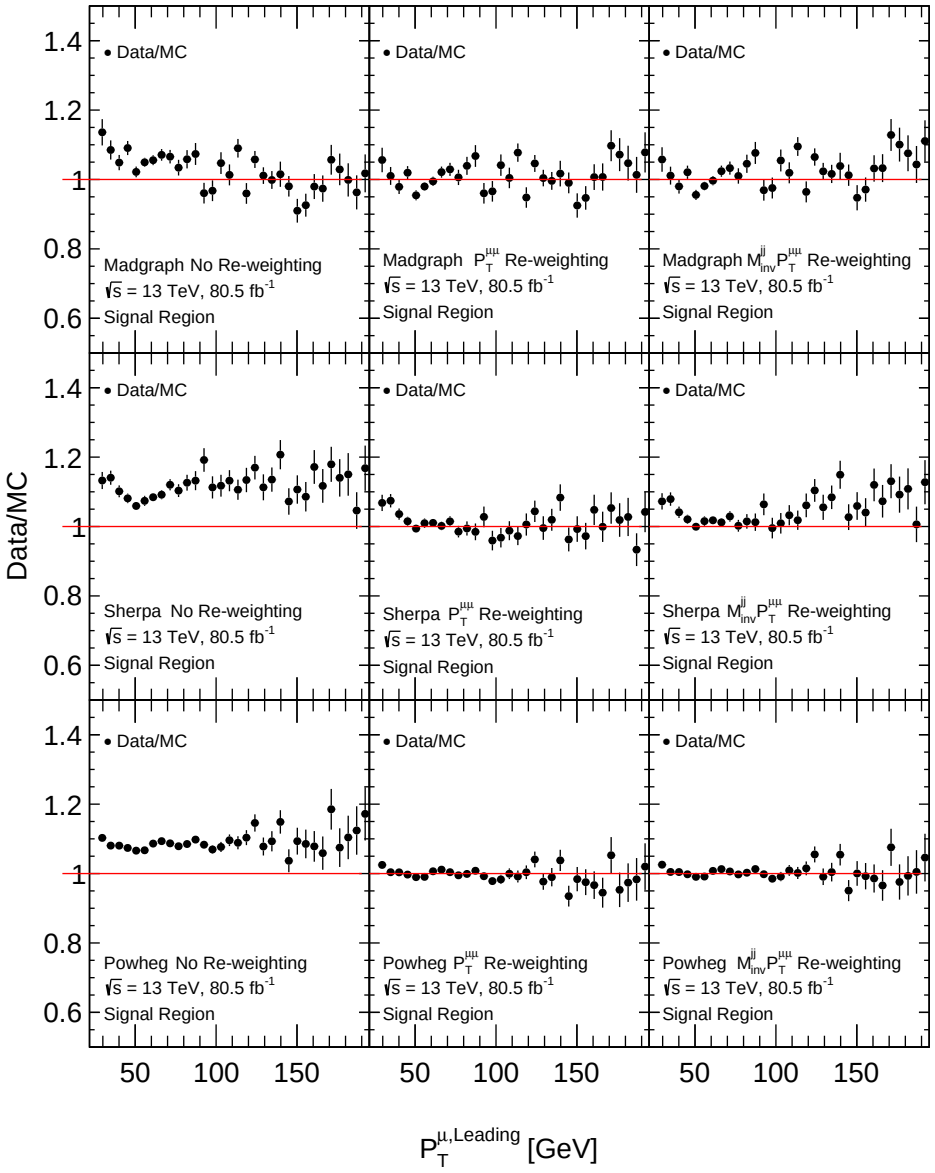

Figure B.0.10: Comparisons between data and MC for $P_T^{\mu,\text{Leading}}$ in the signal region before (left) and after the application of the $P_T^{\mu\mu}$ (middle) and M_{inv}^{jj} (right) re-weightings described in Section 7.1. Madgraph, Sherpa and Powheg have been used for the generation of the Drell-Yan MC used in the top, middle and bottom rows respectively.

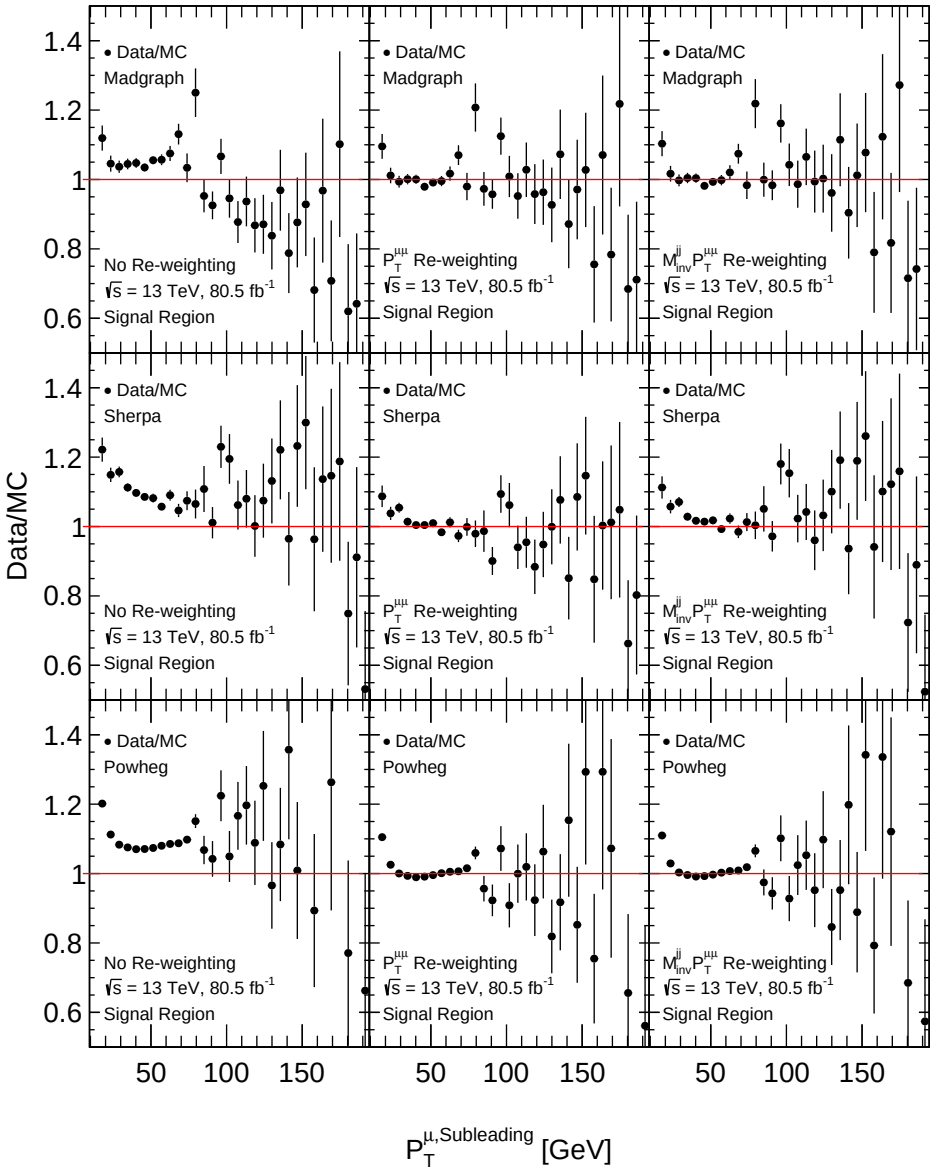

Figure B.0.11: Comparisons between data and MC for $P_T^{\mu,\text{Subleading}}$ in the signal region before (left) and after the application of the $P_T^{\mu\mu}$ (middle) and M_{inv}^{jj} (right) re-weightings described in Section 7.1. Madgraph, Sherpa and Powheg have been used for the generation of the Drell-Yan MC used in the top, middle and bottom rows respectively.

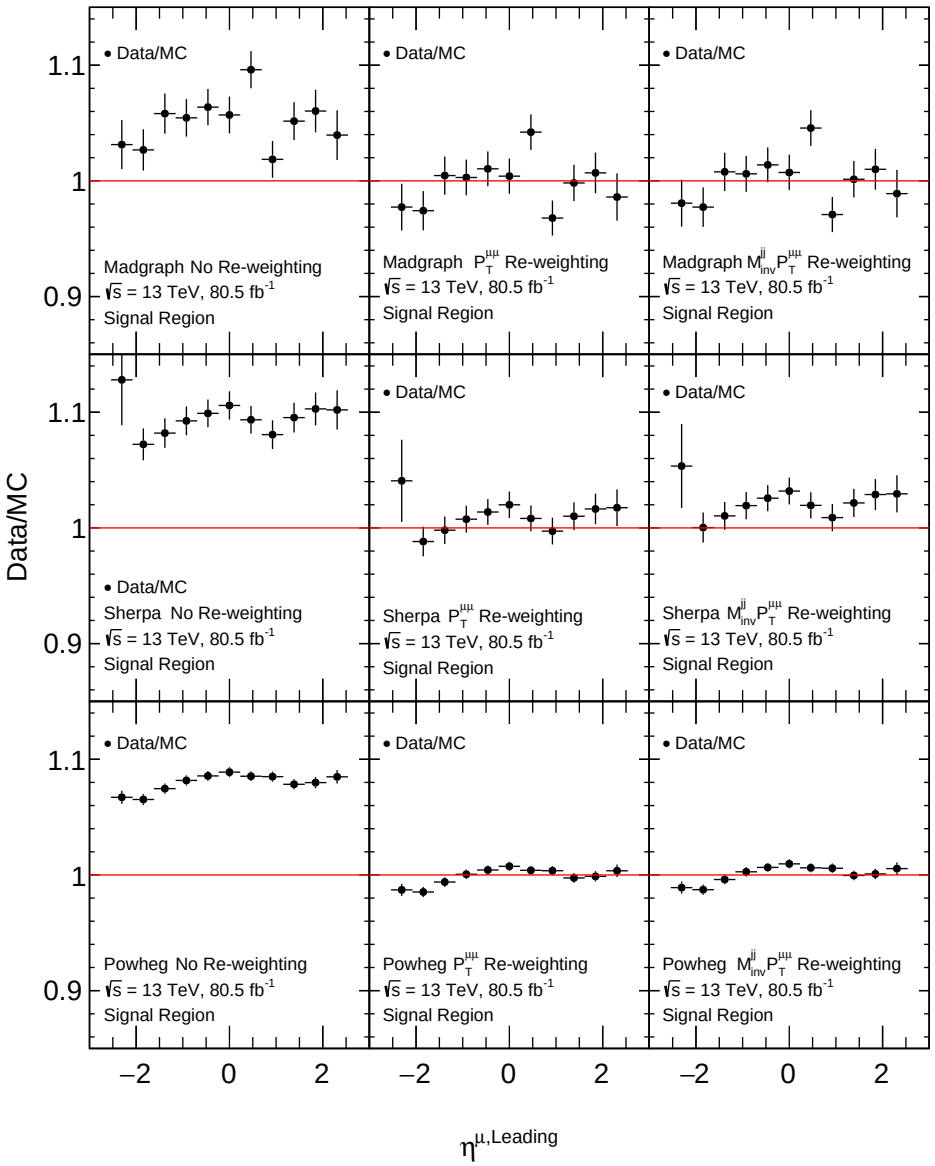

Figure B.0.12: Comparisons between data and MC for $\eta^{\mu,\text{Leading}}$ in the signal region before (left) and after the application of the $P_T^{\mu\mu}$ (middle) and M_{inv}^{jj} (right) re-weightings described in Section 7.1. Madgraph, Sherpa and Powheg have been used for the generation of the Drell-Yan MC used in the top, middle and bottom rows respectively.

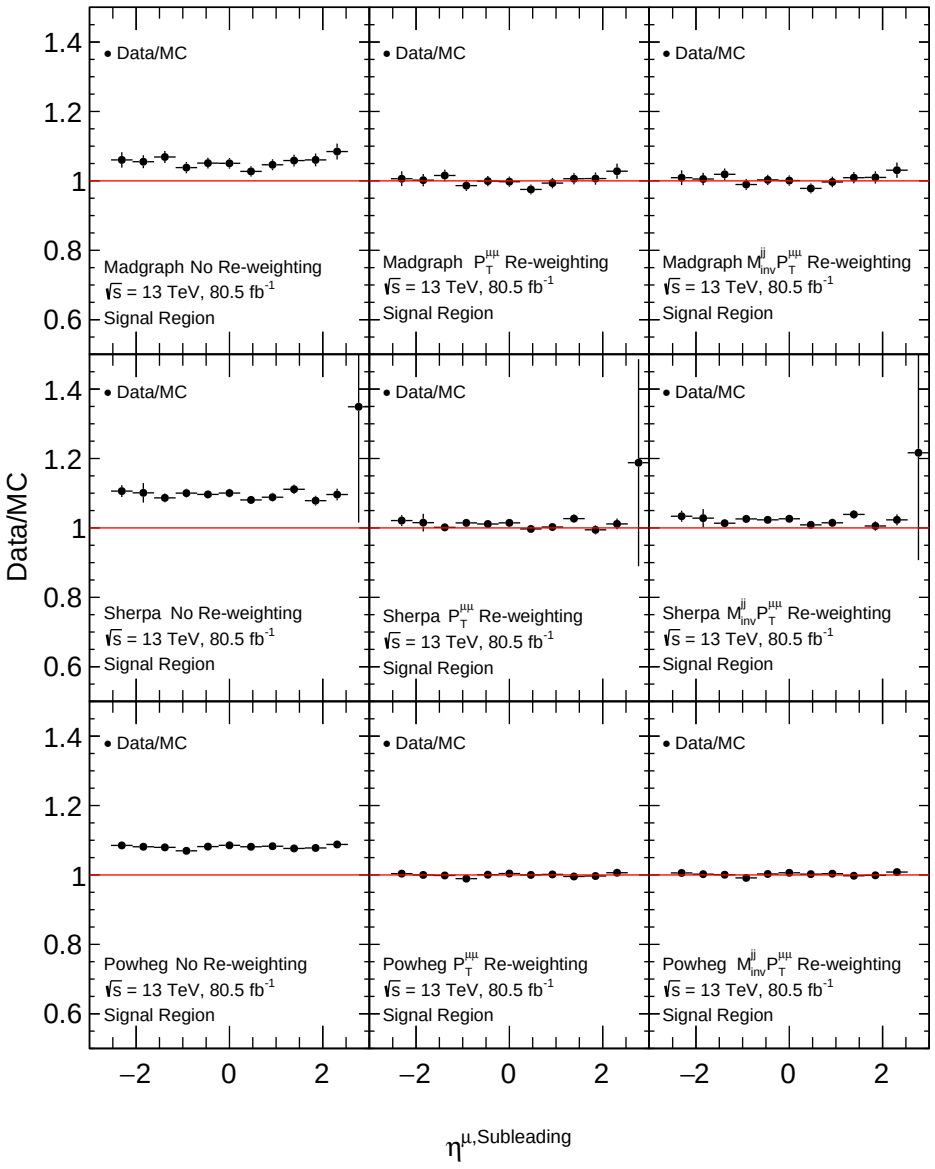

Figure B.0.13: Comparisons between data and MC for $\eta^{\mu,\text{Subleading}}$ in the signal region before (left) and after the application of the $P_T^{\mu\mu}$ (middle) and M_{inv}^{jj} (right) re-weightings described in Section 7.1. Madgraph, Sherpa and Powheg have been used for the generation of the Drell-Yan MC used in the top, middle and bottom rows respectively.

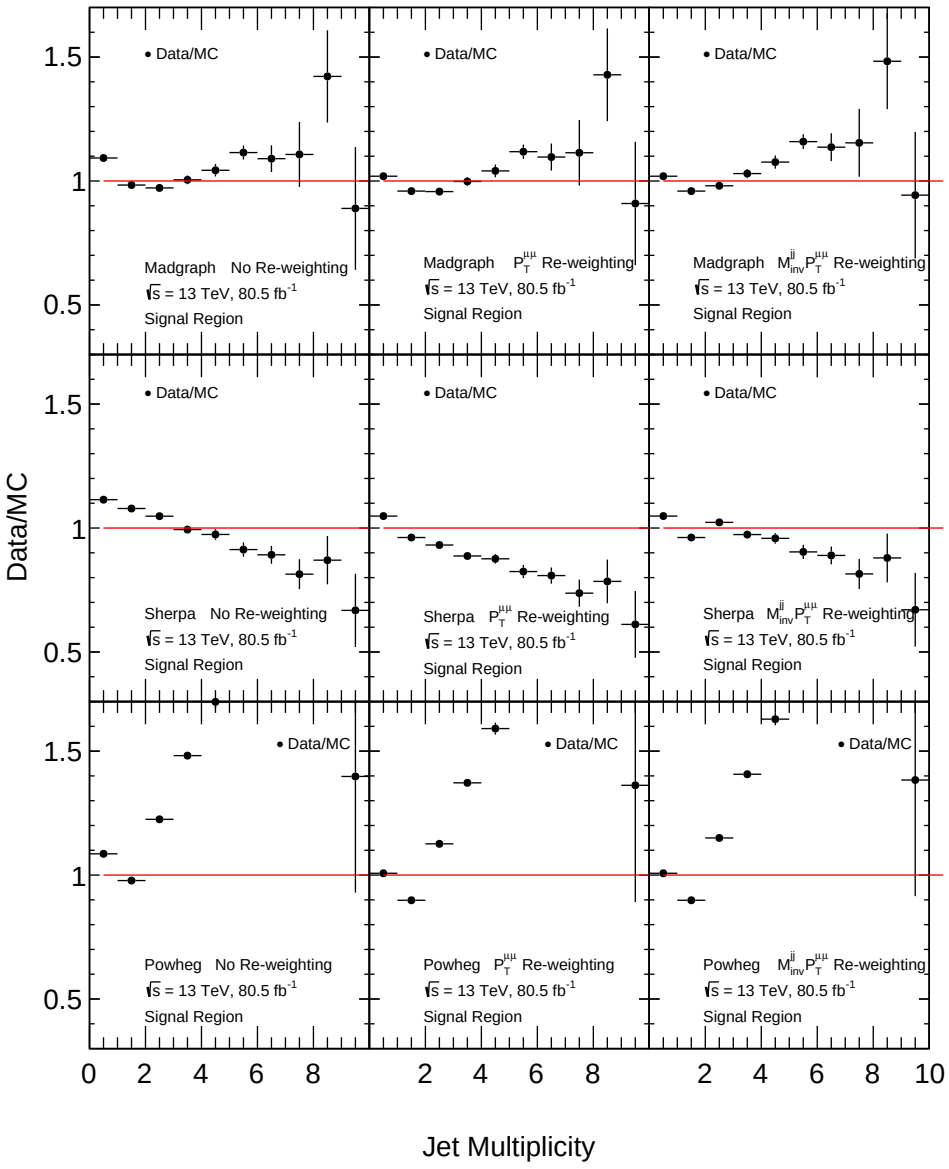

Figure B.0.14: Comparisons between data and MC for jet multiplicity in the signal region before (left) and after the application of the $P_T^{\mu\mu}$ (middle) and M_{inv}^{jj} (right) re-weightings described in Section 7.1. Madgraph, Sherpa and Powheg have been used for the generation of the Drell-Yan MC used in the top, middle and bottom rows respectively.

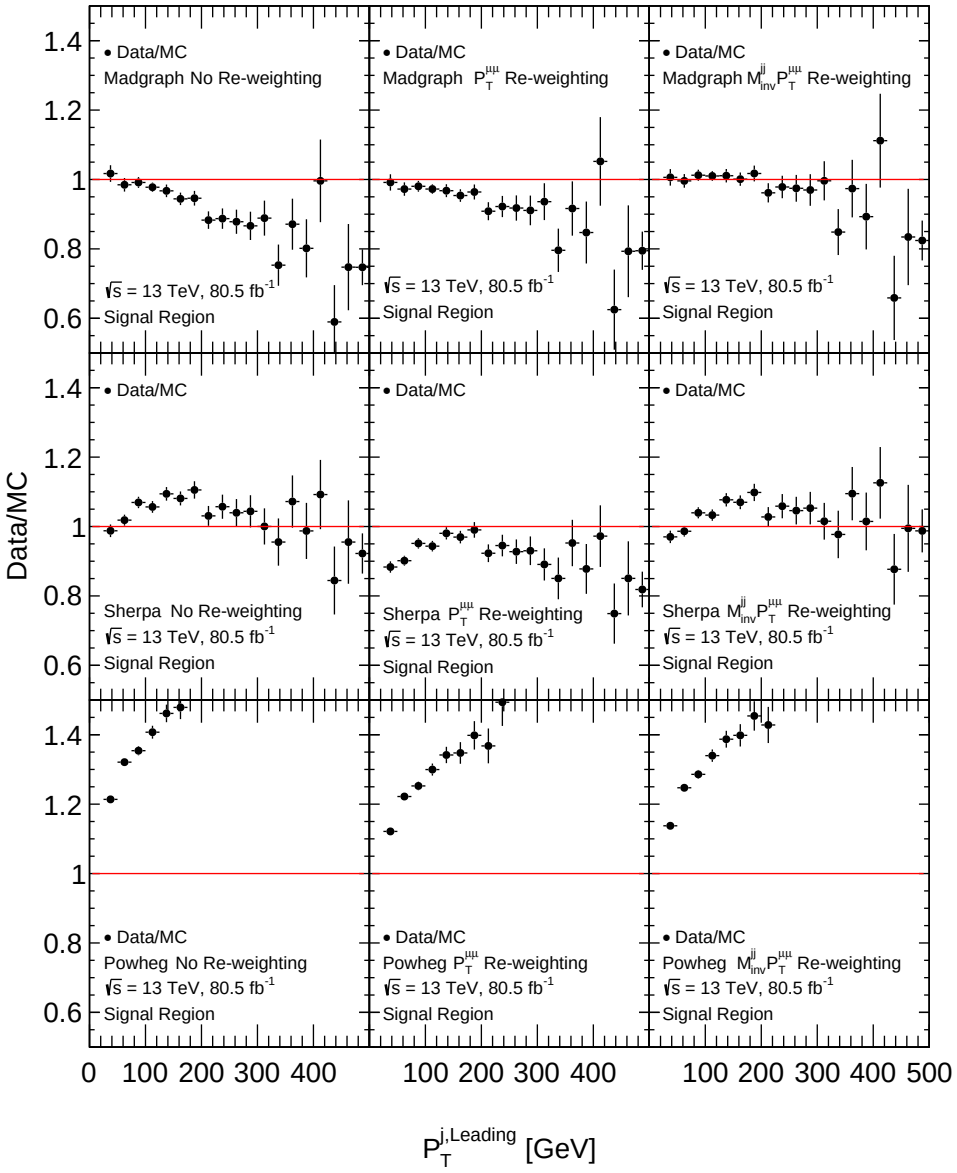

Figure B.0.15: Comparisons between data and MC for $P_T^{j,\mathrm{Leading}}$ in the signal region before (left) and after the application of the $P_T^{\mu\mu}$ (middle) and M_{inv}^{jj} (right) re-weightings described in Section 7.1. Madgraph, Sherpa and Powheg have been used for the generation of the Drell-Yan MC used in the top, middle and bottom rows respectively.

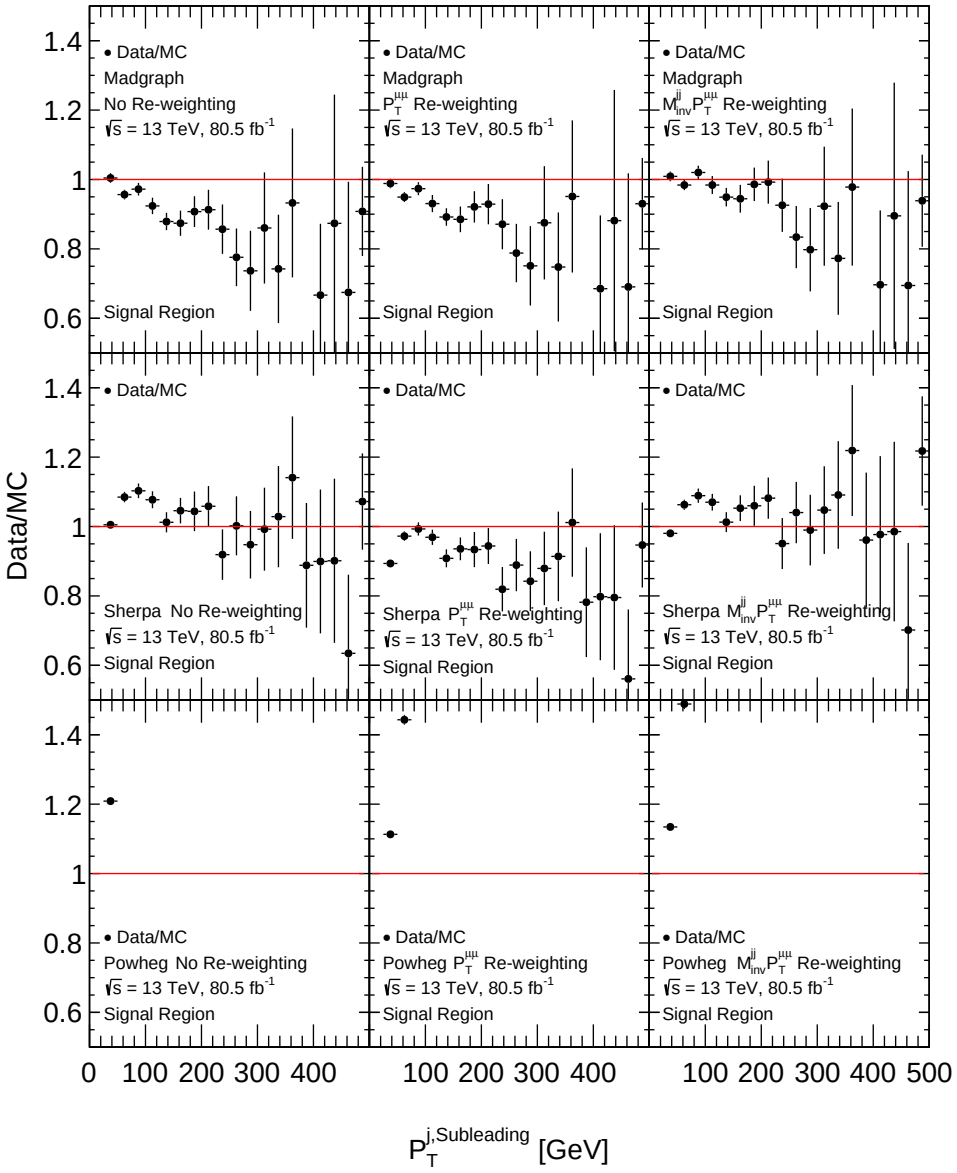

Figure B.0.16: Comparisons between data and MC for $P_T^{j,\text{Subleading}}$ in the signal region before (left) and after the application of the $P_T^{\mu\mu}$ (middle) and M_{inv}^{jj} (right) re-weightings described in Section 7.1. Madgraph, Sherpa and Powheg have been used for the generation of the Drell-Yan MC used in the top, middle and bottom rows respectively.

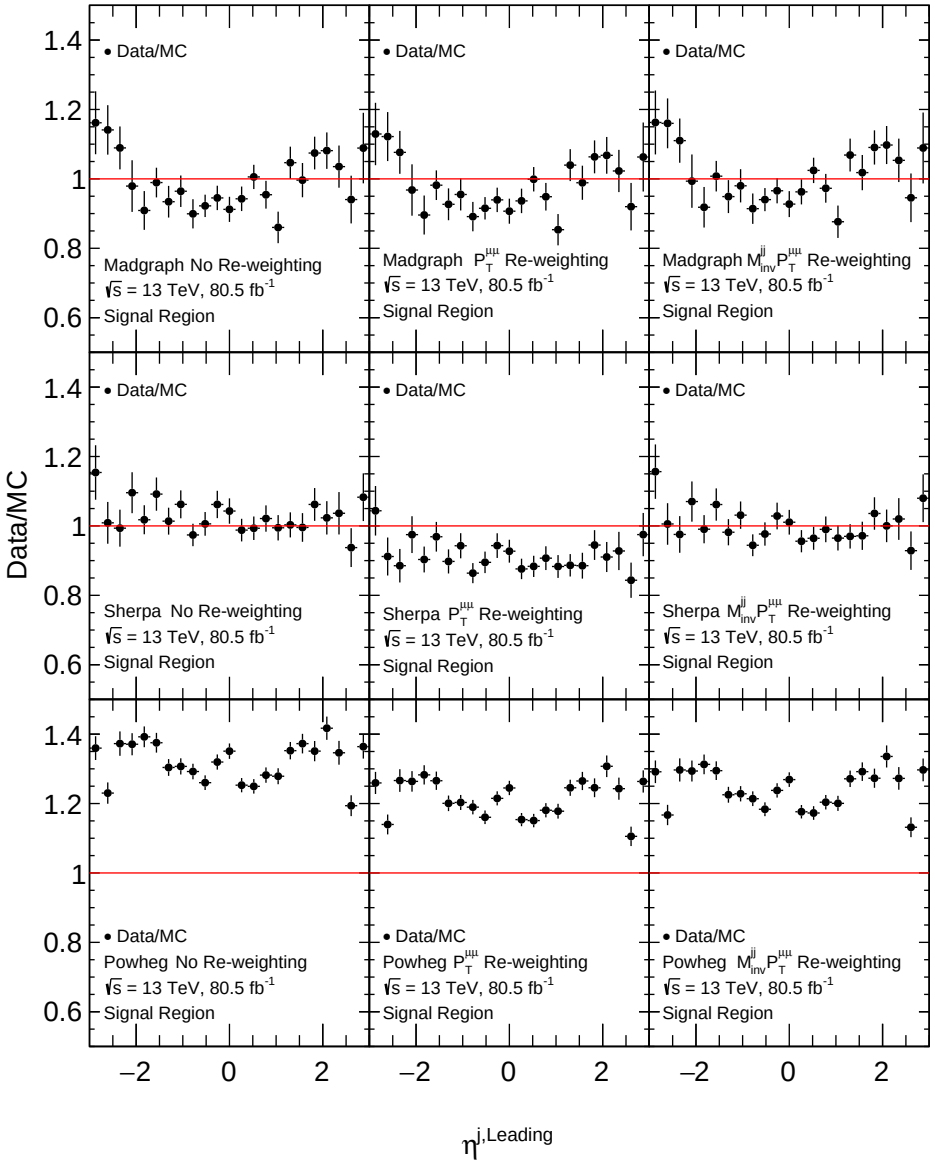

Figure B.0.17: Comparisons between data and MC for $\eta^{j,\mathrm{Leading}}$ in the signal region before (left) and after the application of the $P_T^{\mu\mu}$ (middle) and M_{inv}^{jj} (right) re-weightings described in Section 7.1. Madgraph, Sherpa and Powheg have been used for the generation of the Drell-Yan MC used in the top, middle and bottom rows respectively.

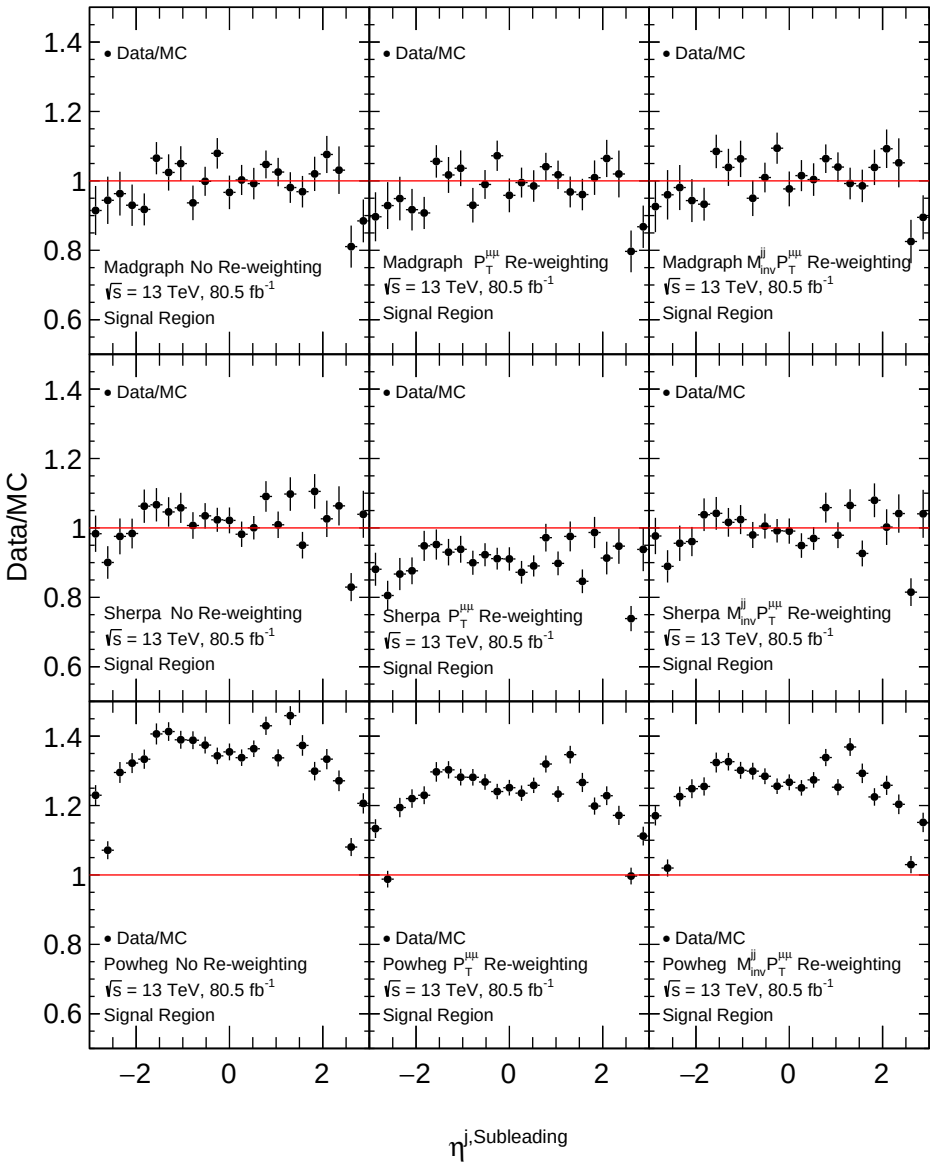

Figure B.0.18: Comparisons between data and MC for $\eta^{j,\text{Subleading}}$ in the signal region before (left) and after the application of the $P_T^{\mu\mu}$ (middle) and M_{inv}^{jj} (right) re-weightings described in Section 7.1. Madgraph, Sherpa and Powheg have been used for the generation of the Drell-Yan MC used in the top, middle and bottom rows respectively.

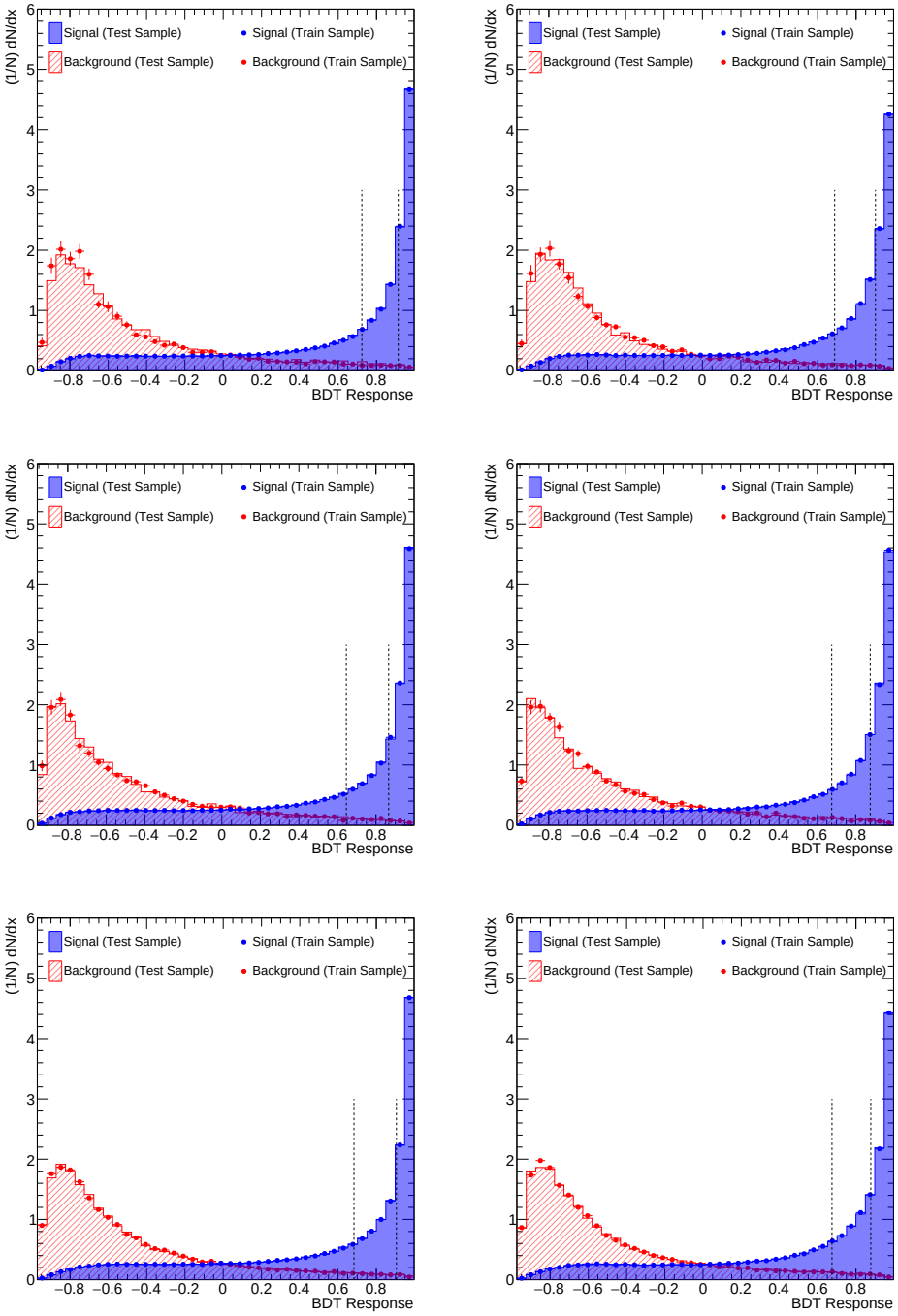

Figure B.0.19: Output distributions of Folds 1 (left) and 2 (right) of the BDTs trained using Madgraph (top), Sherpa (middle) and Powheg (bottom) Drell-Yan MC. Only MC statistical errors are shown. The dashes lines represent the boundaries of the VBF Tight and VBF Loose categories.

	Madgraph		Sherpa		Powheg	
	Fold 1	Fold 2	Fold 1	Fold 2	Fold 1	Fold 2
VBF Tight Cut	0.91	0.90	0.87	0.88	0.90	0.88
VBF Loose Cut	0.72	0.69	0.65	0.68	0.68	0.67

Table B.0.1: Cuts applied to the Madgraph, Sherpa and Powheg Drell-Yan MC BDT output distributions in order to define the VBF Tight and VBF Loose categories. The categories correspond to 98% and 95% signal purity respectively. Differences between folds are due to statistical fluctuations in the MC samples. Cuts devised for Fold 1 are applied exclusively to Fold 2 events (and vice versa).

Appendix C

BDT Correlation Matrices

This chapter presents the variable correlation matrices of BDTs trained using zero-jet, single-jet and multi-jet events. Correlations are presented for the background MC samples used in the analysis. All variables contained within Table 9.0.1 are considered for each applicable selection. The matrices are presented in Figures C.0.1 to C.0.6. Since each BDT was trained using two-fold cross validation, two correlation matrices are presented for each BDT (one for each training fold). As seen in Figures 9.0.1 and 9.0.2 of Chapter 9, correlations greater than 10% are seen between H_T, $P_T^{\mu,\text{Leading}}$, $P_T^{\mu,\text{Subleading}}$ and $M_{\text{inv}}^{\mu\mu}$ for each BDT fold. To avoid shaping the $M_{\text{inv}}^{\mu\mu}$ distributions of background samples processed through the analysis BDTs, H_T, $P_T^{\mu,\text{Leading}}$ and $P_T^{\mu,\text{Subleading}}$ were ignored when training the final analysis BDTs. This was done with the intention of reducing shape biases in the data distributions of each BDT category, from which the $H \to \mu\mu$ signal strength was eventually extracted.

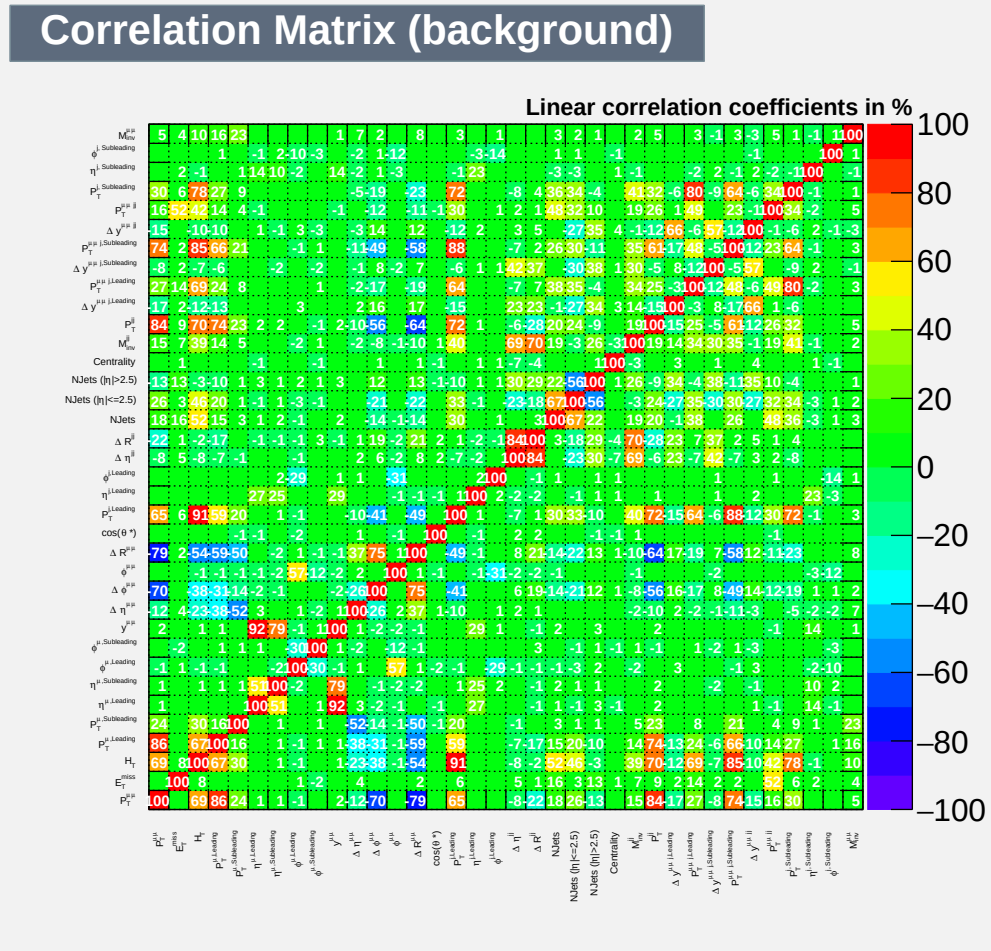

Figure C.0.1: Correlations between variables initially considered for training of the multi-jet selection BDTs. Correlations are presented for Fold 1 of the combined Drell-Yan, di-boson, top and electroweak Z plus jet backgrounds.

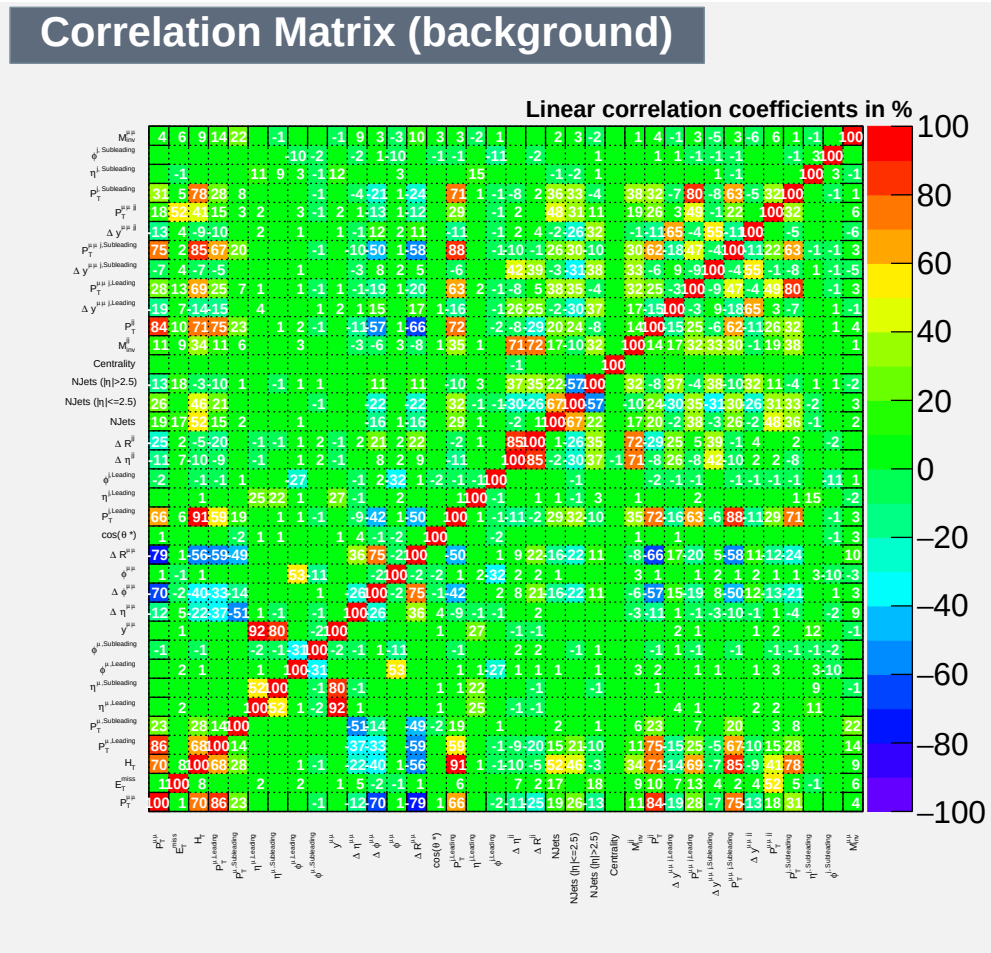

Figure C.0.2: Correlations between variables initially considered for training of the multi-jet selection BDTs. Correlations are presented for Fold 2 of the combined Drell-Yan, di-boson, top and electroweak Z plus jet backgrounds.

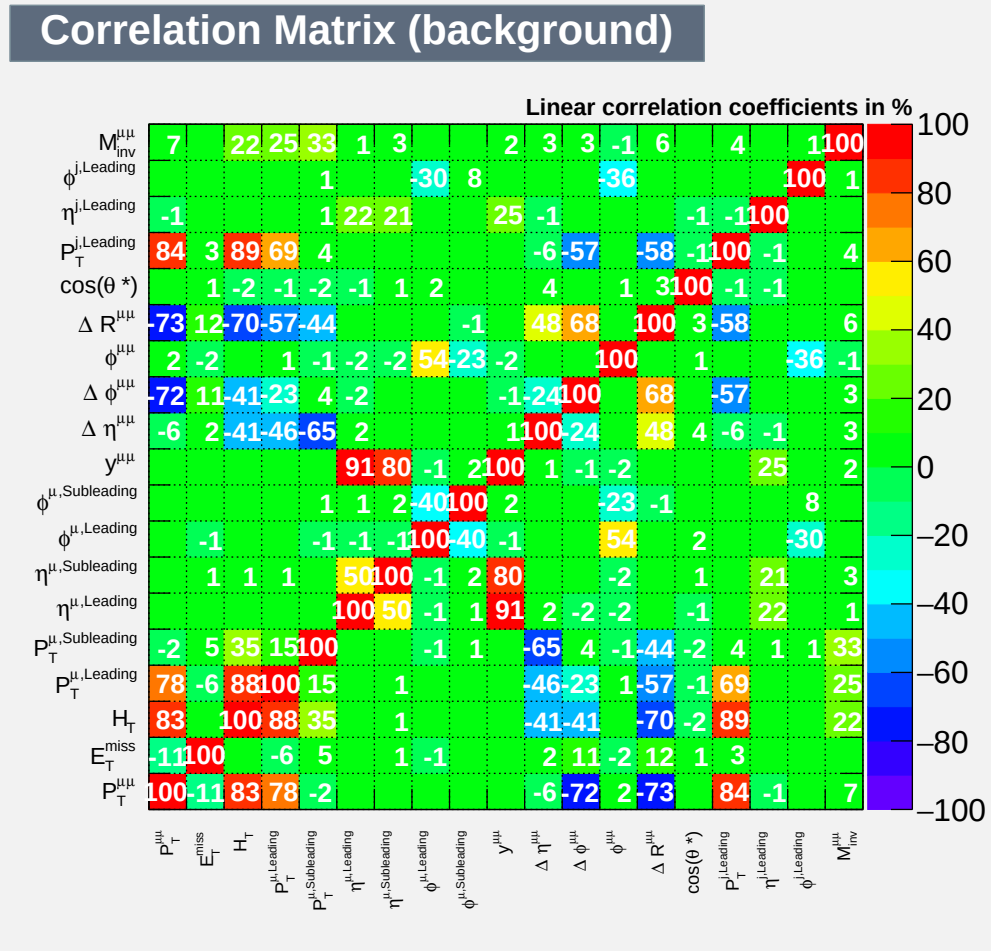

Figure C.0.3: Correlations between variables initially considered for training of the single-jet selection BDTs. Correlations are presented for Fold 1 of the combined Drell-Yan, di-boson, top and electroweak Z plus jet backgrounds.

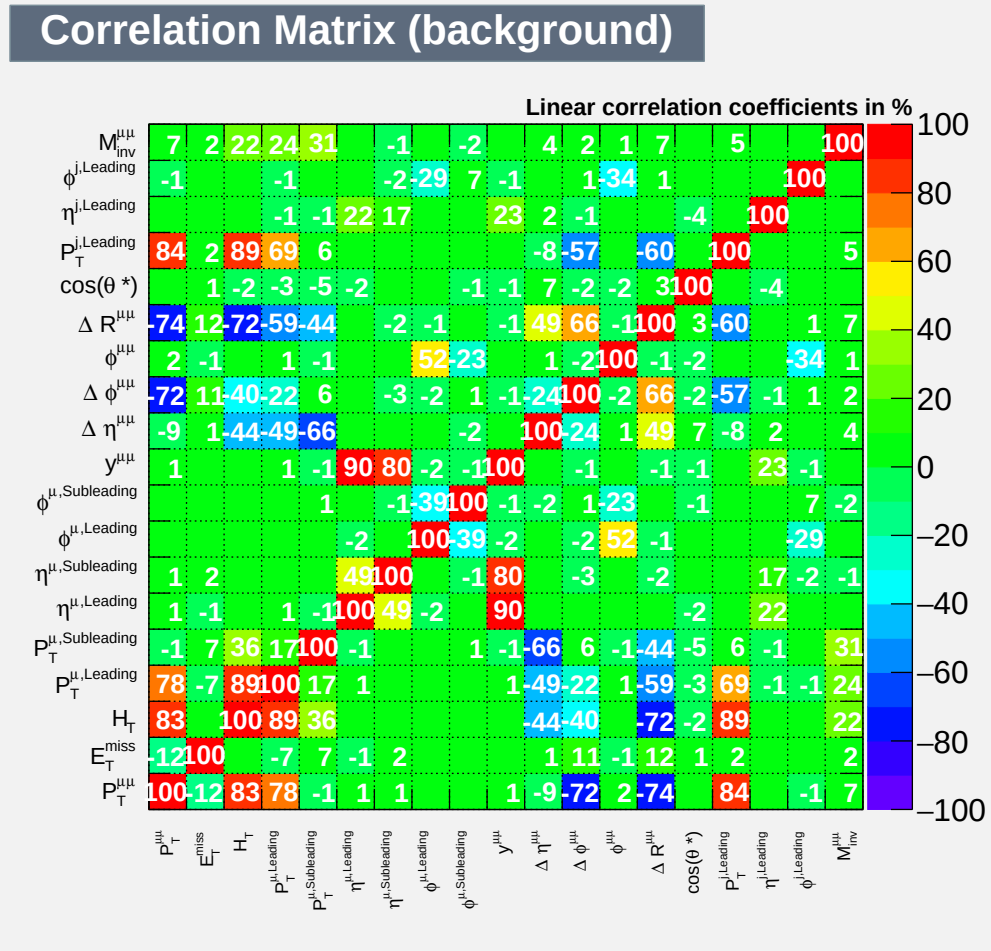

Figure C.0.4: Correlations between variables initially considered for training of the single-jet selection BDTs. Correlations are presented for Fold 2 of the combined Drell-Yan, di-boson, top and electroweak Z plus jet backgrounds.

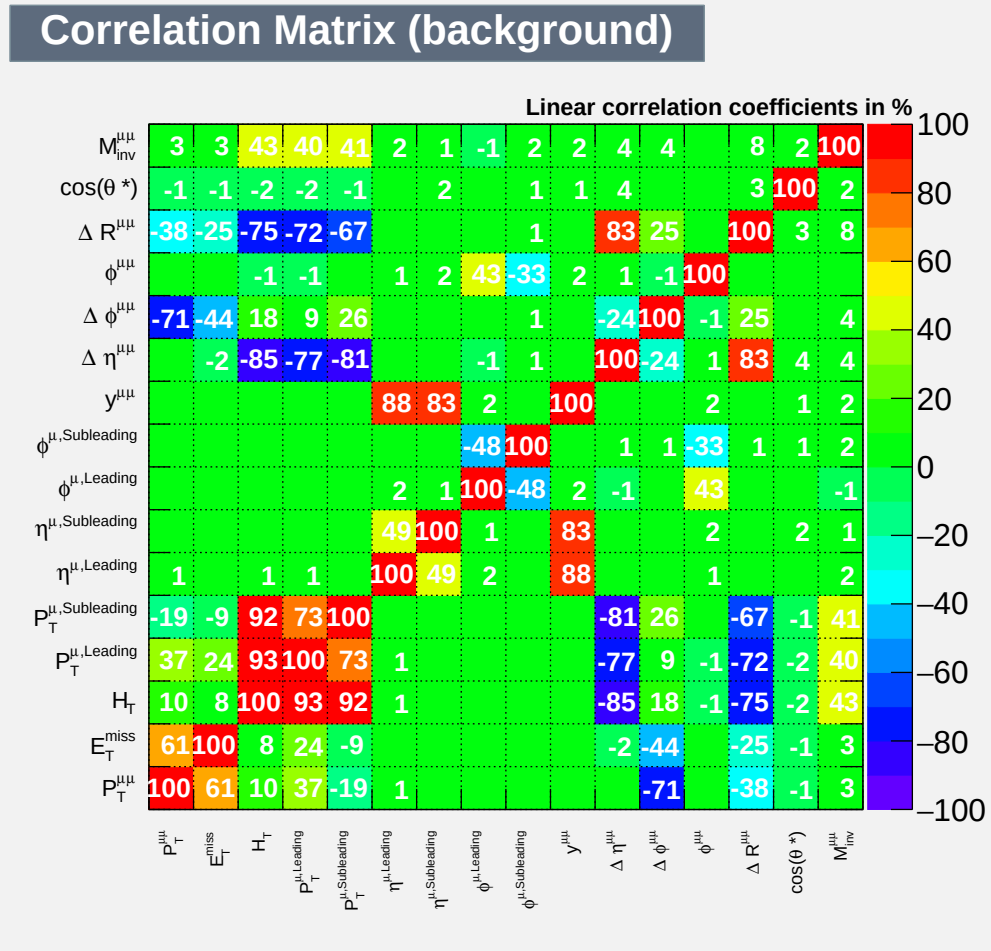

Figure C.0.5: Correlations between variables initially considered for training of the zero-jet selection BDTs. Correlations are presented for Fold 1 of the combined Drell-Yan, di-boson, top and electroweak Z plus jet backgrounds.

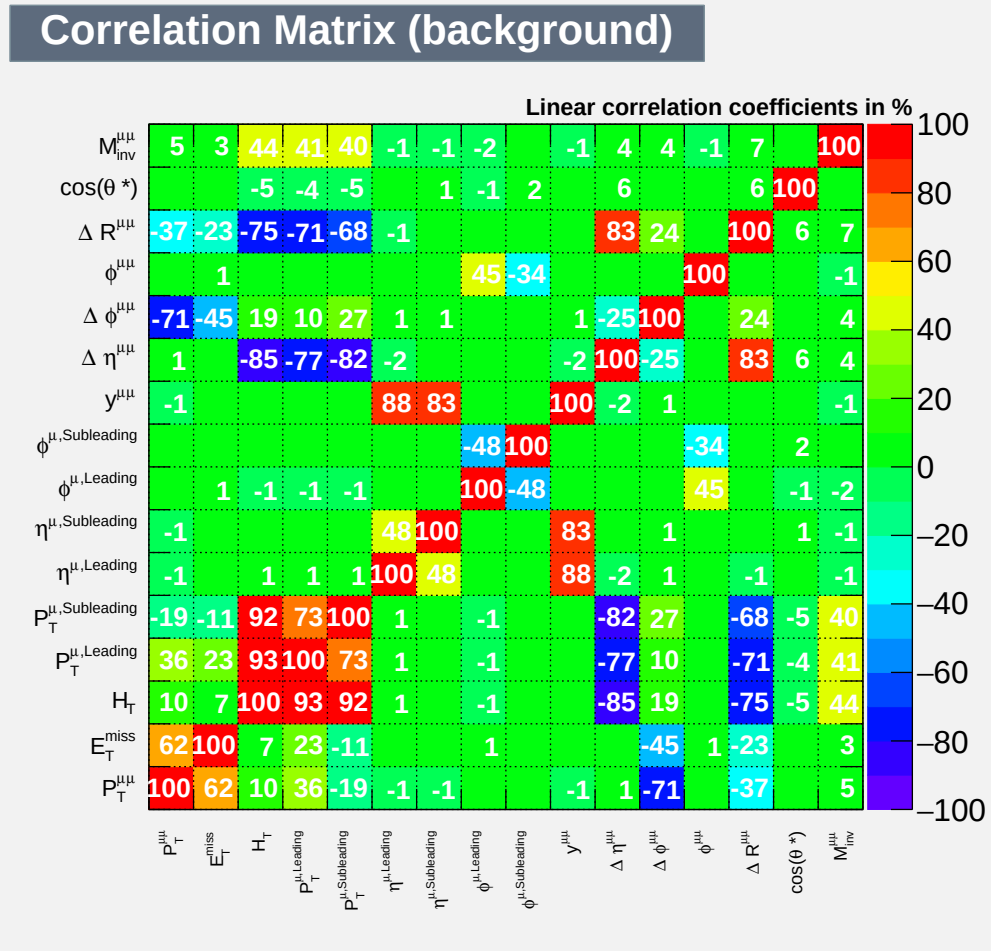

Figure C.0.6: Correlations between variables initially considered for training of the zero-jet selection BDTs. Correlations are presented for Fold 2 of the combined Drell-Yan, di-boson, top and electroweak Z plus jet backgrounds.

Appendix D

BDT Variable Separation

This chapter presents plots comparing the normalised shapes of variables used to train the Dedicated Signal BDTs of Chapter 9. Signal and background MC shapes are shown in red and blue respectively, all normalised to unit area. Figures D.0.1 to D.0.3 present distributions of the variables used to the train the VBF BDT, while Figures D.0.4 to D.0.7 present the variable distributions of the Inclusive, Multi-Jet, Single-Jet and Zero-Jet BDTs.

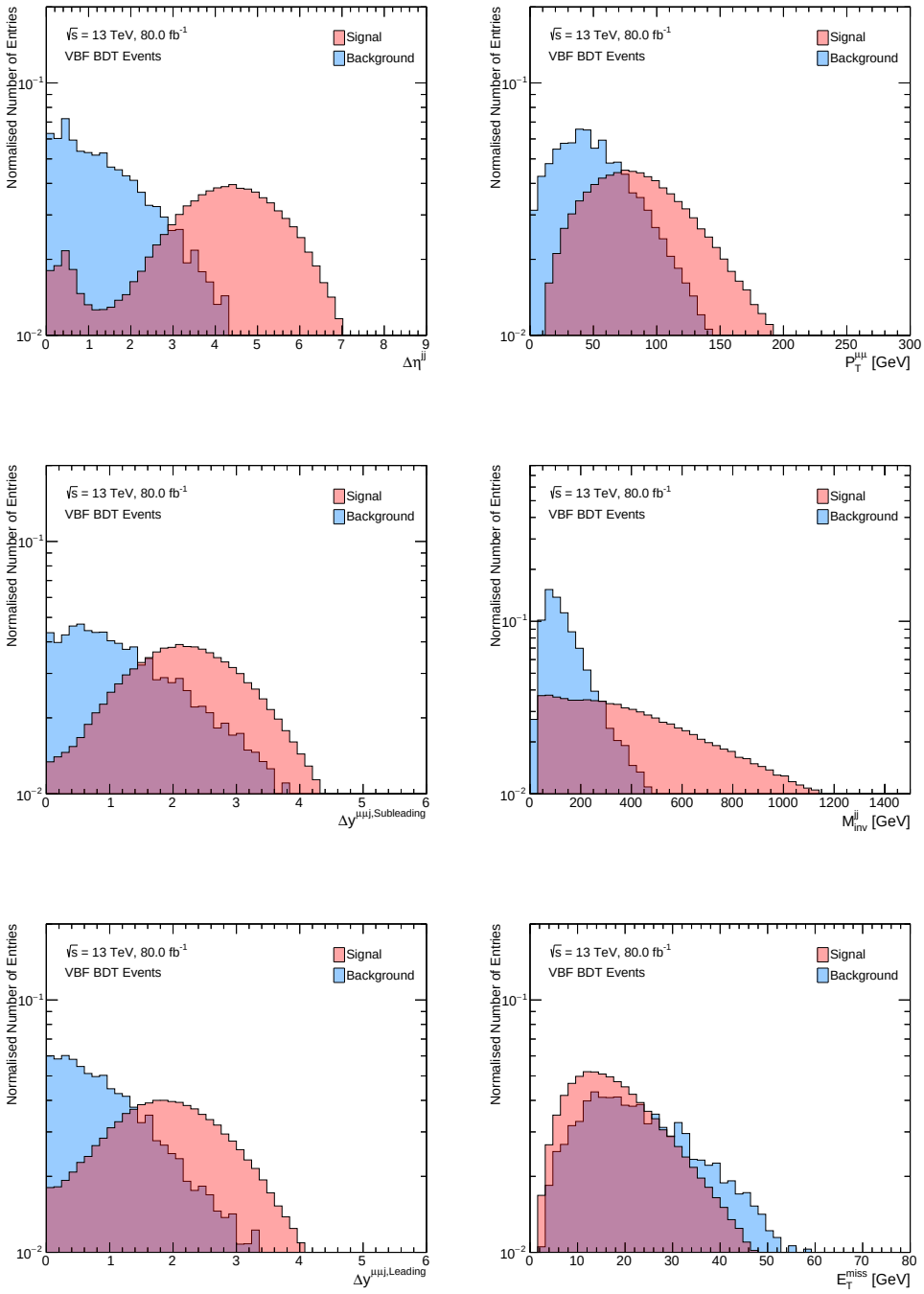

Figure D.0.1: Comparison between the VBF signal and combined background MC distributions for $\Delta\eta^{jj}$ (top left), $P_T^{\mu\mu}$ (top right), $\Delta y^{\mu\mu j,\text{Subleading}}$ (middle left), M_{inv}^{jj} (middle right), $\Delta y^{\mu\mu j,\text{Leading}}$ (bottom left) and E_T^{miss} (bottom right). Samples are normalised to unit area.

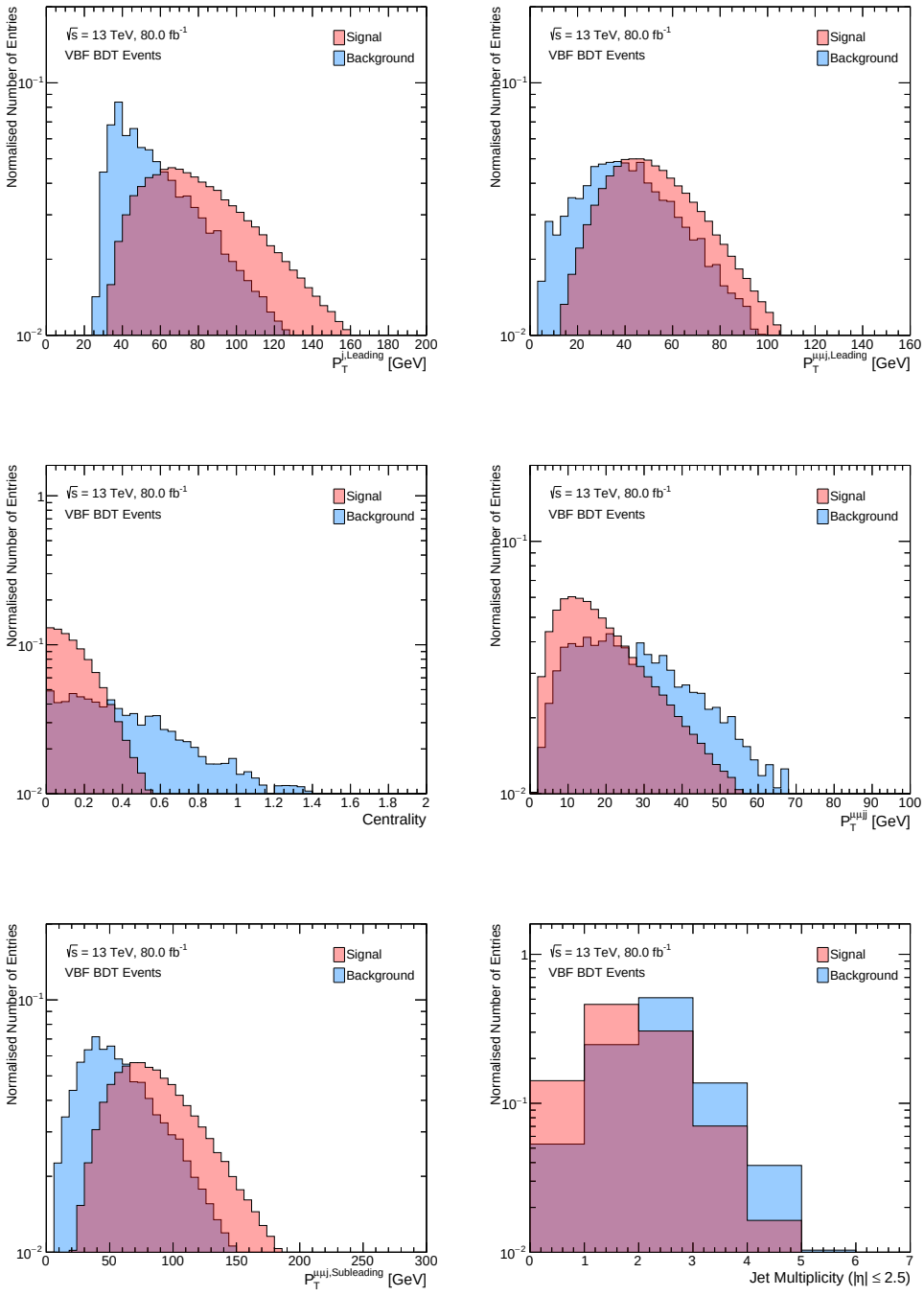

Figure D.0.2: Comparison between the VBF signal and combined background MC distributions for $P_T^{j,\text{Leading}}$ (top left), $P_T^{\mu\mu j,\text{Leading}}$ (top right), Centrality (middle left), $P_T^{\mu\mu jj}$ (middle right), $P_T^{\mu\mu j,\text{Subleading}}$ (bottom left) and Central Jet Multiplicity (bottom right). Samples are normalised to unit area.

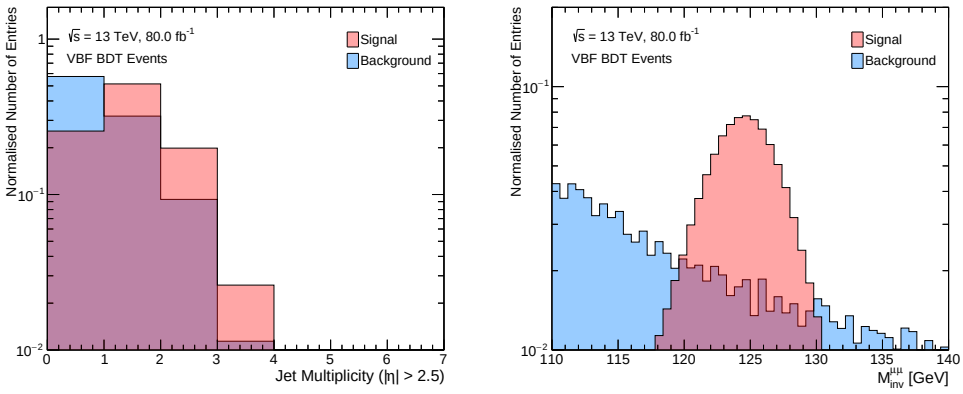

Figure D.0.3: Comparison between the VBF signal and combined background MC distributions for Non-Central Jet Multiplicity (left) and $M_{\text{inv}}^{\mu\mu}$ (right). Samples are normalised to unit area.

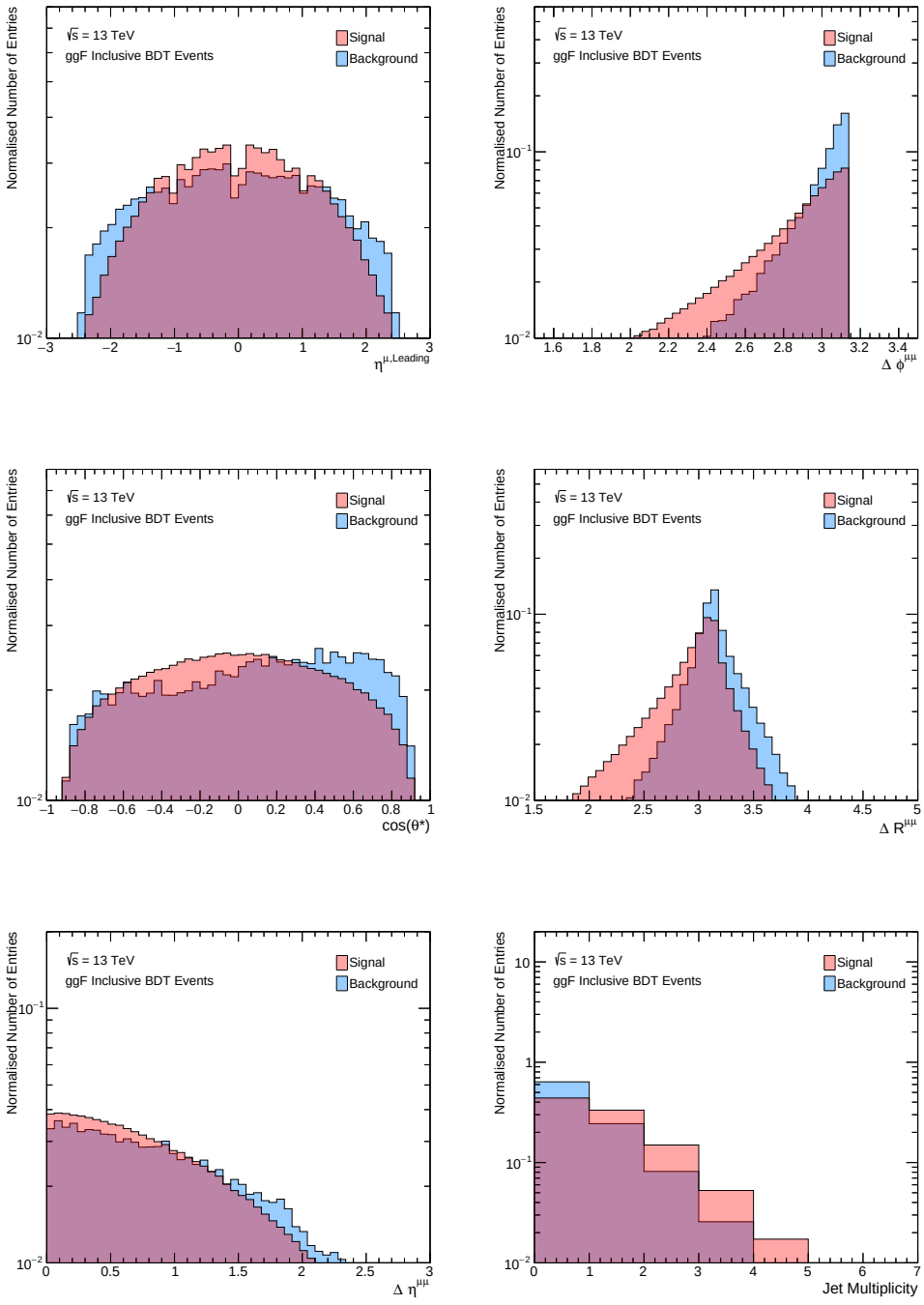

Figure D.0.4: Comparison between the $\eta^{\mu,\text{Leading}}$ (top left), $\Delta\phi^{\mu\mu}$ (top right), $\cos(\theta*)$ (middle left), $\Delta R^{\mu\mu}$ (middle right), $\Delta\eta^{\mu\mu}$ (bottom left) and Jet Multiplicity (bottom right) distributions of signal and background events used to train the dedicated ggF BDT with the inclusive selection. Samples are normalised to unit area.

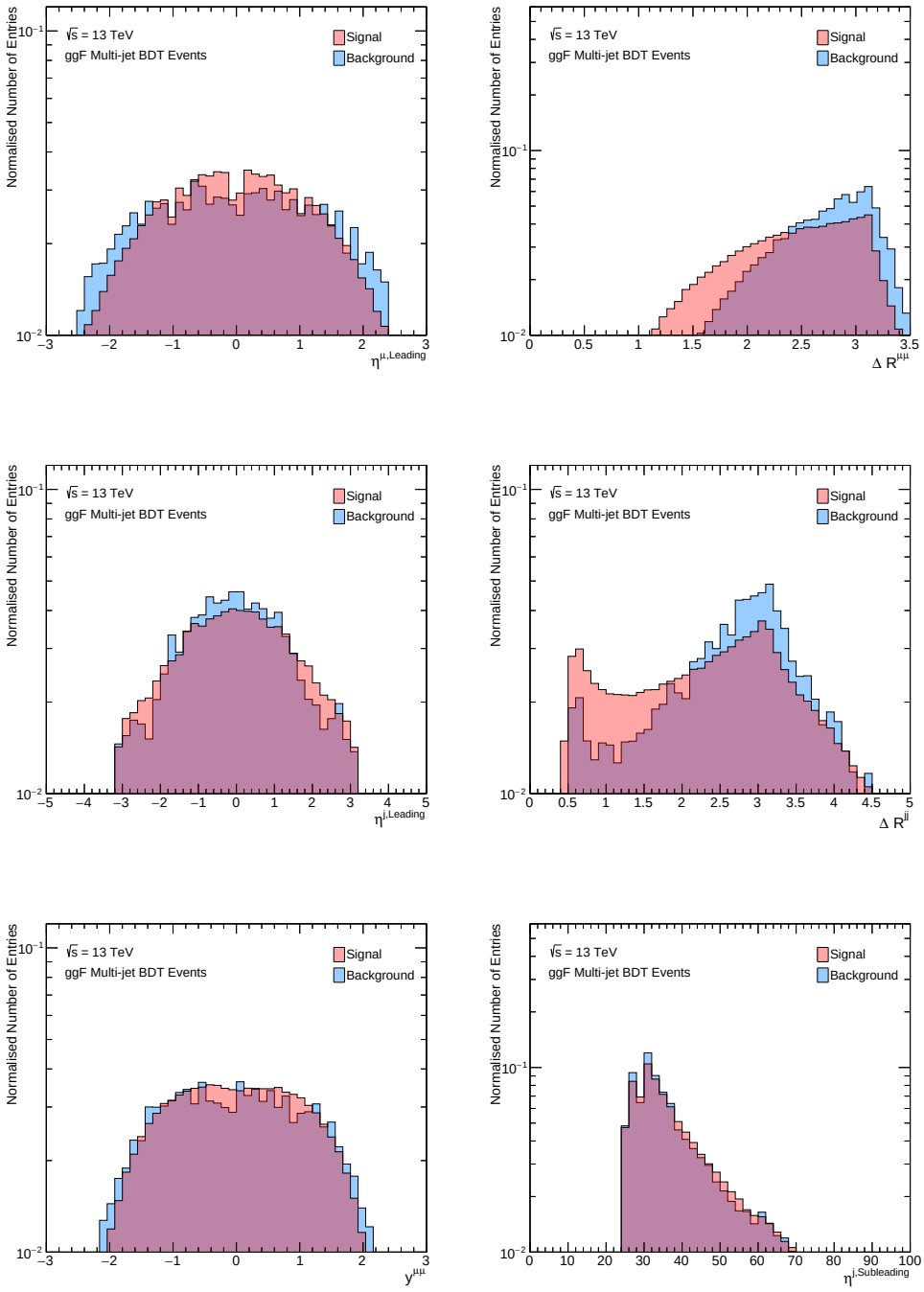

Figure D.0.5: Comparison between the $\eta^{\mu,\text{Leading}}$ (top left), $\Delta R^{\mu\mu}$ (top right), $\eta^{j,\text{Leading}}$ (middle left), ΔR^{jj} (middle right), $\Delta y^{\mu\mu}$ (bottom left) and $\eta^{j,\text{Subleading}}$ (bottom right) distributions of signal and background events used to train the dedicated ggF BDT with the multi-jet selection. Samples are normalised to unit area.

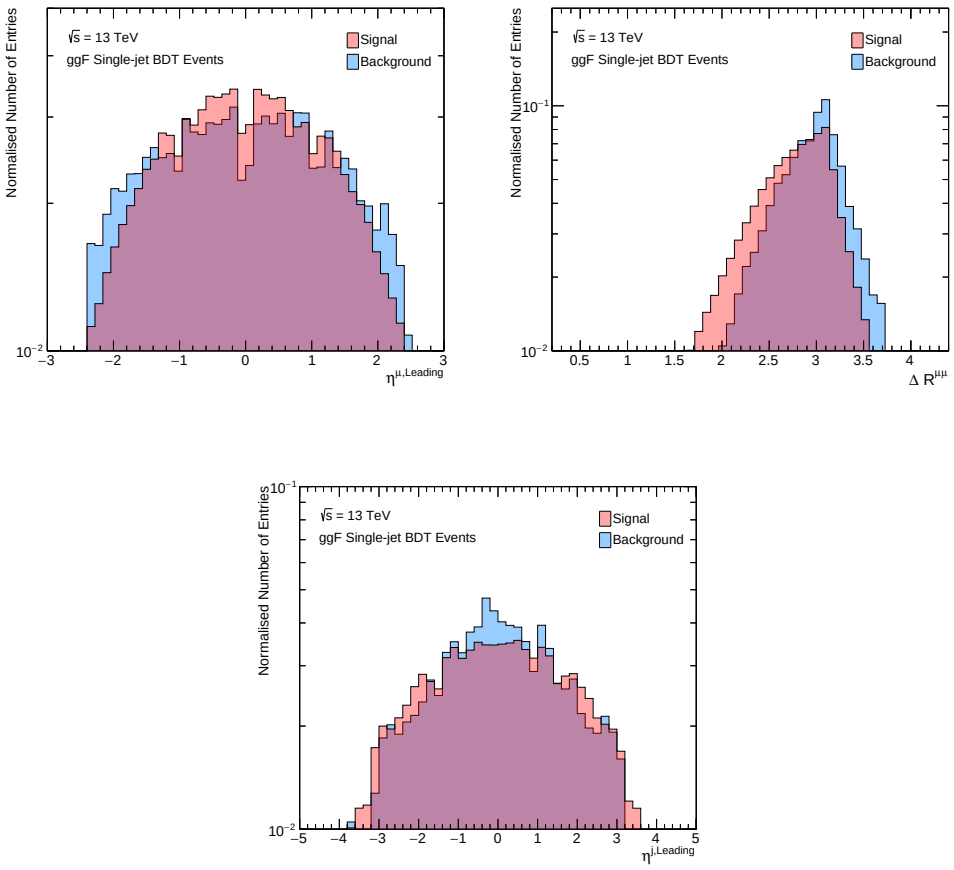

Figure D.0.6: Comparison between the $\eta^{\mu,\text{Leading}}$ (top left), $\Delta R^{\mu\mu}$ (top right) and $\eta^{j,\text{Leading}}$ (bottom) distributions of signal and background events used to train the dedicated ggF BDT with the single-jet selection. Samples are normalised to unit area.

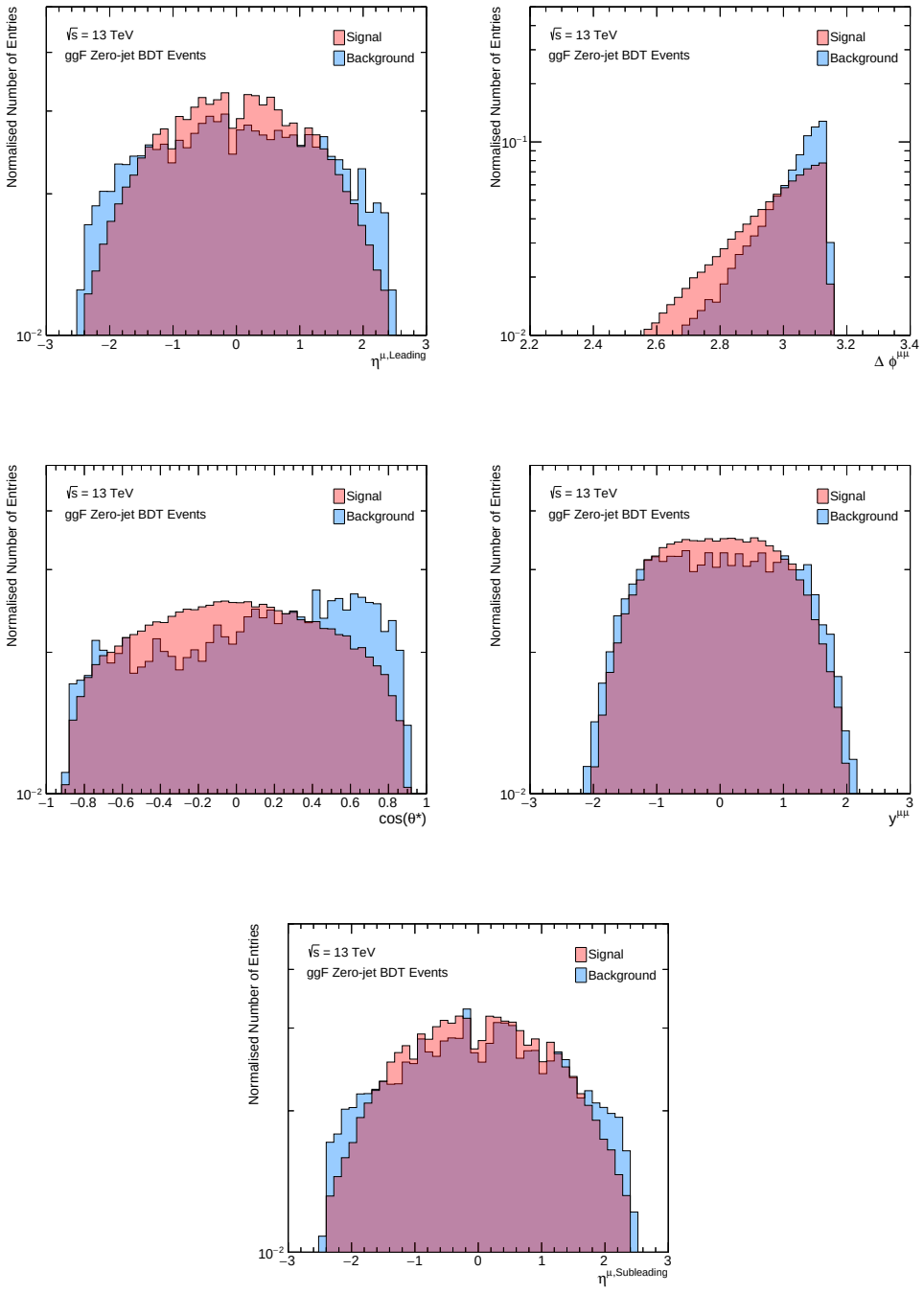

Figure D.0.7: Comparison between the $\eta^{\mu,\text{Leading}}$ (top left), $\Delta\phi^{\mu\mu}$ (top right), $\cos(\theta*)$ (middle left), $y^{\mu\mu}$ (middle right) and $\eta^{\mu,\text{Subleading}}$ (bottom) distributions of signal and background events used to train the dedicated ggF BDT with the zero-jet selection. Samples are normalised to unit area.

Appendix E

$M^{\mu\mu}_{\text{inv}}$ Distributions with Madgraph Drell-Yan MC

Figures E.0.1 to E.0.5 present comparisons of the $M^{\mu\mu}_{\text{inv}}$ distributions of data and MC in each of the categories defined by the Dedicated Signal BDTs of Chapter 9. As opposed to the $M^{\mu\mu}_{\text{inv}}$ distributions seen in Chapter 9, Madgraph Drell-Yan samples have been utilised in these instances. Agreement within 10-20% is seen across most categories, with fluctuations contained within the statistical and systematic error bands. However, the number of Madgraph MC events is significantly limited in some categories, such as Zero-Jet 6, Single-Jet 5, Single-Jet 6 and Multi-Jet 5, leading to disjointed $M^{\mu\mu}_{\text{inv}}$ distributions. These are likely to introduce biases in the background fits, driving the decision to use the smoother Powheg Drell-Yan MC shape instead.

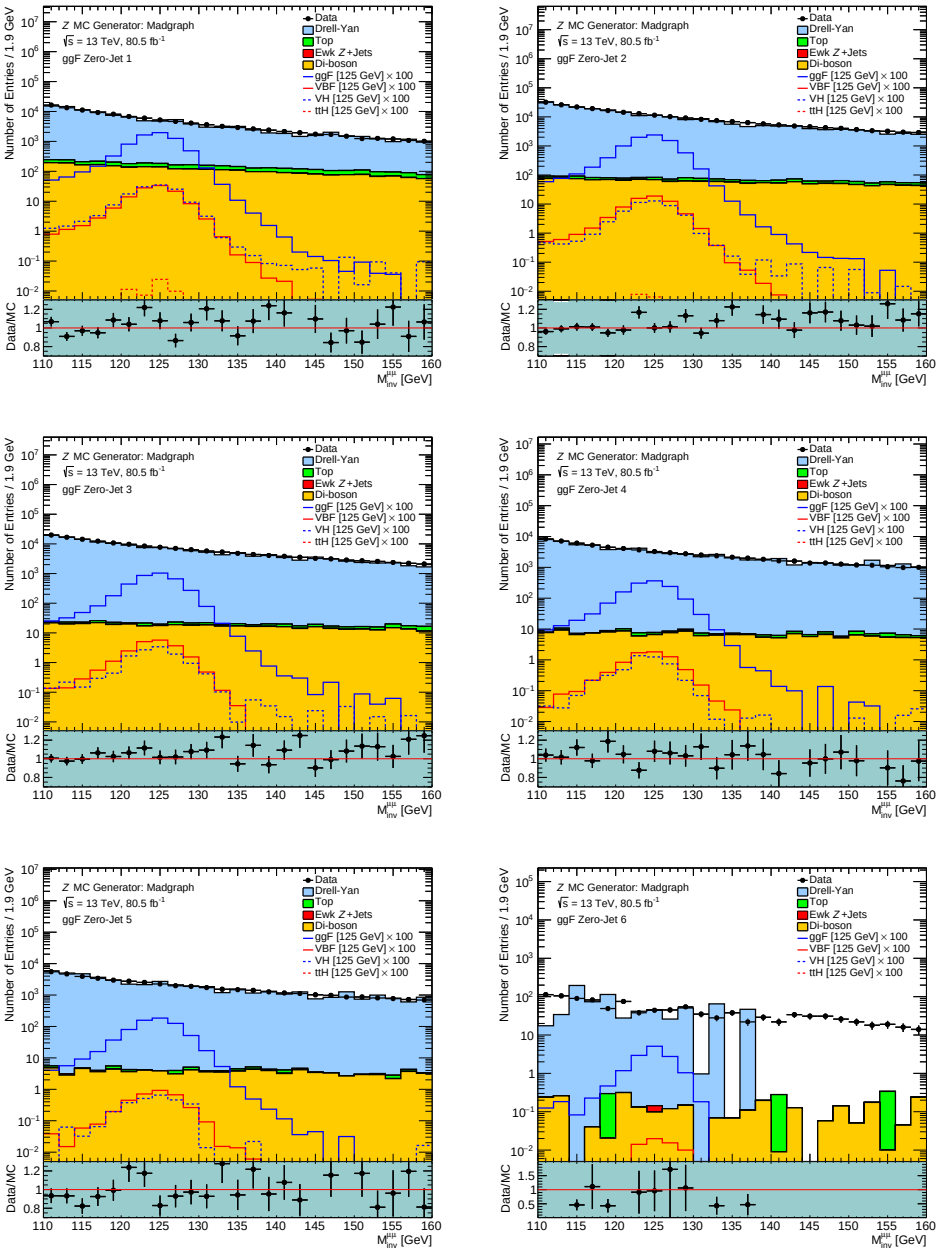

Figure E.0.1: Comparison of the $M^{\mu\mu}_{\text{inv}}$ distributions of data and MC in the ggF Zero-Jet 1 (top left), ggF Zero-Jet 2 (top right), ggF Zero-Jet 3 (middle left), ggF Zero-Jet 4 (middle right), ggF Zero-Jet 5 (bottom left) and ggF Zero-Jet 6 (bottom right) categories. The MC samples have been normalised to 80.5 fb^{-1}, with Madgraph used for the generation of the Drell-Yan events. The systematic bands include statistical, experimental systematic, $P_T^{\mu\mu}$ and M^{jj}_{inv} re-weighting uncertainties.

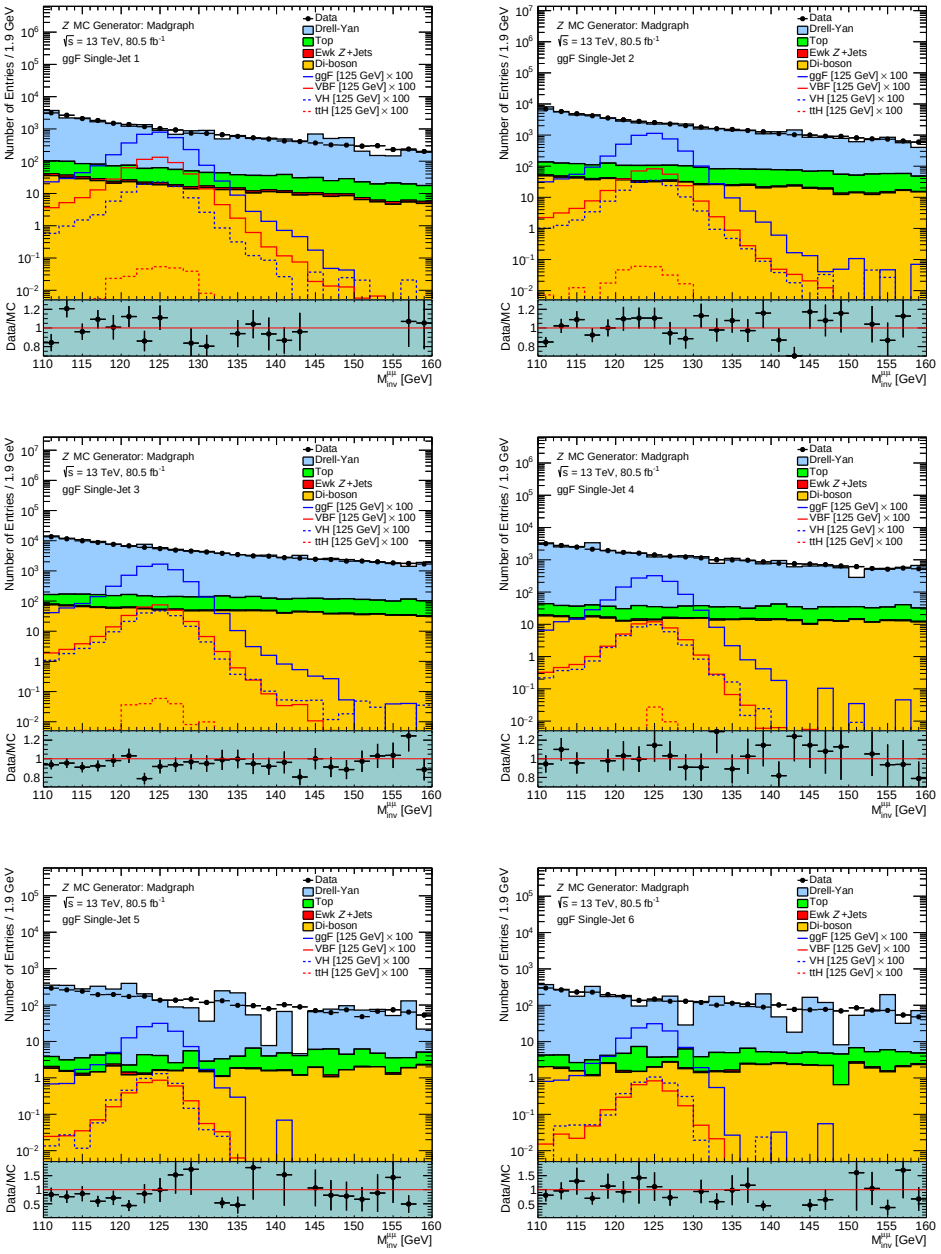

Figure E.0.2: Comparison of the $M_{\text{inv}}^{\mu\mu}$ distributions of data and MC in the ggF Single-Jet 1 (top left), ggF Single-Jet 2 (top right), ggF Single-Jet 3 (middle left), ggF Single-Jet 4 (middle right), ggF Single-Jet 5 (bottom left) and ggF Single-Jet 6 (bottom right) categories. The MC samples have been normalised to 80.5 fb^{-1}, with Madgraph used for the generation of the Drell-Yan events. The systematic bands include statistical, experimental systematic, $P_T^{\mu\mu}$ and M_{inv}^{jj} re-weighting uncertainties.

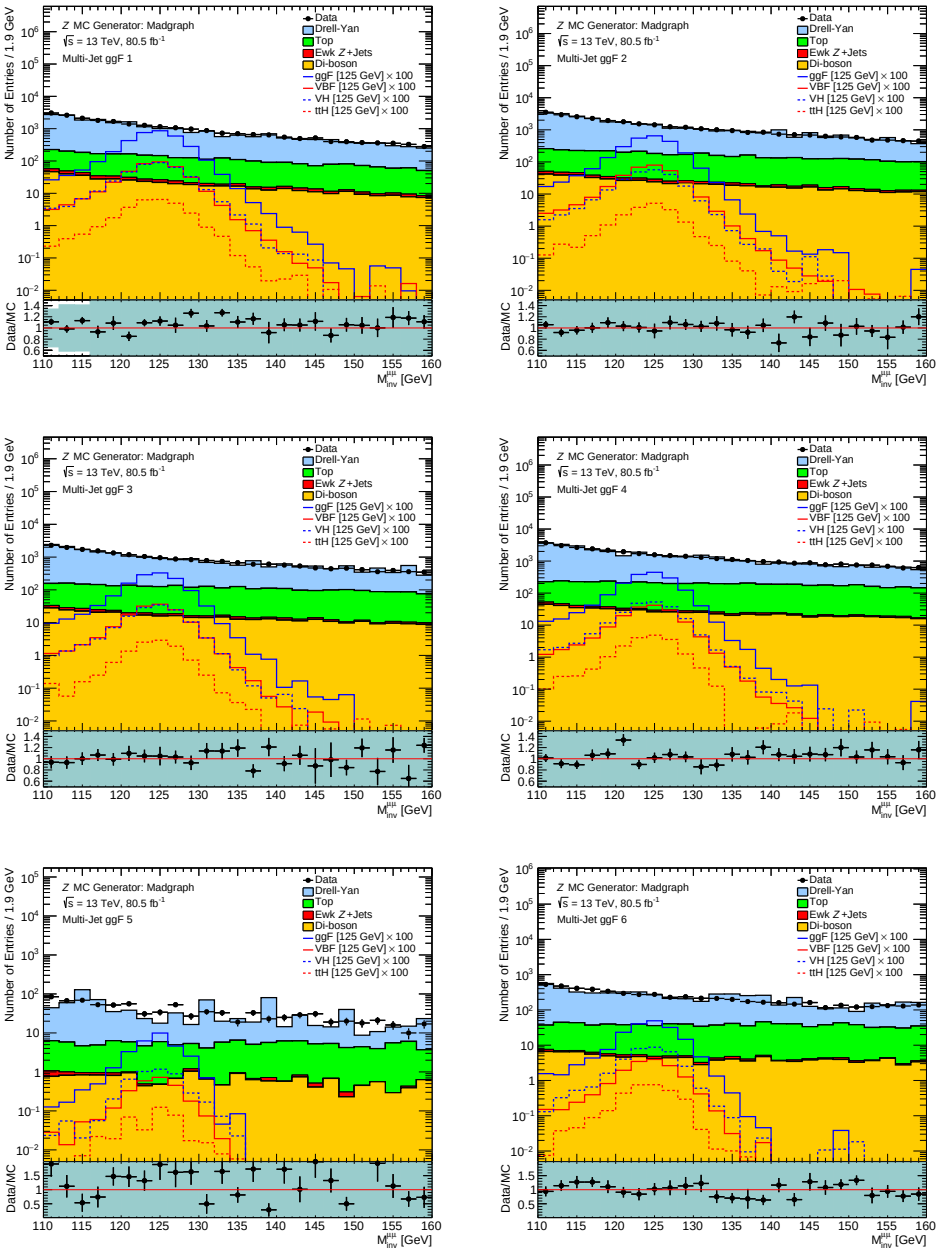

Figure E.0.3: Comparison of the $M^{\mu\mu}_{\text{inv}}$ distributions of data and MC in the ggF Multi-Jet 1 (top left), ggF Multi-Jet 2 (top right), ggF Multi-Jet 3 (middle left), ggF Multi-Jet 4 (middle right), ggF Multi-Jet 5 (bottom left) and ggF Multi-Jet 6 (bottom right) categories. The MC samples have been normalised to 80.5 fb^{-1}, with Madgraph used for the generation of the Drell-Yan events. The systematic bands include statistical, experimental systematic, $P_T^{\mu\mu}$ and M^{jj}_{inv} re-weighting uncertainties.

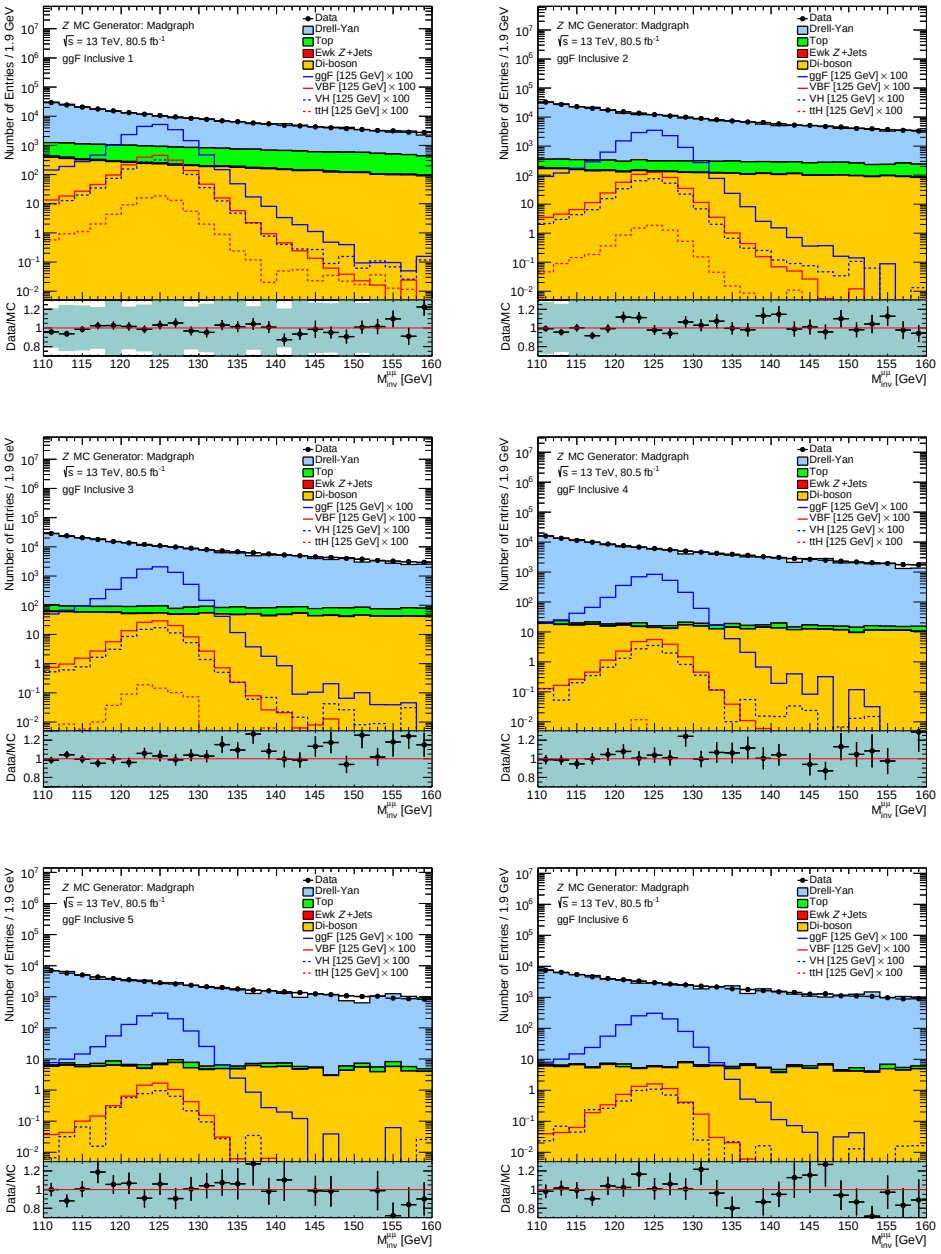

Figure E.0.4: Comparison of the $M^{\mu\mu}_{\text{inv}}$ distributions of data and MC in the ggF Inclusive 1 (top left), ggF Inclusive 2 (top right), ggF Inclusive 3 (middle left), ggF Inclusive 4 (middle right), ggF Inclusive 5 (bottom left) and ggF Inclusive 6 (bottom right) categories. The MC samples have been normalised to 80.5 fb^{-1}, with Madgraph used for the generation of the Drell-Yan events. The systematic bands include statistical, experimental systematic, $P_T^{\mu\mu}$ and M^{jj}_{inv} re-weighting uncertainties.

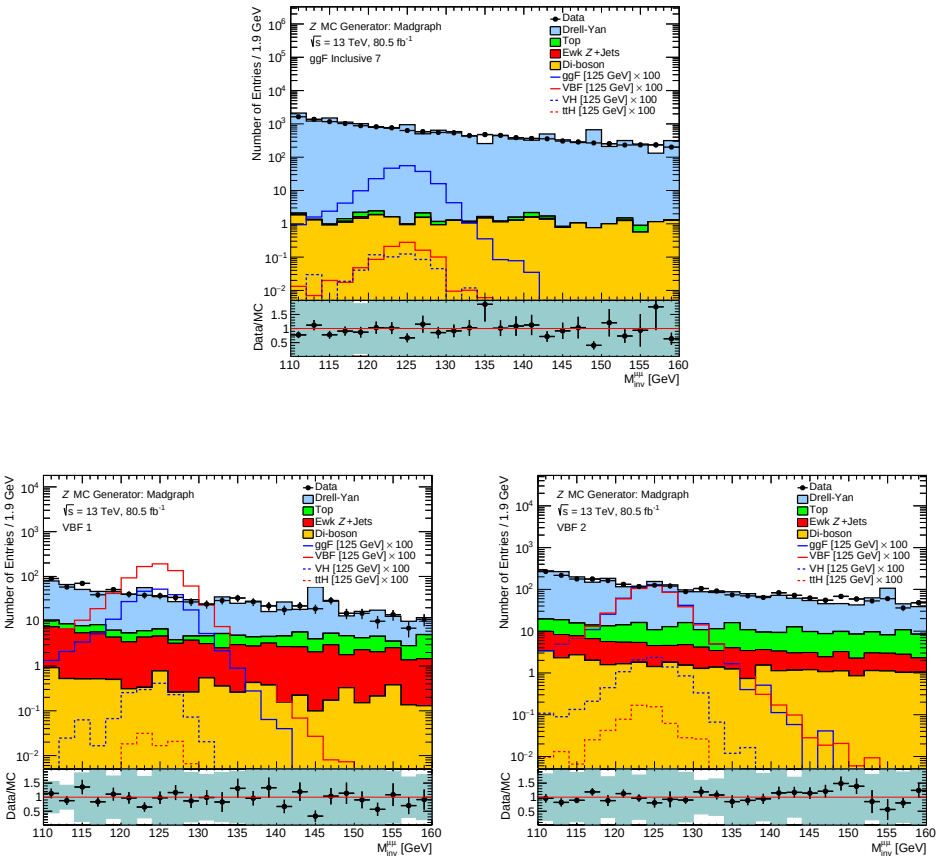

Figure E.0.5: Comparison of the $M_{\text{inv}}^{\mu\mu}$ distributions of data and MC in the ggF Inclusive 7 (top), VBF 1 (bottom left) and VBF 2 (bottom right) categories. The MC samples have been normalised to 80.5 fb^{-1}, with Madgraph used for the generation of the Drell-Yan events. The systematic bands include statistical, experimental systematic, $P_T^{\mu\mu}$ and M_{inv}^{jj} re-weighting uncertainties.

Appendix F

Supplementary Monte Carlo Fits

This chapter presents signal and background fits supplementary to those presented in Chapter 10.

F.1 Signal Fits

Since the final signal plus background fits incorporate contributions from WH, ZH and $t\bar{t}H$ events, the performance of the signal model in fitting $M_{\text{inv}}^{\mu\mu}$ distributions from the aforementioned processes was assessed across all categories. Figures F.1.1 to F.1.10 present the resulting fits, along with their associated pull distributions. No obvious biases were presented in the majority of cases, despite the large statistical uncertainties of the MC samples. A number of categories present null results, due to a lack of MC events with which to fit. Regardless, the processes were expected to contribute little to the final result given the 80.5 fb^{-1} data luminosity.

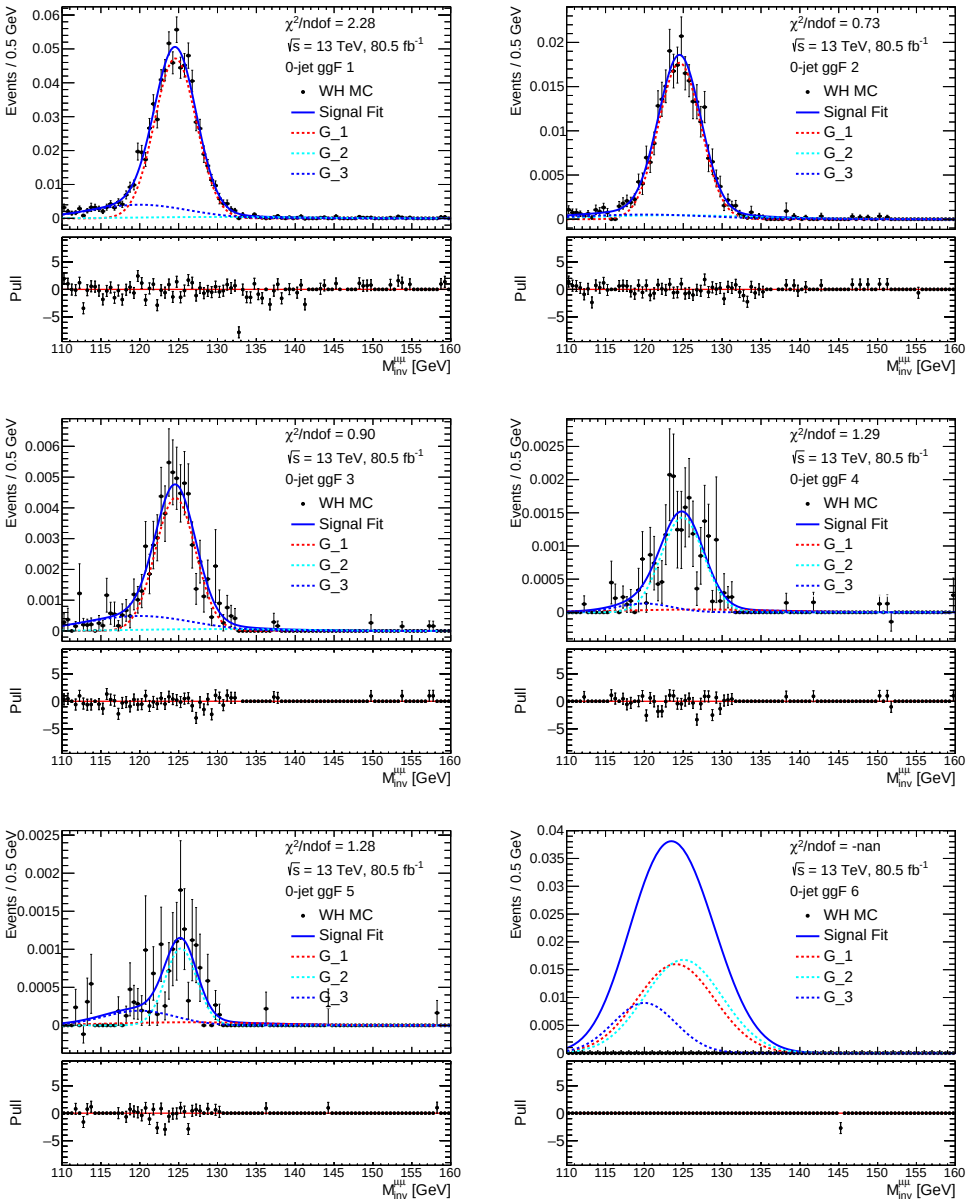

Figure F.1.1: The $M_{\text{inv}}^{\mu\mu}$ distributions of WH MC events in the ggF Zero-Jet 1 (top left), ggF Zero-Jet 2 (top right), ggF Zero-Jet 3 (middle left), ggF Zero-Jet 4 (middle right), ggF Zero-Jet 5 (bottom left) and ggF Zero-Jet 6 (bottom right) categories, fitted using the triple Gaussian signal model described in Chapter 10. The combined signal model is represented by the solid blue line, with the individual Gaussian components represented by the dashed red, cyan and blue lines. The distributions are normalised to 80.5 fb^{-1}, corresponding to the luminosity of the data.

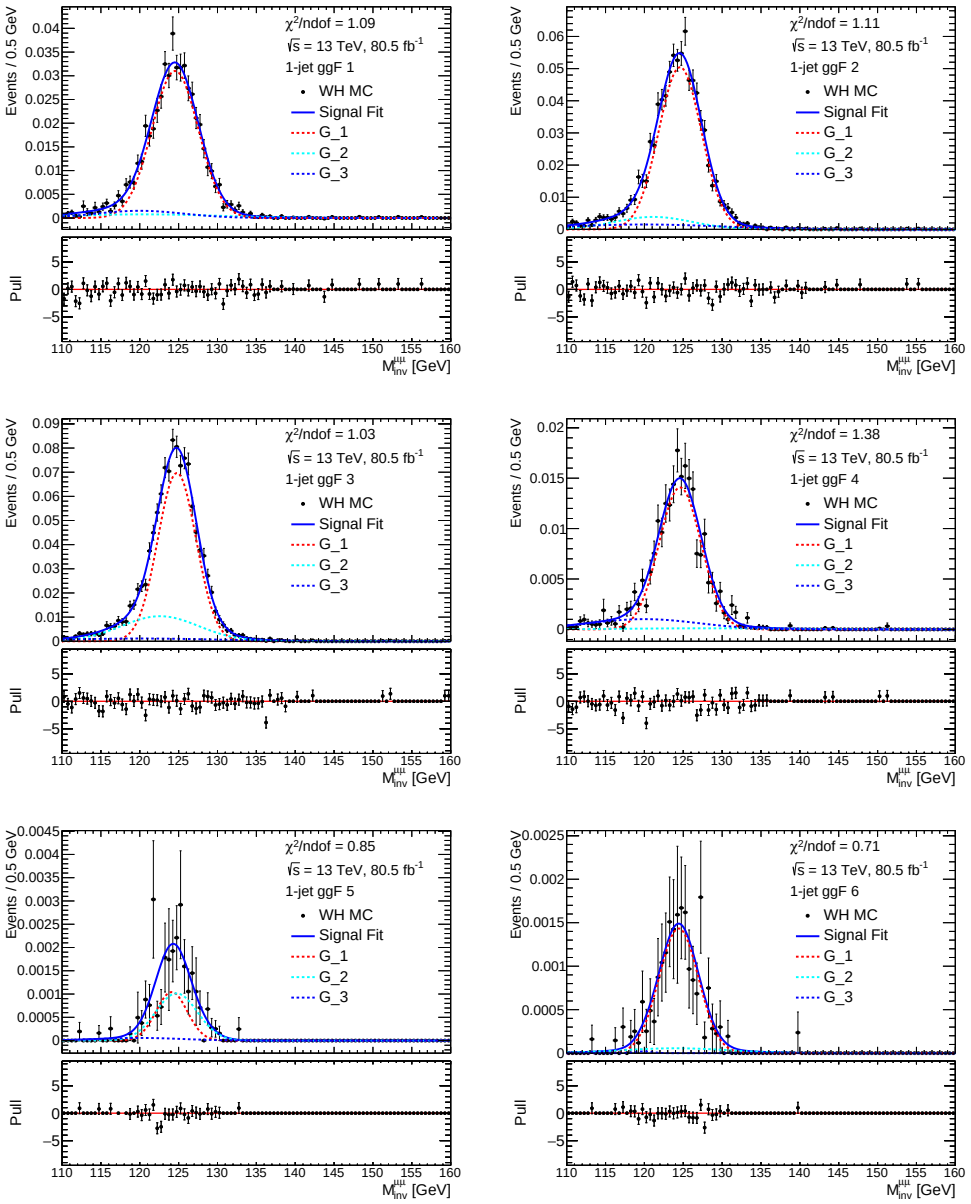

Figure F.1.2: The $M_{\text{inv}}^{\mu\mu}$ distributions of WH MC events in the ggF Single-Jet 1 (top left), ggF Single-Jet 2 (top right), ggF Single-Jet 3 (middle left), ggF Single-Jet 4 (middle right), ggF Single-Jet 5 (bottom left) and ggF Single-Jet 6 (bottom right) categories, fitted using the triple Gaussian signal model described in Chapter 10. The combined signal model is represented by the solid blue line, with the individual Gaussian components represented by the dashed red, cyan and blue lines. The distributions are normalised to 80.5 fb^{-1}, corresponding to the luminosity of the data.

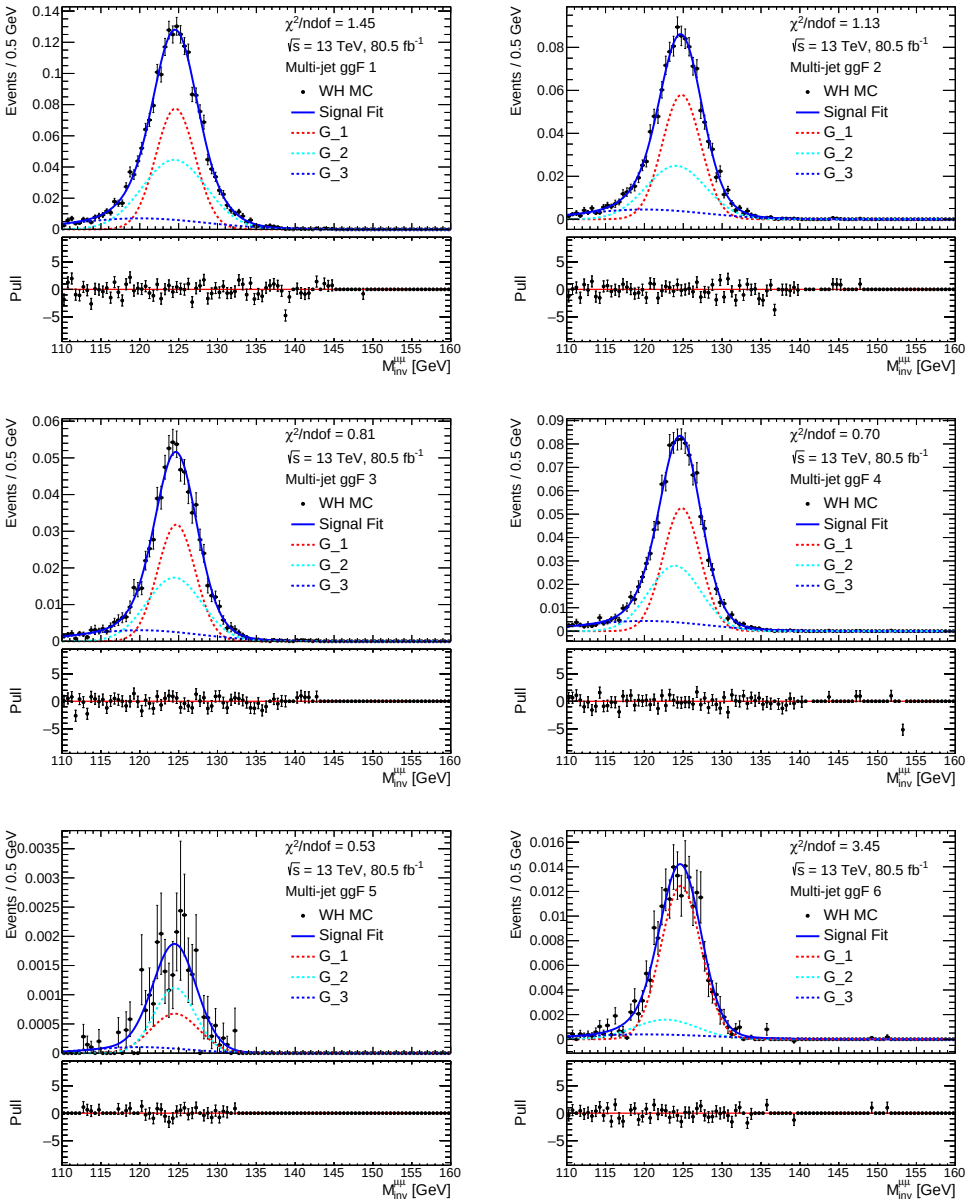

Figure F.1.3: The $M_{\text{inv}}^{\mu\mu}$ distributions of WH MC events in the ggF Multi-Jet 1 (top left), ggF Multi-Jet 2 (top right), ggF Multi-Jet 3 (middle left), ggF Multi-Jet 4 (middle right), ggF Multi-Jet 5 (bottom left) and ggF Multi-Jet 6 (bottom right) categories, fitted using the triple Gaussian signal model described in Chapter 10. The combined signal model is represented by the solid blue line, with the individual Gaussian components represented by the dashed red, cyan and blue lines. The distributions are normalised to 80.5 fb^{-1}, corresponding to the luminosity of the data.

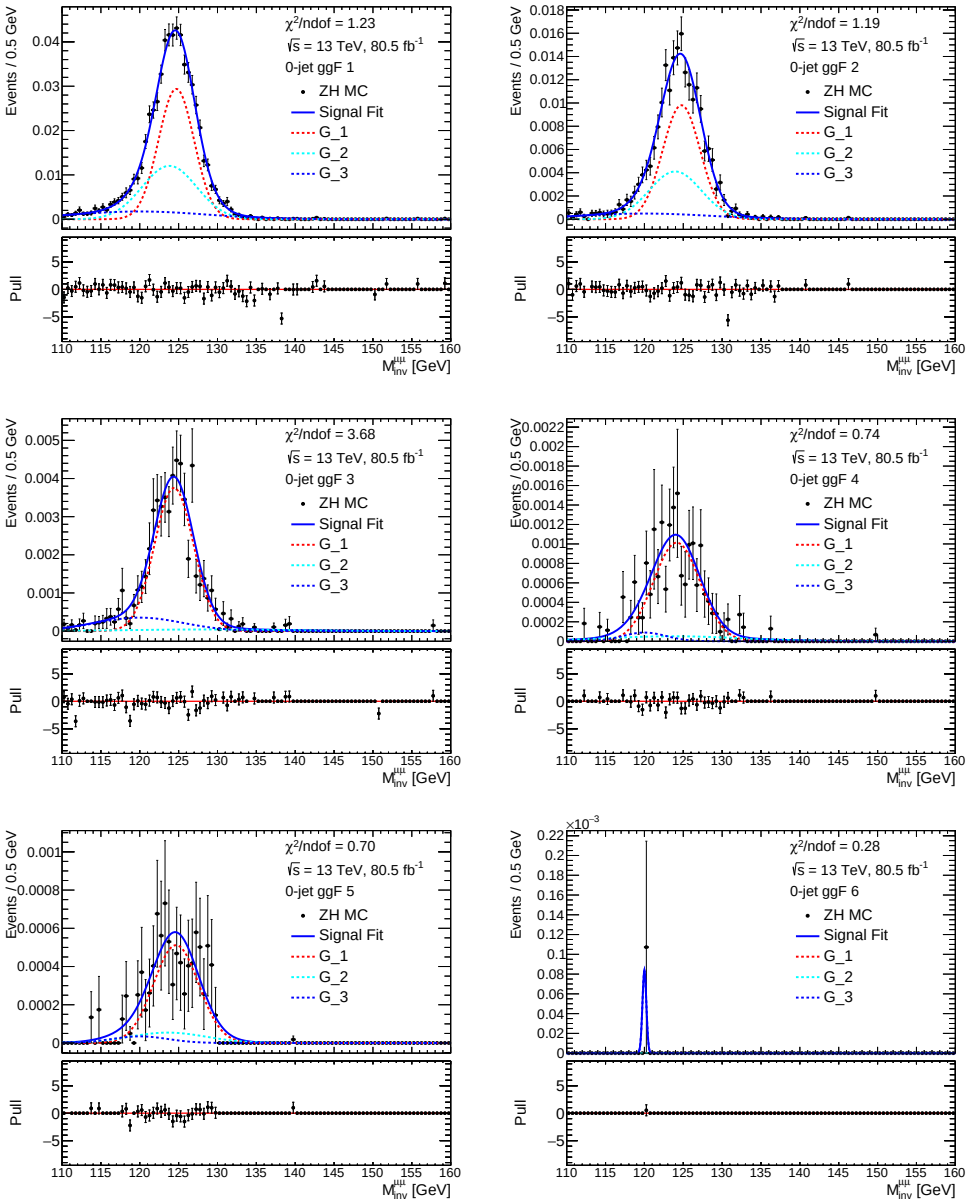

Figure F.1.4: The $M^{\mu\mu}_{\text{inv}}$ distributions of ZH MC events in the ggF Zero-Jet 1 (top left), ggF Zero-Jet 2 (top right), ggF Zero-Jet 3 (middle left), ggF Zero-Jet 4 (middle right), ggF Zero-Jet 5 (bottom left) and ggF Zero-Jet 6 (bottom right) categories, fitted using the triple Gaussian signal model described in Chapter 10. The combined signal model is represented by the solid blue line, with the individual Gaussian components represented by the dashed red, cyan and blue lines. The distributions are normalised to 80.5 fb^{-1}, corresponding to the luminosity of the data.

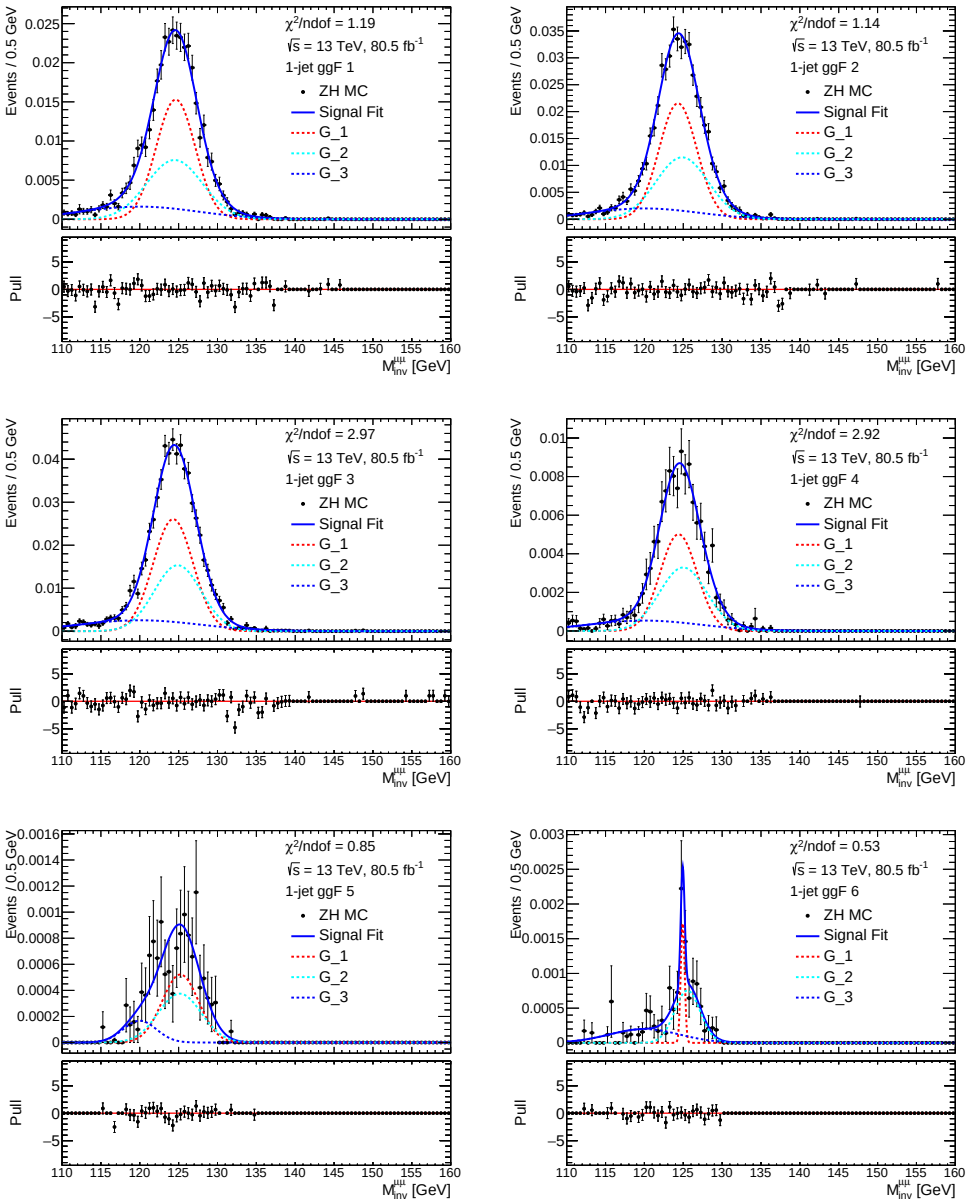

Figure F.1.5: The $M_{\text{inv}}^{\mu\mu}$ distributions of ZH MC events in the ggF Single-Jet 1 (top left), ggF Single-Jet 2 (top right), ggF Single-Jet 3 (middle left), ggF Single-Jet 4 (middle right), ggF Single-Jet 5 (bottom left) and ggF Single-Jet 6 (bottom right) categories, fitted using the triple Gaussian signal model described in Chapter 10. The combined signal model is represented by the solid blue line, with the individual Gaussian components represented by the dashed red, cyan and blue lines. The distributions are normalised to 80.5 fb^{-1}, corresponding to the luminosity of the data.

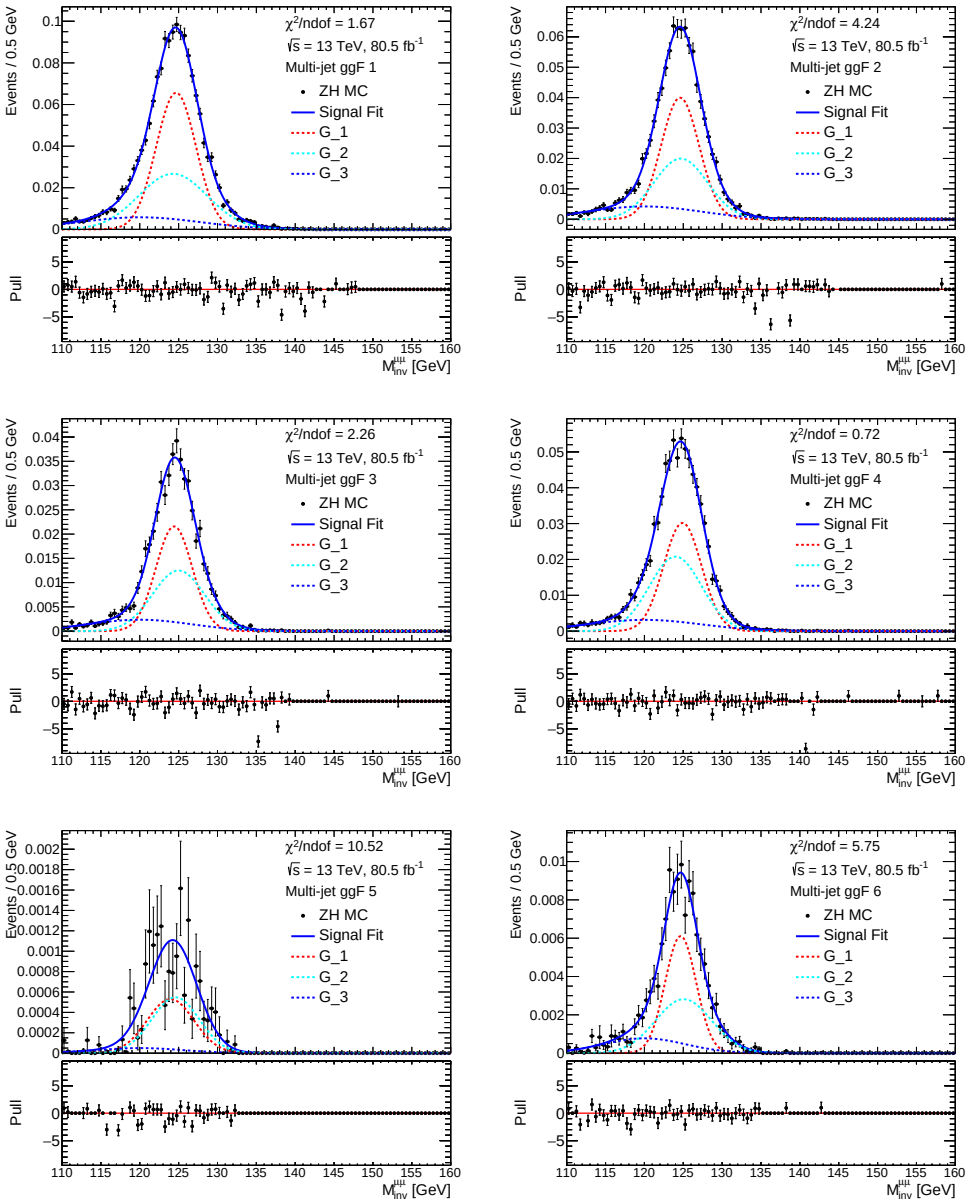

Figure F.1.6: The $M_{\text{inv}}^{\mu\mu}$ distributions of ZH MC events in the ggF Multi-Jet 1 (top left), ggF Multi-Jet 2 (top right), ggF Multi-Jet 3 (middle left), ggF Multi-Jet 4 (middle right), ggF Multi-Jet 5 (bottom left) and ggF Multi-Jet 6 (bottom right) categories, fitted using the triple Gaussian signal model described in Chapter 10. The combined signal model is represented by the solid blue line, with the individual Gaussian components represented by the dashed red, cyan and blue lines. The distributions are normalised to 80.5 fb^{-1}, corresponding to the luminosity of the data.

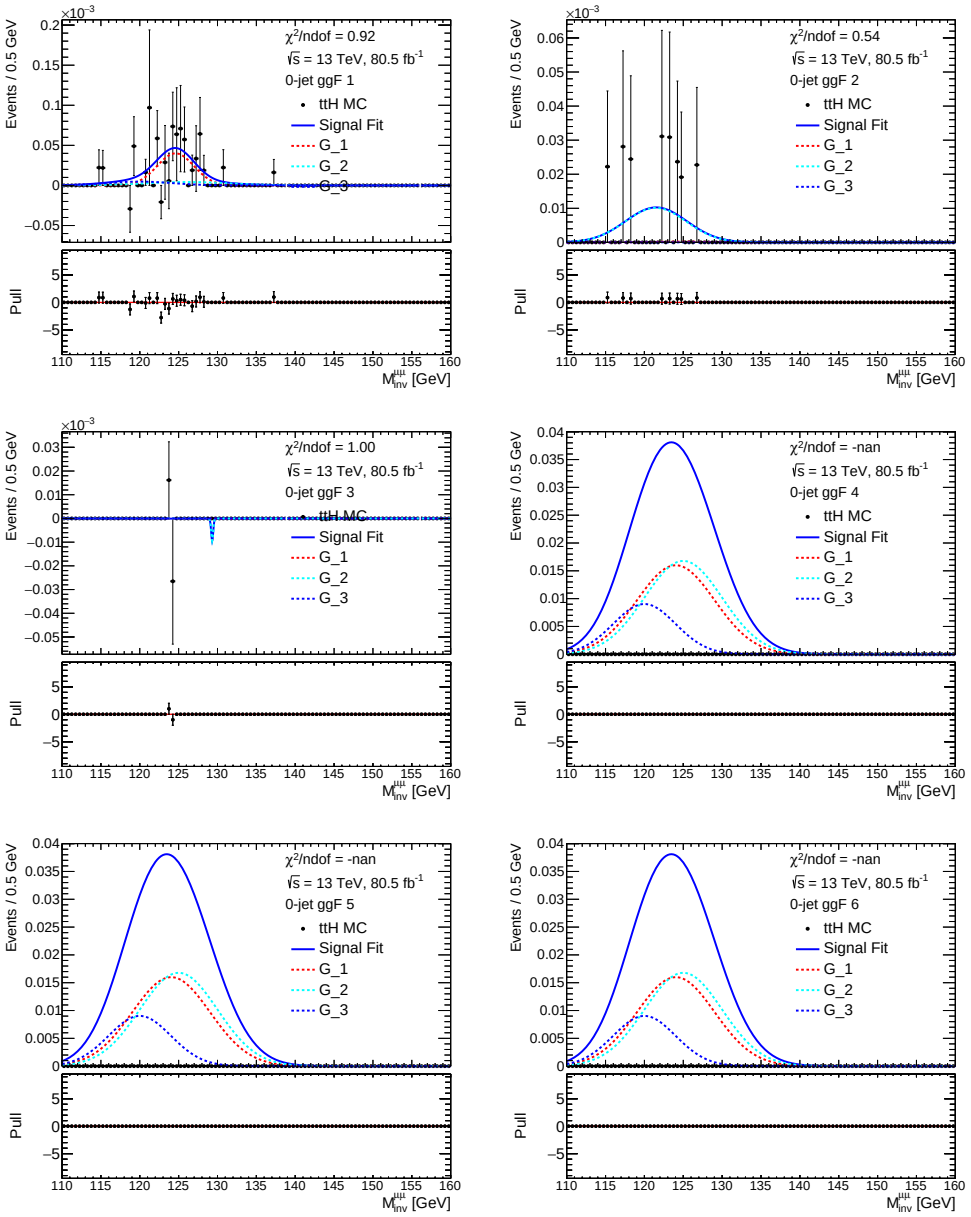

Figure F.1.7: The $M^{\mu\mu}_{\text{inv}}$ distributions of $t\bar{t}H$ MC events in the ggF Zero-Jet 1 (top left), ggF Zero-Jet 2 (top right), ggF Zero-Jet 3 (middle left), ggF Zero-Jet 4 (middle right), ggF Zero-Jet 5 (bottom left) and ggF Zero-Jet 6 (bottom right) categories, fitted using the triple Gaussian signal model described in Chapter 10. The combined signal model is represented by the solid blue line, with the individual Gaussian components represented by the dashed red, cyan and blue lines. The distributions are normalised to 80.5 fb^{-1}, corresponding to the luminosity of the data.

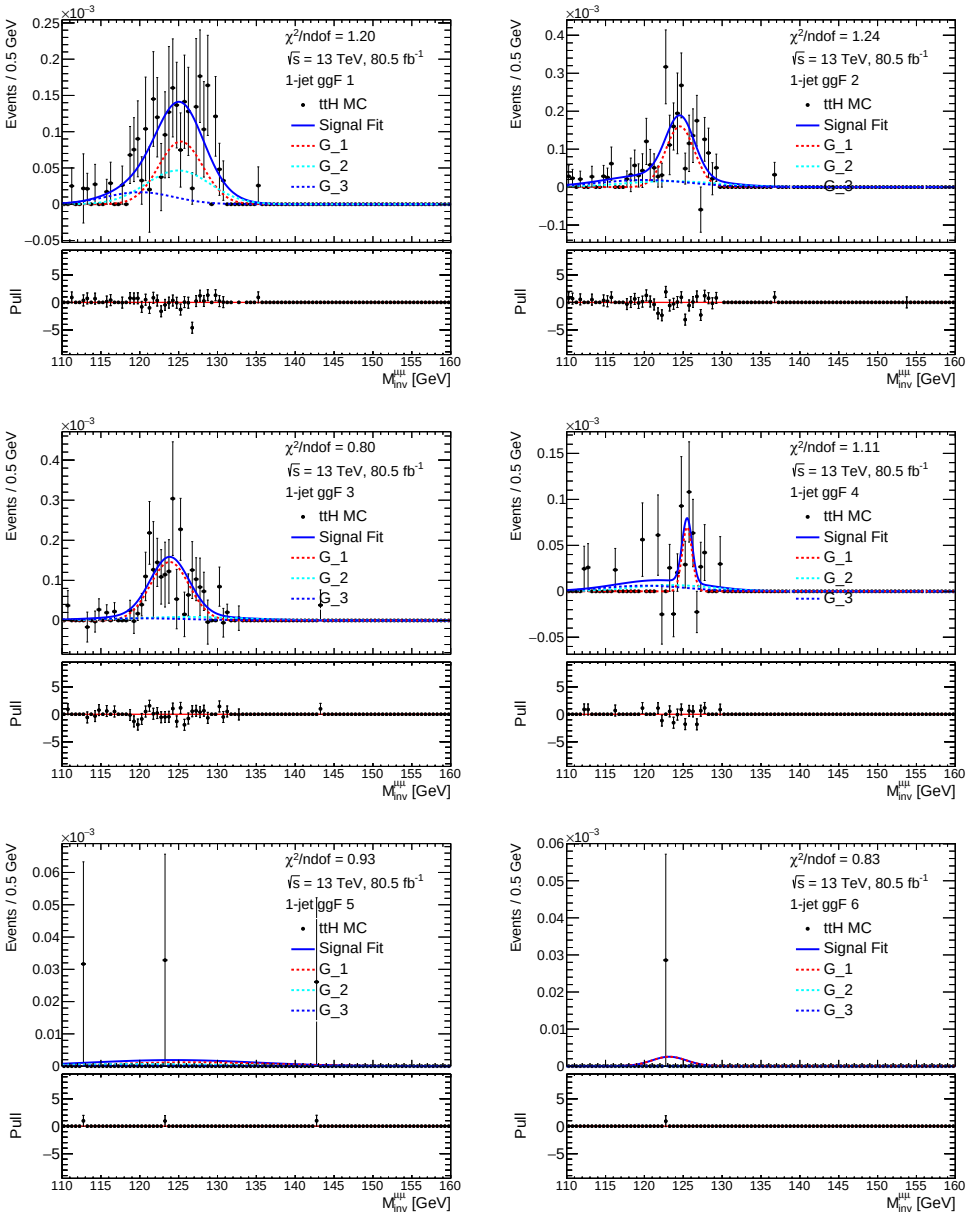

Figure F.1.8: The $M_{\text{inv}}^{\mu\mu}$ distributions of $t\bar{t}H$ MC events in the ggF Single-Jet 1 (top left), ggF Single-Jet 2 (top right), ggF Single-Jet 3 (middle left), ggF Single-Jet 4 (middle right), ggF Single-Jet 5 (bottom left) and ggF Single-Jet 6 (bottom right) categories, fitted using the triple Gaussian signal model described in Chapter 10. The combined signal model is represented by the solid blue line, with the individual Gaussian components represented by the dashed red, cyan and blue lines. The distributions are normalised to 80.5 fb^{-1}, corresponding to the luminosity of the data.

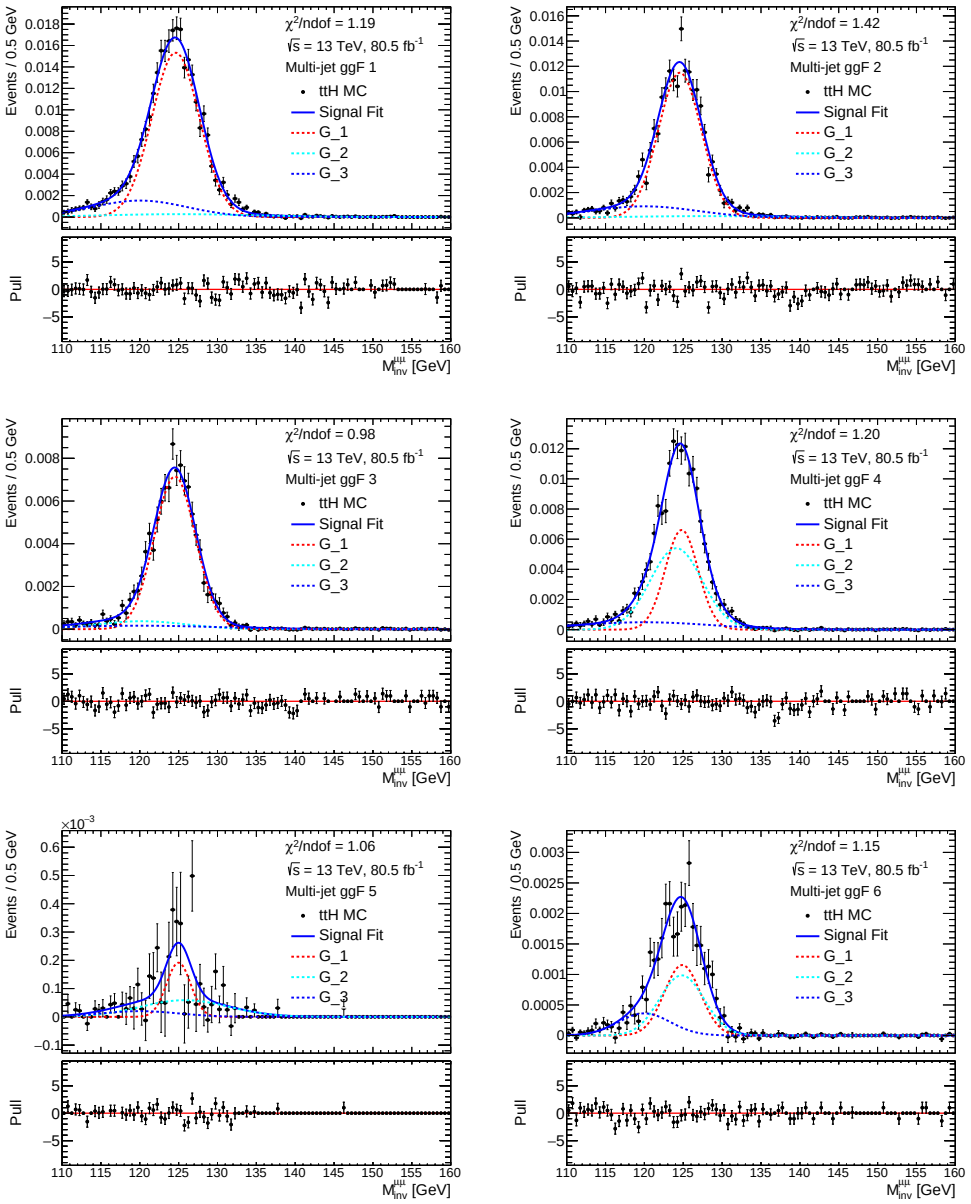

Figure F.1.9: The $M_{\text{inv}}^{\mu\mu}$ distributions of $t\bar{t}H$ MC events in the ggF Multi-Jet 1 (top left), ggF Multi-Jet 2 (top right), ggF Multi-Jet 3 (middle left), ggF Multi-Jet 4 (middle right), ggF Multi-Jet 5 (bottom left) and ggF Multi-Jet 6 (bottom right) categories, fitted using the triple Gaussian signal model described in Chapter 10. The combined signal model is represented by the solid blue line, with the individual Gaussian components represented by the dashed red, cyan and blue lines. The distributions are normalised to 80.5 fb^{-1}, corresponding to the luminosity of the data.

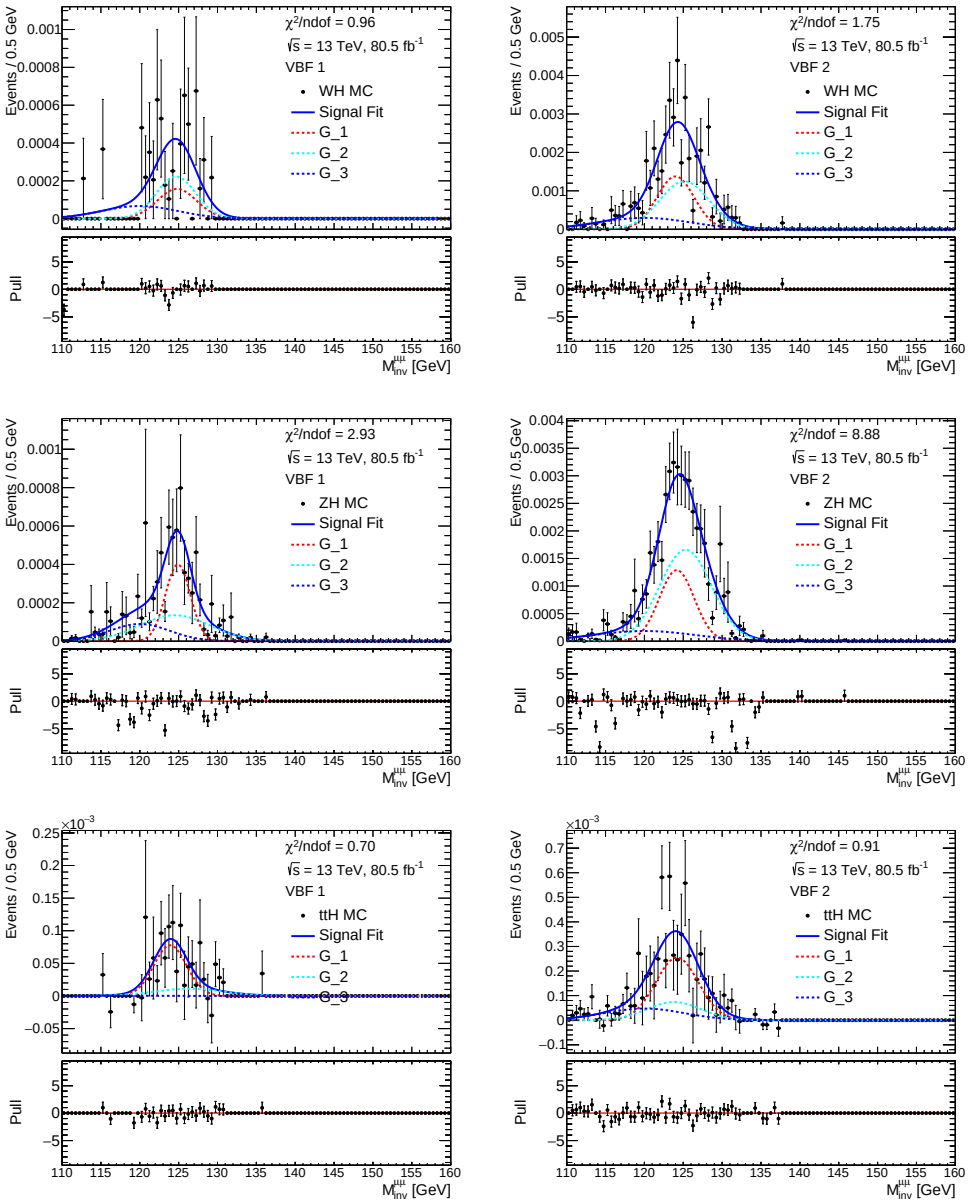

Figure F.1.10: The $M^{\mu\mu}_{\text{inv}}$ distributions of WH, ZH and $t\bar{t}H$ MC events in the VBF 1 (left) and VBF 2 (right) categories, fitted using the triple Gaussian signal model described in Chapter 10. The combined signal model is represented by the solid blue line, with the individual Gaussian components represented by the dashed red, cyan and blue lines. The distributions are normalised to 80.5 fb^{-1}, corresponding to the luminosity of the data.

F.2 Background Fits

Before unblinding the analysis, validation of the background model was performed through fitting background MC $M_{\text{inv}}^{\mu\mu}$ distributions in each of the analysis categories. These fits are presented in Figures F.2.1 to F.2.4, along with their associated pull distributions. Background contributions from Drell-Yan, electroweak Z plus jets, di-boson and top processes were considered. Drell-Yan contributions were modelled using Powheg samples normalised to the event yields of Madgraph. This was done to produce smooth distributions in each category, in order to increase the stability of the fits.

No obvious biases were present in any of the fits, with pulls typically ± 2. Pulls of ± 5 or greater were seen in certain bins, but these were likely due to statistical fluctuations. While the effect could be studied in more detail using larger MC samples, the performance of the background model in each category was satisfactory enough to unblind the analysis.

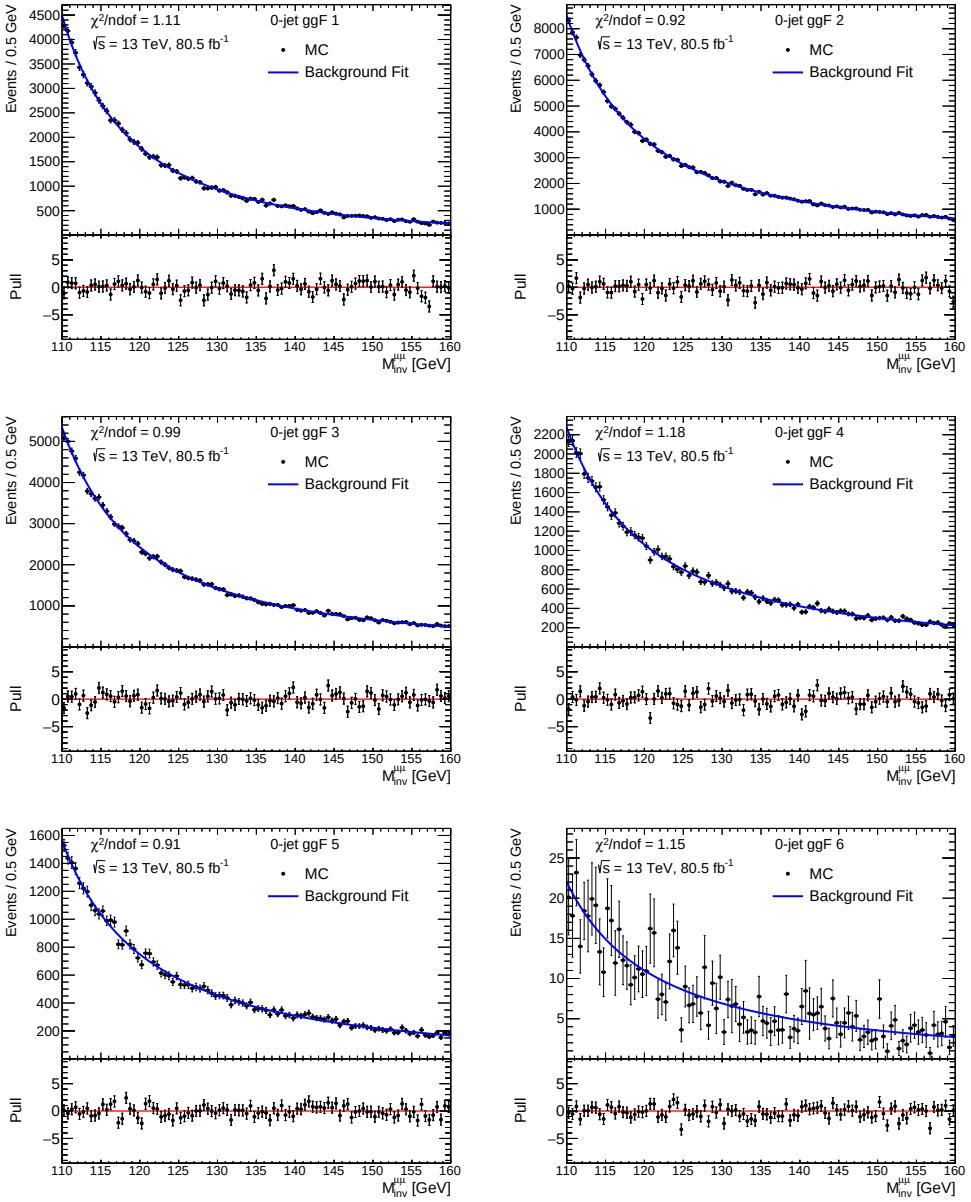

Figure F.2.1: The $M_{\text{inv}}^{\mu\mu}$ distributions of background MC events in the ggF Zero-Jet 1 (top left), ggF Zero-Jet 2 (top right), ggF Zero-Jet 3 (middle left), ggF Zero-Jet 4 (middle right), ggF Zero-Jet 5 (bottom left) and ggF Zero-Jet 6 (bottom right) categories, fitted using the background model described in Chapter 10.

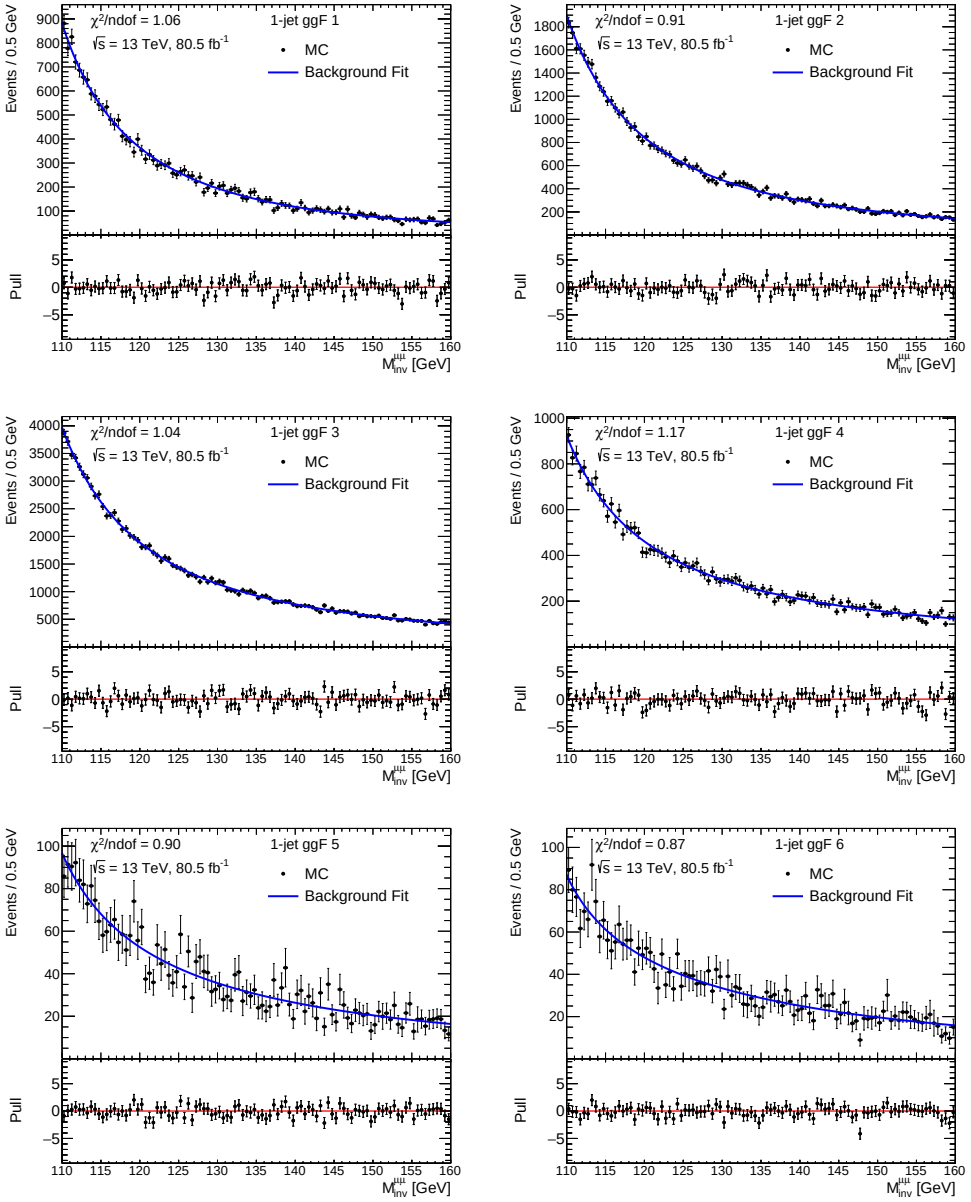

Figure F.2.2: The $M_{\text{inv}}^{\mu\mu}$ distributions of MC events in the ggF Single-Jet 1 (top left), ggF Single-Jet 2 (top right), ggF Single-Jet 3 (middle left), ggF Single-Jet 4 (middle right), ggF Single-Jet 5 (bottom left) and ggF Single-Jet 6 (bottom right) categories, fitted using the background model described in Chapter 10.

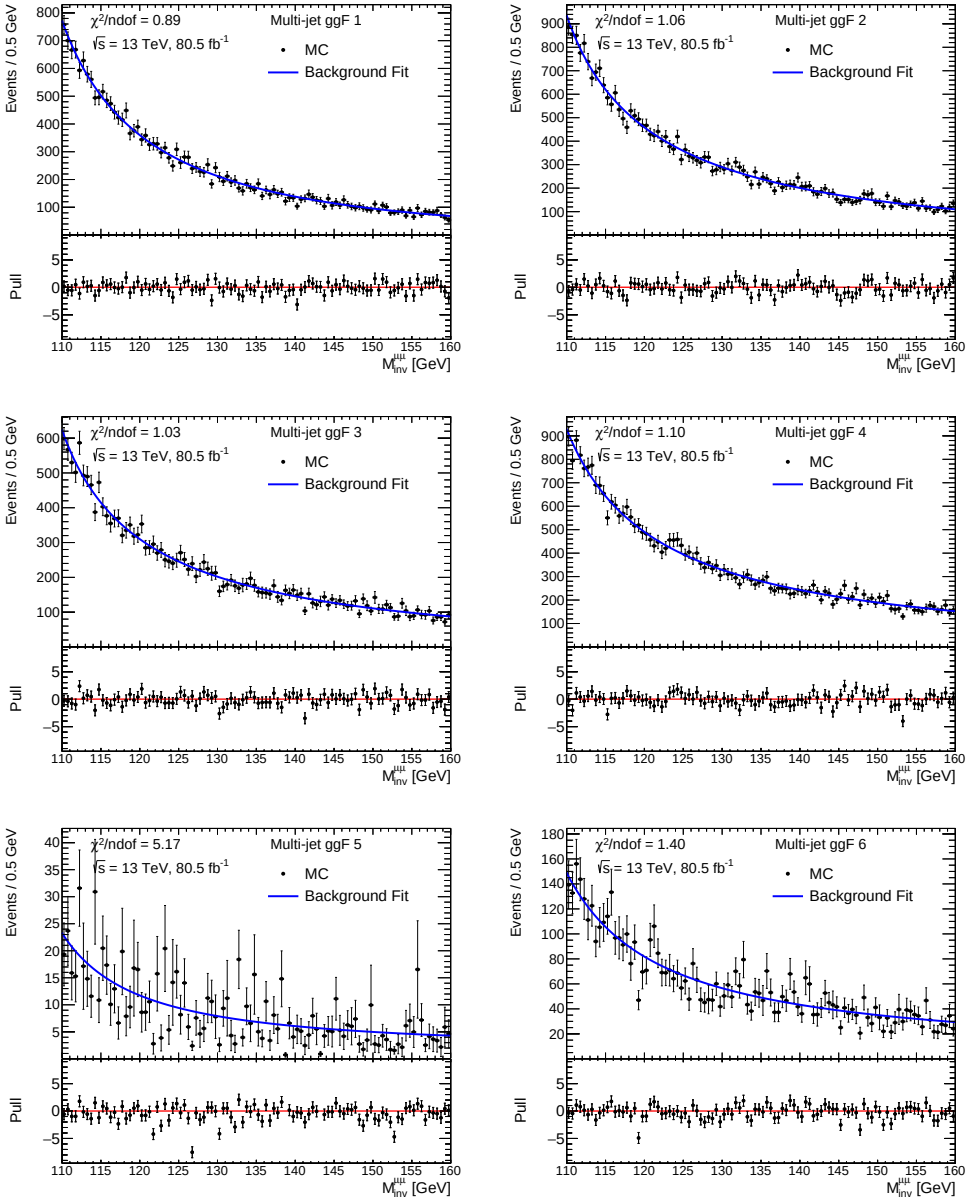

Figure F.2.3: The $M_{\text{inv}}^{\mu\mu}$ distributions of MC events in the ggF Multi-Jet 1 (top left), ggF Multi-Jet 2 (top right), ggF Multi-Jet 3 (middle left), ggF Multi-Jet 4 (middle right), ggF Multi-Jet 5 (bottom left) and ggF Multi-Jet 6 (bottom right) categories, fitted using the background model described in Chapter 10.

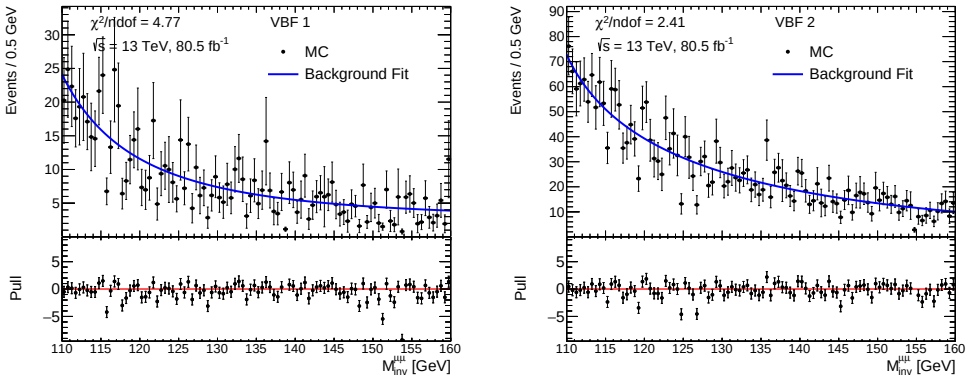

Figure F.2.4: The $M_{\text{inv}}^{\mu\mu}$ distributions of MC events in the VBF 1 (left) and VBF 2 (right) categories, fitted using the background model described in Chapter 10.

Appendix G

Breakdown of Experimental Systematic Uncertainties

This chapter presents the impact of the experimental systematics detailed in Chapter 11 on the ggF and VBF event yields found in the signal region for each category. The yields were normalised to 80.5 fb^{-1} before calculation of the variations, which are summarised in Tables G.0.1 to G.0.20. The largest variations come from the JET_SR1_JET_GroupedNP_1 systematic, along with the JER.

Systematics Type	Up (ggF) [%]	Down (ggF) [%]	Up (VBF) [%]	Down (VBF) [%]
FT_EFF_Eigen_B_0	-0.16	-0.27	-0.10	-0.04
FT_EFF_Eigen_B_1	-0.22	-0.16	-0.30	-0.15
FT_EFF_Eigen_B_2	-0.11	-0.41	0.19	-0.18
FT_EFF_Eigen_C_0	-0.11	-0.18	-0.19	-0.05
FT_EFF_Eigen_C_1	-0.17	-0.10	-0.03	0.21
FT_EFF_Eigen_C_2	-0.39	-0.07	-0.12	-0.38
FT_EFF_Eigen_Light_0	-0.21	-0.17	0.10	-0.11
FT_EFF_Eigen_Light_1	-0.29	-0.18	-0.07	0.09
FT_EFF_Eigen_Light_2	-0.29	-0.19	-0.09	-0.33
FT_EFF_Eigen_Light_3	-0.14	-0.25	0.12	-0.17
FT_EFF_Eigen_Light_4	-0.14	-0.23	-0.09	-0.19
FT_EFF_extrapolation	-0.20	-0.29	-0.37	0.01
FT_EFF_extrapolation_from_charm	-0.07	-0.26	-0.13	-0.11
JET_fJvtEfficiency	-0.22	-0.21	-0.06	-0.27
JET_JER_SINGLE_NP	-1.35	1.44	0.86	-1.12
JET_JvtEfficiency	-0.27	-0.09	-0.29	-0.02
JET_SR1_JET_EtaIntercalibration_NonClosure	-0.31	-0.29	-0.16	0.02
JET_SR1_JET_GroupedNP_1	-9.91	9.93	-16.23	18.83
JET_SR1_JET_GroupedNP_2	-1.07	0.53	-1.37	1.66
JET_SR1_JET_GroupedNP_3	-2.47	1.93	-5.67	5.53
MET_SoftTrk_ResoPara	-0.31	0.13	-0.16	0.09
MET_SoftTrk_ResoPerp	-0.19	0.08	0.14	-0.07
MET_SoftTrk_Scale	-0.15	-0.12	0.05	-0.15
MUON_EFF_ISO_STAT	-0.15	-0.26	0.20	-0.10
MUON_EFF_ISO_SYS	0.04	-0.69	0.51	-0.47
MUON_EFF_RECO_STAT	0.03	-0.64	0.32	-0.66
MUON_EFF_RECO_SYS	0.76	-1.02	0.80	-0.89
MUON_EFF_TrigStatUncertainty	-0.12	-0.24	-0.02	-0.31
MUON_EFF_TrigSystUncertainty	-0.13	-0.23	-0.12	-0.10
MUON_ID	-0.34	-0.21	0.01	0.03
MUON_MS	-0.39	-0.16	-0.20	0.07
MUON_SAGITTA_RESBIAS	-0.16	-0.28	-0.15	0.08
MUON_SAGITTA_RHO	-0.26	-0.25	-0.01	-0.02
MUON_SCALE	-0.37	-0.20	-0.08	-0.32
PRW_DATASF	-1.07	0.40	-0.86	0.97
Total Systematic Uncertainty	10.51	10.39	17.34	19.81

Table G.0.1: Variations of ggF and VBF MC event yields between $110 \leq M_{\text{inv}}^{\mu\mu} \leq 160$ GeV due to experimental systematic variations, for the ggF Zero-Jet 1 category. The samples have been normalised to 80.5 fb^{-1}.

Systematics Type	Up (ggF) [%]	Down (ggF) [%]	Up (VBF) [%]	Down (VBF) [%]
FT_EFF_Eigen_B_0	0.04	0.06	-0.00	-0.29
FT_EFF_Eigen_B_1	0.12	-0.12	0.03	0.17
FT_EFF_Eigen_B_2	0.02	0.33	-0.46	0.03
FT_EFF_Eigen_C_0	-0.02	0.09	0.26	0.28
FT_EFF_Eigen_C_1	0.13	-0.03	0.31	-0.40
FT_EFF_Eigen_C_2	0.23	0.01	0.04	0.55
FT_EFF_Eigen_Light_0	0.17	0.08	-0.51	0.18
FT_EFF_Eigen_Light_1	0.09	0.17	0.06	-0.21
FT_EFF_Eigen_Light_2	0.32	0.09	0.08	0.60
FT_EFF_Eigen_Light_3	0.04	0.18	0.02	0.32
FT_EFF_Eigen_Light_4	0.14	0.09	-0.04	0.49
FT_EFF_extrapolation	0.14	0.13	0.41	0.30
FT_EFF_extrapolation_from_charm	0.02	0.22	-0.15	0.11
JET_fJvtEfficiency	0.09	0.04	0.06	0.41
JET_JER_SINGLE_NP	-1.59	1.52	0.39	-0.14
JET_JvtEfficiency	0.16	0.10	0.47	-0.04
JET_SR1_JET_EtaIntercalibration_NonClosure	0.22	0.17	0.11	0.03
JET_SR1_JET_GroupedNP_1	-5.88	5.48	-13.47	14.63
JET_SR1_JET_GroupedNP_2	-0.29	0.65	-1.47	0.83
JET_SR1_JET_GroupedNP_3	-1.40	1.55	-3.90	4.14
MET_SoftTrk_ResoPara	0.20	-0.12	0.53	-0.85
MET_SoftTrk_ResoPerp	0.02	-0.03	-0.08	-0.38
MET_SoftTrk_Scale	0.20	0.01	0.16	-0.17
MUON_EFF_ISO_STAT	0.01	0.12	-0.15	0.29
MUON_EFF_ISO_SYS	0.68	-0.37	0.39	-0.20
MUON_EFF_RECO_STAT	0.42	-0.17	0.10	0.34
MUON_EFF_RECO_SYS	1.01	-0.83	1.50	-1.18
MUON_EFF_TrigStatUncertainty	0.02	0.13	-0.08	0.47
MUON_EFF_TrigSystUncertainty	-0.07	0.15	0.16	0.03
MUON_ID	0.26	0.17	-0.24	-0.14
MUON_MS	0.22	-0.00	0.29	-0.38
MUON_SAGITTA_RESBIAS	0.02	0.18	0.25	-0.12
MUON_SAGITTA_RHO	0.33	0.14	0.09	-0.10
MUON_SCALE	0.12	0.09	0.25	0.70
PRW_DATASF	-0.72	0.80	-1.48	0.53
Total Systematic Uncertainty	6.48	6.09	14.32	15.41

Table G.0.2: Variations of ggF and VBF MC event yields between $110 \leq M_{\text{inv}}^{\mu\mu} \leq 160$ GeV due to experimental systematic variations, for the ggF Zero-Jet 2 category. The samples have been normalised to 80.5 fb^{-1}.

Systematics Type	Up (ggF) [%]	Down (ggF) [%]	Up (VBF) [%]	Down (VBF) [%]
FT_EFF_Eigen_B_0	-0.03	0.56	0.96	2.62
FT_EFF_Eigen_B_1	0.30	0.22	1.73	1.02
FT_EFF_Eigen_B_2	0.16	-0.22	0.37	0.86
FT_EFF_Eigen_C_0	0.46	0.22	0.58	0.20
FT_EFF_Eigen_C_1	0.21	0.13	0.04	1.25
FT_EFF_Eigen_C_2	-0.01	0.19	0.75	0.25
FT_EFF_Eigen_Light_0	0.02	0.28	1.01	-0.28
FT_EFF_Eigen_Light_1	0.26	-0.01	0.07	0.30
FT_EFF_Eigen_Light_2	-0.08	0.26	0.77	0.23
FT_EFF_Eigen_Light_3	0.20	0.15	-0.44	0.73
FT_EFF_Eigen_Light_4	-0.05	0.43	0.86	0.01
FT_EFF_extrapolation	0.22	0.62	1.51	-1.08
FT_EFF_extrapolation_from_charm	0.16	-0.00	1.58	0.91
JET_fJvtEfficiency	0.35	0.35	0.19	0.38
JET_JER_SINGLE_NP	-1.34	1.55	0.43	1.58
JET_JvtEfficiency	0.09	0.05	-0.06	0.59
JET_SR1_JET_EtaIntercalibration_NonClosure	0.00	0.18	1.06	0.16
JET_SR1_JET_GroupedNP_1	-4.68	4.31	-11.95	14.18
JET_SR1_JET_GroupedNP_2	-0.25	0.27	0.52	3.19
JET_SR1_JET_GroupedNP_3	-1.03	1.30	-2.84	4.78
MET_SoftTrk_ResoPara	0.35	-0.18	0.30	1.22
MET_SoftTrk_ResoPerp	0.16	-0.14	0.64	-0.12
MET_SoftTrk_Scale	0.05	-0.03	1.53	1.11
MUON_EFF_ISO_STAT	0.37	0.07	0.82	-0.74
MUON_EFF_ISO_SYS	0.43	-0.05	0.37	-0.48
MUON_EFF_RECO_STAT	0.64	0.22	1.47	-0.43
MUON_EFF_RECO_SYS	1.27	-0.96	1.39	-1.44
MUON_EFF_TrigStatUncertainty	0.07	0.31	1.56	-0.44
MUON_EFF_TrigSystUncertainty	0.57	0.14	-0.05	0.61
MUON_ID	0.13	0.37	0.34	0.60
MUON_MS	0.17	0.39	0.40	1.26
MUON_SAGITTA_RESBIAS	0.34	0.32	0.38	1.19
MUON_SAGITTA_RHO	0.02	-0.02	1.06	0.31
MUON_SCALE	0.42	0.27	0.21	0.54
PRW_DATASF	-1.03	1.12	0.14	0.65
Total Systematic Uncertainty	5.45	5.20	13.29	16.14

Table G.0.3: Variations of ggF and VBF MC event yields between $110 \leq M_{\text{inv}}^{\mu\mu} \leq 160$ GeV due to experimental systematic variations, for the ggF Zero-Jet 3 category. The samples have been normalised to 80.5 fb^{-1}.

Systematics Type	Up (ggF) [%]	Down (ggF) [%]	Up (VBF) [%]	Down (VBF) [%]
FT_EFF_Eigen_B_0	0.81	-0.47	-2.20	-4.41
FT_EFF_Eigen_B_1	-0.52	1.03	-2.51	-3.59
FT_EFF_Eigen_B_2	0.11	0.71	-2.15	-2.08
FT_EFF_Eigen_C_0	-0.10	0.04	-0.84	-3.73
FT_EFF_Eigen_C_1	-0.20	0.38	-3.19	-4.65
FT_EFF_Eigen_C_2	0.75	-0.06	-2.27	-1.21
FT_EFF_Eigen_Light_0	-0.06	-0.19	-2.57	-0.91
FT_EFF_Eigen_Light_1	0.24	0.09	-1.19	-0.92
FT_EFF_Eigen_Light_2	-0.20	-0.18	-1.97	-2.32
FT_EFF_Eigen_Light_3	-0.02	-0.06	-3.21	-3.05
FT_EFF_Eigen_Light_4	0.30	-0.72	-2.62	-4.77
FT_EFF_extrapolation	-0.61	-0.89	-2.64	-1.09
FT_EFF_extrapolation_from_charm	0.04	0.15	-2.11	-3.23
JET_fJvtEfficiency	-0.33	0.11	-2.54	-0.53
JET_JER_SINGLE_NP	-2.27	1.84	-4.33	1.41
JET_JvtEfficiency	0.54	0.10	-0.77	-2.06
JET_SR1_JET_EtaIntercalibration_NonClosure	0.51	0.08	-3.30	-1.97
JET_SR1_JET_GroupedNP_1	-4.98	4.83	-15.12	9.87
JET_SR1_JET_GroupedNP_2	-0.49	0.98	-5.92	-2.26
JET_SR1_JET_GroupedNP_3	-1.11	0.67	-6.63	2.71
MET_SoftTrk_ResoPara	-0.36	0.79	-0.94	-0.25
MET_SoftTrk_ResoPerp	0.65	0.10	-1.00	1.68
MET_SoftTrk_Scale	-0.03	0.15	-3.08	-4.51
MUON_EFF_ISO_STAT	0.31	0.25	-6.20	-1.61
MUON_EFF_ISO_SYS	0.52	0.30	-2.11	-2.50
MUON_EFF_RECO_STAT	0.18	-0.85	-3.37	-1.59
MUON_EFF_RECO_SYS	0.76	-1.52	-2.61	-0.72
MUON_EFF_TrigStatUncertainty	0.51	-0.24	-3.93	1.00
MUON_EFF_TrigSystUncertainty	-0.57	-0.03	-1.04	-0.41
MUON_ID	-0.18	-0.52	-0.04	-1.64
MUON_MS	0.33	0.13	-1.82	-2.30
MUON_SAGITTA_RESBIAS	-0.03	-0.14	-2.64	-4.19
MUON_SAGITTA_RHO	-0.52	0.48	-4.12	-1.01
MUON_SCALE	-0.43	-0.06	-3.93	-3.91
PRW_DATASF	-1.76	0.57	-3.18	-1.26
Total Systematic Uncertainty	6.33	6.02	23.63	18.01

Table G.0.4: Variations of ggF and VBF MC event yields between $110 \leq M_{\text{inv}}^{\mu\mu} \leq 160$ GeV due to experimental systematic variations, for the ggF Zero-Jet 4 category. The samples have been normalised to 80.5 fb^{-1}.

Systematics Type	Up (ggF) [%]	Down (ggF) [%]	Up (VBF) [%]	Down (VBF) [%]
FT_EFF_Eigen_B_0	-0.32	-0.19	2.26	0.60
FT_EFF_Eigen_B_1	0.06	-0.07	5.06	3.31
FT_EFF_Eigen_B_2	-0.14	-0.13	4.97	5.14
FT_EFF_Eigen_C_0	-0.94	-0.76	0.38	2.81
FT_EFF_Eigen_C_1	-0.53	-0.06	1.66	3.17
FT_EFF_Eigen_C_2	-0.38	-0.36	4.26	3.99
FT_EFF_Eigen_Light_0	0.02	-0.20	5.46	4.41
FT_EFF_Eigen_Light_1	-0.07	-0.33	3.80	1.00
FT_EFF_Eigen_Light_2	-0.18	-0.12	1.71	3.18
FT_EFF_Eigen_Light_3	-0.18	-0.55	4.98	1.98
FT_EFF_Eigen_Light_4	-0.77	0.16	4.33	6.79
FT_EFF_extrapolation	0.27	-0.30	1.21	2.48
FT_EFF_extrapolation_from_charm	-0.42	-0.25	2.64	3.15
JET_fJvtEfficiency	-0.13	-0.51	5.09	0.57
JET_JER_SINGLE_NP	-1.59	1.26	-0.45	-1.50
JET_JvtEfficiency	-0.62	-0.72	3.20	2.08
JET_SR1_JET_EtaIntercalibration_NonClosure	-0.78	-0.25	2.38	2.56
JET_SR1_JET_GroupedNP_1	-5.21	4.03	-9.58	12.88
JET_SR1_JET_GroupedNP_2	-0.24	-0.16	1.76	-0.20
JET_SR1_JET_GroupedNP_3	-1.18	1.48	-0.37	2.59
MET_SoftTrk_ResoPara	-0.56	-0.34	1.74	0.57
MET_SoftTrk_ResoPerp	-0.24	0.07	2.93	-1.45
MET_SoftTrk_Scale	-1.00	0.65	0.87	1.98
MUON_EFF_ISO_STAT	-0.48	-0.61	6.26	4.03
MUON_EFF_ISO_SYS	0.18	-0.97	2.60	2.60
MUON_EFF_RECO_STAT	-0.11	-0.28	4.31	3.76
MUON_EFF_RECO_SYS	1.47	-1.21	3.94	1.02
MUON_EFF_TrigStatUncertainty	-0.40	-0.41	1.25	2.25
MUON_EFF_TrigSystUncertainty	0.15	-0.26	3.83	0.79
MUON_ID	-0.08	-0.59	1.69	2.53
MUON_MS	-0.42	0.15	1.98	2.28
MUON_SAGITTA_RESBIAS	-0.48	-0.69	3.35	1.75
MUON_SAGITTA_RHO	-0.47	0.03	1.16	3.17
MUON_SCALE	-0.18	0.57	3.60	5.27
PRW_DATASF	-0.47	1.53	1.21	5.10
Total Systematic Uncertainty	6.27	5.43	21.33	21.98

Table G.0.5: Variations of ggF and VBF MC event yields between $110 \leq M_{\text{inv}}^{\mu\mu} \leq 160$ GeV due to experimental systematic variations, for the ggF Zero-Jet 5 category. The samples have been normalised to 80.5 fb^{-1}.

Systematics Type	Up (ggF) [%]	Down (ggF) [%]	Up (VBF) [%]	Down (VBF) [%]
FT_EFF_Eigen_B_0	-2.07	0.62	8.61	3.91
FT_EFF_Eigen_B_1	2.45	0.89	-7.18	4.80
FT_EFF_Eigen_B_2	-1.26	4.51	-5.42	-1.54
FT_EFF_Eigen_C_0	4.53	5.40	-26.48	15.51
FT_EFF_Eigen_C_1	-2.11	-1.10	-8.81	-6.56
FT_EFF_Eigen_C_2	5.32	2.43	-25.15	-22.59
FT_EFF_Eigen_Light_0	4.49	-4.81	12.78	-13.70
FT_EFF_Eigen_Light_1	5.75	-0.94	-13.83	2.79
FT_EFF_Eigen_Light_2	1.30	-3.77	-39.57	3.11
FT_EFF_Eigen_Light_3	1.12	8.21	-5.26	-11.44
FT_EFF_Eigen_Light_4	8.69	3.79	-7.93	6.36
FT_EFF_extrapolation	3.08	1.65	-4.09	-0.81
FT_EFF_extrapolation_from_charm	-0.38	-2.81	-2.69	-16.65
JET_fJvtEfficiency	3.37	1.79	-5.60	-19.65
JET_JER_SINGLE_NP	6.31	-4.37	-7.59	13.09
JET_JvtEfficiency	-5.96	-2.55	-6.56	17.36
JET_SR1_JET_EtaIntercalibration_NonClosure	2.86	7.19	6.41	-0.41
JET_SR1_JET_GroupedNP_1	-2.88	7.09	-7.77	8.43
JET_SR1_JET_GroupedNP_2	-4.17	1.90	-5.08	1.75
JET_SR1_JET_GroupedNP_3	-0.71	-0.16	-8.62	7.70
MET_SoftTrk_ResoPara	2.44	-0.93	8.04	-3.38
MET_SoftTrk_ResoPerp	-0.42	-6.28	28.54	4.15
MET_SoftTrk_Scale	-0.19	9.59	12.53	19.13
MUON_EFF_ISO_STAT	1.44	1.09	-12.71	-13.71
MUON_EFF_ISO_SYS	4.73	-2.54	-6.86	10.70
MUON_EFF_RECO_STAT	3.53	2.75	-5.51	-22.60
MUON_EFF_RECO_SYS	-0.51	4.19	-13.24	-27.31
MUON_EFF_TrigStatUncertainty	4.83	-1.55	-2.29	-14.07
MUON_EFF_TrigSystUncertainty	3.26	0.81	-2.00	-30.24
MUON_ID	7.99	2.08	9.72	5.87
MUON_MS	-1.08	0.14	-6.43	0.64
MUON_SAGITTA_RESBIAS	3.48	-4.71	9.64	-20.96
MUON_SAGITTA_RHO	1.10	3.94	2.22	10.31
MUON_SCALE	-5.59	2.03	8.74	-36.38
PRW_DATASF	4.59	2.00	-8.59	10.18
Total Systematic Uncertainty	23.14	23.26	76.02	86.92

Table G.0.6: Variations of ggF and VBF MC event yields between $110 \leq M_{\text{inv}}^{\mu\mu} \leq 160$ GeV due to experimental systematic variations, for the ggF Zero-Jet 6 category. The samples have been normalised to 80.5 fb^{-1}.

Systematics Type	Up (ggF) [%]	Down (ggF) [%]	Up (VBF) [%]	Down (VBF) [%]
FT_EFF_Eigen_B_0	-0.10	-0.02	0.03	0.05
FT_EFF_Eigen_B_1	-0.07	0.14	-0.02	0.06
FT_EFF_Eigen_B_2	0.02	-0.06	-0.02	0.05
FT_EFF_Eigen_C_0	-0.04	0.19	-0.05	0.00
FT_EFF_Eigen_C_1	0.04	-0.00	-0.06	-0.03
FT_EFF_Eigen_C_2	-0.02	0.17	0.06	-0.04
FT_EFF_Eigen_Light_0	0.04	-0.08	0.05	-0.11
FT_EFF_Eigen_Light_1	-0.19	-0.11	-0.08	-0.04
FT_EFF_Eigen_Light_2	-0.13	-0.24	-0.05	-0.03
FT_EFF_Eigen_Light_3	-0.12	-0.08	0.02	-0.05
FT_EFF_Eigen_Light_4	-0.02	0.14	0.05	-0.03
FT_EFF_extrapolation	-0.11	-0.04	0.03	0.05
FT_EFF_extrapolation_from_charm	-0.09	-0.02	-0.13	-0.02
JET_fJvtEfficiency	0.12	0.03	0.12	-0.10
JET_JER_SINGLE_NP	-0.90	1.12	-0.65	0.61
JET_JvtEfficiency	-0.01	-0.16	-0.02	-0.07
JET_SR1_JET_EtaIntercalibration_NonClosure	-0.13	0.19	-0.05	-0.01
JET_SR1_JET_GroupedNP_1	-5.44	4.87	-9.27	9.22
JET_SR1_JET_GroupedNP_2	-0.49	0.47	-0.76	0.71
JET_SR1_JET_GroupedNP_3	-0.78	0.63	-2.83	2.88
MET_SoftTrk_ResoPara	0.10	-0.09	-0.00	-0.09
MET_SoftTrk_ResoPerp	-0.01	0.06	0.06	-0.09
MET_SoftTrk_Scale	-0.08	-0.12	0.11	-0.12
MUON_EFF_ISO_STAT	-0.08	-0.08	0.03	-0.06
MUON_EFF_ISO_SYS	0.36	-0.62	0.43	-0.35
MUON_EFF_RECO_STAT	0.25	-0.26	0.43	-0.29
MUON_EFF_RECO_SYS	0.95	-1.08	0.91	-0.95
MUON_EFF_TrigStatUncertainty	-0.03	-0.05	-0.09	0.02
MUON_EFF_TrigSystUncertainty	-0.06	-0.10	-0.05	0.00
MUON_ID	-0.31	-0.13	-0.03	-0.02
MUON_MS	-0.01	-0.00	0.06	0.06
MUON_SAGITTA_RESBIAS	0.03	-0.05	0.07	-0.08
MUON_SAGITTA_RHO	0.13	0.02	-0.04	0.01
MUON_SCALE	0.05	-0.02	-0.03	0.01
PRW_DATASF	-0.62	0.86	-0.91	0.65
Total Systematic Uncertainty	5.75	5.32	9.86	9.79

Table G.0.7: Variations of ggF and VBF MC event yields between $110 \leq M_{\text{inv}}^{\mu\mu} \leq 160$ GeV due to experimental systematic variations, for the ggF Single-Jet 1 category. The samples have been normalised to 80.5 fb^{-1}.

Systematics Type	Up (ggF) [%]	Down (ggF) [%]	Up (VBF) [%]	Down (VBF) [%]
FT_EFF_Eigen_B_0	0.10	0.13	-0.12	-0.01
FT_EFF_Eigen_B_1	0.28	0.13	-0.02	-0.18
FT_EFF_Eigen_B_2	-0.01	0.32	-0.04	-0.10
FT_EFF_Eigen_C_0	0.30	-0.11	0.28	0.09
FT_EFF_Eigen_C_1	0.02	0.21	0.23	0.03
FT_EFF_Eigen_C_2	0.17	-0.11	0.03	0.10
FT_EFF_Eigen_Light_0	0.10	0.15	-0.08	0.12
FT_EFF_Eigen_Light_1	0.12	0.13	0.22	0.08
FT_EFF_Eigen_Light_2	0.34	0.18	0.02	0.06
FT_EFF_Eigen_Light_3	0.26	0.36	-0.07	0.13
FT_EFF_Eigen_Light_4	0.13	-0.18	-0.12	0.08
FT_EFF_extrapolation	0.12	0.01	0.00	-0.14
FT_EFF_extrapolation_from_charm	0.06	-0.08	0.18	0.06
JET_fJvtEfficiency	-0.24	0.05	-0.10	0.28
JET_JER_SINGLE_NP	-0.04	-0.11	-0.93	0.96
JET_JvtEfficiency	0.24	0.22	0.22	0.14
JET_SR1_JET_EtaIntercalibration_NonClosure	0.18	0.06	0.06	0.23
JET_SR1_JET_GroupedNP_1	-0.44	-0.32	-7.13	6.49
JET_SR1_JET_GroupedNP_2	-0.04	0.11	-0.82	0.70
JET_SR1_JET_GroupedNP_3	0.48	-0.25	-2.10	1.88
MET_SoftTrk_ResoPara	-0.00	-0.12	0.16	-0.12
MET_SoftTrk_ResoPerp	0.22	-0.06	0.11	-0.15
MET_SoftTrk_Scale	0.31	0.17	0.10	-0.14
MUON_EFF_ISO_STAT	0.20	-0.05	0.10	0.20
MUON_EFF_ISO_SYS	0.49	-0.19	0.52	-0.46
MUON_EFF_RECO_STAT	0.42	-0.49	-0.15	-0.43
MUON_EFF_RECO_SYS	0.68	-0.73	1.31	-1.07
MUON_EFF_TrigStatUncertainty	0.15	0.13	0.36	-0.16
MUON_EFF_TrigSystUncertainty	0.33	0.24	0.08	0.05
MUON_ID	0.24	0.12	0.01	0.14
MUON_MS	-0.19	-0.01	-0.22	-0.01
MUON_SAGITTA_RESBIAS	0.09	0.13	-0.06	0.01
MUON_SAGITTA_RHO	-0.21	-0.04	-0.08	-0.07
MUON_SCALE	-0.00	0.30	-0.02	0.02
PRW_DATASF	-0.58	0.27	-0.64	1.07
Total Systematic Uncertainty	1.64	1.35	7.73	7.08

Table G.0.8: Variations of ggF and VBF MC event yields between $110 \leq M_{\text{inv}}^{\mu\mu} \leq 160$ GeV due to experimental systematic variations, for the ggF Single-Jet 2 category. The samples have been normalised to 80.5 fb^{-1}.

Systematics Type	Up (ggF) [%]	Down (ggF) [%]	Up (VBF) [%]	Down (VBF) [%]
FT_EFF_Eigen_B_0	0.01	0.14	0.21	-0.05
FT_EFF_Eigen_B_1	-0.00	-0.08	0.01	-0.05
FT_EFF_Eigen_B_2	0.01	-0.21	-0.15	-0.11
FT_EFF_Eigen_C_0	0.07	0.05	-0.17	-0.24
FT_EFF_Eigen_C_1	0.06	0.09	-0.30	0.10
FT_EFF_Eigen_C_2	0.07	-0.01	-0.14	-0.18
FT_EFF_Eigen_Light_0	0.06	0.00	-0.04	-0.06
FT_EFF_Eigen_Light_1	0.07	0.16	0.07	-0.04
FT_EFF_Eigen_Light_2	-0.09	0.10	-0.04	-0.20
FT_EFF_Eigen_Light_3	0.13	0.05	-0.01	-0.23
FT_EFF_Eigen_Light_4	0.06	0.26	-0.02	-0.22
FT_EFF_extrapolation	-0.04	-0.02	-0.16	0.06
FT_EFF_extrapolation_from_charm	0.12	0.11	0.03	-0.07
JET_fJvtEfficiency	0.15	0.12	-0.02	-0.11
JET_JER_SINGLE_NP	1.19	-1.12	-0.56	0.69
JET_JvtEfficiency	-0.14	-0.05	-0.10	0.04
JET_SR1_JET_EtaIntercalibration_NonClosure	0.17	-0.02	0.09	-0.30
JET_SR1_JET_GroupedNP_1	4.28	-4.81	-5.97	5.20
JET_SR1_JET_GroupedNP_2	0.58	-0.36	-0.31	0.15
JET_SR1_JET_GroupedNP_3	0.90	-0.86	-1.77	1.54
MET_SoftTrk_ResoPara	0.01	-0.01	-0.03	0.09
MET_SoftTrk_ResoPerp	0.10	-0.29	0.12	0.18
MET_SoftTrk_Scale	-0.04	-0.05	-0.18	0.18
MUON_EFF_ISO_STAT	0.11	0.13	0.05	-0.21
MUON_EFF_ISO_SYS	0.46	-0.26	0.11	-0.61
MUON_EFF_RECO_STAT	0.38	0.01	0.50	-0.38
MUON_EFF_RECO_SYS	1.29	-0.95	0.75	-1.02
MUON_EFF_TrigStatUncertainty	0.27	-0.06	-0.34	0.14
MUON_EFF_TrigSystUncertainty	0.08	-0.01	0.06	0.01
MUON_ID	0.11	0.11	-0.03	-0.07
MUON_MS	0.19	0.24	0.08	-0.04
MUON_SAGITTA_RESBIAS	0.12	-0.09	-0.12	0.19
MUON_SAGITTA_RHO	0.11	0.09	0.09	-0.09
MUON_SCALE	0.09	-0.12	0.01	0.01
PRW_DATASF	0.35	0.22	-0.56	0.59
Total Systematic Uncertainty	4.83	5.17	6.39	5.69

Table G.0.9: Variations of ggF and VBF MC event yields between $110 \leq M_{\text{inv}}^{\mu\mu} \leq 160$ GeV due to experimental systematic variations, for the ggF Single-Jet 3 category. The samples have been normalised to 80.5 fb^{-1}.

Systematics Type	Up (ggF) [%]	Down (ggF) [%]	Up (VBF) [%]	Down (VBF) [%]
FT_EFF_Eigen_B_0	-0.08	-0.60	-0.95	-0.29
FT_EFF_Eigen_B_1	-0.54	-0.36	-0.10	0.48
FT_EFF_Eigen_B_2	-0.10	0.24	1.16	0.60
FT_EFF_Eigen_C_0	-0.73	-0.67	0.62	-0.22
FT_EFF_Eigen_C_1	-0.63	-1.00	0.38	-0.11
FT_EFF_Eigen_C_2	-0.76	-0.09	0.25	0.41
FT_EFF_Eigen_Light_0	-0.11	-0.94	0.67	-0.23
FT_EFF_Eigen_Light_1	-0.12	-0.81	-1.05	0.00
FT_EFF_Eigen_Light_2	-0.40	-0.51	0.52	1.08
FT_EFF_Eigen_Light_3	-1.22	-1.26	0.10	0.82
FT_EFF_Eigen_Light_4	-0.47	-1.19	0.08	0.91
FT_EFF_extrapolation	0.35	0.27	0.53	0.10
FT_EFF_extrapolation_from_charm	-0.52	0.05	-0.24	-0.13
JET_fJvtEfficiency	-0.04	-0.82	-0.86	-0.38
JET_JER_SINGLE_NP	0.92	-1.13	-1.37	0.84
JET_JvtEfficiency	0.19	0.30	-0.74	-0.57
JET_SR1_JET_EtaIntercalibration_NonClosure	-1.07	-0.41	-0.64	0.57
JET_SR1_JET_GroupedNP_1	5.94	-7.21	-4.31	3.81
JET_SR1_JET_GroupedNP_2	-0.28	-0.88	0.13	0.73
JET_SR1_JET_GroupedNP_3	0.43	-0.93	-1.94	2.55
MET_SoftTrk_ResoPara	-0.26	0.43	-0.43	0.65
MET_SoftTrk_ResoPerp	-0.78	0.68	-0.70	-0.94
MET_SoftTrk_Scale	-0.01	-0.34	0.62	-0.73
MUON_EFF_ISO_STAT	-0.14	-0.64	-0.19	-0.84
MUON_EFF_ISO_SYS	-0.26	-1.34	0.74	0.52
MUON_EFF_RECO_STAT	-0.38	-1.07	0.75	0.78
MUON_EFF_RECO_SYS	0.53	-1.39	1.49	-1.68
MUON_EFF_TrigStatUncertainty	-1.40	0.22	0.83	-0.01
MUON_EFF_TrigSystUncertainty	-1.32	-0.56	-0.76	-0.72
MUON_ID	-0.41	-0.40	0.45	0.29
MUON_MS	-0.31	-0.70	-0.03	-0.17
MUON_SAGITTA_RESBIAS	-1.06	0.38	-0.02	-0.77
MUON_SAGITTA_RHO	-0.16	-0.37	-0.12	0.38
MUON_SCALE	-0.99	0.03	-0.64	0.22
PRW_DATASF	0.28	-1.23	-0.97	0.32
Total Systematic Uncertainty	7.00	8.46	6.18	5.87

Table G.0.10: Variations of ggF and VBF MC event yields between $110 \leq M_{\text{inv}}^{\mu\mu} \leq 160$ GeV due to experimental systematic variations, for the ggF Single-Jet 4 category. The samples have been normalised to 80.5 fb^{-1}.

Systematics Type	Up (ggF) [%]	Down (ggF) [%]	Up (VBF) [%]	Down (VBF) [%]
FT_EFF_Eigen_B_0	-4.17	0.05	-3.66	6.13
FT_EFF_Eigen_B_1	-2.34	0.09	6.05	4.02
FT_EFF_Eigen_B_2	0.28	-0.94	4.08	4.22
FT_EFF_Eigen_C_0	-1.13	0.20	1.37	0.57
FT_EFF_Eigen_C_1	0.89	0.53	3.42	2.44
FT_EFF_Eigen_C_2	-1.49	1.88	2.01	5.51
FT_EFF_Eigen_Light_0	-1.67	1.04	3.57	3.05
FT_EFF_Eigen_Light_1	-1.13	0.31	0.35	3.00
FT_EFF_Eigen_Light_2	0.09	0.09	1.92	2.28
FT_EFF_Eigen_Light_3	0.76	1.52	3.69	5.39
FT_EFF_Eigen_Light_4	-3.18	1.41	6.31	5.75
FT_EFF_extrapolation	-3.48	-1.57	3.43	1.05
FT_EFF_extrapolation_from_charm	-0.57	-2.47	1.84	4.01
JET_fJvtEfficiency	-1.85	-0.95	3.67	2.50
JET_JER_SINGLE_NP	1.75	-6.34	5.95	-1.84
JET_JvtEfficiency	-3.59	-0.14	0.13	1.44
JET_SR1_JET_EtaIntercalibration_NonClosure	1.44	-0.95	2.62	4.79
JET_SR1_JET_GroupedNP_1	6.82	-5.76	-6.05	10.81
JET_SR1_JET_GroupedNP_2	-1.71	-1.99	2.91	2.24
JET_SR1_JET_GroupedNP_3	0.97	3.31	2.69	7.12
MET_SoftTrk_ResoPara	2.36	-1.08	5.87	-1.74
MET_SoftTrk_ResoPerp	0.31	1.98	0.44	1.78
MET_SoftTrk_Scale	-0.38	-2.47	2.82	1.32
MUON_EFF_ISO_STAT	-3.05	0.64	1.35	6.98
MUON_EFF_ISO_SYS	2.07	0.16	6.04	1.09
MUON_EFF_RECO_STAT	0.77	-1.24	1.07	1.91
MUON_EFF_RECO_SYS	2.37	-3.09	4.94	3.35
MUON_EFF_TrigStatUncertainty	-3.15	-0.94	1.91	-3.79
MUON_EFF_TrigSystUncertainty	0.92	1.30	1.67	3.60
MUON_ID	-2.11	-1.39	-3.30	3.05
MUON_MS	0.83	-0.86	3.75	1.03
MUON_SAGITTA_RESBIAS	-0.26	-2.41	4.83	2.10
MUON_SAGITTA_RHO	0.53	0.88	1.39	2.30
MUON_SCALE	-0.30	1.81	1.57	2.35
PRW_DATASF	0.90	0.50	1.55	-0.85
Total Systematic Uncertainty	13.00	12.12	21.11	23.34

Table G.0.11: Variations of ggF and VBF MC event yields between $110 \leq M_{\text{inv}}^{\mu\mu} \leq 160$ GeV due to experimental systematic variations, for the ggF Single-Jet 5 category. The samples have been normalised to 80.5 fb^{-1}.

Systematics Type	Up (ggF) [%]	Down (ggF) [%]	Up (VBF) [%]	Down (VBF) [%]
FT_EFF_Eigen_B_0	-1.37	-0.82	0.45	-2.00
FT_EFF_Eigen_B_1	-0.45	-1.18	-0.51	1.50
FT_EFF_Eigen_B_2	-1.78	1.09	-3.52	0.97
FT_EFF_Eigen_C_0	-1.63	-0.77	-0.80	-0.12
FT_EFF_Eigen_C_1	-0.36	-1.45	-2.52	-0.87
FT_EFF_Eigen_C_2	0.34	-0.82	-3.62	-0.29
FT_EFF_Eigen_Light_0	-0.84	0.78	0.68	-0.30
FT_EFF_Eigen_Light_1	-1.26	-1.86	-0.64	-0.27
FT_EFF_Eigen_Light_2	-0.53	-0.50	-0.21	-0.50
FT_EFF_Eigen_Light_3	-1.59	-2.37	0.71	-0.86
FT_EFF_Eigen_Light_4	0.56	-0.14	-1.73	-2.22
FT_EFF_extrapolation	-0.06	0.48	-3.23	-1.53
FT_EFF_extrapolation_from_charm	-0.52	-0.77	1.93	0.26
JET_fJvtEfficiency	-0.11	0.39	0.59	0.91
JET_JER_SINGLE_NP	1.79	1.04	-0.19	-4.36
JET_JvtEfficiency	0.21	-4.41	1.00	1.15
JET_SR1_JET_EtaIntercalibration_NonClosure	-2.74	-0.89	-0.40	-5.46
JET_SR1_JET_GroupedNP_1	5.97	-9.52	-3.28	5.94
JET_SR1_JET_GroupedNP_2	0.62	0.01	-1.16	-2.73
JET_SR1_JET_GroupedNP_3	-0.99	-2.36	-4.68	0.54
MET_SoftTrk_ResoPara	0.70	0.93	0.10	-2.76
MET_SoftTrk_ResoPerp	0.32	1.59	2.37	2.13
MET_SoftTrk_Scale	-0.95	-0.90	2.22	-0.67
MUON_EFF_ISO_STAT	-2.27	-1.58	-2.58	-1.40
MUON_EFF_ISO_SYS	0.09	-0.87	0.03	1.05
MUON_EFF_RECO_STAT	-0.25	-2.50	0.22	-1.28
MUON_EFF_RECO_SYS	0.13	-2.93	1.37	1.16
MUON_EFF_TrigStatUncertainty	-1.73	-1.92	-3.95	4.53
MUON_EFF_TrigSystUncertainty	-2.26	-1.22	3.44	-0.91
MUON_ID	-0.71	0.11	4.50	-2.51
MUON_MS	-1.52	-3.08	-0.83	0.54
MUON_SAGITTA_RESBIAS	0.31	-0.06	0.95	2.79
MUON_SAGITTA_RHO	-0.64	-0.83	1.21	-0.86
MUON_SCALE	-0.54	-2.28	0.45	-1.13
PRW_DATASF	-2.62	-1.51	-1.85	-0.82
Total Systematic Uncertainty	9.32	13.43	12.67	12.95

Table G.0.12: Variations of ggF and VBF MC event yields between $110 \leq M_{\text{inv}}^{\mu\mu} \leq 160$ GeV due to experimental systematic variations, for the ggF Single-Jet 6 category. The samples have been normalised to 80.5 fb^{-1}.

Systematics Type	Up (ggF) [%]	Down (ggF) [%]	Up (VBF) [%]	Down (VBF) [%]
FT_EFF_Eigen_B_0	-0.40	-0.02	0.39	0.24
FT_EFF_Eigen_B_1	-0.07	-0.35	0.13	0.21
FT_EFF_Eigen_B_2	-0.02	-0.36	0.10	0.19
FT_EFF_Eigen_C_0	-0.19	-0.16	0.12	0.39
FT_EFF_Eigen_C_1	-0.20	-0.43	0.17	0.33
FT_EFF_Eigen_C_2	-0.28	0.32	0.34	-0.00
FT_EFF_Eigen_Light_0	0.04	-0.25	0.25	0.13
FT_EFF_Eigen_Light_1	-0.21	-0.30	0.16	0.06
FT_EFF_Eigen_Light_2	0.12	-0.29	-0.08	-0.07
FT_EFF_Eigen_Light_3	0.17	-0.41	0.18	0.30
FT_EFF_Eigen_Light_4	0.10	-0.16	0.08	0.12
FT_EFF_extrapolation	0.17	-0.25	0.12	0.23
FT_EFF_extrapolation_from_charm	-0.15	-0.18	0.26	0.28
JET_fJvtEfficiency	-0.17	-0.16	0.05	0.14
JET_JER_SINGLE_NP	0.78	-0.89	2.90	-3.03
JET_JvtEfficiency	0.04	-0.02	0.48	0.11
JET_SR1_JET_EtaIntercalibration_NonClosure	-0.04	0.09	0.11	0.18
JET_SR1_JET_GroupedNP_1	7.96	-7.87	5.37	-4.68
JET_SR1_JET_GroupedNP_2	0.62	-0.86	0.12	-0.12
JET_SR1_JET_GroupedNP_3	1.54	-1.82	1.31	-0.93
MET_SoftTrk_ResoPara	-0.18	-0.05	0.10	0.12
MET_SoftTrk_ResoPerp	-0.14	0.33	0.43	0.02
MET_SoftTrk_Scale	0.14	-0.37	0.09	0.28
MUON_EFF_ISO_STAT	0.07	-0.47	0.34	-0.13
MUON_EFF_ISO_SYS	0.18	-0.47	0.69	-0.29
MUON_EFF_RECO_STAT	0.31	-0.58	0.54	-0.20
MUON_EFF_RECO_SYS	0.90	-0.89	1.10	-1.10
MUON_EFF_TrigStatUncertainty	0.07	-0.30	0.05	0.34
MUON_EFF_TrigSystUncertainty	-0.01	-0.33	-0.01	-0.22
MUON_ID	-0.14	-0.33	0.34	-0.08
MUON_MS	-0.22	-0.26	-0.03	0.19
MUON_SAGITTA_RESBIAS	-0.42	-0.35	0.21	0.13
MUON_SAGITTA_RHO	-0.05	-0.00	0.12	0.00
MUON_SCALE	-0.08	-0.14	0.24	0.24
PRW_DATASF	0.27	-1.17	0.42	-0.77
Total Systematic Uncertainty	8.28	8.46	6.52	5.92

Table G.0.13: Variations of ggF and VBF MC event yields between $110 \leq M_{\text{inv}}^{\mu\mu} \leq 160$ GeV due to experimental systematic variations, for the ggF Multi-Jet 1 category. The samples have been normalised to 80.5 fb^{-1}.

Systematics Type	Up (ggF) [%]	Down (ggF) [%]	Up (VBF) [%]	Down (VBF) [%]
FT_EFF_Eigen_B_0	0.00	0.72	-0.55	-0.24
FT_EFF_Eigen_B_1	-0.07	0.25	-0.41	-0.30
FT_EFF_Eigen_B_2	0.08	0.37	-0.17	-0.19
FT_EFF_Eigen_C_0	0.65	0.23	-0.03	-0.63
FT_EFF_Eigen_C_1	0.44	0.37	-0.11	-0.10
FT_EFF_Eigen_C_2	0.40	-0.26	-0.37	-0.31
FT_EFF_Eigen_Light_0	0.46	0.15	-0.48	-0.38
FT_EFF_Eigen_Light_1	0.22	0.64	-0.33	-0.07
FT_EFF_Eigen_Light_2	0.41	0.08	0.14	0.07
FT_EFF_Eigen_Light_3	0.27	0.24	-0.25	-0.51
FT_EFF_Eigen_Light_4	-0.03	0.28	0.09	0.05
FT_EFF_extrapolation	0.03	0.32	-0.19	-0.19
FT_EFF_extrapolation_from_charm	0.45	0.14	-0.05	-0.22
JET_fJvtEfficiency	0.21	0.20	-0.29	-0.20
JET_JER_SINGLE_NP	3.32	-2.98	2.55	-2.89
JET_JvtEfficiency	-0.25	0.07	-0.28	-0.17
JET_SR1_JET_EtaIntercalibration_NonClosure	0.02	-0.45	0.01	-0.45
JET_SR1_JET_GroupedNP_1	14.97	-12.43	6.39	-6.66
JET_SR1_JET_GroupedNP_2	1.26	-1.11	0.59	-0.47
JET_SR1_JET_GroupedNP_3	4.20	-3.21	1.58	-2.01
MET_SoftTrk_ResoPara	0.20	0.07	-0.18	0.28
MET_SoftTrk_ResoPerp	0.30	-0.63	-0.71	0.48
MET_SoftTrk_Scale	0.07	0.26	-0.15	-0.34
MUON_EFF_ISO_STAT	0.05	0.71	-0.24	0.18
MUON_EFF_ISO_SYS	0.90	-0.10	0.17	-0.55
MUON_EFF_RECO_STAT	0.49	0.02	-0.06	-0.46
MUON_EFF_RECO_SYS	0.99	-1.24	0.89	-0.80
MUON_EFF_TrigStatUncertainty	-0.13	0.74	-0.05	-0.64
MUON_EFF_TrigSystUncertainty	0.19	0.70	-0.31	0.24
MUON_ID	-0.34	-0.01	-0.46	0.03
MUON_MS	0.40	0.50	0.02	-0.42
MUON_SAGITTA_RESBIAS	0.13	0.95	-0.41	-0.31
MUON_SAGITTA_RHO	0.14	0.32	-0.10	-0.28
MUON_SCALE	0.39	0.33	-0.23	-0.15
PRW_DATASF	2.04	-0.65	0.50	-0.76
Total Systematic Uncertainty	16.21	13.50	7.33	7.84

Table G.0.14: Variations of ggF and VBF MC event yields between $110 \leq M_{\text{inv}}^{\mu\mu} \leq 160$ GeV due to experimental systematic variations, for the ggF Multi-Jet 2 category. The samples have been normalised to 80.5 fb^{-1}.

Systematics Type	Up (ggF) [%]	Down (ggF) [%]	Up (VBF) [%]	Down (VBF) [%]
FT_EFF_Eigen_B_0	0.09	-1.59	-0.19	-0.26
FT_EFF_Eigen_B_1	-0.49	-0.46	0.61	0.32
FT_EFF_Eigen_B_2	-0.20	-0.97	-0.07	0.06
FT_EFF_Eigen_C_0	-0.60	-1.39	0.38	-0.19
FT_EFF_Eigen_C_1	-0.49	0.23	-0.25	-0.31
FT_EFF_Eigen_C_2	0.40	-0.69	-0.08	0.10
FT_EFF_Eigen_Light_0	-0.51	-1.06	0.31	0.23
FT_EFF_Eigen_Light_1	-0.51	-1.23	0.11	-0.63
FT_EFF_Eigen_Light_2	-0.84	-0.08	-0.13	0.29
FT_EFF_Eigen_Light_3	-0.49	-1.27	-0.11	-0.82
FT_EFF_Eigen_Light_4	-0.12	-0.68	-0.44	-0.23
FT_EFF_extrapolation	-0.60	-0.34	-0.32	-0.38
FT_EFF_extrapolation_from_charm	-0.66	-0.36	0.25	-0.61
JET_fJvtEfficiency	-1.31	-0.32	0.07	-0.21
JET_JER_SINGLE_NP	2.88	-3.39	1.84	-1.93
JET_JvtEfficiency	0.00	-0.83	0.01	0.10
JET_SR1_JET_EtaIntercalibration_NonClosure	-0.64	-0.16	-1.06	0.10
JET_SR1_JET_GroupedNP_1	15.12	-14.68	7.43	-7.02
JET_SR1_JET_GroupedNP_2	0.50	-1.02	0.34	-1.05
JET_SR1_JET_GroupedNP_3	2.83	-2.65	2.19	-1.91
MET_SoftTrk_ResoPara	-0.33	0.46	-1.05	0.39
MET_SoftTrk_ResoPerp	-0.04	0.49	-0.20	0.62
MET_SoftTrk_Scale	-0.95	-1.07	-0.32	0.11
MUON_EFF_ISO_STAT	-0.81	-0.59	-0.10	-0.66
MUON_EFF_ISO_SYS	-0.34	-0.65	0.71	-0.42
MUON_EFF_RECO_STAT	-0.61	-0.21	0.36	-0.53
MUON_EFF_RECO_SYS	-0.22	-1.46	1.35	-1.84
MUON_EFF_TrigStatUncertainty	-0.32	-1.37	-0.31	0.40
MUON_EFF_TrigSystUncertainty	-1.02	-0.79	-0.00	-0.57
MUON_ID	-0.66	-0.40	-0.39	-0.24
MUON_MS	0.17	-0.52	-0.15	0.13
MUON_SAGITTA_RESBIAS	-0.47	-0.86	-0.04	-0.22
MUON_SAGITTA_RHO	-0.15	-0.54	0.01	0.48
MUON_SCALE	-0.42	-0.50	-0.67	-0.41
PRW_DATASF	0.50	-2.31	0.79	-1.39
Total Systematic Uncertainty	15.97	16.16	8.41	8.23

Table G.0.15: Variations of ggF and VBF MC event yields between $110 \leq M_{\text{inv}}^{\mu\mu} \leq 160$ GeV due to experimental systematic variations, for the ggF Multi-Jet 3 category. The samples have been normalised to 80.5 fb^{-1}.

Systematics Type	Up (ggF) [%]	Down (ggF) [%]	Up (VBF) [%]	Down (VBF) [%]
FT_EFF_Eigen_B_0	0.13	0.46	0.19	0.40
FT_EFF_Eigen_B_1	0.44	0.35	-0.11	-0.06
FT_EFF_Eigen_B_2	-0.26	0.93	0.20	-0.05
FT_EFF_Eigen_C_0	0.39	0.60	0.39	-0.21
FT_EFF_Eigen_C_1	-0.19	0.19	-0.10	-0.15
FT_EFF_Eigen_C_2	-0.13	0.12	0.57	0.24
FT_EFF_Eigen_Light_0	-0.10	0.44	0.53	-0.23
FT_EFF_Eigen_Light_1	0.29	0.33	0.36	0.50
FT_EFF_Eigen_Light_2	-0.27	0.54	0.34	0.38
FT_EFF_Eigen_Light_3	-0.56	1.34	0.66	1.23
FT_EFF_Eigen_Light_4	-0.20	0.25	0.57	0.19
FT_EFF_extrapolation	0.13	0.49	0.65	0.49
FT_EFF_extrapolation_from_charm	0.09	0.44	-0.39	0.83
JET_fJvtEfficiency	0.80	0.31	0.50	0.41
JET_JER_SINGLE_NP	3.71	-3.63	2.12	-1.29
JET_JvtEfficiency	0.27	0.44	0.14	0.11
JET_SR1_JET_EtaIntercalibration_NonClosure	0.28	0.44	0.94	0.63
JET_SR1_JET_GroupedNP_1	16.88	-14.25	7.04	-6.30
JET_SR1_JET_GroupedNP_2	1.38	-0.82	0.87	0.09
JET_SR1_JET_GroupedNP_3	3.28	-3.77	2.33	-1.54
MET_SoftTrk_ResoPara	0.56	-0.32	0.42	-0.48
MET_SoftTrk_ResoPerp	0.27	-0.58	0.26	-0.76
MET_SoftTrk_Scale	0.71	0.82	0.19	0.21
MUON_EFF_ISO_STAT	0.61	0.22	0.37	0.12
MUON_EFF_ISO_SYS	0.38	-0.48	0.55	-0.31
MUON_EFF_RECO_STAT	0.57	-0.46	0.66	-0.31
MUON_EFF_RECO_SYS	2.07	-0.84	1.08	-0.62
MUON_EFF_TrigStatUncertainty	0.09	0.44	0.18	0.21
MUON_EFF_TrigSystUncertainty	0.28	0.09	0.55	0.64
MUON_ID	0.92	0.72	0.43	-0.09
MUON_MS	-0.16	0.18	0.48	0.00
MUON_SAGITTA_RESBIAS	0.95	-0.28	0.21	0.35
MUON_SAGITTA_RHO	-0.06	-0.07	0.15	0.03
MUON_SCALE	-0.19	0.43	0.62	0.29
PRW_DATASF	1.56	-0.75	0.49	0.51
Total Systematic Uncertainty	17.98	15.49	8.22	7.07

Table G.0.16: Variations of ggF and VBF MC event yields between $110 \leq M_{\text{inv}}^{\mu\mu} \leq 160$ GeV due to experimental systematic variations, for the ggF Multi-Jet 4 category. The samples have been normalised to 80.5 fb^{-1}.

Systematics Type	Up (ggF) [%]	Down (ggF) [%]	Up (VBF) [%]	Down (VBF) [%]
FT_EFF_Eigen_B_0	-3.38	-1.16	-0.24	8.75
FT_EFF_Eigen_B_1	-0.35	2.49	7.24	-0.84
FT_EFF_Eigen_B_2	-1.53	2.65	-4.90	1.73
FT_EFF_Eigen_C_0	-1.34	-1.54	0.16	2.45
FT_EFF_Eigen_C_1	2.21	-4.31	-0.57	9.74
FT_EFF_Eigen_C_2	-10.00	-0.10	-0.35	-2.41
FT_EFF_Eigen_Light_0	-3.18	-3.39	-0.50	-1.74
FT_EFF_Eigen_Light_1	-6.54	-1.88	-0.36	4.92
FT_EFF_Eigen_Light_2	-5.32	-3.41	-1.06	0.19
FT_EFF_Eigen_Light_3	-0.82	-4.06	-2.65	-0.54
FT_EFF_Eigen_Light_4	0.65	-5.91	-3.86	-7.84
FT_EFF_extrapolation	-5.46	-2.53	-0.18	0.37
FT_EFF_extrapolation_from_charm	-4.33	-1.98	1.53	-0.75
JET_fJvtEfficiency	1.16	0.05	5.50	-3.95
JET_JER_SINGLE_NP	-1.32	-0.52	2.39	-2.54
JET_JvtEfficiency	-1.93	4.11	1.14	1.11
JET_SR1_JET_EtaIntercalibration_NonClosure	-0.84	1.21	2.30	-2.86
JET_SR1_JET_GroupedNP_1	11.10	-17.15	10.31	-6.36
JET_SR1_JET_GroupedNP_2	1.50	1.65	0.90	-0.73
JET_SR1_JET_GroupedNP_3	-1.09	-4.99	7.73	-4.82
MET_SoftTrk_ResoPara	-3.59	5.74	-3.70	3.04
MET_SoftTrk_ResoPerp	-2.83	5.46	0.19	2.36
MET_SoftTrk_Scale	-3.00	-5.45	8.15	3.07
MUON_EFF_ISO_STAT	-0.33	-4.35	0.10	0.63
MUON_EFF_ISO_SYS	-0.94	-4.68	2.44	-1.19
MUON_EFF_RECO_STAT	-2.23	-0.90	3.44	0.31
MUON_EFF_RECO_SYS	-2.85	-7.73	1.05	-0.16
MUON_EFF_TrigStatUncertainty	-1.64	-7.25	3.43	0.81
MUON_EFF_TrigSystUncertainty	6.73	1.80	-1.94	-0.84
MUON_ID	-4.04	2.25	-3.64	5.38
MUON_MS	2.11	1.44	-1.01	1.10
MUON_SAGITTA_RESBIAS	-4.27	-0.70	7.61	2.28
MUON_SAGITTA_RHO	-2.13	-3.06	2.68	1.09
MUON_SCALE	-0.88	-3.63	2.12	-1.40
PRW_DATASF	2.76	-4.64	1.52	0.41
Total Systematic Uncertainty	23.01	27.67	22.64	20.94

Table G.0.17: Variations of ggF and VBF MC event yields between $110 \leq M_{\text{inv}}^{\mu\mu} \leq 160$ GeV due to experimental systematic variations, for the ggF Multi-Jet 5 category. The samples have been normalised to 80.5 fb^{-1}.

Systematics Type	Up (ggF) [%]	Down (ggF) [%]	Up (VBF) [%]	Down (VBF) [%]
FT_EFF_Eigen_B_0	0.17	0.33	0.78	1.52
FT_EFF_Eigen_B_1	0.63	0.96	3.68	1.56
FT_EFF_Eigen_B_2	0.54	-0.54	0.69	0.45
FT_EFF_Eigen_C_0	-0.74	-0.38	1.63	1.69
FT_EFF_Eigen_C_1	1.29	-0.77	0.42	1.91
FT_EFF_Eigen_C_2	-1.03	0.44	1.68	2.85
FT_EFF_Eigen_Light_0	0.74	-0.88	1.33	0.60
FT_EFF_Eigen_Light_1	0.54	1.19	1.04	-0.80
FT_EFF_Eigen_Light_2	0.17	0.01	-0.16	-0.02
FT_EFF_Eigen_Light_3	1.09	0.59	1.01	1.58
FT_EFF_Eigen_Light_4	0.77	1.85	-0.33	1.31
FT_EFF_extrapolation	-1.13	-2.15	0.65	0.89
FT_EFF_extrapolation_from_charm	0.66	-1.97	1.30	-0.30
JET_fJvtEfficiency	0.25	-0.11	0.02	2.27
JET_JER_SINGLE_NP	6.49	-3.82	0.43	-1.05
JET_JvtEfficiency	-0.15	-0.66	0.39	0.54
JET_SR1_JET_EtaIntercalibration_NonClosure	1.38	0.63	1.74	-0.30
JET_SR1_JET_GroupedNP_1	15.46	-11.83	7.32	-4.72
JET_SR1_JET_GroupedNP_2	1.13	-1.65	2.33	0.42
JET_SR1_JET_GroupedNP_3	3.73	-1.95	0.50	-1.03
MET_SoftTrk_ResoPara	-0.01	-0.39	2.80	-2.98
MET_SoftTrk_ResoPerp	0.25	-0.43	2.27	-2.85
MET_SoftTrk_Scale	0.95	-0.68	-0.89	0.41
MUON_EFF_ISO_STAT	-0.38	-0.13	0.77	0.40
MUON_EFF_ISO_SYS	3.28	-0.02	0.11	0.28
MUON_EFF_RECO_STAT	0.67	0.64	0.52	2.17
MUON_EFF_RECO_SYS	2.10	1.66	3.04	-0.39
MUON_EFF_TrigStatUncertainty	0.07	1.11	1.67	0.93
MUON_EFF_TrigSystUncertainty	-0.44	0.50	2.24	1.92
MUON_ID	1.41	1.27	2.17	0.74
MUON_MS	-1.70	-0.48	-0.28	2.55
MUON_SAGITTA_RESBIAS	-0.41	1.83	3.46	2.63
MUON_SAGITTA_RHO	0.99	-0.58	0.55	0.98
MUON_SCALE	-1.08	-1.63	0.85	-0.89
PRW_DATASF	2.52	-3.16	0.07	-0.82
Total Systematic Uncertainty	18.36	14.22	11.77	9.95

Table G.0.18: Variations of ggF and VBF MC event yields between $110 \leq M_{\text{inv}}^{\mu\mu} \leq 160$ GeV due to experimental systematic variations, for the ggF Multi-Jet 6 category. The samples have been normalised to 80.5 fb^{-1}.

Systematics Type	Up (ggF) [%]	Down (ggF) [%]	Up (VBF) [%]	Down (VBF) [%]
FT_EFF_Eigen_B_0	0.94	0.73	-0.00	-0.04
FT_EFF_Eigen_B_1	0.65	0.51	-0.05	-0.06
FT_EFF_Eigen_B_2	1.13	0.66	-0.03	0.13
FT_EFF_Eigen_C_0	-0.18	0.74	0.08	-0.06
FT_EFF_Eigen_C_1	0.76	1.37	0.04	0.10
FT_EFF_Eigen_C_2	-0.06	0.21	-0.08	-0.04
FT_EFF_Eigen_Light_0	0.82	0.91	0.11	-0.07
FT_EFF_Eigen_Light_1	1.12	0.80	0.08	0.05
FT_EFF_Eigen_Light_2	0.53	1.15	0.01	0.15
FT_EFF_Eigen_Light_3	0.93	0.64	-0.03	-0.01
FT_EFF_Eigen_Light_4	1.19	0.42	0.08	0.01
FT_EFF_extrapolation	0.33	0.54	-0.03	0.02
FT_EFF_extrapolation_from_charm	0.77	0.85	-0.01	0.01
JET_fJvtEfficiency	1.13	0.34	-0.06	-0.03
JET_JER_SINGLE_NP	-1.57	0.61	-3.26	3.26
JET_JvtEfficiency	1.13	0.90	-0.00	0.01
JET_SR1_JET_EtaIntercalibration_NonClosure	0.64	0.05	0.07	0.04
JET_SR1_JET_GroupedNP_1	10.96	-8.83	3.99	-4.83
JET_SR1_JET_GroupedNP_2	1.57	-0.43	0.38	-0.41
JET_SR1_JET_GroupedNP_3	5.26	-2.28	1.71	-1.77
MET_SoftTrk_ResoPara	1.80	-2.21	0.21	-0.25
MET_SoftTrk_ResoPerp	1.36	-1.43	0.26	-0.23
MET_SoftTrk_Scale	2.66	-0.05	0.27	-0.27
MUON_EFF_ISO_STAT	-0.60	0.02	0.04	-0.03
MUON_EFF_ISO_SYS	1.50	-0.19	0.42	-0.37
MUON_EFF_RECO_STAT	0.35	0.37	0.37	-0.25
MUON_EFF_RECO_SYS	1.98	-0.85	1.00	-0.94
MUON_EFF_TrigStatUncertainty	1.64	0.85	-0.03	-0.01
MUON_EFF_TrigSystUncertainty	0.48	1.51	0.06	0.01
MUON_ID	1.55	0.13	-0.07	0.03
MUON_MS	0.07	1.57	-0.09	0.12
MUON_SAGITTA_RESBIAS	0.48	0.23	-0.03	0.09
MUON_SAGITTA_RHO	1.04	0.69	-0.05	-0.02
MUON_SCALE	0.30	1.13	-0.06	0.03
PRW_DATASF	1.18	0.10	-0.22	0.52
Total Systematic Uncertainty	13.82	10.38	5.59	6.24

Table G.0.19: Variations of ggF and VBF MC event yields between $110 \leq M_{\text{inv}}^{\mu\mu} \leq 160$ GeV due to experimental systematic variations, for the VBF 1 category. The samples have been normalised to 80.5 fb^{-1}.

Systematics Type	Up (ggF) [%]	Down (ggF) [%]	Up (VBF) [%]	Down (VBF) [%]
FT_EFF_Eigen_B_0	0.51	0.07	-0.12	0.01
FT_EFF_Eigen_B_1	0.20	0.39	-0.05	-0.02
FT_EFF_Eigen_B_2	0.03	0.31	-0.03	-0.19
FT_EFF_Eigen_C_0	0.01	0.17	-0.11	-0.13
FT_EFF_Eigen_C_1	-0.21	0.19	-0.19	-0.18
FT_EFF_Eigen_C_2	0.46	0.13	-0.06	0.01
FT_EFF_Eigen_Light_0	0.44	0.59	-0.04	-0.08
FT_EFF_Eigen_Light_1	0.31	0.39	-0.22	-0.07
FT_EFF_Eigen_Light_2	0.20	-0.27	-0.13	-0.43
FT_EFF_Eigen_Light_3	-0.10	0.13	-0.15	-0.12
FT_EFF_Eigen_Light_4	-0.40	0.14	-0.27	-0.13
FT_EFF_extrapolation	0.34	0.12	-0.09	-0.15
FT_EFF_extrapolation_from_charm	-0.09	0.50	-0.15	-0.18
JET_fJvtEfficiency	0.16	-0.19	0.02	-0.06
JET_JER_SINGLE_NP	0.81	-1.19	-0.07	0.16
JET_JvtEfficiency	-0.26	0.12	-0.26	-0.08
JET_SR1_JET_EtaIntercalibration_NonClosure	0.19	0.13	-0.26	-0.15
JET_SR1_JET_GroupedNP_1	10.76	-9.20	4.46	-4.48
JET_SR1_JET_GroupedNP_2	1.48	-0.98	0.44	-0.60
JET_SR1_JET_GroupedNP_3	3.45	-3.72	1.35	-1.63
MET_SoftTrk_ResoPara	0.26	-0.98	0.05	-0.02
MET_SoftTrk_ResoPerp	0.71	-0.61	-0.03	-0.17
MET_SoftTrk_Scale	0.17	-0.80	-0.00	-0.14
MUON_EFF_ISO_STAT	0.56	-0.12	-0.07	-0.07
MUON_EFF_ISO_SYS	0.03	-0.47	0.16	-0.49
MUON_EFF_RECO_STAT	0.75	-0.31	0.10	-0.40
MUON_EFF_RECO_SYS	1.17	-0.86	0.99	-1.22
MUON_EFF_TrigStatUncertainty	0.06	0.16	-0.01	-0.08
MUON_EFF_TrigSystUncertainty	0.31	-0.36	-0.13	-0.11
MUON_ID	-0.17	0.89	-0.06	0.15
MUON_MS	-0.27	0.01	-0.05	-0.09
MUON_SAGITTA_RESBIAS	0.53	0.10	-0.07	-0.21
MUON_SAGITTA_RHO	-0.70	-0.08	-0.14	-0.08
MUON_SCALE	-0.07	0.07	-0.17	0.08
PRW_DATASF	0.33	0.30	-0.52	-0.10
Total Systematic Uncertainty	11.65	10.30	4.87	5.05

Table G.0.20: Variations of ggF and VBF MC event yields between $110 \leq M_{\text{inv}}^{\mu\mu} \leq 160$ GeV due to experimental systematic variations, for the VBF 2 category. The samples have been normalised to 80.5 fb^{-1}.

Appendix H

Breakdown of Theoretical Systematic Uncertainties

This chapter presents the $P_T^{\mu\mu,\text{truth}}$ distributions of the ggF and VBF samples used in the determination of the theoretical systematic uncertainties outlined in Chapter 11. Figures H.0.1 to H.0.7 present the variation of acceptance for different underlying event and shower parametrisations, while Figures H.0.8 to H.0.9 present the acceptance of events with varying QCD scale, PDF set and α_s. The uncertainties derived from these distributions for each variation in each category are listed in Tables H.0.1 to H.0.20. The largest contributions come from QCD scale variations, with overall uncertainties greater for ggF in the Multi-Jet and VBF categories, and VBF in the Zero-Jet and Single-Jet categories. This is an intuitive result, considering the event yield contributions of these processes in the respective categories (ggF contributions are largest in the Zero-Jet and Single-Jet categories, with the opposite true for VBF). For low yield categories, variations have a larger impact.

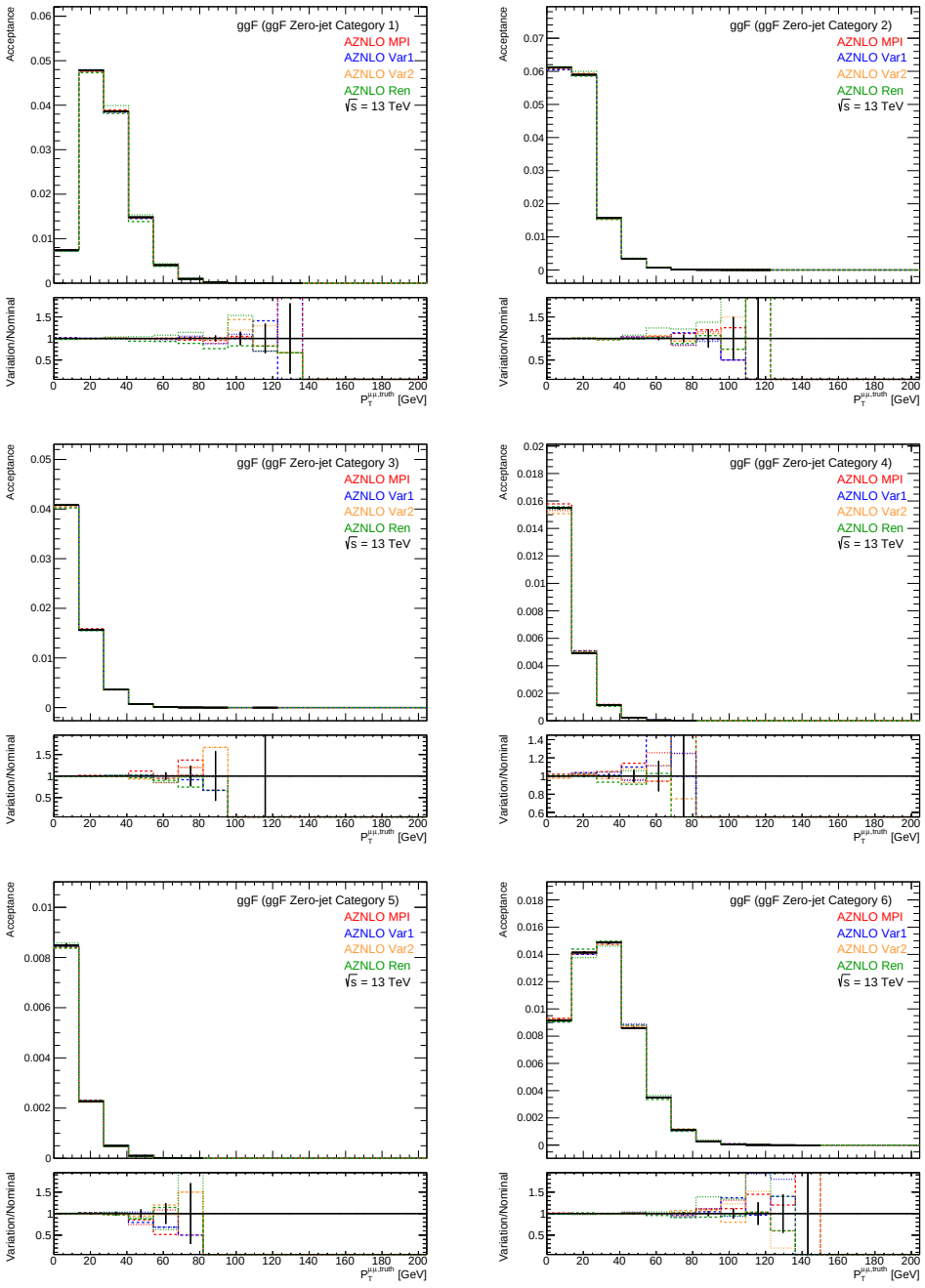

Figure H.0.1: Variation of underlying event and parton shower parameters as a function of $P_T^{\mu\mu,\mathrm{truth}}$ for ggF samples in the ggF Zero-Jet categories. The full analysis selection has been applied to each sample at truth level.

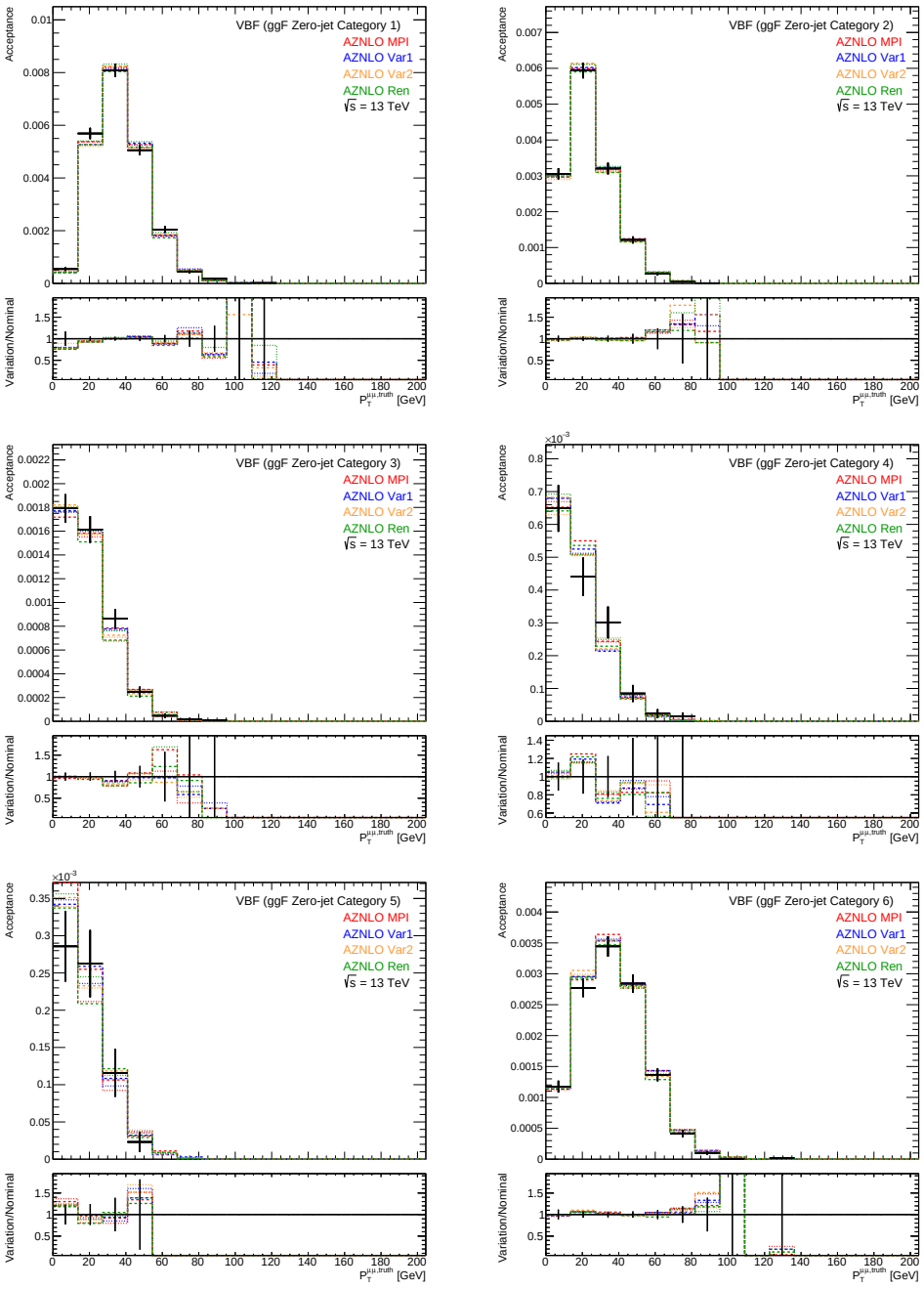

Figure H.0.2: Variation of underlying event and parton shower parameters as a function of $P_T^{\mu\mu,\text{truth}}$ for VBF samples in the ggF Zero-Jet categories. The full analysis selection has been applied to each sample at truth level.

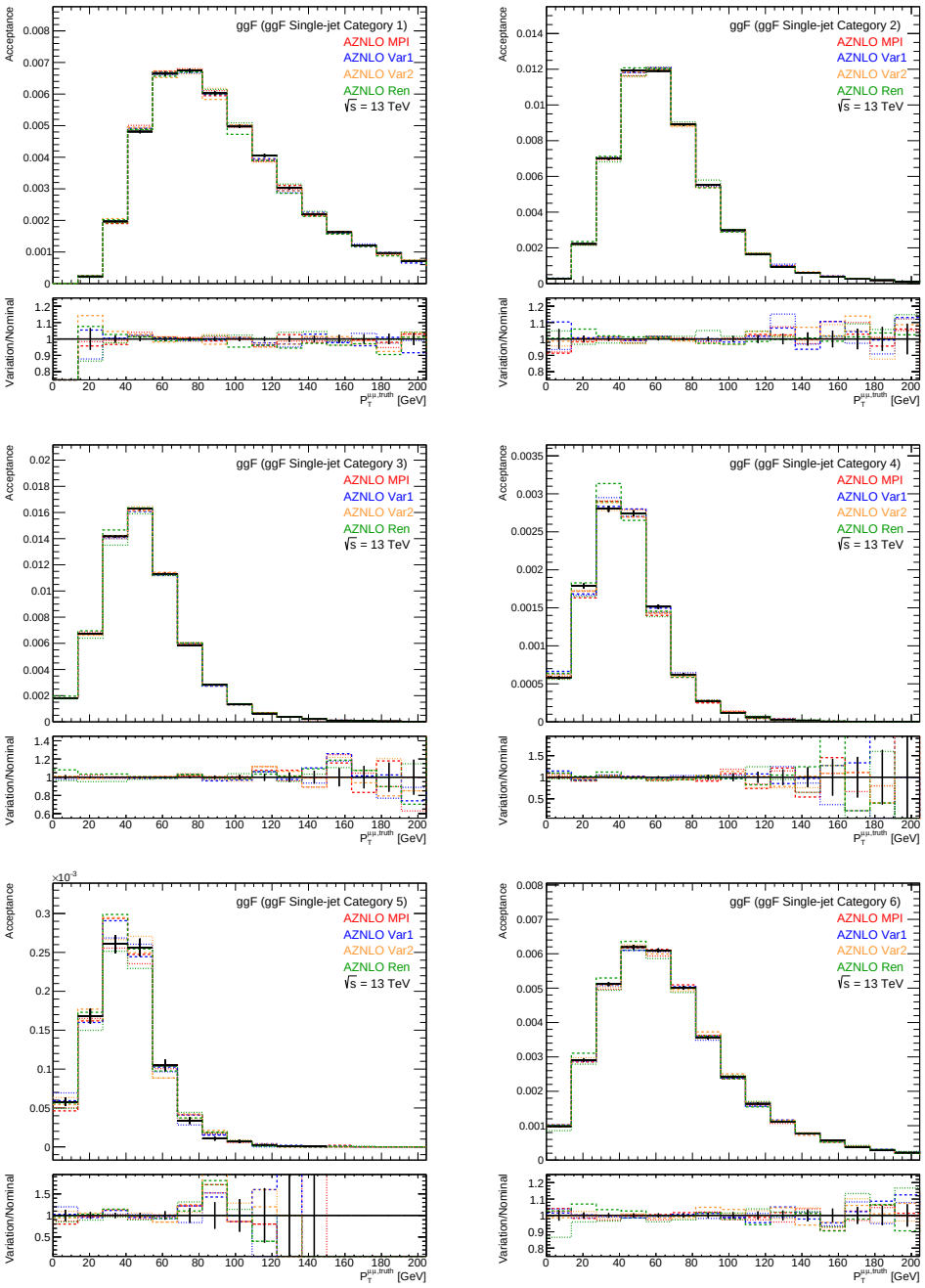

Figure H.0.3: Variation of underlying event and parton shower parameters as a function of $P_T^{\mu\mu,\mathrm{truth}}$ for ggF samples in the ggF Single-Jet categories. The full analysis selection has been applied to each sample at truth level.

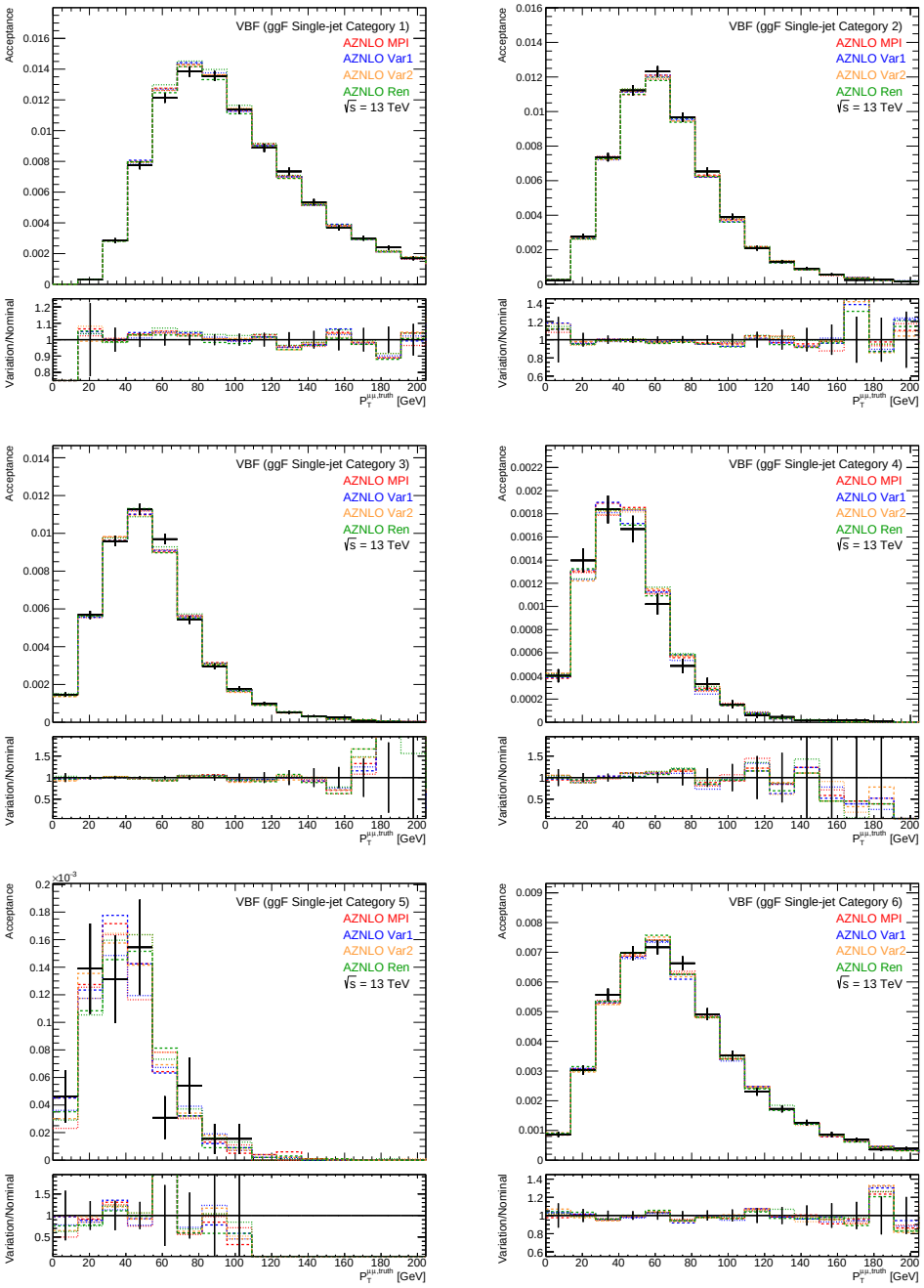

Figure H.0.4: Variation of underlying event and parton shower parameters as a function of $P_T^{\mu\mu,\mathrm{truth}}$ for VBF samples in the ggF Single-Jet categories. The full analysis selection has been applied to each sample at truth level.

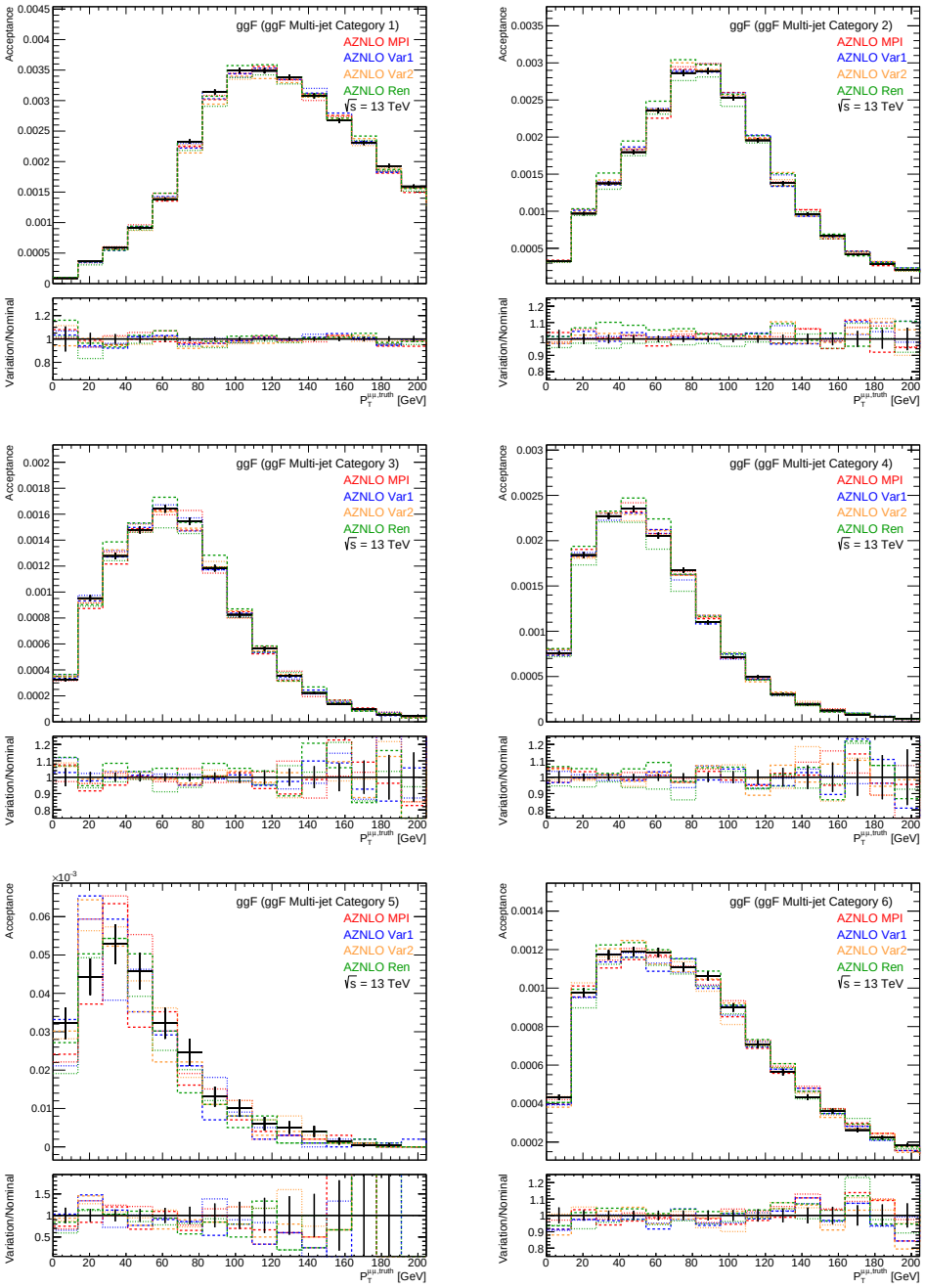

Figure H.0.5: Variation of underlying event and parton shower parameters as a function of $P_T^{\mu\mu,\mathrm{truth}}$ for ggF samples in the ggF Multi-Jet categories. The full analysis selection has been applied to each sample at truth level.

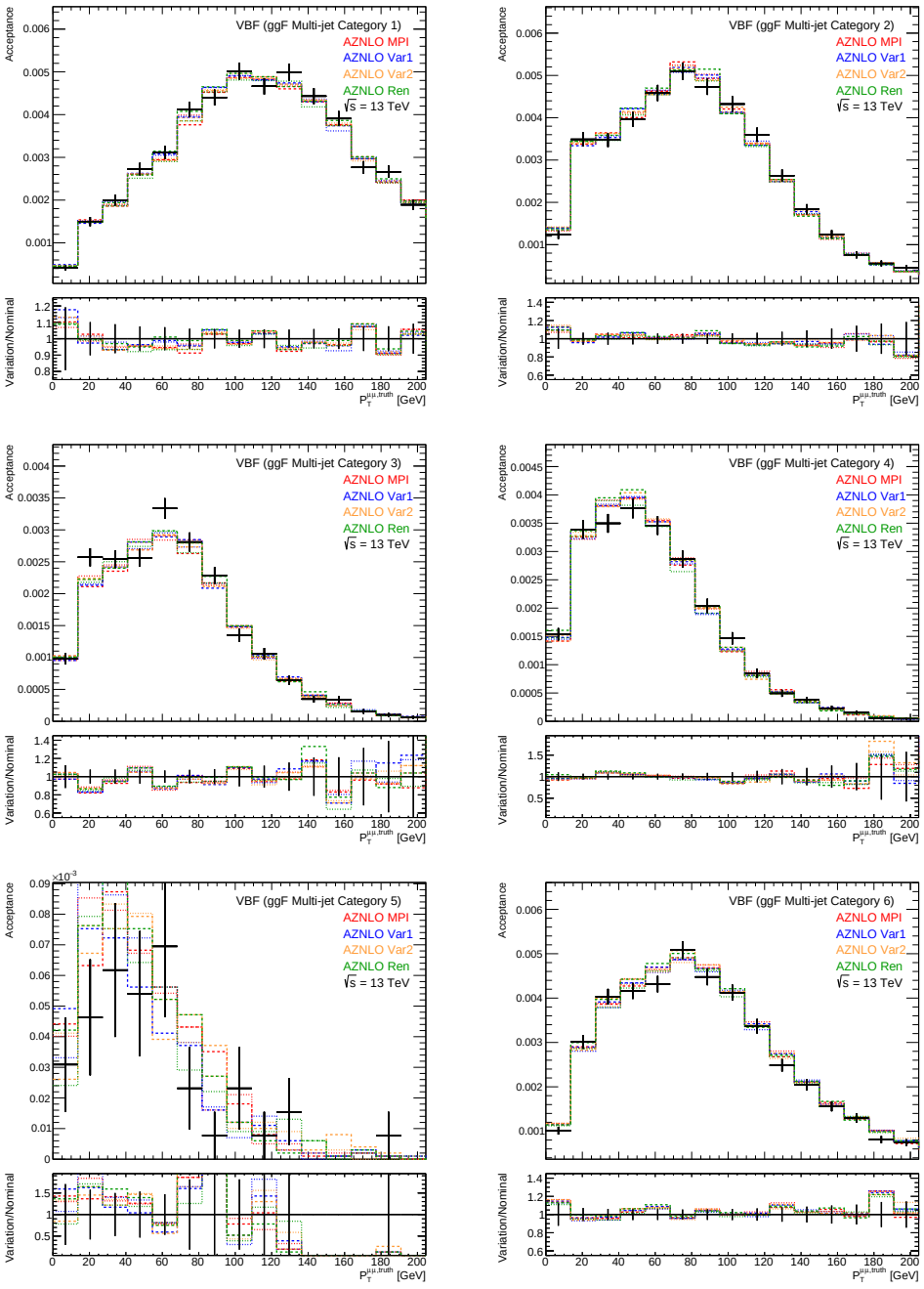

Figure H.0.6: Variation of underlying event and parton shower parameters as a function of $P_T^{\mu\mu,\text{truth}}$ for VBF samples in the ggF Multi-Jet categories. The full analysis selection has been applied to each sample at truth level.

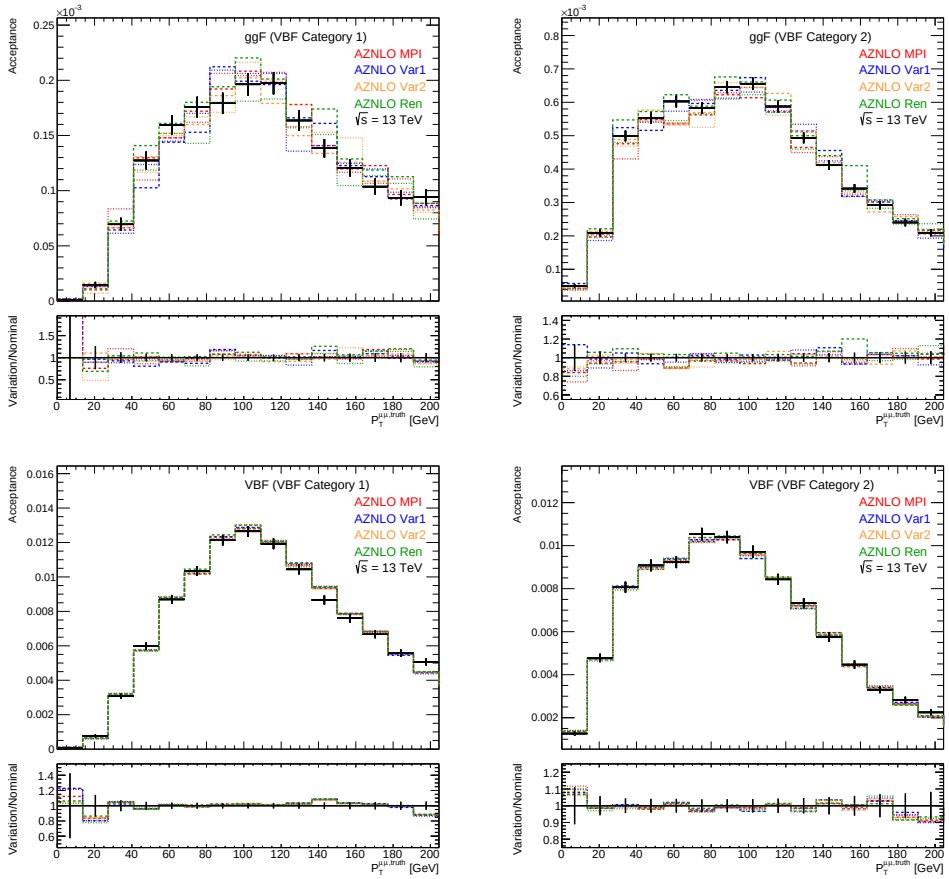

Figure H.0.7: Variation of underlying event and parton shower parameters as a function of $P_T^{\mu\mu,\text{truth}}$ for ggF (top) and VBF (bottom) samples in the VBF categories. The full analysis selection has been applied to each sample at truth level.

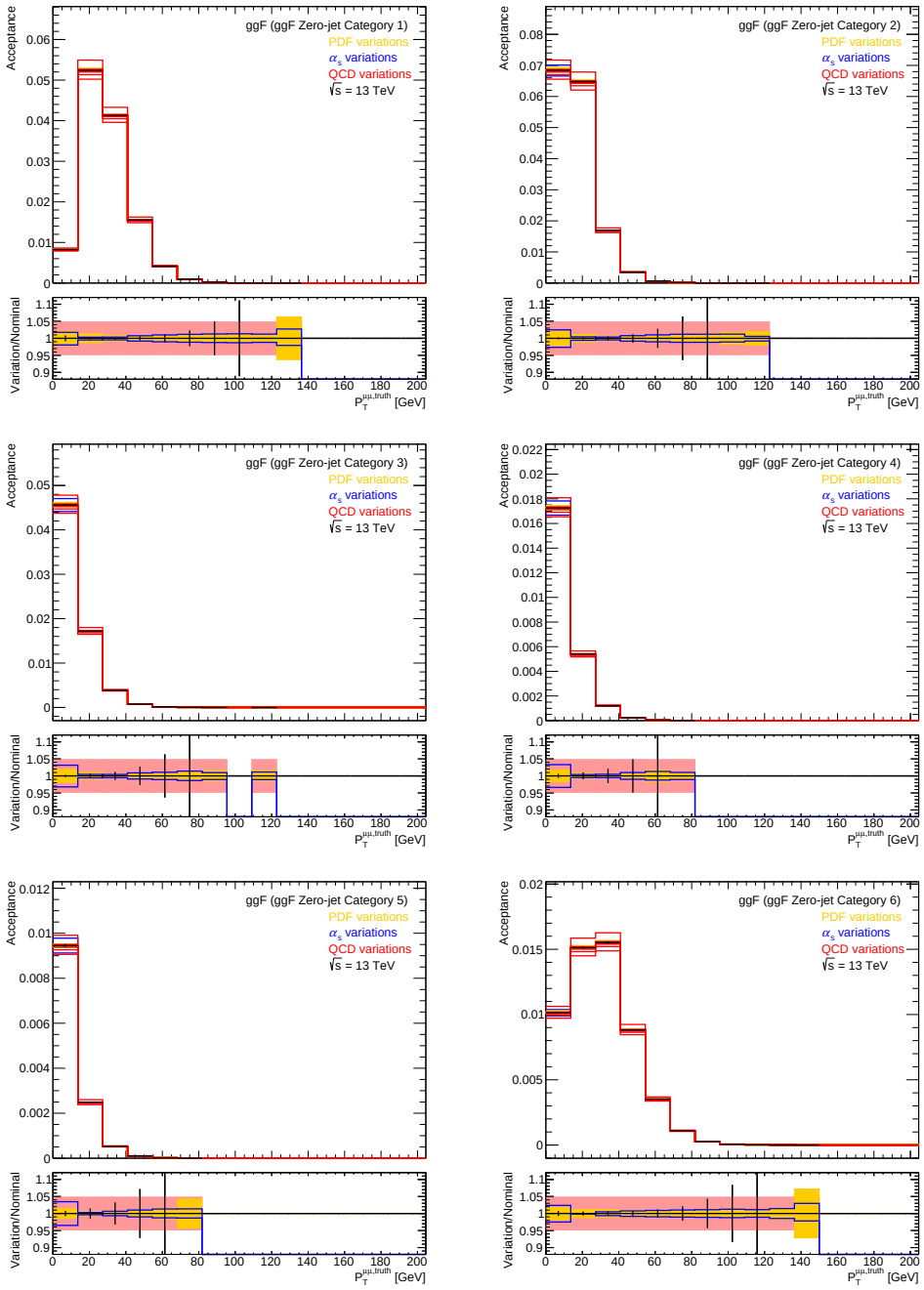

Figure H.0.8: Variation of QCD scale, PDF set and α_s as a function of $P_T^{\mu\mu,\text{truth}}$ for ggF samples in the ggF Zero-Jet categories. The full analysis selection has been applied to each sample at truth level.

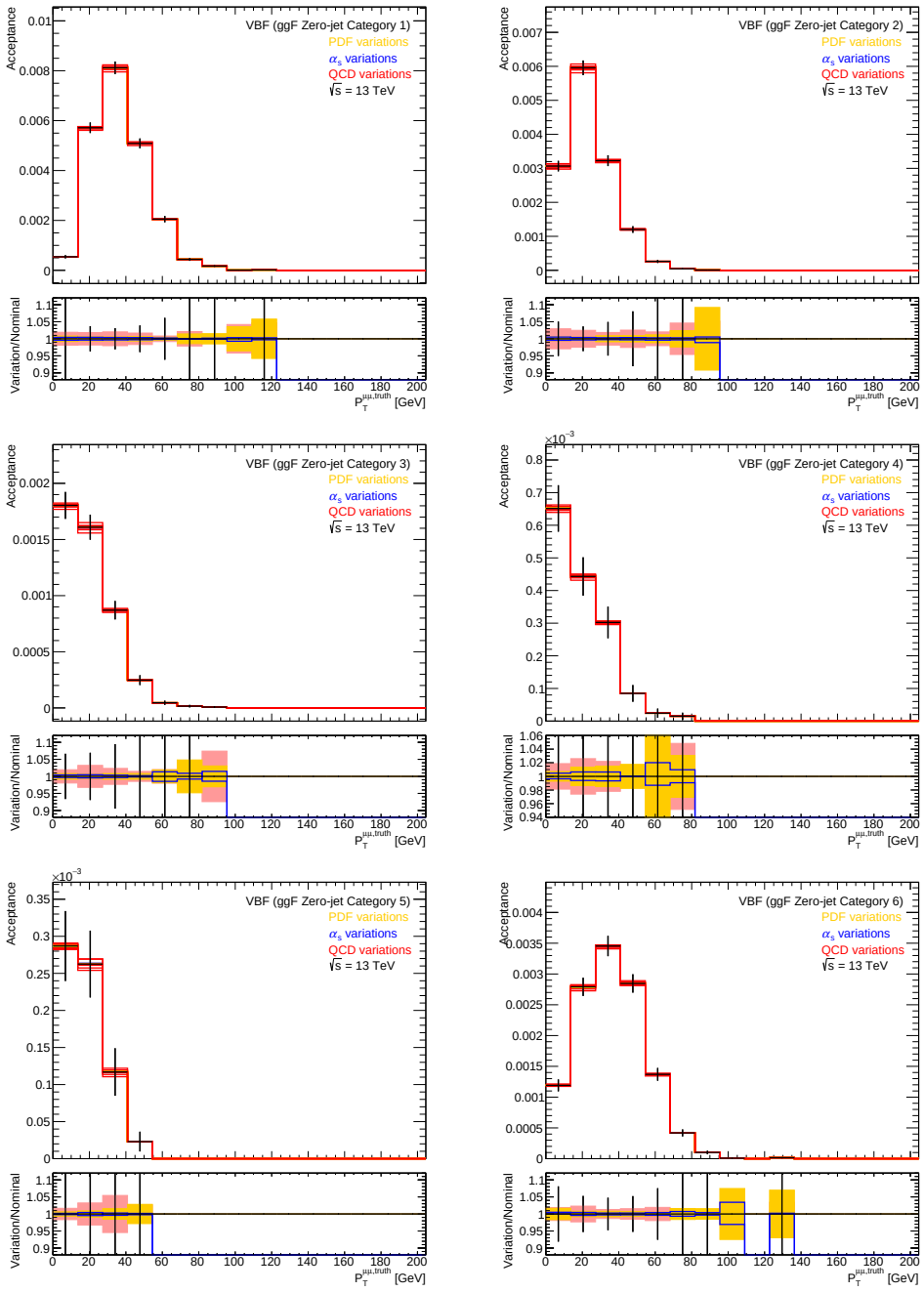

Figure H.0.9: Variation of QCD scale, PDF set and α_s as a function of $P_T^{\mu\mu,\mathrm{truth}}$ for VBF samples in the ggF Zero-Jet categories. The full analysis selection has been applied to each sample at truth level.

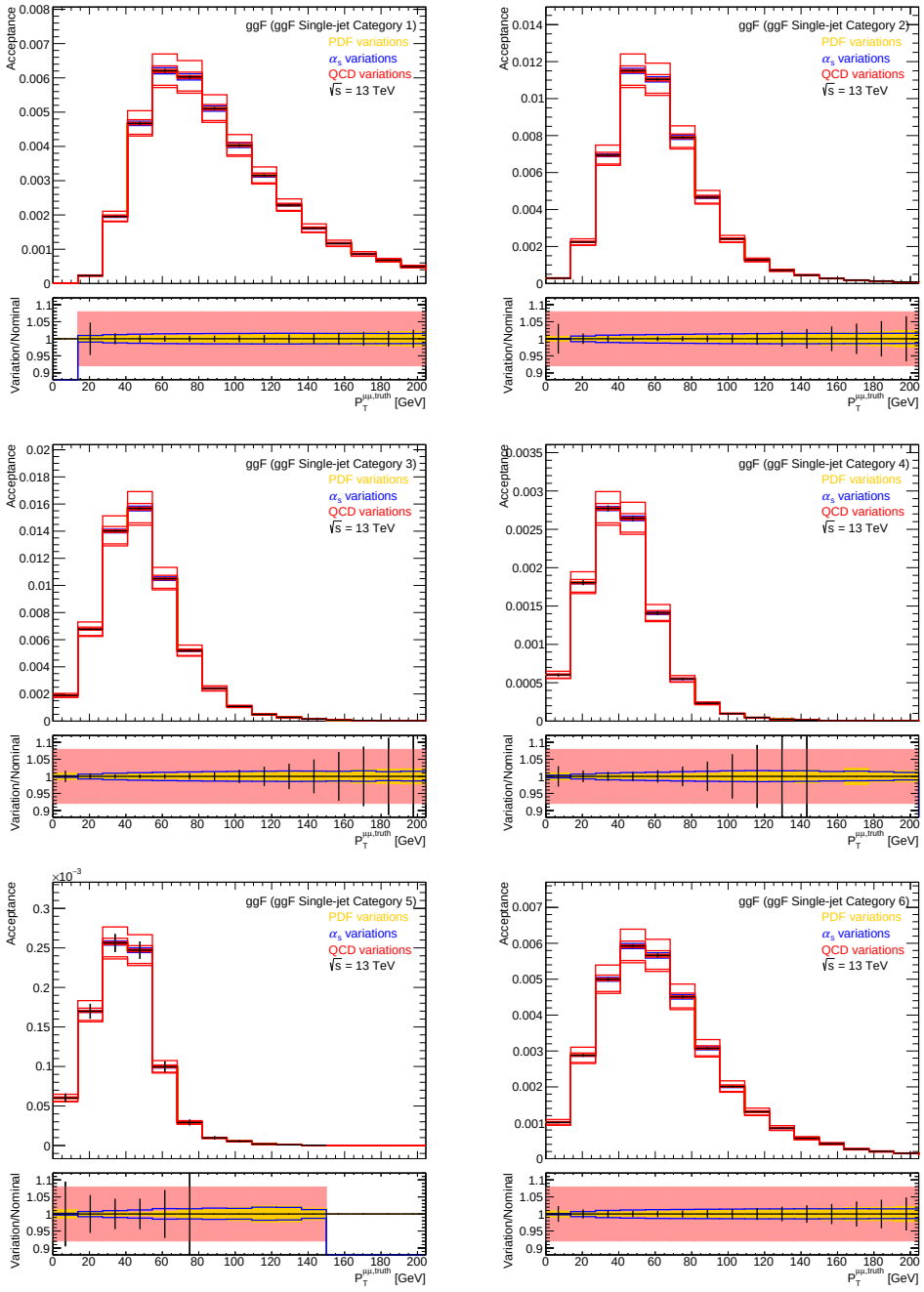

Figure H.0.10: Variation of QCD scale, PDF set and α_s as a function of $P_T^{\mu\mu,\mathrm{truth}}$ for ggF samples in the ggF Single-Jet categories. The full analysis selection has been applied to each sample at truth level.

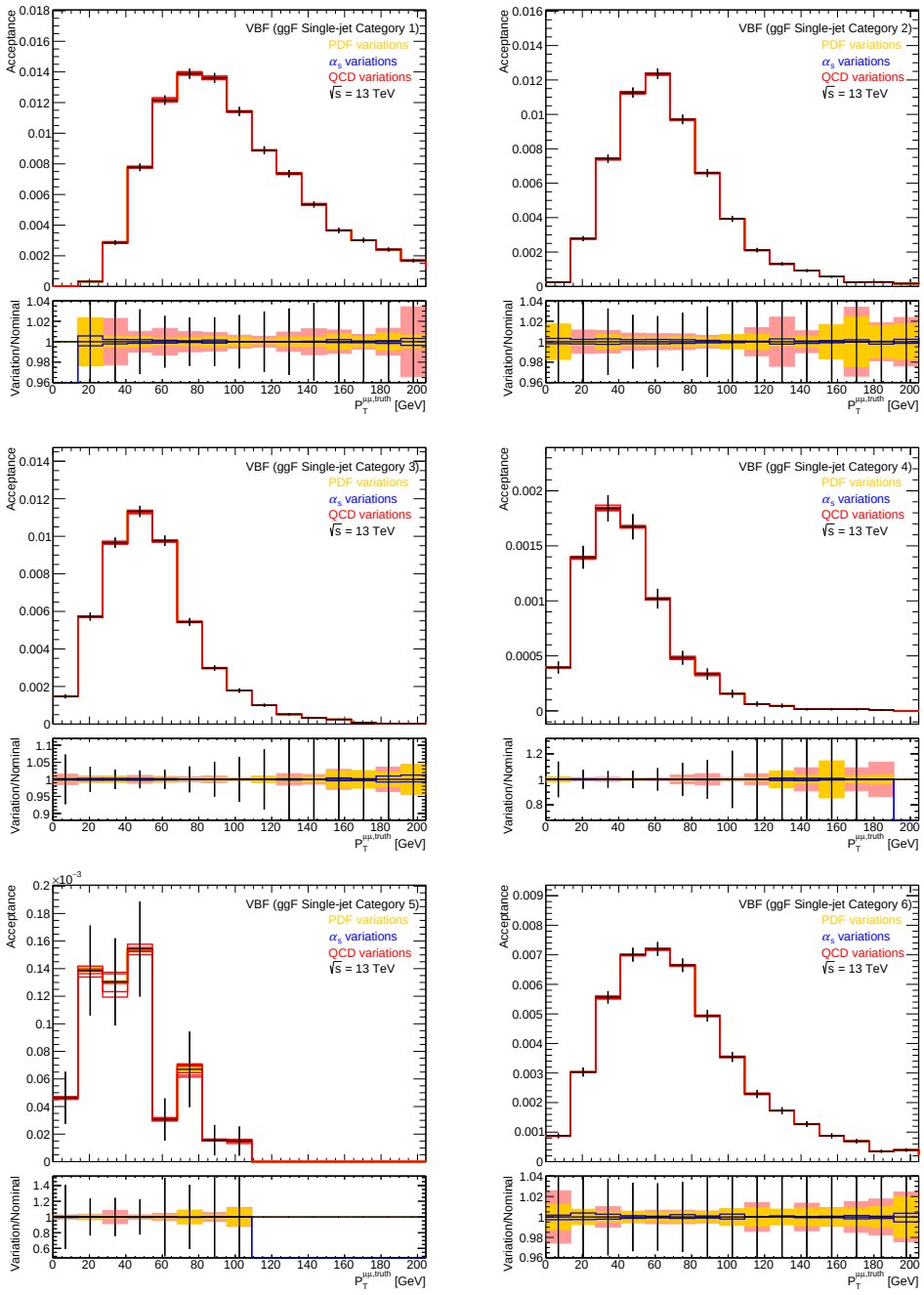

Figure H.0.11: Variation of QCD scale, PDF set and α_s as a function of $P_T^{\mu\mu,\text{truth}}$ for VBF samples in the ggF Single-Jet categories. The full analysis selection has been applied to each sample at truth level.

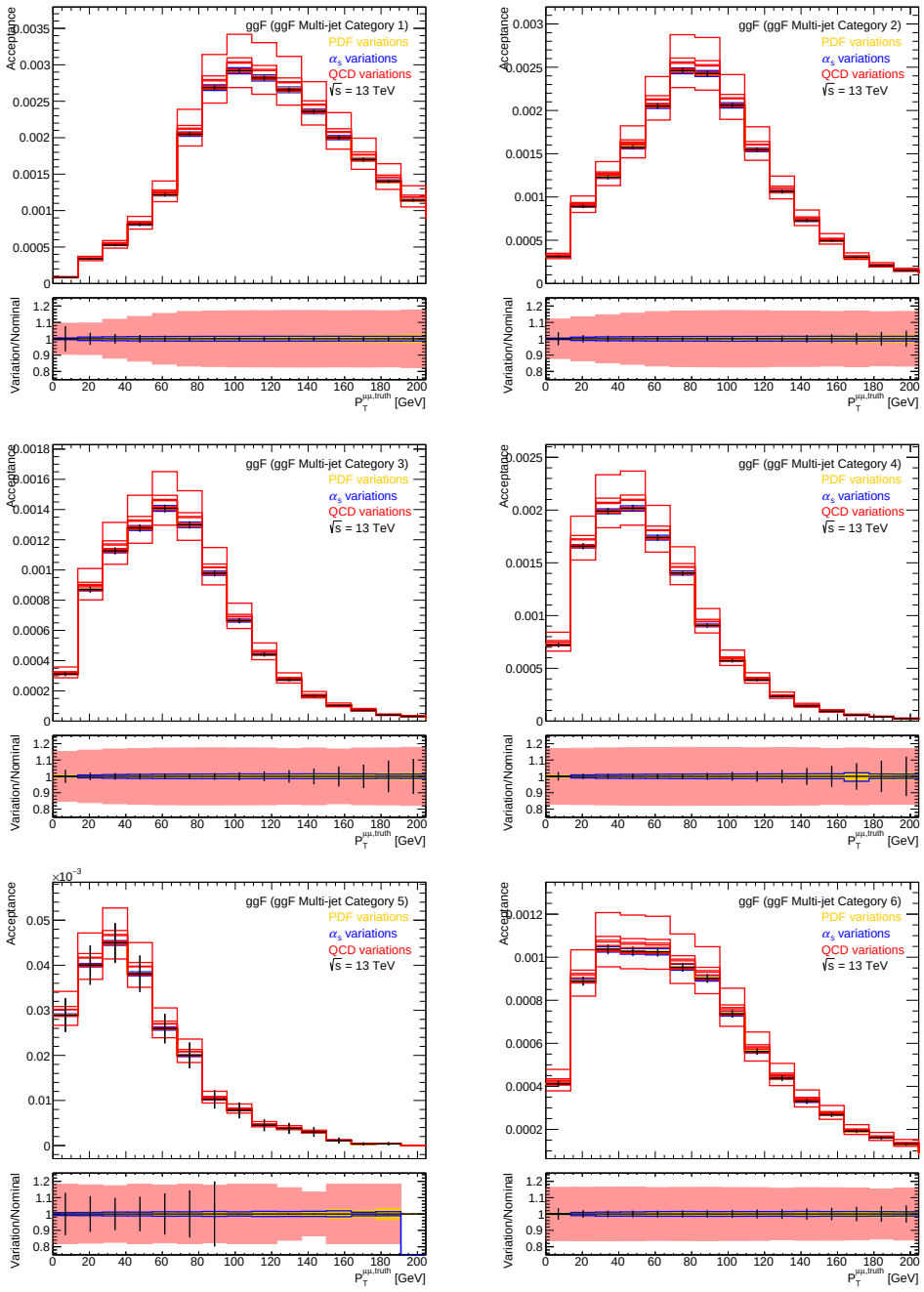

Figure H.0.12: Variation of QCD scale, PDF set and α_s as a function of $P_T^{\mu\mu,\mathrm{truth}}$ for ggF samples in the ggF Multi-Jet categories. The full analysis selection has been applied to each sample at truth level.

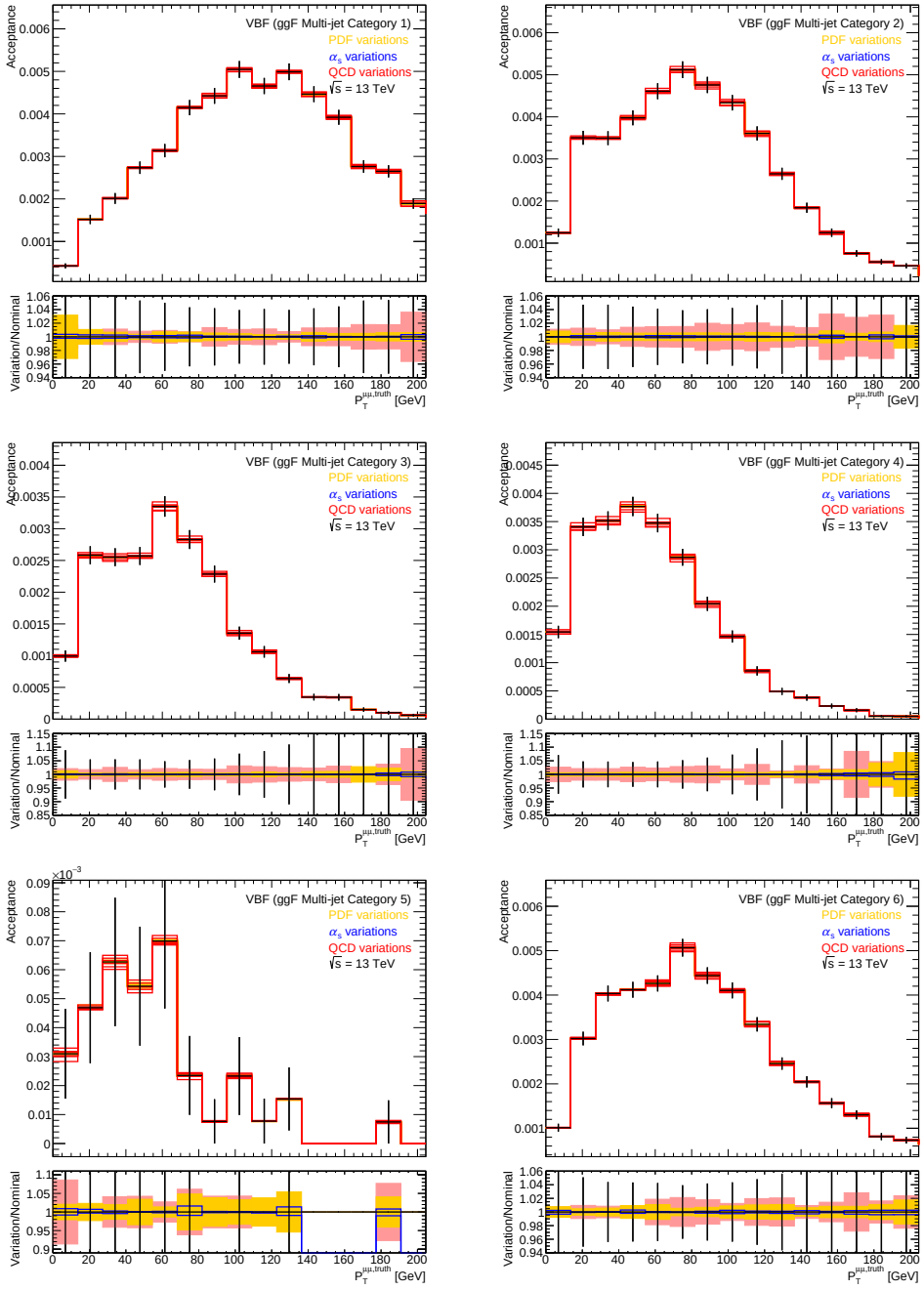

Figure H.0.13: Variation of QCD scale, PDF set and α_s as a function of $P_T^{\mu\mu,\text{truth}}$ for VBF samples in the ggF Multi-Jet categories. The full analysis selection has been applied to each sample at truth level.

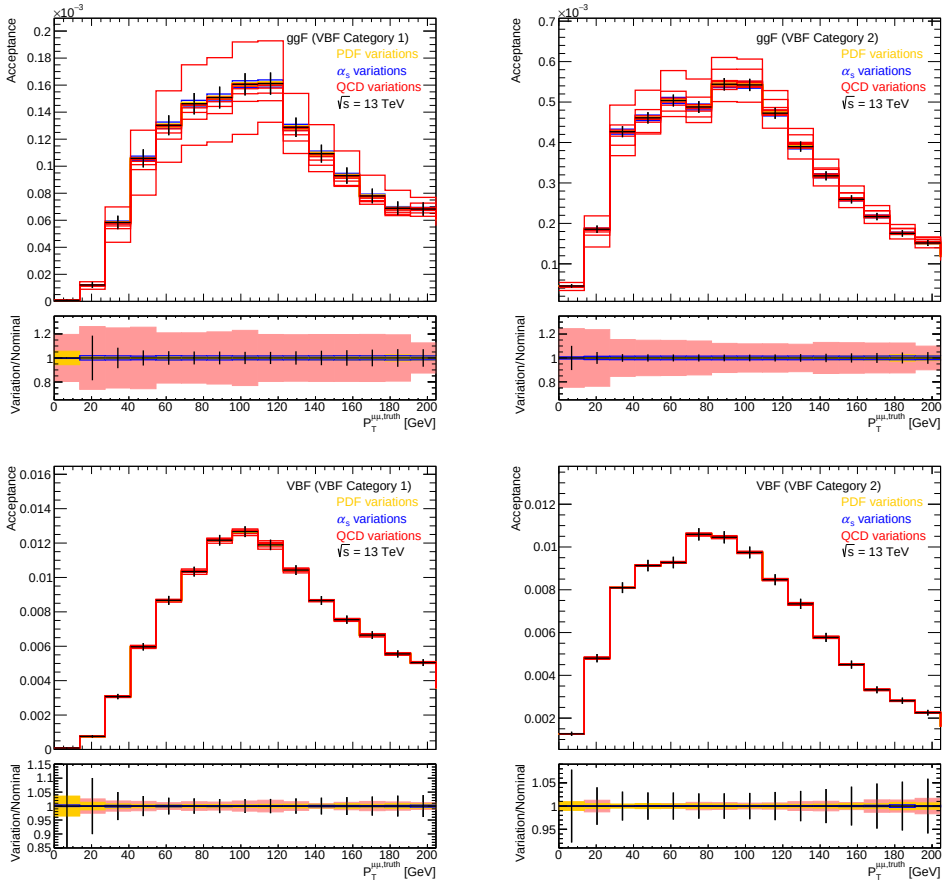

Figure H.0.14: Variation of QCD scale, PDF set and α_s as a function of $P_T^{\mu\mu,\mathrm{truth}}$ for ggF (top) and VBF (bottom) samples in the VBF categories. The full analysis selection has been applied to each sample at truth level.

Systematic	ggF Acceptance Uncertainty [%]	VBF Acceptance Uncertainty [%]
MPI Up	0.14	-1.29
MPI Down	-0.50	-2.44
Var 1 Up	-0.12	-2.33
Var 1 Down	-0.04	-2.06
Var 2 Up	-0.08	-2.28
Var 2 Down	0.06	-2.12
Ren Up	-2.16	-3.94
Ren Down	1.87	0.37
PDF	1.01	0.50
QCD Scale	6.14	16.60
α_s Up	-0.08	0.36
α_s Down	-0.05	-0.32
Total Systematic Uncertainty	6.87	17.85

Table H.0.1: Uncertainty on the acceptance of ggF and VBF events in the ggF Zero-Jet 1 Category for different theoretical parameters. The total systematic uncertainty is equal to the quadrature sum of the preceding contributions.

Systematic	ggF Acceptance Uncertainty [%]	VBF Acceptance Uncertainty [%]
MPI Up	-0.22	0.42
MPI Down	-0.53	-0.11
Var 1 Up	-0.50	0.97
Var 1 Down	-0.38	0.49
Var 2 Up	0.05	0.28
Var 2 Down	-0.46	0.44
Ren Up	-0.81	-1.72
Ren Down	1.27	2.10
PDF	1.44	0.44
QCD Scale	6.14	16.60
α_s Up	-1.35	0.38
α_s Down	1.21	-0.35
Total Systematic Uncertainty	6.80	16.88

Table H.0.2: Uncertainty on the acceptance of ggF and VBF events in the ggF Zero-Jet 2 Category for different theoretical parameters. The total systematic uncertainty is equal to the quadrature sum of the preceding contributions.

Systematic	ggF Acceptance Uncertainty [%]	VBF Acceptance Uncertainty [%]
MPI Up	0.02	-2.99
MPI Down	0.01	-5.90
Var 1 Up	0.01	-2.75
Var 1 Down	-0.12	-3.39
Var 2 Up	-0.74	-3.17
Var 2 Down	-0.03	-4.70
Ren Up	-1.38	-7.50
Ren Down	0.49	-1.35
PDF	1.54	0.55
QCD Scale	6.14	16.60
α_s Up	-2.29	0.43
α_s Down	2.19	-0.37
Total Systematic Uncertainty	7.27	20.72

Table H.0.3: Uncertainty on the acceptance of ggF and VBF events in the ggF Zero-Jet 3 Category for different theoretical parameters. The total systematic uncertainty is equal to the quadrature sum of the preceding contributions.

Systematic	ggF Acceptance Uncertainty [%]	VBF Acceptance Uncertainty [%]
MPI Up	2.22	1.87
MPI Down	0.04	0.21
Var 1 Up	0.97	-0.19
Var 1 Down	0.13	-0.06
Var 2 Up	-1.75	-0.12
Var 2 Down	0.17	-1.32
Ren Up	0.00	-1.12
Ren Down	0.27	2.26
PDF	1.43	0.88
QCD Scale	6.14	16.60
α_s Up	-2.50	0.56
α_s Down	2.42	-0.49
Total Systematic Uncertainty	7.80	16.99

Table H.0.4: Uncertainty on the acceptance of ggF and VBF events in the ggF Zero-Jet 4 Category for different theoretical parameters. The total systematic uncertainty is equal to the quadrature sum of the preceding contributions.

Systematic	ggF Acceptance Uncertainty [%]	VBF Acceptance Uncertainty [%]
MPI Up	0.19	12.75
MPI Down	-0.25	7.78
Var 1 Up	-0.55	9.25
Var 1 Down	0.64	5.89
Var 2 Up	-0.74	8.66
Var 2 Down	-1.18	6.76
Ren Up	-0.80	2.82
Ren Down	1.00	9.83
PDF	1.13	0.68
QCD Scale	6.14	16.60
α_s Up	-2.66	0.19
α_s Down	2.62	-0.21
Total Systematic Uncertainty	7.57	29.06

Table H.0.5: Uncertainty on the acceptance of ggF and VBF events in the ggF Zero-Jet 5 Category for different theoretical parameters. The total systematic uncertainty is equal to the quadrature sum of the preceding contributions.

Systematic	ggF Acceptance Uncertainty [%]	VBF Acceptance Uncertainty [%]
MPI Up	0.00	3.92
MPI Down	0.37	2.29
Var 1 Up	-0.25	2.80
Var 1 Down	0.24	3.23
Var 2 Up	0.25	3.30
Var 2 Down	0.28	2.68
Ren Up	-0.07	0.52
Ren Down	-0.39	2.69
PDF	1.11	0.71
QCD Scale	6.14	16.60
α_s Up	-0.15	0.38
α_s Down	0.03	-0.29
Total Systematic Uncertainty	6.29	18.46

Table H.0.6: Uncertainty on the acceptance of ggF and VBF events in the ggF Zero-Jet 6 Category for different theoretical parameters. The total systematic uncertainty is equal to the quadrature sum of the preceding contributions.

Systematic	ggF Acceptance Uncertainty [%]	VBF Acceptance Uncertainty [%]
MPI Up	-0.31	0.79
MPI Down	0.10	0.02
Var 1 Up	-0.53	0.64
Var 1 Down	-0.74	0.50
Var 2 Up	-0.71	0.36
Var 2 Down	0.03	0.64
Ren Up	-1.83	-0.80
Ren Down	1.09	2.19
PDF	1.19	0.34
QCD Scale	12.56	13.88
α_s Up	1.49	0.04
α_s Down	-1.43	-0.03
Total Systematic Uncertainty	13.02	14.14

Table H.0.7: Uncertainty on the acceptance of ggF and VBF events in the ggF Single-Jet 1 Category for different theoretical parameters. The total systematic uncertainty is equal to the quadrature sum of the preceding contributions.

Systematic	ggF Acceptance Uncertainty [%]	VBF Acceptance Uncertainty [%]
MPI Up	0.03	-1.31
MPI Down	-0.46	-1.50
Var 1 Up	0.37	-1.80
Var 1 Down	0.42	-1.48
Var 2 Up	0.35	-1.51
Var 2 Down	-0.94	-1.69
Ren Up	0.35	-3.07
Ren Down	0.45	-0.37
PDF	0.69	0.40
QCD Scale	12.55	13.88
α_s Up	1.22	0.17
α_s Down	-1.24	-0.15
Total Systematic Uncertainty	12.76	14.73

Table H.0.8: Uncertainty on the acceptance of ggF and VBF events in the ggF Single-Jet 2 Category for different theoretical parameters. The total systematic uncertainty is equal to the quadrature sum of the preceding contributions.

Systematic	ggF Acceptance Uncertainty [%]	VBF Acceptance Uncertainty [%]
MPI Up	-0.02	-1.33
MPI Down	0.43	-1.05
Var 1 Up	-0.43	-1.86
Var 1 Down	-0.29	-1.18
Var 2 Up	0.24	-1.94
Var 2 Down	-0.06	-0.69
Ren Up	1.69	-1.67
Ren Down	-2.11	-0.58
PDF	0.68	0.56
QCD Scale	12.55	13.88
α_s Up	1.01	0.21
α_s Down	-1.07	-0.18
Total Systematic Uncertainty	12.96	14.43

Table H.0.9: Uncertainty on the acceptance of ggF and VBF events in the ggF Single-Jet 3 Category for different theoretical parameters. The total systematic uncertainty is equal to the quadrature sum of the preceding contributions.

Systematic	ggF Acceptance Uncertainty [%]	VBF Acceptance Uncertainty [%]
MPI Up	-2.78	3.42
MPI Down	0.22	2.17
Var 1 Up	0.44	1.71
Var 1 Down	-0.05	0.52
Var 2 Up	-0.81	2.08
Var 2 Down	-1.07	1.86
Ren Up	2.15	0.69
Ren Down	-1.87	3.22
PDF	0.55	0.46
QCD Scale	12.55	13.88
α_s Up	0.94	0.21
α_s Down	-0.99	-0.20
Total Systematic Uncertainty	13.33	15.20

Table H.0.10: Uncertainty on the acceptance of ggF and VBF events in the ggF Single-Jet 4 Category for different theoretical parameters. The total systematic uncertainty is equal to the quadrature sum of the preceding contributions.

Systematic	ggF Acceptance Uncertainty [%]	VBF Acceptance Uncertainty [%]
MPI Up	2.37	4.33
MPI Down	-3.31	-3.88
Var 1 Up	2.60	3.82
Var 1 Down	1.37	-4.74
Var 2 Up	3.82	2.45
Var 2 Down	1.93	7.41
Ren Up	4.71	-1.49
Ren Down	-5.09	2.28
PDF	0.38	1.42
QCD Scale	12.56	13.88
α_s Up	1.00	0.01
α_s Down	-1.03	-0.07
Total Systematic Uncertainty	15.86	18.27

Table H.0.11: Uncertainty on the acceptance of ggF and VBF events in the ggF Single-Jet 5 Category for different theoretical parameters. The total systematic uncertainty is equal to the quadrature sum of the preceding contributions.

Systematic	ggF Acceptance Uncertainty [%]	VBF Acceptance Uncertainty [%]
MPI Up	0.25	-1.19
MPI Down	-1.03	-0.88
Var 1 Up	-0.08	-0.93
Var 1 Down	-0.74	-1.41
Var 2 Up	0.33	-0.93
Var 2 Down	-0.21	-1.29
Ren Up	0.94	-0.73
Ren Down	-1.87	-0.62
PDF	0.71	0.34
QCD Scale	12.55	13.88
α_s Up	1.19	0.14
α_s Down	-1.19	-0.10
Total Systematic Uncertainty	12.92	14.19

Table H.0.12: Uncertainty on the acceptance of ggF and VBF events in the ggF Single-Jet 6 Category for different theoretical parameters. The total systematic uncertainty is equal to the quadrature sum of the preceding contributions.

Systematic	ggF Acceptance Uncertainty [%]	VBF Acceptance Uncertainty [%]
MPI Up	-0.61	-2.54
MPI Down	-0.43	-1.71
Var 1 Up	-0.67	-1.61
Var 1 Down	-0.22	-1.28
Var 2 Up	-2.17	-1.98
Var 2 Down	-1.30	-1.38
Ren Up	0.70	-0.50
Ren Down	-2.56	-2.99
PDF	1.72	0.33
QCD Scale	19.95	10.34
α_s Up	1.47	0.01
α_s Down	-1.36	0.02
Total Systematic Uncertainty	20.48	11.65

Table H.0.13: Uncertainty on the acceptance of ggF and VBF events in the ggF Multi-Jet 1 Category for different theoretical parameters. The total systematic uncertainty is equal to the quadrature sum of the preceding contributions.

Systematic	ggF Acceptance Uncertainty [%]	VBF Acceptance Uncertainty [%]
MPI Up	0.91	0.48
MPI Down	1.42	-0.14
Var 1 Up	1.13	-0.21
Var 1 Down	2.17	0.36
Var 2 Up	2.52	-0.09
Var 2 Down	0.86	0.23
Ren Up	5.01	0.64
Ren Down	-2.51	-1.16
PDF	1.04	0.45
QCD Scale	19.44	10.34
α_s Up	1.36	0.07
α_s Down	-1.33	-0.04
Total Systematic Uncertainty	20.73	10.46

Table H.0.14: Uncertainty on the acceptance of ggF and VBF events in the ggF Multi-Jet 2 Category for different theoretical parameters. The total systematic uncertainty is equal to the quadrature sum of the preceding contributions.

Systematic	ggF Acceptance Uncertainty [%]	VBF Acceptance Uncertainty [%]
MPI Up	-1.78	-5.32
MPI Down	-0.12	-2.74
Var 1 Up	-0.74	-3.67
Var 1 Down	1.33	-3.89
Var 2 Up	0.04	-3.99
Var 2 Down	-0.79	-3.78
Ren Up	3.65	-1.94
Ren Down	-3.09	-3.75
PDF	0.80	0.50
QCD Scale	19.98	10.34
α_s Up	1.25	0.05
α_s Down	-1.24	-0.02
Total Systematic Uncertainty	20.78	14.82

Table H.0.15: Uncertainty on the acceptance of ggF and VBF events in the ggF Multi-Jet 3 Category for different theoretical parameters. The total systematic uncertainty is equal to the quadrature sum of the preceding contributions.

Systematic	ggF Acceptance Uncertainty [%]	VBF Acceptance Uncertainty [%]
MPI Up	0.34	-0.20
MPI Down	1.24	1.31
Var 1 Up	-0.38	0.63
Var 1 Down	-0.23	-0.61
Var 2 Up	0.29	0.38
Var 2 Down	-0.76	1.05
Ren Up	3.90	2.24
Ren Down	-5.53	-1.73
PDF	0.71	0.57
QCD Scale	20.48	10.34
α_s Up	1.18	0.03
α_s Down	-1.19	-0.01
Total Systematic Uncertainty	21.70	10.91

Table H.0.16: Uncertainty on the acceptance of ggF and VBF events in the ggF Multi-Jet 4 Category for different theoretical parameters. The total systematic uncertainty is equal to the quadrature sum of the preceding contributions.

Systematic	ggF Acceptance Uncertainty [%]	VBF Acceptance Uncertainty [%]
MPI Up	-12.04	25.07
MPI Down	4.89	22.76
Var 1 Up	-1.00	10.63
Var 1 Down	-6.52	21.61
Var 2 Up	-6.15	19.59
Var 2 Down	3.42	25.36
Ren Up	-6.52	29.70
Ren Down	-11.30	12.65
PDF	0.69	1.09
QCD Scale	20.79	10.34
α_s Up	1.16	0.22
α_s Down	-1.17	-0.12
Total Systematic Uncertainty	29.45	62.48

Table H.0.17: Uncertainty on the acceptance of ggF and VBF events in the ggF Multi-Jet 5 Category for different theoretical parameters. The total systematic uncertainty is equal to the quadrature sum of the preceding contributions.

Systematic	ggF Acceptance Uncertainty [%]	VBF Acceptance Uncertainty [%]
MPI Up	-1.83	1.46
MPI Down	0.58	2.22
Var 1 Up	-2.36	2.02
Var 1 Down	-1.67	0.73
Var 2 Up	-0.64	2.74
Var 2 Down	-0.10	0.90
Ren Up	2.43	2.90
Ren Down	-3.18	0.63
PDF	0.97	0.58
QCD Scale	19.25	10.32
α_s Up	1.31	-0.16
α_s Down	-1.27	0.13
Total Systematic Uncertainty	20.08	11.65

Table H.0.18: Uncertainty on the acceptance of ggF and VBF events in the ggF Multi-Jet 6 Category for different theoretical parameters. The total systematic uncertainty is equal to the quadrature sum of the preceding contributions.

Systematic	ggF Acceptance Uncertainty [%]	VBF Acceptance Uncertainty [%]
MPI Up	-0.19	0.60
MPI Down	0.22	0.94
Var 1 Up	-0.70	0.81
Var 1 Down	-0.15	0.89
Var 2 Up	-3.34	0.65
Var 2 Down	-0.98	0.73
Ren Up	5.91	1.44
Ren Down	-5.37	0.18
PDF	1.79	0.63
QCD Scale	23.58	10.33
α_s Up	1.72	-0.20
α_s Down	-1.59	0.18
Total Systematic Uncertainty	25.32	10.63

Table H.0.19: Uncertainty on the acceptance of ggF and VBF events in the VBF 1 Category for different theoretical parameters. The total systematic uncertainty is equal to the quadrature sum of the preceding contributions.

Systematic	ggF Acceptance Uncertainty [%]	VBF Acceptance Uncertainty [%]
MPI Up	-2.69	-0.87
MPI Down	-3.12	-0.32
Var 1 Up	0.74	-0.80
Var 1 Down	-1.19	-0.38
Var 2 Up	-0.10	-0.68
Var 2 Down	-1.40	-0.83
Ren Up	4.22	-0.07
Ren Down	-3.83	-1.06
PDF	1.32	0.33
QCD Scale	15.65	10.34
α_s Up	1.54	-0.03
α_s Down	-1.45	0.04
Total Systematic Uncertainty	17.45	10.53

Table H.0.20: Uncertainty on the acceptance of ggF and VBF events in the VBF 2 Category for different theoretical parameters. The total systematic uncertainty is equal to the quadrature sum of the preceding contributions.

Appendix I

Muon Momentum Smearing Distributions

This chapter presents the $P_T^{\text{reco}}/P_T^{\text{truth}} - 1$ distributions taken from the official mc15c Powheg Drell-Yan MC sample, from which the momentum smearing corrections applied to the privately generated spurious signal systematic sample were derived. Figures I.0.1 to I.0.4 present the remaining 302 distributions not shown in Chapter 11. Across all η^{truth} bins, the muon momentum resolution appears to degrade with increasing P_T^{truth}, an effect tied to the reduced curvature of higher P_T tracks.

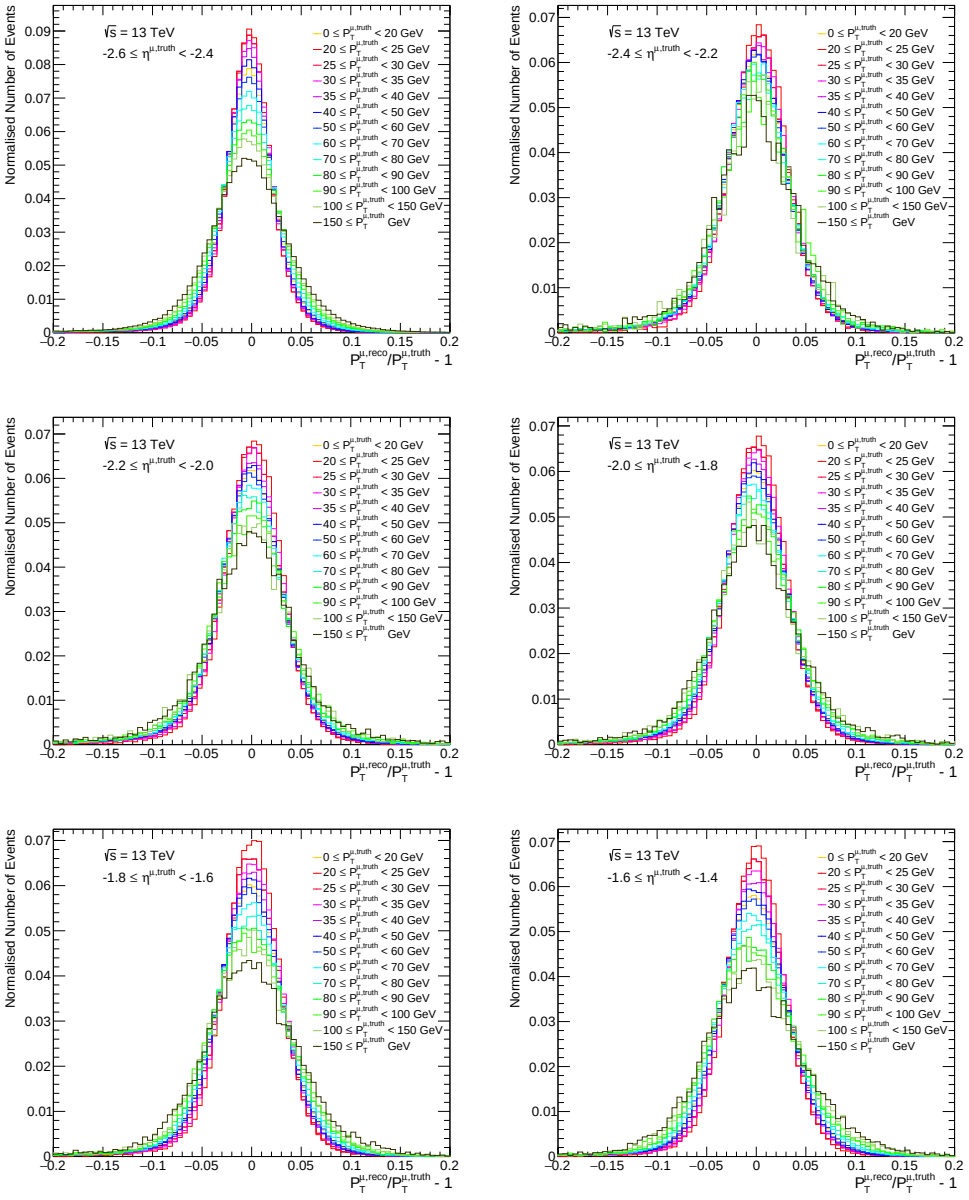

Figure I.0.1: The difference in P_T between truth- and reco-level muons in bins of $P_T^{\mu,\text{truth}}$ and $\eta^{\mu,\text{truth}}$. The distributions are normalised to $P_T^{\mu,\text{truth}}$. $P_T^{\mu,\text{truth}}$ bins are represented by differently coloured histograms, with each plot corresponding to a different $\eta^{\mu,\text{truth}}$ bin. Shown here are the $-2.6 \leq \eta^{\mu,\text{truth}} < -2.4$ (top left), $-2.4 \leq \eta^{\mu,\text{truth}} < -2.2$ (top right), $-2.2 \leq \eta^{\mu,\text{truth}} < -2.0$ (middle left), $-2.0 \leq \eta^{\mu,\text{truth}} < -1.8$ (middle right), $-1.8 \leq \eta^{\mu,\text{truth}} < -1.6$ (bottom left), and $-1.6 \leq \eta^{\mu,\text{truth}} < -1.4$ (bottom right) $\eta^{\mu,\text{truth}}$ ranges. The PDFs associated with the distributions are used to perform a binned smearing of truth-level muons in the spurious signal systematic sample to reco-level.

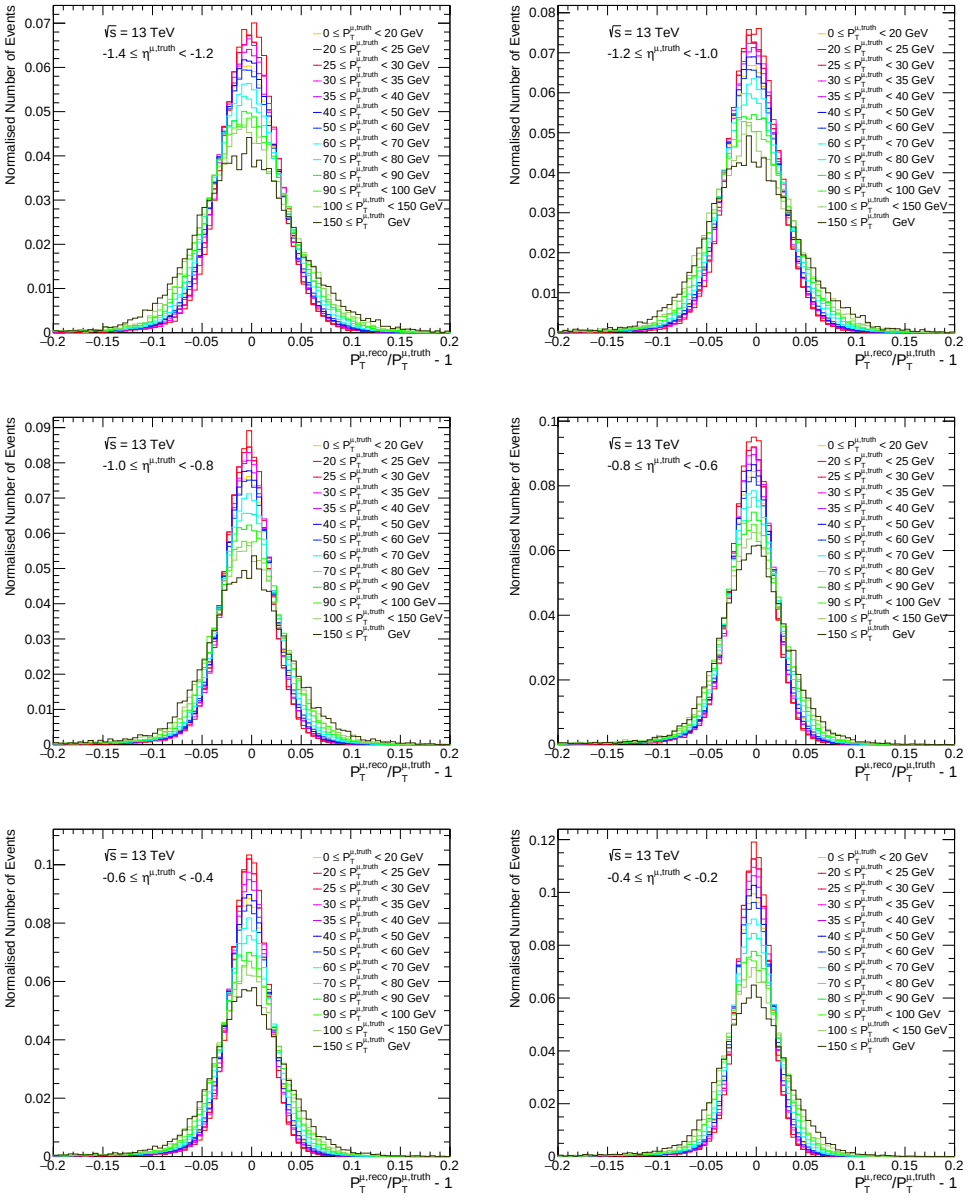

Figure I.0.2: The difference in P_T between truth- and reco-level muons in bins of $P_T^{\mu,\text{truth}}$ and $\eta^{\mu,\text{truth}}$. The distributions are normalised to $P_T^{\mu,\text{truth}}$. $P_T^{\mu,\text{truth}}$ bins are represented by differently coloured histograms, with each plot corresponding to a different $\eta^{\mu,\text{truth}}$ bin. Shown here are the $-1.4 \leq \eta^{\mu,\text{truth}} < -1.2$ (top left), $-1.2 \leq \eta^{\mu,\text{truth}} < -1.0$ (top right), $-1.0 \leq \eta^{\mu,\text{truth}} < -0.8$ (middle left), $-0.8 \leq \eta^{\mu,\text{truth}} < -0.6$ (middle right), $-0.6 \leq \eta^{\mu,\text{truth}} < -0.4$ (bottom left), and $-0.4 \leq \eta^{\mu,\text{truth}} < -0.2$ (bottom right) $\eta^{\mu,\text{truth}}$ ranges. The PDFs associated with the distributions are used to perform a binned smearing of truth-level muons in the spurious signal systematic sample to reco-level.

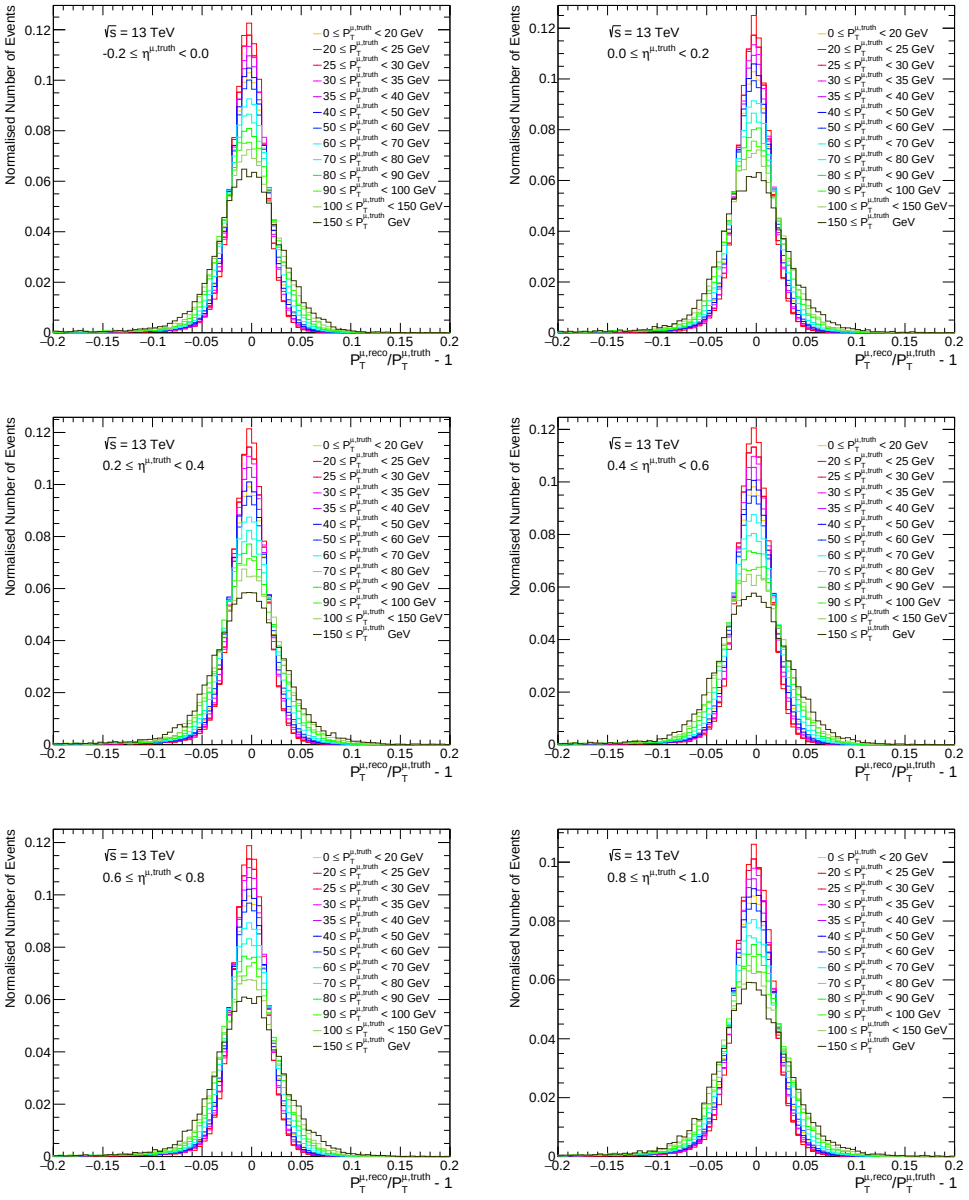

Figure I.0.3: The difference in P_T between truth- and reco-level muons in bins of $P_T^{\mu,\text{truth}}$ and $\eta^{\mu,\text{truth}}$. The distributions are normalised to $P_T^{\mu,\text{truth}}$. $P_T^{\mu,\text{truth}}$ bins are represented by differently coloured histograms, with each plot corresponding to a different $\eta^{\mu,\text{truth}}$ bin. Shown here are the $-0.2 \leq \eta^{\mu,\text{truth}} < 0.0$ (top left), $0.0 \leq \eta^{\mu,\text{truth}} < 0.2$ (top right), $0.2 \leq \eta^{\mu,\text{truth}} < 0.4$ (middle left), $0.4 \leq \eta^{\mu,\text{truth}} < 0.6$ (middle right), $0.6 \leq \eta^{\mu,\text{truth}} < 0.8$ (bottom left), and $0.8 \leq \eta^{\mu,\text{truth}} < 1.0$ (bottom right) $\eta^{\mu,\text{truth}}$ ranges. The PDFs associated with the distributions are used to perform a binned smearing of truth-level muons in the spurious signal systematic sample to reco-level.

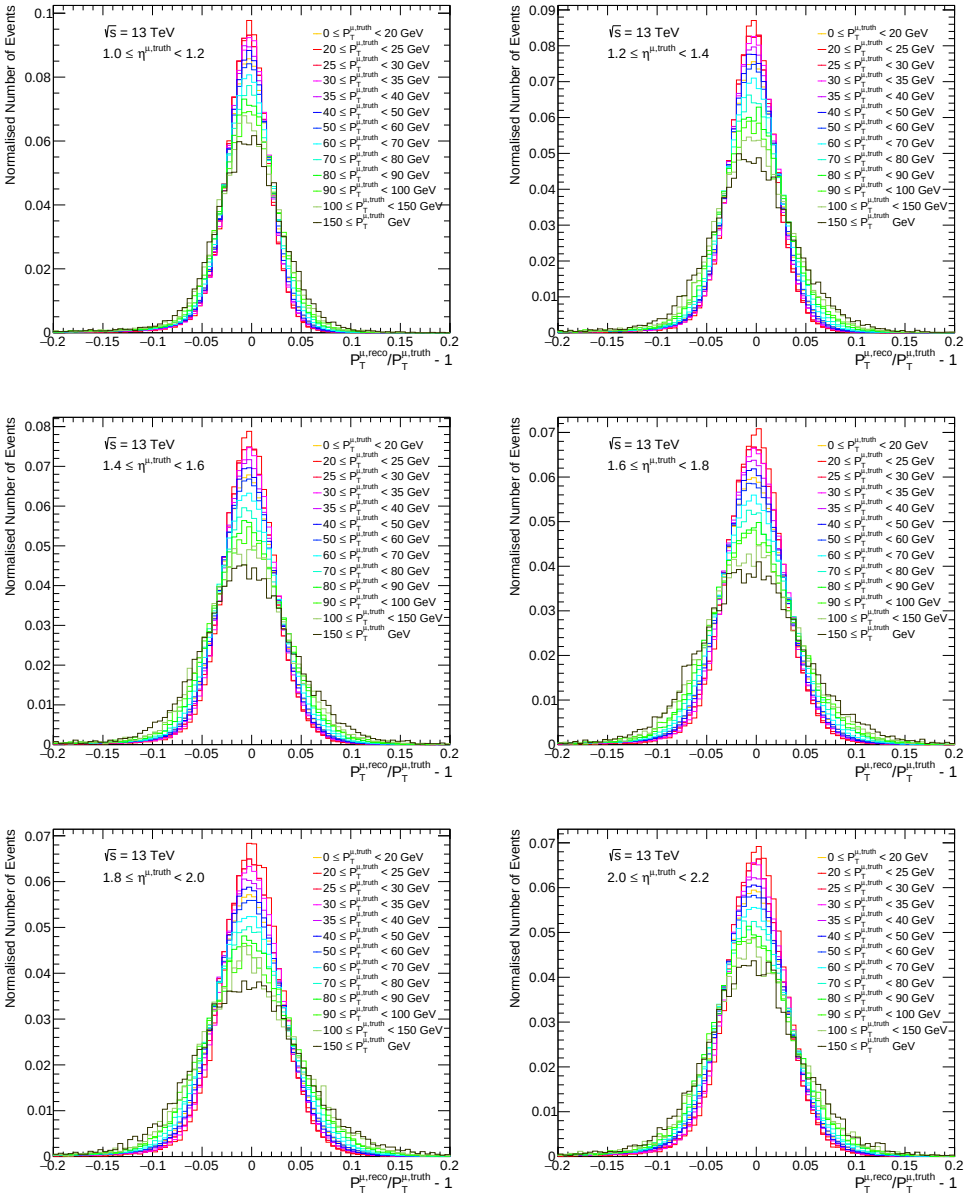

Figure I.0.4: The difference in P_T between truth- and reco-level muons in bins of $P_T^{\mu,\text{truth}}$ and $\eta^{\mu,\text{truth}}$. The distributions are normalised to $P_T^{\mu,\text{truth}}$. $P_T^{\mu,\text{truth}}$ bins are represented by differently coloured histograms, with each plot corresponding to a different $\eta^{\mu,\text{truth}}$ bin. Shown here are the $1.0 \leq \eta^{\mu,\text{truth}} < 1.2$ (top left), $1.2 \leq \eta^{\mu,\text{truth}} < 1.4$ (top right), $1.4 \leq \eta^{\mu,\text{truth}} < 1.6$ (middle left), $1.6 \leq \eta^{\mu,\text{truth}} < 1.8$ (middle right), $1.8 \leq \eta^{\mu,\text{truth}} < 2.0$ (bottom left), and $2.0 \leq \eta^{\mu,\text{truth}} < 2.2$ (bottom right) $\eta^{\mu,\text{truth}}$ ranges. The PDFs associated with the distributions are used to perform a binned smearing of truth-level muons in the spurious signal systematic sample to reco-level.